DATE DUE

8	1984		
4-27-90 ILL	5768672		
1-3-95	Xerox		
1-25-95 ILL	EPA		

NBS SPECIAL PUBLICATION 455

U.S. DEPARTMENT OF COMMERCE / National Bureau of Standards

Electrocatalysis on Non-Metallic Surfaces

NATIONAL BUREAU OF STANDARDS

The National Bureau of Standards[1] was established by an act of Congress March 3, 1901. The Bureau's overall goal is to strengthen and advance the Nation's science and technology and facilitate their effective application for public benefit. To this end, the Bureau conducts research and provides: (1) a basis for the Nation's physical measurement system, (2) scientific and technological services for industry and government, (3) a technical basis for equity in trade, and (4) technical services to promote public safety. The Bureau consists of the Institute for Basic Standards, the Institute for Materials Research, the Institute for Applied Technology, the Institute for Computer Sciences and Technology, and the Office for Information Programs.

THE INSTITUTE FOR BASIC STANDARDS provides the central basis within the United States of a complete and consistent system of physical measurement; coordinates that system with measurement systems of other nations; and furnishes essential services leading to accurate and uniform physical measurements throughout the Nation's scientific community, industry, and commerce. The Institute consists of the Office of Measurement Services, the Office of Radiation Measurement and the following Center and divisions:

> Applied Mathematics — Electricity — Mechanics — Heat — Optical Physics — Center for Radiation Research: Nuclear Sciences; Applied Radiation — Laboratory Astrophysics[2] — Cryogenics[2] — Electromagnetics[2] — Time and Frequency[2].

THE INSTITUTE FOR MATERIALS RESEARCH conducts materials research leading to improved methods of measurement, standards, and data on the properties of well-characterized materials needed by industry, commerce, educational institutions, and Government; provides advisory and research services to other Government agencies; and develops, produces, and distributes standard reference materials. The Institute consists of the Office of Standard Reference Materials, the Office of Air and Water Measurement, and the following divisions:

> Analytical Chemistry — Polymers — Metallurgy — Inorganic Materials — Reactor Radiation — Physical Chemistry.

THE INSTITUTE FOR APPLIED TECHNOLOGY provides technical services to promote the use of available technology and to facilitate technological innovation in industry and Government; cooperates with public and private organizations leading to the development of technological standards (including mandatory safety standards), codes and methods of test; and provides technical advice and services to Government agencies upon request. The Institute consists of the following divisions and Centers:

> Standards Application and Analysis — Electronic Technology — Center for Consumer Product Technology: Product Systems Analysis; Product Engineering — Center for Building Technology: Structures, Materials, and Life Safety; Building Environment; Technical Evaluation and Application — Center for Fire Research: Fire Science; Fire Safety Engineering.

THE INSTITUTE FOR COMPUTER SCIENCES AND TECHNOLOGY conducts research and provides technical services designed to aid Government agencies in improving cost effectiveness in the conduct of their programs through the selection, acquisition, and effective utilization of automatic data processing equipment; and serves as the principal focus within the executive branch for the development of Federal standards for automatic data processing equipment, techniques, and computer languages. The Institute consists of the following divisions:

> Computer Services — Systems and Software — Computer Systems Engineering — Information Technology.

THE OFFICE FOR INFORMATION PROGRAMS promotes optimum dissemination and accessibility of scientific information generated within NBS and other agencies of the Federal Government; promotes the development of the National Standard Reference Data System and a system of information analysis centers dealing with the broader aspects of the National Measurement System; provides appropriate services to ensure that the NBS staff has optimum accessibility to the scientific information of the world. The Office consists of the following organizational units:

> Office of Standard Reference Data — Office of Information Activities — Office of Technical Publications — Library — Office of International Relations — Office of International Standards.

---

[1] Headquarters and Laboratories at Gaithersburg, Maryland, unless otherwise noted; mailing address Washington, D.C. 20234.

[2] Located at Boulder, Colorado 80302.

Electrocatalysis on Non-Metallic Surfaces

Proceedings of a workshop held at the
National Bureau of Standards
Gaithersburg, Maryland, December 9-12, 1975

Edited by

Alan D. Franklin

Institute for Materials Research
National Bureau of Standards
Washington, D.C. 20234

Sponsored by

National Bureau of Standards

National Science Foundation

Energy Research and Development
Administration

U.S. DEPARTMENT OF COMMERCE, Elliot L. Richardson, Secretary
Edward O. Vetter, Under Secretary
Dr. Betsy Ancker-Johnson, Assistant Secretary for Science and Technology

NATIONAL BUREAU OF STANDARDS, Ernest Ambler, Acting Director

Issued November 1976

Library of Congress Catalog Card Number: 76-600062

National Bureau of Standards Special Publication 455
Nat. Bur. Stand. (U.S.), Spec. Publ. 455, 372 pages (Nov. 1976)
CODEN: XNBSAV

U.S. GOVERNMENT PRINTING OFFICE
WASHINGTON: 1976

For sale by the Superintendent of Documents, U.S. Government Printing Office
Washington, D.C. 20402 - Price $4.45

Stock No. 003-003-01699-3/Catalog No. C 13.10:455

GENERAL ABSTRACT

This book presents the proceedings of a Workshop on Electrocatalysis on Non-metallic Surfaces held at the National Bureau of Standards, Gaithersburg, Maryland, on December 9-12, 1975. The Workshop was sponsored by the Institute for Materials Research, NBS, the Division of Materials Research of the National Science Foundation, and the Division of Conservation Research and Technology of the Energy Research and Development Administration. The purpose of the Workshop was to review the most recent experimental and theoretical investigations on electrocatalysis on non-metals and related topics, and to bring together electrochemists, surface scientists, and solid state physicists and chemists involved in research related to this topic. A total of thirty-one invited and contributed papers are here presented, together with a summary report of the final panel discussion. These proceedings are arranged to reflect, with some small exceptions, the program of the Workshop. The main groupings of papers are: Theory of Electrocatalysis and Related Topics; Characterization; Electrochemical Processes on Non-metallic Surfaces (1,2, and 3); Electrochemistry at Solid Electrolyte Interfaces. In addition, a final panel discussion considered major problems, advances, and opportunities revealed by the Workshop.

Key Words: Catalysis; characterization; chemisorption; electrocatalysis; electrochemistry; electrode processes; non-metals; photoelectrolysis; solid electrolytes; surfaces

Disclaimer:

In order to describe experiments adequately, it has been necessary to identify commercial materials and equipment in this book. In no case does such identification imply recommendation or endorsement by the National Bureau of Standards, nor does it imply that the material or equipment is necessarily the best available for the purpose.

FOREWORD

The dissemination of research results is almost as important as the scientific work that produced the results in the first place. As part of its role in making available to the scientific and engineering community fundamental data on the properties of materials, the Institute for Materials Research of the National Bureau of Standards from time to time holds symposia and workshops on various aspects of materials research. Such meetings provide opportunities for exchanges of ideas and results, and the proceedings, when published, often become benchmarks in the development of the field. Other institutions, inside or outside of the Federal Government, often join in various aspects of these meetings.

This Workshop, sponsored not only by the National Bureau of Standards, but also by the National Science Foundation and the Energy Research and Development Administration, was concerned with the topic of Electrocatalysis on Non-metallic Surfaces. It brought together electrochemists, surface scientists, and solid state physicists and chemists with a common interest in electron transfer reactions at interfaces. Indeed, it was a major purpose of the Workshop to provide a meeting ground for these somewhat disparate groups. The field of electrocatalysis entails study of the electronic structure and transport in the solid, the nature and chemistry of the interface on both sides, including adsorbed layers, the disposition of the electrolyte and its components at and near the interface, and the nature of electron transfer reactions through the interface. It is a truly interdisciplinary field, hence the emphasis on representation among the participants from the several relevant disciplines.

The National Bureau of Standards takes pleasure in presenting these proceedings of the Workshop on Electrocatalysis on Non-metallic Surfaces. This, too, is an opportune place to express our thanks to those who contributed to the Workshop and these proceedings, including the participants from the United States and those who came from abroad, and our sister institutions, the National Science Foundation and the Energy Research and Development Administration, whose support was essential to this successful outcome.

John D. Hoffman
Director
Institute for Materials Research
National Bureau of Standards

PREFACE

Electrochemistry as a science dates back almost two hundred years, to the work of Galvani, Volta, Faraday, and others. In the course of development of this science a great deal has been learned about electrocatalysis and the nature of electrochemical reactions on electrodes. Most attention, however, has been given to the development of highly reproducible metallic electrodes, such as the dropping mercury electrode or platinum. What work has been done on semiconductors has been concentrated on again the well-known, reproducible materials--silicon, germanium, zinc oxide, etc.

Recently, new impetus for the study of electrode processes and electrode materials has come in the wake of renewed interest in fuel cells for electricity generation. While traditional electrode materials such as platinum and its alloys work well (but not perfectly) in fuel cells, they are so costly as to be discouraging to commercial development. One remedy is to find new, less costly, materials that perform as well, or better, as fuel cell electrocatalysts. Non-metallic solids offer a promising class of materials.

Current development of fuel cells is concentrated on only a few types. The alkaline cell, while efficient and reliable as a result of extensive development for the use in the space program, is presently excluded in the competition for utility application by its sensitivity to CO_2. Closest to commercial realization is the hot (150-200 °C) phosphoric acid cell, with the molten carbonate cell some years away and the solid electrolyte cell still further behind.

At the air electrode in both acid and alkaline media, present catalysts (including Pt) reduce the oxygen at least partially to peroxide rather than to water. The working voltage for the peroxide reaction is lower than that possible with the water reaction, and therefore, the achievable efficiency of conversion of chemical to electrical energy is also lowered. The development of catalysts for oxygen reduction, particularly in the acid cell, that avoid the peroxide reaction or minimize it could result in significant increases in efficiency which may be necessary in the second-generation cells and beyond. It is interesting to note that some highly-conducting metal oxides (*e.g.*, IrO_2, RuO_2) appear to catalyze oxygen reduction directly to water. Unfortunately, they are very unstable in acids, but may ultimately be useful with neutral (buffered) electrolytes.

In a very practical sense, the *application* of fuel cells in the extensive way needed in the not-too-distant future may well depend upon progress in the *science* of electrocatalysis as applied to non-noble metal surfaces, with particular but not exclusive reference to the oxygen electro-reduction processes. This is a field at the boundary between two disciplines, electrochemistry on the one hand, and solid state physics and chemistry on the other.

Semiconductors have long been used as heterogeneous catalysts, especially for oxidation and reduction reactions. Early uses of such materials as electrocatalysts included the oxides of Cu and Ag. Silver has found extensive use at the oxygen electrode in alkaline fuel cells; probably as an oxide. Lithiated NiO at temperatures above about 100 °C has also operated successfully as an oxygen electrode in alkaline media. More recently, work has been done using spinels such as $CoAl_2O_4$ and perovskites such as Sr-doped $LaCoO_3$. The latter use is obviously related to the use of the perovskites ABO_3, where A represents rare earth, Pb, or alkaline earth ions, and B is Co or Mn, for oxidation of Co and reduction of NO_x in automotive exhaust catalysts. Some of the early, exciting non-metallic electrocatalysts, for both hydrogen oxidation and oxygen reduction were the tungsten bronzes and related compounds. However, more recent work has shown that the observed high catalytic activity probably depends upon the presence of Pt, which in some way activates the oxide in a synergistic fashion. A fairly detailed body of theory has been worked out for electrochemical processes on semiconductors and insulators.

With this a background, the time appeared ripe for a Workshop on Electrocatalysis on Non-metallic Surfaces to review the most recent experimental and theoretical investigations, to consider what are the problems most important for scientific progress in this field, and to strive for some common understanding on how to approach those problems. A fundamental purpose of the Workshop was to bring together electrochemists, surface scientists, and solid state physicists and chemists to stimulate as much interdisciplinary interaction as possible.

The organization and running of the Workshop and the publication of these Proceedings required the cooperation and enthusiastic support of a number of people. The Steering Committee, composed of A. J. Bard, L. H. Bennett, U. Bertocci, M. W. Breiter, R. J. Brodd, S. Bruckenstein, E. Cohn, R. deLevie, A. Fickett, H. P. R. Frederikse, H. Gerischer, J. B. Goodenough, and W. S. Horton, provided invaluable guidance in the planning of the Workshop. The Institute staff, particularly R. B. Johnson, R. F. Martin, and their assistants, and Mrs. Sara R. Torrence and her staff from the NBS Office of Information Services, performed yeoman service in the actual detailed running of the Workshop. Mrs. Rosemary Maddock, as Format Editor, deserves much of the credit for gathering the Proceedings into a coherent whole, and the IMR Text-Editing Facility for correcting and preparing some of the manuscripts.

Alan D. Franklin
Technical Editor

CONTENTS

THEORY OF ELECTROCATALYSIS AND RELATED TOPICS

CHARACTERIZATION

THEORY OF ELECTROCATALYSIS AND RELATED TOPICS

National Bureau of Standards Special Publication 455, *Electrocatalysis on Non-Metallic Surfaces*,
Proceedings of Workshop held at NBS, Gaithersburg, Md., December 9-12, 1975. (Issued November 1976)

Electron Transfer and Electrocatalysis

H. Gerischer
Fritz-Haber-Institut der Max-Planck-Gesellschaft
1 Berlin-Dahlem, West-Germany

Non-catalysed electron transfer is reasonably defined as an electron exchange between an electron donor or acceptor and an electrode under the condition of very weak interaction between the reactants and the electrode. The case of strong interaction between reactants and electrodes is analysed with respect to its catalytic effect on electron transfer. It is pointed out that strong interaction may often inhibit electron transfer for a single electron transfer step at its individual equilibrium potential. Electrocatalysis is however found in multistep electron transfer reactions when the adsorption of intermediates in the reaction path brings the individual standard potentials of the single electron transfer steps closer to that of the overall redox potential. Examples for this effect of adsorptive interaction are given for metal and non-metallic electrodes. It is further analysed where the electron energy levels of the adsorbed reactants are located with respect to the characteristic energy levels in the metallic or non-metallic electrodes and in the non-adsorbed species in solution. The important role of surface states at a non-metallic electrode for chemisorption and electrocatalysis is emphasized.

Key words: Chemisorption; electrocatalysis; electron transfer theory; multistep redox reactions; semiconductor surface states.

1. Introduction

This lecture is supposed to act as a bridge between the "Workshop on the Electron Factor in Catalysis on Metals" and the "Workshop of Electrocatalysis on Non-metallic Surfaces" by discussing the problem of electron transfer. However, there is a fundamental difference between electron transfer in chemical catalysis and in electrocatalysis. In chemical catalysis, electron transfer can occur only during a transitory state and is finally compensated by the reverse electron transfer, since the reactants and the products are electroneutral. But, in electrocatalysis the final products are obtained by single or multiple electron transfer and differ in net electric charge. One can control direction and rate of the catalysed reaction, at least to some extent, by an external variation of the driving force with help of the so-called electrode potential.

There is only one particular situation where electrocatalysis is equivalent with chemical catalysis, namely when anodic and cathodic electron transfer processes just compensate each other so that the external current is zero and the driving force of the reaction is solely the free energy difference between reactants and products as in chemical catalysis. One can consider this special case as an electrochemical mechanism of normal chemical catalysis. For instance, H_2O_2-decomposition in electrolytes in contact with metals can be described [1,2][1] in this way.

This relation between chemical and electrochemical heterogeneous catalysis is demonstrated in Fig. 1 for one special type of reaction. The common feature of both types of catalys-

---

[1] Figures in brackets indicate the literature reference at the end of this paper.

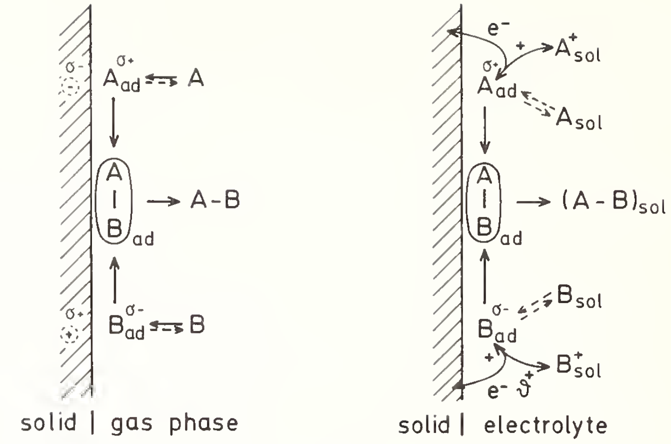

heterogeneous catalysis

$A + B \rightarrow A - B$

electrocatalysis

$A^+ + B^+ + 2e^- \rightarrow AB$

$A^+ + B + e^- \rightarrow AB$

$A + B^+ + e^- \rightarrow AB$

Fig. 1. Comparison: heterogeneous- and electrocatalysis.

sis is the strong interaction between the reactants and the catalysts in the intermediate stage of the reaction where the interaction species are in an adsorbed state. The way in which the reactants reach and the products leave this state is, however, different. The electric forces play a minor role in chemical catalysis but a dominating one in electrocatalysis. All analogies can therefore be only very limited.

2. Non-Catalysed Electron Transfer at Electrodes

We cannot understand electrocatalysis without knowing what we mean with an uncatalysed electron transfer reaction. Let us consider as a reasonable definition of an uncatalysed electron transfer a redox reaction where the interaction between the redox species and the electrode during electron transfer is so weak that its influence on the energy of those electronic quantum states, which are involved in the electron transfer, can be neglected. A statistical theory for adiabatic electron transfer under such weak interaction conditions has been developed by R.A. Marcus [3,4]. A quantum mechanical treatment of similar character with perturbation theory for describing the electron transfer has been worked out by Levich and his co-workers [5-7]. Both theories give the identical result that the activation energy for electron transfer in the case of weak interaction with the electrode is primarily controlled by the reorganisation energy which is needed to reach a structure of the solvent around the electron exchanging species which is identical before and after electron transfer.

This type of reaction can be interpreted [8], based on the early work of Gurney [9] as an electron transfer between real or virtual electronic quantum states of equal energy which are filled at one side of the interface and vacant at the other side [2]. Such a process is represented by the following equation

$$(\text{acceptor})^+_E + (\text{occupied state})^-_E \rightleftharpoons (\text{donor})_E + (\text{vacant state})_E \qquad (1)$$

---

[2] This model neglects electron transfer with energy dissipation by excitation of vibrations in neighbouring molecules or by phononemission, processes which are important in reactions with release of large energies.

The reaction rate is controlled by the probability to find quantum states of equal energy E during an encounter between the electron acceptor or donor components of a redox couple and the electrode. Such electron transfer can occur in parallel at different energy levels. The net electron exchange rate must therefore be obtained from an integration over all electron transfer steps at various energies. The general formula for such an electron transfer rate is given in the following 2 equations:

$$j^{+} \sim c_{don} \int_{-\infty}^{\infty} K(E)\, D_{vacant}(E) \cdot W_{don}(E)\, dE \tag{2a}$$

$$j^{-} \sim c_{acc} \int_{-\infty}^{\infty} K(E)\, D_{occup.}(E) \cdot W_{acc}(E)\, dE \tag{2b}$$

where D(E) represents the density of states in the electrode and $c_{don} \cdot W_{don}(E)$ the energy distribution of donor states in solution which is proportional to the donor concentration c_{don}. The energy distribution of acceptor states is represented by $c_{acc} \cdot W_{acc}(E)$ and is proportional to the acceptor concentration c_{acc}.

For a calculation of the electron transfer rates one needs information on the distribution of filled and vacant electron states in the solid and in the electrolyte. The formulation for the solid can be taken from band theory and Fermi distribution statistics. For the electrolyte it has been derived that the distribution of electron energy states is of the Gaussian type if one takes into account only the square terms [10]. The maxima of the distribution functions represent characteristic energy levels for the acceptor and the donor of every individual redox system [11].

The position of these characteristic energy levels can be derived from a thermodynamic cycle. Fig. 2 shows in a very simplified way the influence of the interaction between the donor or the acceptor states and their surroundings in an electrolyte (the solvation shell primarily) on the position of the energy level for electron exchange. Assuming that electron transfer occurs under Franck-Condon conditions, the energy level for electron exchange is then given by the distance between the two energy curves of the acceptor and the donor state at constant reorganisation coordinates. The redox reaction is formulated in part (a) of the picture as an electron transfer between the redox species and the electron at the vacuum level. In part (b) the electron transfer occurs at equilibrium conditions between the redox species and the electron in an electrode. This means the electron is at the Fermi level of the redox system E^{o}_{redox} which is equivalent to the Fermi level of electrons in an electrode in equilibrium with this particular redox system. The correlation between the electron energy scale related to the vacuum level and the electrochemical potential scale is [12]:

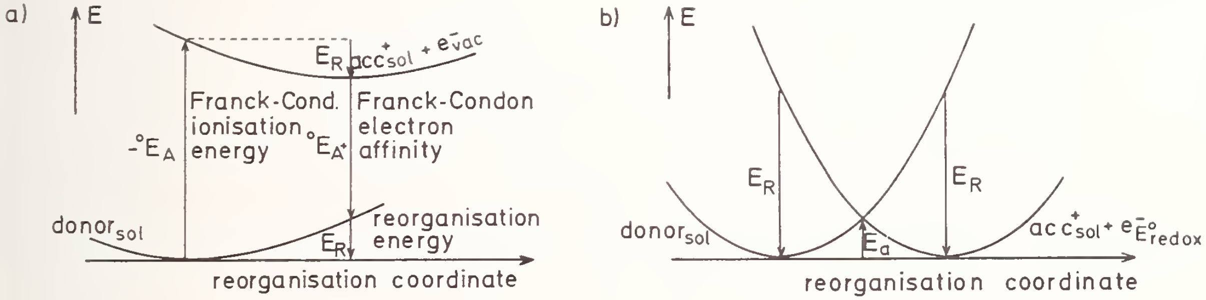

Fig. 2. (a) Energy profile for electron transfer under Franck-Condon conditions between redox species and electrons at vacuum level;

(b) the same for electron transfer between redox species and electrons at the Fermi level of an electrode being at equilibrium with the redox couple.

$$E_F = \text{Const.} - U_o \tag{3}$$

with Const. $\approx$ - 4.5 eV.

The interaction with the surroundings can bring both species to the same electron energy as shown in part (b) of Fig. 2 in the point of intersection. This solvation structure characterizes the intermediate state which has to be reached for adiabatic electron transition. The energy necessary to reach this state is the activation energy for electron transfer under Franck-Condon conditions. The result is that the minimum activation energy between the redox species and their surroundings is, in the parabolic approximation of the energy surfaces, one fourth of the reorganisation energy E_R which is the energy released after electron transfer under Franck-Condon conditions from the initial states with minimum free energy (compare Fig. 2b). The distribution function of the electron exchange levels of redox species in electrolytes has in this simplest case the form [10],

$$W(E) = (4\pi\ E_R kT)^{-1/2} \exp\left(-\frac{(E-{}^{o}E)^2}{4E_R kT}\right) \qquad (4)$$

The translation of this model into the formulation given in equ. (2) for electron transfer between quantum states at both sides of the interface is shown in Fig. 3. In the equilibrium situation, the electron transfer occurs preferentially in the close neighbourhood of the Fermi level with equal rate in both directions. If one applies another electrode potential the result is a net current in the one or the other direction. This is described in this model by a shift of all energy levels in the metal electrode relative to the Fermi level in the redox system. It has the consequence that now the electron transfer rates from the electrode to the redox system or reverse do no longer compensate each other. If the shift of the Fermi level goes far enough, the electron transfer occurs only in one direction as shown in Fig. 4. All these theories lead to the long known Volmer-Butler equation for the rate of redox reactions in dependence on the applied overvoltage, $\eta = U - U_o$ [8].

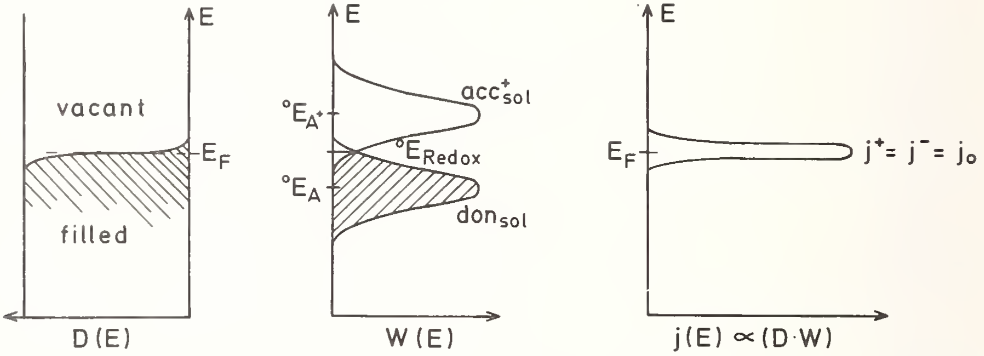

Fig. 3. Energy distribution of electronic states at equilibrium between a metal electrode and a redox couple; energy spectrum of electron exchange rates.

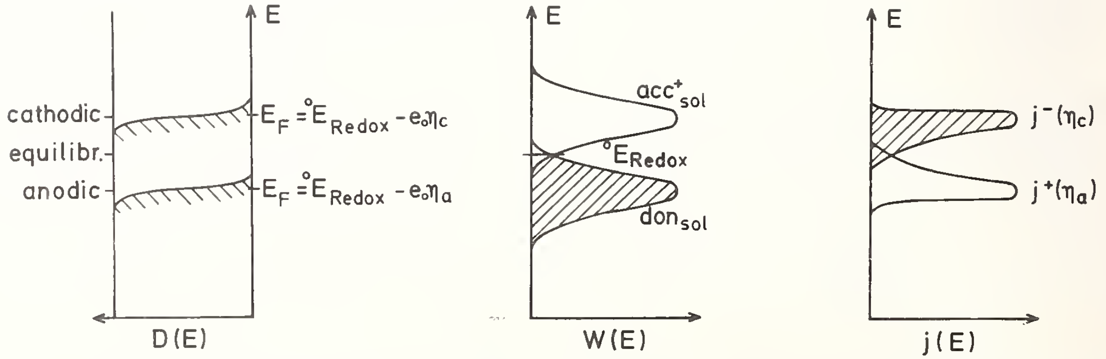

Fig. 4. The same as in Fig. 3 for anodic (η_a) and cathodic (η_c) polarisation of the electrode against the Fermi level of the redox couple.

The characteristic kinetic parameter of an electron transfer reaction is the exchange current density at the standard potential of the redox system. This is mainly controlled by the reorganisation energy. A general experience is that one electron transfer steps are normally fast, E_R being in the order of 0.8 - 1.6 eV if no kinetic complication arises. This means one electron transfer reactions cannot be accelerated very much by catalysis. We shall see later that in correspondence with this the main field of electrocatalysis is multiple electron transfer reactions.

3. Electron Transfer with Strong Interaction between Electrode and Redox Components

In the uncatalysed electron transfer reaction the electrode plays only the role of a source or sink for electrons. What happens with regard to the electron transfer rates when now the reactants interact strongly with the electrode? We shall be inclined to consider this situation as a case of catalysis and expect that the rate of electron transfer will increase. But we shall see that strong adsorption of the redox species can in the range of the equilibrium potential also have an inhibiting effect on electron transfer.

For so close an approach to the electrode that strong interaction becomes possible, the redox species have to enter the region of the Helmholtz double layer. The interaction with the surroundings compared with the situation in solution is then drastically modified in two ways:

(a) A great part of the interaction which was prior directed to the solution is now replaced by the interaction with the electrode. This applies as well to the outer solvation shell as in many cases to the interaction with the inner solvation shell. Some ligands may be lost in compensation for strong adsorption.

(b) By entering the inner region of the Helmholtz layer the electrostatic forces become important for all redox species having an excess electric charge or a dipole moment. This makes the situation very complicated and difficult for a quantitative treatment of electron transfer kinetics. Therefore, we shall discuss the consequences only qualitatively.

One consequence is that the polarisation interaction is no longer the most important coordinate for electron transfer. The distance from and even the particular site on the surface become the more important the stronger the interaction energy. A multidimensional representation of energy surfaces becomes unavoidable. We shall discuss in the following three different cases distinguished by the degree of interaction of the acceptor and the donor state of the redox system with the electrode.

Fig. 5 shows the situation where, at equilibrium potential, both redox species are adsorbed at the electrode with about equal adsorption energy. In part (a) the energy of both sides of a redox reaction is plotted against the distance of the redox species from the electrode with the electron energy level at the Fermi-energy of the redox system (the equilibrium condition). From this picture we obtain an energy for desorption and adsorption at equilibrium. For calculating the activation energy of electron transfer we need, however, a multidimensional representation, since we have to take into account also the different interaction energy of the redox species with their surroundings. We must expect that the interaction with the surroundings in the adsorbed state of a redox system is much less different for the two components than in solution. This is indicated in part (b) of Fig. 5 where the influence of the reorganisation coordinates on free energy is plotted for the redox components at 3 different distances from the electrode. The conclusion is that the activation barrier for electron transfer in the adsorbed state is much smaller than in solution. The electron exchange rate in the adsorbed state may often be so high that the different oxidation states become indistiguishable as has been pointed out already by Plieth and Vetter [13]. The result is that in case of equal adsorption of both components the rates of desorption will become the rate controlling steps for the redox reaction, as Fig. 5a indicates.

A variation of the electrode potential changes the energy position of the reactants in

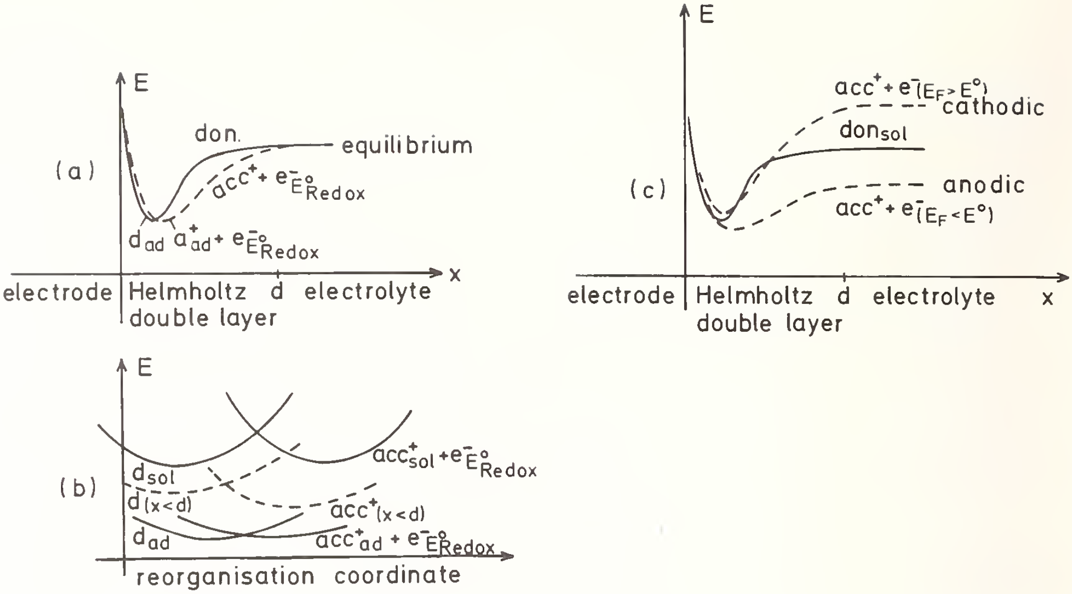

Fig. 5. Energy profiles for adsorption of both redox components at various electrode potentials in dependence on the position in the double layer

(a) at equilibrium potential;

(b) energy profiles in dependence on the reorganisation coordinate for 3 positions in the double layer at equilibrium potential;

(c) for anodic and cathodic polarisation.

solution relatively to each other, and the energies for desorption shift in different direction. This is shown in Fig. 5c for an anodic and a cathodic overvoltage. How much the electrode potential influences the energy of both components in the adsorbed state depends on the double layer structure, the charge of the adsorbed species and their position in the Helmholtz double layer. It dependes also on the strength of the interaction with the substrate. In case of very strong interaction, the electron exchange levels of the adsorbed species can be treated like a surface states of a solid. This case is closest to normal chemical catalysis.

In most real systems with strong adsorption, the one or the other component of the redox system has large preference in adsorption. This will usually be the electroneutral component which is the stronger adsorbed one because electrostatic interaction would in any case prevent too high coverage of the surface with charged species. Strong adsorption of charged molecules involves other complications connected with a change in double layer structure which cannot be discussed here.

The situation for an uncharged donor species being stronger adsorbed is shown in Fig. 6. The surface at equilibrium potential in this case is widely covered with the donor and the exchange rate between the adsorbed state and the state in solution will be slow. Electron exchange in the adsorbed state will not occur because of the too different adsorption energies. If electron transfer is not possible via tunnel transitions between the electrode and the redox components in solution, the electron exchange rate at equilibrium potential will be very slow. It needs a high anodic polarisation to reduce the barrier for oxidative desorption of the reduced species where the electron transfer occurs somewhere on the path of desorption. This is shown in Fig. 6. If polarized in cathodic direction, the surface will be more and more covered with the reduced product, the desorption of which remains the rate determining step. It is assumed in Fig. 6 that the reduced species has no electric charge and that the desorption energy therefore does not depend on electrode potential. We find such a situation, for example, in the first step of the reduction of protons from solution, $H^+_{sol} + e^- \longrightarrow H_{ad}$, where the hydrogen atoms are strongly adsorbed at all electrodes and desorption of H-atoms

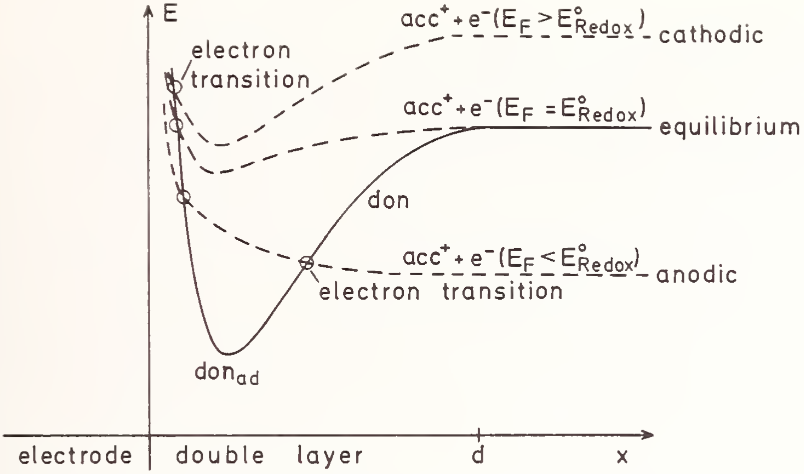

Fig. 6. Energy profiles for preferential adsorption of the reduced component of a redox couple at various electrode potentials.

does not occur. That in this system the reaction proceeds further is only due to consecutive reactions generating the hydrogen molecule. We shall come back to this reaction later.

The opposite case where the acceptor is the uncharged species and much stronger adsorbed, is shown in Fig. 7. At equilibrium the electrode is now covered by the adsorbed acceptor component, the desorption rate of which is very slow. A variation of the electrode potential causes in this case a drastic shift of the energy of the acceptor in the adsorbed state plus electron in the electrode and also of the acceptor in solution plus electron in the electrode, as is shown in part (b) of Fig. 7. Since the donor state has an electric charge its energy varies also in the adsorbed state in correspondence with the local potential in the double layer, but to a smaller extent than for the acceptor state.

By applying a cathodic voltage a reductive desorption of the donor can occur connected with an electron transition occurring at some distance from the electrode. For anodic polarisation, we see in Fig. 7b that the oxidation of the donor will occur very rapidly in the adsorbed state but the desorption of the product is slow and rate determining. A situation like this of Fig. 7 is found in the reaction $OH^- \rightleftarrows OH_{ad} + e^-$, since the OH radicals are

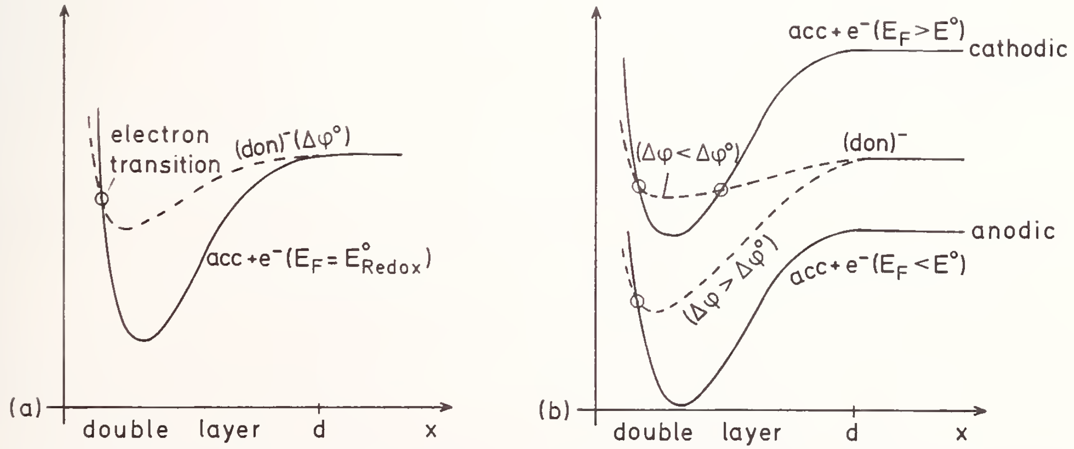

Fig. 7. Energy profiles for preferential adsorption of the oxidized component of a redox couple:

(a) at equilibrium potential

(b) at anodic and cathodic polarisation.

strongly adsorbed on nearly all substrates. A reaction progress in anodic direction is again caused only by consecutive steps.

To complete our picture in terms of electronic energy levels, we have to discuss where the electronic states in the adsorbed species at the electrode are found energetically. We shall begin with a thermodynamic argument and ask what is the standard redox potential for the redox system in the adsorbed state (standard state: both components present at equal concentration). If the interaction with both oxidation states of the redox couple is equal, then the standard redox potential of this system in the adsorbed state will be the same as in solution. This means that the electronic energy levels for electron exchange must remain in the range around the standard Fermi level E^{o}_{Redox} as defined for the system in solution. We have previously seen in Fig. 3 that the most probable energy level for the donor state of the redox system is located at $E^{o}_{Redox}-E_R$ and the most probable acceptor state at $E^{o}_{Redox}+E_R$. We expect a narrowing of the distance between the most probable energy levels for both oxidation states in the adsorbed position because the interaction with the solvent has decreased. The consequences are shown in Fig. 8 as a comparison between the energy distribution of the electron levels in solution and in the adsorbed state. If the electron exchange in the adsorbed state is slow enough that two different oxidation states can be distinguished, we shall still have two maxima for the adsorbed species in their different state of charge (Fig. 8b). If the electron exchange with the electrode is so fast that both states become indistinguishable, we shall find a situation as shown in Fig. 8c.

The broadening of the electronic levels in Fig. 8c for strongly adsorbed species is mainly caused by the interaction between the manifold electronic states of the solid and the electronic states of the adsorbate. This picture is equivalent to the assumptions in the Anderson model for chemisorption of atoms on metals [14,15]. To some extent the broadening into an "energy band" will also be caused by fluctuations in the remaining interaction with the solvent. The occupation of electronic levels in this "energy band" of the adsorbed species is controlled by the position of the Fermi level. Since the location of adsorbed species extends into the region of the Helmholtz double layer, the position of the Fermi level in this band will be shifted to some extent by a variation of the electrode potential, which causes a variation of the average charge on adsorbed redox species with the applied voltage.

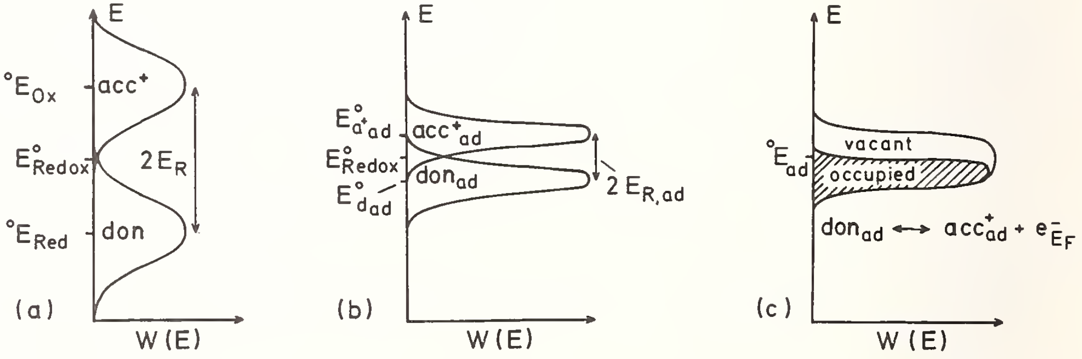

Fig. 8. Distribution of electron exchange energy levels of a redox couple with about equal interaction between both redox species and the electrode

(a) in solution; (b) in adsorbed state with medium interaction energy; (c) in adsorbed state with strong interaction energy.

The electron level distributions for the two cases with very different adsorption energies of the donor or the acceptor species are schematically represented in Fig. 9 for electronic equilibrium. In the case of strong adsorption the electronic energy levels of the adsorbate are practically part of the electron system of the electrode. Whether they are occupied or not in the adsorbed state depends on their relative position against the Fermi level in the electrode. If the reduced (donor) state is stronger adsorbed than the oxidized (acceptor) state, the standard Fermi level for the adsorbed species will be far below the Fermi level

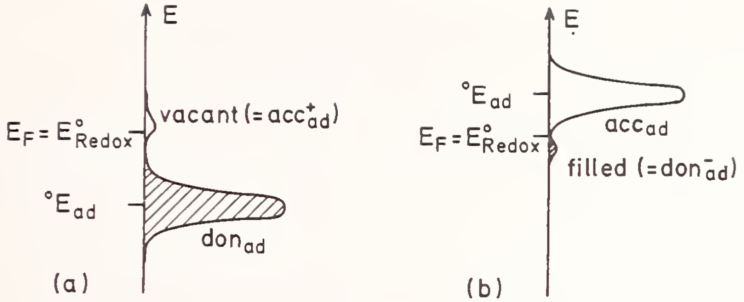

Fig. 9. Distribution of electron exchange energy levels in the adsorbed state of a redox couple with (a) preferential adsorption of the reduced state; (b) preferential adsorption of the oxidized state.

of the redox system in solution and vice versa for a preferential adsorption of the acceptor state at the electrode. It is obvious that in the latter case the electron state of the acceptor species which controls electron transfer (the redox orbital) is not involved in the adsorption interaction. This must be caused by other electron states at deeper energies which intercombine with electron states of the electrode.

Fig. 9 shows such a hypothetical energy term distribution for electrodes in equilibrium contact with two different redox systems. In case (a) the stable adsorbed state is the occupied one, in (b) it is the vacant state. The standard redox potential in the adsorbed state of the redox system may be defined as the energy level where the electron terms of the adsorbed species would be half-filled. This is $^0E_{ad}$ in Fig. 9, which will shift nearly in parallel with the electrode potential relative to the Fermi energy of the redox system in solution as does the Fermi energy of the electrode.

The small maxima above E_F in Fig. 9a and below E_F in Fig. 9b indicates a slight stabilisation of the differently charged states by the fluctuating interaction with the polar solvent to which the adsorbed species are partially exposed. This contribution will, however, be of very little importance at strong adsorption.

4. Catalysis of Electron Transfer in Multi-Step Redox Reactions

We have explained that adsorption in a one-step electron transfer reaction usually does not increase the reaction rate in the neighbourhood of the equilibrium potential but may often cause the contrary. The interesting systems for electrocatalysis are therefore those where the reaction is slow because more than one electron transfer step is needed in the overall reaction and intermediates are formed which may interact strongly with the electrode. A few examples may be given.

reaction:	possible intermediates:
$2H^+ + 2e^- \rightleftarrows H_2$	H
$O_2 + 2H^+ + 4e^- \rightleftarrows 2OH^-$	O_2^-, HO_2^-, OH, O^-, O
$2NH_3 \longrightarrow N_2 + 6H^+ + 6e^-$	NH_2, NH, N_2H_3, N_2H_2, N_2H, N, H
$CH_3OH + H_2O \longrightarrow CO_2 + 6H^+ + 6e^-$	H, CH_3O, CH_2O, CHO, CHOOH, COOH

The common feature of all these reactions is that some intermediates with a high energy have to be generated before the reaction can proceed to form the final products. An easier generation of such intermediates due to interaction with the electrode will increase the reaction rate in such multi-electron step processes, and this is the general reason of electrocatalysis in all systems of practical interest. For simplicity, we shall discuss this for a reaction with two electron transfer steps. The conclusions are valid for all systems independent of the number of electrochemical and chemical reaction steps.

$$\text{Overall reaction:} \quad A^+ + 2e^- \rightleftharpoons B^- \qquad \text{standard potential:} \quad E^o_{A^+/B^-} \tag{5}$$

$$\text{reaction steps:} \quad A^+ + e^- \rightleftharpoons I \qquad E^o_{A^+/I} \tag{5a}$$

$$I + e^- \rightleftharpoons B^- \qquad E^o_{I/B^-} \tag{5b}$$

where the intermediate I acts as an electron donor in the first reaction and as an electron acceptor in the second one. If we define the standard redox potentials for the two different electron transfer reactions as usual (with standard concentrations of the species in solution) we have from thermodynamics a simple correlation between the redox potential of the overall reaction and the redox potentials of the single steps (the principle of Luther [16]).

$$E^o_{A^+/B^-} = \frac{1}{2}\left(E^o_{A^+/I} + E^o_{I/B^-}\right) \tag{6}$$

For a reaction with a chemical reaction step involved like:

$$\text{overall reaction:} \quad A^+ + 2e^- + C \rightleftharpoons B^- \qquad E^o_{A^+,\,C/B^-} \tag{7}$$

$$\text{1st electrochem. step} \quad A^+ + e^- \rightleftharpoons I_1 \qquad E^o_{A^+/I} \tag{7a}$$

$$\text{chem. step} \quad I_1 + C \rightleftharpoons I_2 \qquad \Delta G^o_{\text{chem.}} \tag{7b}$$

$$\text{2nd electrochem. step} \quad I_2 + e^- \rightleftharpoons B^- \qquad E^o_{I_2/B^-} \tag{7c}$$

this principle gives:

$$2\,E^o_{A^+,C/B^-} = E^o_{A^+/I_1} + \Delta G^o_{\text{chem}} + E^o_{I_2/B^-} \tag{8}$$

A demonstration of this thermodynamic relation in terms of the position of electron-exchange energy levels for the two respective redox reactions of equ. (6) is given in Fig. 10a and 10b. For starting the reduction of A^+ in solution one has to apply an overvoltage in the order of the difference between the standard redox potentials of the overall reaction and the first electron transfer step. The second reaction will follow very fast because the acceptor state of the intermediate is at a much lower energy level having a very high electron affinity.

If, however, the intermediate is strongly adsorbed, the energy levels in the adsorbed state are shifted for I as a donor into negative direction of the electron energy scale and for I as an acceptor into the opposite direction as shown in Fig. 10c.

This means, thermodynamically, that the standard redox potential of the first step is shifted in the adsorbed state to more positive values; that is a more negative Fermi level in our absolute energy scale of Fig. 10. The standard redox potential of the second reaction is shifted into the opposite direction (see Fig. 10a). The consequences of adsorption of such an intermediate for the kinetics are obvious. The reaction can proceed now in cathodic and in anodic direction at much lower overvoltages measured against the standard redox potential of the overall reaction, because the intermediates can be formed with much less excess energy. We see that the shift of electronic energy states due to adsorption can have an enormous catalytic effect on the reaction rate of electron transfer reactions with two or more one-electron transfer steps of very different standard redox potentials. This is a common situ-

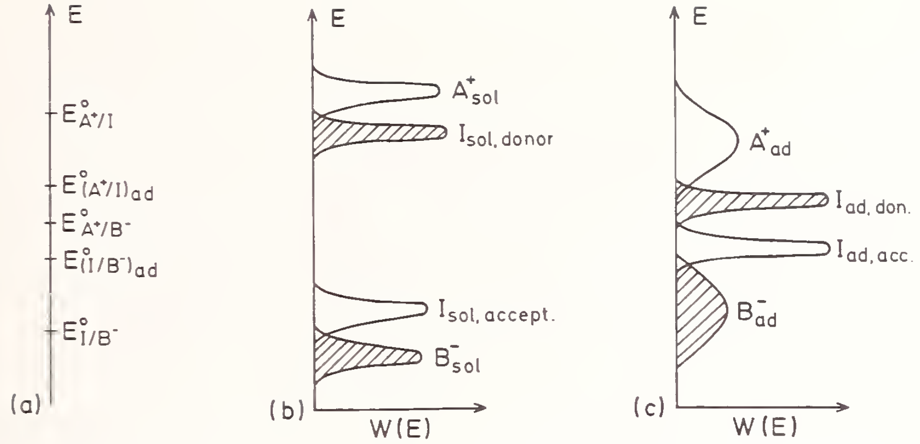

Fig. 10. Two-step redox reaction $A^+ + 2e^- \rightleftarrows B^-$ with intermediate I.
(a) Standard redox potentials in absolute scale (= Fermi levels);
(b) distribution of energy levels in solution;
(c) distribution of energy levels in the adsorbed state.

ation in the kinetics of organic electrode reactions, where radicals are formed as intermediates. The classical example, however, is the hydrogen electrode reaction which we now shall discuss very briefly from this thermodynamic point of view.

Let us assume that the hydrogen evolution reaction follows the electrochemical desorption path. In the absence of interaction with the electrode, we have the following situation for the overall reaction and the single reaction steps:

$$2H^+_{sol} + 2e^- \rightleftarrows H_{2,sol} \qquad \Delta E^o_{2H^+/H_2} = 0 \tag{9}$$

$$H^+_{sol} + e^- \rightleftarrows H_{sol} \qquad \Delta E^o_{H^+/H} = +\,2.1\ \mathrm{V} \tag{9a}$$

$$H_{sol} + H^+_{sol} + e^- \rightleftarrows H_{2,sol} \qquad \Delta E^o_{H + H^o_o/H_2} = -2.1\ \mathrm{V} \tag{9b}$$

$$H_{sol} + H_{sol} = H_{2,sol} \qquad \Delta G^o_{H,ad} = -\,4.2\ \mathrm{eV}$$

$$\text{with} \quad \Delta E^o_i = E^o_i - E^o_{2H^+/H_2} \tag{9c}$$

The two standard redox potentials of reaction (a) and (b) are shifted by adsorption of H-atoms at the electrode by an equal amount into opposite directions. They coincide when the free energy of adsorption of H-atoms $\Delta G^o_{H,ad}$ just compensates the differences of $\Delta E^o_{H^+/H}$. This is shown in Fig. 11 by plotting the standard Fermi energy of the adsorbed redox systems as function of $\Delta G^o_{H,ad}$. We see that the evolution of hydrogen by electrolysis would for $\Delta G^o_{H,ad} = 0$ need an enormous negative overvoltage to reach the first intermediate. Only because hydrogen atoms are strongly adsorbed can the reduction start at much lower cathodic potentials. The first step remains rate determining for the cathodic process as long as the second step does not reach a more negative redox potential than the first one. This is seen in Fig. 11 where an inversion of E^o for the two partial reactions occurs when

$$\left|\Delta G^o_{H,ad}\right| > \frac{1}{2}\left|\Delta G^o_{2H \rightarrow H_2}\right| .$$

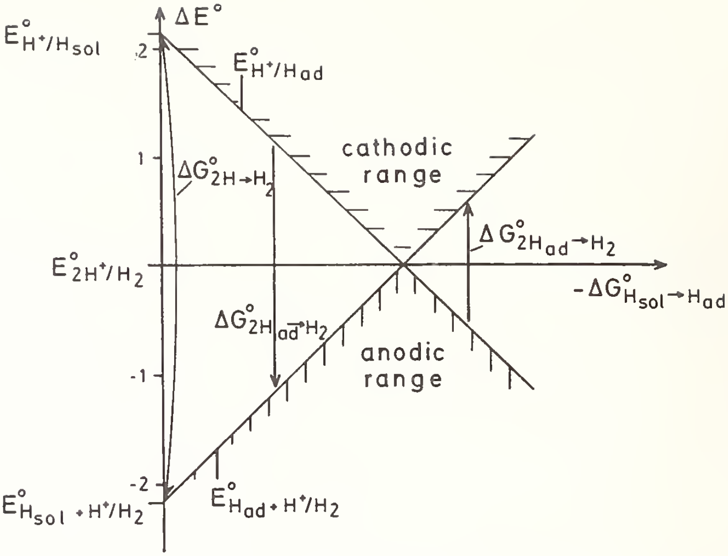

Fig. 11. The hydrogen electrode; dependence of the standard redox potentials (Fermi levels) for the partial reaction steps on free energy of adsorption at the electrode.

When this point is reached, the formation of the adsorbed H-atoms gets fast, but the desorption reaction becomes slow, a well known idea of the mechanism for the hydrogen generation at electrodes with very high adsorption energies for hydrogen atoms [17,18].

A general conclusion is that the highest rates or the optimal catalysis can be expected when the Fermi energies for all single electron transfer steps coincide approximately. The real kinetic picture which has been given by Parsons and by myself at an earlier occasion [17,18] is more complicated than this thermodynamic discussion can show. For a more specific discussion of the kinetics one has not only to use the exact rate equations and their dependence on electrode potential but also to include the recombination step. The driving force for this step can be taken from the scheme of Fig. 11 as the difference between the 2 Fermi energies of the single redox reactions, but the kinetics of this step are quite different from electron transfer steps. This means the optimum can be shifted to a somewhat different adsorption energy of H_{ad} than $\frac{1}{2}\Delta G^{0}_{2H\rightarrow H_2}$ but this is only a minor correction.

The reduction of oxygen via the hydrogen peroxide path or the oxide path and the electrolytic oxygen evolution can be discussed analogously [19]. In such a complex reaction with four electron transfer steps, however, the adsorption of different intermediates can have a compensating effect. This is demonstrated in Fig. 12 for the peroxide path. One can derive from such a figure what kind of interaction at the surface should be favourable and what not. The optimum will again be obtained when the standard potentials of all single electron transfer steps approximately coincide with the standard potential of the overall reaction. Fig. 12 shows that for this mechanism we would need the following free energies of adsorption to approach this optimum;

$$OH_{sol} \longrightarrow OH_{ad}: \quad \Delta G = -1.6 \text{ eV}; \quad O^{-}_{2,sol} \longrightarrow O^{-}_{2,ad}: \quad \Delta G = -1 \text{ eV}$$

$$HO^{-}_{2,sol} \longrightarrow HO^{-}_{2,ad}: \quad \Delta G = -0.6 \text{ eV}$$

The oxygen electrode reaction can contain, however, different intermediates than here assumed, for instance, the formation of O_{ad}, O_2H_{ad}, which would need a different optimisation of adsorption energies if such a reaction path should be more favourable. For real kinetics, such

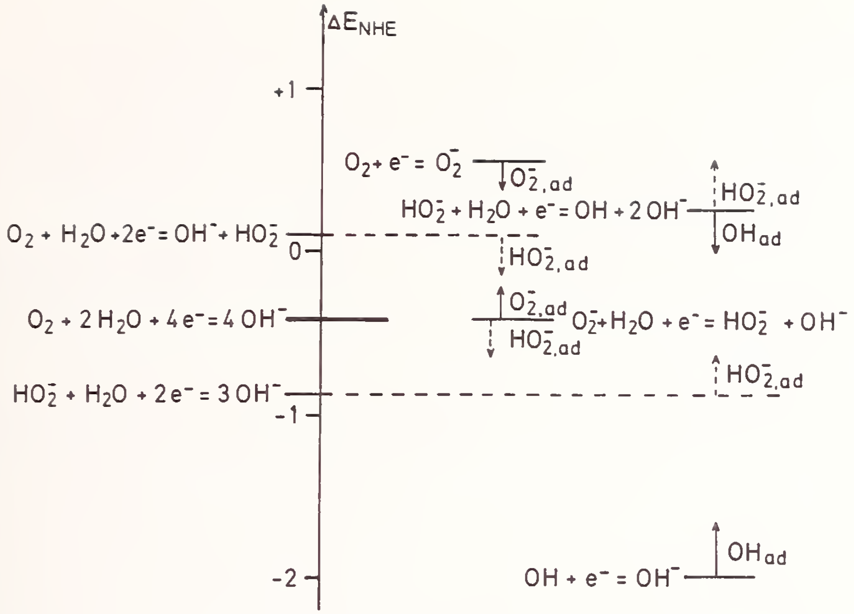

Fig. 12. The oxygen electrode; dependence of the standard redox potentials (Fermi levels) of four possible electron transfer steps on the free energy of adsorption of the respective intermediates O_2^-, HO_2^-, OH, assumed in one particular reaction path.

a thermodynamic consideration can again only give the general background, but no reliable prediction of rates.

5. Electron Transfer at Non-Metallic Electrodes

In our previous discussion we have assumed a metal-like behaviour of the electrode with the Fermi energy located within a continuous energy band. A variation of the electrode potential in this case changes the voltage drop in the double layer between the electrode surface and the electrolyte but has no effect on the charge distribution in the bulk of the electrode. For non-metallic electrodes this can be quite different. The electronic system there contains a band gap which means that a smaller number of electronic quantum states will be available for exchange interaction with adsorbed species. Therefore, the adsorption interaction will normally be weaker than on metals, if there is not a specific bond formation due to interaction between localized electron states in the surface (surface states) and the adsorbate.

We shall discuss now a non-metallic electrode with the Fermi energy in the band gap, but high enough conductivity to be usable for electrolysis. Non-catalysed electron transfer can here be described in the same way as for metals but with the restriction that all energy levels of a redox system which correspond to energies in the forbidden gap of the semiconductor are excluded from electron exchange [20]. It is therefore very important to know where the electronic energy levels of a redox system are located relative to the energy levels of the band edges in the surface of a semiconductor. Fig. 13 gives a survey of typical situations for different redox couples in contact with a semiconductor. For simplicity the semiconductor is assumed to be at a particular electrode potential, the so-called flat band potential, where we have no excess charge in the bulk of the electrode. In Fig. 13a, the redox system I has a redox Fermi level above the flat band Fermi level E_{FB} of the semiconductor, but below the conduction band edge. The consequence is a slow rate of electron injection into the conduction band from thermally excited levels of the reduced species which have reached the energy range of the conduction band. The second redox system II of Fig. 13a has the redox Fermi level below E_{FB}, but above the valence band edge. The consequence is an electron transfer from the valence band to acceptor states of the redox system which have reached the

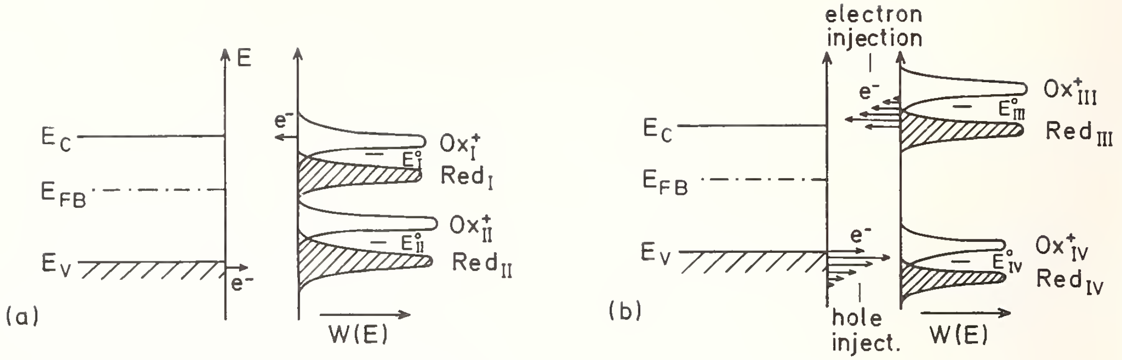

Fig. 13. Energy distribution of electron exchange levels for various redox systems in contact with a semiconductor at flat band potential. Indication of electron transfer rates by arrows.

energy of the valence band by thermal activation. This is equivalent to a hole injection into the semiconductor.

In Fig. 13b we see the situation where the Fermi levels of the redox systems are either in the range of the conduction band or in the range of the valence band. The consequence is a fast electron injection into the conduction band or a fast hole injection into the valence band respectively. While the electron transfer rates in the situation of Fig. 13b are high, comparable with metals or even higher, the rates of electron transfer in the situation of Fig. 13a are much smaller than for metals. If the band gap is wide enough and the Fermi energy of the redox system is located in the middle range of the band gap, electron transfer can practically be fully prevented.

The influence of the electrode potential on the relative position of the electron energy levels can vary to a large extent. It depends on the concentration of mobile electric charge carriers in the semiconductor and on the presence of surface states, their concentration and energetic position. In systems with a wide band gap and a not too high donor or acceptor concentration ($<10^{18}$ cm^{-3}) and in the absence of surface states, a potential variation affects primarily the charge distribution in the semiconductor and can be described by an equivalent band bending. This means for a redox system with a Fermi level E^{o}_{Redox} closer to the conduction band than to the valence band that a more cathodic electrode potential will shift the Fermi level in the semiconductor upwards and cause an increase of electron density in the surface of the semiconductor. In this way the reduction via electron transfer from the conduction band to the vacant levels of the redox system is accelerated as indicated in Fig. 14a The concentration of electrons in the surface and the density of vacant electron states of the redox system at the band edge control the rate.

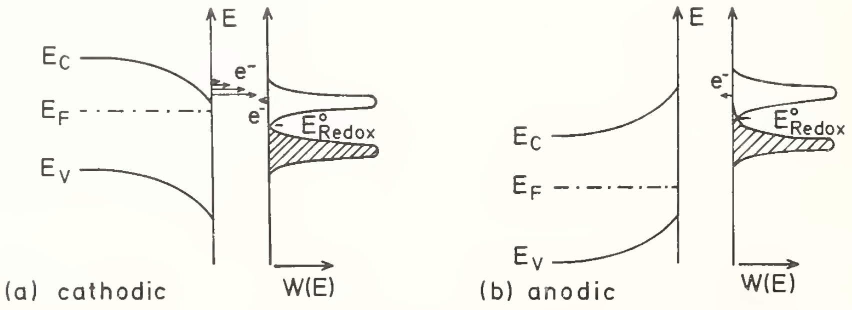

(a) cathodic (b) anodic

Fig. 14. Influence of cathodic and anodic polarisation on electron transfer between a redox couple and a semiconductor with preference of electron exchange in the conduction band.

Polarization in the anodic direction lowers the Fermi level in the semiconductor but leaves the oxidation by injection of electrons into the conduction band at a nearly constant rate as long as no holes are generated in the surface of the semiconductor (compare Fig. 14b). Since semiconductors with a wide band gap can usually not form an inversion layer, the oxidation by means of holes normally plays no role at an n-type semiconductor with a wide band gap.

For p-type semiconductors we have the inverse situation and normally all electron transfer steps occur via the valence band. At anodic polarisation, the concentration of holes in the surface increases and the current grows in parallel. At cathodic polarisation, the current is limited by the injection rate of holes and remains constant as long as no electrons are generated in the conduction band.

6. Catalysis of Electron Transfer at Semiconductors by Surface States

Semiconductors with a wide band gap are normally uninteresting for catalysis because they not only imply a high barrier for electron transfer, but they are normally also inactive for chemisorption. This can be different by two reasons if surface states are present. The surface states can be energetically located within the range of the band gap with the result that charge can be accumulated in the surface forming a variable countercharge for a Helmholtz double layer. The variation of charge in such surface states with the applied voltage makes the semiconductor behave like at a metal electrode with regard to the double layer behaviour. The other consequence is that surface states can specifically form bonds with adsorbates, which can catalyse electron transfer.

If surface states interact with the components of a redox couple, charge can be easily exchanged with the electrolyte by alternating adsorption and desorption of the redox species. To complete the charge transfer with the bulk of the semiconductor, however, the coupling between bulk states and surface states must be strong enough. This condition is often not fulfilled for semiconductors with a wide band gap and a low concentration of donor or acceptor states, because the electrons cannot pass the energy barrier between the electron surface states and the bulk states if the barrier is high and too extended. With a high enough concentration of mobile charge carriers, however, the space charge layer becomes thin and transparent for electrons via tunnelling [21]. Electron transfer is also possible to a more or less extent if the energetic position of the surface states is close to the band edges and therefore the barrier height for electron transfer between surface states and the bulk states remains low. A variation of the electrode potential in these cases mainly changes the concentration of excess charge in surface states but only slightly the charge distribution in the bulk. This has been shown in some experiments with artificially created surface states [22].

Fig. 15 characterizes four situations of an n-type semiconductor with surface states close to the conduction band edge being in contact with the electron states of a redox electrolyte. It shows their relative energy position and also schematically the energy spectrum for electron transitions between the redox electrolyte and the electrode in these four cases. Electron transfer occurs in this system primarily via the surface states of the semiconductor and the relative shift between E_F and E^o_{Redox} is mainly caused by a variation of the potential drop in the Helmholtz double layer with the voltage applied.

For a p-type semiconductor with surface states around the valence band edge one finds the analogous situation as shown in Fig. 16. Electron transfer is described in this figure as hole injection and extraction into or from the semiconductor occurring via the surface states.

Fig. 17 demonstrates the influence of surface states, with energies located in the band gap, on electron transfer in the absence of strong interaction between the reactants and the electrode. Continuous current flow is in such systems only possible if the potential barrier between the bulk states and the surface states is so thin that tunnelling is efficient, which needs a high donor or acceptor concentration [21]. The previous discussion of electrocatalysis has, however, shown that only strong interaction between intermediates of a multistep redox reaction and the electrode can make an important contribution to an increase in overall reaction rate. Therefore, we shall now consider the consequences of strong interaction between a non-metallic electrode and the intermediates of redox reactions.

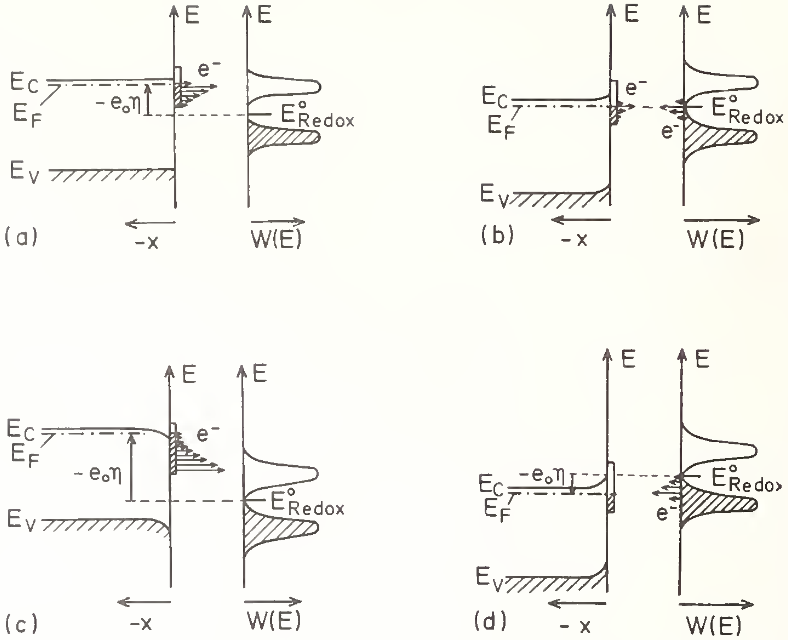

Fig. 15. Correlation of electron exchange energy levels for redox couple in contact with an n-type semiconductor having surface states around the conduction band edge. Situation at various potentials; (a) flat band (cathodic), (b) equilibrium, (c) strongly cathodic, (d) anodic.

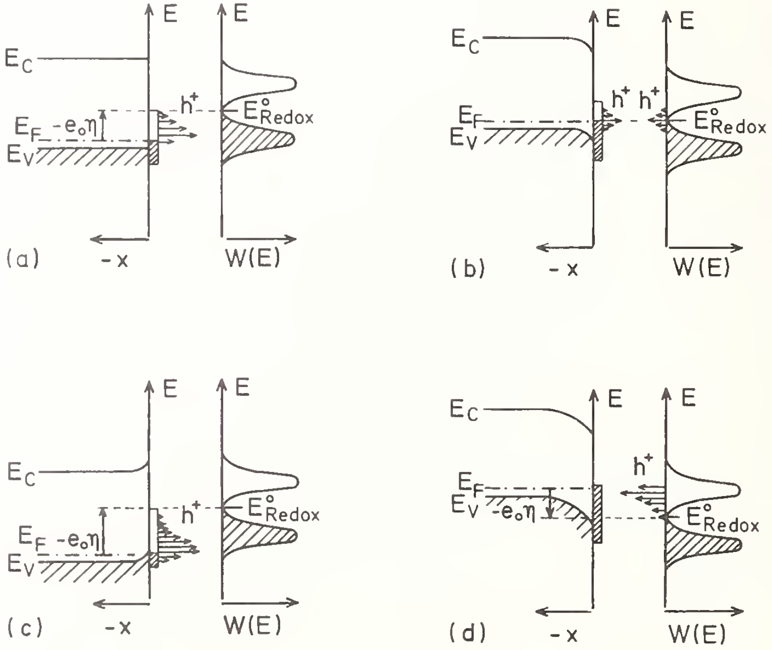

Fig. 16. Correlation of electron exchange energy levels for redox couple in contact with a p-type semiconductor having surface states around the valence band edge. Situation at various potentials; (a) flat band (anodic), (b) equilibrium, (c) strongly anodic, (d) cathodic.

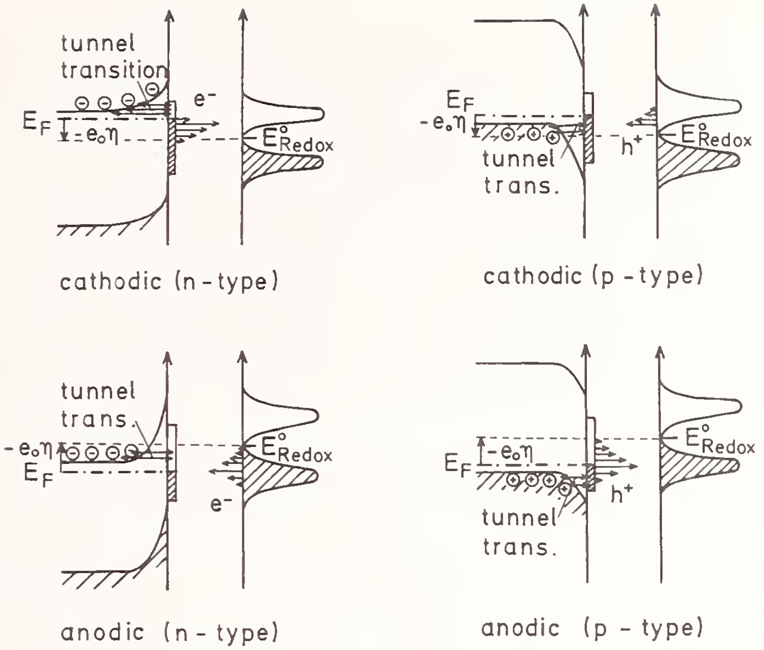

Fig. 17. Electron exchange levels of redox system in contact with an n-type or p-type semiconductor having surface states in the band gap energy range; various states of polarisation.

We discuss the hypothetical intermediate I of equ. (5) which can act as the electron donor state in reaction (5a) and the electron acceptor state in reaction (5b). The electron exchange term for the first step may have a rather negative standard redox potential $E^0_{A^+/I}$ for the non-catalysed redox process in solution; the standard redox potential E^0_{I/B^-} of the second step may be rather positive in the electrochemical scale. Fig. 18 represents this situation for a contact between two semiconductor electrodes at equilibrium with the net redox system. For simplicity, this equilibrium potential is assumed to coincide with the flat band potential. $E^0_{A^+/I}$ may be located in the range of the conduction band, E^0_{I/B^-} in the range of the valence band. This means, according to Fig. 13, that electron injection from I (oxidation) into the conduction band would be fast and also hole injection from I (reduction) into the valence band. The intermediate is therefore not stable at equilibrium conditions as already indicated by the large difference between $E^0_{A^+/I}$ and E^0_{I/B^-}. The overall reaction (5) will therefore be blocked in both directions as long as one does not apply high overvoltages.

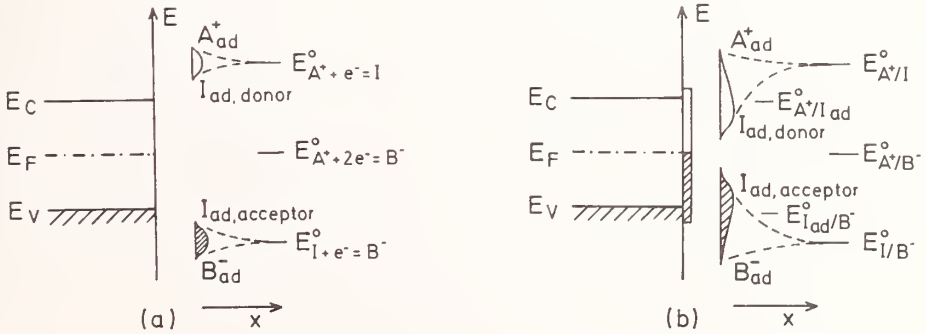

Fig. 18. Electron exchange levels of redox couple with 2 electron transfer steps and one intermediate broadened by interaction with a semiconductor surface.
(a) no surface states on the semiconductor.
(b) with surface states in the energy range of the band gap.

The semiconductor of Fig. 18a is supposed to have no surface states. It is to be expected in this case that interaction is weak because the wave functions of the electronic semiconductor bulk states decay very rapidly in front of the surface. A weak interaction is indicated in Fig. 18a by a small broadening of the electron exchange terms for the intermediate acting as a donor state (reaction 5a) and as an acceptor state (reaction 5b).

In the presence of surface states the interaction will be much stronger and results in a wide broadening of the electron exchange levels. This is schematically shown in Fig. 18b where the surface states are supposed to form a continuous band over the range of the gap. The principal consequence is that the donor and the acceptor levels of the intermediate I come much closer together and approach the range of the standard Fermi energy of the redox system. It has been assumed in Fig. 18b that this range is not yet reached, and therefore, the exchange current at equilibrium potential of the overall reaction will still be negligible. If the interaction is so strong that the energy range of E_F is reached in the adsorbed state, the exchange current starts to increase, and this means efficient electrocatalysis.

In the absence of surface states, as in Fig. 18a, a polarisation of the electrode at medium overvoltages will only vary the band bending but not the relative position between the band edges at the surface and the energy levels of the redox system. Only if degeneracy of electron states is reached in the surface, the system begins to behave like a metal electrode, and the potential drop in the Helmholtz double layer increases until electron or hole injection become possible. This means a very high overvoltage, much higher than for metal electrodes.

The much more promising situation is to be expected in presence of surface states which strongly interact with the electronic bulk states and the intermediates. A slight polarisation of the electrode is then sufficient to bring the Fermi level to the range of electronic levels of the reactants, as is schematically shown in Fig. 19, because now the amount of charge accumulated in the surface varies with the applied voltage. Such a variation of the voltage drop between the surface and the electrolyte causes a relative shift between the energy levels of the electrode and the solution similar to a metal electrode, as indicated in Fig. 19. Electron transfer starts in cathodic direction when the Fermi level in the surface states reaches the acceptor levels of the oxidized species because the acceptor levels of the intermediate can then pick up electrons from the lower filled states of the surface (compare Fig. 19a). The respective situation at anodic polarisation with electron injection into surface states is shown in Fig. 19b.

This discussion has shown that surface states can catalyse electron transfer at non-metallic electrodes in both cathodic and anodic directions for multiple electron transfer reactions in the same way as electrocatalysis acts at metal electrodes. Is there to be expected any advantage from the use of nonmetallic electrodes? One favourable possibility is

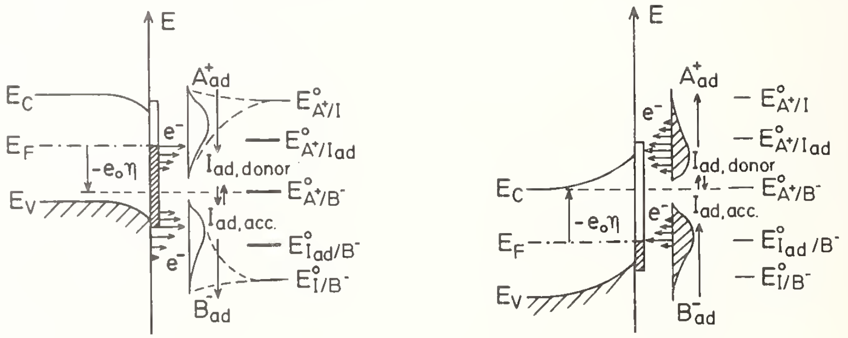

(a) cathodic (b) anodic

Fig. 19. Electron exchange levels of a 2-step redox reaction with strong interaction between the intermediate and surface states in the energy range of the band gap. Demonstration of electron transfer catalysis in cathodic and anodic direction by such an interaction.

that the interaction with particular intermediates may be more specific than on metals. A non-metallic electrode can have surface sites of very different character, especially if the surface consists of different elements which can form specific chemical bonds. Structural defects, special crystal faces or surface places may form favourable reaction sites. No generalizing prediction can at present be made for the usefulness of non-metallic electrodes besides that the individual properties of the constituents, the variety of lattice structures and of the electronic properties of such materials present an enormous reservoir of different possibilities. This seems to be the principal challenge in using non-metallic electrodes for catalysis. However, one should not forget that the necessary high conductivity and strong coupling between electronic bulk and surface states implies serious limitations to the use of such materials in electrochemistry. To some extent the conductivity problem can perhaps be overcome by using very thin layers on highly conductive substrates. However, the stability of such layers of different chemical composition will always remain a critical problem. The conclusion is that one should not expect catalytic miracles from non-metallic electrodes, but in some cases and for some specific reactions, as with the Ruthenium Oxide on Titanium substrates for the Chlorine and Oxygen electrolysis (23,24), one might be especially lucky with such materials.

7. References

[1] Weiss, J. Trans. Faraday Soc. 31, 1547 (1935).
[2] Gerischer, H. and Gerischer R., Z. physik. Chem.(Frankfurt) 6, 178 (1956).
[3] Marcus, R.A., Can. J. Chem. 37, 155 (1959); J. Chem. Phys. 43, 679 (1965).
[4] Marcus, R.A., Ann. Rev. Phys. Chem. 15, 155 (1964).
[5] Levich, V.G. and Dogonadze, R.R., Dokl. Akad. Nauk SSSR, 124, 123 (1959).
[6] Levich, V.G., Adv. Electrochem. Electrochem. Eng., 4, 249 (1966).
[7] Dogonadze, R.R. in "Reactions of Molecules at Electrodes", ed. by N.S. Hush, Wiley-Intersciences, New York-London-Sidney-Toronto 1971, p. 135.
[8] Gerischer, H., Z. physik. Chem.(Frankfurt), 26, 223, 325 (1960); 27, 48 (1961).
[9] Gurney, R.W., Proc. Roy. Soc. (London) A 134, 137 (1931).
[10] Gerischer, H., Photochem. Photobiol. 16, 243 (1972).
[11] Gerischer, H. in "Adv. Electrochemistry Electrochem. Eng.", 1, 139 (1961).
[12] Lohmann, F., Z. Naturforschung 22a, 843 (1967).
[13] Plieth, W.J. and Vetter, K.J., Z. physik. Chem. (Frankfurt) 61, 282 (1968).
[14] Anderson, P.W., Phys. Rev. 124, 41 (1961).
[15] Gadzuk, J.W., Surface Sci. 6, 133 (1967); 43, 44 (1974).
[16] Luther, R., Z. physik. Chem. 34, 488 (1900); 36, 385 (1901).
[17] Parsons, R., Trans. Faraday Soc. 54, 1053 (1958).
[18] Gerischer, H., Z. physik. Chem. (Frankfurt) 8, 137 (1956); Bull. Chim. Soc. Belge 67, 506 (1958).
[19] Appleby, A.J. Catalysis Rev. 4 (2), 221 (1970), Marcel Dekker Inc., New York.
[20] Gerischer, H., Physical Chem. Vol. IX A (Electrochemistry) ed. by Eyring, Henderson, Jost, Academic Press 1970.
[21] Memming, R. and Möllers, F., Ber. Bunsenges. physik. Chem. 76, 469, 475 (1972).
[22] Gerischer, H., Pettinger, B. and Luebke, M., Proc. Symposium on Electrocatalysis, p. 162 (ed. by M. Breiter), The Electrochemical Society, Princeton 1972.
[23] Kuhn, A.T. and Mortimer C.J., J. Electrochem. Soc. 120, 231 (1973).
[24] Grady, W.O., Iwakura, C., Huang, J., and Yeager, E., Proc. Symposium on Electrocatalysis, p. 286 (ed. by M. Breiter), The Electrochem. Soc., Princeton 1972.

National Bureau of Standards Special Publication 455, *Electrocatalysis on Non-Metallic Surfaces*,
Proceedings of Workshop held at NBS, Gaithersburg, Md., December 9-12, 1975. (Issued November 1976)

SURFACE STATES, CHEMISORPTION AND CATALYTIC PROCESSES ON TRANSITION METAL OXIDES

T. Wolfram, F. J. Morin[1] and R. Hurst

Department of Physics
University of Missouri-Columbia
Columbia, Missouri 65201

A discussion of the bulk and surface electronic states of transition metal oxides such as the perovskites is presented. The factors which determine the surface electronic structure are described and several examples of surface states and surface energy bands are presented using both cluster and energy band models.

The role of d-electron surface states in chemisorption and catalytic processes on transition metal oxides is considered. Several examples of surface reactions are given using a cluster model for the substrate. These examples include the chemisorption of OH^- ions, the dissociative adsorption of H_2 and the hydrogenation of ethylene.

A detailed description of a Green's function theory for surface reactions is given in which both the reacting molecule and the solid are described by local basis states. The concept of the spectral weight function (local density of states) is used to describe delocalized bonding of molecules to a solid surface. As an example of the application of the theory the formation of localized electronic states associated with the adsorption of OH^- ions is considered.

Key words: Catalysis; chemisorption; cluster states; electronic structure; energy bands; perovskites; surface states; transition metal oxides.

1. Introduction

When a crystalline solid is terminated by a surface new electronic states appear, associated with the surface and derived from the bulk band structure. The surface states have wavefunctions which can hybridize with the orbitals of reacting molecules to produce a surface complex. Chemisorption involves the formation of a stable surface complex while catalysis involves the surface complex as an intermediate or transient state which facilitates a molecular transformation.

The transition metals and transition metal compounds dominate the science and technology of catalysis and a great deal of effort is currently directed towards understanding the mechanisms by which molecules interact with the surface of such solids.

Models for chemisorption and catalysis have tended to emphasize one or the other of two extremes. One approach is developed around the concept of a surface molecule in which the effects of electron delocalization in the catalyst due to energy band formation are

---

[1] Permanent address: Science Center, Rockwell International, Thousand Oaks, California 91360

regarded as secondary or negligible. The solid is approximated by a small cluster of atoms and the interaction of molecules with the solid is expressed in terms of molecular bonding concepts. Such models are of considerable value in isolating and identifying possible mechanisms of surface reactions. They cannot be employed to calculate heats of adsorption or activation energy barriers because solid state effects such as band formation, screening and polarization and delocalization of surface bonds significantly alter the energetics of surface reactions.

The second type of model, based on energy band concepts, emphasizes the delocalized character of the electrons of the catalyst. The interaction of reactant molecules with the solid is expressed in terms of matrix elements between molecular orbitals and all of the energy band states of the solid. In principle, such models are capable of describing the formation of localized chemical bonds. However, until recently approximations were frequently employed which minimized or negated the role of surface states and which tended to obscure local bonding mechanisms. This type of model has applicability to some metals and has provided insight into mechanisms of screening by mobile carriers and delocalization of chemical bonds.

The transition metal compounds present a particularly interesting and difficult class of materials for theoretical models. Their surface chemical properties can not be described successfully by either a completely localized or a completely delocalized electron model. The challenge here is clearly the development of models which treat both local and solid state properties on an equal footing.

In this paper we describe some initial efforts to integrate local and band concepts into a model for understanding chemisorption and catalysis on the transition metal oxides. We have selected certain materials as model compounds upon which to base a theoretical program for the study of the mechanisms of chemisorption and the mechanisms by which the interaction between two molecules is catalyzed by a solid surface.

Surface reactions involved in chemisorption and catalysis are so complex that no single model or theoretical approach can be expected to correlate the wide diversity of real situations. Even in the case of a simple, specific surface reaction understanding of the actual mechanisms of chemisorption or catalysis is minimal. Nevertheless there are a number of factors which are known to be of primary importance in surface reactions. In this paper we discuss some of the factors believed to be fundamental in considerations of surface chemistry on transition metal oxides. These include:

1. a high density of d-electron and p-electron surface states located in the forbidden energy gap.

2. the formation of localized electronic states involving electrons shared between surface states and molecular orbitals.

3. the effects of surface perturbations such as changes in the electrostatic potentials and coordinatively unsaturated surface ions.

4. the effects of energy band formation on the character of chemisorption bonds.

We begin in section 2 with a discussion of the bulk electronic states of the transition metal oxides. For concreteness we present examples of the electronic properties of the simple cubic perovskites. In this discussion we present both the localized cluster model and the energy band model and also show relation between the two models. A discussion of the various types of surface states is given and examples of surface energy bands on $SrTiO_3$ are presented. The importance of the electrostatic Madelung potentials in controlling the energies of surface states is emphasized. Detailed calculations of surface states derived from the cluster model and from energy band theory are presented. Finally, some experimental results relating to surface states on TiO_2 and Ti_2O_3 are briefly described.

In section 3 qualitative examples of chemisorption and catalytic processes on transition metal oxides are presented. The localized cluster model is employed to show how the electronic levels of surface ions can hybridize with the molecular orbitals of reacting molecules to form stable and unstable surface complexes. As examples we consider the chemisorption of OH^- ions, the dissociative adsorption of H_2 and the hydrogenation of ethylene.

In section 4 we discuss an energy band model for chemisorption. The theory employs a Green's function formalism based on localized basis states for both the solid and the reacting molecule. The concept of the spectral weight function (local density of states) and its relation to chemisorption is described. A simplified model of OH^- adsorption is described and the relation of the various chemisorption states to those of the cluster model are discussed.

2. The Transition Metal Oxides

2.1. Recent Applications

The transition metal oxides have been of interest for many years because of their catalytic and electrocatalytic properties. An abbreviated list of the oxides belonging to several structural families is presented in Table I. Some of these oxides have received particular attention recently including the perovskites and their various mixed crystals, and TiO_2.

Table 1. Some examples of transition metal oxides.

ROCKSALT STRUCTURE		
Antiferromagnetic Mott insulators		Metals
MnO (d^5)		TiO (d^2)
FeO_x (d^6)		VO (d^3)
CoO (d^7)		
NiO (d^8)		
PEROVSKITE AND RELATED STRUCTURES		
Wide band gap insulators	Magnetic semiconductors	Metals
$SrTiO_3$ (d^0)	$LaCoO_3$ (d^6)	ReO_3 (d^1)
$BaTiO_3$ (d^0)	$LaMnO_3$ (d^4)	$LaTiO_3$ (d^1)
$KTaO_3$ (d^0)		$KMoO_3$ (d^1)
WO_3 (d^0)		$CaMoO_3$ (d^2)
$PbZrO_3$ (d^0)		$LaNiO_3$ (d^7)
RUTILE STRUCTURE		
Wide band gap insulators		Metals
TiO_2 (d^0)		VO_2 (d^1) (S.C. $\rightleftarrows$ metal)
		CrO_2 (d^2) ferromagnetic
CORUNDUM STRUCTURE		
Antiferromagnetic Mott insulators		Metals
α-Cr_2O_3 (d^3)		Ti_2O_3 (S.C. $\rightleftarrows$ metal)
α-Fe_2O_3 (d^5)		V_2O_3 (d^2) (S.C. $\rightleftarrows$ metal)

Pedersen and Libby [1][2] suggested that the rare-earth cobalt oxides might provide inexpensive catalysts for the oxidation of CO and the reduction of the oxides of nitrogen. Voorhoeve et al. [2,3] reported on the use of mixed crystals such as $(La_{1-x}Pb_x)MnO_3$ and $(Pr_{1-x}Pb_x)MnO_3$ which have the cubic perovskite structure and Libby and Aegerter [4] found that reduced $SrTiO_3$ and $BaTiO_3$ are both active catalysts for isomerization, hydrogenation, hydrogenolysis synthesis and cracking.

---

[2] Figures in brackets indicate the literature references at the end of this paper.

In the area of electrocatalysis Tseung and Bevan [5] investigated various compositions of $(La_xSr_{1-x})CoO_3$ as candidate oxygen electrodes. They reported that $La_{0.5}Sr_{0.5}CoO_3$ performs as a nearly ideal reversible electrode in a 45% KoH aqueous electrolyte at 25 and 80°C.

The possibility of utilizing solar radiation for the production of hydrogen by electrochemical photodecomposition of water has stimulated a number of studies on transition metal oxide electrodes. Fujishima and Hondo [6] demonstrated the feasibility of such photodecomposition using a TiO_2 anode. More recently Mavroides et al. [7] reported studies of the photoelectrolysis of water using TiO_2 and $SrTiO_3$ anodes. Quantum efficiencies for band gap radiation (~3eV) were found to be near 100%. The search for a material whose band-gap is matched to the peak in the solar radiation distribution (~2.4eV) is currently focused on the transition metal oxides because many of these materials are stable as anodes in an electrochemical environment.

2.2. Bulk Electronic Properties

The oxides include a wide range of different structures and electronic properties. They include insulators, semiconductors, metals and superconductors. Examples of ferromagnetics, ferrimagnets, antiferromagnets and ferroelectrics can be found. Some oxides possess delocalized d-bands while others have localized d-electrons and transitions from localized to delocalized behavior may occur and semiconductor to metal transitions are common. For the purposes of our theoretical investigation of d-band surface states and catalysis, an ideal structural form is the perovskite. This is because the simple structure makes it theoretically tractable and because essentially all of the electronic properties found among the transition metal oxides may be realized in the perovskites by metal ion substitution.

A large class of ionic oxides having the formula unit ABO_3 crystallize in the perovskite structure (the structural details of which are illustrated in fig. 1.).

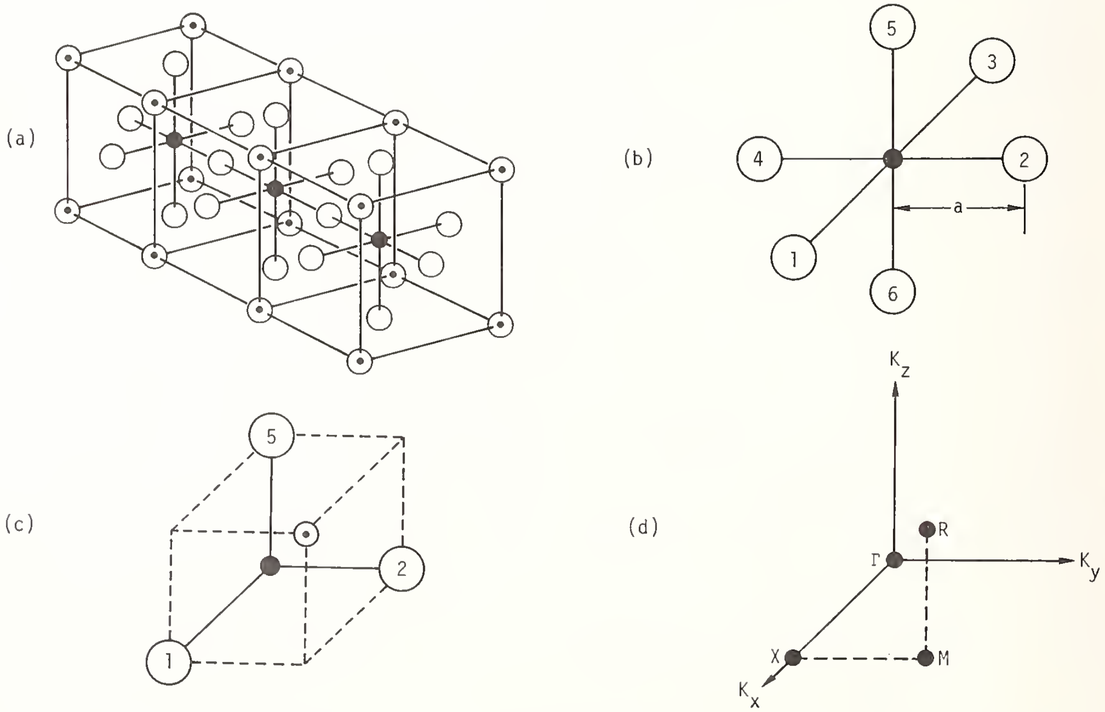

Fig. 1. (a) Cubic perovskite structure containing octahedral clusters; (b) BO_6 octahedral cluster, B = transition metal ion, O = oxygen ion; (c) unit cell for the perovskite structure; (d) symmetry points in the Brillouin zone for the cubic perovskite structure. structure.

(A=larger cation, B=small cation.) The stability of the structure derives primarily from the Madelung energy achieved when cations occupy oxygen octahedra which share corners. This requires that the B cations have a strong preference for octahedral coordination. In the discussion to follow, we are interested in the case where B=transition metal ion. Also, we shall consider only the (001) surface which contains the B cations. Presumably this is a catalytically active surface and, due to its stability, the surface likely to be exposed to a chemical reaction rather than the (001) surface which contains the A cation. Furthermore, for our purposes, the ABO_3 oxides of interest are not only those having the cubic structure, of which $SrTiO_3$ is typical, but also those whose structure may be considered to be distorted cubic such as $LiNbO_3$ (rhombohedral), $NaTaO_3$ (orthorhombic), $PbTiO_3$ (tetragonal). Cation formal charge varies in these structures over the range A (3+ to vacant site), B (3+ to 6+) so that, when mixed crystals are included, a very large number of oxide perovskites are possible. Their electrical properties include d-band insulators, metals, Mott insulators and superconductors. A general survey of these materials has been compiled by Goodenough and Longo [8].

The bulk energy bands of perovskites are reviewed in this section, using $SrTiO_3$ as an example, in order to provide a basis for the description of the surface states to follow. The properties of the perovskites are dominated by the properties of the electronic states derived from O^{2-} and the B ion. The A ion contributes strongly to the Madelung potentials but has only a minor influence on the low-energy electronic and optical properties because its energy levels lie much higher than those of the B ion. Therefore, for the purpose of determining the structure of the d-bands, we ignore the A ion so that effectively we regard the perovskites as transition metal trioxides BO_3. From this point of view ReO_3 is a typical member of the d-band perovskite family. Figure 2 summarizes the major energy parameters which influence the electronic structure. The energy levels of the free ions relative to vacuum are shown on the left of figure 2a before the ions are combined to form the crystal. These levels include the ionization energy for the reaction $Ti^{3+} \rightarrow Ti^{4+} + e$ (-43.2eV) and the electron affinity of oxygen, $O^{-} + e \rightarrow O^{2-}$ (+9.2 eV). When these ions are brought together to form the perovskite structure large electric potentials arise which shift the energy levels.

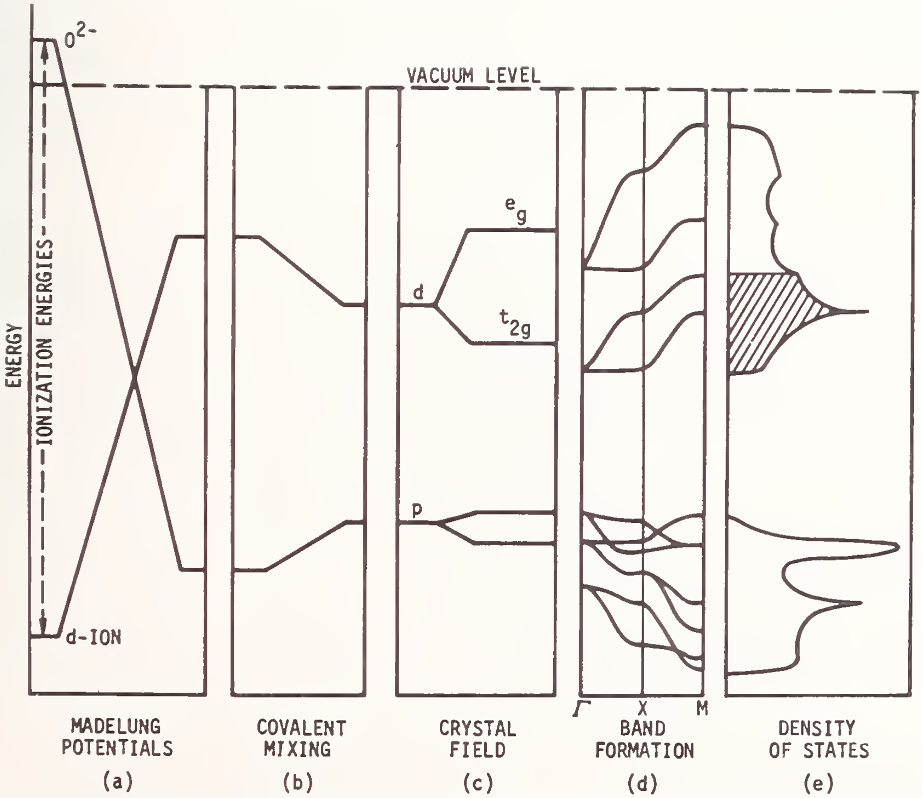

Fig. 2. Schematic of the major energies involved in the electronic structure of a perovskite.

The electrostatic field acting on any site in the lattice can be expressed in terms of various electric multipoles. The monopole contribution produces large Madelung potentials while the higher-order poles produce a crystal field effect. The effect of the Madelung potential on the energy levels of the free ions is illustrated in figure 2a. The negatively charged oxygen ions produce a repulsive Madelung potential at the B-ion sites. These repulsive potentials decrease the effective ionization energy (raise the energy levels) for electrons on the B ions. For example, in $SrTiO_3$, the full Madelung potential at the Ti^{4+} site is 45 eV. Similarly, the positively charged B ions provide an attractive Madelung potential of -20 eV at the oxygen site which lowers the O^{2-} level below the B-ion levels. In the d-band insulating perovskites such as $SrTiO_3$ and $LiNbO_3$ the O^{2-} levels will be filled and the B-ion levels will be unoccupied.

The perovskites are not completely ionic and there is some covalent sharing of charge. This has the effect of altering the formal charge on the ions. This effect in $SrTiO_3$, for example, reduces the formal charge on the oxygen ion from -2 to about -1.8 and a corresponding reduction in the cation formal charges. Reduction of the formal charge reduces the Madelung potentials, and changes the energy levels as illustrated in figure 2b. This in turn reduces the energy gap from 17 eV to 3.2 eV.

Next we consider the qualitative effects of the crystal field. The B ion is surrounded by an octahedron of oxygen atoms which produce a cubic crystal field. The d-levels are split by this field into the familiar t_{2g} and e_g levels as illustrated in figure 2c. The d-orbitals transforming according to the t_{2g} representation are d_{xy}, d_{xz}, and d_{yz}. The doubly degenerate e_g level includes the $d_{x^2-y^2}$ and d_{z^2} states. The t_{2g} states have their wavefunction lobes directed in between the repulsive oxygen-ions while the lobes of the e_g states point directly into the repulsive oxygen-ion sites. As a consequence, the t_{2g} states are lowered in energy while the e_g states are raised in energy. The "center of gravity" of the d-level of course in unaffected by the higher order multipoles producing the crystal fields. The oxygen-ions experience an axial crystal field due to the cations and the p-orbitals may be classified as P_σ and P_π according to the orientation of the p-orbital lobes with respect to the cation-anion axis.

Now we proceed to a discussion of the energy band effects, as illustrated in figure 2d for three points in the Brillouin zone. A number of studies, using a variety of techniques, have been reported on the energy band structure. In terms of the simple LCAO model, the largest energies which contribute to the formation of energy bands are:

1) The (pdσ) transfer integral which leads to mixing of the e_g states with p-orbitals (2-4 eV).
2) The (pdπ) transfer integral which leads to mixing of the t_{2g} states with the $p_\perp$-orbitals (1-2 eV).
3) The (ppσ) and (ppπ) transfer integrals which couple p-orbitals on different oxygen sites (few tenths of an eV).

Spin orbit coupling, polaron effects, anion distortion effects, and more distant neighbor interactions are not important in determining the qualitative features and will be ignored in subsequent discussions. The (pdσ) interaction broadens the e_g levels into a conduction band with width of the order of 3-4 eV. The (pdπ) interaction produces a t_{2g} conduction band with width of the order of 2-3 eV. Similar band widths are produced in the valence bands due to both (pdσ) and (pdπ). Additional broadening of the valence band is also produced by (ppπ) and (ppσ). At the point Γ, the t_{2g} and e_g band wavefunctions have pure d character, the mixing with the p-orbitals occurring away from Γ. Note that the t_{2g}-e_g band edge separation at Γ is not equal to the crystal field splitting.

We shall be mainly interested in the lower or t_{2g} conduction band. The surface states which derive from this band and exist in the energy gap between the valence and conduction band have been shown to possess the t_{2g} symmetry important in catalytic activity.

A feature to note in connection with the t_{2g}-bands is the "flat-band" region between Γ and X. This characteristic can be traced directly to the two-dimensional nature of the (pd) transfer integral. For example, in the two center approximation d_{xy} interacts with p_x and p_y but not with p_z; d_{xz} interacts with p_x and p_z but not with p_y and finally d_{yz} interacts with p_y and p_z but not with p_x. As shown quantitatively in our previous papers [9,10,11], this effect leads to three equivalent energy bands, $E_{\alpha\beta}$, ($\alpha\beta$=sy,xz, and yz) each of which depends upon two components of the wavevector (k_α, and k_β) but not on the third. The flat band region results from the lack of dependence on the third component. A more exacting band-theory calculation [12], of course, does not predict an absolutely flat band but does predict very small dispersion and therefore effectively confirms features exhibited here.

There are a great many perovskites, $LaMnO_3$ is an example, which are Mott insulators because exchange and correlation energies are larger than the band width and thus d-electron localization rather than energy band formation results. For these materials the d-electronic structure is nearer to that illustrated by figure 2c than to the band representation of figure 2d.

Figure 2e illustrates the density of electronic states expected for d-band perovskites. The shaded portion is the density of states associated with the three t_{2g} bands. The abrupt jump in the density at the band edges and the approximate logarithmic singularity in the center of the band are a result of the two-dimensional characters of the t_{2g} conduction bands. These properties are easily picked out in density of states histograms, published by Mattheiss [12] based on APW calculations for ReO_3, $SrTiO_3$, $BaTiO_3$, and $KTaO_3$. These features also produce characteristic structure in the optical properties of these perovskites. In a previous paper [11] we developed approximate analytical expressions, from a simple LCAO model, for the energy bands, wavefunctions, density of states,frequency-dependent dielectric function and reflectivity. The structure in the energy dependence of the dielectric function and reflectivity was shown to be in excellent agreement with the experimental data of Cardona [13] on $SrTiO_3$. These analytic expressions provide the basis for a description of the surface states [18].

Density of states diagrams for perovskite materials with localized d-electrons are not shown in figure 2e, but clearly they consist of delta function peaks at the t_{2g} and e_g energies.

We have emphasized the two-dimensional character of the t_{2g} bands because this characteristic is important in relating the d-electron states to the catalytic activity on perovskites. For example, the abrupt jump in the t_{2g}-band density of states in the band edge means that a high density of nearly pure d-electron states exist in a narrow range of energies. This argument, for the perovskites having localized d-electrons, is even stronger.

Where d-electron localization occurs, as in $LaCO_3$, conduction occurs by a "hopping" process. In $LaCoO_3$ the B ion configuration at low temperatures is thought to be $t_{2g}^6\ e_g^0$, but the small energy separation between the filled t_{2g} and empty e_g levels results in a room temperature mixture of "low-spin" ($t_{2g}^6\ e_g^0$) and "high-spin" ($t_{2g}^4\ e_g^2$) cobalt ions (designated Co^{III} and Co^{3+} in the literature). Electron transport involves hopping of electrons between B ions creating Co^{+2} and Co^{+4} electron-hole pairs. p or n-type conduction occurs in doped material. For example, when Sr^{+2} is substituted for La^{+3} in $(La^{+3}_{1-x}Sr^{+2}_x)(Co^{+3}_{1-x}Co^{+4}_x)O_3$ transport involves hopping of Co^{+4} holes in the Co^{+3} lattice. Similarly in the doped $^3(La^{+3}_{1-x}Th^{+4}_x)(Co^{+3}_{1-x}Co^{+2}_x)O_3$ transport involves hopping of Co^{+2} electrons in the Co^{+3} lattice.

In the case of perovskites with localized d-electrons the electronic structure is closer to that described by the crystal field picture, figure 2c. The "cluster" approach is more appropriate than the energy band method. In the cluster model the electronic properties of the perovskite are approximated by those of a BO_6 octahedral complex which is shown in figure 1. The electronic states of similar clusters have been investigated recently by Tossel, Vaughan and Johnson [14] using a self-consistent $X\alpha$ approximation and utilized to interpret the properties of rutile, wustite and hematite. In the application of the cluster method to the perovskites, the effects of the Madelung potentials which are present in the bulk material must be included.

We have studied the character of the cluster states of the BO_6 cluster and their relation to band states in d-band perovskites. A schematic of some of the levels of a typical BO_6 cluster spectrum are shown in figure 3a. The various states are labeled according to octahedral group theoretical notation.

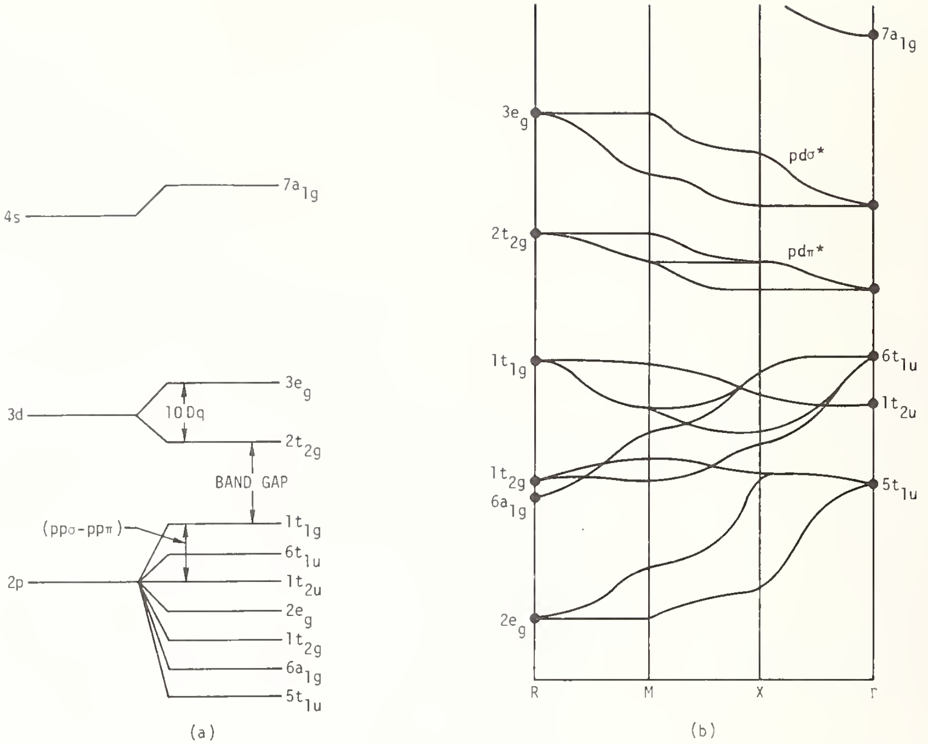

Fig. 3. Cluster and energy band states: (a) states of a BO_6 octahedral cluster; (b) energy bands. The band states with equivalent cluster symmetry are indicated.

The crystal field $3e_g$ and $2t_{2g}$ states correspond to d-orbitals with a 20 to 30% covalent admixture of oxygen 2 p-orbitals. The corresponding valence states, $2e_g$ and $1t_{2g}$, are mostly oxygen 2 p-orbitals with a 20 to 30% admixture of d-orbitals. The t_{2u}, t_{1g} and t_{1u} states are essentially non-bonding states since they involve no hybridization with the cation orbitals. Additional cluster states arise when the B-cation 4s and 4p and oxygen 2s states are included.

In addition to the states discussed previously new states appear because of the added 4p and 2s basis states. The group, $5a_{1g}$, $1e_g$ and $4t_{1u}$ are essentially oxygen 2s states and the $7t_{1u}$ level is derived from the 4p cation states. The 4p states also enter the $5t_{1u}$ levels so that these levels have some bonding character.

There is a strong correlation between the cluster states and the energy band states of the corresponding solid at points of high symmetry in the Brillouin zone [15]. The correspondence for the perovskites is particularly simple. The group of the k-vector possesses full cubic symmetry (O_h) at the points Γ and R in the Brillouin zone. The cluster wavefunctions and energies can be approximately related to the energy band wavefunctions and energies at either Γ or R in the Brillouin zone. These relationships are indicated in figure 3b on the energy band diagram. For example, the upper valence band state at Γ possesses the same symmetry as the $6t_{1u}$ cluster state. One may imagine constructing the band state wavefunction by repeating a cluster wavefunction of $6t_{1u}$ symmetry in every unit cell throughout the entire crystal. Similarly the $pd\pi^*$ band state at R may be constructed by repeating a cluster wavefunction of $2t_{2g}$ symmetry in each unit cell with the phase reversed in adjacent cells. This process is illustrated in figure 4 for the band state Γ_{25} in terms of a cluster state of $1t_{2u}$ symmetry.

The cluster states are mixtures of particular symmetry coordinates which transform according to the irreducible representations of the cubic group (O_h). Specific relationships among the orbitals which make up ligand symmetry coordinates are fixed by symmetry.

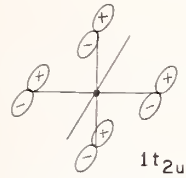

CLUSTER STATE

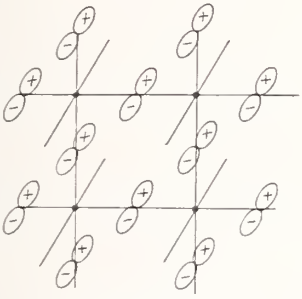

Γ_{25} BAND STATE

Fig. 4. Illustration of symmetry relationship between cluster and band wavefunctions.

In the band model the point group symmetry depends upon the wavevector k. For an arbitrary k-vector arbitrary phase relationships exist among the orbitals making up the energy band wavefunction. As these phases vary with k so do the energies. The dependence of the energy on k determines the energy bands of the solid.

In the insulating oxides such as $SrTiO_3$, $BaTiO_3$, $KTaO_3$ or TiO_2 at the point Γ in the Brillouin zone the $1t_{1g}$ is the highest filled state and the $2t_{2g}$ is the lowest unfilled state. The energy separation between these levels approximates the energy gap which tends to be on the order of 3 eV. The energy difference between the $3e_g$ and the $2t_{2g}$ states is the crystal field splitting 10 Dq.

The insulating materials can be made semiconducting or metallic by introducing oxygen vacancies or by substitution doping. This results in partial occupancy of the $2t_{2g}$ states. In materials such as ReO_3, VO_2 or Ti_2O_3 the cationic configuration is d^1. This additional electron resides in the $2t_{2g}$ state (or $pd\pi^*$-band) and these materials are metallic.

For magnetic materials the exchange and correlation interactions lead to a situation in which the cluster states have different energies for different spin orientations as has been illustrated in recent calculations of Johnson and Messmer [16] for antiferromagnetic NiO. In this case the filling of the spin dependent levels with electrons would not be equal and a net spin results on each cation.

The cluster model serves as a preliminary model for examining the local electronic structure of the oxides and is reasonably appropriate for oxides in which the d-electrons are localized as would be expected in, for example, $LaCoO_3$. On the other hand, there are many oxides for which the d-electrons are delocalized, TiO_2, Ti_2O_3, $SrTiO_3$, $KTaO_3$, and $KMoO_3$ are examples, and the effects of energy band formation must be considered.

2.3. Surface States

Whenever a solid is terminated by a surface or interface, special electronic states occur whose wavefunctions are localized at and near the surface. If a sufficiently large portion of the surface (eg. 100 Å x 100 Å) is regular then the surface states will be characterized by a two-dimensional (real) wavevector $\underset{\sim}{K}$ and two-dimensional surface energy bands E(K) will result. The wavefunctions of the surface state will be characterized by $\underset{\sim}{K}$ and by a complex constant $\gamma(K)$ which determines the decrease of the amplitude of the wavefunction $\psi(K)$ normal to the surface. In most cases the surface state charge density $e|\psi|^2$ will decrease exponentially as $e^{-2\gamma(K)z}$ with increasing distance z into the solid as illustrated in figure 5.

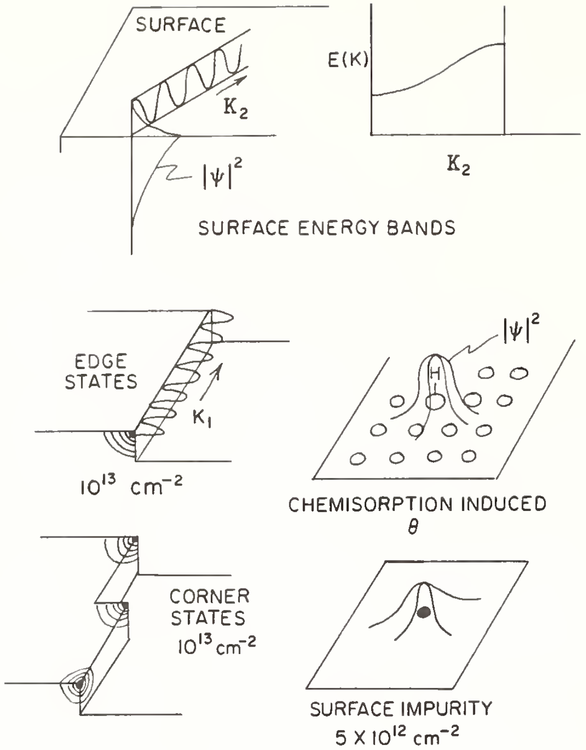

Fig. 5. Schematic of the various types of surface states and approximate densities of states.

A second type of surface state shown in figure 5 is associated with atomic edges or steps, grain boundaries, dislocations or other "line" discontinuities. These states are characterized by a one-dimensional wavevector K_1 and complex decay constants which determine the manner in which the wavefunctions decays perpendicular to the line.

Finally atomic-like surface states occur at the site of a vacancy, intersitial, impurity or chemisorbed atom or molecule. The intersection of a dislocation with a surface or an atomic corner may also produce localized surface states.

The densities of these various possible surface states can be estimated from general considerations. A typical oxide crystal will have 10 d-electron states in a unit cell of 4 Å on a side thereby producing 1.6 x 10^{23} d-electron states/cm^3. Then there will be a 6 x 10^{15} states/cm^2 for two-dimensional surface states.

Assuming one line structure (step or edge) in each square 100 Å on a side leads to a density of line states of the order of 10^{13} cm^{-2}. An impurity content of 10^{19} cm^{-3} would produce 5 x 10^{12} surface impurities/cm^2. All of these densities are significant in an electrochemical reaction. For example, if 6.3 x 10^{12} impurities centers per square centimeter are sites for a reaction in which the reaction time is on the average one millisecond an electrochemical current of one milliampere per cm^2 would result. Chemisorption-induced surface states are of importance by definition and their density will be equal to the surface coverage, θ. Approximate locations of different types of surface states are indicated in figure 6 on the energy band diagram for $SrTiO_3$.

The degree of localization of a surface state on a solid having energy bands increases with the energy separation between the surface state and the corresponding bulk energy. Highly localized surface states occur only in energy regions forbidden to the normal bulk states. Thus if highly localized surface states occur they will be found in energy gaps. In this respect non-metallic materials such as insulators and semiconductors provide more opportunity for the occurrence of well defined, highly localized surface states than do metals. Insulators and semiconductors have a global energy gap in which surface states can occur. By contrast a transition metal does not possess a global energy gap in the energy range near the d-bands. Instead surface states can only exist in small local energy regions provided by the sp-d hybridization gaps.

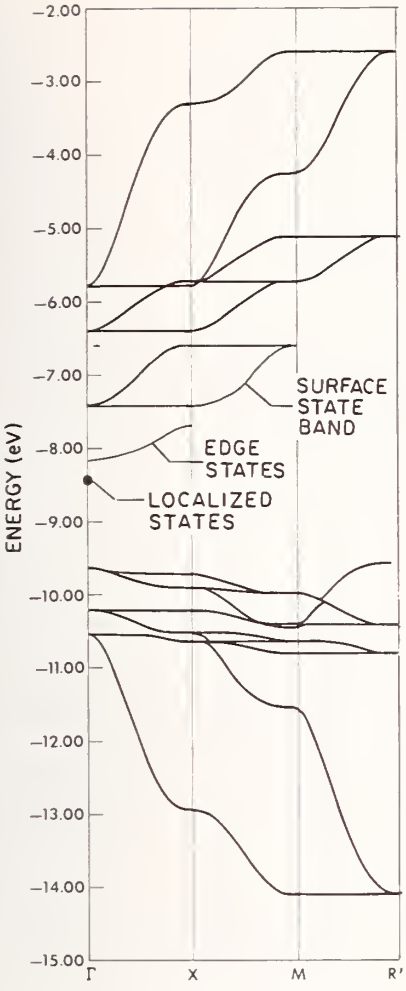

Fig. 6. Energy bands of $SrTiO_3$. Solid curves full LCOAO model.

2.4. Origion of Intrinsic Surface States

Surface states which occur on a surface in the absence of foreign atoms are called intrinsic surface states. The major factors which produce intrinsic surface states and which influence the energy of such states are:

(a) Missing neighboring atoms
(b) Changes in the electrostatic potentials at a surface
(c) Changes in the covalent bonding interactions at the surface
(d) Relaxation of the surface layers and changes in the interlayer spacings
(e) Reconstruction of the surface structure

In ionic crystals such as the oxides the electrostatic potentials acting on the surface ions are substantially altered due to missing neighbors. This effect can be calculated exactly [9]. Variation in the Madelung potentials at Ti or oxygen surface site is illustrated in figure 7 for a type I configuration of a (001) surface (see fig. 8) of $SrTiO_3$. The Madelung potential at the surface Ti site is reduced by about 2 eV while that for a surface oxygen is essentially unchanged from its bulk value. On a type II surface (obtained by removing the top layer from the type I surface, see fig. 8) the oxygen and strontium ions are exposed while the titanium ion is buried in the next layer. For the type II surface the oxygen Madelung potential is increased (towards vacuum) by 3 eV while the Ti potential is unchanged from its bulk value.

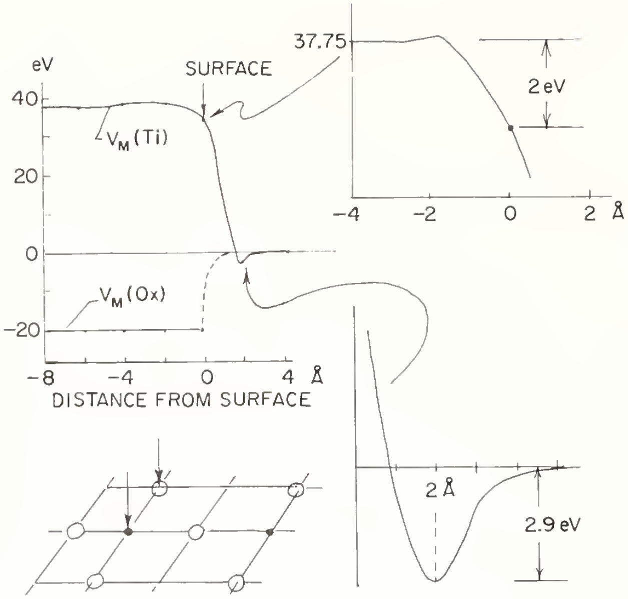

Fig. 7. Madelung potentials as a function of distance above and below a (001) surface on $SrTiO_3$.

TYPE I SURFACE (a)

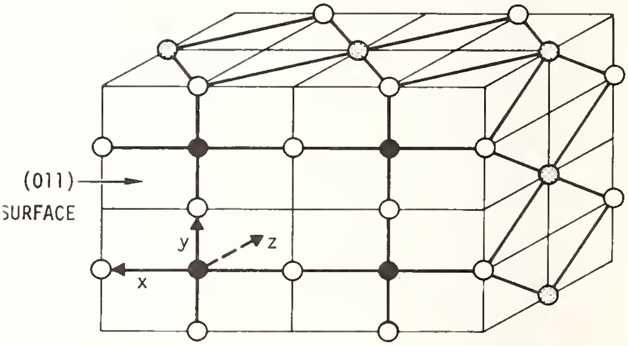

TYPE II SURFACE (b)

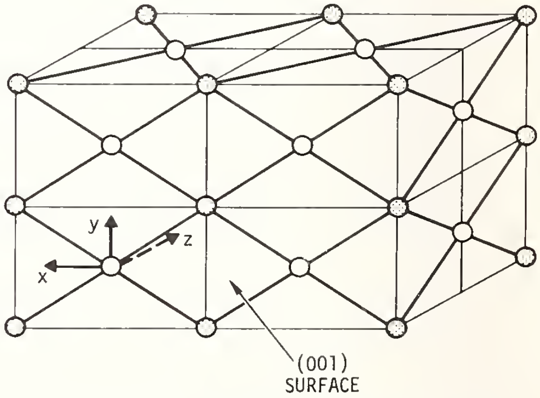

Fig. 8. Illustration of the type I and type II (001) surfaces of a perovskite structure. ○ = A ions; ● = B ions; ○ = oxygen.

A second feature of the surface is that due to the missing neighbors the electrostatic crystalline field is no longer cubic. An axial field appears which can cause further splitting of the levels. This is illustrated in figure 9.

Also from figure 7 it is clear that a large electric field will be present at the surface. An estimate places the field in the 10^8 volts/cm range at the Ti surface site.

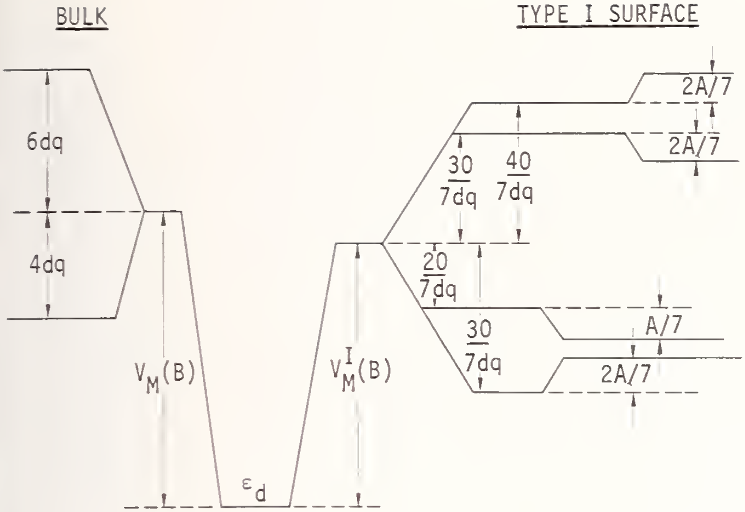

Fig. 9. Crystal field splitting of d-levels including an axial field at a surface ion.

A large electric field will also act on the surface oxygen ion. These fields tend to move the ions out of their normal surface positions. This tendency is countered by elastic restoring forces. However, because for small displacements the electrostatic energy is linear in the displacement while the elastic energy is quadratic, the electric forces prevail as in the Jahn-Teller effect. It can also be shown that small displacements of the surface ions leads to increased electronic bonding [10]. One possible result of these forces is to produce "puckering" of the surface ions or an undulating surface. The precise configuration of the surface ions is not yet known, but recent electron spin resonance measurements suggest that the axial field component produced at the surface is only a few percent of the crystal field energy (10 Dq) indicating that the electric field has been greatly reduced. We shall ignore the possible Stark splitting due to surface electric fields in this discussion.

It is also clear from figure 7 that the electrostatic Madelung fields extend several angstroms out beyond the surface. The potential above a Ti ion, for example, exhibits a 3 eV attractive minimum at about 2 Å above the surface. This attractive minimum is believed to be important in attracting surface reactants to cation sites at the initiation of a surface reactions. We shall return to this possibility later.

2.5. Cluster and Energy Band Surface States

As an introduction to surface states which occur on the transition metal oxides we consider a cluster consisting of a transition metal cation surrounded by an octrahedron of oxygen ions. The cluster analogs of the surface states are defined as follows. The type I states correspond to a BO_5 cluster with a reduction in the electrostatic Madelung potential acting on the cation. Type II cluster surface model corresponds to a BO_6 cluster with the Madelung potential of one of the oxygen ions increased.

The surface cluster levels are shown in figure 10b and compared with the unperturbed cluster levels. The center panel is the unperturbed cluster states. Figure 10c shows the Type I cluster surface states and figure 10a shows the Type II cluster surface states.

For the discussions here the important cluster surface states are those derived from the $2t_{2g}$ and $3e_g$ states labeled xy, xz, yz and x^2-y^2 and z^2 in figure 10c. We shall also discuss the valence states e and a_2 derived from the $1t_{1g}$ level. In order to simplify the diagram we show on figure 11 only these levels. The wavefunctions for two of the cluster surface states are shown. The xz, yz surface states derived from the $2t_{2g}$ d-states have d-orbitals pertruding normal to the surface which can react with molecules coming in contact with the surface. The (doubly degenerate) e states have p_z orbital extending normal to the surface.

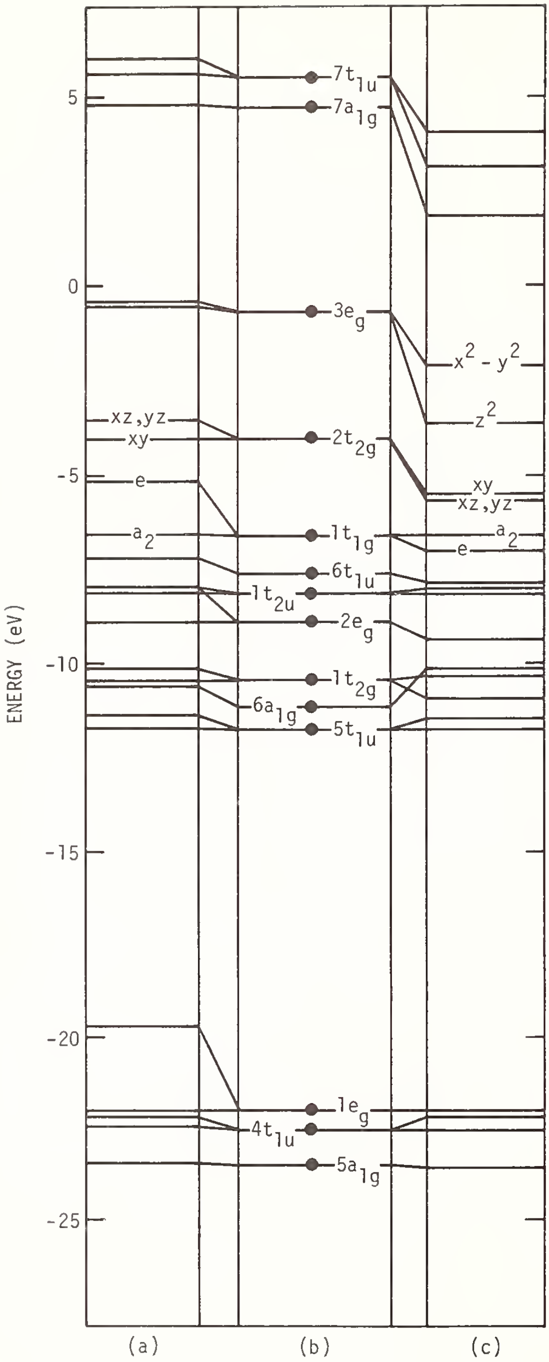

Fig. 10. Cluster states: (a) surface cluster states for a BO_6 cluster corresponding to a type II surface; (b) BO_6 cluster states corresponding to bulk levels; (c) BO_5 surface cluster states corresponding to a type I surface.

When the d-electron surface states are occupied with electrons they provide orbitals of the proper symmetry for strong interaction with the antibonding states of molecular species such as H_2, O_2, and CO and other diatomic molecules. Transfer of electrons from surface states into empty molecular antibonding orbitals by means of hybridization is often important in facilitating dissociative chemisorption. These states also provide ideal orbitals for adsorption of OH^- ions and for interaction with the π electrons of hydrocarbons. We have previously described a model which illustrates the catalytic role of d-band surface states in facilitating the concerted reaction of two ethylene molecules to form cyclobutane [17].

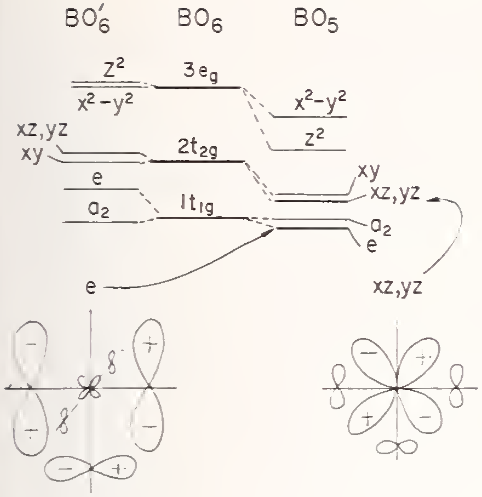

Fig. 11. Cluster states and wave functions of the d- and p-orbital surface states.

In an energy band model surface bands are found which are the analogs of the cluster states just described. The oxides possess a high density of localized d-electron and p-electron surface energy band states in the energy gap between the valence and conduction bands. In previous work [10,17] we showed that for a (001) surface the density of surface states possessed square-root singularities at the band edges. This behavior is characteristic of a 1-dimensional energy band and is a direct consequence of the two-dimensional character of the lower conduction band. The energies and density of states are shown in figure 12 for $SrTiO_3$. The dashed curves indicate the bulk energy bands while the surface states are shown as solid curves. The cross-hatched regions of the surface density of states indicates a small energy range which each contain 10% of the total density of

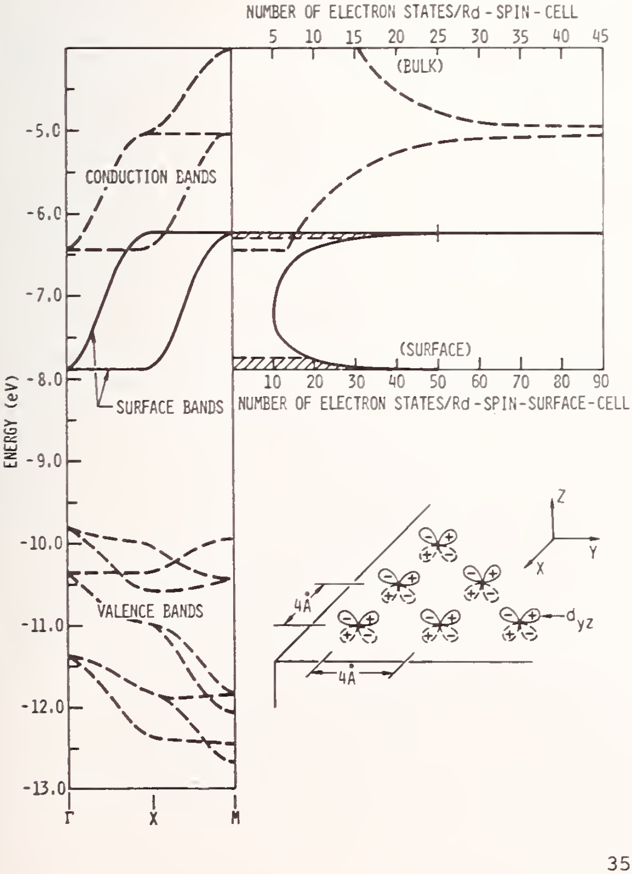

Fig. 12. Bulk and surface energy bands for $SrTiO_3$. The density of states for the bulk and surface band are shown on the right hand side of the figure. The hatched areas each contain 10 % of the total surface state density (1.2×10^{14} states/cm^2). The lower right portion illustrates one of the two equivalent d-orbital surface states near the bottom of the surface band.

states. The states corresponding to the lower cross-hatched region are nearly pure d-electron states having the t_{2g} symmetry. This region contains about 1.2×10^{14} states per cm^2. The surface state wave function for states in this region is shown on the right hand side to consist of an array of d_{yz} orbitals. Equivalent surface states composed of d_{xz} orbitals are degenerate with the d_{yz} states.

Surface states are also split-off from the pdσ* bands and from the oxygen valence bands. One type of surface band derived from the pdπ valence band having p_z symmetry is believed to play an essential role in one mechanism for the dissociation of H_2. This will be discussed in the next section.

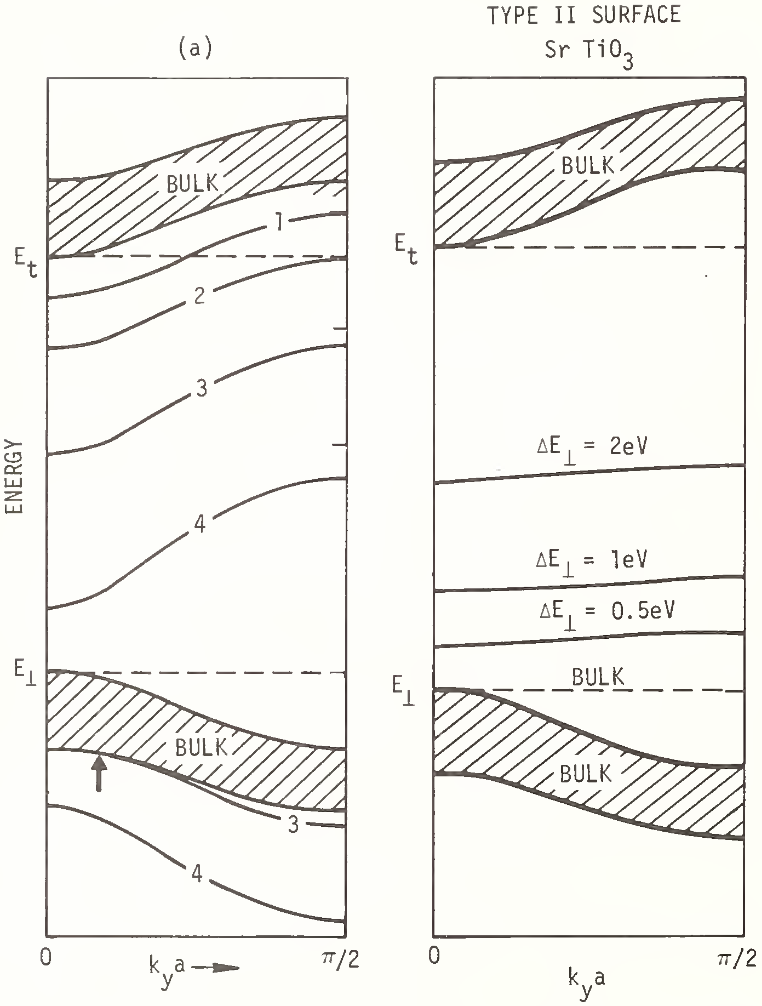

Fig. 13. Surface energy bands on $SrTiO_3$. The numbered curves correspond to different surface perturbations. For details see reference [10].

In previous work we reported a study of the dependence of surface energy bands on surface perturbations. Some of these results are shown in figure 13. The different surface bands correspond to different surface perturbation parameters. The details are described in reference 10. The point to be noted here is that both d-band and p-band surface states occur in the energy gap and that on a non-uniform surface a distribution of such bands may be anticipated corresponding to various crystallographic facets and surface irregularities.

A comparison of the d-electron surface bands for an ideal (001) type I surface of $SrTiO_3$ with the corresponding cluster surface states is shown in figure 14. The cluster energies are the same as those shown in figure 10. The unperturbed cluster levels $3e_g$ and $2t_{2g}$ are shown at R in the Brillouin zone and the cluster surface states are shown at M in the zone for reasons described earlier. The solid curves are the bulk energy bands and the dashed curves are the surface energy bands.

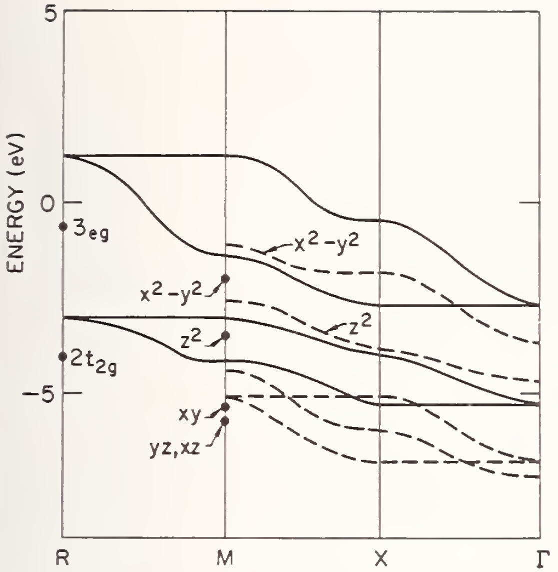

Fig. 14. Comparison of cluster states with the energy band states of $SrTiO_3$. The BO_6 cluster states $3e_g$ and $2t_{2g}$ are compared to band states at R in the Brillouin zone. The cluster surface states x^2-y^2, z^2, xy, xz and yz are compared with band states at M.

The electronic structure of TiO_2 and Ti_2O_3 surfaces has been studied recently by Henrich, Dresselhaus and Zeiger [19] using electron energy-loss spectroscopy. They observe a large peak at 1.5 to 2 eV in the electron energy-loss spectrum of freshly broken samples of Ti_2O_3 but not for TiO_2. After sputter-etching with Ar ions the TiO_2 samples also exhibited the 2 eV peak. Subsequent exposure to oxygen removed the peak in TiO_2 and diminished the intensity in Ti_2O_3. The sputter-etching by Ar ions was believed on the basis of Auger studies to reduce the surface.

Henrich, Dresselhaus and Zeiger suggest that the 2 eV peak may be associated with $Ti^{+3}(3d^1)$ surface ions on Ti_2O_3 or created on TiO_2 by the sputter-etching process. The 2 eV energy is then attributed to transitions between the crystal-field-split levels of the $3d^1$ states of Ti^{+3} ions.

Transitions between crystal field surface states, $XZ \rightarrow Z^2$ may be involved. According to cluster calculations 10Dq is about 3 to 3.5 eV and therfore the transition for an octahedrally coordinated Ti ion would be too large to explain the 2 eV peak. However, as illustrated in figure 10, the splitting of the d-electron states of a TiO_5 cluster $(E_{XZ}-E_{Z^2})$ is reduced to about 2.0 eV. The band model gives the same result.

Frank et. al [20] have obtained electrochemical data for the standard potential of a number of redox couples in nonaqueous acetonitrile from which they were able to deduce the existence of surface states on n-type TiO_2 and other semiconducting electrodes. Their results indicate a density of surface state at energies about 1 eV below the conduction band. This is in rough agreement with our theoretical results which show the XZ, YZ surface states lie about 1.5 eV below the $2t_{2g}$ level (see figure 10).

3. Chemisorption and Catalytic Processes

In this section we discuss in a qualitative fashion some mechanisms for chemisorption and catalysis which can be described utilizing the cluster and energy band surface states from the previous section.

3.1. A Mechanism for Adsorption of OH^- Ions

It is well known that oxides have an affinity for adsorption of OH^- ions. The surface coverage can be substantial, particularly when the surface is in aqueous solution.

It is obvious that a surface O^{2-} anion can form an OH^- ion by accepting a proton from a hydronium ion (H_3O^+) in solution. This process is energetically favorable since the positively charged H_3O^+ ion will be attracted by the Madelung potential to a position directly above the oxygen ion (see figure 8) and σ-bonding to a p_z oxygen orbital can occur. Electrostatic energy is also gained when a surface O^{2-} ion is oxidized to a OH^- ion.

The process by which an OH^- ion becomes bound to a surface cation is less obvious. One possible mechanism is illustrated in figure 15 which shows the molecular orbitals of the OH^- ion together with cluster surface orbitals which bond strongly. For the discussion here we treat the non-bonding OH^- states as simply the oxygen $2p_x$ and $2p_y$ orbitals and the bonding state is an oxygen $2p_z$ orbital σ-bonded to a hydrogen 1s state. The OH^- ion is assumed to be attracted to the surface by the attractive Madelung potential 2Å directly above the cation site (see fig. 7). For discussion of this example we use the TiO_5 cluster results. The OH^- energy levels are determined approximately by several estimates. The ionization energy and dissociation energies of OH^- are 2.1 and 5 eV respectively [21,22]. The separation between the non-bonding and bonding states is approximated by one half of the dissociation energy; 2.5 eV. The ionization energy refers to the liberation of an electron from a non-bonding state. Thus we locate p_x and p_y at $-2.1 -2.9 = -5$ eV below the vacuum level where the -2.9 eV term is the attractive Madelung potential above a Ti surface ion. The bonding state then is located at -7.5 eV below the vacuum level.

In solution solvation of the OH^- ion and the Helmholtz layer will alter these gas phase energies in a manner which is not known precisely. It would be expected that the energies will be shifted towards the vacuum level. However, the energies of the surface states will also be shifted towards vacuum for a typical semiconducting electrode because of band bending at the surface. In the absence of more information we assume these shifts are comparable and therfore omit them in the energy level diagram. This approximation should not invalidate the mechanisms of adsorption to be discussed, however, the numerical results should not be taken too seriously.

The hybridized energy levels are determined by using the values of the two-center LCAO transfer integrals determined by Mattheiss [12] or Wolfram, Hurst and Morin [15] which both give $(pd\sigma)\sim 2$ eV, $(pd\pi)\sim 1$ eV for $SrTiO_3$ or TiO_2.

From figure 15 it is clear that levels (a) and (b) represent the antibonding states of an OH^- surface complex. Except for the proton the wavefunctions are very similar to the bulk 3 e_g and $2t_{2g}$ BO_6 cluster states. Occupation of these antibonding states by electrons will reduce the OH^- binding energy and therefore it follows that the maximum bond will occur on an insulating crystal such as $SrTiO_3$ or TiO_2. Minimum bonding of OH^- will occur when the xz, yz and z^2 surface states are occupied. In $LaCoO_3$ and its

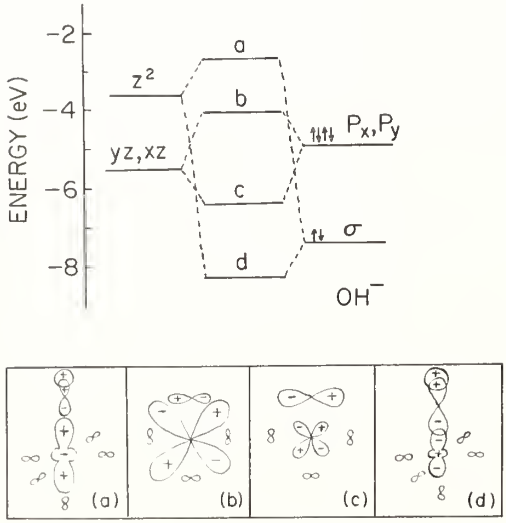

Fig. 15. Energy levels and wavefunctions for the hybridization of OH^- non-bonding states with d-electron surface states.

mixed crystals the bulk $3e_g$ states are partially occupied and on the basis of figure 15 a smaller binding energy would be expected as compared with TiO_2, for example.

Alternately the antibonding levels can be occupied by application of a cathodic bias which may also tend to move the OH^- towards OH^{2-}. Thus with cathodic bias OH^- may be discharged leaving an exposed cation. This cation may then serve as a catalytic site for the associative desorption of H_2 by combining hydrogen atoms attached to adjacent surface oxygen anions. The inverse process, the dissociative adsorption of H_2, will be discussed subsequently.

Finally we note that for OH^- attached to a surface cation it may be energetically favorable for the proton to migrate to an adjacent surface anion and then to an interior anion.

3.2. A Mechanism for Dissociative Adsorption of H_2

We consider H_2 in the gas phase interacting with a n-type reduced or doped oxide such as $SrTiO_3$ or TiO_2. The filled bonding states, $\sigma(H_2)$, and the empty antibonding states, $\sigma(H_2)^*$, of molecular hydrogen are located at about -15 and -10 eV respectively. The Fermi-level of the substrate is assumed to lie within the lower conduction band at about -5.5 eV (xz state, figure 10) so that in the cluster picture the xz surface state is occupied while the z^2 state is empty. When the H_2 molecule approaches the surface as illustrated in figure 16, hybridization of the xz and $\sigma(H_2)^*$ and hybridization of the z^2 and $\sigma(H_2)$ orbitals occurs. Because of the large energy separation between the z^2 and $\sigma(H_2)$ states the latter process is unimportant in <u>this</u> example. The hybridization of xz and $\sigma(H_2)^*$ leads to electron transfer from the substrate to the molecule. The electrons residing in the hybrid state have several effects. First, they constitute the formation of Ti-H bonds. Second they weaken the H-H bond and third, they cause the H-H internuclear bond length to increase. Finally, they cause the $\sigma(H_2)^*$ state to rise in energy (towards the affinity level of H_2^- which is only -0.7 eV) due to the Coulomb repulsion among the electrons. As the state rises in energy the interaction between $\sigma(H_2)^*$ and xz is enhanced because these levels move closer together in energy and because the molecule is being pulled in towards the surface. Thus a positive feed back situation exists in which the transfer of charge invites the transfer of even more charge. The process is terminated by two factors. The first factor is that eventually the effective energy of $\sigma(H_2)^*$ would rise above the Fermi-level of the substrate due to Coulomb repulsion. Second, as charge transfer occurs the H-H bond length increases eventually moving the hydrogen atoms away from the Ti ion as the molecule proceeds along the reaction coordinate. The maximum bonding to the Ti ion

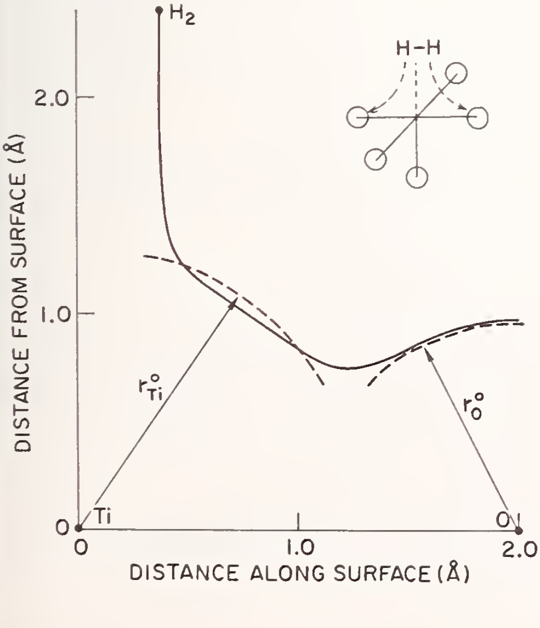

Fig. 16. Bond order model calculation for the dissociative chemisorption of H_2 on $SrTiO_3$ showing the trajectory of H atoms along the reaction coordinate.

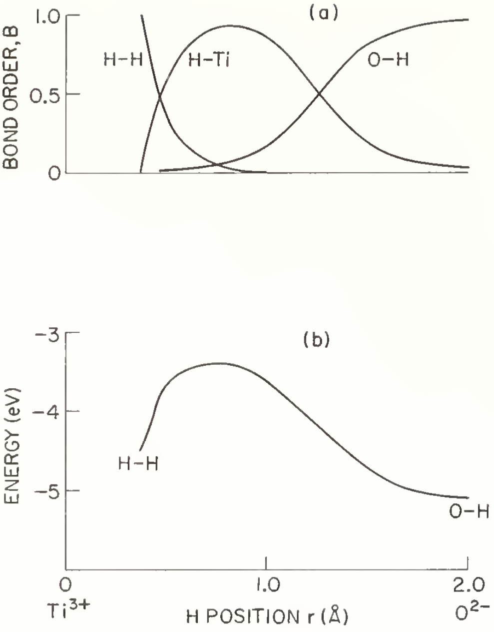

Fig. 17. Bond order calculation of the dissociative chemisorption of H_2 on $SrTiO_3$ showing (a) the bond order and (b) the total bond energies as a function of the reaction coordinate.

occurs when the H-Ti bond length is about 1.2 Å as shown in figure 17 and the H-H bond length has increased from 0.75 Å to about 1.5 Å. This means that the molecule is effectively dissociated.

The formation of OH^- ions now proceeds by interaction of the individual atomic hydrogen atoms with the e oxygen surface states (see figure 10) which have p_z orbitals projecting normal to the surface. As can be seen from figure 17 (b) the process is energetically favorable. As the hybridization with the e oxygen states proceeds the Ti-H bonds are weakened. Conceptually the weakening of the Ti-H bonds means that electrons are flowing out of the $\sigma(H_2)^*$ state and back into the xz surface state. This lowers the coulomb repulsion energy and drops the hydrogen levels into registry with the e oxygen states. Again a positive feedback situation exists so that as charge leaves the extended hydrogen molecule the individual hydrogens become strongly bound to the surface oxygen ions. The protons may now migrate over the surface and into the crystal so that the same site is again available for catalysis.

The results displayed in figures 16 and 17 were obtained by use of a bond-order model similar to that described by Weinberg et al.[23] but modified to include the presence of a Fermi level.

According to figure 17 the process has a 1.1 eV activation energy in the gas phase. This barrier may be greatly reduced for reactions in solution where the coulomb repulsion energy is reduced by solvation effects and by mobile electrolyte ions in the Helmholtz layer.

The inverse of the reaction described here would lead to hydrogen evolution at an oxide cathode.

Several other mechanisms for the dissociative adsorption of H_2 are also conceivable. For example, Burwell has suggested a "heterolytic" process in which one hydrogen atom adsorbs to an oxygen surface ion while the other adsorbs on the adjacent surface cation. The relative importance of various mechanisms is not well established.

3.3. Role of d-Electron Surface States in Concerted Reactions

We present here a schematic discussion of the concerted reaction of molecular hydrogen with ethylene to form ethane. The purpose here is to illustrate qualitatively how the hybridization of reactants with surface orbitals can lower an electronic activation energy barrier.

Hydrogenation of an alkene such as ethylene is an exothermic reaction but it does not proceed in the gas phase without the aid of a catalyst such as a transition metal or transition metal oxide. α-Cr_2O_3 (chromia), for example, will catalyze the hydrogenation of ethylene [24].

There are several different mechanisms that have been proposed for the hydrogenation process. Most of these assume the dissociative adsorption of H_2 on the catalyst as an initial step. Here we describe how the concerted reaction might be catalyzed by the surface states of a transition metal oxide. The relative importance of this mode of hydrogenation is not known and therefore this example should be regarded as illustrative.

Consider first the reaction of H_2 with C_2H_4 in the gas phase without a catalyst. The hydrogen and ethylene molecules are assumed to approach each other along the reaction coordinate shown in figure 18. On the right of the figure we show the approximate locations of the bonding, $\sigma(e)$, and antibonding, $\sigma(e)^*$, states of the C-H bonds which are formed in the reaction. On the left of the figure we show the approximate locations of the relevant bonding and antibonding states of the non-interacting reactants. These energies are based on experimental and theoretical results in the literature [25-27].

The reaction coordinate is the C-H distance of the incipient bonds and the reaction proceeds from left to right on the diagram. The diagram is schematic but we have attempted to indicate typical energies.

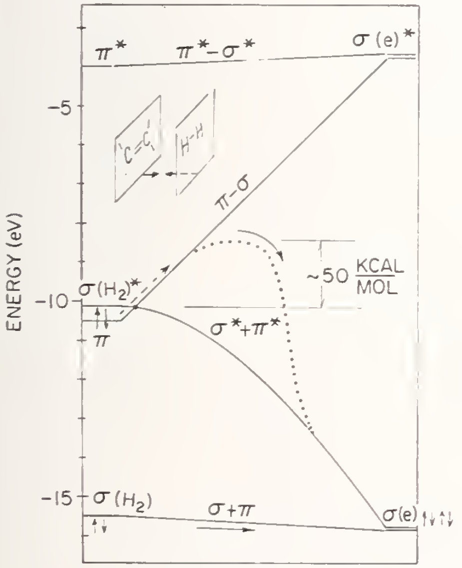

Fig. 18. Schematic of the correlation diagram for the concerted reaction of H_2 with ethylene to produce ethane. Arrows indicate electron flow. The dotted curve illustrates an activation energy of about 50 Kcal/mol per electron.

As the distance between the reactants decreases (left to right) various hybrid orbital states are formed representing the intermediate states of a $H_2 \ldots C_2H_4$ complex. The strongly interacting combinations are: $\sigma(H_2)$ with π to form the bonding combination designated as $\sigma(H_2)+\pi$ and the antibonding combination $\pi-\sigma(H_2)$; $\sigma(H_2)$ with π^* to form the bonding combination $\sigma(H_2)+\pi^*$ and the antibonding combination $\pi^*-\sigma(H_2)$. Bonding here means those combinations which concentrate charge in the region in which the new C-H bonds are formed. Antibonding combinations deplete charge from the C-H regions. From such considerations it is evident how to connect the various branches to the product states $\sigma(e)$ and $\sigma^*(e)$. A schematic of the energies of different branches along the reaction coordinate is given in figure 19.

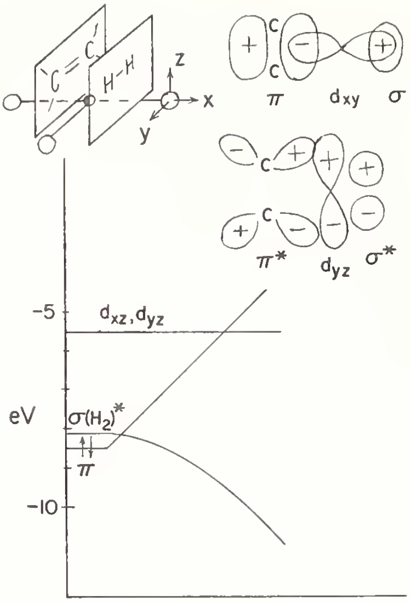

Fig. 19. Correlation diagram showing the d-electron surface state level before hybridization. Strongly bonding combinations of molecular and surface state orbitals are indicated at the top of the figure.

In the non-interacting condition the $\sigma(H_2)$ and π levels are each occupied by a pair of electrons. Both of these pairs must be delivered to the $\sigma(e)$ levels of ethane for a ground state reaction to occur. The problem is that the occupied π-$\sigma(H_2)$ branch does not correlate with $\sigma(e)$ but rather with $\sigma^*(e)$. At cross-over between the π-$\sigma(H_2)$ and $\sigma^*(H_2)+\pi^*$ it could be assumed that the electron pair switches branches. Woodward and Hoffman [28] have argued that such a transfer is symmetry forbidden because gross charge redistribution would have to occur. Thus electron flow is constrained to the π-$\sigma(H_2)$ branch as indicated by the dashed arrow. It can be argued that at some point of close approach this symmetry selection rule must break down due to the imperfect alignment, asymmetrical vibrations and electron-electron interactions. The result will be that the pair of electrons in the π-$\sigma(H_2)$ branch will eventually switch to the $\sigma^*(H_2)+\pi^*$ branch whereupon they may be delivered to the $\sigma(e)$ levels of ethane. The branch switching and electron flow as indicated schematically in figure 19 by the dotted curve and the solid arrow.

There still remains a sizable energy barrier of the order of 50 to 100 Kcal/mole which is a direct result of the failure of the hybridized reactant states to correlate properly with the ground state orbitals of the product. Consideration of grossly asymmetrical reaction configurations does not improve the situation because then geometrical barriers can arise which are larger than the activation energy for the symmetrical case [29].

The assumption that the electrons do not switch branches near cross-over in figure 18 does not rest entirely upon symmetry considerations. Suppose that transfer from π-$\sigma(H_2)$ to $\sigma^*(H_2)+\pi^*$ does occur. Because the crossing is so near to the $\sigma^*(H_2)$ and the π energies the approximate electronic configurations after electron transfer would be $\sigma(H_2)^2\sigma^*(H_2)^2$ for the hydrogen molecule and π^0 for the ethylene molecule. These configurations correspond to $H_2{}^{2-}$ and $C_2H_4{}^{2+}$ and thus a large energy would be required for the creation of such species. This is not apparent in a one-electron energy level diagram such as figure 18 because the effects of changes in orbital populations are not included. If such effects were included the actual crossing of energy levels would occur near the apex of the dotted correlation curve in figure 18. At the apex of this curve the molecules are sufficiently close to each other that the energy loss in H-H bonding and in π bonding is compensated by the formation of the new C-H bonds. The charge in the $\sigma^*(H_2)+\pi^*$ branch now resides in orbitals which approximate those of an ethane molecule with extended C-H bonds rather than in orbitals resembling those of $H_2{}^{2-}$ or $C_2H_4{}^{2+}$.

Now consider the reaction as it occurs on a catalytic substrate. When the reactants come in contact with a solid surface the ionization potentials will be modified due to molecular relaxation [30] and screening [31]. For example, DeMuth and Eastman found that the effective ionization potential of the π-level of ethylene on nickel was shifted by 2.1 eV towards the vacuum level. This type of shift is separate from bonding shifts due to chemisorption.

Similar relaxation shifts were also found for benzene and acetylene on nickel. As an estimate of these effects we shall assume that all of the relevant molecular levels are shifted by 2 eV towards vacuum as shown in figure 19. The xz, yz surface state of the TiO_6 cluster located at -5.5 eV are shown before interaction in figure 19a.

The strongly bonding combinations of molecular and surface orbitals are π and $\sigma(H_2)$ with d_{xz} and π^* and $\sigma^*(H_2)$ with d_{yz}. Next, assuming that the surface states interact with the appropriate molecular states through a two-center transfer integral with a maximum strength of 1 eV we arrive at the diagram shown schematically in figure 20. There are two important effects. First, we note that if the d_{yz} state is occupied with electrons then hybridization with the $\pi^*+\sigma^*(H_2)$ branch provides a symmetry-allowed path for transfer of electrons from the surface state into the $\sigma(e)$ levels of ethane. Second, due to hybridization of π-$\sigma(H_2)$ with d_{xz} electrons in this branch can be transferred from the reactants to the surface state. Along the reaction coordinate both transfer process occur so there is little or no net charge transfer between the surface states and the reactant molecules. To emphasize this aspect we use the charge transferred from d_{yz} into $\sigma^*(H_2)+\pi^*$ as the reaction coordinate in figure 20. The charge transferred from π-$\sigma(H_2)$ to d_{xz} is assumed to be equal. At the completion of the reaction the surface state is unchanged as it must be in a catalytic process.

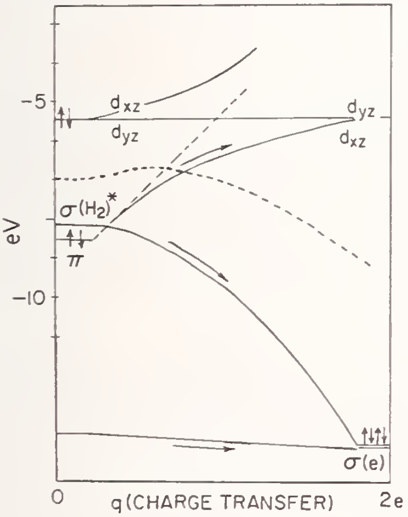

Fig. 20. The effect of d-electron surface states on the hydrogenation of ethylene correlation diagram. The dashed line is a schematic of the total energy of the surface complex as a function of the charge transfer, q.

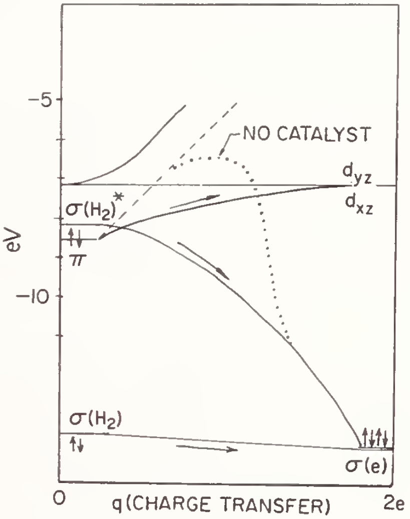

Fig. 21. The effect of d-electron surface states near the $(H_2)^*$ level on the correlation diagram for the dydrogenation of ethylene.

The total energy for the electrons involved in the surface complex is shown schematically by the dashed curve in figure 20. The diagram suggests that the activation energy can be substantially lowered by hybridization with surface states of the proper symmetry.

We note that this catalytic mechanism requires that the surface states be partially occupied with electrons and that the effectiveness is increased as the surface state energy approaches the $\sigma^*(H_2)$ energy. In figure 21 a correlation diagram is illustrated for surface states which are close in energy to the π-level.

4. Energy Band Theory of Chemisorption

Many of the transition metal oxides of interest have d-electron energy bands. A more realistic treatment of the mechanisms of chemisorption and catalysis should include the effects of electron delocalization. In this section we describe a band theory model for investigating chemisorption and catalysis on transition metal oxides such as the perovskites.

The cluster model approximation is valuable in understanding the local electronic structure of strong chemisorption bonds, but the effects of energy band formation are not included. When the states of the substrate form bands of substantial width (several eV), the nature of the hybridization of surface orbitals with molecular orbitals can be altered significantly from that suggested by a simple cluster model. The energy levels associated with chemisorption bonds can be displaced and broadened into bands. A greater variety of symmetries are represented by band wavefunctions so that a greater variety of geometries for molecule-solid interactions are possible.

These effects mean that the chemisorption process involves the formation of virtual localized electronic states in which the bonds are shared by many substrate atoms because of electron delocalization. The chemisorption energy can no longer be computed from a "single bond" model.

Various approaches to an energy band model have been employed recently [34-37] which make use of Green's function methods. The solid is usually characterized by energy band states and the chemisorbing atom by a single atomic state. The interaction between the molecule and the solid is described by matrix elements between the atomic state and each band state.

There are several problems encountered in a band theory. First, the interaction matrix elements are complex function of the k-vector and their form is difficult to obtain. Often, the k-vector dependence is ignored and an average matrix element is employed as a parameter. Such approximations are very poor and obscure the nature of molecule-solid hybridization--that is the actual mechanisms of chemisorption. A second problem is that surface states rather than bulk states are involved in surface reactions. In principal surface states are included in the usual formalisms. In practice, however, surface states are seldom included in evaluation of the model. The symmetry properties of the d-orbitals are often neglected in applications of existing band models.

The basic problem in beginning with states characterized by a wavevector for the solid is that it is a poor starting point for describing localized surface interactions which lead to the formation of localized electronic states (chemisorption bonds). A reasonably accurate picture of the localized interactions, hybridization, and bonding in terms of molecular orbitals already exists. Therefore a suitable model for describing chemisorption should take advantage of this knowledge. This can be accomplished by beginning from a description in which the solid and reacting molecules are treated on an atomic orbital basis. In such a basis a large amount of existing quantum chemistry can be inserted directly into the model.

4.1. Localized Orbital Model for Chemisorption on a Perovskite Surface

We describe a relatively simple model for the interaction of a molecule with a perovskite surface. The oxide is represented by the cation d-orbitals and anion 2p-orbitals and their interactions. The molecule is represented by the atomic orbitals of its constitutent atoms and by their mutual interactions. Since we may wish to be able to describe a process such as the dissociative chemisorption of H_2 we want to employ atomic rather than molecular orbitals because when dissociation occurs molecular orbitals become inappropriate states. The interactions between the atoms of the molecule and those on the surface of the solid are also expressed in terms of atomic orbitals. In this representation we can make use of quantum chemical calculations of atomic overlap and transfer integrals and their dependence on distance. The symmetry constraints which dominate orbital interactions are also easily accounted for in this approach.

The Hamiltonian for the system is

$$H = H_M + H_S + H_{MS}. \tag{4.1.1}$$

The component H_M describes the molecule, H_S describes the substrate and H_{MS} describes the molecule-solid interactions. The Hamiltonian for the atoms of the molecule is

$$H_M = \sum_{\alpha j\sigma} \varepsilon_a \; n_{\alpha j\sigma} + \frac{1}{2} \sum_{\alpha j\sigma} U_{\alpha j} \, n_{\alpha j\sigma} \, n_{\alpha j-\sigma} + \sum_{ij\alpha\beta} V_{ij\alpha\beta} \, a^+_{\alpha i\sigma} \, a_{\beta j\sigma} \tag{4.1.2}$$

where ε_a is the effective ionization energy for an electron in an atomic orbital of the molecule. The subscripts α,j,σ designate the atoms (α=1,2,...), the orbital (j = s, p_x, p_y, p_z, etc.), and the spin respectively. Operators $a^+_{\alpha j\sigma}$ and $a_{\alpha j\sigma}$ create and destroy electrons in localized atomic states. The quantity $U_{\alpha j}$ is the Coulomb repulsion integral for electron-electron interactions and the operators $n_{\alpha j\sigma}$ are number operators for each atom and spin-orbital and $V_{ij\alpha\beta}$ are the interactions matrix elements between the atoms of the molecule which produce molecular states. In the absence of substrate interactions H_M is an approximate Hamiltonian for the molecule.

We also treat the solid in an atomic orbital representation in terms of linear combinations of atomic orbitals or Wannier functions. For H_S we have:

$$H_S = H_d + H_p + H_{pd}, \tag{4.1.3}$$

$$H_d = \sum_{Rk\sigma} \varepsilon_{dk} c^+_{Rk\sigma} c_{Rk\sigma} + \frac{1}{2} U_d \sum_{Rk\sigma} n_{Rk\sigma} n_{Rk-\sigma}, \tag{4.1.4}$$

$$H_p = \sum_{R'm\sigma} \varepsilon_{pm} d^+_{R'm\sigma} d_{R'm\sigma}, \tag{4.1.5}$$

$$H_{pd} = \frac{1}{2} \sum_{R,R'km\sigma} \{T_{RR'km} c^+_{Rk\sigma} d_{R'm\sigma} + c.c.\} \tag{4.1.6}$$

ε_{dk} is the effective ionization energy of the d-electron in one of the orbitals including the Madelung potential and electrostatic splitting ($\varepsilon_{dk} = \varepsilon(t_{2g})$ or $\varepsilon(e_g)$ for k = xy,xz, yz or k = x^2-y^2 or z^2) and the operator $c^+_{Rk\sigma}$ and $c_{Rk\sigma}$ create and destroy electrons respectively in d-orbitals with spin σ at a lattice site located at R. The Coulomb integral is U_d and $n_{Rk\sigma}$ is the number operator for the d-ion at R. The Hamiltonian for the oxygen ions is given by (4.1.5). Here ε_{pm} is the effective affinity energy for adding an electron to a 2p-orbital (m = p_x,p_y and p_z) on an O^- ion to create an O^{2-} ion and includes the Madelung potential and electrostatic static splitting; $\varepsilon_{pm} = \varepsilon_\sigma$ or ε_π for orbitals parallel and perpendicular to the M-O axis in a ABO_3 perovskite. The operators $d^+_{R'm\sigma}$ and $d_{R'm\sigma}$ create and destroy respectively electrons with spin σ in 2p-orbitals at a lattice site located at R'.

The quantities $T_{RR'km}$ are two-center integrals for the interaction of d-orbital of k-type at lattice site R with a p-orbital of m-type at lattice site R'. The elements of $R_{RR'km}$ are the two-center transfer integrals such as pdπ and pdσ. Cation-cation or anion-anion interactions between atoms in different unit cells may also be added in a similar fashion.

The eigenstates of H_S (in the absence of H_{SM}) are the energy bands of a finite solid perovskite including surface states. Our previous work has shown that this model leads to a reasonably good representation of d-band perovskites [10,11].

The interaction between the atoms of the molecule with those of the substrate is written as

$$H_{SM} = \sum_{R_s \alpha k\sigma j} \{T_{R\alpha k\sigma}\, c^+_{Rk\sigma}\, a_{\alpha j\sigma} + c.c\} + \sum_{R'_s \alpha m\sigma j} \{T_{R'\alpha m\sigma}\, d^+_{R'm\sigma}\, a_{\alpha j\sigma} + c.c\} \tag{4.1.7}$$

The two-center integrals $T_{R\alpha k\sigma}$ and $R_{R'\alpha m\sigma}$ correspond to the parameters for interaction between the atoms of the molecule and the cations and anions of the substrate. The sum over R_s and R'_s in eq. 4.1.7 refers to a sum which includes only a few substrate surface atoms; that is, only those surface atoms which have a direct bonding to the atoms of the interacting molecule. These parameters are strong functions of the reaction coordinate since they depend on the atom-atom internuclear separation and on the atom-substrate geometry. The results of a bond order model and the cluster calculations can be used to determine these parameters as a function of the bond lengths.

The operators a, c and d are Fermions and obey the usual anticommutator relations. The effect of molecule-substrate overlap has been stressed by Schrieffer and Gomer in their "Induced Covalent Bond" model [38]. An approximate method for including overlap has been suggested by Madhukar [39] in which the commutator relations are modified. In this scheme:

$$[a_{\alpha j\sigma}, c^+_{R_s k\sigma'}] = \delta_{\sigma\sigma'} D_{\alpha R_s jk}, \tag{4.1.8}$$

$$[a_{\alpha j\sigma}, d^+_{R'_s m\sigma'}] = \delta_{\sigma\sigma'} D_{\alpha R_s jm}, \tag{4.1.9}$$

where the $D_{\alpha R_s jh}$ and $D_{\alpha R'_s jm}$ are atom-substrate overlap integrals which vanish except for those surface atoms which directly participate in the chemical bonding.

The information characterizing the molecular reaction is contained in the matrix of Green's functions. These functions [40] are defined in general by:

$$G(t)_{A,B} = -i\theta(t) < [A(t), B(t)]_+ >, \tag{4.1.10}$$

$$G(\omega)_{A,B} = \int_{-\infty}^{\infty} e^{-i\omega t} G(t)_{A,B}\, dt, \tag{4.1.11}$$

where A and B are creation and destruction operators and $\theta(t)$ is a unit step function in t (time).

A supermatrix of such functions with diagonal blocks $G^d(\omega)$, $G^{Ox}(\omega)$, and $G^M(\omega)$ are defined by the elements:

$$G^d(t)R_1R_2k_1k_2\sigma\sigma' = -i\theta(t) < [c(t)_{R_1k_1\sigma} c^+(0)_{R_2k_2\sigma'}]_+ > \tag{4.1.12}$$

$$G^{Ox}(t)_{R'_1R'_2m_1m_2\sigma\sigma'} = -i\theta(t) < [d(t)_{R'_1m_1\sigma}, d^+(0)_{R'_2m_2\sigma'}]_+ > \tag{4.1.13}$$

$$G^M(t)_{\alpha\alpha'jj'\sigma\sigma} = -i\theta(t) < [a(t)_{\alpha j\sigma}, a^+(0)_{\alpha'j'\sigma'}]_+ > \tag{4.1.14}$$

The off-diagonal blocks are $G^{d-Ox}(\omega)$, $G^{d-M}(\omega)$, $G^{Ox-d}(\omega)$, $G^{M-d}(\omega)$, $G^{Ox-M}(\omega)$ and $G^{M-Ox}(\omega)$. A typical element of an off-diagonal is, for example,

$$G^{M-d}(\omega)_{\alpha Rjk\sigma\sigma'} = -i\theta(t) < [a_{\alpha j\sigma}(t), c^{+}(0)_{Rk\sigma'}]_{+} > \qquad (4.1.15)$$

A matrix of spectral weight functions (or local density of states) is derived from these Green's functions. Spectral weight functions for an atom of the molecule are, for example,

$$\rho(\omega)_{\alpha j\sigma} = -\mathrm{Im}\; G(\omega)_{\alpha\alpha jj\sigma\sigma} \qquad (4.1.16)$$

For the isolated molecule $\rho_{\alpha j\sigma}(\omega)$ will consist of a (normalized) weighted sum of delta-functions at energies corresponding to the molecular states. When the molecule interacts with the solid the character of $\rho(\omega)$ changes to reflect the formation of hybridized molecule-solid bonds. The spectral weight function can possess both bands and delta-functions which are peaked at energies different from those of the free molecule. The broadening of a peak into a band occurs when a localized state is formed at an energy within the energy range of the bands of the substrate.

The bonding among substrate atoms is also altered by the chemisorption process. This information is contained in the spectral weight functions of surface atoms, $\rho(\omega)_{Rk\sigma}$ and $\rho(\omega)_{R'm\sigma}$, which are defined by

$$\rho(\omega)_{Rk\sigma} = G^{d}(\omega)_{RRkk\sigma\sigma} \qquad (4.1.17)$$

$$\rho(\omega)_{R'm\sigma} = G^{Ox}(\omega)_{R'R'mm\sigma\sigma} \qquad (4.1.18)$$

For the non-interacting substrate $\rho(\omega)_{Rk\sigma}$ (and $\rho(\omega)_{R'm\sigma}$) have a distribution of spectral weight characteristic of the admixture of d-orbital (p-orbital) in the valence and conduction bands including surface states. When interaction occurs the spectral weight of the surface atoms is shifted. Some additional density now occurs at the energies of the chemisorption bonding and antibonding states and some density reduction occurs at substrate band energies. This shifting of spectral weight characterizes the participation of substrate electrons in covalent bonds formed with the atoms of the reacting molecule. A schematic of these features is shown in figure 22.

The energy of chemisorption (heat of adsorption) E_c, can be determined from

$$E_c = E_M^o + E_S^o - E_{SM},$$

where E_M^o and E_S^o are the total energies respectively of the non-interacting molecule and substrate and E_{SM} is the final energy of the interacting systems after chemisorption. This quantity is determined by

$$E_{SM} = -\mathrm{Im}\int_{-\infty}^{E_f} d\omega\; \omega \mathrm{Tr}\{\overline{G}(\omega)\}, \qquad (4.1.19)$$

where E_F is the substrate Fermi-energy, Tr indicates the trace of a matrix and $\overline{G}(\omega)$ is the entire super matrix of Green's functions.

The formal application of the model is fairly simple, but obtaining self-consistent solutions is a major problem. The Green's function matrix elements can be calculated if suitable approximations are made to treat the electron-electron terms. Assuming suitable approximations are made, the Green's functions may be calculated in terms of certain (unknown) quantities such as the electronic occupation of various eigenstates. The actual energy of these states is dependent on a knowledge of their occupation because of the electron-electron interaction terms. The occupations in turn are dependent upon the

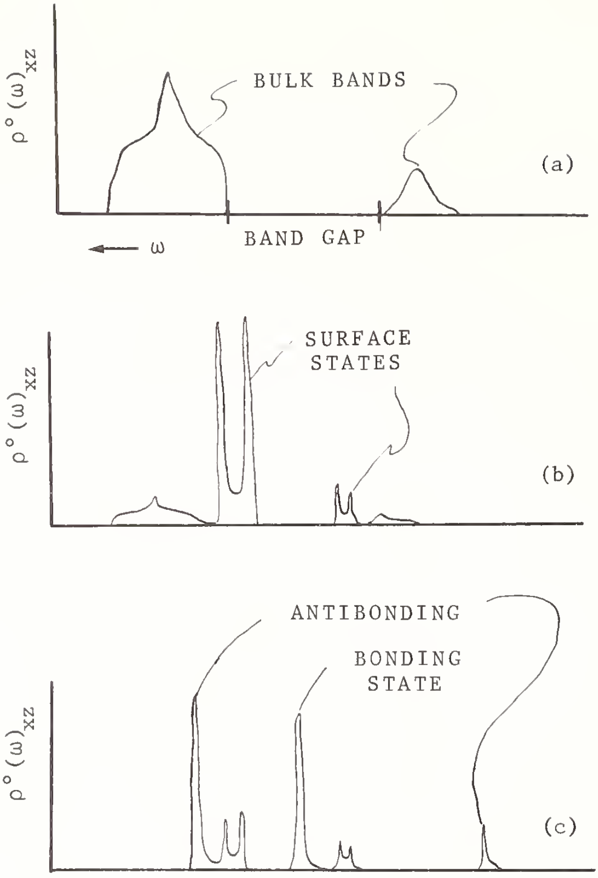

Fig. 22. Schematic of the local density of states function of a cation. (a) the spectral weight function for a d_{xz} state of an interior cation. (b) the spectral weight function for a surface d_{xz} state before interaction with a molecule. (c) the spectral weight function for a surface d_{xz} state interacting with a molecule.

spectral weight functions. For example, the number of electrons in the jth orbital of the α-th atom with spin σ of the reacting molecule is given by:

$$n_{\alpha j\sigma} = \int_{-\infty}^{E_f} d\omega \, \rho_{\alpha j\sigma}(\omega) \ , \qquad (4.1.20)$$

where $\rho_{\alpha j\sigma}(\omega)$ is a function of $n_{\alpha j\sigma}$. Thus an iteration procedure is required to obtain self-consistent solutions for the Green's functions.

The approximation used in treating the electron-electron terms in most band theory models is the Hartree-Foch approximation. This leads to the replacement of the ionization and affinity levels by a single average level. As discussed recently by Madhulkar and Bell [41] the Hartree-Foch approximation can lead to an incorrect structure for the single particle Green's function. A more complete treatment leads to the preservation of both the effective ionization and affinity levels.

It is complicated but straight-forward to apply the formal theory to problems of chemisorption of diatomic molecules on a perovskite surface. We are currently using this model for the investigation of the dissociative chemisorption of H_2 and O_2. These studies will be discussed elsewhere.

4.2. Relation of the Band Model to the Cluster Model

The application of the theory to any realistic situation requires fairly complicated numerical calculations. However, using a highly simplified version of the theory the connection between the band model and local models such as were discussed in section 3 can be demonstrated. Our purpose here is to illustrate how localized chemical bonds appear in a band model. In particular, we consider the hybridized states which an OH^- molecule forms with the t_{2g} d-orbitals of the solid. These states are represented by the levels b and c of figure 15.

We consider the simplified Hamiltonian:

$$H = H_s + H_m + H_{sm}, \qquad (4.2.1)$$

$$H_s = \sum_{\alpha,R} E_d(R)c^+(R)_\alpha c(R)_\alpha + \sum_{\beta R'} E_p d^+(R')_\beta d(R')_\beta$$

$$+ \sum_{\alpha\beta RR'} \{T(RR')_{\alpha\beta} c^+(R)_\alpha d(R')_\beta + H.C.\}, \qquad (4.2.2)$$

$$H_m = \sum_\gamma E_m a^+_\gamma a_\gamma \qquad (4.2.3)$$

$$H_{sm} = \sum_{\gamma\alpha} V_{\gamma\alpha} a^+_\gamma c(0)_\alpha + V^+_{\gamma\alpha} c^+(0)_\gamma a_\alpha \qquad (4.2.4)$$

In eq. 4.2.2, $E_d(R) = E_d$ for interior cations and $E_d + \Delta V_M$ for cations on the surface where ΔV_M is the change in the Madelung potential at the surface. The index α designates xz, yz or xy d-orbitals and R runs over the cation sites. The index β designates p_x, p_y or p_z orbitals and R' runs over the anion sites and E_p is the anion energy including electrostatic potentials. The interaction between near neighbor cation and anions is represented by $T(RR')_{\alpha\beta}$ which is equal to the two-center transfer integral $(pd\pi)$ or vanishes depending upon the relative orientation of the p and d-orbitals.

The non-bonding p-orbitals of the OH^- molecule are represented by $\gamma = p_x$ or p_y and their energy before interaction with the surface but including electrostatic potentials is E_m. These non-bonding orbitals can π-bond to a surface cation. The interaction, represented by $V_{\gamma\alpha}$, is equal to V or vanishes depending upon γ and α. The chemisorption is assumed to occur at R = 0 which designates a surface cation site.

The details of the calculation of the various Green's functions will not be described here. Instead we present some of the results and discuss the interpretation. The Green's function for the molecular levels

$$G^M(\omega) = \{\omega-\varepsilon_m-v^2(\omega-\varepsilon_p)G^\circ(\omega)\}^{-1} \qquad (4.2.5)$$

$$G^\circ(\omega) = \frac{1}{2\pi}\int_{-\pi}^{\pi} \frac{dk}{\Delta p(\omega)-e^{-i\theta(\omega,k)}} \qquad (4.2.6)$$

In equations 4.2.5 and 4.2.6 ω is expressed in units of $(pd\pi)$ and the parameters are defined by the following equations

$$\varepsilon_p = E_p/(pd\pi); \qquad v = V/(pd\pi); \qquad \Delta v_M = \Delta V_M/(pd\pi)$$

$$\varepsilon_d = E_d/(pd\pi); \qquad -2\cos\theta = (\omega-\varepsilon_d)(\omega-\varepsilon_p)-4+2\cos k; \qquad \varepsilon_m = E_m/(pd\pi);$$

$$\Delta p(\omega) = 1+(\varepsilon_p-\omega)\Delta v_M. \qquad (4.2.7)$$

The function $G^{o}(\omega)$ has several important properties. Consider the denominator of the integrand in equation (4.2.6). We have shown in our work on surface states [10] that the condition for the existence of a surface state with wavevector K is

$$\Delta p(\omega) = e^{-i\theta(\omega,k)} \tag{4.2.8}$$

The function $e^{-i\theta}$ is real in the energy gap between the d and p bands of the solid. Solutions of equation (4.2.8) as a function of k determine the surface state energy band $\omega_s(K)$. Thus the poles of the integrand of $G^{o}(\omega)$ correspond to the surface energy bands. Since these poles form a continuum as a function of k the existence of a surface band produces a real and imaginary contribution to $G^{o}(\omega)$. The imaginary part is directly related to the density of surface states and therefore vanishes for ω outside of the surface band frequency regime.

Second, the function $e^{-i\theta}$ is complex for ω inside the bulk energy bands. Consequently $G^{o}(\omega)$ will also have an imaginary part for ω coincident with a bulk energy. In this energy range the imaginary part is related to the bulk density of states. Therefore we express $G^{o}(\omega)$ in the form:

$$G^{o}(\omega) = R(\omega) + iN(\omega) \tag{4.2.9}$$

where $N(\omega)$ is related to the bulk density of states or the surface state density of states in the relevant range of ω. In the band gap but outside of the surface state bands $N(\omega) = 0$.

Now we consider the molecular Green's function given by equation (4.2.5). It may be written in the form

$$G^{M}(\omega) = \{\omega-\varepsilon_m-\Delta(\omega)-i\Gamma(\omega)\}^{-1} \tag{4.2.10}$$

where

$$\Delta(\omega) = v^2\ (\omega-\varepsilon_p)R(\omega), \tag{4.2.11}$$

$$\Gamma(\omega) = v^2(\omega-\varepsilon_p)N(\omega)$$

The density of states $\rho^{M}(\omega)$ for the chemisorbed OH^- molecule is given by:

$$\rho^{M}(\omega) = \frac{1}{\pi}\ \mathrm{Im}G^{M}(\omega) = \frac{1}{\pi}\ \frac{\Gamma(\omega)}{[\omega-\varepsilon_m - \Delta(\omega)]^2 + \Gamma(\omega)^2} \tag{4.2.12}$$

The resonances of $\rho^{M}(\omega)$ correspond to the formation of localized chemisorption states which for this example are admixtures of the p and d orbitals of the solid with the non-bonding orbitals of the OH^- molecule. In the non-interacting case $v = 0$ and $\rho^{M}(\omega) \to \delta(\omega-\varepsilon_m)$. This means a discrete level at the assumed molecular energy E_m. When interaction between the molecule and the surface occurs, $v \neq 0$, then $\Delta(\omega)\neq 0$ and the molecular energy is shifted. The function $\Delta(\omega)$ describes the hybridization of the molecular level with the continuum of bulk and surface states. The new state will be discrete if $\Gamma(\omega)$ vanishes at the ω for which

$$\omega_r = \varepsilon_m + \Delta(\omega_r) \tag{4.2.13}$$

If $\Gamma(\omega_r) \neq 0$ then the localized state is broadened into a band whose width is governed by $\Gamma(\omega)$. Since $\Gamma(\omega)$ is a strong function of ω the resonance in $\rho^M(\omega)$ does not have a simple shape.

We may conclude from equation (4.2.12) that localized hybrid states which resemble those described for the cluster model in section 3 will occur if the states are formed in the energy gap but not within the surface bands. When this condition is not met the chemisorption bond is shared by many surface atoms--that is, delocalized. The degree of localization depends on $\Gamma(\omega)$. The smaller $\Gamma(\omega)$ is the greater the degree of localization.

It should be noted that in general $\rho^M(\omega)$ will have several resonances corresponding to bonding and antibonding combinations of molecular and band states.

The Green's functions in this example may be calculated and the various functions evaluated. Typical solutions have the form shown schematically in figure 23 for the parameters (pdπ) = V = 1 eV and E_m = -5 eV corresponding to OH^- chemisorbing on a Ti ion of $SrTiO_3$ on a (001) surface.

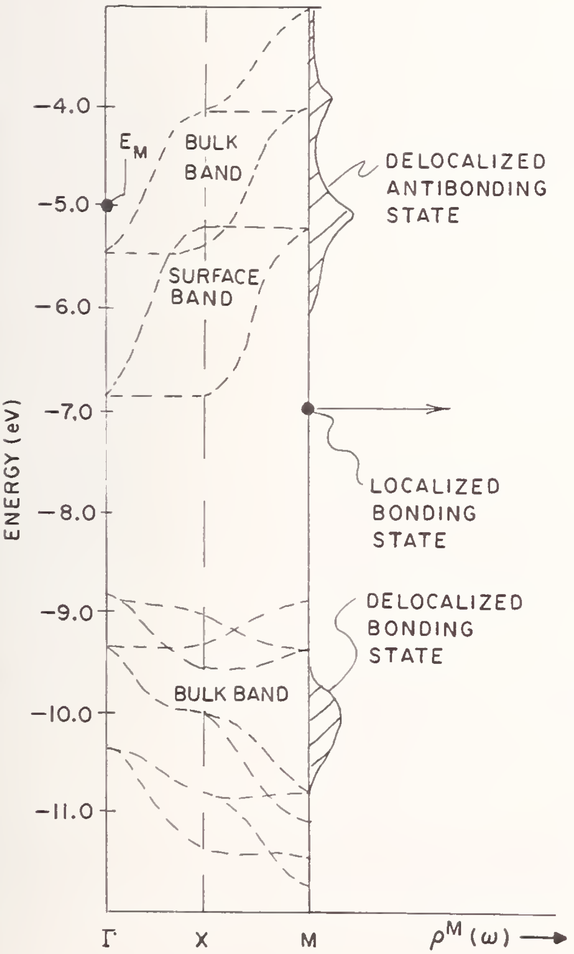

Fig. 23. Schematic of typical solutions to the Green's function model for chemisorption of an OH^- molecule on a surface cation. $\rho^M(\omega)$ is the molecular density of states function.

The qualitative features of figure 23 are to be compared with those of figure 15. The localized bonding state corresponds to level c and the delocalized antibonding state to level b of figure 15. It is clear that the hybridization mechanisms operating in the energy band model are the same as those discussed in the cluster model. It is equally clear that the effects of band formation can not be neglected in any quantitative treatment.

5. Summary

In this paper we have attempted to introduce the concepts which are believed to play an important role in surface chemistry on transition metal oxide materials. The models are crude and refinement is needed in order to produce quantitative results. Such calculations may be expected in the near future. A strong driving force for increased theoretical effort will develop as the new experimental techniques of surface physics are turned to the investigation of transition metal oxide surfaces.

6. References

[1] L.A. Pedersen and W.F. Libby; Science 176, 1355 (1972).
[2] R.J. Voorhoeve, J.P. Remika, P.E. Freeland and B.T. Matthias; Science 177, 353 (1972).
[3] R.J. Voorhoeve, J.P. Remika and D.W. Johnson, Jr., Science 18, 62 (1973).
[4] W.F. Libby and S. Aegerter (unpublished report).
[5] A.C.C. Tseung and H.L. Bevan; J. Electroanal. Chem. and Interfacial Electrochem. 45, 429 (1973).
[6] A. Fujishima and K. Honda; Nature 238, 37 (1972).
[7] J.G. Mavroides, D.I. Tchernev, J.A. Kafalas, and D.F. Kolesar; Mat. Res. Bull. 10, 1023 (1975).
[8] J.B. Goodenough; Progress in Solid State Chemistry 5, 149 (1971) (ed. H. Reiss).
[9] E.A. Kraut, T. Wolfram and W.F. Hall; Phys. Rev. B6, 1499 (1972).
[10] T. Wolfram, E.A. Kraut and F.J. Morin; Phys. Rev. B7, 1677 (1973).
[11] T. Wolfram; Phys. Rev. Letters 29, 1383 (1972).
[12] L.F. Mattheiss; Phys. Rev. 181, 987 (1967); Ibid B2, 3918 (1970); Ibid B4, 3548 (1971).
[13] M. Cardona; Phys. Rev. A140, 651 (1965).
[14] J.A. Tossel, D.J. Vaughan and K.H. Johnson; Am. Mineralogist 59, 319 (1974).
[15] T. Wolfram, R. Hurst and F.J. Morin, "Surface States on $SrTiO_3$, $BaTiO_3$ and TiO_2" to be published.
[16] K.H. Johnson and R.P. Messmer, J. Vac. Sci. Technol. 11, 236 (1974).
[17] T. Wolfram and F.J. Morin, Appl. Phys. 8, 125 (1975).
[18] F.J. Morin and T. Wolfram; Phys. Rev. Letters 30, 1214 (1973).
[19] V.E. Henrich, G. Dresselhaus and H.J. Zeiger; Thirty-Fifth Annual Conference on Physical Electronics, Penn. State University, June 2-4, 1975.
[20] S.N. Frank, D. Laser, K.L. Hardee and A.J. Bard, "Characterization of Semiconductor Electrodes in Nonaqueous Solvents", presented at the Workshop on Electrocatalysis on Non-Metallic Surfaces, National Bureau of Standards, Gaithersburg, Md., Dec. 9-12, 1975.
[21] F.H. Field and I.L. Franklin, "Electron Impact Pehnomena", Academic Press, New York, 1957.
[22] J.W. Maskowitz and M.C. Harrington; J. Chem. Phys. 42, 3612 (1965).
[23] H. Weinberg and R.P. Merrill; Surf. Sci. 33, 493 (1972); H. Weinberg, M. Lambert, C.M. Comrie and J.W. Linnett, Surf. Sci. 30, 299 (1972).
[24] S.W. Weller and S.E. Voltz, J. Amer. Chem. Soc. 76, 4695 (1975).
[25] R. Hoffmann, J. Chem. Phys. 39, 1397 (1963).
[26] H.A. Germer, J. Chem. Phys. 58, 3524 (1972).
[27] J.W. Moskowitz, M.C. Harrison, J. Chem. Phys. 42, 1726 (1965).
[28] R.B. Woodward and R. Hoffmann; The Conservation of Orbital Symmetry (Verlag-Chimie, Weinheim, F.R., Germany, 1970).
[29] See for example, hydrogen exchange reaction.
[30] D.R. Hamann, Chem. Phys. Lett. 22, 301 (1973).
[31] D.A. Shirley, Chem. Phys. Lett. 16, 220 (1972).
[32] J.E. DeMuth and D.E. Eastman, Phys. Rev. Letters 32, 1123 (1974).
[33] F.D. Mango and J.H. Schachtschneider, J. Am. Chem. Soc. 89, 2484 (1967); F.D. Mango, Adv. Catalysis 20, 291 (1969).
[34] D.M. Newns, Phys. Rev. 179, 1123 (1969).
[35] T.B. Grimley, J. Vac. Sci. Technol. 8, 31 (1971).
[36] T.B. Grimley in "Molecular Processes on Solid Surfaces", McGraw-Hill, New York (1969).
[37] J.W. Gadzuk, "Interaction of Atoms and Molecules with Surfaces" in Surface Physics of Crystalline Materials, Academic Press, J.M. Blakely, Ed.
[38] J.R. Schrieffer and R. Gomer, Surf. Sci. 25, 315 (1971).
[39] A. Madhukar, Phys. Rev. B8, 4458 (1971).
[40] D.N. Zubarev, Sov. Phys. Uspechi 3, 320 (1960).
[41] A. Madhukar and B. Bell, Phys. Rev. Letters 34, 1631 (1975).

National Bureau of Standards Special Publication 455, *Electrocatalysis on Non-Metallic Surfaces*, Proceedings of Workshop held at NBS, Gaithersburg, Md., December 9-12, 1975. (Issued November 1976)

Hartree-Fock Calculations of Hydrogen Adsorption on Nickel, Copper, and Magnesium Oxide[1]

A. B. Kunz, M. P. Guse, and R. J. Blint
Department of Physics and Materials Research Laboratory
University of Illinois
Urbana, Illinois 61801

The potential energy curves for NiH, HNiH, CuH, and HCuH resulting from the ground and first excited state atomic configurations are calculated using the unrestricted Hartree-Fock and generalized valence bond methods. NiH bonding in the $3d^84s^2$ configuration and CuH bonding in the $3d^94s^2$ configuration is by means of an sp hybrid orbital which comes from the $4s^2$ shell leaving a singly occupied orbital free to bond to another hydrogen atom. The bonding in the NiH$3d^94s$ and CuH$3d^{10}4s$ configurations is to the 4s orbital leaving in NiH a hole in the nickel 3d shell which interacts with another hydrogen only weakly and in CuH a closed 3d shell resulting in a repulsive potential energy curve. The interaction of hydrogen with a cluster representing a magnesium oxide surface V_I center was calculated using UHF. The lowest energy results when the Mg and O are singly ionized rather than doubly as in the bulk resulting in a surface radical. The hydrogen is bound over one of the oxygen atoms.

Key words: Adsorption; catalysis; copper hydride; magnesium oxide; molecular structure; nickel hydride.

INTRODUCTION

The interaction of hydrogen with surfaces is important in a multitude of catalytic processes. In the hope of learning something about this interaction for at least a few cases we have studied the much simpler problem of hydrogen bonding to small molecules approximating the essential features of the surface. We have used self consistent Hartree-Fock methods to calculate potential energy curves for hydrogen interacting with Ni, NiH, Cu, CuH, and a small MgO cluster.

Two methods of calculation were used in this work, unrestricted Hartree-Fock (UHF) and perfect pairing generalized valence bond (GVB). The UHF wavefunction is

$$\Psi^{UHF} = A[\phi_1 \cdots \phi_i \phi_{i+1} \cdots \phi_n \alpha_1 \cdots \alpha_i \beta_{i+1} \cdots \beta_n] \tag{1}$$

where A is the antisymmetrizer, the ϕs are the spatial one electron orbitals, and the αs and βs are the corresponding spin functions. The one electron orbitals need not be doubly occupied so that the spin up and spin down electrons can occupy different spatial orbitals. The ϕs are varied self consistently with no restriction on their symmetry.

The perfect pairing GVB wave function

$$\Psi^{GVB} = A[\phi_1 \cdots \phi_{i-1}(\phi_{ia}^2 - c\phi_{ib}^2)\phi_{i+1} \cdots \phi_n \chi] \tag{2}$$

---

[1] This research was supported by the National Science Foundation under Grant DMR 72-03026.

is in effect a two-configuration, optimized wavefunction where χ is the spin eigenfunction [1].[2] All orbitals are restricted Hartree-Fock in nature except for the pairs which are GVB split. In both UHF and GVB methods, bonds are allowed to dissociate properly.

The valence shell of a nickel atom in its ground state (^3F) has the configuration $3d^84s^2$. The first excited state (^3D) is only about .03 electron volts (eV) higher in energy and has the configuration $3d^94s$. Our Hartree-Fock calculations find the $3d^94s$ state to be about 1.7 eV higher than the $3d^84s^2$ state. Consequently we have considered NiH and HNiH resulting from both of these configurations.

The potential energy curves of $Ni(3d^84s^2)H$ were calculated using UHF and are shown in Figure 1a. From $Ni(^3F)$ and $H(^2S)$ we can form NiH with spin 3/2 or 1/2. The high spin state in Figure 1a is a nearly pure quartet while the low spin state is a mixture $.81|1/2\rangle+.58|3/2\rangle$. At the potential minimum the energy of this state is lower than the pure doublet state by about .07 eV.

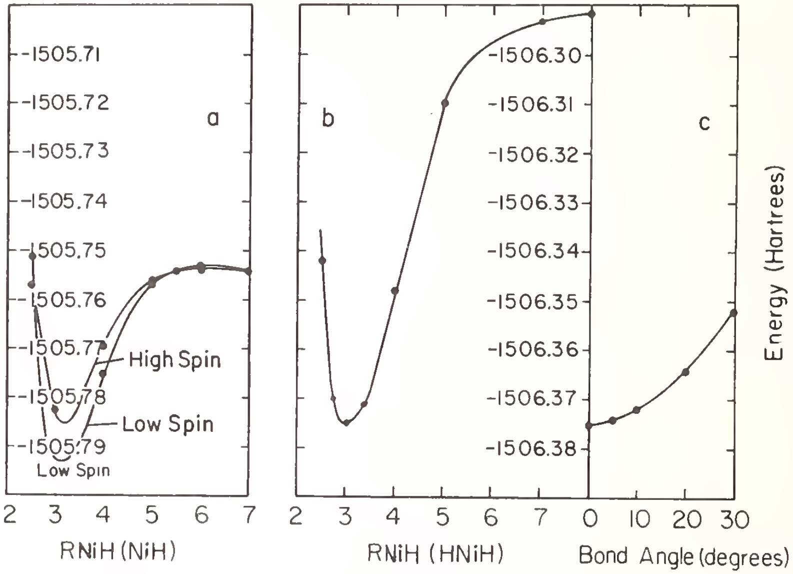

Fig. 1. In part a, the bonding curves for NiH in the doublet and quartet states are shown as a function of Ni-H separation. In part b, the bonding curve arising from forming a linear HNiH molecule from the doublet NiH molecule is shown. The one H is held at the NiH equilibrium separation and the other one is moved around. In part c, the resistance to bond bending of the HNiH molecule is seen. The NiH distances are held to those for minimum energy. Energies are in hartree (1Hy = 27.2 eV), length are in a.u. (1 a.u. = 0.529 Å).

In order to determine the nature of the binding in NiH we examined the valence orbitals of the molecule for large and small internuclear separations. The orbitals for the high spin state are almost identical to those of the low spin state, which are shown in Figure 2. It is immediately clear that the nickel 3d orbital does not contribute significantly to the bonding. This agrees with the findings of Blyholder [2] and Melius [3] for the adsorption of hydrogen on nickel. As the internuclear separation decreases the doubly occupied nickel $4s^2$ orbital splits into two essentially sp hybrid orbitals. One of these forms a covalent bond with the hydrogen atom while the other becomes a singly occupied nonbonding orbital directed away from the hydrogen. This is identical to the bonding we found in ScH and MnH [4-5].

A second hydrogen atom interacts strongly with the NiH radical to form a linear HNiH molecule. Figure 1b shows the potential energy curve for H approaching the low spin

---

[2] Figures in brackets indicate the literature references at the end of this paper.

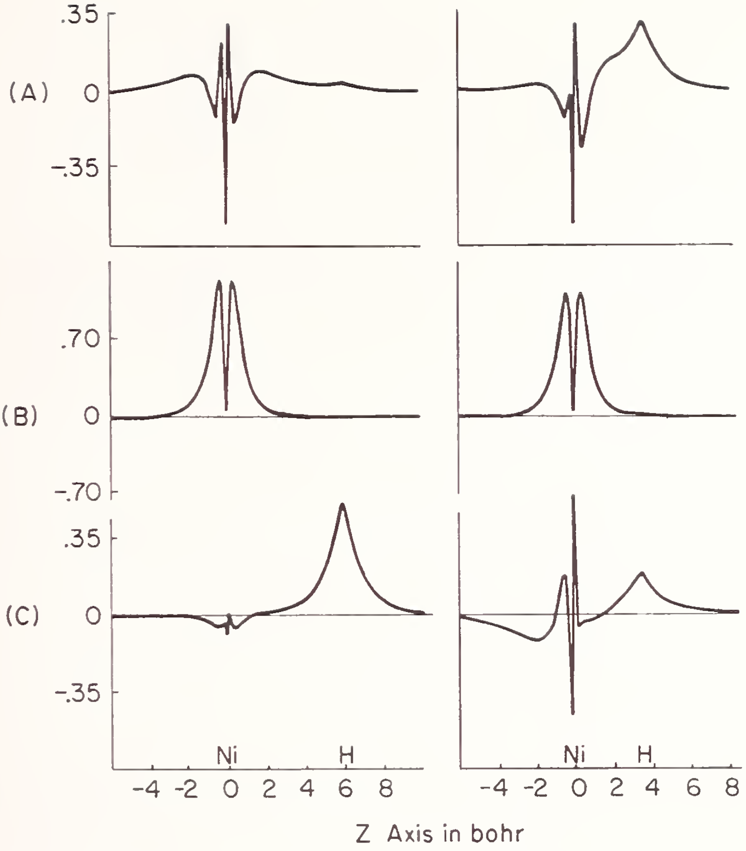

Fig. 2. Amplitudes of the three valence orbitals as a function of inter-nuclear separation. A is the doubly occupied $Ni4s^2$ orbital, B the Ni $3d_z2$ orbital and C the hydrogen 1s orbital. The origin is at the Ni atom and the plane includes the Ni and H nuclei.

$Ni(3d^84s^2)H$ radical calculated using UHF. The ground state is a nearly pure spin triplet with the hydrogen binding to the NiH non-bonding 4sp hybrid orbital. The energy required to bend this second bond while keeping the Ni-H distance fixed is shown in Figure 1c.

The potential energy curves of $Ni(3d^94s)H$ were calculated for the doublet state using both UHF and GVB and are shown in Figure 3. The full curve is shown for the $^2\Sigma^+$ state while the energies of the $^2\pi$ and $^2\Delta$ GVB states are shown at 3.0 Bohr. Taking into account the experimental fact that the $Ni3d^94s$ and $3d^84s^2$ states are nearly degenerate we find the ground state of NiH to be the $^2\Delta$ state resulting from the Ni $3d^94s$ configuration. In each of these states the bond involves the Ni4s and H 1s orbitals leaving a single hole in the nickel d shell.

The H $Ni(3d^94s)H$ potential energy curve was calculated using GVB with both one and two GVB pairs. The initial NiH state is $^2\Sigma^+$ with the second hydrogen 1 s orbital GVB paired with the Ni $3d_z2$ orbital to form the $^1\Sigma^+$ state of HNiH. Both curves are shown in Figure 4. It may be seen that hydrogen interacts very weakly with the 3d electron showing that the ground state of HNiH is derived from the $3d^84s^2$ configuration of nickel. We are unable to find solutions to H-NiH arising from the $3d^94s$ state of Ni for H-NiH separation less than shown in Figure 4 because the solution jumps to the branch derived from the $3d^84s^2$ Ni configuration which has lower energy. We have also studied H adsorption by Ni bonded to a surface of SiO_2 and find the chemisorption behavior in these cases to be similar to that for the H-NiH system.

A similar study was done on copper using GVB. The CuH molecule may have both a $^1\Sigma^+$ and $^3\Sigma^+$ state arising from the Cu $3d^{10}4s$ ground state. As is seen from Figure 5a only the

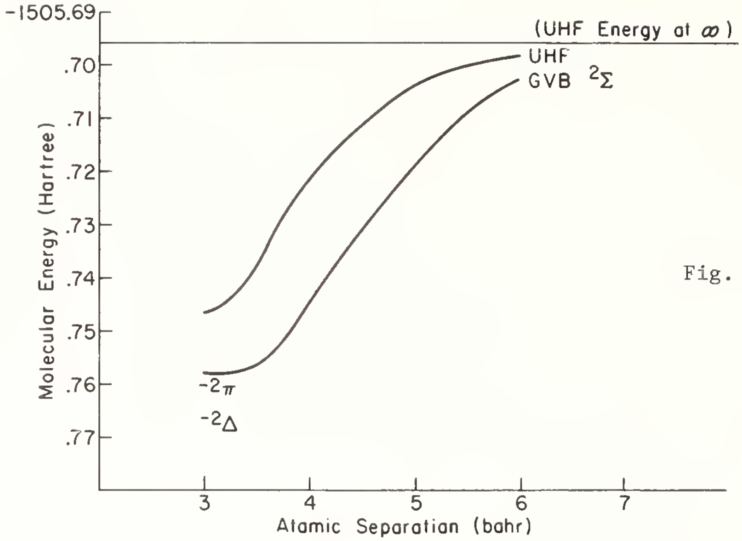

Fig. 3. The potential energy curves for $Ni(3d^94s)$. The energy is in hartrees and the lengths are in bohr.

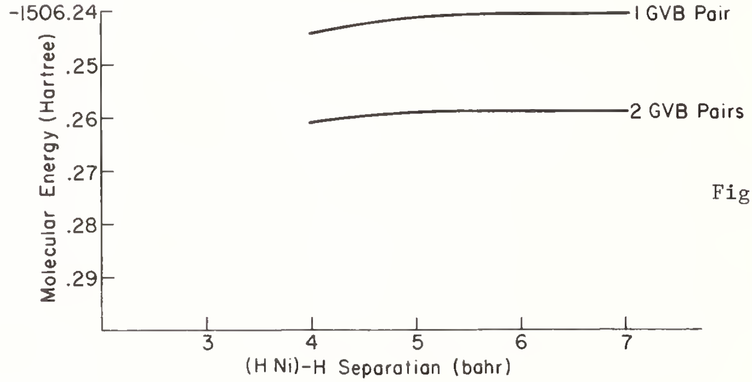

Fig. 4. The potential energy curves for a second hydrogen on the $^2\Sigma$ state of NiH $(3d^94s)$ in the perfect pairing GVB method. The energy is in hartrees and the lengths are in bohr.

$^1\Sigma^+$ state arising from the Cu ground state is bonding. The ground state $^3\Sigma^+$ is antibonding and this is in contrast to the first period transition metals for which all states arising from the atomic ground state are bonding. The first excited state of copper has the configuration $3d^94s^2$. The excited CuH constructed from this configuration can exist in the $^3\Sigma^+$ state. The potential energy curve for this state has a deep minimum. In making up Figure 5 the experimental energy difference for the Cu atom $3d^{10}4s$ and $3d^94s^2$ are used to determine the infinite R_{CuH} energy separation, rather than the less accurate theoretical value. When we bring a second hydrogen up to CuH we find that the linear HCuH molecule exists only when it is derived from the Cu $3d^94s^2$ level as seen in Figure 5b. The form of bonding is identical to that of $Ni(3d^84s^2)H$. We see that a hydrogen atom approaching a copper surface must overcome an activation barrier in order to bond to the $3d^94s^2$ configuration. This is consistent with the experimental observation that Cu adsorbs dissociated H but is not able to adsorb H_2.

The above calculations suggest that hydrogen does not bind to a nickel surface by means of the 3d-electrons but rather by means of the 4s-4p electrons. If a surface nickel atom exists in the $3d^84s^2$ configuration one of the 4s electrons may be involved in the nickel-surface bond while the other lies in a nonbonding orbital forming a surface radical to which a hydrogen atom may bind. The strength of this hydrogen-nickel bond will be just over half that of the H_2 bond in the Hartree-Fock limit (3.4 eV) so that an H_2 molecule will tend to dissociate with each hydrogen bonding to a nickel atom. For a surface atom in the $3d^94s$ configuration the 4s electron is involved in the nickel-surface bond and the d electron-hydrogen interaction leads to at most weak adsorption. We might then guess that the catalytic ability of a transition metal would correlate with the ability of its atoms to exist in the d^ns^2 configuration.

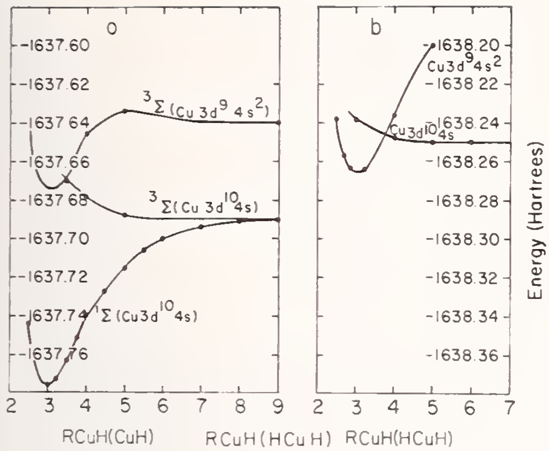

Fig. 5. In part a, the bonding curve for CuH is shown for the singlet and triplet state. In part b, the curve arising from forming a linear HCuH molecule from the $^1\Sigma^+$ ground state of CuH is shown. The first H is held at the CuH equilibrium separation and the other one is moved around. Energies are in hartrees and length in a.u.

This mechanism is consistent with the constancy of relative catalytic activity across the first transition metal series since the ground state for these atoms is already the $3d^n4s^2$ configuration. The ground state of atoms in the second transition series is predominantly $4d^n5s$. We would then expect the catalytic activity of the second transition series to depend on the ease with which the atoms are excited to the $4d^{n-1}5s^2$ configuration. The minimum energy for this promotion occurs for the middle of the second transition series [6] and the Boltzman occupation factor for the $4d^{n-1}5s^2$ state correlates directly with the relative activities for hydrogenolysis of ethane as found by Sinfelt [7]. This is seen in Figure 6. The experimental data are due to Sinfelt and the specific activities are with respect to Cu for the first transition series and Pd for the second transition series. In the theoretical determination, we assume the activity is directly proportional to the probability of occupation of the d^ns^2 state of the atom. As is seen from Figure 5b for Cu, the actual barrier is less than the atomic ground state to d^ns^2 state energy splitting. We use a factor of 1/3 the atomic energy value in preparing this curve. This factor of 1/3 is our only parameter and is used universally for Cu and the second transition series elements. T is 205°C as is the case experimentally. This then seems capable of predicting the strong dependence of activity with element for the second transition series.

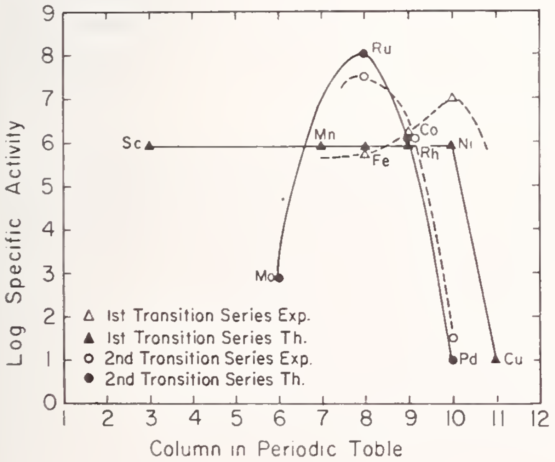

Fig. 6. The experimental activities for hydrogenolysis of ethane are shown [2]. The theoretical relative activities are also given on the assumption the activity is proportional to the occupancy of the d^ns^2 energy state. This probability is proportional to $C^{-\Delta/kT}$. We use a Δ which is 1/3 the atomic excitation energy from the ground state and T is 205°C as it is experimentally. The theoretical rates are relative with that of Cu being 10 for the first transition series and that of Pd being 10 for the second transition series.

Magnesium oxide catalyzes the H_2-D_2 equilibration reaction at low temperatures. Boudart has studied this reaction [8] and determined that the active catalytic site involves a paramagnetic triangular array of O^-ions situated on a (111) plane of MgO which he calls a V_I center. In order to study the interaction of hydrogen with this site we constructed a cluster consisting of an equilateral triangle of oxygen atoms overlaying a similar array of magnesium atoms rotated 60° (Table 1).

Table 1. The positions of atoms in the MgO cluster.

	x	y	z (bohr)
O_1	.00000	-3.24533	0.00000
O_2	2.81054	1.62266	0.00000
O_3	-2.81054	1.62266	0.00000
Mg_1	0.00000	3.24533	-2.29479
Mg_2	-2.81054	-1.62266	-2.29479
Mg_3	2.81054	-1.62266	-2.29479

We began with the system in the $Mg^{++}O^{=}$ state as it is found in the bulk and calculated the potential energy curve of H along the cluster axis using UHF. We found that this is an excited state. The state $Mg^{+}O^{-}$ is over 3 eV lower in energy. This suggests that the surface radical is energetically favorable. The potential energy curves for bringing H down over various points on the cluster are shown in Figure 7. The lowest energy results when the H sits directly over one of the oxygens. This indicates that the V_I site may be able to accomodate three hydrogen atoms. This study seems to be fully consistent with the results of Boudart. There is one important similarity between the behavior of the MgO cluster and the supported Ni system. In both cases the H atom is found to adsorb into an existing "surface radical".

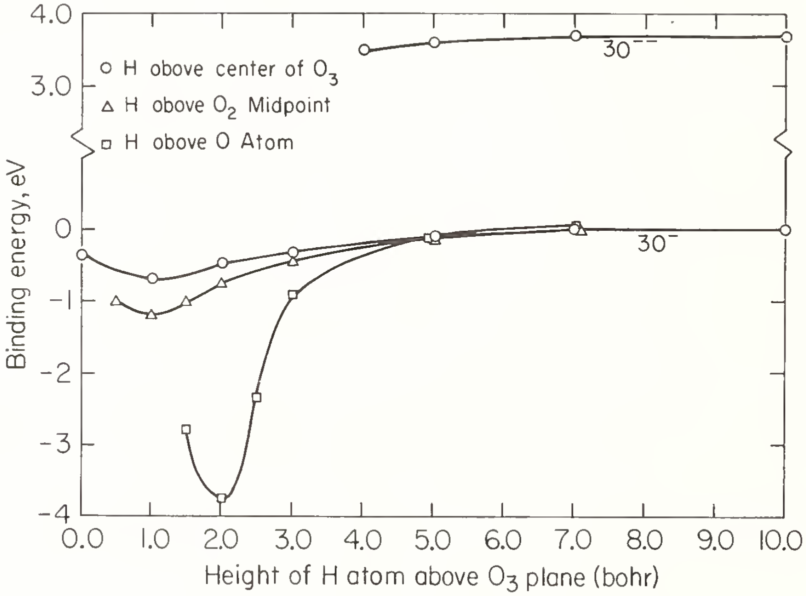

Fig. 7. Potential energy curves for hydrogen on MgO V_I cluster. The vertical axis gives binding energy in electron volts. The horizontal axis gives the height of the H atom above the O_3 plane in bohr.

REFERENCES

[1] Hunt, W. J., Hay, P. J., and Goddard, W. A., J. Chem. Phys. 97, 738 (1972).
[2] Blyholder, G., J. Chem. Phys. 62, 3193 (1975).
[3] Melius, C., 1975, Private Communication.
[4] Kunz, A. B., Guse, M. P., and Blint, R. J., J. Phys. B: Atom. Molec. Phys. 8, L358 (1975).
[5] Blint, R. J., Kunz, A. B., and Guse, M. P., Chem. Phys. Lett. 36, 191 (1975).
[6] Moore, D. E., Atomic Energy Levels, (NSRDS-NBS Circular 35, Washington, D.C.), Vol. I-III.
[7] Sinfelt, J., Advances in Catalysis 23, 91 (1973).
[8] Boudart, M., Delboville, A., Derovane, E. G., Indovina, V., and Walter, A. B. J. Am. Chem. Soc. 94, 6622 (1972).

National Bureau of Standards Special Publication 455, *Electrocatalysis on Non-Metallic Surfaces*, Proceedings of Workshop held at NBS, Gaithersburg, Md., December 9-12, 1975. (Issued November 1976)

Stark Model of the Excitonic Surface States Observed on MgO[1]

H. J. Zeiger, Victor E. Henrich, and G. Dresselhaus
Lincoln Laboratory, Massachusetts Institute of Technology
Lexington, Massachusetts 02173

Using the energy and angle-of-incidence dependence of the electron energy loss spectra of MgO, we have separated the excitonic transitions from the Mg core levels to the excited states into those of bulk and surface origin. The bulk transitions are very nearly those of the free Mg^{2+} ion. The (100) surface-state transitions can be described by Stark-splitting of the energy levels of the surface Mg^{2+} ions in the intense Madelung electric fields at the crystal surface. The observations on other crystal faces of MgO and in amorphous MgO, however, suggest the possibility of the presence of surface Mg^{+} ions.

Key words: Bulk excitons; electron loss spectroscopy; ionic crystals; Madelung potential; Mg^{+}; Mg^{2+}; MgO; Stark spectrum; surface excitons.

1. Introduction

While the electronic surface states of covalent semiconductors such as Si, Ge and GaAs have been widely studied over the last few years, less attention has been paid to the surface electronic structure of highly ionic materials. We have extended the technique of reflection electron energy loss spectroscopy (ELS) to the study of intrinsic surface states on MgO. By using both the angle-of-incidence and primary-electron-energy dependence of the ELS spectra, we have been able to unambiguously separate transitions from the Mg(2p) and Mg(2s) core levels to excited states [1][2] into those of bulk and surface origin. The energies of the bulk excitonic transitions are in good agreement with the optically observed excited states of the free Mg^{2+} ion [2]. The surface-state transitions on a (100) face can be described well by a simple, one-parameter model for the Stark splitting of the bulk Mg^{2+}-like excitonic states in an electric field $\mathcal{E}_s$ at the position of a surface Mg^{2+} ion. The experimentally determined value of $\mathcal{E}_s$ is 3.0×10^8 V/cm, compared to the value of 3.7×10^8 V/cm calculated for the electric field produced by the Madelung potential gradient. However, as we discuss below (see Section 4), observations on other faces of MgO and on amorphous MgO suggest the possibility that Mg^{+} ions are present on the surfaces.

2. Experimental Observations

By varying the energy and angle-of-incidence of the primary-electron beam, a wide range of effective depths can be sampled in ELS. The electron mean free path in a solid increases from 4-5 Å for energies between about 40 to 150 eV to 20-30 Å for 2000 eV electrons [3]. Thus an ELS spectrum taken with a primary-electron energy $E_p \sim 2000$ eV at normal incidence will be dominated by transitions of bulk origin, whereas a normal-incidence spectrum taken with $E_p \sim 100$ eV will exhibit both bulk and surface transitions. The contribution of bulk transitions to the spectrum can be virtually eliminated by using a primary beam of ~ 100 eV at grazing incidence. We have used this approach to separate our spectra into structure of bulk and surface origin. By using a double-pass cylindrical-mirror electron spectrometer and retarding the emitted electrons to a constant energy of 50 eV, an energy-independent resolution of 0.8 eV was maintained. Modulation (0.4 eV peak-to-peak) was applied to the gun accelerating voltage; this eliminated Auger peaks from the spectra. First-derivative energy loss spectra were obtained by recording dn(E)/dE, where E is the electron kinetic energy in vacuum, vs energy loss E_L. The location of peaks in n(E) was determined from midpoints of negative slopes in dn(E)/dE; most peaks could be located to within ± 0.2 eV.

The MgO samples were (100) surfaces cleaved from a single crystal and etched in boiling H_3PO_4 (83%). The surfaces were then sputter-etched in an ultrahigh vacuum system with 260 eV Ar ions

---

[1] This work was sponsored by the Department of the Air Force.

[2] Figures in brackets indicate the literature references at the end of this paper.

incident at about 70° to the surface normal. Auger spectroscopy showed the surfaces to be atomically clean. Some samples were also annealed for 5 minutes at about 1200°C. The Auger spectra for these surfaces showed traces of Ca. Both treatments yielded very good LEED patterns and gave the same energy loss spectra.

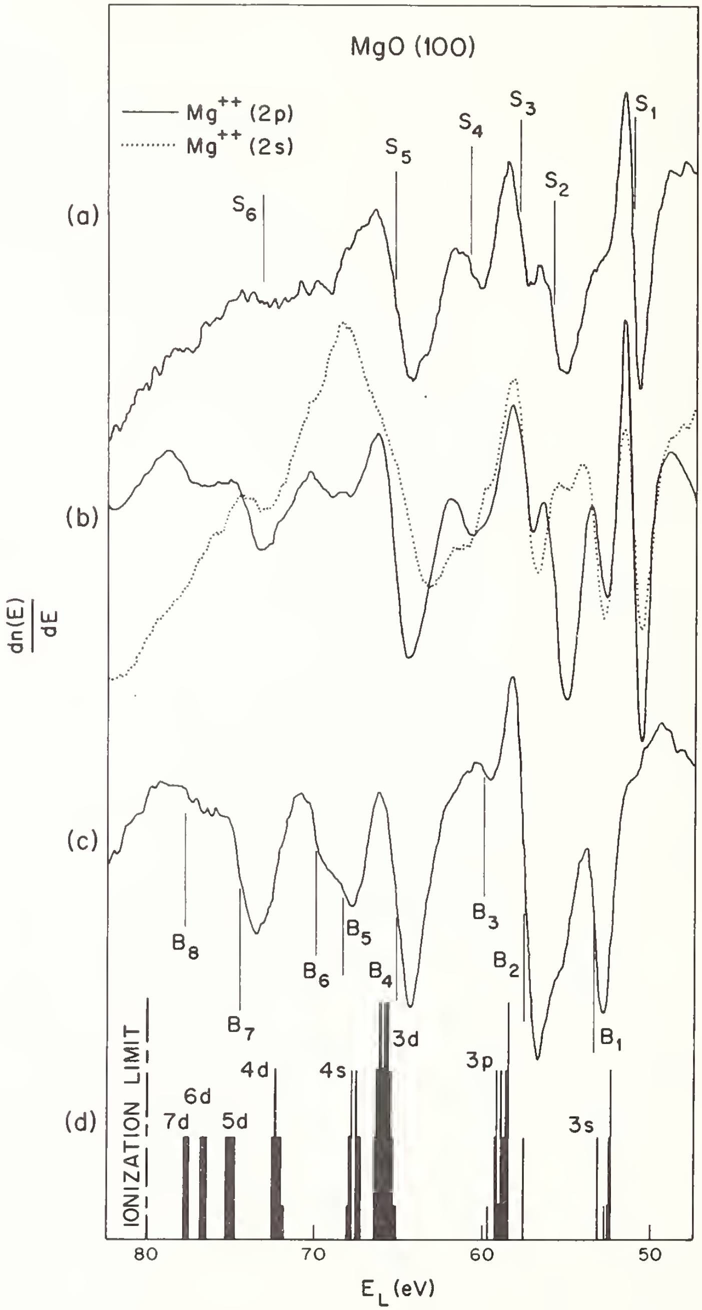

Fig. 1. First-derivative energy loss spectra, dn(E)/dE vs energy loss E_L, for transitions from the Mg(2p) (solid lines) and Mg(2s) (dotted line) core levels in MgO(100). (a) E_p = 120 eV, grazing incidence; (b) E_p = 120 eV (solid line) and E_p = 200 eV (dotted line), normal incidence; (c) E_p = 2000 eV, normal incidence; (d) observed Mg^{2+} free-ion spectrum from ref. 2. The Mg(2s) spectrum has been shifted down by 38.4 eV to align it with the Mg(2p) spectrum. The positions of bulk peaks B_1 through B_8 and surface peaks S_1 through S_6 are indicated in (c) and (a), respectively.

The experimental ELS spectra for transitions from the Mg(2p) and Mg(2s) core levels to excited states are shown in figure 1a-c. The solid curves are Mg(2p) spectra; they can be compared directly with the optically observed Mg^{2+} free-ion spectrum in figure 1d [2]. The spectra for transitions from the Mg(2s) core level, which lies 38.4 eV below the Mg(2p) level, show similar excited-state structure; one such spectrum is shown by the dotted curve in figure 1b. The spectrum in figure 1c is for $E_p = 2000$ eV, normal incidence, and the positions of peaks in n(E) are labeled B_1 through B_8, indicating their bulk origin. The locations of these peaks, which are given in Table 1, are in good agreement with those for transitions from the Mg(2p) core level to excited states observed by high-energy transmission ELS [4], x-ray absorption spectroscopy [5] and ultraviolet reflectivity [6], all of which are basically bulk probes. The energies of peaks B_1, B_2, B_4 and B_5 are very close to the 3s, 3p, 3d and 4s levels, respectively, in the Mg^{2+} $2p \rightarrow n\ell$ series in figure 1d [2]. Additional peaks are seen up to the ionization limit of the free Mg^{2+} ion, with no further structure until the onset of the Mg(2s) spectrum at $E_L \approx 90$ eV. Peak B_3, which is only present for $E_p \geq 500$ eV, may be due to the excitation of both a Mg^{2+} ion and an O^{2-} ion.

Table 1

Observed Mg(2p) - Excited State Transitions in MgO

This Work (eV)		Previous Experiments (eV)		
Surface[a]	Bulk[b]	Trans. ELS[c]	X-Ray Abs.[d]	UV Refl.[e]
51.3				
	53.7	54	53.5	53.5
56.0		55.8(vw)		
58.0	57.8	57.9	57.4	57.3
	60.1	60.5(w)	60.5(w)	
60.9				
65.4	65.4	65	65.0	64
	68.6(w)		68.2	
	70.2	69.5	70.5	
73.2				
	74.5	74		
	77.5		76.5	

a) S_1 through S_6 in Fig. 1a.
b) B_1 through B_8 in Fig. 1c.
c) From Fig. 1 of Ref. 4.
d) Ref. 5.
e) From Fig. 1 of Ref. 6.

As the primary-electron energy is lowered, surface-state transitions appear in the energy-loss spectrum, and at $E_p = 120$ eV, normal incidence (fig. 1b), the bulk and surface contributions are of comparable magnitude. The Mg(2s) spectrum in figure 1b, taken with $E_p = 200$ eV, normal incidence, also contains peaks arising from both bulk and surface transitions. On going to grazing incidence at $E_p = 120$ eV (fig. 1a), only surface-state transitions should remain in the spectrum [7]; that is confirmed here by the disappearance of peak B_1, and we have labeled the peaks S_1 through S_6. The locations of these surface-state peaks in n(E) are given in Table 1. Both the bulk and surface peaks listed in Table 1 were observed in our earlier ELS measurements on MgO [1], but we were unable to distinguish between them either experimentally or theoretically.

3. Stark Model of Surface States

The similarity between the excited-state spectrum of a free Mg^{2+} ion and the ELS spectrum of bulk transitions from the Mg(2s) and Mg(2p) states in MgO suggests that an ionic description is also applicable to the surface transitions. As discussed by earlier workers [8], an ion at the surface of a crystal does not experience the same Madelung potential as the same ion in the bulk. The Madelung shifts of the initial and final states of a surface ion should be essentially the same, producing no net shift in its transition energies. However, in an ionic insulator there is a large gradient of the Madelung potential at the surface, giving rise to a strong electric field that should produce a Stark mixing of ionic states (see fig. 2). We have applied a simple model of this effect to the calculation of the Stark-split spectrum of the Mg^{2+} surface ions in MgO.

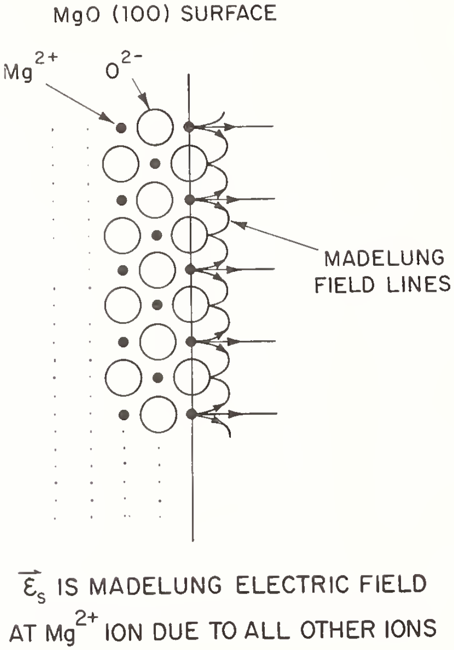

Fig. 2. Schematic representation of the (100) surface of an MgO crystal.

We have formulated a ligand field description of this model of the MgO surface. The potential seen by an Mg^{2+} excited state electron is of the form,

$$V_B(\vec{r}) = V_{0B}(r) + V_{4B}(r)[Y_4(\theta,\varphi)]_{cubic} + \ldots\ldots$$

in the bulk, and of the form,

$$V_S(\vec{r}) = V_{0S}(r) + V_{1S}(r)Y_1^0(\theta,\varphi) + V_{2S}(r)Y_2^0(\theta,\varphi) + \\ + V_{4S}(r)[Y_4(\theta,\varphi)]_{fourfold} + \ldots\ldots \qquad (1)$$

at the surface. Here, $[Y_4(\theta,\varphi)]_{cubic}$ and $[Y_4(\theta,\varphi)]_{fourfold}$ are respectively fourth rank spherical harmonic combinations of cubic and fourfold symmetry, and the symmetry axis for the spherical harmonics is the normal to the surface. The terms $V_{0B}(r)$ and $V_{0S}(r)$ produce shifts of the 2s, 2p, 3s, 3p, ... levels. The terms proportional to $V_{4B}(r)$ and $V_{4S}(r)$ produce ligand field splittings of the 3d, 4d, ... levels, which are presumably less than the widths of the observed transitions (~ 1 eV). The terms proportional to $V_{1S}(r)$, $V_{2S}(r)$, ... split and mix the 3s, 3p levels, and the largest term is expected to be $V_{1S}(r)Y_1^0(\theta,\varphi)$.

If we assume that $V_{0B}(r)$ and $V_{0S}(r)$ produce essentially identical small shifts of transition energy, then the most important difference between the bulk and surface Mg^{2+} ion potential is the presence of the surface term $V_{1S}(r)Y_1^0(\theta,\varphi) \rightarrow \mathcal{H}_{Stark} = -e\vec{\mathcal{E}}_S \cdot \vec{r}$, where $\vec{\mathcal{E}}_S$ is the average electric field at the position of a surface Mg^{2+} ion, and is normal to the surface.

In evaluating the Stark effect we consider only the contribution of the one-electron 3s, 3p, 3d, 4s, 4p, 4d and 4f states of the excited Mg^{2+} ion. Term structure due to the interaction of the core hole and the excited electron is neglected. The Stark shifts of the 2s and 2p core holes are also neglected, since they are calculated to be less than 3% of the 3s Stark shift. The matrix elements of the Stark interaction for the Mg^{2+} ion are written, $\langle n'\ell' m_\ell | \mathcal{H}_{Stark} | n\ell m_\ell \rangle = -\vec{\mathcal{E}}' \cdot \langle n'\ell' m_\ell | \vec{r} | n\ell m_\ell \rangle$, where $\vec{\mathcal{E}}' = e\vec{\mathcal{E}}_s / Z_{eff}$, Z_{eff} is an effective charge seen by the electron in its excited orbit, and the $\langle n'\ell' m_\ell | \vec{r} | n\ell m_\ell \rangle$ are the matrix elements of $\vec{r}$ for the hydrogen atom [9]. The value for the 3s, 3p, 3d, 4s, 4p, 4d and 4f energy levels are taken from the observed bulk peaks ($B_1, B_2, B_4, B_5, B_5, B_6$ and B_7, respectively), and each one lies roughly within the range of multiplet energies for the corresponding level of the Mg^{2+} free ion spectrum [2]. The identification of the peaks beyond B_5 is not critical to the location of the surface peaks S_1 through S_5.

The results of a Stark effect computer calculation including 3s through 4f levels are summarized in figure 3, which shows the energy levels of the Mg^{2+} excited states as a function of the parameter $\mathcal{E}'$ expressed in atomic units (au). The levels above ~ 70 eV are not accurate because of the neglect of $n = 5$ and higher states. The best overall fit to the observed surface peak energies, indicated by the circles and triangle in figure 3, is obtained for $\mathcal{E}' \cong 0.035$ au. For the Mg^{2+} free-ion spectrum, a rough fit of the energy levels for $n = 3 \rightarrow \infty$ relative to the ionization limit is given by a hydrogenic series with a screened charge of $Z_{eff} \sim 3$, as expected. For $\mathcal{E}' = 0.035$ au, this value of Z_{eff} gives the average surface electric field seen by an excited Mg^{2+} electron as $\mathcal{E}_s \sim 0.11$ au (3.0×10^8 V/cm). This value of $\mathcal{E}_s$ is in satisfactory agreement with the calculated Madelung electric field at the center of a Mg^{2+} ion on the undisplaced (100) surface of MgO, $\mathcal{E}_s = 0.136$ au (3.7×10^8 V/cm).

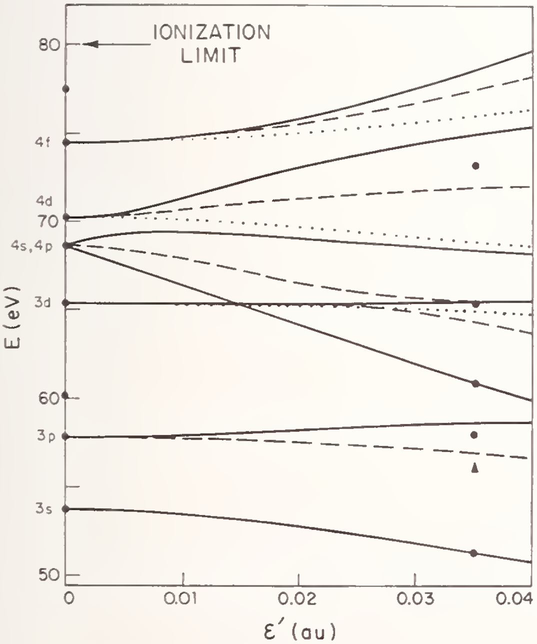

Fig. 3. Energy of Stark-split Mg^{2+} excited states vs normalized surface electric field (in atomic units). Full lines represent $m_\ell = 0$ levels, dashed lines are $m_\ell = \pm 3$ levels, and dotted lines are $m_\ell = \pm 2$ levels. The $m_\ell = \pm 3$ level associated with 4f is not shown. Squares are observed bulk peaks, dots and triangle are observed surface peaks. The triangular point is inferred to be an $m_\ell = \pm 1$ level in view of the selection rule discussed in the text.

It should be noted that we have included the $n = 4$ levels in our Stark effect calculation, but have neglected $n = 5$ and higher levels. While it is well known that the higher n-states all contribute to low-lying energy levels [10], it is also known that these levels rapidly broaden out with increasing n, because excited electrons "leak out" of the quasi-bound Stark levels. We must assume, in our interpretation, that the lowest $n = 4$ Stark level is barely resolved, and that for $n = 5$ and higher, the low-lying Stark levels are washed out.

Additional evidence for the Stark-effect model of the surface states is provided by the very small amplitude of peak S_2 in the $2s \rightarrow n\ell$ surface spectrum at normal incidence (see dotted curve of fig. 1b). Because the interaction of the Mg^{2+} surface ion with a normally incident electron beam has cylindrical symmetry, the resulting transitions should have $\Delta m_\ell = 0$ (assuming small angle scattering [11]) so that the $(2s, m_\ell = 0) \rightarrow (n\ell, m_\ell = \pm 1)$ transitions are forbidden. When the electron beam is tipped away from normal incidence, the symmetry selection rule breaks down. We do indeed observe a strong increase in the relative intensity of the $(2s, m_\ell = 0) \rightarrow (3p, m_\ell = \pm 1)$ transition at grazing incidence. The

($2p, m_\ell = 0$) and ($2p, m_\ell = \pm 1$) states are almost degenerate, and therefore transitions from the 2p levels to final states with $m_\ell = 0$ or ± 1 are observed even at normal incidence.

4. Discussion

Although the phenomenological identification of the ELS spectra of the Mg ion in MgO with the spectrum of the free Mg^{2+} ion appears satisfactory, a conceptual difficulty remains. For $Z_{eff} \sim 3$, a rough hydrogenic value for the size of the Mg^{2+}, n = 3 orbit is $r \sim (3n^2/2Z_{eff})a_{Bohr} \sim 2.25$ Å. Since the distance between the Mg^{2+} ion and the O^{2-} ion in MgO is only 2.1 Å, there is a large overlap of the Mg^{2+}, n = 3 orbit with the O^{2-} charge cloud, suggesting the importance of banding. Nevertheless, as demonstrated in ref. 1, we have found that the Mg excited states observed in MgO are in poor agreement with the conventional one-electron band picture of MgO.

Preliminary ELS spectra on MgO (110) and (111) and on amorphous MgO films showed small but reproducible shifts ($\leqslant 0.5$ eV) of the surface peaks compared to the (100) surface. The above model predicts larger Stark shifts on ideal (110) and (111) faces, however. Since the surface Madelung potential is smaller than the bulk value, Mg^+ and O^- surface ions could be more stable than Mg^{2+} and O^{2-} ions, and we should consider the possibility of such states. Our observations are consistent with the presence of Mg^+ surface ions in a much reduced surface Stark field (see fig. 4).

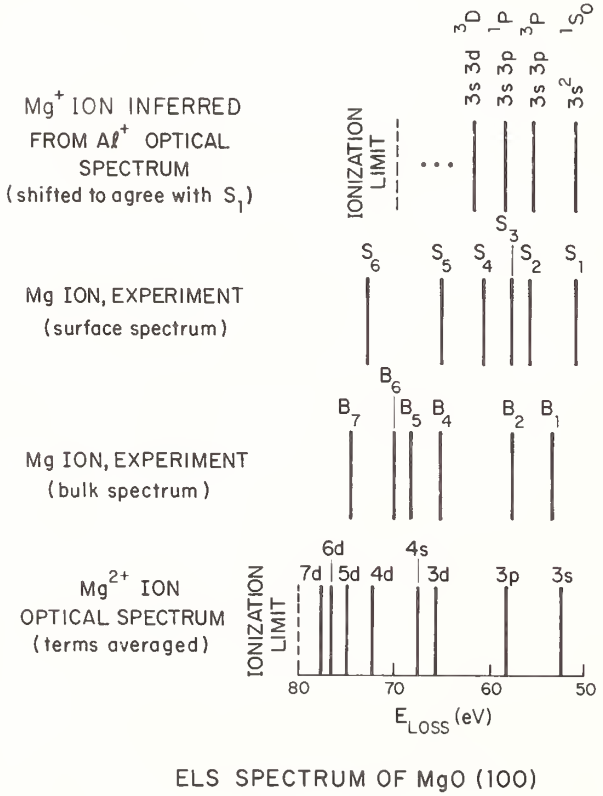

Fig. 4. Comparison of the observed magnesium bulk and surface transitions observed by (LES) in MgO with the optical spectrum of the free Mg^{2+} ion, and the spectrum inferred for the free Mg^+ ion from that observed for the free $A\ell^+$ ion.

On the other hand, the (110) and (111) faces tend to form facets of the more stable (100) surface, and had poorer LEED patterns than the (100) surface. Alternatively, then, the observations on (110), (111) and amorphous MgO surfaces may be due to a restructuring of the surface to produce a (100)-like local environment about an Mg^{2+} ion. Additional experimental and theoretical work on the localized nature of the excitonic states in ionic crystals is necessary for a detailed understanding of this class of materials.

The authors thank B. J. Palm for assistance with the computer programming and B. Feldman for technical assistance.

References

[1] Henrich, V. E. and Dresselhaus, G., Solid State Commun. 16, 1117 (1975).

[2] Moore, C. E., Atomic Energy Levels, Vol. 1, N.B.S. Circular No. 467, U. S. Government Printing Office, Washington (1949).

[3] Tracy, J. C., Electron Emission Spectroscopy (W. Dekeyser et al., Eds.) D. Reidel, Dordrecht (1973), p. 305; Palmberg, P. W. (personal communication) finds escape depths in MgO no more than 50% greater than in metals at energies larger than several times the band gap.

[4] Venghaus, H., Opt. Commun. 2, 447 (1971).

[5] Fomichev, V. A., Zimikina, T. M., and Zhukova, I. I., Soviet Phys. Solid State 10, 2421 (1969).

[6] Hanson, W. F., Arakawa, E. T., and Williams, M. W., J. Appl. Phys. 43, 1661 (1972).

[7] Lucas, A. A. and Sunjic, M., Prog. in Surf. Sci. 2, 75 (1972)

[8] Levine, J. D. and Mark, P., Phys. Rev. 44, 751 (1966).

[9] Condon, E. U. and Shortley, G. H., The Theory of Atomic Spectra, Cambridge Univ. Press, Cambridge (1951), p. 133.

[10] Rice, M. A. and Good, R. H., Jr., J. Opt. Soc. Am. 52, 239 (1962).

[11] Mott, N. F. and Massey, H. S. W., The Theory of Atomic Collisions, Oxford University Press, Oxford (1959), Chap. XI.

National Bureau of Standards Special Publication 455, *Electrocatalysis on Non-Metallic Surfaces*,
Proceedings of Workshop held at NBS, Gaithersburg, Md., December 9-12, 1975. (Issued November 1976)

QUANTUM CHEMISTRY AND CATALYSIS

R. P. Messmer
General Electric Corporate Research and Development
Schenectady, New York 12301

and

K. H. Johnson
Department and Materials Science and Engineering
Massachusetts Institute of Technology
Cambridge, Massachusetts 02139

A number of recent theoretical calculations on model systems relevant to chemisorption and catalysis is discussed. The approach taken is basically chemical in nature, emphasizing the local active site concept and employing a cluster of atoms to represent the substrate which interacts with the molecular or atomic adsorbate. The computational procedure used in these studies has been the self-consistent-field $X\alpha$ scattered wave (SCF-$X\alpha$-SW) method.

Key words: Catalysis; chemisorption theory; metal clusters; molecular orbitals; quantum chemistry; transition metal complexes.

1. Introduction

While the major focus of this workshop is on the subject of electrocatalysis on nonmetallic surfaces, the science of catalysis, in the broadest perspective, is as diverse as chemistry itself. For example, it includes reactions catalyzed heterogeneously by metallic and nonmetallic surfaces, reactions catalyzed homogeneously by transition-metal complexes in solution, acid or base catalyzed polymerization of organic molecules, certain reactions catalyzed in the upper atmosphere, photocatalytic reactions, and biochemical reactions catalyzed by enzymes.

For the theorist who wishes to investigate catalysis from a fundamental electronic point of view, the problems are enormous. For example, if one concentrates on heterogeneous catalysis and, in particular, on catalysis by metallic or bimetallic particles dispersed on a support, should the metal particles be considered from the band-theory point of view of the solid-state physicist or from the molecular point of view of the chemist? Since chemisorption is a precursor in heterogeneous reactions on supported catalysts, what are the most important adsorbate-particle configurations? What are the effects of the supporting material on chemisorption and catalytic activity? Since the theorist investigating electronic structure is accustomed to starting with the arrangement and positions of atoms in a solid or molecule, structural information is crucial. Unfortunately, such information is often lacking for heterogeneous catalysts. This is in contrast to the isolated transition-metal complexes involved in homogeneous catalysis and enzymes or proteins involved in biocatalysis, where the molecular structure and coordination chemistry are often known to reasonable accuracy.

Assuming that one has at least some idea of the molecular structure of the catalyst, a new set of questions can be asked. What is the mobility or lability of the adsorbates on the catalyst surface? What reaction intermediates or decomposition products of the adsorbates, if any, are important after the initial step of chemisorption? How do these intermediates convert or interact with other adsorbed species to yield the reaction products? These questions are related to the reaction kinetics and, from a theoretical point of view, are much more complex than those regarding simple chemisorption. In view of the rather poor status of first-principles theories for the kinetics of even the simplest chemical reactions, it is unlikely that accurate quantitative calculations for the "potential surfaces" of catalytic reactions will be practical for many years to come. However, with the proper guidance from experiment, calculations on a few configurations and not the entire potential surface may be sufficient to elucidate key features of the reaction kinetics.

With these limitations in mind, one may take a more optimistic outlook and consider how quantum chemistry can presently be employed in understanding aspects of catalysis at the electronic level. Since it is clear that chemisorption is a precursor in heterogeneous catalysis, it is important to try to understand the possible structures and bonding of adsorbates on clusters of atoms which simulate the active centers of supported metallic and bimetallic catalysts or the active centers of oxide and other nonmetallic catalysts. It is also important, from the theoretical point of view, to try to understand the coordination chemical bonding of ligands in isloated transition-metal complexes of the type important in homogeneous catalysis and the electronic structure of the active centers of enzymes and proteins involved in biocatalysis. As we will attempt to show in this paper, there are striking analogies between the chemisorption of molecules on the surfaces of transition-metal aggregates and the chemical bonding of the same molecules as ligands in isolated transition-metal coordination complexes, as well as equally striking analogies between the active centers of certain metalloproteins and the active centers of supported metal catalysts. Such analogies are probably not fortuitous. They should be investigated and their common basis elucidated.

The self-consistent-field-Xα-scattered-wave (SCF-Xα-SW) approach to molecular-orbital theory is ideally suited for the quantitative investigation of such systems. In the following sections, we will describe recent applications of this method to prototype clusters and complexes of importance in heterogeneous, homogeneous, and biological catalysis.

2. Discussion of Applications

2.1. Transition and Noble Metal Clusters

The electronic structures of small transition- and noble-metal aggregates (clusters less than 10 Å in size) are of considerable current interest and importance. For example, the active centers of heterogeneous catalysts often consist of small metallic, bimetallic, or multimetallic clusters, typically based on Group-VIII and IB elements, supported on a porous refractory material such as silica or alumina [1-3][1]. The electronic structures of small metal clusters are also intrinsically interesting in the ways they are related to the bulk electronic band structures and surface states of the corresponding crystalline metals.

In comparison with the large number of band-structure calculations for crystalline metals and alloys [4,5], relatively little fundamental work has been directed to the electronic structures of small metallic clusters. Band theory, in its conventional form, is based on the assumptions of long-range crystalline order, Bloch's theorem, and reciprocal- or $\vec{k}$-space representation, which do not apply to small clusters, where there is at most only short-range order.

Molecular-orbital (MO) theory, on the other hand, is well suited, in principle, for describing metal-cluster electronic structure but is limited by the accuracy and practicality of available MO techniques. The recently developed self-consistent-field

---

[1] Figures in brackets indicate the literature references at the end of this paper.

X-alpha scattered-wave (SCF-Xα-SW) approach to MO theory [6] is based on the combined use of the Xα density-functional approximation to exchange correlation [7] and the multiple-scattered-wave method of solving the one-electron Schrödinger equation [8]. This approach has been successfully applied to a wide range of polyatomic molecules and to clusters simulating local environments in nonmetallic solids, as summarized in a recent review article [9].

Small lithium clusters were the first metallic aggregates investigated by the SCF-Xα-SW method [10]. Results of these studies that are of possible general significance to the properties of small metal aggregates are: (1) there is a gradual increase of cohesive energy with increasing cluster size, approaching the value for the bulk solid; (2) there is a gradual decrease of first ionization potential (calculated by the SCF-Xα "transition-state" method [6,7]) with increasing cluster size, approaching the bulk work function; (3) the cluster with icosahedral geometry is the most energetically stable of all the clusters considered.

Because the required computation time does not increase inordinately with the number of electrons per atom, the SCF-Xα-SW method is ideally suited for the study of small transition- and noble-metal clusters. During the past year, we have been carrying out such calculations, with initial emphasis on elemental Cu, Ni, Pd, Pt, and Fe clusters and Cu-Ni and Cu-Fe bimetallic clusters having cubic, cubo-octahedral, and icosahedral geometries. Calculations have been completed and analyzed for Cu, Ni, Pd, and Pt clusters and are in progress for Fe, Cu-Ni, and Cu-Fe clusters.

As an illustrative example, we may consider the results obtained for 13-atom copper and nickel clusters having the cubo-octahedral geometry shown in figure 1, the structure characteristic of the local arrangement of atoms in a face-centered cubic (fcc) crystal. First of all, the MO representation of the electronic wavefunctions of the cluster and the use of orbital symmetries immediately allow one to distinguish between those orbitals which have no components on the "interior" central atom of the cubo-octahedron and which therefore are localized on the 12 equivalent "surface" atoms (hereafter called "surface orbitals"), and those orbitals which have components on all 13 atoms or are predominantly localized on the central atom (hereafter called "bulk orbitals"). Obviously, the distinction between "surface" and "bulk" orbitals of such a small cluster is academic since most of the atoms are actually surface atoms. Nevertheless, we shall adopt this terminology because it allows one to discuss the cluster results in relation to the bulk and surface electronic states of the corresponding crystals. Indeed, the rotational equivalence of the surface atoms of the cubo-octahedron in analogous to the translational equivalence of the surface atoms on an fcc crystal. However, the cubo-octahedral cluster includes both "(100)"

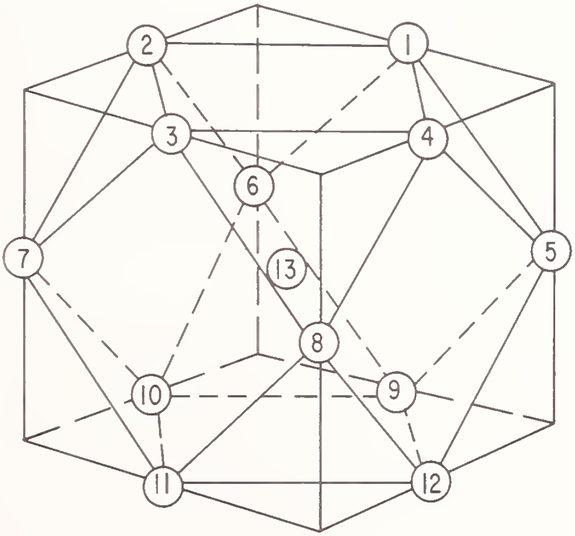

Fig. 1. Cubo-octahedral cluster containing 13 atoms.

and "(111)" type surface planes (see fig. 1), so that it is actually analogous to a faceted or polycrystalline surface, rather than a single-crystal one.

Using the orbital symmetries associated with the electronic energy levels of Cu_{13} and Ni_{13} clusters, we can separate the "bulk" and "surface" orbitals, resulting in the energy-level diagrams shown in figure 2. The levels are labeled according to the irreducible representations of the cubic (O_h) symmetry group. The first thing to note is the high density of surface orbitals in the vicinity of the Fermi level in the case of Ni_{13}. These are antibonding and nonbonding d-orbitals which are spatially oriented away from the surface of the cluster, as exemplified by the orbital contour maps shown in figures 3 through 5. In figures 3 and 4, respectively, the occupied a_{2g} orbital of Ni_{13} just below the Fermi level is mapped in a plane passing through the four nuclei (numbered 1, 2, 3, and 4 in fig. 1) in a square face of the cubo-octahedron and in an equatorial plane containing four surface atoms and the central atom (numbered 5 through 8 and 13, respectively, in fig. 1). The equatorial map in figure 4 clearly shows the absence of any contribution of the central atom to the wavefunction, consistent with the surface localization of the a_{2g} orbital.

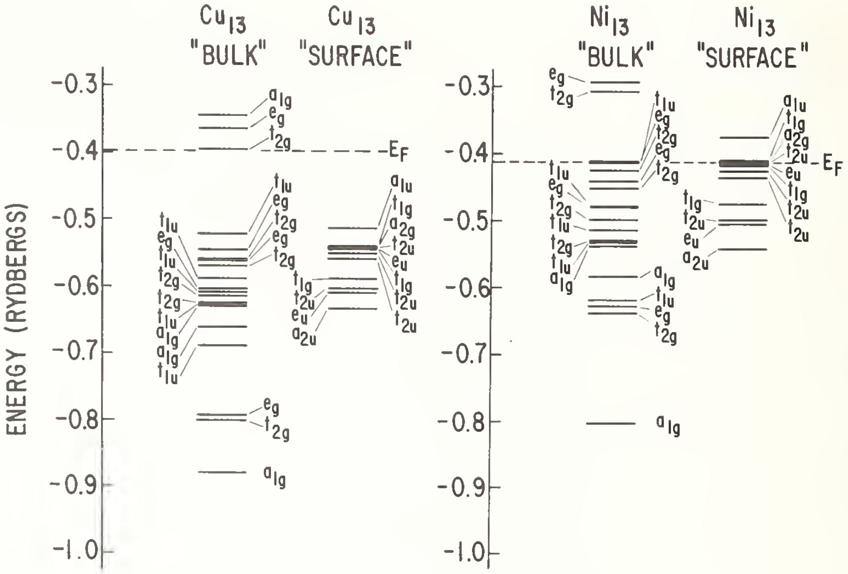

Fig. 2. Separation of the SCF-Xα-SW electronic energy levels for Cu_{13} and Ni_{13} clusters into "bulk" and "surface" components.

The unoccupied Ni_{13} a_{1u} orbital lying above the Fermi level in figure 2 is mapped in figure 5 in the plane of a square face of the cubo-octahedron. The splitting off of this d-orbital from the manifold of closely spaced d-levels around the Fermi energy may be viewed, in the simplest approximation, as a "surface ligand-field" effect arising from the repulsion of neighboring surface atomic d-orbitals. Because it is an empty "surface state" which is spatially directed away from the surface, it could possibly overlap and effectively accept electrons from interacting adsorbate atoms and molecules. On the other hand, in Cu_{13} the a_{1u} orbital is fully occupied and lies below the Fermi energy (see fig. 2). In fact, the entire manifold of surface and bulk d-levels in Cu_{13} lies well below the Fermi energy, which itself coincides with an energy level (t_{2g}) that corresponds to a highly delocalized s,p-like orbital [2]. This is very similar to the well known band structure of crystalline copper, where the d-band is completely occupied and lies well below the Fermi level. Thus, it is not expected that the d-orbitals will play a dominant role in the interaction of adsorbates with a small copper aggregate or crystallite, as they do in the case of the surface reactivity of transition metals such as nickel, where the density of surface d-orbitals around the Fermi level is high. How this situation changes as a function of "alloying" copper with nickel, to form a bimetallic cluster, is currently under investigation.

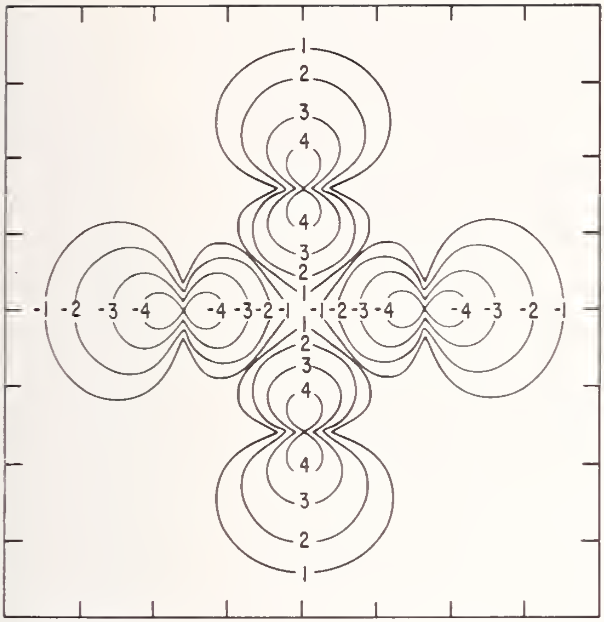

Fig. 3. Contour map for the occupied a_{2g} antibonding "surface" orbital of a Ni_{13} cluster, corresponding to the energy level -0.413 Ry shown in figure 2, plotted in the plane of the square face containing atoms 1, 2, 3, and 4 of the cubo-octahedron illustrated in figure 1.

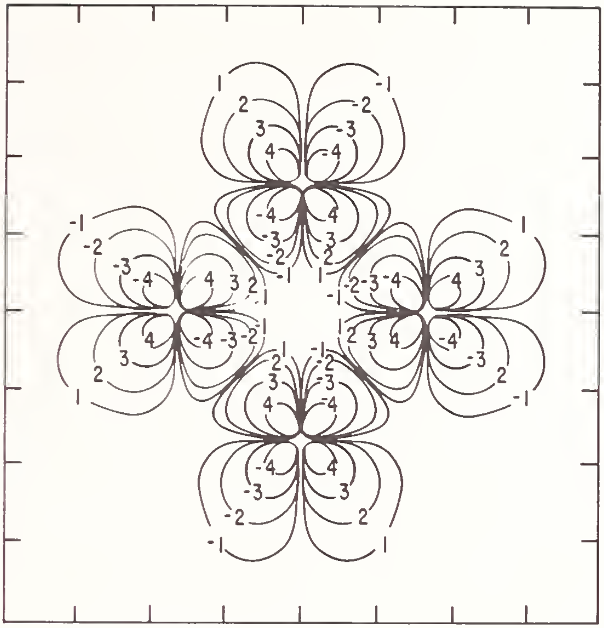

Fig. 4. Contour map for the occupied a_{2g} antibonding "surface" orbital of a Ni_{13} cluster, corresponding to the energy level -0.413 Ry shown in figure 2, plotted in the equatorial plane containing atoms 5, 6, 7, 8, and 13 of the cubo-octahedron illustrated in figure 1.

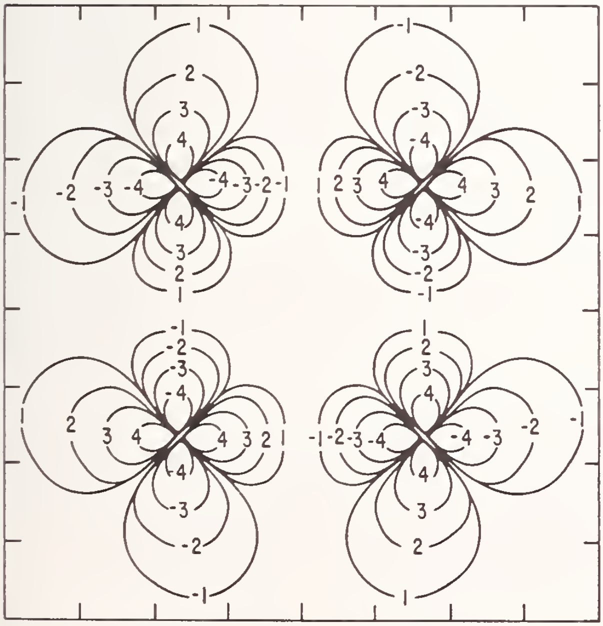

Fig. 5. Contour map for the unoccupied a_{1u} antibonding "surface orbital of a Ni_{13} cluster, corresponding to the energy level -0.376 Ry shown in figure 2, plotted in the plane of the square face containing atoms 1, 2, 3, and 4 of the cubo-octahedron illustrated in figure 1.

The calculations also suggest a slight depletion of electronic charge and therefore a slight positive charge on the surface atoms of the cluster, compensated for by a buildup of excess electronic charge on the central atom of the cubo-octahedron to preserve total electrical neutrality of the cluster. The effective surface charge (+0.06 e/atom) on Ni_{13} is somewhat larger than the value (+0.04 e/atom) for Cu_{13} and would be expected to be especially significant on transition-metal aggregates where there is a large percentage of surface atoms with relatively low coordination number, such as those at "corners" and "edges" of facets. The number of surface sites of low coordination number will tend to decrease rapidly with increasing particle size, for ideally shaped crystallites.

Further details of these results, including the effects of magnetic spin polarization on the electronic structure of nickel clusters and electronic structures for palladium and platinum clusters, are described in a recent publication [11].

One frequently hears the statement that small metallic clusters are intrinsically "different" in their catalytic behavior from larger particles or crystalline surfaces, especially in regard to so-called "demanding" or structure-sensitive reactions [1]. The higher fraction of corner and edge atoms on the surface of a small cluster, as compared with an ideal "flat" crystal surface, and the presence of spatially directed surface d-orbitals at these corners and edges (e.g., see figs. 3-5) could possibly contribute to the structure sensitivity of catalytic reactions through the preferential chemisorption of reacting molecules on these sites. Furthermore, the effective positive charges of these sites and their associated electric fields could enhance the interaction of the reacting molecules through electrostatic polarization or attraction of the adsorbate charge distributions. Other things being equal, the relatively high ionization potentials (∿7 eV) and electron affinities (∿4 eV) calculated for small transition-metal clusters by the SCF-Xα-SW "transition-state" procedure [6,7] will also tend to promote electron transfer from a nucleophilic adsorbate to cluster. The cluster ionization potential and electron affinity gradually approach the bulk work function (∿5 eV) with increasing cluster size [11].

2.2 Bimetallic Clusters and Effects of Alloying

Bimetallic and multimetallic clusters have become increasingly important in the design of active centers of supported heterogeneous catalysts, particularly those that are selective for specific reactions [2]. For example, the hydrogenolysis of ethane and dehydrogenation of cyclohexane are reactions which are both activated by elemental nickel catalysts. However, as copper is alloyed with nickel, the rate of hydrogenolysis decreases precipitously with increasing copper concentration, while the dehydrogenation reaction remains relatively constant over a wide range of composition [12]. Two factors of possible relevance to this behavior are that the hydrogenolysis reaction is structure sensitive, whereas the dehydrogenation reaction is normally structure insensitive, and there may be surface segregation of copper in the Cu-Ni aggregates.

We have begun to investigate the effects of alloying on the electronic structures of transition-metal clusters, with initial emphasis on bimetallic clusters of Group-VIII and IB elements. This can be accomplished by systematically substituting the "impurity" atoms in the host metal aggregate and then carrying out SCF-Xα-SW calculations for the electronic structure of the composite system.

For example, suppose we wish to study a Cu-Ni cluster, and the host aggregate is a Cu_{13} cluster having the cubo-octahedral geometry shown in figure 6. Then we can construct the bimetallic clusters by selectively substituting Ni atoms for Cu atoms in the cubo-octahedron, allowing for possible relaxations of interatomic distance. The effects of surface segregation of Cu can be modeled by embedding small "islands" of Ni atoms, e.g., Ni_2 diatoms, in a "sea" of surface Cu atoms and then calculating the electronic structure of the composite cluster. The effects of alloying and surface segregation on chemisorption

---

[2] In this case, the t_{2g} wavefunction s- and p-components on the outer 12 atoms are dominant over the d-components on the central and outer atoms.

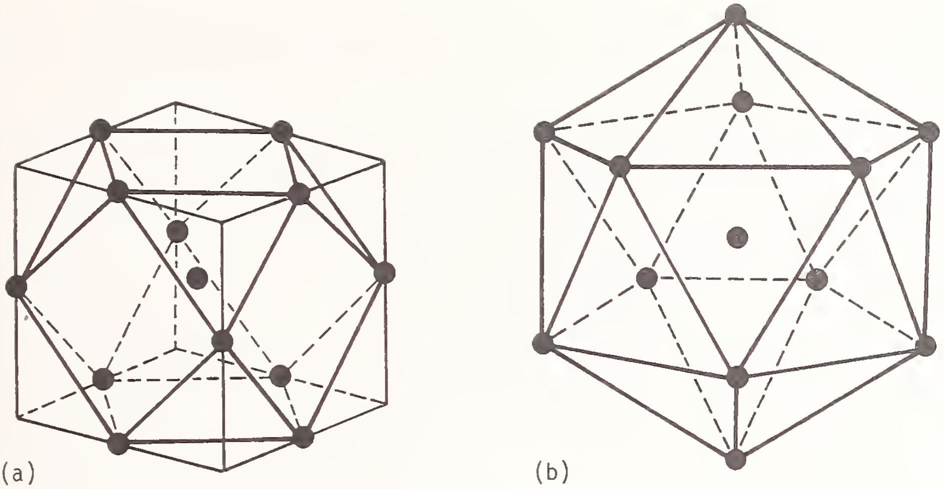

Fig. 6. 13-atom clusters: (a) Cubo-octahedral geometry; (b) Icosahedral geometry.

can then be modeled, in turn, by allowing adsorbates to interact with the bimetallic cluster and comparing this interaction with the results obtained for chemisorption on pure Ni_{13} and Cu_{13} clusters. This procedure can, in principle, be carried out over a range of cluster compositions and geometries, including the effects of typical supporting environments. Calculations for 13-atom Cu-Ni clusters are in progress.

It is possible to study the effects of magnetic spin polarization on the electronic structures of transition-metal clusters and the changes in magnetic behavior with alloying, using the spin-unrestricted SCF-Xα-SW method. For example, the spin-polarized orbital energies for a cubo-octahedral Ni_{13} cluster are shown in figure 7. The levels are displayed on two energy scales, one encompassing the entire d-band and overlapping s,p-levels, and the other resolving the upper part of the d-band on a much finer energy mesh. The "Fermi level" E_F, separates the unoccupied spin orbitals from the occupied ones and passes through a high density region of minority-spin levels. Note that the spin splitting of the energy levels corresponding to orbitals which are predominantly s,p-like is smaller than that of the d-levels. The spin magneton number per atom in Ni_{13} is 0.46, assuming the net spin density, arising from the six unpaired spins in the topmost occupied $t_{1u}\uparrow(-0.425\ \mathrm{Ry})$ and $t_{1g}\uparrow(-0.427\ \mathrm{Ry})$ spin-orbitals, to be delocalized uniformly over all 13 atoms. This value may be compared with the magneton number (0.25) per atom calculated for the smaller cluster, Ni_8 [11], and with the value (0.54) characteristic of ferromagnetic crystalline nickel. Although we have thus far investigated the spin polarization in nickel clusters of rather limited size and geometry, the results are consistent with the experimental observation of Carter and Sinfelt [13] that the paramagnetic magneton number for small nickel crystallites decreases continuously from the bulk value as the crystallite size is reduced from 100 Å to approximately 10 Å. The so-called "superparamagnetism" of such metal aggregates is often utilized at a measure of the particle size and dispersion of supported metal catalysts [2].

Although our theoretical studies of bimetallic clusters have been initially focused on the Cu-Ni and Cu-Fe systems, we plan to investigate other bimetallic systems as well. For example, a recent experimental investigation of Pt-Fe clusters supported on alumina, using Mössbauer spectroscopy, chemisorption measurements, and kinetic studies of the synthesis of hydrocarbons from CO and H_2 (Fischer-Tropsch synthesis) indicate that Fe, which is normally a good Fischer-Tropsch catalyst, becomes catalytically inert in the CO-H_2 synthesis when alloyed in the form of Pt-Fe clusters [14]. The inert behavior of Fe in the Pt environment is attributed to a decrease in electron density on the Fe atoms, as suggested by the Mössbauer isomer shift data [14]. We plan to carry out SCF-Xα-SW studies of Pt-Fe clusters, using our recent results for elemental Pt clusters as the starting point [11]. Other bimetallic systems of catalytic importance which are readily within the scope of the SCF-Xα-SW method include Pd-Ag and Pd-Au clusters.

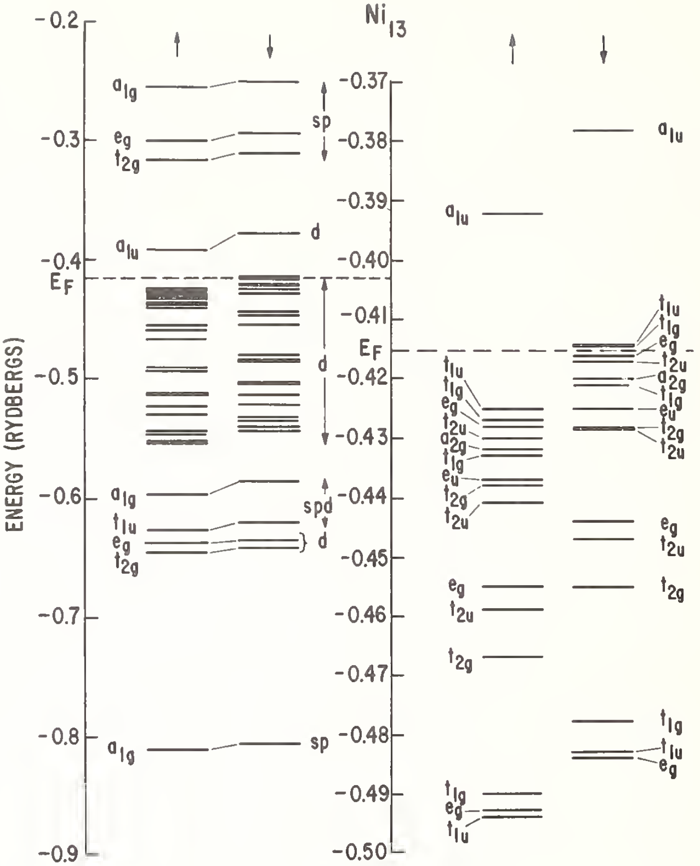

Fig. 7. Spin-polarized SCF-Xα-SW electronic energy levels for a cubo-octahedral Ni$_{13}$ cluster with nearest-neighbor internuclear distance equal to that for bulk crystalline nickel. The levels are labeled according to the irreducible representations of the O_h symmetry group. The "Fermi level" E_F separates the occupied levels from the unoccupied ones.

2.3 Effects of the Supporting Environment

When utilized as the active centers of a heterogeneous catalyst, small metal clusters are usually supported in a porous refractory material such as silica or alumina [3]. If the sensitivity of a catalytic reaction cannot be explained solely in terms of the surface morphology or intrinsic electronic structure of the clusters themselves, then it is possible that the supporting material itself may be involved [1]. Most supporting materials are oxides and may effectively withdraw electrons from the small metal clusters in contact with them, much in the same way as the ligands of a simple transition-metal atom. The electron depletion could then allow the small metal cluster to interact with adsorbates in a different manner from the elemental clusters themselves. On the other hand, for larger metal aggregates or particles in a support, the electron withdrawing effect of the surrounding material may be largely screened out, by the intervening metal atoms, from the surface of the particle. Thus for these larger particles the main effect on catalytic behavior might be determined by the effective surface area.

For example, clusters of fewer than six platinum atoms contained in the supercages of a Y-zeolite containing multivalent cations exhibit a catalytic activity per surface Pt atom which is enhanced by a factor of about five over that of other platinum catalysts for the hydrogenation of ethylene, a reaction that is normally structure insensitive [15]. They also chemisorb less oxygen than larger platinum crystallites. This fact and the enhanced catalytic activity have been attributed to electron transfer from the small platinum clusters to the zeolite support, as if platinum were behaving more like its neighbor, iridium, to the left in the periodic table [15].

We have begun to construct quantitative theoretical models for the effects of supporting materials such as Y-zeolite, SiO_2, and Al_2O_3 on the electronic structures of small transition- and noble-metal clusters. For example, in considering a small platinum cluster supported in Y-zeolite, the cluster is embedded in a local molecular environment simulating that of the zeolite, and SCF-Xα-SW calculations will be carried out for the composite system. The amount of effective charge transfer between the metal cluster and zeolitic framework can then be determined from a comparison of the electronic structure of the composite system and that of the isolated metal cluster. The effects of multivalent cations (e.g., Mg^{2+}, Ca^{2+}) in the Y-zeolite on the metal clusters will also be investigated. Recent applications of the SCF-Xα-SW method to SiO_2 and Al_2O_3 [16] show that only relatively small clusters are needed to simulate the electronic structures and properties of these materials, and these results can be utilized in the modeling of Y-zeolite.

A possible effect of electron transfer from a metal cluster to its supporting environment is to increase the effective work function and electron affinity of the cluster, thereby promoting its interaction with nucleophilic adsorbates but diminishing its interaction with electrophilic adsorbates. Such calculations as described above should provide an accurate oheck of this naive argument.

Somewhat related to the issue of metal-support interactions is the nature of the electronic structure of the 4-Fe active sites in ferredoxin and "high-potential" proteins which are important as electron-transfer agents in the metabolism of bacteria, plants, and animals [30]. The active site, an $Fe_4S_4(S\text{-}Cys)_4$ cluster, consists of an approximately cubic array of Fe and S atoms on alternate vertices, with four outer sulfur atoms attaching the cluster to the surrounding protein via cysteinyl groups. The sulfur atoms may be viewed as providing a "support" for the Fe_4 cluster, and therefore possible analogies with the effects described in the preceding section are obvious. Indeed, the results of preliminary SCF-Xα-SW calculations for $[Fe_4S_4(SCH_3)_4]^{2-}$, a prototype model of oxidized ferredoxin and reduced "high-potential" proteins, in which methyl groups have been substituted for the cysteinyl moieties, suggest significant amounts of charge transfer and orbital delocalization of the Fe_4 electrons onto the surrounding sulfur ligands, with each iron site in the effective $Fe^{+2.5}$ valence state [17]. The distorted cubane geometry of the active centers of oxidized ferredoxin, the reduced high-potential proteins, and their analogs are explained in terms of the Jahn-Teller instability of the cubic (T_d) symmetry, and spin-orbital occupancy in the lower (D_{2d}) symmetry is consistent with measured temperature-dependent magnetic properties [17].

There are probably many useful analogies to be made between supported metal cluster catalysts and the active centers of metallo-proteins and enzymes like ferredoxin. Such analogies are probably <u>not</u> fortuitous. They should be sought after and the common basis of understanding elucidated.

2.4 Models for Chemisorption and Reactivity on Metallic and Non-Metallic Substrates

Let us now consider some theoretical models for chemisorption on Ni, Pd, Pt, Fe, and Cu-Ni clusters, with emphasis on those molecular species and configurations which are believed to be important as reaction intermediates in the activation of the chemical reactions

$$CO + 3H_2 \rightarrow CH_4 + H_2O$$

$$N_2 + 3H_2 \rightarrow 2NH_3$$

$$C_2H_4 + H_2 \rightarrow C_2H_6$$

by supported metal and bimetallic heterogeneous catalysts.

In regard to the nature of chemisorption on transition-metal clusters, it is important to note the occurrence in inorganic chemistry of metal cluster complexes [18] such as the iron carbonyl carbide [19] illustrated in figure 8. This is a case where linear and bridged carbonyl groups occur, both of which have been speculated to form in the chemisorption of CO on transition-metal surfaces and to be important as surface species in catalytic reactions involving CO. The existence of such cluster complexes suggests how small metal clusters of the type that may be found as the active centers of heterogeneous catalysts can form more or less normal chemical bonds on the cluster periphery and particularly at corners and edges of a faceted cluster surface. The cluster complex shown in figure 8, which is only one of many examples [18], is a true molecular analogue of CO chemisorbed on iron carbide, since there is a central carbon atom coordinated octahedrally by Fe atoms at almost the precise Fe-C distance characteristic of bulk iron carbide [19]. Therefore, it may be no coincidence that iron carbide is an excellent catalyst for the Fischer-Tropsch synthesis of hydrocarbons from CO [20].

Our investigation of CO chemisorption on transition-metal and bimetallic clusters draws on the knowledge and experience gained in recent extensive SCF-Xα-SW studies of the molecular transition-metal carbonyls, $Ni(CO)_4$, $Fe(CO)_5$, $Cr(CO)_6$, $W(CO)_6$, $Mo(CO)_6$, $Mn_2(CO)_{10}$, and $Fe_2(CO)_9$, carried out in collaboration with W. G. Klemperer [21]. The systematic study of these simpler mononuclear and binuclear metal carbonyls is an absolutely essential prerequisite before calculations on polynuclear carbonyls and cluster models for CO chemisorption are attempted.

It is also important to observe that the study of metal clusters "saturated" by adsorbates, as shown in figure 8, is likely to be relevant to the high surface coverage of adsorbates characteristic of catalytic reactions which normally occur on heterogeneous catalysts at relatively high pressures, whereas theoretical studies which focus on a single adsorbate bonded to an extended substrate are likely to be relevant to low-pressure chemisorption on a single-crystal surface. The SCF-Xα-SW molecular-orbital treatment of a metal cluster more or less symmetrically covered with adsorbate atoms automatically includes the effects of adsorbate-adsorbate interactions along with metal-adsorbate bonding.

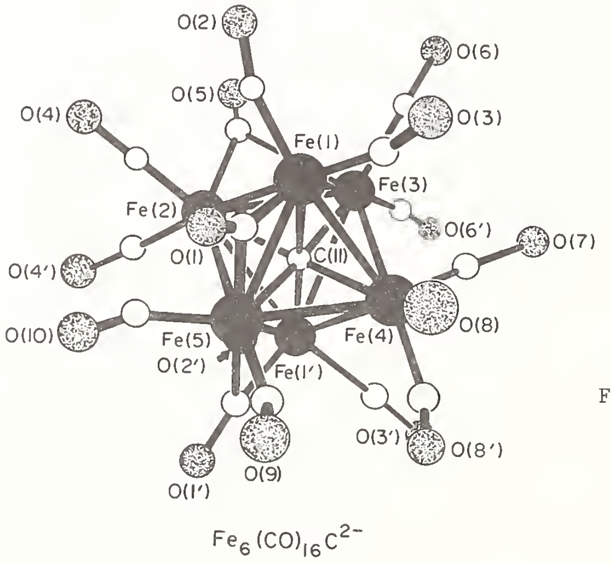

Fig. 8. Structure of the iron carbonyl carbide molecular ion, $Fe_6(CO)_{16}C^{2-}$.

To illustrate the type of information an SCF-Xα-SW molecular-orbital study of chemisorption provides, when implemented properly, we consider recent studies of prototype transition-metal-olefin systems of catalytic importance, carried out in collaboration with N. Rösch [22-24]. Olefins are involved in many chemical reactions which are catalyzed <u>heterogeneously</u> and/or <u>homogeneously</u>. For example, in figure 9 we schematically represent possible catalytic precursors and reaction intermediates in the <u>heterogeneous</u> hydrogenation of ethylene (C_2H_4) on a supported transition-metal cluster and homogeneous hydrogenation of ethylene by a "square-planar" transition-metal coordination complex. The major steps in the heterogeneous reaction shown in Fig. 9(a) are: the molecular chemisorption of ethylene and dissociative chemisorption of hydrogen; transfer of chemisorbed hydrogen atoms to chemisorbed ethylene; desorption of ethane. The major steps in the homogeneous reaction shown in figure 9(b) are: the molecular addition of ethylene and dissociative addition of hydrogen as ligands of the transition metal, with ligand exchange; the transfer of hydrogen ligands to the ethylene ligand; dissociation of the hydrogenated ethylene ligand as ethane. It is clear that there is a one-to-one correspondence between the chemisorption of ethylene and hydrogen on the metal cluster and the addition of ethylene and hydrogen as ligands of the isolated metal complex. It has therefore been one of our principal objectives to determine the degree to which chemisorption and heterogeneous reactivity on the active sites of supported metal or bimetallic catalysts are governed by the same principles of coordination chemistry which underlie the chemical bonding and homogeneous reactivity of isolated transition-metal complexes. Since transition-metal complexes tend to be more selective or specific with respect to the reactions they catalyze and are generally more resistant to

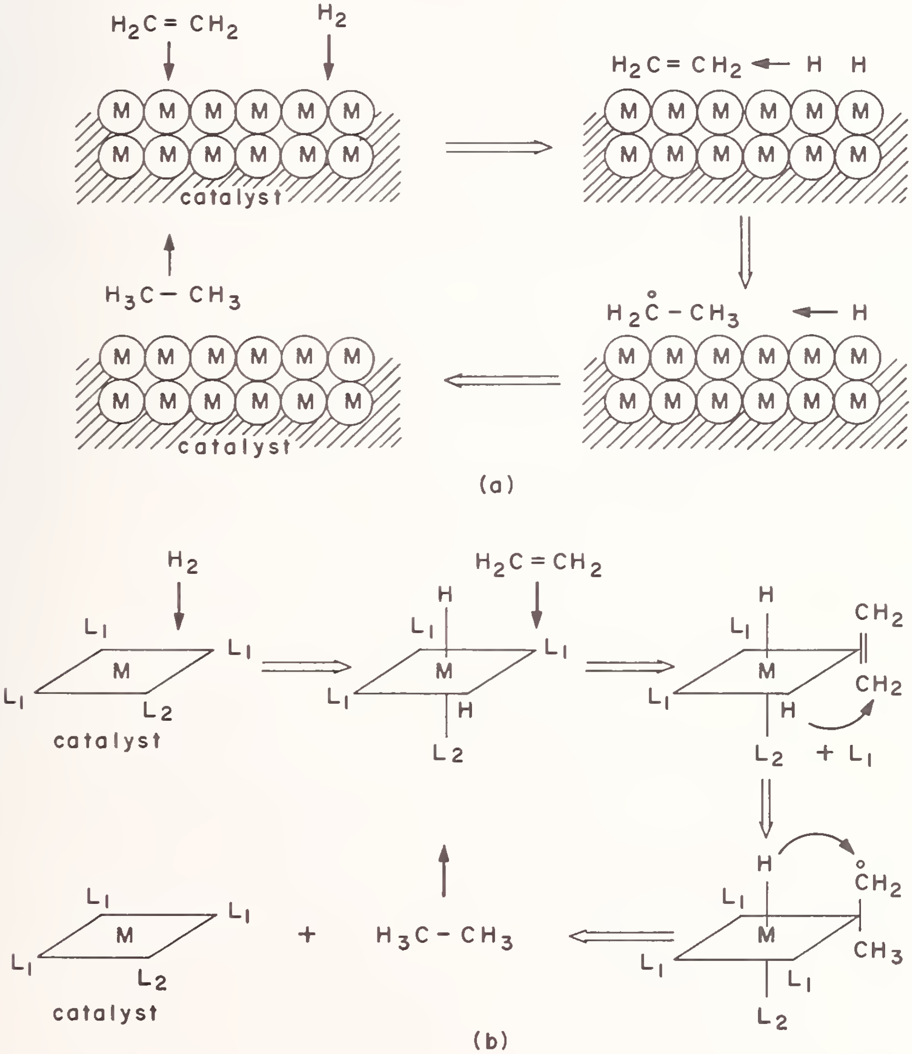

Fig. 9. Heterogeneous vs. homogeneous catalysis. (a) Schematic representation of heterogeneous catalysis of ethlene hydrogenation on the surface of a supported transition metal aggregate; (b) Schematic representation of the homogeneous catalysis of ethylene hydrogenation by an isolated transition-metal complex.

catalyst poisoning than are the extended surfaces of much larger metal aggregates [25], a fundamental understanding of how the local site symmetry and coordination of a transition-metal atom affect its chemical bonding could ultimately aid in the design of very small metal or bimetallic cluster complexes which exhibit optimum catalytic activity, selectivity, and stability.

As a first step toward this long-range objective, we have initiated a study of the bonding of ethylene to very small aggregates and complexes of Ni, Pd, and Pt. The intent of this study is to establish how the metal-olefin chemical bonding varies with the composition and size of the metal aggregate, supporting environment, and presence of coordinated nonmetallic ligands.

The simplest case to start with and the one that is also most directly comparable with isolated transition-metal complexes that homogeneously catalyze the hydrogenation of ethylene [25] is that of a single ethylene molecule bonded to a single atom of Ni, Pd, or Pt. In figure 10 we show the resulting SCF-Xα-SW orbital energies for these systems, calculated for a metal-ethylene bond distance equal to that used in earlier theoretical studies of the platinum-olefin complex, Zeise's anion $[Pt(C_2H_4)Cl_3]^-$, by the SCF-Xα-SW method [22]. This bond distance was chosen for comparison of the bonding of C_2H_4 to Ni, Pd, and Pt because many ethylene compexes of these Group-VIII metals have bond distances which are within 0.1 Å of this value. The metal-ethylene orbital energies in figure 10 are labeled according to the C_{2v} symmetry group, and the highest occupied level in each case is the one labeled $5a_1$. Also shown for comparison are the SCF-Xα-SW orbital energies for the isolated ethylene molecule, labeled according to the symmetry group.

In figure 10, the related orbitals are connected by broken lines. The ethylene orbitals from $2a_g$ up to $1b_{3g}$ undergo an almost uniform shift, with only a slight upward shift on going from Pt to Pd to Ni. The π and π* levels of ethylene on the other hand

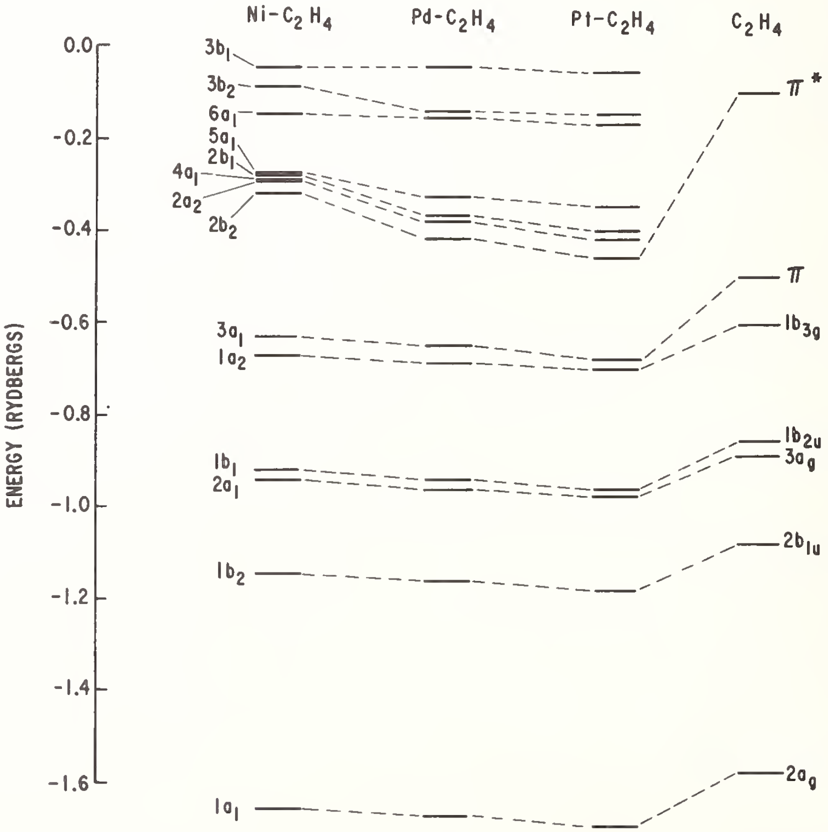

Fig. 10. Comparison of calculated electronic energy levels for Ni-C_2H_4, Pd-C_2H_4, Pt-C_2H_4 and C_2H_4. The same geometry was employed for all calculations.

experience a rather profound change on interacting with an atom of Pt, Pd, or Ni. Thus the $3a_1$ and $2b_2$ orbitals are in each case primarily responsible for the bonding, through the overlap and interaction of metal d orbitals (d_{z^2} and d_{yz}, respectively, if the metal-ethylene and carbon-carbon bond directions are along the z and y axes, respectively) with the ethylene π and π* orbitals. The metal s and p orbitals also participate in the bonding but to a lesser extent. The $2a_2$, $4a_1$, and $2b_1$ levels correspond principally to nonbonding d_{xy}, $d_{x^2-y^2}$, and d_{xz} atomic orbitals, whereas the $5a_1$ level corresponds to a metal d_{z^2} orbital that is slightly antibonding with respect to the ethylene π orbital. These characteristics of the orbitals are revealed in figures 11(a)-11(d) and 12(a)-12(d), where contour maps of the $3a_1$, $4a_1$, $5a_1$, and $2b_2$ wavefunctions are shown in the z-y plane containing the metal atom and carbon atoms of ethylene. The overlap of the axially symmetric metal d_{z^2} orbital with the ethylene π orbital in the $3a_1$ wavefunction is evident in figures 11(a) and 12(a), corresponding to the classic "σ-donation" or ethylene π electrons into the unoccupied metal d_{z^2} atomic orbital as originally postulated for transition-metal-olefin bonding by Dewar, Chatt, and Duncanson [26]. In figures 11(d) and 12(d) for the $2b_2$ wavefunction, we see the overlap of the four-lobe d_{yz} orbital of the metal with the ethylene π* orbital, corresponding to the "π-back donation" of metal d_{yz} electrons into the unoccupied π* orbital postulated by Dewar, Chatt and Duncanson [26].

The increasing stabilization of the $2b_2$ orbital and the increasing overlap of the metal d_{yz} orbital with the ethylene π* orbital in the $2b_2$ wavefunction as one goes from Ni to Pd to Pt [see figs. 10, 11(d), and 12(d)] suggest increasing metal-to-ethylene back donation from Ni to Pt. In this regard, it is interesting to note that Pd, which exhibits a degree of back-bonding to ethylene intermediate to that of Ni and Pt, is an order of magnitude

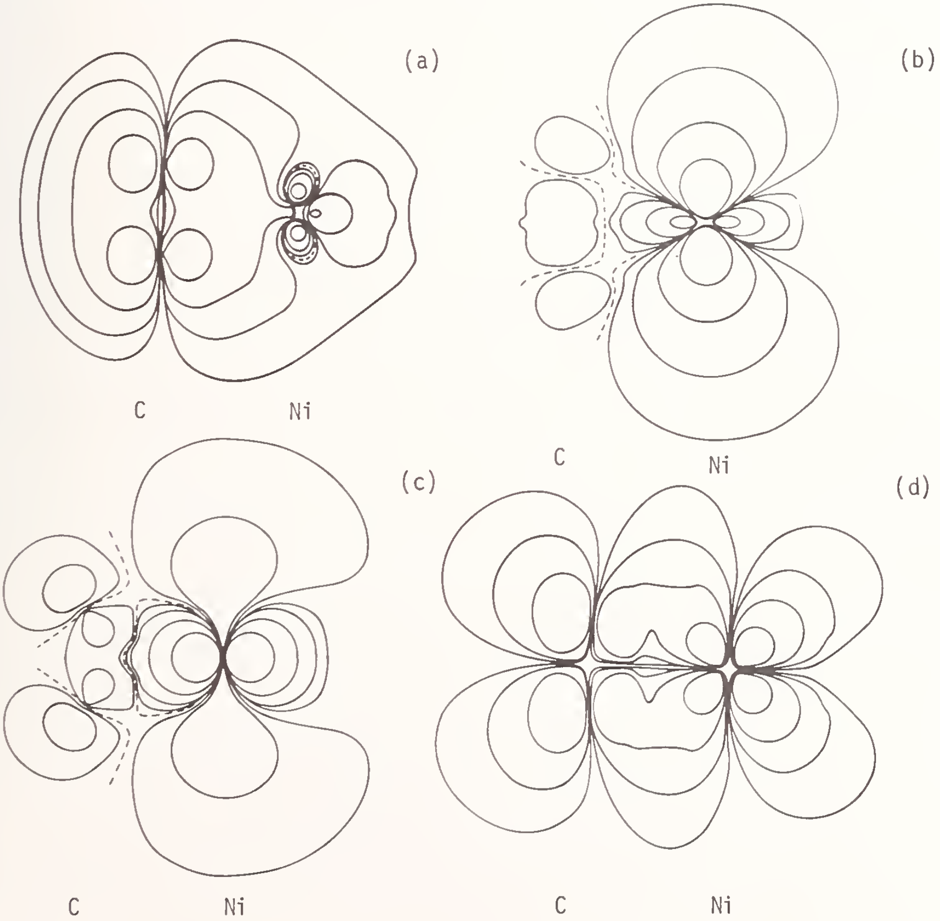

Fig. 11. Contour maps of the (a) $3a_1$; (b) $4a_1$; (c) $5a_1$; and (d) $2b_2$ orbitals of Ni-C_2H_4. Nodes are indicates by dashed curves.

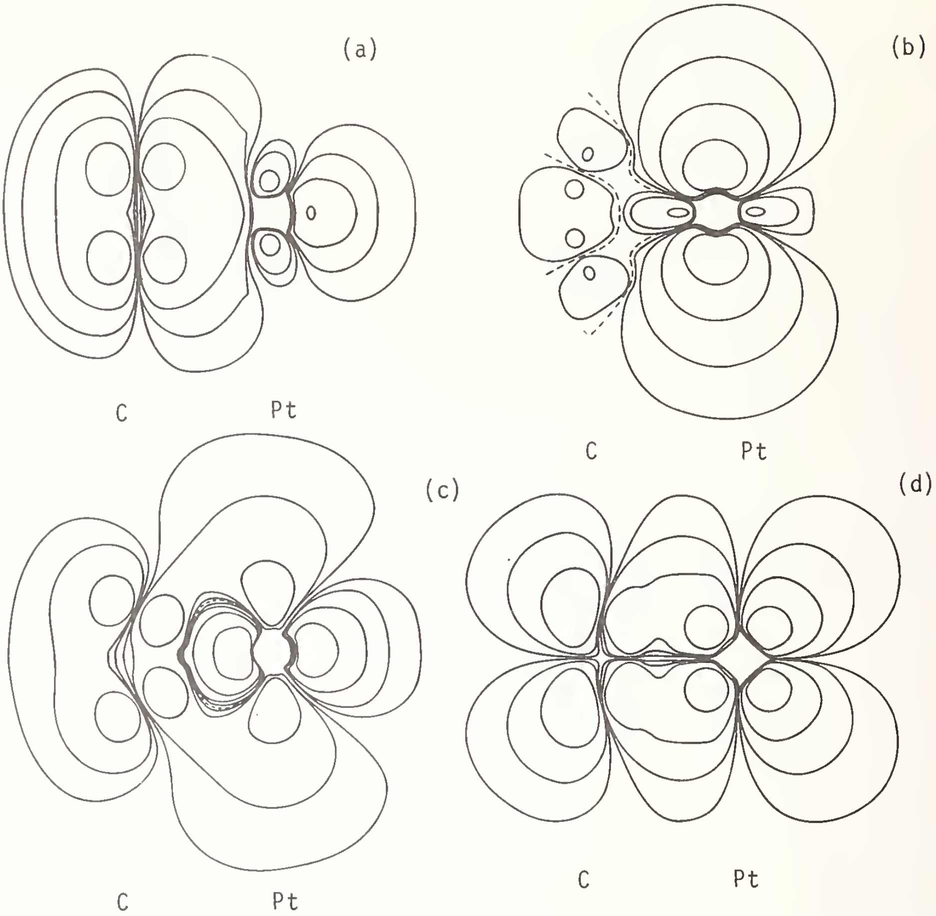

Fig. 12. Contour maps of the (a) $3a_1$; (b) $4a_1$; (c) $5a_1$; and (d) $2b_2$ orbitals of Pt-C_2H_4. Nodes are indicated by dashed curves.

more catalytically active for the hydrogenation of ethylene than are Ni and Pt [27]. It has been suggested that metal-olefin chemical bonding of "moderate" strength, rather than bonding that is "too weak" or "too strong," is the optimum precursor in transition-metal catalyzed olefin hydrogenation [28].

Of course, the above described study of the molecular orbitals for ethylene bonded to a single transition-metal atom at fixed internuclear distance, while instructive as to the principal components of metal-olefin bonding and their systematic variation from Ni to Pd to Pt, is rather far removed from the interaction of olefins with metal clusters and complexes of the type illustrated in figure 9 which are important in heterogeneous and homogeneous olefin catalysis. As a preliminary study of the effects of gradually increasing the size of the metal aggregate [see fig. 9(a)] and adding electronegative ligands [see fig. 9(b)] on metal-olefin chemisorption, the following prototype examples have been investigated: (1) adding another metal atom to the M-C_2H_4 complex and (2) adding three planar chlorine ligands to the M-C_2H_4 complex. In the former case, the M_2-C_2H_4 complex has been considered in two alternative configurations: (1) with the C_2H_4 molecule attached to the metal diatomic "end-on" (the "linear" configuration) and (2) with the carbon-carbon bond direction parallel to the metal-metal bond (the "bridged" configuration). Both configurations are speculated to be important in the chemisorption and reactivity of olefins on larger transition-metal aggregates and extended surfaces. In the case of Ni_2-C_2H_4, such calculations have also been made by others, using the SCF-Xα-SW method [29].

A direct comparison of the orbital energies calculated for Ni-C_2H_4 and Ni_2-C_2H_4 (in the "linear" bonded configuration) is shown in figure 13. The broken lines in figure 13 connect orbitals which are related in the two cases and are of particular importance in

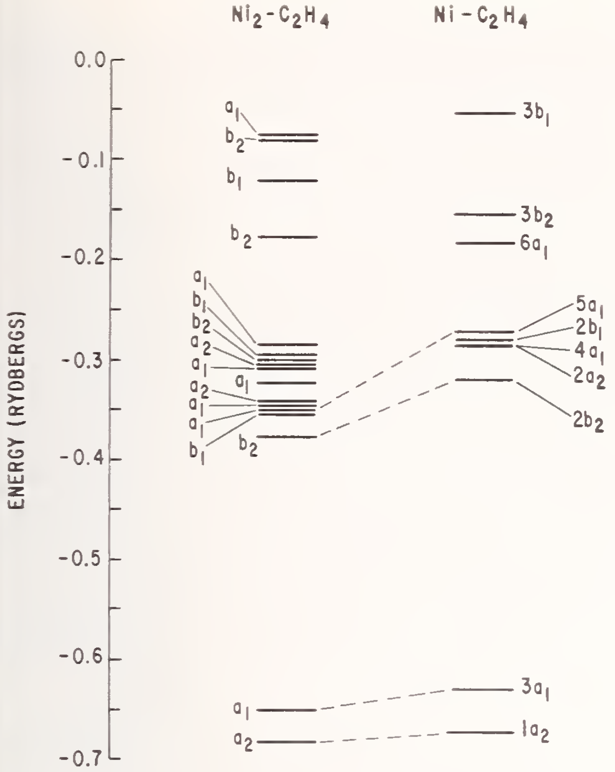

Fig. 13. Comparison of calculated electronic energy levels for Ni–C$_2$H$_4$ and Ni$_2$–C$_2$H$_4$; the latter one from Rösch and Rhodin [29].

understanding the effects of adding the extra metal atom on the bonding of ethylene σ orbital, remains relatively unchanged. The 3a$_1$ level, which corresponds to the ethylene π orbital that effectively "donates" electrons into the metal d_{z^2} orbital, is slightly lowered in energy in the case of Ni$_2$-C$_2$H$_4$, indicating that the second Ni atom, although not directly bonded to ethylene in the "linear" configuration, contributes to the stabilization of this orbital. The 2b$_2$ level, which corresponds to the metal d_{yz} orbital that effectively "back donates" electrons into the ethylene π* orbital, is also somewhat lowered by the presence of the second metal atom. However, the most dramatic change occurs in the 5a$_1$ level which, while slightly antibonding in the case of Ni-C$_2$H$_4$, is significantly stabilized by the addition of the second Ni atom. This orbital is lowered in energy below the nonbonding d orbitals and contributes to the metal-ethylene bonding in Ni$_2$C$_2$H$_4$. Similar results, differing however in important details, have also been obtained for Ni$_2$-C$_2$H$_4$ in the "bridged" configuration. Contour maps for the most important molecular orbitals of Ni$_2$-C$_2$H$_4$, in both the "linear" and "bridged" configurations, may be seen in Ref. 29 and compared directly with the orbital contour maps for Ni-C$_2$H$_4$ shown in figures 11(a)-(d).

It is, of course, highly desirable to establish, from first principles, the relative energetic stabilities of the linear, bridged, and other possible geometric configurations in metal-olefin bonding, especially in regard to the precursors, reaction paths, and kinetics of olefin catalysis. The same issues also arise in the chemisorption and catalytic reactions of other molecules, such as CO, on transition metals. This requires the calculation of total energies and their differences as a function of molecular geometry, often to an accuracy of a few kilocalories per mole. We are currently attempting to improve our present computational procedure for calculating total energies, starting with the recently proposed "overlapping-sphere" extension of the SCF-Xα-SW method [30-32], which allows one to compensate for errors arising from the "muffin-tin" representation without sacrificing the computational efficiency of the method. Indeed, overlapping atomic spheres were used in the metal-ethylene molecular-orbital calculations described above. Whether this approach is ultimately accurate enough to serve as the basis for calculating catalytic reaction paths remains to be seen, particularly for larger metallic and bimetallic clusters based on Ni, Pd, and Pt, where the total energies are very large numbers and the pertinent energy differences are very small numbers.

Therefore, it is very important to attempt to develop alternative concepts of catalytic reactivity, based purely on "one-electron" quantities that can be computed accurately and efficiently with the SCF-Xα-SW method for both small and large systems. An example of the latter is Slater's "transition-state" concept [7], which has already been successfuly applied to a wide range of molecules and clusters [8,9] to determine electronic excitation energies, including orbital relaxation effects. Electronic excitations of optical energies are, of course, crucial to photocatalytic and other photochemical behavior [33]. Such excitations redistribute electronic charge in the molecule, often making it more susceptible to chemical reaction than the molecule in its ground state. Electronic excitations of lower energy (e.g., thermal energy) and those effectively induced through charge transfer between adsorbate and catalyst probably underlie other types of catalytic activity. For example, the combined effects of donating ethylene π electrons into the d orbitals of a transition-metal catalyst and back donation of d electrons into the ethylene π* orbital can be viewed as an effective partial excitation of electrons between the π and π* orbitals, redistributing charge in ethylene so as to make it more susceptible for chemical reaction with certain other atoms and molecules.

Orbital symmetry rules, such as those introduced by Woodward and Hoffmann [34] and Fukui [35] and further developed by Mango and Schachtschneider [36] and Pearson [37] can also be used to elucidate certain features of chemical reaction paths. The basic idea is that, for a chemical reaction to occur with reasonable activation energy, there must be a low lying unoccupied molecular orbital (LUMO) for the reacting system having the same symmetry as the highest occupied molecular orbital (HOMO), and the energy gap between the HOMO and LUMO must be reasonably small (a few eV or less). The requirement that the HOMO and LUMO have the same symmetry is equivalent to the requirement that these two orbitals have a net positive overlap. Implicit in the application of these rules is the notion of electron flow between the HOMO and LUMO.

A catalyst can often be viewed as providing a pathway for electrons to flow between the reactants, where such flow is normally prevented to occur by orbital symmetry restrictions. In other words, a primary role of the catalyst is to <u>break</u> the orbital symmetry restrictions through the coordination chemical bonding of reactions and to permit the reaction to occur at low activation energy. A good example is olefin hydrogenation, e.g.,

$$C_2H_4 + H_2 \rightarrow C_2H_6$$

where the transfer of electrons directly from the filled π orbital of the olefin to the empty σ* orbital of H_2 is forbidden by the orbital symmetries. However, hydrogen atoms that have first been dissociated by a transition-metal catalyst can be readily transferred to an olefin molecule that is d_{yz}-π* back-bonded to the metal resulting in the formation and evolution of the hydrogenated species (ethane). As shown in figure 9, this process can take place heterogeneously on the surface of a supported metallic or bimetallic aggregate or homogeneously through exchange of ligands by an isolated transition-metal coordination complex. As emphasized, however, in the recent excellent review of heterogeneous catalysis by Madey <u>et al</u>. [38], the application of orbital symmetry rules to catalysis is based on the assumption of <u>concerted</u> reactions with high symmetry transition states, whereas alternative mechanistic schemes are sometimes more likely [39].

In regard to the chemisorption and reactivity of hydrogen on transition-metal aggregates, it has recently been suggested that delocalized metal s orbitals, and <u>not</u> localized orbitals, are responsible for the chemical bonding and catalytic reactivity of hydrogen [40]. While metal s orbitals may indeed contribute significantly to the chemisorption and lability of atomic hydrogen (SCF-Xα calculations indicate that metal s orbitals are important), the d orbitals are essential to the activation of H_2 dissociation and, as we have shown above, to the coordination chemical bonding and reactivity of olefins on transition metals. Preliminary theoretical studies of the interaction of CO with transition metals also show that metal d orbitals are primarily responsible for the bonding, whereas metal s and p orbitals participate in the bonding to a lesser extent [21].

The SCF-Xα-SW method is particularly well suited for the quantitative implementation of orbital symmetry rules in catalysis, since the ordering of both the occupied and unoccupied molecular orbitals (HOMO and LUMO) <u>and</u> the corresponding orbital energies as a function of occupation number are automatic consequences of the self-consistent-field-Xα-density-functional representation of molecular-orbital theory [7]. In this regard, it should be emphasized that the orbital energies in the SCF-Xα theory are rigorously equal to <u>derivatives</u> of the total energy with respect to occupation number, i.e.,

$$\varepsilon_{ix\alpha} = \partial \langle E_{x\alpha} \rangle / \partial n_i$$

and therefore should <u>not</u> be identified with Hartree-Fock orbital energies, which are equal to the <u>differences</u>

$$\varepsilon_{iHF} = \langle E_{HF}(n_i=1) \rangle - \langle E_{HF}(n_i=0) \rangle$$

between total energies calculated when the ith orbital is occupied and when it is empty (fixing the remaining occupied orbitals) [7]. In the conventional Hartree-Fock approach, moreover, the unoccupied ("virtual") orbitals are represented less accurately than the occupied ones, whereas in the Xα method the unoccupied and occupied orbitals are treated to the same degree of accuracy. The Xα orbital energies, in fact, correspond closely to the "orbital electronegativities" defined by Hinze <u>et al</u>. [41] as a generalization of Mulliken's definition of electronegativity. Therefore, the relative positions of the Xα energy levels for reacting molecules, as exemplified in figure 10 for the case of ethylene interacting with Ni, Pd, and Pt, are an approximate measure of the relative amounts of electron transfer between the reactants. Slater's transition-state procedure [7], applied in conjunction with the SCF-Xα-SW method to the HOMO and LUMO of reacting molecules, leads to remarkably accurate ionization potentials, electron affinities, and electron excitation energies, including spin-orbital relaxation and the effects of averaging over many-electron multiplet states which are usually beyond the scope of conventional molecular-orbital theories [8,9].

The unique characteristics of the Xα orbitals described above greatly facilitate the application of orbital symmetry rules and the concept of electron flow between reacting molecules via the coordination chemical bonding of reactants to the catalyst.

As mentioned earlier, another important concern is to determine the effects on chemisorption and reactivity of adding nonmetallic ligands to small transition-metal aggregates, in part, to model metal-support interactions in heterogeneous catalysis [see fig. 9(a)] and, in part, to determine the electron-withdrawing effects of such ligands in homogeneous catalysis by isolated transition-metal complexes [see fig. 9(b)].

As a simple prototype, we may consider the effects of adding planar electronegative ligands to a platinum-olefin complex. This is just the situation in the classic platinum-ethylene-chlorine complex, Zeise's anion $[Pt(C_2H_4)Cl_3]^-$, for which SCF-Xα-SW calculations have already been completed [22]. To illustrate the effects of the chlorine ligands on platinum-ethylene bonding, we may compare the molecular-orbital energies for $[Pt(C_2H_4)Cl_3]^-$ directly with those shown in figure 10(c) for $Pt-C_2H_4$. This comparison is made in figure 14. The σ orbitals (due to ethylene) of $Pt-C_2H_4$, i.e., the levels labeled 1a, up to $1a_2$, remain relatively unperturbed by the addition of the Cl ligands. The localized Cl 3s levels are found at approximately -1.5 Ry in $[Pt(C_2H_4)Cl_3]^-$, as indicated in figure 14. A very striking effect occurs, however, for those levels that are derived primarily from the π and π* orbitals of ethylene. The levels in $[Pt(C_2H_4)Cl_3]^-$ which are derived from the ethylene π orbitals are labeled by "†" and those derived from the π* orbitals are labeled by "*". The broken line rectangle indicates the region in which the energies of predominantly nonbonding Cl 3p orbitals are found. The strongly antibonding orbitals (not shown) are found at approximately -0.3 Ry.

The highly electronegative chlorine ligands effectively withdraw electrons from the central Pt atom, giving the latter atom a formal oxidation number of +2, and promoting the bonding between ethylene and platinum by allowing the $4a_1$ and $5a_1$ orbitals, which correspond respectively to nonbonding Pt $d_{x^2-y^2}$ and slightly antibonding Pt d_{z^2} orbitals in $Pt-C_2H_4$, to become significantly bonding in $[Pt(C_2H_4)Cl_3]^-$. Moreover, the $3a_1$ and $2b_2$ orbitals which are responsible for $Pt(d_{z^2})-C_2H_4(\pi)$ and $Pt(d_{yz})-C_2H_4(\pi^*)$ bonding in $Pt-C_2H_4$ are more strongly bonding in $[Pt(C_2H_4)Cl_3]^-$ due to the influence of the chlorine ligands.

A classic example in heterogeneous catalysis of the stereochemical effects of coordinating transition-metal atoms with electron-withdrawing ligands is the group of transition-metal halide crystals, such as $TiCl_3$, which catalyze the polymerization of

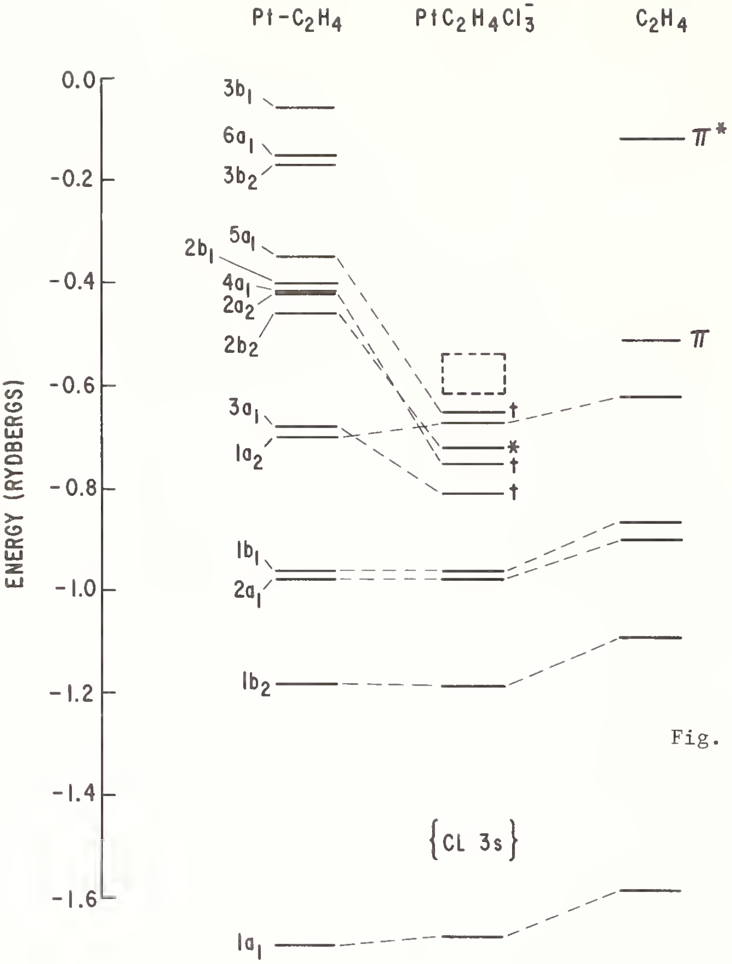

Fig. 14. Comparison of calculated electronic energy levels for Pt-C_2H_4, $PtC_2H_4Cl_3$- and C_2H_4. The levels for $PtC_2H_4Cl_3$- are from Rösch, Messmer and Johnson [22].

olefins, as discussed by Ziegler and Natta [42,43]. The chemisorption and polymerization of the parent olefin (e.g., ethylene), as originally postulated by Cossee and Arlman [44], is envisioned to occur in the vicinity of a transition-metal atom, specifically titanium in the +3 oxidation state, which is incompletely coordinated by chlorine ligands near the surface of an α-$TiCl_3$ crystal, as represented schematically in Fig. 15 (L=Cl, R=alkyl).

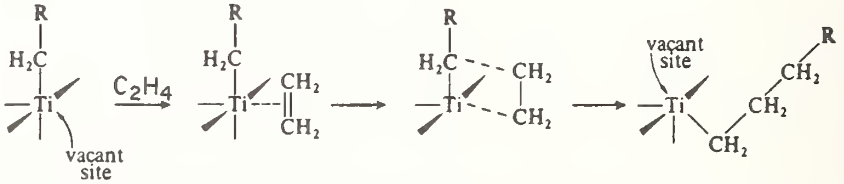

Fig. 15. Proposed mechanism for the Ziegler-Natta catalytic polymerization of olefins. [see Ref. 44].

Note that the geometry of the surface titanium-olefin complex is similar to that of the isolated transition-metal complex shown in Fig. 9(b) which homogeneously catalyzes olefin hydrogenation, although the Ziegler-Natta catalysis of olefin polymerization occurs heterogeneously. We have recently carried out SCF-Xα-SW studies (described in Ref. 24) of titanium-ethylene complexes which simulate the first step shown in Fig. 15. These results again suggest the crucial role of the electron-withdrawing ligands in determing the metal-olefin bonding. Such effects are also probably important in chemisorption and catalytic reactivity on the surfaces of transition-metal compounds such as NiO, TiO_2, and perovskites [38].

3. References

[1] M. Boudart, in Proceedings of the Robert A. Welch Foundation Conference on Chemical Research. XIV Solid State Chemistry, edited by W. O. Milligan (The Robert A. Welch Foundation, Houston, Texas, 1970), p. 299.

[2] J. H. Sinfelt, in Annual Review of Materials Science, edited by R. A. Huggins, R. H. Bube, and R. W. Roberts (Annual Reviews, Palo Alto, California, 1972), V. 2, p. 641.

[3] J. F. Anderson, Structure of Metallic Catalysts (Academic, New York, 1975).

[4] Energy Bands in Metals and Alloys, edited by L. H. Bennett and J. T. Waber (Gordon and Breach, New York, 1968).

[5] Electronic Density of States, edited by L. H. Bennett (National Bureau of Standards Spec. Pub. 323, Washington, D. C., 1971).

[6] J. C. Slater and K. H. Johnson, Phys. Rev. B5, 844 (1972); K. H. Johnson and F. C. Smith, Jr., Phys. Rev. B5, 831 (1972).

[7] J. C. Slater, in Advances in Quantum Chemistry, Vol. 6, edited by P.-O- Lowdin (Academic, New York, 1972), p. 1; J. C. Slater, The Self Consistent Field for Molecules and Solids, Vol. 4 of Quantum Theory of Molecules and Solids (McGraw-Hill, New York, 1974).

[8] K. H. Johnson, J. Chem. Phys. 45, 3085 (1966); in Advances in Quantum Chemistry, Vol. 7, edited by P.-O. Lowdin (Academic, New York, 1973), p. 143.

[9] K. H. Johnson, in Annual Review of Physical Chemistry, Vol. 26, edited by H. Eyring, C. J. Christensen, and H. S. Johnston (Annual Reviews, Palo Alto, California, 1975), p. 39.

[10] J. G. Fripiat, K. T. Chow, M. Boudart, J. B. Diamond, and K. H. Johnson, J. Molec. Catal. (in press); C. Y. Yang and K. H. Johnson (unpublished work).

[11] R. P. Messmer, S. K. Knudson, K. H. Johnson, J. B. Diamond, and C. Y. Yang, Phys. Rev. Feb. 15, 1976 Issue.

[12] J. H. Sinfelt, J. L. Carter, and D. J. C. Yates, J. Catal. 24, 283 (1972).

[13] J. L. Carter and J. H. Sinfelt, J. Catal. 10, 134 (1968).

[14] M. A. Vannice and R. L. Garten, J. Molec. Catal. (in press).

[15] R. A. Dalla Betta and M. Boudart, in Proceedings of the Vth International Congress on Catalysis, edited by J. W. Hightower (North Holland, Amsterdam, 1973), p. 1329.

[16] J. A. Tossell, D. J. Vaughan, and K. H. Johnson, Chem. Phys. Letters 20, 329 (1973); J. A. Tossell, J. Am. Chem. Soc. 97, 4840 (1975); J. A. Tossell, J. Phys. Chem. Solids 36, 1273 (1975).

[17] C. Y. Yang, K. H. Johnson, R. H. Holm, J. G. Norman, Jr., J. Am. Chem. Soc. 97, 6596, (1975).

[18] F. A. Cotton, Quart, Rev. (London) 20, 389 (1966); Accounts Chem. Res. 2, 240 (1969).

[19] M. R. Churchill, J. Wormwald, J. Knight, and M. J. Mays, J. Am. Chem. Soc. 93, 3073 (1971).

[20] G. C. Bond Catalysis by Metals (Academic, New York, 1962), p. 357.

[21] W. G. Klemperer and K. H. Johnson, Chem. Phys. Letters (manuscript in preparation).

[22] N. Rosch, R. P. Messmer, and K. H. Johnson, J. Am. Chem. Soc. 96, 3855 (1974).

[23] R. P. Messmer, in The Physical Basic of Heterogeneous Catalytic, edited by R. I. Jaffee and E. Drauglis, (Plenum, New York, 1975) p. 261.

[24] N. Rosch and K. H. Johnson, J. Molec. Catal. (submitted for publication).

[25] G. C. Bond, in Homogeneous Catalysis, ACS Advances in Chemistry Series, edited by R. F. Gould, Vol. 70 (American Chemical Society, Washington, D.C., 1968), p. 25.

[26] M. J. S. Dewar, Bull, Soc. Chem. France 18, C79 (1951); J. Chatt and L. A. Duncanson, J. Chem. Soc. 2939 (1953).

[27] G. C. A. Schuit and L. L. van Reijen, Adv. Catal. 10, 242 (1958).

[28] G. C. Bond and P. B. Wells, Adv. Catal. 15, 92 (1964).

[29] N. Rosch and T. N. Rhodin, Phys. Rev. Letters 32, 1189 (1974).

[30] F. Herman, A. R. Williams, and K. H. Johnson, J. Chem. Phys. 61, 3508 (1974).

[31] J. G. Norman, Jr., J. Chem. Phys. 61, 4630 (1974); Mol. Phys. (in press).

[32] D. R. Salahub, R. P. Messmer, and K. H. Johnson, Mol. Phys. (in press).

[33] V. Balzani and V. Carassiti, Photochemistry of Coordination Compounds (Academic, New York, 1970).

[34] R. G. Woodward and R. Hoffmann, Accounts Chem. Res. 1, 17 (1968); The Conservation Of Orbital Symmetry (Academic, New York, 1969).

[35] K. Fukui, Bull. Chem. Soc. Japan 39, 498 (1966); K. Fukui and H. Fujimoto, Bull. Chem. Soc. Japan 39, 2116 (1966).

[36] F. D. Mango and J. H. Schachtschneider, in Transition Metals in Homogeneous Catalysis, edited by G. N. Schrauzer (Marcel Dekker, New York, 1971), p. 223; F. D. Margo, Adv. Catal. 20, 291 (1969).

[37] R. G. Pearson, Theoret. Chem. Acta (Berlin) 16, 107 (1970); Accts. Chem. Res. 4, 152 (1971).

[38] T. E. Madey, J. T. Yates, Jr., D. R. Sandstrom, R. J. H. Voorhoeve, in Treatise on Solid State Chemistry, edited by N. B. Hannay (Plenum, New York, in press).

[39] J. Halpern, in Proceedings of the 14th International Conference on Coordination Chemistry, Toronto, 1972, p. 698.

[40] A. B. Kunz, M. P. Guse, and R. J. Blint. J. Phys. B8, L358 (1975).

[41] J. Hinze, M. A. Whitehead, and H. H. Jaffe, J. Am. Chem. Soc. 85, 148 (1963).

[42] K. Ziegler, E. Holzkamp, E. Breil, and H. Martin, Angew. Chem. 67, 541 (1955).

[43] G. Natta and I. Pasquon, Adv. in Catal. 11, 1 (1959).

[44] P. Cossee, J. Catal. 3, 80 (1964); E. J. Arlman, J. Catal. 3, 89 (1964); E. J. Arlman and P. Cossee, J. Catal. 3, 99 (1964).

National Bureau of Standards Special Publication 455, *Electrocatalysis on Non-Metallic Surfaces*, Proceedings of Workshop held at NBS, Gaithersburg, Md., December 9-12, 1975. (Issued November 1976)

Relationship Between Electronic Structure and Catalytic Behavior of Transition Metal Carbides[1]

Dwight R. Jennison, David L. Klein, A. Barry Kunz, Kent M. Hall, and Wendell S. Williams
Department of Physics and Materials Research Laboratory
University of Illinois at Urbana-Champaign
Urbana, Illinois 61801

We have studied the electronic structure of TiC within the unrestricted Hartree-Fock approximation. We find that strong covalent bonding occurs between the carbon 2s and 2p and the metal 3d orbitals. An absence of strong metal-metal bonding was noted. We tested various configurations on the metal atoms and found $4s^0 3d^n$ energetically favored. Thus the formation of the carbon-metal bonds results in a loss of 4s character in the electronic structure. Cluster calculations confirm that the strength of the bonds is sufficient to prevent the reestablishment of 4s character on a surface. The recent studies of Kunz, Guse, and Blint indicate that H bonds strongly to the 4s level, but not to the 3d. Although Ti metal can dissociate H_2, our results explain why the carbide apparently can not. Similar results are anticipated on WC, suggesting a carbon deficient surface may have properties intermediary to W and WC.

Key words: Adsorption; catalysis; electronic structure; surface states; transition metal carbide.

1. Introduction

The transition metal carbides are not only useful for many technological applications, but they also present a challenge to basic science in that their properties are difficult to interpret theoretically [1].[2] Here we concentrate on some properties relevant to electrocatalysis, specifically the nature of the surface bonding and chemisorption.

As Dr. Stonehart has pointed out in the previous paper, WC has been shown [2,3] to selectively chemisorb H_2 in H_2/CO mixtures. It is comparable to Pt as a fuel cell anode catalyst as it is not poisoned by CO. Additionally, the specific activity of WC_x for hydrogen oxidation is enhanced when $x<1$, i.e., when carbon vacancies exist in the material and at the surface. The key questions are, what changes occur to the electronic properties of a transition metal upon the introduction of carbon, and how do these changes depend on carbon concentration, x? We begin with one of the simpler transition metals, Ti. Our results will then be generalized to other species.

TiC_x is stable in the rocksalt fcc structure when $0.5 \leq x \leq 1.0$. This great stability, along with other unusual properties such as its great hardness and high melting temperature [1], indicates that an unusual bonding relationship exists between the Ti and C atoms.

---

[1] This research was supported in part by the U.S. Energy Research and Development Administration under Contract E(11-1)-1198, and in part by the National Science Foundation under Grant DMR 72-03026.

[2] Figures in brackets indicate the literature references at the end of this paper.

Ti readily dissociates hydrogen as does W. The probable limiting factor in the use of Ti as a catalyst for H_2 oxidation is that it bonds oxygen too strongly. This factor has also been suggested for W [4]. However, TiC has been observed not to dissociate H_2 [5]. Apparently the addition of carbon greatly weakens adsorbate-surface binding. This immediately suggests that a carbon-deficient carbide may have intermediary properties, accounting for the above mentioned observation on WC_x. Deficient TiC has indeed been observed to react with hydrogen [5].

We briefly describe our theoretical methods, then present the results for the bulk and surface electronic structure. We close by interpreting our structures in terms of the recent calculations of Kunz, Guse, and Blint [14] on H-transition metal binding, and show that their calculations are consistent with the above mentioned carbide catalytic behavior.

2. Theory

Our theoretical philosophy excludes the use of variable parameters which may prejudice our results. We obtain accurate Hartree-Fock (HF) solutions for systems of interest. For those properties not well described by HF theory alone, such as the bulk optical and Fermi surface properties, we then add electron correlation effects.

The HF solution for the bulk is obtained by utilizing a computationally advantageous Hilbert space transformation given by the Adams-Gilbert equation [6]. This permits us to self-consistently solve for a set of localized orbitals from which the proper HF density matrix, $\rho(r,r')$, may be found. Having found ρ, we may then construct Hamiltonian matrices (in a Bloch representation) which differ only by a phase factor at two points in reciprocal space. Thus a lengthy self-consistent procedure is avoided at each point, and we may economically use a dense mesh in the Brillouin zone. The local orbitals part of the calculation is done by rigorously calculating single site parts (including full non-local exchange) while expanding the intersite parts in a rapidly converging series, using the overlap matrix, $S_{ai,bj} \equiv \langle ai|bj \rangle$ as a smallness parameter. We use the notation that $|ai\rangle$ is the $\underline{i}^{\underline{th}}$ local orbital on atomic site $\underline{a}$. Kunz has shown [7] that for a wide variety of materials sufficient accuracy is obtained by taking the series to first order in overlap. These materials are ionic and inert gas solids and some metals, such as calcium. Kunz, Hall, and Jennison [8] have recently shown that excellent results may be obtained on a high-overlap solid (diamond) when the ground state is constructed from a linear combination of Slater determinants, which maintains nearest-neighbor valence local orbital orthogonality by virtue of spin. Thus we may still take the series to first order in overlap. This method also permits "left-right" electron correlation and results in an unrestricted HF (UHF) solution for the solid. Details of the TiC bulk solution will appear soon [9].

To calculate surface properties, we simulate the surface by a cluster of atoms with dangling bonds tied off by hydrogens. A space-spin unrestricted HF solution is obtained in terms of Gaussian basis functions.

Poor HF results may be obtained if the theorist unnaturally restricts the variational freedom in the spin and/or spatial sense, e.g., if he requires the one-electron wavefunctions to have unnatural symmetry. Such restricted HF (RHF) calculations have occasionally been unfairly cited as examples of poor HF results. Poor results may also be obtained if one attempts to use only HF theory to calculate properties greatly affected by electron correlation, e.g., optical properties. One should not expect <u>any</u> one electron theory which yields decidedly non-local, one-electron wavefunctions to correctly account for an optical excitation which is decidedly a local event. However, the HF solution forms a proper many body vacuum state. From this state one may calculate the correlation corrections in the configuration interaction sense, which then must be added. On all materials so far attempted [10,11], HF, when corrected for correlation, has consistently yielded better agreement with experiment than any other method.

3. Results

In a UHF calculation, a strong covalent bond in the bulk is indicated by a deep interpenetration of the atomic-like charge densities, rather than by a localized increase in charge density in the bond (i.e. above those produced by a superposition of atomic-like densities). This point has been conclusively shown for diamond and silicon [8,12]. A measure of this interpenetration is the spatial local orbital overlap matrix which ranges from ~.5 in diamond to ≤.1 in ionic solids.

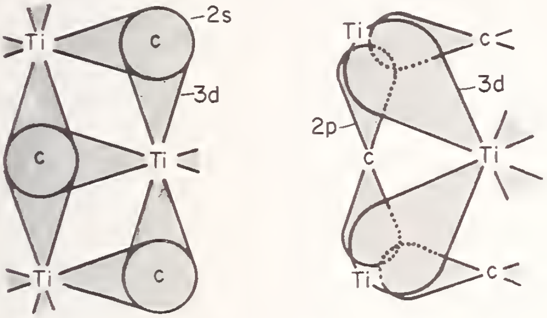

Fig. 1. Schematic of those local orbitals forming covalent bonds in TiC.

Upon examining the bulk solution for TiC, we indeed find evidence for strong C-Ti bonds of the pdπ and sdσ types as shown in Fig. 1. Overlaps of ~.25 indicate that there is an optimal match between the size of the Ti3d lobes (expanded somewhat from free atom size) and the carbon valence orbitals (about the same as the free atom sizes). We would not expect this match to be as ideal with transition metals having smaller and atomic-like d-orbitals, as are found in Groups VII and VIII. Indeed, by Group VII (Group VI in the first series), other phases, such as graphite, successfully compete energetically and prevent the formation of a mono-carbide.

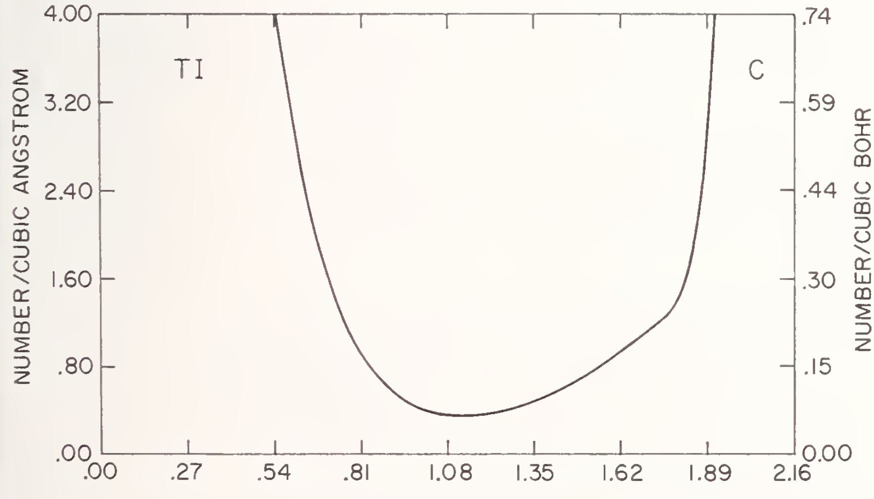

Fig. 2. TiC electron density along (100).

Evidence of the covalent bonding is also found in the position and magnitude of the electron density minimum between nearest neighbors, Fig. 2. The approximate bands, Fig. 3, found from the Coulomb potential of the local orbitals UHF calculation, are reproduced here to illustrate the hybridization. It must be mentioned that, unlike simpler solids, there is no immediate knowledge of the proper local orbitals (LO's) electron configuration (i.e., whether to assume Ti to be $4s^2 3d^2$, $4s^0 3d^4$, etc.). However, within the fractional occupation sense given by the equivalence and symmetry restrictions of Nesbet and adapted to LO theory by Kunz [13], the Hilbert space spanned by the LO's must be isomorphic to that

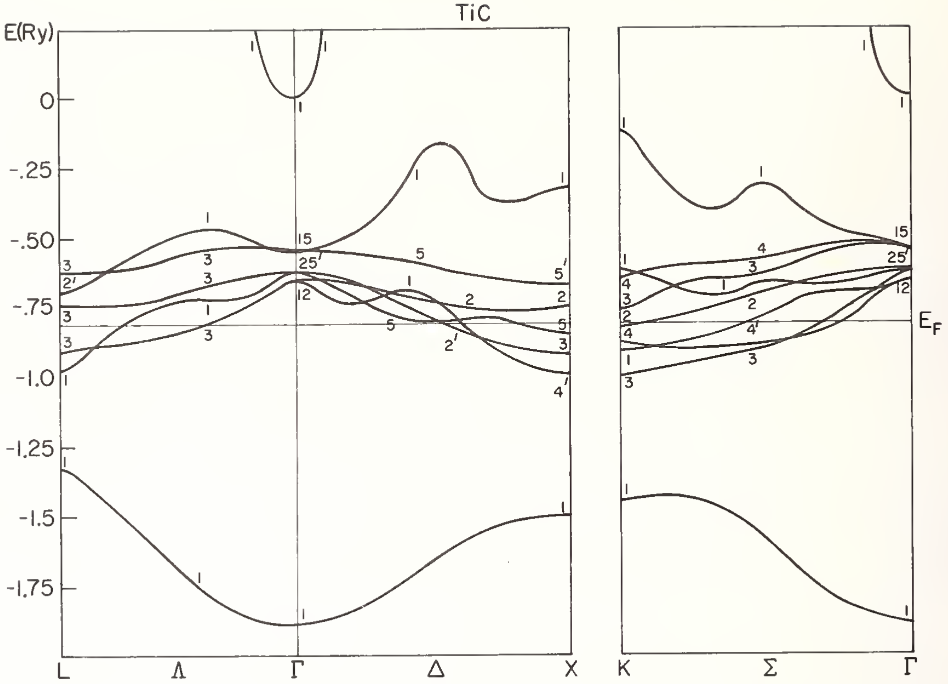

Fig. 3. Approximate RHF bands shown only to illustrate bonding. Exact bonds with calculated optical properties will be presented soon [9].

spanned by the Bloch functions. At least in the complicated case of TiC, we must find the occupied Bloch functions to determine whether the configuration we chose for the LO's is self-consistent with the bands. The bands shown are not fully self-consistent, but are approximately so, Thus they should not be used except as a qualitative indication as to the nature of the bonding. Quantitative properties, e.g. optical and Fermi surface properties, are calculated from the fully self-consistent bands which will be presented shortly.

The lowest band in Fig. 3 is predominantly C2s like with some d hybridization occurring near L. Strong pd hybridization is found in the bands coming from the pure 3d Γ_{12} and $\Gamma_{25'}$ points and the pure 2p Γ_{15} point. For example, the next lowest Δ_1 band begins pure d at Γ_{12} but ends pure p at X_4'. The reverse is noted along the next higher Δ_1 band. The highest Γ_1 band is Ti4s like and is obviously empty.

An explanation of the changes which occur to Ti metal upon the introduction of carbon becomes apparent. The atomic levels Ti3d and C2p are about the same energy. Ti4s is higher than these and C2s is lower. Due to the large overlap and the energy differences between Ti4s and C2s, the 4s level in the compound is raised in energy, while the 2s is lowered somewhat. This drains the atomic $4s^2$ level and the two electrons are shared by the C2p-Ti3d bands. The C2s level remains full. The compound thus has a Ti$4s^0 3d^n$, C$2s^2 2p^{6-n}$ bulk configuration with n being about 3-4.

Thus we may characterize the bulk solid as having strong, but unsaturated, sdσ and pdπ covalent bonds between the Ti and C atoms. The spatial orientation of these bonds (see Fig. 1) suggests the stability of the fcc structure.

Two characteristics of the solid indicate the surface will be electronically very similar to the bulk. These are the great stability of the fcc structure and the very high activation energies for diffusion (~8eV for Ti and ~5eV for C [1]). Thus we expect the surface geometry and composition to be the same as the bulk. TiC favors cleavage along the {100} plane since this breaks only one bond per surface atom. We simulate this surface by a TiC_5H_{13} cluster shown in Fig. 4. We obtain a full UHF solution, taking the free atom configurations as an initial guess. The results are seen in Fig. 5 where the

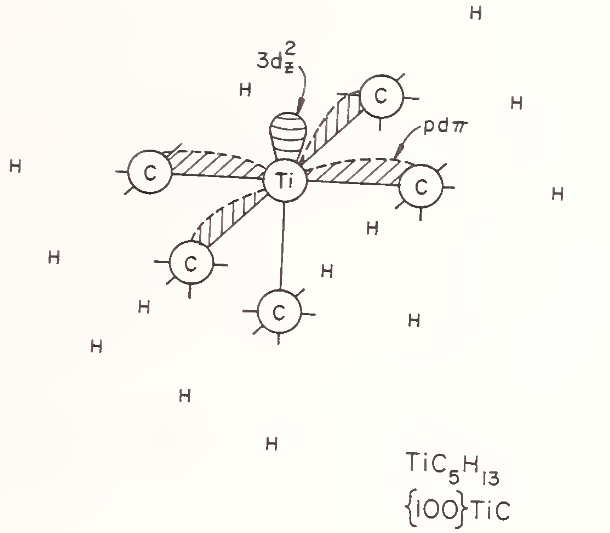

Fig. 4. Schematic of TiC_5H_{13} cluster showing pdπ bonds on surface and dangling $3d_z{}^2$ orbital on Ti.

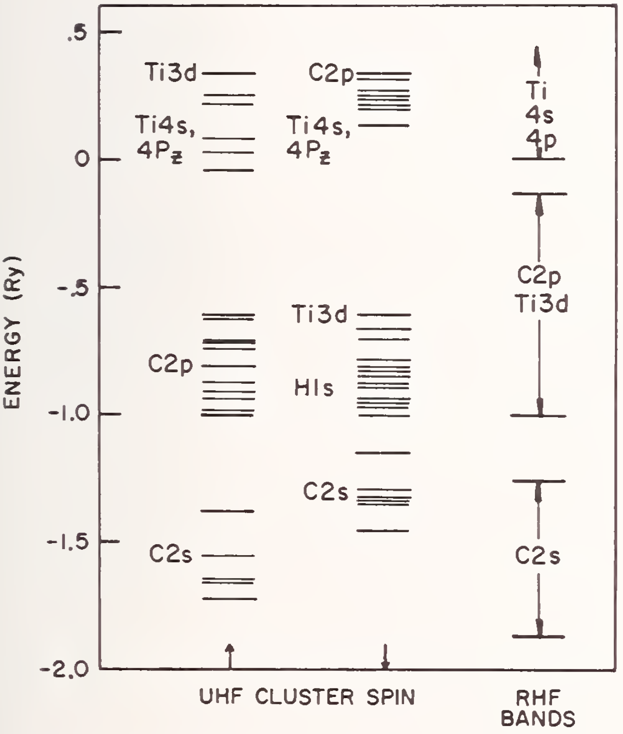

Fig. 5. UHF eigenvalues from TiC_5H_{13} cluster presented with RHF band energies for comparison. Eigenvalues are identi-ied fied by spin and by dominant component. Note strong "left-right" correlation and empty $4s-4p_z$ levels.

eigenvalues are identified by spin and by the dominant basis functions of the corresponding eigenvectors. The band eigenvalues are also shown for ease of comparison. Strong "left-right" correlation is seen in the separation of the predominantly C2p and Ti3d eigenfunctions by spin. The same bonds as seen in the bulk are again indicated by the interpenetration and phases of the C2s, C2p and Ti3d cluster orbitals. In spite of our first guess, the Ti4s-$4p_z$ hybrid orbital at the surface is virtual and lies considerably above the Fermi surface. This result strongly suggests that this orbital is not available to bond an adsorbate. However, a dangling lobe of almost pure $3d_z{}^2$ type is occupied by $<1\underline{e}^-$ and is available to bond adsorbates. Other Ti3d orbitals are tied to the neighboring C2p orbitals through the pdπ bonds, which are strong and thus not easily disrupted. In summary, the independent UHF cluster calculation confirms the results of the local orbitals bulk studies.

4. Discussion

One might expect that the TiC {100} surface with its dangling d-lobes would present an attractive surface for catalysis. However, recent calculations of Kunz, Guse and Blint [14] have shown that on both extremes of the first row of transition metals (Sc and Ni), H bonds well to the 4s level but not to the 3d lobes. They concluded that any bonding to the 3d level would be much weaker than to the 4s, and show that the H-4s bond is sufficient to permit H_2 dissociation. Their studies indicated this to be the case not only for isolated Ni atoms, but also for Ni clusters and Ni atoms bonded to oxygens and hydrogens simulating a silicate substrate. Thus we would expect the unavailability of the 4s level in TiC to greatly reduce the hydrogen-surface bond strength relative to the metal, as is observed experimentally. One would also expect that the H-Ti bonding would be stronger given C vacancies on a surface. The 4s level would lower energetically upon the progressive removal of nearest neighbor carbons, until it would again be available for bonding.

Several calculations immediately are suggested. We will bring hydrogen down upon our present cluster and determine the bonding curve. Then we will proceed to TiC_nH_m clusters with $n<5$ and m appropriate to tie off the dangling bonds. Thereby, we will investigate the defective carbide surface. Finally we will turn to WC and other carbides. These results will be reported soon.

It is seen that our preliminary studies indicate a carbide behavior well consistent with experimental observations to date. As the high activation energies for diffusion keep surface composition constant, the possibility of tailoring a catalyst by varying the carbon content in a carbide seems to exist.

5. References

[1] For a review article see Williams, Wendell S., in Progress in Solid State Chemistry (H. Reiss, Ed.) 6, 57 (1971).

[2] Ross, P. N. Jr., Macdonald, J., and Stonehart, P., J. Electroanal. Chem. 63, 450 (1975).

[3] Ross, Philip N. Jr. and Stonehart, Paul, J. Catalysis 39, 298 (1975).

[4] Levy, R. B. and Boudart, M., Science 181, 547 (1973).

[5] Goretzki, H., Bittner, H., and Nowotny, H., Monatsh 95, 1521 (1964).

[6] Gilbert, T. L. in Molecular Orbitals in Chemistry, Physics and Biology (P-O Löwdin, Ed.), Academic, N.Y., 1964, p. 405.

[7] Kunz, A. Barry, Phys. Status Solidi 36, 301 (1969).

[8] Kunz, A. B., Hall, K. M., and Jennison, D. R., to be published.

[9] Jennison, D. R., Kunz, A. B., Hall, K. M., and Williams, W. S., to be published.

[10] For an independent comparison of theoretical results see Poole, R. T., et al., Phys. Rev. B11, 5190 (1975).

[11] On calcium see Mickish, Daniel J., Kunz, A. Barry, and Pantelides, Sokrates T., Phys. Rev. B10, 1369 (1974).

[12] Hall, K. M., Jennison, D. R., and Kunz, A. B., to be published.

[13] Kunz, A. B., Phys. Stat. Sol. 46, 385 (1971).

[14] Kunz, A. B., Guse, M. P., and Blint, R. J., these proceedings.

National Bureau of Standards Special Publication 455, *Electrocatalysis on Non-Metallic Surfaces*,
Proceedings of Workshop held at NBS, Gaithersburg, Md., December 9-12, 1975. (Issued November 1976)

The Role of Intramolecular Quantum Modes in Electrode Reactions via Intermediate States

Yu. I. Kharkats and J. Ulstrup

Institute of Electrochemistry of the
Academy of Sciences of the USSR
Leninskij Prospect 31, Moscow V-71, USSR

Chemistry Department A, Building 207
The Technical University of Denmark
2800 Lyngby, Denmark

The importance of intermediate electronic states, of energy-nonconserving (virtual) nature in various molecular processes has been recognized recently. In homogeneous and heterogenous electron transfer reactions such states participate effectively, when they provide good electronic and/or Franck Condon overlap integrals with both the initial and final manifold of vibrational states. For weak interactions the electron transfer probability, averaged overall vibrational and electronic states, is calculated by second order quantum mechanical perturbation theory. Account can thus be taken of reorganization of both solvent (classical) and intramolecular modes (essentially quantum) resulting in physically transparent expressions for the reaction probability. Also adiabaticity of the overall reactions can be incorporated in the theory. Explicit summation can be performed for various model systems (Fermi distribution functions, harmonic or Morse potentials et.), which again leads to theoretical free energy relationships (Brønsted or Tafel plots) qualitatively different from such relationships for direct reactions. The electrochemical reduction of molecular oxygen on various phthalocyanine catalysts is analyzed on the basis of the formalism presented.

Key words: Bridge mechanism; classical modes; electrocatalysis; electron transfer theory; intermediate states; intramolecular quantum modes; oxygen reduction; phthalocyanines.

1. Introduction

The theory of electron transfer reactions (ET) in polar solutions is now developed to such an extent that at least simple ET, in which no chemical bonds are broken or established, enjoy a fairly complete description [1,2][1]. Thus, within the dielectric formalism for the solvent outside the first coordination sphere of the reactants, the nature of the activational process and the reorganization of the quantum subsystems are reasonably well understood. Furthermore, the same ideas have been ex-

---

[1] Figures in brackets indicate the literature references at the end of this paper.

tended to cover more complicated situations. This bears first of all to electrode reactions [2], but also to reactions in homogenous solution which are accompanied by substantial intramolecular restructuration (ligand substitution [3] and inner sphere ET reactions [4]).

In the most important theoretical formulations the ET is considered as the radiationless decay of a "supermolecule" consisting of the reactants and the surrounding solvent. The decay probability, W_{fi}, is calculated by time dependent perturbation theory

$$W_{fi} = \frac{2\pi}{\hbar} Av_i \sum_f |<\Psi_f|\tau|\Psi_i>|^2 \delta(E_i - E_f) \tag{1}$$

where Av_i indicates averaging over all initial states, and $\sum_f$ summation over all final states, E the total energy, and Ψ_i and Ψ_f the wave functions representing the stationary initial and final states, i.e. the solutions of the equations

$$H_i\Psi_i = E_i\Psi_i \text{ and } H_f\Psi_f = E_f\Psi_f \tag{2}$$

The total Hamiltonian can be written

$$H = H_i + V_i = H_f + V_f \tag{3}$$

which then gives the form of the operator τ

$$\tau = V_i + V_f(E_i - H + i\gamma)^{-1}, \ \gamma \rightarrow 0+ \tag{4}$$

In the first Born approximation eq (1) takes the form

$$W_{fi} = \frac{2\pi}{\hbar} Av_i \sum_f |<\Psi_f|V_i|\Psi_i>|^2 \delta(E_i - E_f) \tag{5}$$

If the first order matrix elements in the expansion of τ vanish, higher order perturbation theory is required in the calculation of W_{fi}. If there are other states, d, for which V_{fd}, $V_{di} \neq 0$, the second order matrix elements become

$$H_{i\rightarrow f} = \sum_d \frac{V_{fd} \ V_{di}}{E_i - E_d} \tag{6}$$

This is usually interpreted as if the reaction proceeds from i to f via the virtual intermediate states d, but really is based on the time evolution of the system in terms of eigenfunctions of the unperturbed Hamiltonians.

Virtual intermediate states have been considered in various physical processes such as intramolecular radiationless transitions [5], transitions in molecular crystals [6], photochemical reactions [7], superexchange [8], and also in homogeneous and heterogenous ET [9,10]. Application of second order perturbation theory to ET was originally prompted by a wish of formulating a theory for inner sphere ET. The intermediate state here corresponds to the localization of the electron in an orbital of a common ligand (M) for the donating (D) and accepting (A) metallic centres. Figure 1a shows schematically the pathway of an electron in such

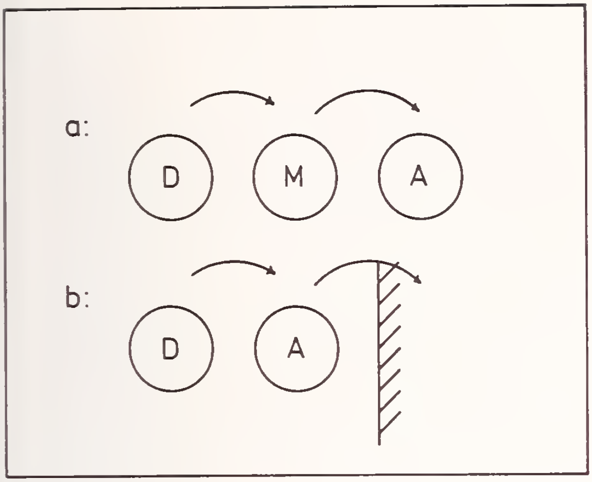

Fig. 1. a: Electron transfer pathway in a collision complex of bridge structure in homogeneous solution; b: the same for an electrode reaction.

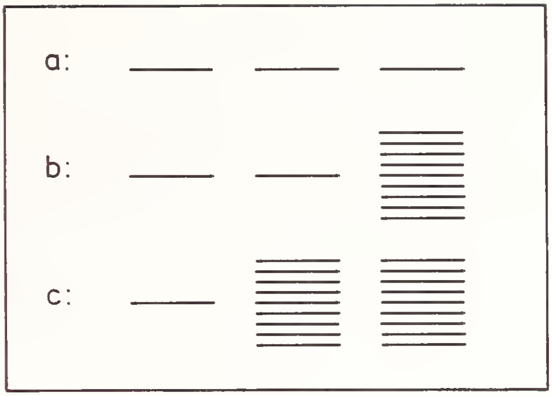

Fig. 2. a: Electronic levels in a bridge-assisted homogeneous ET; b: electronic levels for an electrode reaction via discrete surface states; c: electronic levels for an electrode reaction via surface bands.

a collision complex. Figure 1b shows the analogous electrochemical reaction, in which e.g. the acceptor has been replaced by the electrode. M can here be a ligand on the depolarizer, or in a wider sense some discrete surface state, the nature of which might in principle be understood, e.g. from calculations of the kind presented in the previous workshop.

Figure 2a shows schematically the three discrete electronic levels on D, M, and A. For electrode reactions many levels in the electrode must be included, and also, if the surface states interact, they may form a band instead of discrete levels [11]. These two cases are illustrated in figures 2b and 2c.

For both homogeneous and heterogeneous reactions the system in each electronic state can be divided into three subsystems, a) the electrons, b) the intramolecular quantum modes, and c) the solvent. Due to the large differences in characteristic frequencies, the Born-Oppenheimer approximation can be applied twice, i.e. the wave functions of the total system in each state can be written

$$\Psi_{i,d,f}(X,Q;q) = \psi_{i,d,f}(X,Q;q)\phi_{i,d,f}(Q;q)\chi(q) \qquad (7)$$

where ψ, ϕ, and χ are the wave functions of the electrons, the intramolecular modes, and the solvent, respectively, and X, Q, and q the corresponding coordinates. The electronic terms take the form

$$U_{i,d,f} = U^{o}_{i,d,f} + f_{i,d,f}\,(q) + g_{i,d,f}\,(Q) \qquad (8)$$

where f and g are potential energy functions of the solvent (including ion-solvent interaction) and intramolecular modes, respectively. In the dielectric formalism [1]

$$f_{i,d,f}(q) = \tfrac{1}{2}\sum_{\nu,\mathbf{k}} \hbar\omega_{\nu k}(q_{\nu k} - q^{o}_{\nu k})^2 \qquad (9)$$

where the boson coordinate $q_{\nu k}$ is related to the polarization vector of the medium; $\omega_{\nu k}$ are the associated frequencies, ν and k refer to the nature of the elementary excitation and the momentum states, respectively, and $q^{o}_{\nu k}$ is the solvent coordinate shift by the interaction with the reactants. The fundamental expression for the second order transition probability is [12]

$$W_{fi} = \frac{2\pi}{\hbar} Av_{i} \sum_{f}\Big|\sum_{d} \frac{<\Psi_f|V_d|\Psi_d><\Psi_d|V_i|\Psi_i>}{E_i-E_d+i\gamma}\Big|^2 \delta(E_i-E_f),\ \gamma\to 0+ \qquad (10)$$

Using the Condon approximation, and performing the summations with respect to the solvent system we can write eq (10) as

$$W_{fi}\propto |L_{fd}|^2|L_{di}|^2 Z_{int}^{-1} \sum_{n,m} \exp(-\varepsilon_n/kT) \otimes$$
$$\otimes |<\phi_f|\phi_d>|^2 |<\phi_d|\phi_i>|^2 \exp(-E_a^{n,m}/kT) \qquad (11)$$

where L_{fd} and L_{di} are electronic matrix elements coupling the intermediate state with the final and initial state, respectively, Z_{int} is the statistical sum of the high-frequency intramolecular modes, n and m the quantum numbers of these modes in the initial and final states, ε_n the corresponding energies, and $E_a^{n,m}$ an activation energy depending on the nature of all the classical modes.

Equations (7)-(11) provide a general nonadiabatic theory for the second order ET including account of all solvent and intramolecular modes. It is noted that there are no restrictions in the nature of the intramolecular modes, which means that effects such as frequency and coordinate shifts, anharmonicity etc. can be included in the description. In order to see the physical meaning of the results we shall consider the four different cases described below.

2. Results

2.1 Reorganization of Classical Modes Only

If only classical modes (e.g. solvent modes) undergo coordinate and/or frequency shifts during the reaction, then eq (11) contains only one term in the sum over n and m. Depending on the character and number of modes various expressions for W_{fi} can be obtained, of which we only present results for a one-dimensional harmonic representation with no frequency shifts. For the two relative positions of the various intersection regions of the terms shown in figures 3b and 3a W_{fi} is found to be [13]

$$W_{fi} = \frac{\pi^{3/2}|L_{fd}|^2|L_{di}|^2 \exp[-(U_{di(fd)}-U_i^{o})/kT]}{\hbar^2\ \omega(E_s^{di}\ E_s^{fd})^{1/2}|U_{di}-U_{fd}|^{1/2}(kT)^{1/2}} \qquad (12)$$

and

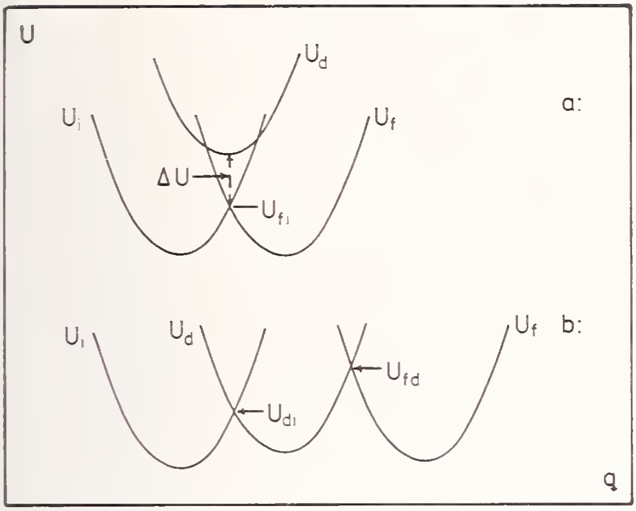

Fig. 3. One-dimensional electronic terms for ET through an intermediate state of a: high and b: low energy.

$$W_{fi} = \frac{\pi^{1/2} |L_{fd}|^2 |L_{di}|^2}{\hbar |\Delta U|^2 (E_s^{fi} kT)^{1/2}} \exp [-(U_{fi} - U_i^o)/kT] \qquad (13)$$

respectively, where E_s are the reorganization energies (e.g. $E_s^{fi} = \frac{1}{2} \hbar\omega(q_f^o - q_i^o)^2$). In the case of a high-energy intermediate state (figure 3a and eq 13) the system thus reaches the intersection region between the intermediate and final state with a probability given by the activational factor. In this region the electronic subsystem is reorganized with a probability given by the pre-exponential factor, and via the intermediate state which in this case is an energy nonconserving state. If the intermediate state has a low energy, the activation energy is determined by the highest intersection region of the intermediate state with either the initial or final state. In this case the system moves classically on the energy surface corresponding to the intermediate state which is now converted to an essentially energy conserving state. However, as opposed to two consecutive one-electron transfers, this description covers the situation in which the system does not relax into the equilibrium configuration of the intermediate state.

2.2 Reorganization in Quantum Modes

If reorganization occurs in the high-frequency intramolecular modes as well, it is convenient to introduce electron-intramolecular modes terms. They represent three series of surfaces like the ones shown, corresponding to all the possible vibrational quantum numbers for each electronic state. The result for W_{fi} has to be presented as the sum of eq (11) with the appropriate expressions for $E_a^{n,m}$ (eqs (12) and (13))and the Franck Condon factors inserted. This sum expresses the independent probabilities of reaction between each quantum state. Both the Franck Condon factors [14] and the activational factors [15] have recently been considered in some detail for various model systems. Thus, the energies of the intersection regions of the intermediate terms with the initial and final terms are (fig. 4)

$$U_{di} = (E_s^{di} + \Delta U_{di}^o + \varepsilon_m^d - \varepsilon_n^i)^2 / 4E_s^{di} + U_i^o + \varepsilon_n^i \qquad (14)$$

and

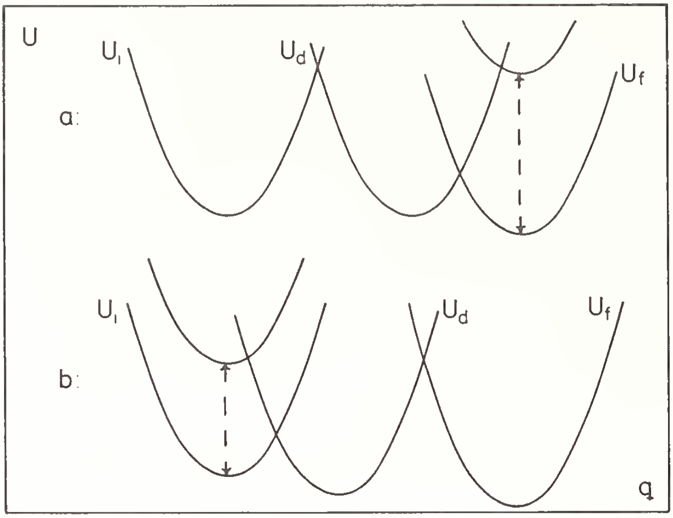

Fig. 4. One-dimensional electron-intramolecular modes, terms and intervals showing the effective number of participating vibrational quantum states. a: $U_{di}^o > U_{fd}^o$; b: $U_{di}^o < U_{fd}^o$.

$$U_{fd} = (E_s^{fd} + \Delta U_{fd}^o + \varepsilon_m^f - \varepsilon_n^i)^2/4E_s^{fd} + U_i^o + \Delta U_{di}^o + \varepsilon_m^d - \varepsilon_n^i \qquad (15)$$

Due to the exponentially rapid decrease of W_{fi} with increasing n or m, the dominating terms of the sum in eq (11) are those shown in figures 4a and 4b. For example, in figure 4a they are the ones lying between the ground initial state and the initial state which equalizes the initial - intermediate intersection region with the intermediate - final intersection region for the ground states. Furthermore, due to the rapid increase of the Franck Condon factors with increasing quantum numbers, the highest of the latter within these intervals gives the main contribution to the sum. For example, for the position of the terms of figure 4a this number, n^*, can be found from the equation

$$(E_s^{di} + \Delta U_{di}^o - \varepsilon_{n^*}^i)^2/4E_s^{di} = (E_s^{fd} + \Delta U_{fd}^o)^2/4E_s^{fd} + U_{di}^o \qquad (16)$$

2.3 Electrochemical Reactions

If electrochemical reactions are considered, account must be taken of the quasicontinuous electronic spectrum of the metal or semiconductor electrode, and possibly of the set of intermediate states, by summing and averaging over these states as well as over the vibrational states. Each term of eq (11) therefore has to be modified by a factor which expresses the probability that a particular level can donate or accept an electron. In the one-electron approximation this gives for discrete intermediate states, e.g. for an anodic reaction [10]

$$W_{fi}^{n,m} = \int [1-n(\varepsilon_\alpha)]\rho(\varepsilon_\alpha)W_{fi}^{n,m}(\varepsilon_\alpha, e\eta)d\varepsilon_\alpha \qquad (17)$$

where $e\eta$ is the overvoltage, ε_α represents a particular metal or semiconductor electronic level, $\rho(\varepsilon_\alpha)$ the level density, $n(\varepsilon_\alpha)$ the distribution function, and $W_{fi}^{n,m}(\varepsilon_\alpha, e\eta)$ the transition probability to the level ε_α. Similarly, for a band of intermediate states [11]

$$W_{fi}^{n,m} = \iiint [1-n_1(\varepsilon_\alpha)][1-n_2(\varepsilon_{\beta 1})]n_2(\varepsilon_{\beta 2})\rho_1(\varepsilon_\alpha)\rho_2(\varepsilon_{\beta 1})\rho_2(\varepsilon_{\beta 2}) \boxtimes$$

$$\boxtimes \quad W_{fi}^{n,m}(\varepsilon_\alpha,\varepsilon_{\beta 1},\varepsilon_{\beta 2},e\eta)d\varepsilon_\alpha d\varepsilon_{\beta 1}d\varepsilon_{\beta 2} \tag{18}$$

where ρ_1 and ρ_2 are the level densities of the electrode and the surface band, respectively, n_1 and n_2 the corresponding distribution functions, and $\varepsilon_{\beta 1}$ and $\varepsilon_{\beta 2}$ the accepting and donating levels, respectively, of the surface band. These integrals can be calculated by various approximations depending on the concrete forms of the n's and ρ's, and for various kinds of intramolecular modes. A general presentation of the results is

$$W_{fi} \propto \Delta N_1(\varepsilon_\alpha^{*})\Delta N_2(\varepsilon_{\beta 1}^{*})\Delta N_3(\varepsilon_{\beta 2}^{*})|L_{fd}(\varepsilon_\alpha^{*},\varepsilon_{\beta 1}^{*},\varepsilon_{\beta 2}^{*})|^2 \boxtimes$$

$$\boxtimes\ |L_{di}(\varepsilon_\alpha^{*},\varepsilon_{\beta 1}^{*},\varepsilon_{\beta 2}^{*})|^2 Z_{int}^{-1} \sum_{n,m} S_{fd}(n,m)S_{di}(n,m)\exp[-E_a(\varepsilon_\alpha^{*},\varepsilon_{\beta 1}^{*},\varepsilon_{\beta 2}^{*},n,m,e\eta)/kT] \tag{19}$$

where the ε^{*}'s are the electronic levels giving the main contributions to the integrations, the ΔN's numbers of electronic levels effectively participating in the reaction, and the S's the Franck Condon factors. From this equation theoretical Tafel plots can be calculated, which for suitable values of the parameters of the system are qualitatively different from Tafel plots for direct (i.e. two-level) reactions.

2.4 Adiabatic Reactions

The formalism presented can be extended to stronger interactions between the reactants, leading to completely or partially adiabatic reactions [16]. Several different situations may arise, and no systematic presentation of all the variants will be made here. However, it should be emphasized that several important predictions, such as free energy relationships, are basically unaffected by the possible adiabaticity of the reactions, i.e. the stronger interactions between the reactants. This is also relevant to the analysis of the experimental data below.

For adiabatic as well as for nonadiabatic reactions the thermally averaged transition probability is

$$W_{fi} = Av_i\{[T_i(E)]^{-1}W_{fi}(E)\} \tag{20}$$

where $T_i(E)$ is an oscillation period in the initial state, and $W_{fi}(E)$ is the transition probability at given energy E. Considering classical modes only, the reaction proceeds when E is sufficiently high that the system can move classically over the barriers from the initial to the final state. Depending on the slopes of the zero order surfaces in the intersection regions, different pathways become possible also giving different expressions for W_{fi}. For example, the relative positions of the three terms shown in figure 5 give for W_{fi} [16]

$$W_{fi}(E) = (1-e^{-2\pi\gamma_{di}})(1-e^{-2\pi\gamma_{fd}})/(1-\tfrac{1}{2}e^{-2\pi\gamma_{di}}) \tag{21}$$

where γ is the Landau-Zener parameter. For $\gamma_{di},\gamma_{fd} \ll 1$ eq (21) reduces to eq (12) corresponding to a totally nonadiabatic reaction. On the other

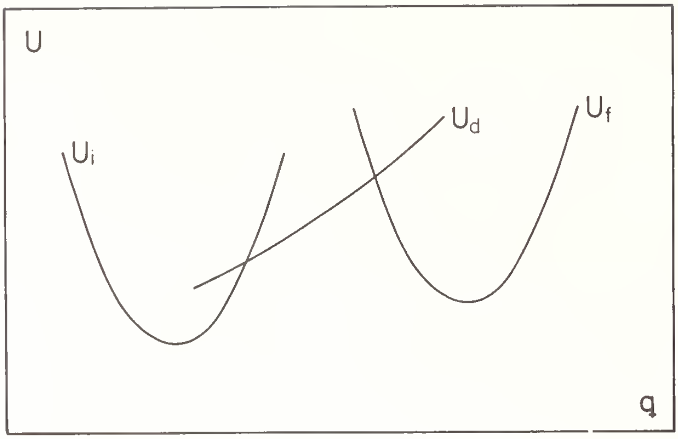

Fig. 5. One-dimensional electronic terms for ET in a case of strong interactions between reactants.

hand, if one γ is much smaller than unity, and the other one much larger, a partially nonadiabatic reaction results. For example, if $\gamma_{di} << 1$, and $\gamma_{fd} >> 1$, the reaction is nondiabatic in the initial-intermediate step and adiabatic in the intermediate-final step. W_{fi} then becomes

$$W_{fi} = 4\pi\gamma_{di}(Z\cdot 2\pi\hbar/kT)^{-1} \exp[-(U_{fd}-\Delta E_{fd}/2)/kT] \qquad (22)$$

where Z is the statistical sum of the classical modes, and ΔE_{fd} the splitting energy in the intermediate-final state intersection region. Analogous expressions can be derived for other term positions [16].

3. Application to Experimental Data

The formalism for second order ET presented has had a certain success in the interpretation of various experimental data. This is so in particular for homogeneous inner and outer sphere bridge-assisted ET [17] but also for proton transfer reactions [15], some of which proceed through intermediate states by polyfunctional catalysis. We shall here show briefly how a semiquantitative analysis of experimental data on the electrocatalysis of the reduction of molecular oxygen on various phthalocyanines can be performed in an analogous way. The present formalism provides a theoretical justification of part of a recent empirical analysis [18] but contains necessarily many reservations due to the limited number of parameters available. Equation (19) is the basis of the interpretation, which considers a) the logi-eη relationship for a particular metal (i.e. at fixed ΔU^o_{di}, ΔU^o_{fd}); b) logi-ΔU^o_{di} relationships for different metals, at fixed eη; c) Catalytic activity, i.e. eη-ΔU^o_{di} relationships for different metals at fixed current density. Correlations between electrocatalytic activity and either magnetic moments or gas phase activity are not considered, since this would be reflected in both the electronic matrix elements and the activational factor in a very inaccurately predictable way.

Certain simplifying assumptions about the system are necessary. Thus, firstly it will be assumed that the reaction proceeds at discrete surface sites (eq (17)). This should really correspond to a monolayer of phthalocyanine, and the data of Savy et al. [19] on carbon-supported polymeric phthalocyanines are therefore used, since they seem to be most closely related to the model. However, as indicated by eq (19), band structure could also be incorporated. Secondly, it has been suggested [19] that the O_2 reduction may proceed via excited states of the central metal ion, induced by coupling with the unpaired spins of the O_2 molecule. Inclusion of this point would require an additional summation in eq (19) over such states, but in view of the present uncertainty about the exact role of the excited states in the process, this point will be omitted here. Thirdly, the effective potential distribution in the catalyst layer should be known. Two limiting cases were previously considered [11,12]. The whole electrode-solution potential drop could either occur in the catalyst-solution or in the electrode-catalyst interface. For the phthalocyanine systems the former situation is likely to prevail, as pointed out below. Finally, the ET may proceed in two ways. Either an electron is transferred from the catalyst to O_2, and the "hole" is filled by an ET from the electrode (pull push mechanism). This is the pathway implicit in previous interpretations and also supported by the considerations below. Or, the ET may proceed at first from electrode to catalyst and then from catalyst to O_2 (push pull mechanism).

Since the first two correlations are not basically affected by the presence of intramolecular quantum modes, we shall at first ignore such modes. The activation energy for the pull push mechanism, and the former of the two potential distributions is then

$$E_a = (E_s^{di} + \Delta U_{di}^o + e\eta)^2/4E_s^{di} \qquad (23)$$

when the initial-intermediate intersection region is the higher, and

$$E_a = \Delta U_{di}^o + e\eta + (E_s^{fd} + \Delta U_{fd}^o)^2/4E_s^{fd} \qquad (24)$$

when the intermediate-final intersection region is the higher (figures 3 and 4). Assuming constant E_s values eq (23) gives an approximately 118 mv Tafel slope (normal region), whereas eq (24) gives a 59 mv slope (barrierless region); the second potential distribution would lead to independence of $\log i$ on $e\eta$ in the low overpotential region, and 118 mv in the high overpotential region. For the phthalocyanines of Ni, Cu, and Co 100-120 mv laws are observed experimentally [19], whereas 45-60 laws are observed for the Fe complex. Since furthermore the oxidation potential is substantially lower for the Fe complex [20], the data are compatible with the first step having the higher activation energy for Ni, Cu, and Co, and the second step for Fe. Of course this does not exclude other possible mechanisms for the reaction at the Fe complex, such as a pre-equilibrium in the first step. For the push pull mechanism the experimental Tafel plots are compatible with the second of the two limiting potential distributions. Strictly speaking this can not be ruled out, but it would require that Fe(I) is the most readily formed, and that Cu(I) and Ni(I) are about equally readily formed, which seems less likely.

Equation (23) also predicts a relationship between the current density and the oxidation potentials of the phthalocyanines as expressed by ΔU_{di}^o. Useful correlations can here only be made if the same step is rate determining throughout the series, which is then restricted to Ni, Cu, and Co. Since furthermore the potentials and catalytic activities of Ni and Cu are very similar, the $\log i$-ΔU_{di}^o correlation is of limited applicability. A value of $\partial \log i/\partial(\Delta U_{di}^o) = 0.23 \pm 0.06$ can be obtained in the overvoltage region of about -0.7 v.

A linear relationship of unit slope between the oxidation potential and the catalytic activity (i.e. overvoltage at a fixed current density) is predicted by eqs (23) and (24). The slope found experimentally is, however, less than unity and seems to increase with increasing oxidation potential. This can be understood qualitatively on the basis of eq (19) and can be explained by the excitation of intramolecular modes of relatively low frequencies in the cathodic overpotential region. The effective energy of reaction is then $\Delta U_{di}^{o} + \varepsilon_m^d$, where $\varepsilon_m^d(>o)$ is the excitation energy for the state giving the main contribution to the sum. For increasing potential (decreasing negative ΔU_{di}^{o}) m decreases, and the slope thus approaches unity.

4. Acknowledgement

One of us (JU) would like to thank Statens naturvidenskabelige Forskningsråd for financial support.

5. References

[1] Dogonadze, R. R. and Kuznetsov, A. M., *Fizicheskaya Khimiya. Kinetika*, Viniti (1973).

[2] Dogonadze, R.R., in *Reactions of Molecules at Electrodes* (N. S. Hush, Ed.), John Wiley and Sons (1971).

[3] German, E. D. and Dogonadze, R. R., J. Res. Inst. Catalysis, Hokkaido Univ. 20, 34 (1972).

[4] Dogonadze, R. R. Ulstrup, J. and Kharkats, Yu. I., J. C. S. Faraday Trans. II 68, 744 (1972).

[5] Fischer, S. F., Chem. Phys. Lett. 17, 25 (1972).

[6] Jortner, J. and Rice, S. A., J. Chem. Phys. 44, 3364 (1966).

[7] Grimley,T. B., Faraday Disc. 58, 7 (1974).

[8] Anderson, P. W., Phys. Rev. 79, 350 (1950).

[9] Vol'kenstein, M. V., Dogonadze, R. R., Madumarov, A. K. and Kharkats, Yu. I., Dokl. Akad. Nauk SSSR, Ser. Fiz. Khim. 199, 124 (1971).

[10] Dogonadze, R. R., Ulstrup, J., and Kharkats, Yu. I., J. Electroanal. Interfac. Electrochem. 39, 47 (1972).

[11] Dogonadze, R. R., Ulstrup, J., and Kharkats, Yu. I., J. Electroanal. Interfac. Electrochem. 43, 161 (1973).

[12] Landau, L. D. and Lifshitz, E. M., *Quantum Mechanics*, Pergamon (1965).

[13] Levich, V. G., Madumarov, A. K., and Kharkats, Yu. I., Dokl. Akad. Nauk SSSR, Ser. Fiz. Khim. 203, 135 (1972).

[14] Ulstrup, J. and Jortner, J., J. Chem. Phys. 63, 4358 (1975).

[15] Dogonadze, R. R., Ulstrup, J., and Kharkats, Yu. I., J. C. S. Faraday Trans. II, 70, 64 (1974).

[16] Kuznetsov, A. M. and Kharkats, Yu. I., Elektrokhimiya, in press.

[17] Ulstrup, J., Acta Chem. Scand. 27, 1067 (1973).

[18] Randin, J.-P., Electrochim. Acta 19, 83 (1974).

[19] Savy, M., Andro, P., Bernard, C., and Magner, G., Electrochim. Acta 18, 191 (1973).

[20] Manassen, J. and Bar-Ilan, A., J. Catal. 17, 86 (1970).

Comment on the Papers of H. Gerischer, "Electron Transfer and Electrocatlysis Reactions," and of Yu. I. Kharkats and J. Ulstrup, "The Role of Intramolecular Quantum Modes in Electrode Reactions via Intermediate States"

C. B. Duke

Xerox Webster Research Center
800 Phillips Road
Webster, NY 14580

The equations for the electrode current utilized in both of these papers are of the form

$$i = \int_{-\infty}^{\infty} K(E)\, D(E)\, W(E)\, dE \tag{1}$$

for a single-step reaction. In eq. (1), K(E) is a transfer probability as a function of energy, E; D(E) is a measure of the occupied (cathodic) or unoccupied (anodic) electronic states in the electrode; and W(E) is a measure of the corresponding states ("redox orbitals") in the electrolyte. Because the electron-vibration coupling in the electrode [D(E)] and solution [W(E)] is written in separable form as a simple product $D(E) \cdot W(E)$, the validity of eq. (1) is highly circumscribed. In particular, it is not correct in some of the limits for which its use was cited in the papers referred to above.

A consideration of the limits in which formulae like eq. (1) are valid for electron or exciton transfer processes has been given for conventional solid state tunneling by C. B. Duke, "Tunneling in Solids," (Academic Press, NY, 1969), Chapter VII, and for electron and exciton transfer between localized states by T. F. Soules and C. B. Duke, Phys. Rev. B3, 262 (1971). Specifically, the form of eq. (1) is correct if and only if the electron is coupled to independent vibrational fields in the initial and final state and the transfer operator is not a functional of either field. This limit corresponds to the Förster/Dexter model of resonant energy transfer (Soules and Duke, eqs. (3.10)-(3.12)) and to the concept of electron interactions in the electrodes of both normal and superconducting tunnel junctions (Duke, Secs. 20 and 21).

The coupling of both the initial and final states to the *same* polarization or vibration field (*e.g.*, to the "medium" modes in the case of electron transfer reactions in solution) invalidates eq. (1), as discussed in detail by Soules and Duke. In conventional quantum-field-theory language, the propagator renormalization diagrams which lead to eq. (1) are in large measure canceled by vertex corrections in which the common ("medium") polarization field links the initial and final states (see, *e.g.*, Duke, pp. 244-245). Thus, eq. (1) is not expected to be correct if the electron in both the initial and final states interacts with the same vibrational or polarization field.

A second process not described by eq. (1) is inelastic tunneling in which case the electron actually loses energy during the electron-transfer process (Duke, Sec. 22; A. J. Bennett, C. B. Duke and S. D. Silverstein, Phys. Rev. 176, 969 (1968)). These processes are known to be of importance for electron transfer in semiconductors and insulators (A. M. Andrews, H. W. Korb, N. Holonyak, Jr., C. B. Duke, and G. G. Kleiman, Phys. Rev. B5, 2273 (1972)). Thus, one would anticipate that their omission from eq. (1) is likely to constitute a serious flaw in the theory of electron transfer reactions.

Finally, the coupling of the transferred electron to low-energy particle-hold excitations or polar fluctuations in the solution can cause infrared divergences which modify eq. (1). These are well known for piezoelectric semiconductors (C. B. Duke and G. D. Mahan, Phys. Rev. 139, 1965 (1965)) and x-ray absorption and photoemission by metals (J. J. Hopfield, Comments on Solid State Phys. 2, 40 (1969)), and hence, would be expected to be of relevance to the analysis of electron transfer reactions, especially for metal electrodes.

In summary, there are three phenomena which can lead to substantive conceptual alterations in the derivation and interpretation of the formula, cited at this workshop, for electrode currents associated with electron transfer reactions. These phenomena are well known to be important in analogous areas in solid-state physics, and hence, should be considered by electrochemists prior to accepting uncritically the analysis leading to eq. (1) or its generalizations as discussed by Kharkats and Ulstrup.

Reply to Comments by C. B. Duke on a Paper by Yu. I. Kharkats and J. Ulstrup, "The Role of Intramolecular Quantum Modes in Electrode Reactions via Intermediate States"

J. Ulstrup

Chemistry Department A, Building 207
The Technical University of Denmark
2800 Lyngby, Denmark

The equation for the electrode current is not written as claimed by Dr. Duke, but has the form

$$i = \int_{U_{io}}^{\infty} K(E)W(E)dE \int_{-\infty}^{\infty} D(\varepsilon)d\varepsilon$$

where U_{io} is the minimum of the initial state potential energy surface, E refers to vibrational solvent and intramolecular levels, and ε to electronic levels in the metal. The separable form, $W(E)D(\varepsilon)$, is therefore related to the averagings over the different subsystems, and in fact, inherent in the Born-Oppenheimer approximation. For the analogous homogeneous reactions, the integrations are carried out over E only. In this case, the energy distribution is characterized by a single function of the medium energy states, even though the part concerning the high-frequency intramolecular modes is written in separable form. However, this is fully justified in view of the nature of these modes. Dr. Duke's comments, therefore, only relate to other kinds of processes, such as the Förster/Dexter model of resonance energy transfer.

The theory outlined in the paper, as well as many descriptions of intramolecular radiationless transitions, do not contain tunnelling in the Gamow sense, although other formulations of electron transfer theory in the literature do. However, by Franck Condon restrictions, both formalisms are incompatible with electron energy loss during electron transfer in the saddle point region of the classical modes. Of course, energy transfer occurs during the total act of electron transfer and is equivalent to the phonon emission processes in the paper quoted by Dr. Duke in his second comment.

The third comment is, in fact, already answered by this. In summary, we do not believe that the comments have revealed a necessity of substantive reformulation or reinterpretation of the theory of thermal electron transfer reactions as outlined at this workshop and other places. On the other hand, we think that a more detailed comparison between such reactions and the processes mentioned by Dr. Duke would be useful.

CHARACTERIZATION

National Bureau of Standards Special Publication 455, *Electrocatalysis on Non-Metallic Surfaces*, Proceedings of Workshop held at NBS, Gaithersburg, Md., December 9-12, 1975. (Issued November 1976)

The Study of Electrode Surfaces by Electrochemical Methods

B. E. Conway and H. Angerstein-Kozlowska
Chemistry Department, University of Ottawa
Ottawa K1N 6N5 Canada

Electrochemical methods for the study of surfaces are reviewed. Unlike high-vacuum techniques, they measure changes in the state of surfaces by virtue of occurrence of electrode surface processes, rather than giving information on the state of the surface itself. However, electrochemical procedures have high sensitivity down to 2% of a monolayer and multiple states of chemisorption can be distinguished with an energy resolution of 100-200 small calories. Interactions in the ad-layer can also be derived from the form of electrical transients. Combination of electrochemical methods with optical techniques, such as relative reflectivity and ellipsometry, provides a new dimension for studies in electrochemical surface science.

Key words: Atomic layers; chemisorption; cyclic-voltammetry; electrochemical adsorption; monolayers; surface processes.

1. Introduction

In this review, it must first be pointed out that electrochemical methods, by their nature, detect *changes* of state of metallic and non-metallic surfaces due to the passage of charge. In these respects they are unlike diffraction techniques, or optical and electron spectroscopy, which give information directly on the state of a surface itself, apart from any modifications of the surface introduced by the necessary ion or electron bombardment pre-treatment procedures required to produce a clean surface in the high-vacuum environment.

It must also be recognized that purely electrochemical techniques are not so generally applicable to the study of non-metallic electrocatalyst surfaces as they are to metals, unless the bulk conductivity is reasonably high. However, this condition is fulfilled for some materials, e.g., mixed oxide electrocatalysts such as the La, Sr cobaltites, other materials such as WC and tungsten bronzes, and also a number of almost metallic sulfides such as PbS, Cu_2S, etc. Hitherto, few electrochemical surface studies on such materials have been published, partly because their surface stability is, in many cases, lower than that of noble metals.

For non-metallic electrode materials that are semi-conductors, electrochemical techniques combined with the study of photo-effects (e.g., as in the work of Gerischer[1][1]) have been most profitable. For such systems, however, both bulk and surface properties are involved in the observed experimental behavior under photon irradiation.

The electrochemical procedures basically depend on counting charge for Faradaic processes occurring in the formation or removal of surface layers, often monolayers or less in extent. The relation between charge passed and electrode potential, measured

---

[1] Figures in brackets indicate the literature references at the end of this paper.

with respect to some constant-potential reference electrode in the circuit, gives additional information about the processes occurring in electrochemical surface studies as a function of their relative free energy changes since distinction of processes occurring on an electrode-potential scale is equivalent to distinction on a scale of free energies. In electrochemical terms, this is hence analogous to spectroscopy.

Since surface processes of necessity are chemically and electrochemically limited in extent by the quantity of material that can be changed, or introduced or removed on a surface, e.g., deposition or removal of a layer of H atoms at Pt, electrochemical methods for study of surfaces must employ transient procedures in which a time-dependent current i is registered, e.g., on an oscilloscope or recorder, in response to a change of potential V or in which a time-dependent change of potential is recorded in response to an impressed current. Because i and V are conjugate variables in electrochemical experiments, these two types of procedures give the same information in different ways. In current work, controlled-potential methods involving the use of an electronic potentiostat programmed by means of a function generator are preferred.

In addition to observation of changes of state of a surface, electrochemical methods also give information on the change of state of the electric double-layer at the electrode/solution interface. Over some potential ranges at various metals, e.g., between 0.35 and 0.75 V on Pt or between 0.0 and 1.37 V on Au in aq. H_2SO_4 solutions, the electrochemical transient methods give information on the double-layer charging processes alone, since no other Faradaic surface processes (e.g., deposition of H or oxidation of the surface) occur. The transient electric currents i_t that pass under these conditions in response to a change of potential dV/dt in time are "non-Faradaic" currents associated with changing the charge on the double-layer capacitance C; in general, $i_t = C(dV/dt)$. At semi-conductor electrodes the distributed space-charge, within the electrode material, due to p or n charge carriers, also contributes a capacitance which is measured in transient experiments. For quantitative evaluation of surface processes themselves, separation of the non-Faradaic from the Faradaic component in the overall current or potential response of the system is necessary. Since non-Faradaic processes are usually fast because they are associated with short-range movements of ionic and electron charge near the electrode interface, they have relaxation times of the order of 10^{-6}-10^{-7} sec and hence can be separated by measurements on short time scales. Alternatively, various semi-empirical procedures can be employed.

2. Conditions for Deposition of Atomic Layers at Electrodes

With a number of systems, an array of metal, H atoms or OH and O species, can be deposited uniformly over a surface up to approximately a monolayer before deposition of the species in bulk form occurs. This means that the initial ad-layer deposit is laid down at electrode potentials below the thermodynamic reversible potential for the substance in bulk form. This phenomenon has been called "underpotential deposition" (UPD) and is to be contrasted with the normal mode of electrodeposition of most substances which occurs by growth of nuclei deposited at significant overpotential. UPD can be studied most conveniently at noble metal surfaces as substrates where corrosion or dissolution currents for the substrate itself are negligible. For an adsorbate A and a substrate M, UPD arises when the bonding of A to M is stronger than that of A to A. This is expressed thermodynamically by the condition that $\Delta G^\circ_I<0$ for the process

$$\text{A-A} + 2\text{M} \xrightleftharpoons{\Delta G^\circ_I} 2\ \text{A-M}, \qquad (\text{I})$$

if coverage by the underpotential-deposited species A on S is to be significant (e.g., >2%, a conveniently detectable limit) before the reversible potential for deposition of bulk A in the process

$$2A^{\pm} \pm 2e \xrightleftharpoons{\Delta G^\circ_{II}} A_2 \qquad (\text{II})$$

is attained. Alternatively, the condition for UPD to be observed is $\Delta G^\circ_I < \Delta G^\circ_{II}$. In process

II,"bulk A" is represented as "A_2", e.g., if bulk A were a diatomic molecule such as H_2, O_2. If A is a metal, bulk A would, of course, be a lattice A_n.

3. Basis of Electrochemical Methods for Study of Surface Processes

For quantitative studies of coverage of species on an electrode, it is necessary that the species be "electroactive" i.e., the species can be adsorbed or desorbed with passage of charge in a quantitative way according to Faraday's laws on a microscopic scale, as represented in process II above. When this is the case, electrochemical techniques provide a very sensitive method for study of surface processes since e.g., formation or removal of a monolayer of H atoms on a Pt (111) surface ($PtH_{ads} + H_2O \rightarrow Pt + H_3O^+_{aq} + e$) requires a charge of ca. 220 μ coulombs per real cm^2 which can be accurately measured and in fact, electrochemical methods are sensitive down to 2% of monolayer coverage. Also, passage of the charge during the transient can be followed on a potential scale with a practical accuracy of 0.1 to 1 mV and with a resolution, when multiple surface processes occur (see below), of ca. 5-10 mV, i.e., 115-230 small calories in (free) energy for a 1e surface process. (It is to be noted that this is a much finer resolution on the energy scale for surface processes than that afforded, e.g., by current electron spectroscopic techniques.)

A summary of the direct electrical transient techniques for electrochemical study of surfaces is given below (Table 1). Some other indirect techniques which are required for study of electro-<u>in</u>active adsorbates will be described separately later in this review.

Table 1. Electrical methods[a] for study of surface processes.

Method	Transient measured	Results Obtained
1. Controlled current pulse	Time-dependent potential, V_t	Charge and coverage for change of state of surface.
2. Controlled current pulse with electronically differentiated output	Time-dependent potential and dV_t/dt resolved	As in (1) but with better resolution of surface processes.
3. Controlled potential pulse (potential-step)	Time-dependent current, i_t	As in (1) but with possibility of more direct charge evaluation as $\int i_t\,dt$. Kinetic applications convenient.
4. Controlled charge pulse (coulostatic method)	Time-dependent potential	As in (3). Kinetic applications possible.
5. Linear voltage sweep $V = V_0 \pm St$ $S = \frac{dV}{dt}$	Time-dependent current i_t in cyclic mode	Direct evaluation of charge and coverage from $\int i_t dt$. Excellent resolution of successive surface processes.
6. A.c. current or applied a.c. potential (a.c. impedance)	Periodic i or V response	Impedance analysis, Ohmic and capacitative components of a.c. can be analysed with equivalent circuit. Kinetic information obtainable.
7. Electrical transient, e.g., linear sweep method, combined with reflectance or ellipsometry technique: chronoellipsometry	i_t as $f(V_t)$, $\Delta R/R$ or Δ and ψ as $f(V_t)$ or t	Optical data on surface refractive index changes coupled with change of surface coverage and charge (Interpretation complex).

[a] Some other advanced methods exist such as Faradaic rectification, harmonic analysis or time-domain reflectometry using the sampling oscilloscope, but they have not been applied to surface studies.

In addition to the purely electrochemical techniques listed in Table 1 (entries 1-6) should be mentioned the use of optical techniques coupled with controlled change of the electric potential. Methods based on measurement of relative reflectivity change $d\frac{\Delta R}{R}/dV$, in polarized light and on changes of the ellipsometric parameters ψ (the amplitude change) and Δ (the phase shift) in response to change of potential are being profitably used for study of electrode surfaces. They may also be applied to non-metallic surfaces. The interpretation of the changes of optical properties with potential are complex [2,3,4] as they involve the real and imaginary components of the refractive indices of the double-layer, the surface film and of the underlying metal, and the thickness of the film. Also, the electronic refractive index of the surface region of the electrode itself within the Thomas-Fermi screening distance is modulated by the electric potential due to its effect on surface electron charge density. Further, the optical properties of the double-layer on the solution-side of the interface are modulated by potential due to changes of population of anions and cations, and to orientation and electrostrictive compression of solvent molecules [3,5]. Corrections for these double-layer effects can be made semi-empirically [4] or they may be minimized by use of an appropriate angle of incidence [2].

The coupled optical electrochemical procedures for study of surfaces provide one of the few methods whereby *in situ* "spectroscopic" information on electrode surfaces can be obtained, in these cases, by measuring $\Delta R/R$ (or Δ and ψ) as a function of wave-length over a range of potentials. Applications to semi-conductor electrode interfaces have been extensive [6] and information on inter-band transitions has been obtained.

4. Relation to High-vacuum Methods

In addition to the above methods, it is desirable to be able to characterize electrode surfaces themselves by means of high-vacuum techniques such as LEED, HEED and scanning electron microscopy, as well as by photo-electron spectroscopic methods such as Auger and ESCA. Such approaches present serious experimental problems for electrochemists since removal of an electrode from solution eliminates the potential control required for generation of a definite state of the surface. Only in the case where stable oxide films can exist on an electrode, or when the metal surface itself is to be examined, will characterization by high-vacuum techniques be meaningful. Also, pre-treatment techniques may introduce changes in state of the electrode surface to be examined. Some ESCA studies of oxide films on electrodes, e.g., Pt and Au, have been carried out severally by Parsons, Dickenson, Winograd and others, but it is uncertain if the electrogenerated films remain unchanged in the vacuum system.

5. Solution Purification

In all the electrochemical techniques referred to above, and in Table 1, it is essential that ultra-pure solutions be used. Special care must be exercised in all work to ensure that (a) depositable heavy-metal impurities are absent [7] and (b) that adsorbable organic impurities that may block the surface or be themselves electroactive are not present in the solution. A technique for pyrodistillation of water has been described by Conway et al. [8] which gives very pure solutions with high purity grade H_2SO_4 or $HClO_4$ and criteria for evaluation of solution purity have been established. Since coverage of an electrode by an organic impurity of mw *ca.* 100 requires only *ca.* 1.7 x 10^{-10}moles cm^{-2}, it is readily seen that meaningful work in electrochemical surface science can only be achieved by working with ultra-purified solutions [7,8]. Unfortunately, this has not been the case with much of the earlier published work in the literature, although Schuldiner's work, in many papers, must be commended for its attention to the important question of solution purity. Fortunately, in some cases, adsorbed impurities can be removed *in situ* at electrode surfaces by appropriate electrochemical pre-treatment, e.g., in an anodic oxidation pulse or sweep[8], but impurities tend to be readsorbed if the solution is insufficiently clean as soon as the oxidized electrode-surface is returned to the metallic state in a following reduction cycle.

6. The Potential Sweep or Potentiodynamic Method for Study of Electrode Surface Processes (cyclic-voltammetry; method 5, Table 1)

One of the most useful techniques for study of electrode surface processes is the linear potential sweep method or cyclic-voltammetry as it is called when applied in a repetitive manner with successive cathodic-and anodic-going changes of potential. Originating from a fast polarographic technique described by Sevčik [9], the application of the potential sweep technique to study of electrode surface processes was developed by Will and Knorr [10] and employed in many papers by Breiter, Knorr and co-workers. Single-sweep techniques were used by Gilman [11] and the current pulse method by Brummer et al. [12,13] for characterization of chemisorbed organic residues which were not directly electroactive (see below).

The basis of the method is as follows: currents for an electrode surface process of the kind $A^- + M \rightarrow MA_{ads} + e$ are represented by the equation

$$\overrightarrow{i} = z\ Fk_1(1-\theta_A)C_{A^-} \exp \beta VF/RT \tag{1}$$

and

$$\overleftarrow{i} = z\ Fk_{-1}\ \theta_A \exp -(1-\beta)\ VF/RT \tag{2}$$

where V is the metal/solution potential difference and β ($\simeq \frac{1}{2}$) is a symmetry factor for the charge transfer process. For a surface process such as deposition or desorption of A, to or from a monolayer limit, $\overrightarrow{i}$ or $\overleftarrow{i}$ are not continuous and can only be observed by some transient technique; thus, $\overrightarrow{i} \rightarrow o$ as $\theta_A \rightarrow 1$ and $\overleftarrow{i} \rightarrow o$ as $\theta_A \rightarrow o$. Generally, $\overrightarrow{i}$ or $\overleftarrow{i}$ is a function of time t in the sweep as V is varied linearly with time at a sweep-rate S=dV/dt. The time-dependent current $\overrightarrow{i}$ or $\overleftarrow{i}$ we denote as i_t. Then coverage θ_A at any point in the sweep is

$$\theta_A = \int \frac{i_t dt}{Q} \tag{3}$$

where Q is the charge for monolayer coverage. Introducing S = dV/dt for the sweep experiment enables eq (3) to be rewritten as

$$\theta_A = \int \frac{i_t}{Q} \frac{dV}{S} \tag{4}$$

Correspondingly

$$\theta_A = \theta_{initial,A} - \int \frac{i_t dV}{Q\ S} \tag{5}$$

Coverages are hence evaluated from the integral of the i-V_t profile generated by application of the potential sweep to the electrode where

$$V_t = V_{initial} \pm St\ . \tag{6}$$

Alternatively, since i = dq/dt in general, where dq is charge passed by the current i in time dt, i can be written

$$i = \frac{dq}{dt} \equiv \frac{dq}{dV} \cdot \frac{dV}{dt} = \frac{dq}{dV} \cdot S \tag{7}$$

dq/dV is the capacitance associated with the electrode process, C, i.e., i = CS. C is made up of a double-layer charging component and a component arising from potential dependence of coverage θ_A of the surface by A. The latter is the so-called adsorption pseudocapacitance for A, $C_A = dq_A/dV$. Thus, $C = C_{d.l.} + C_A$. Since θ_A and q_A are related by $\theta_A = q_A/Q$ for any coverage < 1,

$$i = C_{d.l.}\ S + Q\cdot\frac{d\theta_A}{dV}\cdot S \tag{8a}$$

$$= C_{d.l.}\ S + C_A S \tag{8b}$$[2]

The profile of i with changing potential at the rate S (= dV/dt) hence gives $d\theta_A/dV$ which is the differential coefficient of the electrochemical isotherm for adsorption of A in the process $A^- + M \rightarrow MA_{ads} + e$. The double-layer charging contribution $C_{d.l.}S$ in eq (8) can usually be subtracted from i by calculation, by an empirical procedure or by high-frequency measurements, as mentioned earlier.

The kinetic equations (1) or (2) can be expressed in terms of S under sweep conditions by writing e.g., for (1).

$$i_t = \frac{dq}{dt} = ZFk_1\ [1-\int \frac{\vec{i}dt}{Q}]\ \exp \beta(V_{initial} \pm St)F/RT \tag{9}$$

which can be evaluated numerically to give the i-V profile for the surface process as θ_A goes from $0 \rightarrow 1$, or vice versa, in the sweep.

7. Relation between i-V Profiles in Cyclic-voltammetry of Surface Processes and the Adsorption Isotherm

When a process such as $A^- + M \rightleftarrows MA_{ads} + e$ is at equilibrium, i.e., when $\vec{i} = \overleftarrow{i}$ in eqs (1) and (2), a reversible cyclic voltammetry i-V profile is generated in a potential sweep experiment and corresponds to the differential coefficient of the electrochemical isotherm $\theta_A = f(C_{A^-}, V, T)$ for electrochemisorption of A on the substrate M. For the Langmuir case $\ell n[\theta_A/(1-\theta_A)] = KC_{A^-} \exp VF/RT$ where K is an equilibrium constant k_1/k_{-1}. More generally, when interaction effects are involved, the adsorption isotherm takes the form $\ell n[\theta_A/(1-\theta_A)] = K \exp{-g\theta_A}\cdot C_{A^-}\cdot\exp VF/RT$ where g measures the change of binding energy with coverage. When g is finite, the effect is to make the range of electrode potentials over which θ_A goes from near zero to near unity increase in approximate proportion to g (Fig. 1). In fact, the half-widths of i-V profiles provide a good basis for evaluation of g [14].

The differential coefficient of the isotherm to which the current in cyclic-voltammetry of a surface process is proportional, is proportional to pseudocapacitance C_A [eqs (8a, b)].

Thus, for the general isotherm with interaction effects,

$$C_A = \frac{dq_A}{dV} = \frac{FQ}{RT}\cdot\frac{\theta_A(1-\theta_A)}{1 + g\ \theta_A(1-\theta_A)} \tag{10}$$

applies [15] for reversible deposition or ionization of A.

---

[2] Pure surface processes are distinguished by this relation from diffusion-controlled processes for which currents are proportional to $S^{\frac{1}{2}}$.

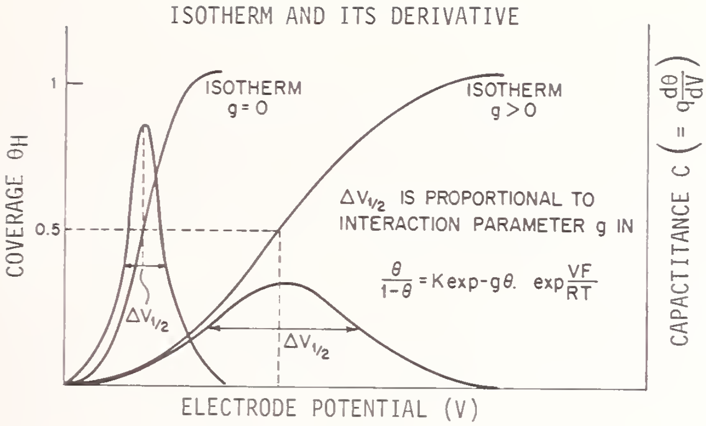

Fig. 1. Relation between electrochemical isotherm and pseudocapacitance as a function of potential for adsorption with (g >0) and without (g = o) interaction effects [14].

The maximum value of C_A corresponds to the current maximum in the sweep experiment and arises, for a reversible surface process, at $\theta_A = \frac{1}{2}$; i.e., $(C_A)_{max} = FQ/4RT \cdot 1/(1+ g/4)$. Also the potential range for appreciable C_A is increased approximately proportionally to g for the same reason referred to in the discussion of the isotherm itself. The form of C_A with potential in relation to isotherms with various g values is illustrated in Fig. 1.

When a surface process is irreversible, eq (10) no longer applies and the θ_A or f(V) relation, and the corresponding C_A, must be calculated [16] from eq (1) or (2) and not from both at equilibrium. The i-V profile is then asymmetric and its peak shifts by $2.3RT/\beta F$ volts for every 10-fold increase in sweep rate S. This provides a convenient way of examining the kinetics of electrochemical surface processes [17,18]. Practically, the reversibility of a surface process in relation to the range of S values employed experimentally is characterized by the ratio, k/S of the rate constant to the sweep rate as discussed further below. Reversible and irreversible i-V profiles are illustrated in Fig. 2.

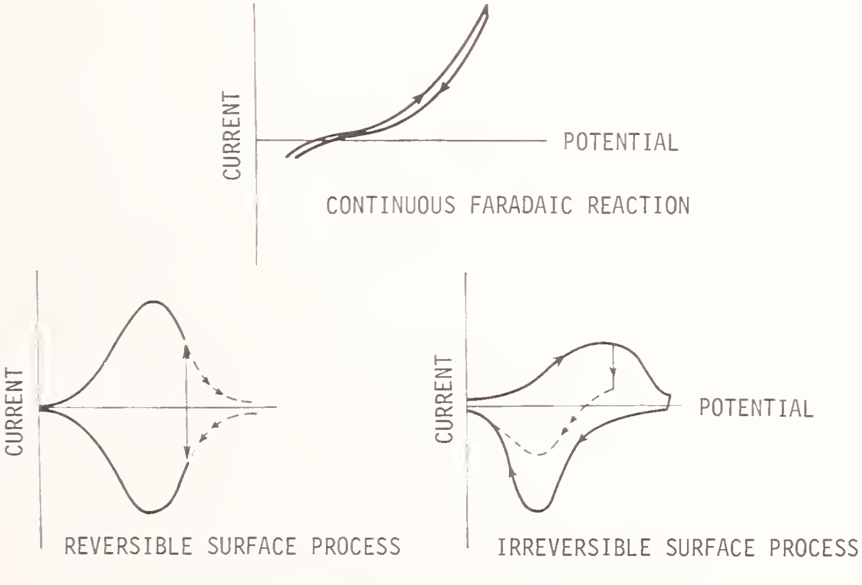

Fig. 2. Comparison of reversible and irreversible i-V profiles generated in cyclic voltammetry of a surface process.

8. Multiple States of Chemisorption below a Monolayer

Contrary to the current-potential response expected for a single chemical species electrodeposited on, or ionized from, a surface, the experimental behavior of many systems e.g., H, Cu, on Pt, Pb, Bi, Te, Cu on Au, OH and O on Pt and Au reveals that UPD of atoms, with the eventual formation of a monolayer, occurs in a succession of four or more submonolayer states in a very reproducible way. For H on Pt [19,20], four states are resolved over an energy range of ca. 8 kcal. mol^{-1}, while for Pb on Au, about 7 states are resolved over an energy range of ca. 11 kcal. mol^{-1}.

An obvious question arises [19,20] whether these states arise simply on account of intrinsic heterogenity of the surface, e.g., exposure of various crystal planes of a polycrystalline surface. Two types of experimental facts indicate this is not the case: (a) experiments on well prepared single crystal surfaces of Pt, e.g., in the (111) (110) or (100) orientations, give [19] more rather than less resolution of the 4-peaked i-V profile in cyclic voltammetry of H adsorption (Fig. 3); (b) changing anion of the electrolyte, e.g., from SO_4^{2-} or ClO_4^- in acid solution to HCO_3^-, CO_3^{--} or OH^- in alkaline solution, reveals a radical redistribution of adsorbed H amongst the 4 states, two being now filled to greater coverages and two to less in comparison with the situation in acid medium. This cannot be accounted for in terms of intrinsic heterogeneity since if a given peak in acid solution conditions corresponded to filling of elements of a given orientation on a polycrystalline surface, such elements could hardly become more filled simply by changing the anion of the electrolyte. These conclusions apply to results obtained in dilute solutions (0.02 N) when specific adsorption of anion is not significant (e.g., the i-V profiles for H on Pt become independent of H_2SO_4 concentration with increasing dilution and then become identical with the behavior in dilute $HClO_4$). Strongly adsorbed ions such as Cl^-, Br^- etc. do have redistribution effects, but this is due to blocking of the surface at the relative positive end (0.25-0.35 V E_H) of the potential range for H adsorption.

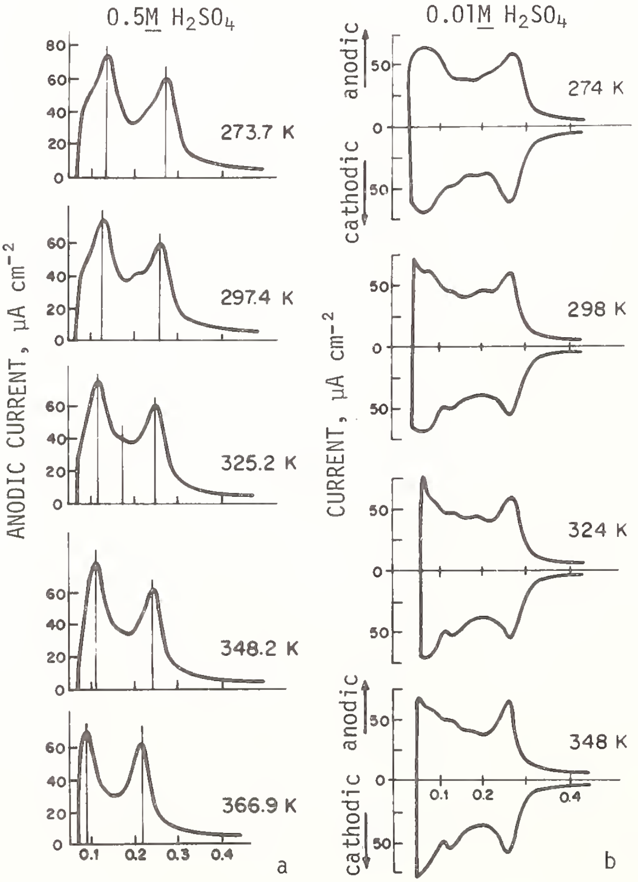

Fig. 3a. Resolution of 4 states of H adsorption at Pt in dilute acid solution at various temperatures. These diagrams show the i-V profiles generated by cathodic and anodic sweeps at the same dV/dt [19].

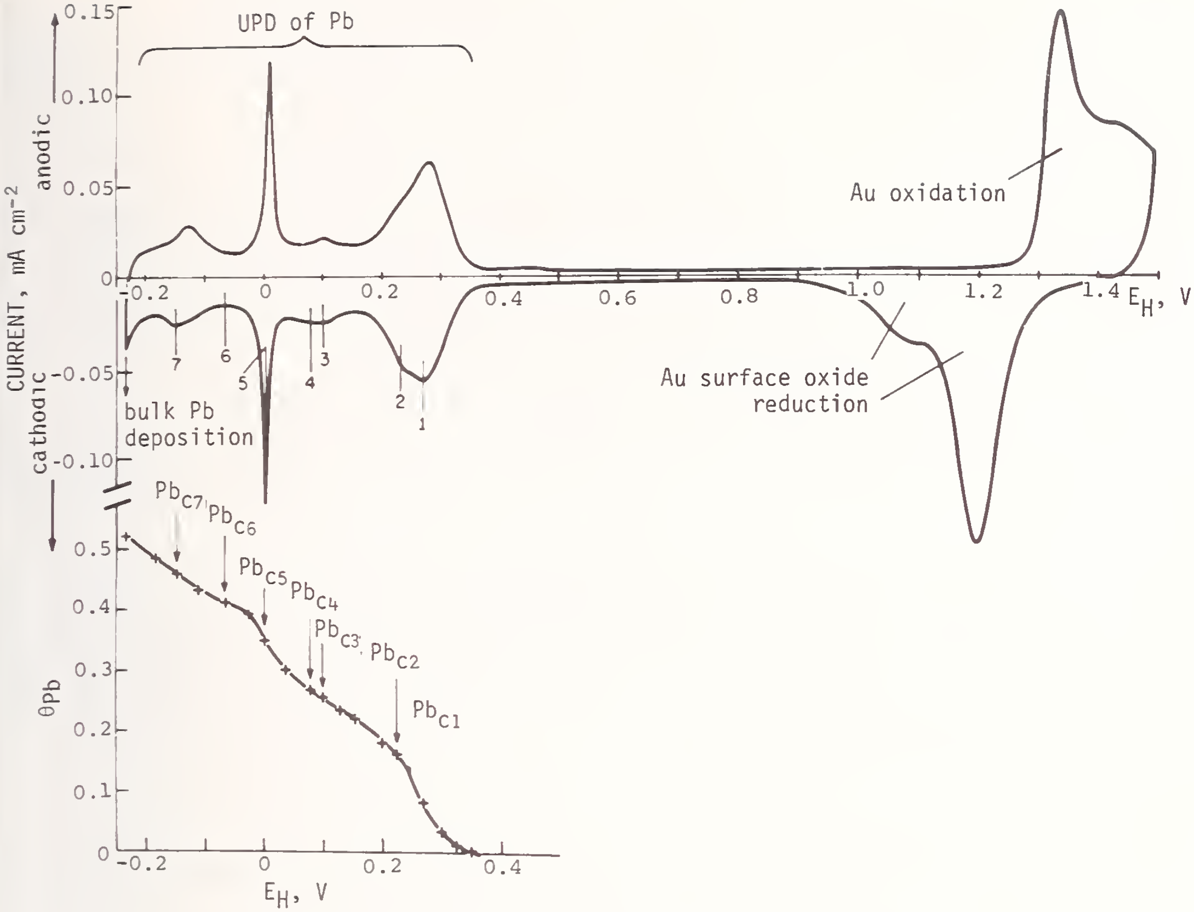

Fig. 3b. Resolution of 7 states of Pb atom deposition on Au with the isotherms.

The observation of multiple states of chemisorption of H on Pt (also observed on Rh and Ir) below a monolayer is paralleled by the results of thermal desorption experiments on dispersed Pt when several states of adsorption bonding of hydrogen are distinguished over an estimated energy range of ca. 8 kcal. mol^{-1} as in the electrochemical experiments. However, kinetic effects are involved in thermal desorption experiments while the electrochemical results for H on Pt correspond to equilibrium binding free energies since the deposition and ionization of H at Pt is a very reversible process.

The observation of multiple states of adsorption in deposition (or removal) of atoms or radical species is general and, for a given substrate metal, the general form of the peaks is similar for various atom adsorbates.

No present theories of chemisorption are able to account for the behavior observed, and structure in the electron density-of-states function for various metals is on too coarse a scale [21] (electron volts) to be able to account for the relatively fine resolution demonstrated in electrochemical experiments. We may speculate that the behavior observed (in the absence of major intrinsic heterogeneity effects) arises from "induced heterogeneity" associated with one or more of the following effects [19]:

(a) use of various available hybrid orbitals on the surface as relative coverage approaches an epitaxial or a geometric limit of 1; orbital energy splitting with change of θ_A.
(b) modification of the electronic properties of the surface in a communal way by all the adatoms at a given coverage as that coverage increases towards a monolayer,
(c) occupation successively of various different coordination positions on the surface (e.g. on substrate atoms, between pairs of atoms, in trigonal or square holes depending on orientation of the crystal face). This probably would be a result of (a) and/or (b) above.

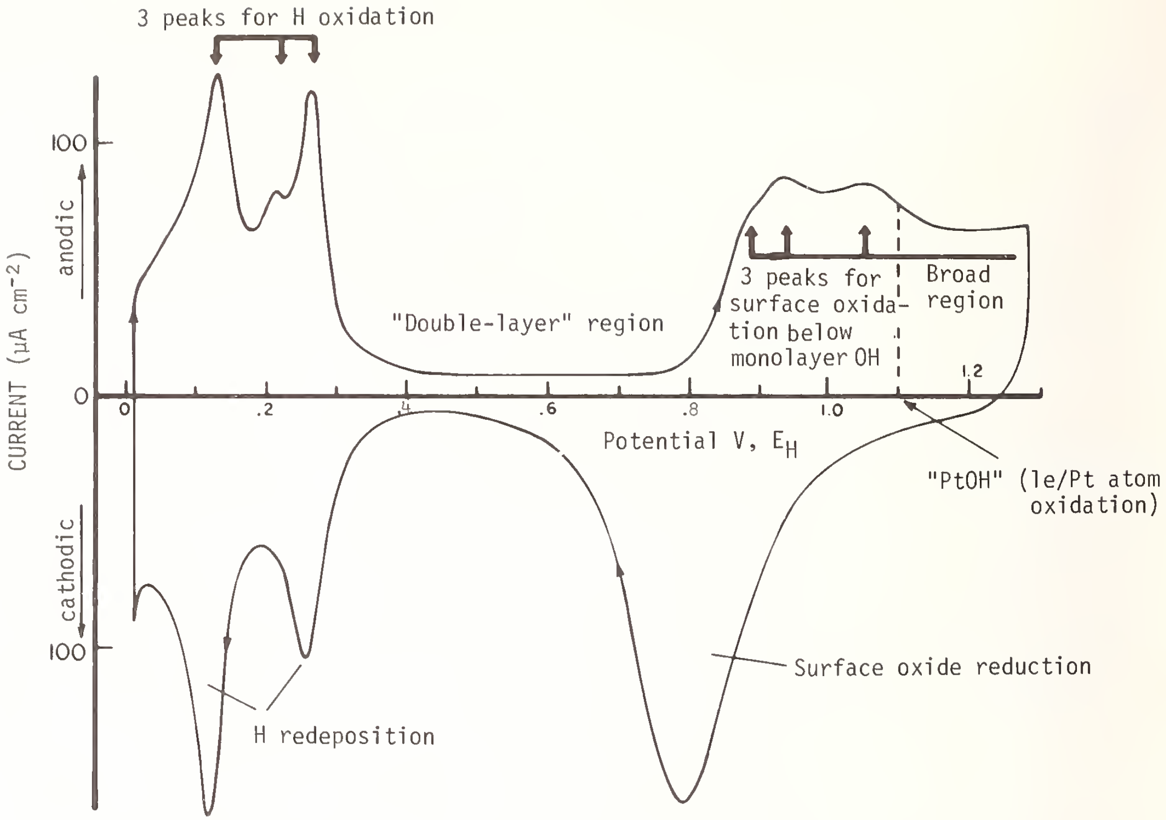

Fig. 3c. Resolution of 3 peaks in surface oxidation of Pt below monolayer coverage.

(d) long-range electronic interactions between ad-atoms on the surface (e.g., as discussed by Newns, Grimley, Koutečky, etc.).

(e) reactive-reconstruction of the substrate/adsorbate layer as coverage by ad-atoms increases towards a monolayer, with resultant development of successive 2-dimensional lattices in the ad-layer.

Probably [19], a combination of the above factors rather than any single one, determines the observed multiplicity of states of chemisorption of ad-atoms below a monolayer. The well-defined experimental behavior provides a challenge to surface chemists and physicists for quantitative interpretation.

9. Information on the Kinetics of Surface Processes at Electrodes from the Potentiodynamic Sweep Method and other Procedures

In principle, analysis of a transient which represents a kinetic relaxation response to a stimulus applied to the reaction, (in this case, voltage) can give information on the kinetics of the reaction. Potential-step, current-pulse and a.c. impedance methods, e.g., by Gerischer, Breiter, Bagotskii and others, have been applied for this purpose. Similar information is conveniently afforded by the potential sweep method by recording i-V profiles for a surface process over a sufficiently wide range (2-3 decades) of sweep rates that the process changes from a reversible to an irreversible one. Two kinds of kinetic information are obtained [17,18]: (a) the Tafel slope $RT/\beta F$ for the surface process and (b) the limiting sweep rate, S_0, corresponding to the exchange current density, i_0, below which the process is thermodynamically reversible, i.e., perturbation by a sweep at a rate $S < S_0$ does not significantly disturb the reaction from reversible behavior.

The Tafel slope is obtained [18] by plotting peak potential V_p vs. $\log S$ for $S > S_0$.

The S_0 is obtained by extrapolation of anodic and cathodic peak currents as a function of log S to a common point with appropriate allowance for interaction effects [14,17]. The required equations representing this situation have been developed by Angerstein-Kozlowska and Conway [17]:

$$V_{P,irrev} = V_{P,rev} + \frac{RT}{\beta F} \ln \frac{\beta F}{k_0 RT} + \frac{RT}{\beta F} \ln S \qquad (11)$$

where $RT/\beta F$ (= b/2.3) is the Briggsian Tafel slope, k_0 is a standard rate constant [$k_0 = k_1 \exp \beta V° F/RT = k_{-1} \exp -(1-\beta)V° F/RT$] for the standard potential V° for the surface process defined as the peak potential ($\theta_A = \frac{1}{2}$) when the process behaves reversibly. Equation (11) follows from analysis of a surface process in terms of eqs such as (1), (2) and (9). Equation (11) leads to the useful relation

$$V_{P,\ irrev} - V_{P,\ rev} = -b \log S_0 + b \log S \qquad (12)$$

(cf., the Tafel equation $\eta = -b \log i_0 + b \log i$). In eq (12), S_0 has been defined from eq (11) as

$$S_0 = \beta F/k_0 RT \qquad (13)$$

It is seen that S_0 characterizes the kinetics of a surface process like i_0 does for a regular continuous Faradaic process. It has the advantage (contrast i_0) for kinetic evaluations in electrocatalysis that the real-area of the electrode is not a required parameter. Hence the general problem in evaluation of electrocatalysis of separating the real-area factor from the intrinsic catalytic effectiveness of a surface is conveniently avoided in this approach.

When lateral interactions on the surface are significant ($g > o$), experimentally

$$V_{P,irrev} - V_{P,rev} = -b \log S_0' + b \log S \qquad (14)$$

where $\ln S_0 = \ln S_0'$ (experimentally evaluated by extrapolation) +

$$\text{[correction term due to interaction effects]} \qquad (15)$$

Since (for a 1e process) $V_{P,\ rev} = V° + RT/F\ g\ \theta_{P,rev}$ and $\theta_{P,rev} = \frac{1}{2}$, Angerstein-Kozlowska and Conway [17] showed that

$$V_{P,irrev} = \frac{RT}{\beta F} \ln \frac{S}{S_0} - \frac{RT}{\beta F} \ln \left[1 + \beta g\left(1-\theta_{P,irrev}\right)\right] + \frac{RT}{\beta F} (1-\beta)\ g\ \theta_{P,irrev} \qquad (16)$$

which gives a final general relation for $\log S_0$:

$$\log S_0 = \log S_0' - \log\left[1 + \frac{g}{2}\left(1 - \theta_{P,irrev}\right)\right] + \frac{g}{4.6} (\theta_{P,irrev} - \tfrac{1}{2}) - V°/2.3\ b \qquad (17)$$

where $\theta_{P,irrev}$ is [16] 0.63. Hence the kinetically significant S_0 can be evaluated if g is known from the half-width [14] of the i-V profile.

The electrochemical kinetics of surface processes, including those for resolved submonolayer states, can hence be completely characterized since b and S_0 as well as the coverage and relative energy of the states can be measured.

An illustration of the method is given schematically in Fig. 4 and with respect to experimental results for two of the states of H deposition in Fig. 5.

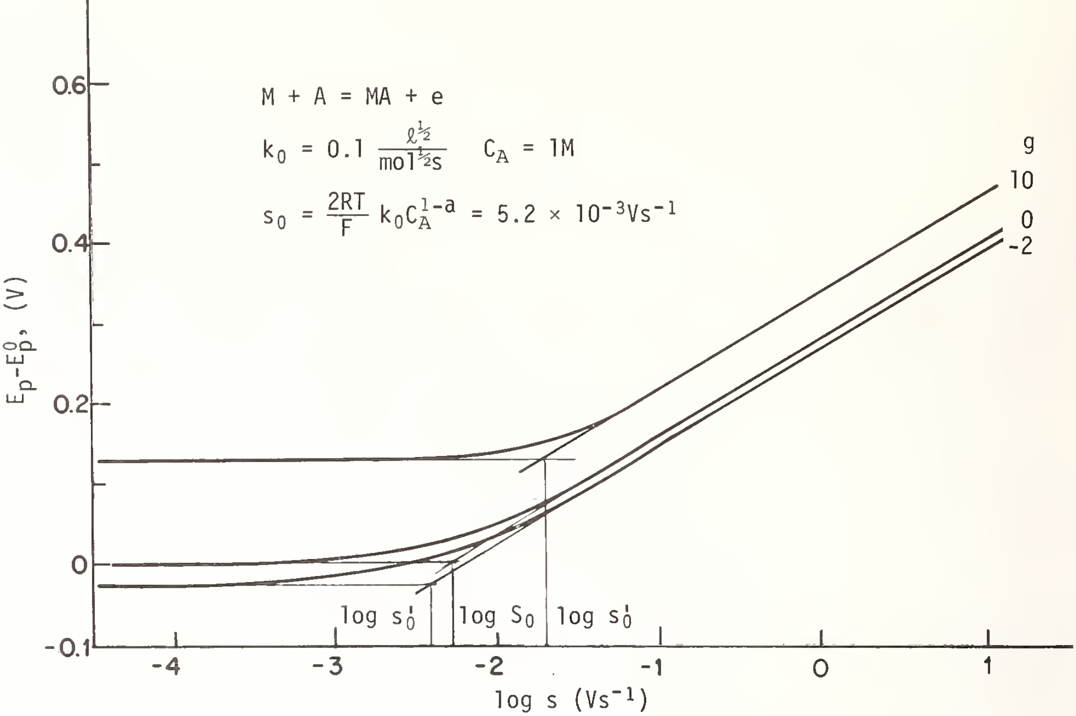

Fig. 4. Schematic relation between peak currents and log S for transition from reversibility to irreversibility in an electrochemical surface process studied by cyclic voltammetry [19]. (a) without interaction effects, g = 0. (b) with interaction effects taken into account, g ≠ 0.

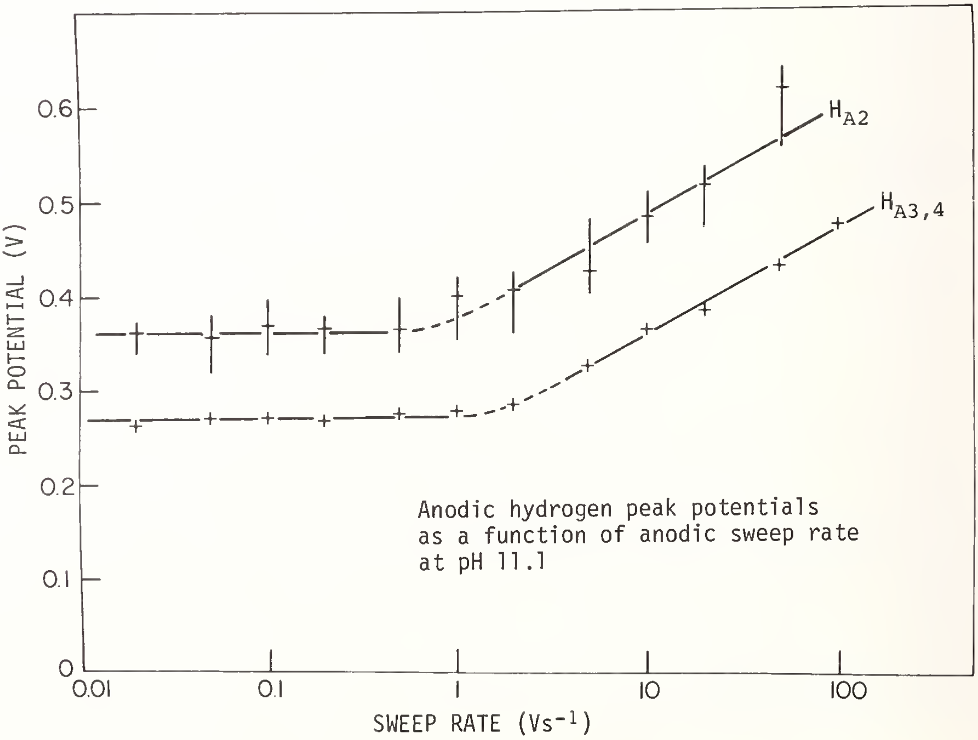

Anodic hydrogen peak potentials as a function of anodic sweep rate at pH 11.1

Fig. 5. Experimental relation between peak currents and log S for two of the states of chemisorbed H at Pt at 25 °C in 0.1N aqueous.

10. Resolution of Information on Co-adsorbed Species which give Overlapping Peaks

In a number of cases, species are co-adsorbed and may react electrochemically on a surface over the same range of potentials. Their relative coverage and electrochemical behavior cannot then be distinguished under equilibrium conditions. However, if the kinetics of the surface reaction processes are different, they may be distinguished by their kinetic relaxation characteristics, e.g., in terms of the current response to an impressed voltage sweep. This possibility arises if the rate constants, e.g., for two surface processes a and b, are sufficiently different that for an impressed sweep at a rate S, either

$$S_{o,a} < S < S_{o,b} \tag{18a}$$

or

$$S_{o,b} < S < S_{o,a} \tag{18b}$$

Condition (18a) corresponds to process b remaining reversible while a is perturbed from equilibrium by the sweep, while condition (18b) corresponds to process a remaining reversible while b is perturbed.

Experimentally, if the rate S_1 of an initially slow sweep is suddenly increased say 10 or 100 fold successively at various potentials over the overlapping i-V profile for a pair of co-adsorbed electroactive species, the current increase will be immediate for the fast process (say a) if $10S_1$ or $100S_1 < S_{o,a}$ for the fast process but will be slower for the slow process, b, for which $10S_1$ or $100S_1 > S_{o,b}$. Hence, fast and slow processes a and b can be distinguished in an overlapping i-V profile by the locus of fast current responses for the more reversible process in the profile [22]. Similar distinction can be made by using an a.c. modulated potential sweep [23].

These methods were applied by Angerstein-Kozlowska, Conway and MacDougall [22] to distinguish between extents of coverage by H and by chemisorbed acetonitrile at Pt which reacts in the adsorbed state over the potential region where H is co-adsorbed. Theoretical calculations were also carried out [23] to establish the basis of this method.

11. Initial Stages of Metal Oxidation

The sensitivity of electrochemical techniques allows the very initial stages of metal oxidation, or passivation in corrosion, to be studied at coverages by O species down to 2% of a monolayer[13]. For the noble metals, a rather general behavior is found initially, O species (or OH) are deposited as arrays which are determined by the crystal orientation of the surface, and give distinguishable states of the chemisorbed film below a monolayer (e.g., see Fig. 3c for Pt). The first 15%, approximately, of the monolayer on Pt is reversibly chemisorbed [13] but with progressively increasing extent of oxidation of the surface, the oxidation becomes more and more irreversible in the sense that a more cathodic potential is required to reduce the oxide film. At Au, this effect already sets in at ca. 2% coverage by OH. The effect is due to rearrangement ("place exchange" [14]) of the adsorbed layer from a chemisorbed film of OH or O species "on" the metal substrate surface to a two-dimensional lattice of OH and O species amongst metal atoms (or cations) in the metal surface; in fact, a surface compound is formed. The rearranged layer is thermodynamically more stable than the chemisorbed ad-layer, so that hysteresis between formation and reduction of the surface oxide film occurs. The rearrangement is driven by (a) repulsive forces in the initial ad-layer, (b) the field at the interface and (c) by the free-energy change of the transformation ad-layer → surface compound. Experimental behavior for Au is shown in Fig. 6.

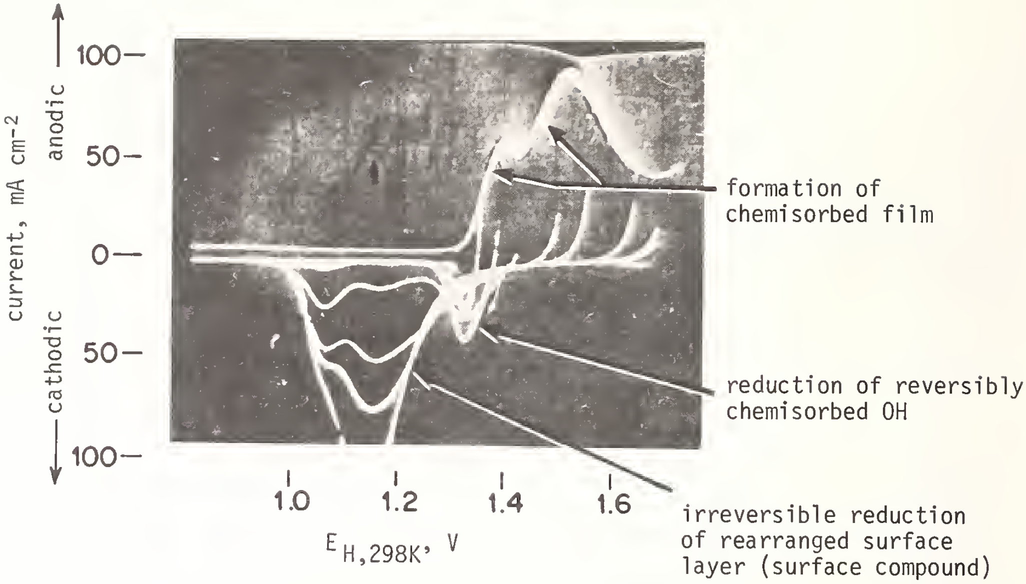

Fig. 6. Experimental distinction between reversibly reduced chemisorbed OH layer on Au and irreversibly reduced rearranged layer. (1<u>M</u> aq. $HClO_4$, 293 K, sweep rate 50 $V \cdot s^{-1}$.)

The rearrangement process and the consequent hysteresis can be looked upon in terms of electrochemical kinetics as a post-electrochemical step that drains off the electro-active chemisorbed species A on M and thus prevents the electrochemisorption reaction $A^{\pm} \pm e + M \rightarrow MA$ from being reversible. The situation may be represented by the scheme below:

Reversible Faradaic deposition process for adsorption of A atoms on M.

$$A^- + M \underset{k_{-1}}{\overset{k_1}{\rightleftharpoons}} A - M + e \qquad \text{I}$$

Reversible Faradaic deposition process with reversible following step.

$$\begin{tikzcd}
A^- + M \arrow[r, shift left] & A - M + e \arrow[l, shift left] \arrow[d, shift right, "k_2"'] & \text{II} \\
& M\text{-}A \arrow[u, shift right, "k_{-2}"'] \arrow[ul, dashed, "e"] & \text{(Place exchange)}
\end{tikzcd}$$

Reversible Faradaic deposition process for totally irreversible following step—hysteresis.

$$\begin{tikzcd}
A^- + M \arrow[r, shift left] & A - M + e \arrow[l, shift left] \arrow[d, "k_2"] & \text{(III)} \\
& M\text{-}A \arrow[ul, "e"] & \text{(Place exchange)}
\end{tikzcd}$$

A combination of II and III can arise in practice at low coverages and in II there is probably some residual hysteresis component (--➤) under certain conditions. Resolution of the reversible electrochemisorption process I in III from the irreversible place-exchange will, in practice, depend on the sweep-rate in relation to the rate constants k_1, k_{-1} and k_2.

The general behavior of chemisorbed atoms at electrodes, formed in a process such as $M + A^{\pm} \pm e \rightleftarrows A - M$. may be illustrated comparatively for various conditions by the following scheme, where U's are energies of interaction between adsorbed atoms A and metal substrate M; χ terms in branch (iii) are electronegativities of A and M:

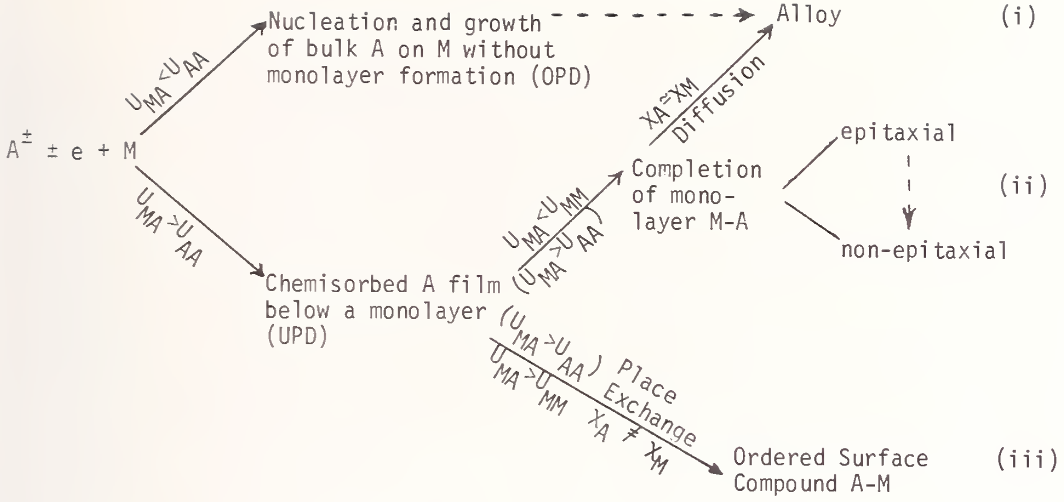

12. Indirect Studies on Chemisorbed Species

12.1. Cathodic and anodic sweep response

A number of substances chemisorb at electrodes but are not themselves directly "electroactive" in the same way as are H and metal atoms. In such cases, two related methods are used (cf. Gilman [11], Brummer et al.[12,13]) to characterize the adsorbed species. First, the substance is adsorbed at equilibrium at a potential where no surface processes can normally occur, e.g., at *ca*. 0.5V E_H on Pt. A cathodic sweep is applied and the accommodation of the surface for electrodeposited H is measured in relation to that for a clean surface. This gives (by difference) the number of H-sites which are blocked by the chemisorbed species. Secondly, an anodic sweep is applied and the substance is oxidatively removed (usually by reaction with anodically generated surface oxide of the metal). The number of electrons required for oxidation of the adsorbate per H-site occupied can then be calculated and the chemisorption characterized. This method has been used to study the adsorption of many organic substances at Pt.

12.2. Anodic H-displacement currents

An effect discovered by Conway, MacDougall and Angerstein-Kozlowska [24] can be used to evaluate coverage by species which chemisorb competitively with H. If an adsorbable substance, e.g., thiourea, is added at a controlled potential in the H adsorption region at Pt, an *anodic* current transient arises. It becomes *larger* the *less* positive is the potential at which it is adsorbed (Fig. 7). Hence, the current transient cannot be due to any reduction process. It arises by displacement of the initially adsorbed H, anodically; thus

$$A + MH_{ads} \rightarrow MA_{ads} + H^{+} + e$$

Integration of the anodic current transient and measurement of the potentiodynamic i-V profile before and after addition of the chemisorbing additive, quantitatively confirms the interpretation of this effect. Some substances, e.g., nitriles, chemisorb by anodic H displacement and are themselves partially reduced. Study of the anodic H displacement effect then gives a procedure for quantitatively following the surface electrochemistry of the ad-species [22,23]. The effect is a general one and is observed with a variety of substances that chemisorb at Pt.

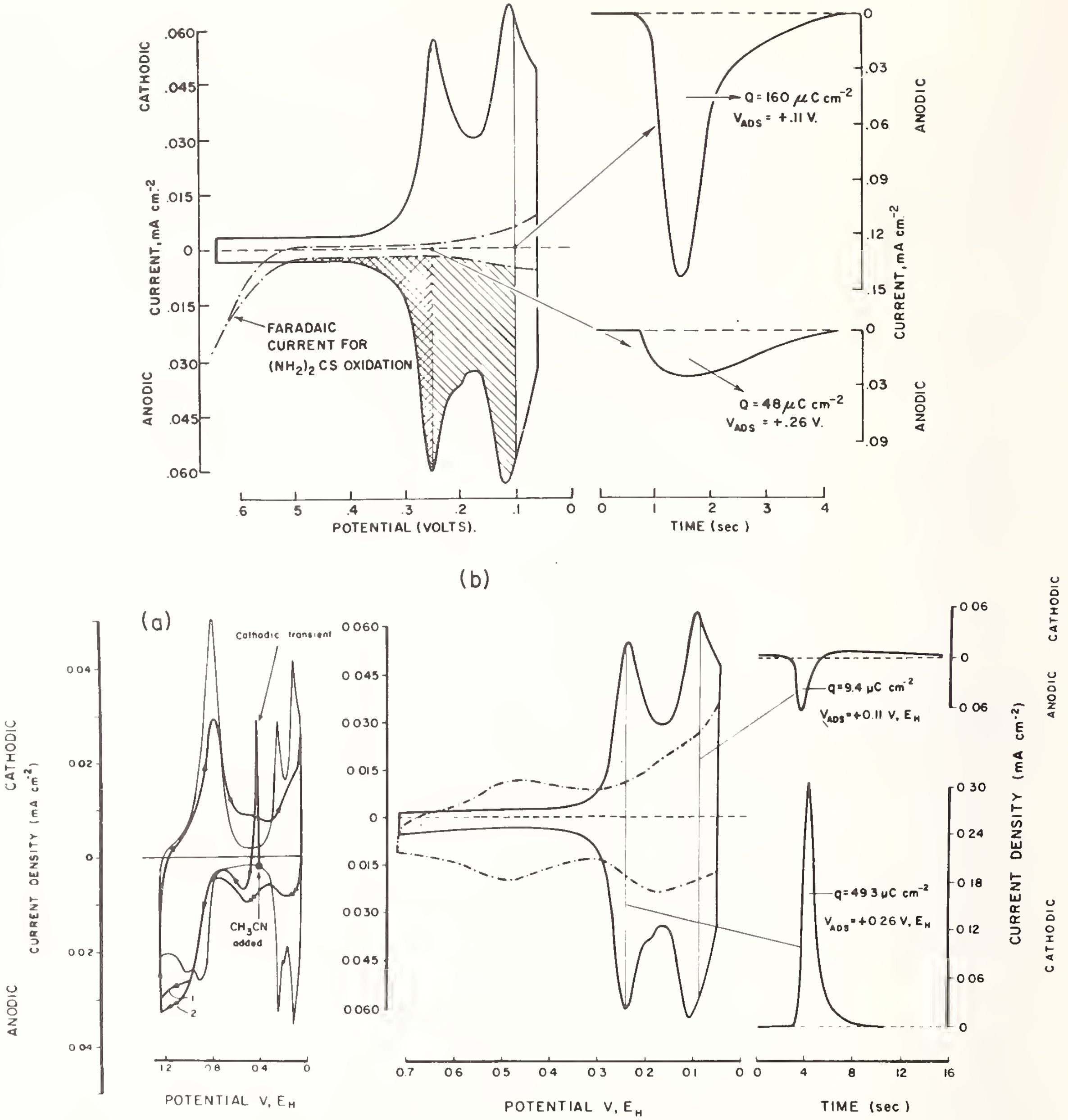

Fig. 7. Anodic H desorption effect with (a) thiourea and (b) acetonitrile desorption at Pt [24].

13. Applications to Non-metallic Surfaces [25,26]

In the case of non-metal surfaces where direct electrochemical changes can be introduced, studies similar to those described above for metals may be made, provided the ohmic resistance is not excessive. Also, the optical methods may be applied. Examples where electrochemical techniques have been applied are conducting oxides and sulfides (PbS, Cu_2S), carbon (very important in electrocatalyst technology), tungsten carbide and various tungsten bronzes.

14. Conclusion

It is convenient to conclude with a summary of information derivable from electrochemical methods of study of surfaces; this is given in tabular form below.

Table 2. Electrochemical studies of surfaces: information derivable.

1. Resolution of distinguishable bonded states below a monolayer, down to 2% coverage (monolayer of H on Pt is equivalent to 220 μ coulombs cm^{-2}; 2.20×10^{-9} F cm^{-2}).
2. State energies determinable to 5 mV (= 100 calories mol^{-1}).
3. Reaction rates of distinguishable adsorbed species below a monolayer determinable.
4. Resolution of behavior of co-adsorbed species can be made by kinetic relaxation studies.
5. Interaction forces in sub-monolayer states of adsorbed species determinable from current-potential profile half-widths.
6. Electronic and optical data determinable by single reflection measurements as a function of potential.
7. Surface space requirement determinable from extent of ads. H-blocking.
8. Coverages and properties of electro-inactive adsorbates determinable by H-blocking and indirect oxidation experiments.

15. Acknowledgement

Grateful acknowledgement is made to the National Research Council of Canada for support of work referred to in this review.

16. References

[1] E.g., see H. Gerischer, Z. Phys. Chem., 26, 223; 325 (1960); F. Beck and H. Gerischer, Z. Elektrochem., 63, 500 (1969); Record Chem. Prog., 23, 135 (1962); Z. Phys. Chem., N.F. 13, 389 (1957).

[2] J.D. McIntyre, Adv. Electrochem. Electrochem. Eng., 9, 61 (1973); Surface Sci., 37, 658 (1973).

[3] S. Gottesfeld and B.E. Conway, J. Chem. Soc. Faraday Trans. I, 69, 1090 (1973).

[4] B.E. Conway, L. Laliberté and H. Angerstein-Kozlowska, J. Electrochem. Soc., 121, 1596 (1974).

[5] B. Bewick and J. Robinson, J. Electroanal. Chem., 60, 163 (1975).

[6] E.g., see B.O. Seraphin, Chapter 1, in Semiconductors and Semimetals, Vol. IX, Modulation Techniques, Ed. R.K. Willardson and A. Beer, Academic Press, N.Y. (1972); and D.E. Aspnes and N. Bottka, Chapter 6 in Semiconductors and Semimetals, Vol. IX, Modulation Techniques, Ed. R.K. Willardson and A. Beer, Academic Press, N.Y. (1972).

[7] A.M. Azzam, B.E. Conway, J.O'M. Bockris and H. Rosenberg, Trans. Faraday Soc., 46, 918 (1950).

[8] B.E. Conway, H. Angerstein-Kozlowska, W.B.A. Sharp and E. Criddle, Anal. Chem., 45, 1331 (1973).

[9] A. Sevčik, Coll. Czeck. Chem. Comm., 13, 349 (1948).
[10] F. Will and C.A. Knorr, Zeit. Elektrochem., 64, 258 (1960).
[11] S. Gilman, J. Phys. Chem., 67, 78 (1963); Trans. Faraday Soc., 61, 2456; 2561 (1965).
[12] S.B. Brummer and A.C. Makrides, J. Phys. Chem., 68, 1448 (1964).
[13] S.B. Brummer, J.I. Ford and M.J. Turner, J. Phys. Chem., 69, 3424 (1965).
[14] B.E. Conway, E. Gileadi and M. Dzieciuch, Electrochim. Acta., 8, 143 (1963).
[15] B.E. Conway and E. Gileadi, Can. J. Chem., 42, 90 (1964).
[16] S. Srinivasan and E. Gileadi, Electrochim. Acta., 11, 321 (1966).
[17] H. Angerstein-Kozlowska and B.E. Conway, J. Electroanal. Chem., (Barker 60th Birthday Volume), in press, (1976).
[18] D. Gilroy and B.E. Conway, Can. J. Chem., 46, 875 (1968).
[19] B.E. Conway, H. Angerstein-Kozlowska and W.B.A. Sharp, Symposium on Electrocatalysis, The Electrochemical Society, San Francisco, 1973, p. 94.
[20] F. Will, J. Electrochem. Soc., 112, 481 (1966).
[21] D.R. Penn, Surface Science, 39, 333 (1973).
[22] H. Angerstein-Kozlowska, B. MacDougall and B.E. Conway, J. Electroanal. Chem., 39, 287 (1972).
[23] B.E. Conway, H. Angerstein-Kozlowska, B. MacDougall, F.C. Ho and J. Klinger, Faraday Disc., Chem. Soc. London, 56, 199 (1973).
[24] B.E. Conway, B. MacDougall and H. Angerstein-Kozlowska, J. Chem. Soc. Faraday Trans. I, 68, 1566 (1972).
[25] R. Woods, J. Phys. Chem., 75, 354 (1971); Proc. Aust. Inst. Min. Met., 241, 53 (1972).
[26] F.C. Ho and B.E. Conway, in course of publication.

National Bureau of Standards Special Publication 455, *Electrocatalysis on Non-Metallic Surfaces*, Proceedings of Workshop held at NBS, Gaithersburg, Md., December 9-12, 1975. (Issued November 1976)

Electroreflectance Study of the Defect States in Reduced n-type Titanium Dioxide[1]

Samuel S. M. Lu, Fred H. Pollak and Paul M. Raccah
Belfer Graduate School of Science, Yeshiva University
New York, New York 10033

We have investigated the electroreflectance spectrum of reduced n-type TiO_2, particularly below the fundamental absorption edge (~ 3 eV), in aqueous electrolyte, metal-semiconductor and metal-oxide-semiconductor configurations. We have observed for the first time in electroreflectance features in the spectrum for $\hbar\omega < 3$ eV which are related to the defect states. It is found that this structure is strongly dependent on the applied bias electric field. One optical peak appears at about 1.7 eV, an energy region in which structure has been observed in various other measurements which are related to both bulk (optical transmission, photoconductivity) and surface (electrochemical, electron loss spectroscopy) states. The intimate relationship between the bulk defect levels introduced by reduction and surface states will be discussed. Our results will be interpreted in terms of a recent model of Morin and Wolfram for d-electron surface states in transition metal oxides.

Key words: Defect states; d-electrons; electrolyte electroreflectance; surface states; titanium dioxide; transition-metal oxides.

1. Introduction

Considerable attention has recently been given to the transition metal oxides because of their possible application as catalysts. For example TiO_2[1,2][2] and $SrTiO_3$ [2] have been observed to catalyze the photoelectrolysis of water. This result has aroused interest in the possible use of photoelectrolysis for the large scale production of gaseous hydrogen, which can be conveniently stored and transported. It is generally believed that the catalytic properties of these materials are associated with the role of the d-electrons in the surface states. With regard to the nature of the d-electron states these materials may be classified into two broad categories, i.e. intrinsic and extrinsic (or defect). In the former class there exist occupied d-electron orbitals (or bands) in the intrinsic, stoichiometric material (e.g., Ti_2O_3,NbO_2) while in the latter the d-electron states are empty but can be populated by means of changes in stoichiometry (e.g., $SrTiO_3$, $BaTiO_3$, TiO_2). These latter oxides are not good catalysts in their intrinsic state but do become active when the d-electron states are populated by reduction or by the action of band-gap light. For example, it is only in their reduced states that TiO_2[1,2] and $SrTiO_3$[2] are active catalysts in the photoelectrolysis of water.

The process of reducing the intrinsic material so as to create those d-electron surface states that appear to be related to the catalytic action also introduces a set of "defect" levels and/or bands. These "defect" states then have a specific connection with

---

[1] Work supported in part by the National Science Foundation.

[2] Figures in brackets indicate the literature references at the end of this paper.

the d-electron states and may, in some cases, actually consist of d-orbitals (or bands). For example, the process of reducing TiO_2 introduces oxygen vacancies as well as creating Ti^{3+} states. In fact the relation between defect states and catalytic activity may be very general in the case of non-metallic catalysts. It has been pointed out that from the standpoint of widespread application it is extrinsic semiconductors that are of absorbing interest [3]. It is in this spirit that we have undertaken an investigation of the defect states in reduced n-type TiO_2 by means of the electroreflectance (electric-field modulated reflectivity) technique. Electroreflectance (ER) is particularly relevant in this situation since it can be performed in an electrolytic configuration[4,5]. This represents an in situ observation of the properties of materials in relation to their catalytic activities, such as, for example, the photoelectrolysis of water.

We have investigated the ER spectrum of reduced n-type TiO_2, particularly below the fundamental absorption edge (~ 3 eV), in aqueous electrolyte, metal-semiconductor (MS) and metal-oxide-semiconductor (MOS) configurations. We have observed for the first time in ER features in the spectrum for $\hbar\omega < 3$ eV which are related to the defect states. It is found that this structure is strongly dependent on the applied bias electric field. One optical peak appears at about 1.7 eV, an energy region in which structure has been observed in other measurements related to both bulk (optical transmission[6,7], photo-conductivity[8,9])and surface (electrochemical[10], electron loss spectroscopy[11]) states. The relationship between the bulk defect states introduced by reduction and surface states will be discussed. Our results will be interpreted in terms of a recent model of Morin and Wolfram[12] for d-electron surface states in transition metal oxides.

2. Experimental Details

Modulation techniques, particularly ER, have been employed over the past several years in optical measurements of solids to achieve greater sensitivity and resolution[5]. They have been extremely successful in enhancing small structure in optical spectra. Uniform electric fields for ER can be applied to the surface of a solid by a number of different techniques including the electrolyte[4], metal-semiconductor (MS), or metal-oxide-semiconductor (MOS) methods[5]. There are similarities between these approaches since the interface between the solid and an electrolyte solution behaves very much like a metal-semiconductor diode, in which the applied field modulates the space-charge layer at the interface. In an electrolyte-solid interface this is accomplished by means of the Gouy layer, which is typically about 5 Å thick. In all these techniques large electric fields can be obtained at the interface with relatively small modulating voltages (~ 1 - 10 V).

The experimental arrangement for measuring ER spectra has been described extensively in the literature and hence will not be repeated here[4,5].

Pure, single crystal TiO_2 was obtained from the Adolph Meller Company[13] and was cut into parallelepipeds of dimensions 5x5x1 mm. The samples were reduced by annealing at 800°C for about 2 hours in a sealed, evacuated (10^{-4} Torr) quartz ampoule. The broad faces [(100) face] were prepared for optical investigation by polishing with various grades of diamond paste and finally by Siton[14], the latter for a period of several hours. This procedure resulted in a high quality optical finish on the surface. The TiO_2, which was originally clear in color, became a deep uniform blue after this procedure indicating that the oxygen vacancy concentration was rather uniform throughout the crystal. Ohmic indium contacts were soldered onto the unpolished faces of the sample, which were also sandblasted and painted black to avoid back surface reflection effects. The MS samples were prepared by evaporating a semitransparent layer of about 70 Å of Ni onto the polished surface of the TiO_2 in a vacuum of about 10^{-6} Torr, thus giving rise to a Schottky type barrier. The MOS samples were prepared by first evaporating a dielectric layer of about 1000 Å of SiO and then the semitransparent 70 Å Ni layer onto the TiO_2 surface, also under high vacuum.

3. Experimental Results

Shown in figures 1 and 2 are the electrolyte ER spectra of reduced n-type TiO_2 for light polarized parallel and perpendicular to the c-axis, respectively, in the range 1.5 - 4.5 eV for different values of the dc bias. The sense of the bias is taken relative to a

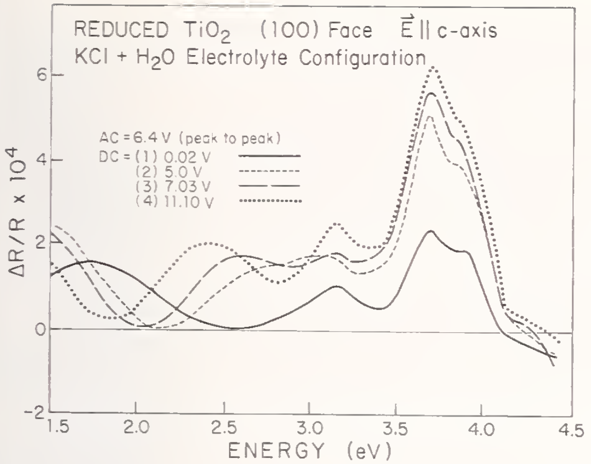

Fig. 1. Electroreflectance spectra of reduced n-type TiO_2 in the electrolyte configuration for light polarized parallel to the c-axis at various values of the dc bias.

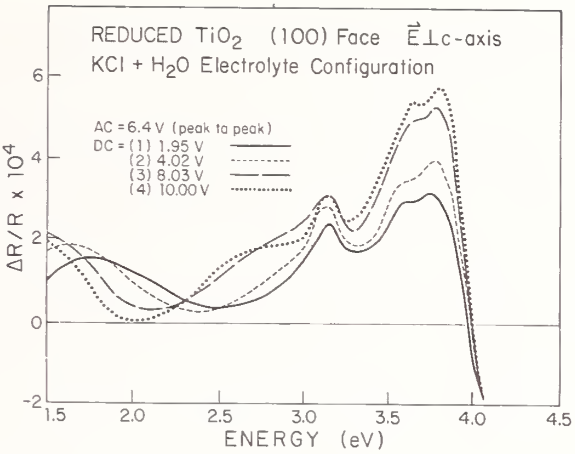

Fig. 2. Electroreflectance spectra of reduced n-type TiO_2 in the electrolyte configuration for light polarized perpendicular to the c-axis at various values of the dc bias.

platimum electrode, i.e. positive bias indicates the sample is positive with respect to the electrode. The electrolyte used was approximately 1 molar KCℓ in water[4]. At the lowest value of the bias several features are observed above 3 eV and a peak is seen at about 1.7 eV. In general, the structure above 3 eV is similar to that which has been reported previously[9,15,16] with only some minor differences. These peaks have been assigned to various interband optical transitions of the intrinsic material. We shall return to a discussion of these features shortly. What is of considerable interest is the optical structure around 1.7 eV, for both polarization directions, which has not been observed before in reflection[17] or ER[9,15,16]. As the bias is increased there are two main effects on the spectrum: (a) the 1.7 eV peak shifts to lower energies and (b) a new structure appears which is split off from the 3.15 eV interband peak which also moves to lower energies. These two field dependent features appear to shift at the same rate with applied dc voltage. This new peak is observed at the highest bias at about 2.4 eV in figure 1, for which it is clearly resolved, and 2.6 eV in figure 2 (note that the biases are different for the two polarizations). The structure due to the interband transitions above 3 eV have been left relatively unaffected by the increase in dc bias. The dc bias voltages used in this study were kept low enough to avoid oxygen evolution at the sample. Although we have not been able to completely follow the shift of the field-dependent features we can estimate their change in energy from the shift of the minima (~ 2.5 eV at the lowest bias) since the line shape does not change with field. We have determined the shift of the minima for both polarizations and found that in a certain bias range it is linear in $\sqrt{V}$, where V is the applied bias. These results are shown in figure 3. For a fully depleted space change layer it can be

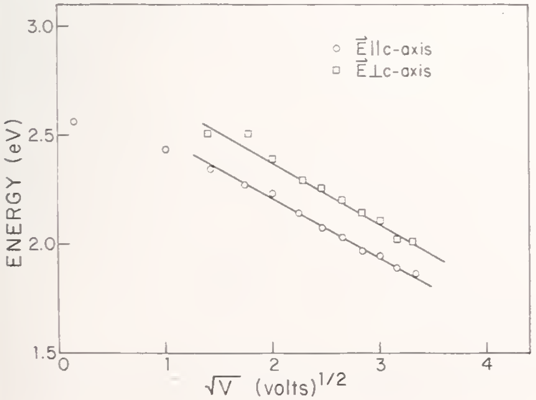

Fig. 3. Voltage dependence of the minima in the electrolyte ER spectra for $\hbar\omega < 3$ eV. This shift is representative of the voltage dependent structure in the spectra.

demonstrated that the average surface field E_s is proportional to $\sqrt{V}$[4,18]. Therefore, the results of figure 3 indicate that the shift of these structures is linearly dependent on the surface field E_s.

The optical structure for $\hbar\omega > 3$ eV corresponds to that observed by previous workers [9,15,16], the main difference being that their spectra shows a large single structure in the range $3.5 < \hbar\omega < 4$ eV, while in this region we find a doublet structure for this feature for both polarization directions. The reasons for this difference are not understood at this time.

The ER spectrum for the MS configuration is shown in figures 4 and 5 for light polarized parallel and perpendicular to the c-axis, respectively, while in figures 6 and 7 are plotted to ER data for the MOS configuration for the two light polarizations. For both the MS and MOS cases the sample bias is taken in reference to the Ni electrode.

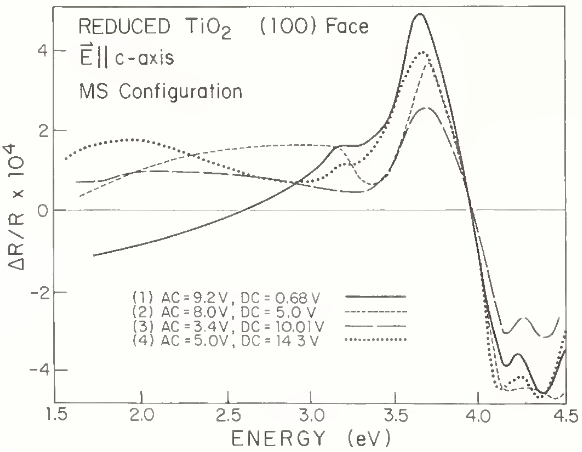

Fig. 4. MS electroreflectance spectra of reduced n-type TiO_2 for light polarized parallel to the c-axis.

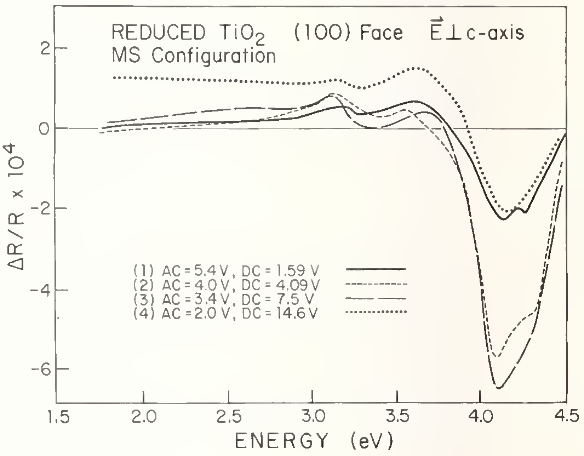

Fig. 5. MS electroreflectance spectra of reduced n-type TiO_2 for light polarized perpendicular to c-axis.

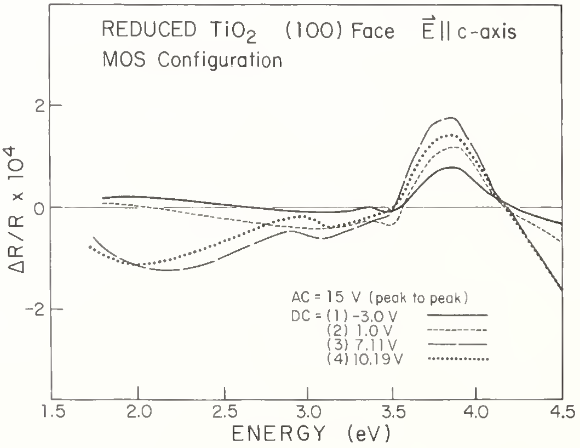

Fig. 6. MOS electroreflectance spectra of reduced n-type TiO_2 for light polarized parallel to the c-axis.

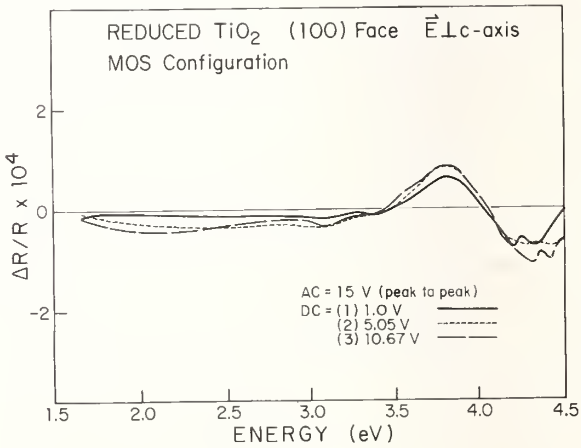

Fig. 7. MOS electroreflectance spectra of reduced n-type TiO_2 for light polarized perpendicular to the c-axis.

For the cases of "dry" configuration these spectra show, in general, features at the same energy above 3 eV as for the case of aqueous ER (see figures 1 and 2), although there are some differences in line-shape. Below 3 eV there is some indications of the 1.7 eV structure but it is not as clear as in the case of the electrolyte ER. For example, figure 4 shows that as the bias is increased an optical feature in the range of 1.8 eV begins to emerge. This can be seen clearly for the case of the 14.3 V bias. Figure 6 shows structure in this energy range for bias values of 7.11 and 10.19 V although here the phase is inverted. No field-induced splitting of the 3.15 eV optical structure is observed for the dry configuration ER spectra. The differences between the aqueous and "dry" ER data is probably due to the fact that higher surfaces fields are generally attainable in the electrolyte case.

No hysterisis effects were found for any of the three ER configurations employed. After data at the highest bias was recorded the lowest bias spectrum could be recovered without any compensation of the dc voltage.

The possible interpretation of our data for $\hbar\omega < 3$ eV in terms of interference effects can be eliminated. For example, it might be argued that in the electrolytic configuration it is possible to form a layer on the material due to electrochemical action. In the MS or MOS case a semi-insulating layer might be formed at the TiO_2 surface by the field-induced migration of the oxygen vacancies near the interface. The field-induced modulation of the thickness or refractive index of such a layer could produce interference effects. Such considerations can be ruled out since it has been clearly demonstrated that interference effects of this nature produce oscillatory spectra with a well defined phase change[19,20], i.e. the spectra would swing positive and negative. We have not observed this pattern in any of our data for $\hbar\omega < 3$ eV. In addition, the lack of hysteresis seems to rule out the formation of any layer, particularly in the electrolyte case.

4. Discussion of Results

The main results of this work are the observation in the ER spectra of structure at 1.7 eV (below the direct gap), the field-induced splitting of the 3.15 eV peak and the strong electric field dependence of these structures. We will now discuss the relationship of these results to the defect and surface states in reduced TiO_2.

Intrinsic TiO_2 has its lowest direct gap at about 3.2 eV and an indirect gap at a somewhat lower energy of about 3 eV[15,16]. The direct transition is presumably due to O(2p) - Ti(3d) transitions and is characteristic of the perovskite-type materials in which the Ti ion is in a TiO_6 octahedral environment. Therefore, in agreement with previous workers we attribute our ER peak at 3.15 eV to the direct transition of the intrinsic material.

While optical absorption measurements of stoichiometric TiO_2 show no structure for $\hbar\omega<3$ ev, after reduction optical transitions are observed in this region[6,7]. Of particular interest is the fact that a number of investigators report structure around 1.7 eV[6-9]. The photoconductivity spectra also shows a peak in this general region[9]. These experiments reveal that in the process of reduction levels are introduced in the band gap in the region around 1.7 eV above the valence band (and hence about 1.5 eV below the conduction band). Our data reveals the first indication of these levels in a reflection or ER experiment and their strong field dependence.

Surface state experiments have also found a response in this energy range. Using energy loss spectroscopy Henrich et al[11] have reported surface state transitions at about 1.5 eV. Frank et al. have investigated the electrode response of n-type TiO_2 in acetonnitrile with a large number of electroactive compounds differing widely in their standard potentials. They report a level located about 1.2 eV below the conduction band[10].

The above mentioned studies show that there are levels in both the bulk and surface of reduced TiO_2 at about 1.5 eV below the conduction band. These results suggest that there is a close connection between the bulk defect and surface states in this material. This is not completely unexpected if one considers the following situation. The bulk Ti atoms in TiO_2 are in a 4 + valence state and hence have no d-electrons. Surface ions would have a 3+ valence due to the absence of some of the ligands that are present in the bulk. But creation of such a surface is analogous to the process of reduction in which oxygen vacancies are created with the resultant change in valence of a neighboring Ti atoms. In fact, Henrich et al only see a signal in their energy loss measurements on pure TiO_2 after Ar-ion bombardment of the surface which sputters off oxygens thus leaving the Ti^{3+} ions on the surface. It is therefore not surprising to find this intimate connection between bulk defect states and surface states in reduced TiO_2.

We next turn our attention to the field-induced splitting of the 3.15 eV peak and the strong field dependence of this and the 1.7 eV structure. Morin and Wolfram have calculated d-electron surface states in this class of transition metal oxides by considerations of the termination of some of the d-electron orbitals of the intrinsic material. As has been discussed above there is an intimate relationship between the d-electron surface states and defect states introduced by reduction of the material[12]. Hence, we will use the model of these authors to interpret our results and will henceforth talk about d-electron surface/defect states.

Morin and Wolfram report surface bands which are lowered by about 1.5 eV from the conduction bonds at Γ in the Brillouin zone. In addition the shape of the surface/defect bands is such that at the M point they are at the same energy as the intrinsic conduction bands at Γ. On this basis the 1.7 eV peak is assigned to transitions from the top of the valence band to the surface/defect states at Γ. There are two degenerate transitions at about 3 eV, one from the valence to intrinsic conduction band at Γ and another from the valence band to the surface/defect states at the M point. If we further assume that the effect of the dc bias electric field is to uniformly displace the surface/defect bands to lower energies the field-induced-splitting of the 3.15 eV structure and shift of the 1.7 eV feature are explained. The former effect is accounted for by the removal of the energy degeneracy between the intrinsic conduction band at Γ and the surface/defect states at M. Also the field-induced lowering of these bands would explain the shift to lower energies of the field-dependent structures.

Such field-induced shifts are not completely unreasonable when it is considered that the position of the surface/defect bands have been deduced from the changes in surface electrostatic potential at the transition metal site. In addition, large field-induced changes of ER positions ($\sim$ 0.5 eV) have been observed in $KTaO_3$ in the electrolyte configuration for surface fields of about 10^6 V/cm. If we assume an electron density of about 10^{19} cm^{-3} then for a bias of 10 V our surface fields are estimated to be about 2 x 10^6 V/cm [4,5,16].

The intimate connection in TiO_2 between defect states introduced by reduction and d-electron surface states has been strongly suggested by this study and other recent investigations. The results of this experiment can be qualitatively explained on the basis of the Morin and Wolfram d-electron surface/defect state model. These conclusions may also be applicable to other transition-metal oxides of this class such as $SrTiO_3$.

We wish to thank T. Wolfram for several very useful discussions.

References

[1] Fujishima, A., and Honda, K., Nature 238, 37 (1972). Hardee, K. L., and Bard, A. J., J. Electrochem. Soc. 122, 739 (1975).

[2] Marvroides, J. G., Tchernev, D. I., Kafalas, J. A., and Kolesar, D. F., paper presented at the workshop.

[3] Sastri, M. V. C., Srinivasan, V., and Viswanathan, B., in Modern Aspects of Solid State Chemistry (Rao, C. N., Ed.), Plenum Press, New York (1970), p. 425.

[4] Cardona, M., Shaklee, K. L., and Pollak, F. H., Phys. Rev. 154, 696 (1967).

[5] Cardona, M. in Modulation Spectroscopy (Seitz, F., Turnbull, D., and Ehrenreich, H., Ed.) Academic Press, New York (1969), and references therein.

[6] Cronemeyer, D. C., Phys. Rev. 87, 876 (1952).

[7] Breckenridge, R. G., and Hosler, W. R., Phys. Rev. 91, 793 (1953).

[8] Addiss, R. R. Jr., Ghosh, A. K., and Wakim, F. G., Appl. Phys. Letters 12, 397 (1968).

[9] Ghosh, A. K., Wakim, F. G., and Addiss, R. R. Jr., Phys. Rev. 184, 974 (1969).

[10] Frank, S. N., Laser, D., Hardee, K. L., and Bard, A. J., paper presented at this workshop.

[11] Henrich, V. E., Zeiger, H. J., and Dresselhaus, G., paper presented at this workshop.

[12] Morin, F. J., and Wolfram, T., Phys. Rev. Letters 30, 1214 (1973) and references therein. Wolfram, T., paper presented at this workshop.

[13] Adolph Meller Co., Providence, R.I.

[14] Manufactured by Monsanto Co., New York, N.Y.

[15] Frova, A., Boddy, P. J., and Chen, Y.S., Phys. Rev. 157, 700 (1967).

[16] Vos, K., and Krusemeyer, H. J., Solid State Comm. 15, 949 (1974).

[17] Cardona, M., and Harbeke, G., Phys. Rev. 137, A 1467 (1965).

[18] See, for example, Sze, S. M., in Physics of Semiconductor Devices, Interscience, New York (1969).

[19] Subashiev, V. K., Surface Science 37, 947 (1973).

[20] Aspnes, D. E., J. Opt. Soc. Am. 63, 1380 (1973).

National Bureau of Standards Special Publication 455, *Electrocatalysis on Non-Metallic Surfaces*, Proceedings of Workshop held at NBS, Gaithersburg, Md., December 9-12, 1975. (Issued November 1976)

Electron Energy Loss Spectroscopy of Surface States on Titanium and Vanadium Oxides[1]

Victor E. Henrich, H. J. Zeiger, and G. Dresselhaus
Lincoln Laboratory, Massachusetts Institute of Technology
Lexington, Massachusetts 02173

Using electron energy loss spectroscopy, we have studied the surface electronic structure of TiO_2, Ti_2O_3, $TiO_{0.87}$ and V_2O_3. A surface-state transition in the region of 1.5 to 2.5 eV is present in all of these materials when the surface is reduced by Ar-ion bombardment. Subsequent exposure of the surfaces to oxygen or water vapor reduces or completely eliminates this transition. The origin of the transition in terms of d-electron population of surface cations is discussed.

Key words: Adsorption; electron spectroscopy; ligand-field splitting; surface excitons; surface states; transition-metal oxides.

We are reporting here electron energy loss measurements made under ultrahigh-vacuum conditions on single crystals of TiO_2, Ti_2O_3 and V_2O_3, and on polycrystalline TiO_x, where x = 0.87. Our interest in these materials stems from the recent observation that TiO_2 and other transition-metal oxides catalyze the photoelectrolysis of water [1];[2] and we are investigating the surface electronic structure of these catalysts.

In electron energy loss spectroscopy, a monoenergetic electron beam of energy E_o strikes the surface of a solid, and some of the electrons excite electronic transitions of energy Δ in the sample and emerge with energy $E_o - \Delta$. This is just the electron analog of Raman scattering. The extreme surface sensitivity of this technique arises from the very short mean free paths of electrons in solids. Electrons with energies between about 40 and 150 eV have mean free paths of only 4 or 5 Å [2], so surface-state transitions can contribute structure to an energy loss spectrum comparable in magnitude to that due to bulk transitions.

The samples were either oriented and polished or fractured to expose fresh surfaces before mounting in the ultrahigh vacuum system. All samples were then Ar-ion sputter-etched to produce atomically clean surfaces. This treatment produced enough disorder on the surfaces that no low-energy-electron-diffraction patterns were observed, except in one case that will be discussed later.

We will concentrate on the low-energy region of the energy loss spectra, and this is shown for TiO_2 in figure 1. The first derivative of the secondary-electron energy distribution n(E) was recorded vs energy loss, so peaks in n(E) occur at midpoints of negative slopes. The resolution in these measurements is about 0.6 eV. The elastically reflected peak has been attenuated relative to the rest of the spectrum. Four peaks are seen in this region of the spectrum, and their locations are indicated by the arrows. The method used for determining peak amplitude and width is also indicated. Peaks B, C and D, which occur at 5.5, 10 and 13.5 eV, are present in all of the titanium oxides. We attribute them to cross transitions from the ground state of the O^{2-} ion to the relatively narrow, high density-of-states band of titanium d-levels.

Peak A, which occurs at about 1.5 eV, is of primary interest here. It is due to a surface-state transition, and its amplitude varies tremendously on different crystal surfaces and as a function of exposure to ambient gases. Figure 2 shows the energy loss spectra for Ar-ion sputtered surfaces of TiO_2, Ti_2O_3 and TiO_x. Peak A is much larger on the last two samples, while the triplet is similar on all crystals. A very weak peak is sometimes seen between peaks B and C, and it is shown on the insert below the bottom trace. This happens to be for a TiO_x surface that had been exposed to water vapor, although water vapor is not necessary for the presence of this peak. We have not as yet determined its origin.

---

[1] This work was sponsored by the Department of the Air Force.

[2] Figures in brackets indicate the literature references at the end of this paper.

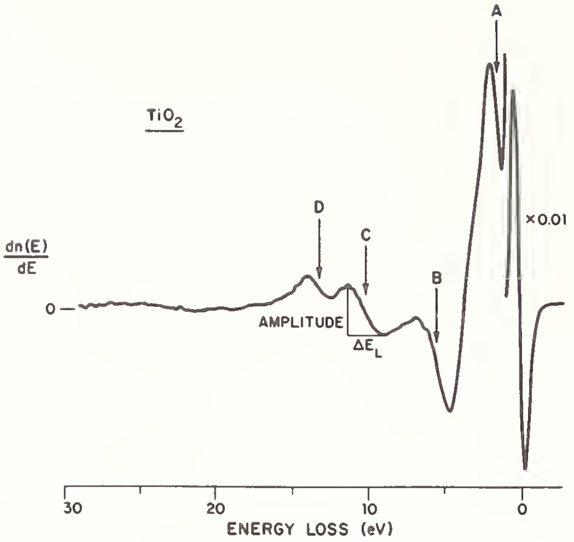

Fig. 1. Electron energy loss spectrum for Ar-ion sputtered TiO_2. The derivative of the secondary-electron energy distribution, dn(E)/dE, is plotted vs energy loss. Locations of peaks in n(E) are indicated by the arrows.

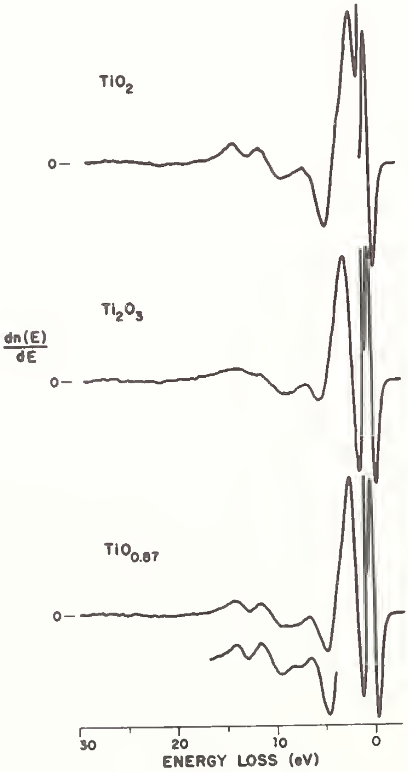

Fig. 2. Electron energy loss spectra for Ar-ion sputtered TiO_2, Ti_2O_3 and $TiO_{0.87}$. The insert shows a small peak that is sometimes present at about 8 eV.

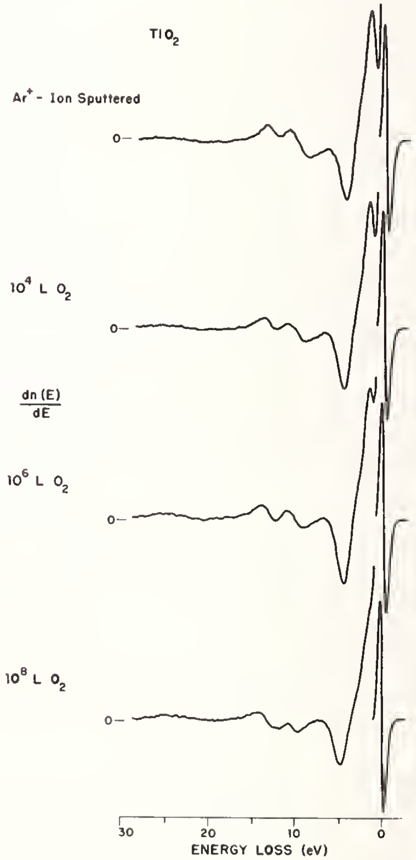

Fig. 3. Electron energy loss spectra for TiO_2 after Ar-ion sputtering and subsequent exposure to O_2.

Peak A is affected dramatically by exposure of the surfaces to either oxygen or water vapor. Figure 3 shows the effect of oxygen exposure on the spectra for TiO_2. As little as 1 Langmuir of oxygen begins to reduce the amplitude of peak A relative to the rest of the spectrum, and on heavy exposure the peak can completely disappear. The exposures shown here are 10^4, 10^6 and 10^8 Langmuir of oxygen. A similar reduction in the amplitude of peak A with oxygen exposure is seen for Ti_2O_3 and TiO_x, although on those surfaces the peak never completely disappears. The results of measurements on several crystals are summarized in figure 4, where the amplitude of peak A, normalized to that of peak C, is plotted vs surface oxygen concentration as measured by Auger electron spectroscopy. Peak A always decreases with increasing surface oxygen concentration, although different surfaces have somewhat different functional dependences. The spectra from other surfaces of TiO_2 and Ti_2O_3 that we have measured, most of them fractured and thus not having high symmetry orientations, lie in the range of these data but do not lie right on these curves. This implies a dependence on crystal face symmetry as well as on oxygen concentration. We are currently examining this dependence in more detail.

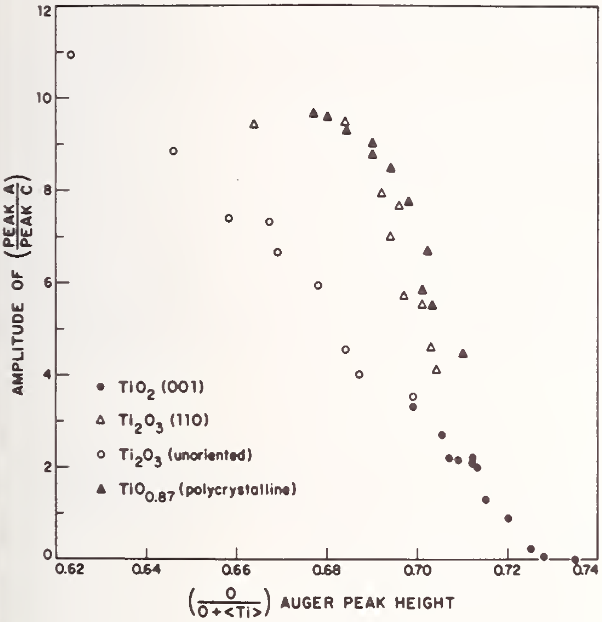

Fig. 4. Amplitude of peak A, normalized to peak C, vs surface oxygen concentration as determined by Auger spectroscopy for several samples.

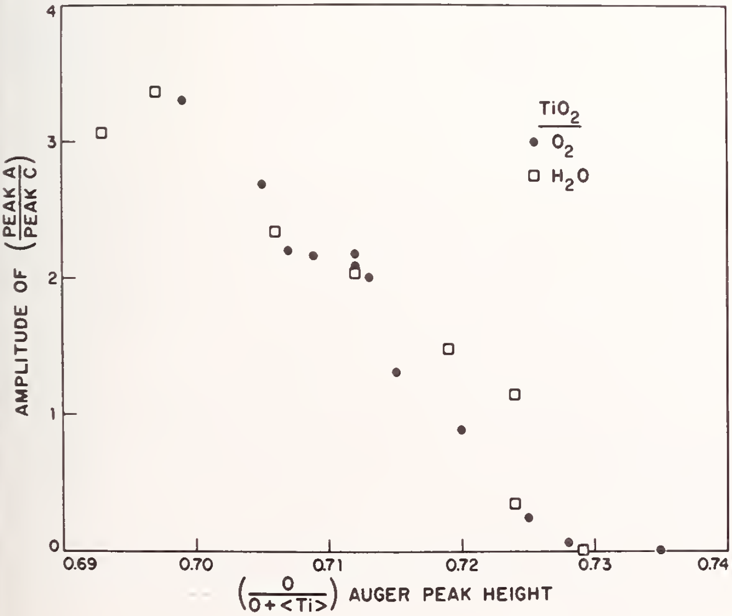

Fig. 5. Effect of H_2O and O_2 exposure on amplitude of peak A for TiO_2.

Ar-ion sputtered surfaces of these materials always have the lowest oxygen concentration, with the concentration increasing with oxygen exposure. It thus appears that ion bombardment is preferentially removing oxygen from the surface, leaving it titanium-rich compared to the bulk. This is corroborated by the absence of peak A on TiO_2 surfaces that have been fractured in ultrahigh vacuum, where the surface has essentially the stoichiometry of the bulk. Oxygen exposure restores the missing oxygen atoms, thus changing the environment of the surface titanium ions.

Exposure of the surfaces to water vapor oxidizes them in the same manner as does oxygen, and figure 5 compares the effects of oxygen and water vapor on a surface of TiO_2. The ordinate and abscissa are the same as in figure 4. No differences are seen in the spectra for samples exposed to oxygen or water vapor.

Although the dependence of the amplitude of peak A on surface oxygen concentration is somewhat different for different samples, the spectra from all of the oxides are indistinguishable for a given amplitude of peak A. This is shown in figure 6, where we have plotted both the location and full width of peak A versus its amplitude, normalized to peak C. These are data for all three compounds, and for exposure to both oxygen and water vapor. The location of the peak varies from 1.4 eV when its amplitude is almost zero to 2.0 eV at the maximum amplitude, and its width increases from less than 0.5 eV to about 1.4 eV.

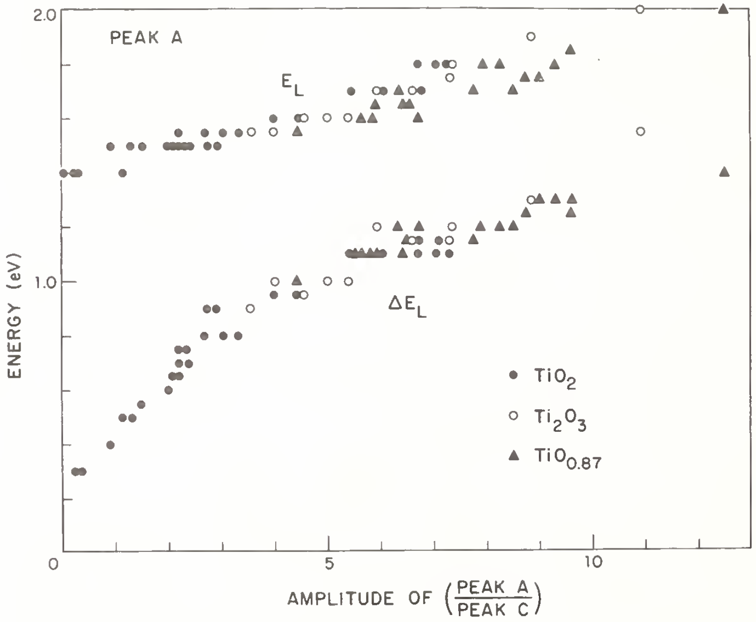

Fig. 6. Energy loss, E_L, and width, ΔE_L, of peak A vs amplitude of peak A for several samples.

The electronic structure of even a highly ordered crystal surface is invariably more complicated than that of the bulk, and we do not yet have a clear picture of the origin of the surface states on the titanium oxides. However, one can consider some simple, purely ionic, models which are consistent with most of the experimental observations. One extreme is to consider the ions to be essentially free-ion-like. The bulk Ti ions in TiO_2 will be in a 4+ valence state, but the surface ions, even on a cleaved surface, could have a 3+ valence due to the absence of some of the ligands that are present in the bulk. Neither the Ti^{3+} nor Ti^{4+} free ions have any observed transitions in the vicinity of 2 eV [3]. Removal of surface oxygen atoms, however, could create Ti^{2+} ions on the surface, and the free Ti^{2+} ion does have optically observed transitions between 1.0 and 1.8 eV [3]. Peak A in TiO_2 would then be attributed to these transitions. In Ti_2O_3, where the bulk Ti ions have a 3+ valence, the surface Ti ions could be 2+, by the same argument used for TiO_2. Peak A would then always be seen on Ti_2O_3, even when the surface had essentially the bulk stoichiometry.

Another approach to the surface-state transitions is to consider the ligand-field-split levels of the Ti d-electrons. If we assume that the Ti ions on a TiO_2 surface that has not had any oxygen sputtered off are in a 4+ valence state, they will have no d-electrons. Removal of some oxygen would create Ti^{3+} ions on the surface, and they have a $3d^1$ configuration. The d-levels will be split by ligand fields, and peak A would then correspond to transitions between these ligand-field-split 3d states. In Ti_2O_3, even the bulk Ti ions have a $3d^1$ configuration, so peak A should always be present. When some oxygen is sputtered off of Ti_2O_3, Ti^{2+} ions could then be created on the surface. The ligand-field-split spectrum for the resulting $3d^2$ configuration would be more complicated, with several transitions over a range of 1 or 2 eV [4]. As more oxygen atoms are removed from the surface of either oxide, more different valence states and ligand environments are possible for the surface titanium ions, and this should cause peak A to broaden and shift to higher energy as its amplitude increases, as we have observed.

A more sophisticated approach to the problem of surface states on transition-metal oxides, which allows for their partially ionic nature, is currently being taken by Wolfram [5]. He is performing cluster calculations in the tight-binding approximation and finds surface states arising from d-to-d transitions in the surface titanium ions. We are currently extending our energy loss measurements to the atomic core levels of both surface and bulk ions in an attempt to determine which of these models is applicable.

We have also looked at the low-energy region of the energy loss spectrum of V_2O_3, and this is shown in figure 7. Two peaks, B and C, occur within 0.5 eV of the location of two of the peaks in the titanium oxides, but no third peak is seen. Peak C is quite a bit broader than in the titanium oxides, however, and the third peak may just not be resolvable. These transitions presumably have the same origin as those in the titanium oxides. Two peaks occur at very low energies in V_2O_3, peak I at 1.3 eV and peak II at 2.6 eV in this sample. Peak II has a sensitivity to oxygen similar to that of peak A in the titanium oxides, and figure 8 shows the decrease in amplitude of peak II with relatively small oxygen exposures and its disappearance after large exposures. Peak I is essentially unaffected by oxygen. V_2O_3 has the same crystal structure as Ti_2O_3, the major difference being one additional electron on the V ion. Although we have not performed as extensive a set of experiments on V_2O_3 as on the titanium oxides, we can say that peak II clearly arises from a surface-state transition, and its origin is probably analogous to that of peak A in the titanium oxides. Peak I, on the other hand, could arise from either a surface or a bulk transition.

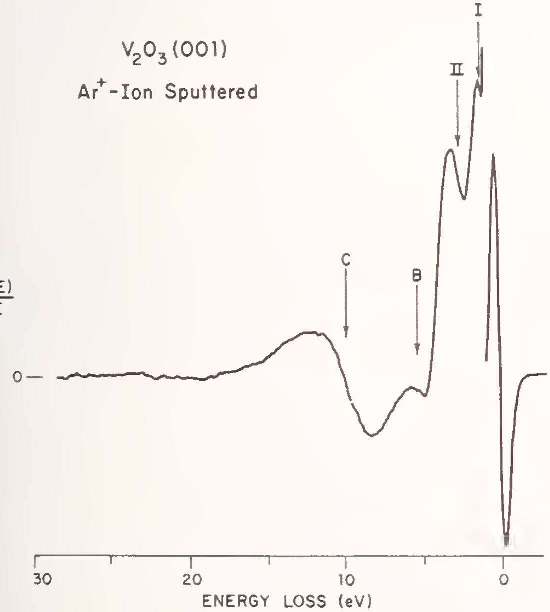

Fig. 7. Electron energy loss spectrum for Ar-ion sputtered $V_2O_3(001)$. Locations of peaks in n(E) are indicated by arrows.

We have just begun to study peaks B, C and D in TiO_2 in greater detail. Excellent (110) surfaces of TiO_2 can be prepared by annealing to about 800°C in vacuum. We have made preliminary measurements of the energy loss spectra from this surface for 100 eV primary energy at both grazing and normal incidence and at 2000 eV primary energy, normal incidence. The 100 eV, grazing incidence spectrum should be dominated by surface transitions, while the 2000 eV spectrum should arise almost entirely from bulk transitions. All three peaks occur in all of the spectra, but peak D is much weaker at 100 eV, grazing incidence, than in the other two spectra, indicating that it has more bulk character than the other peaks.

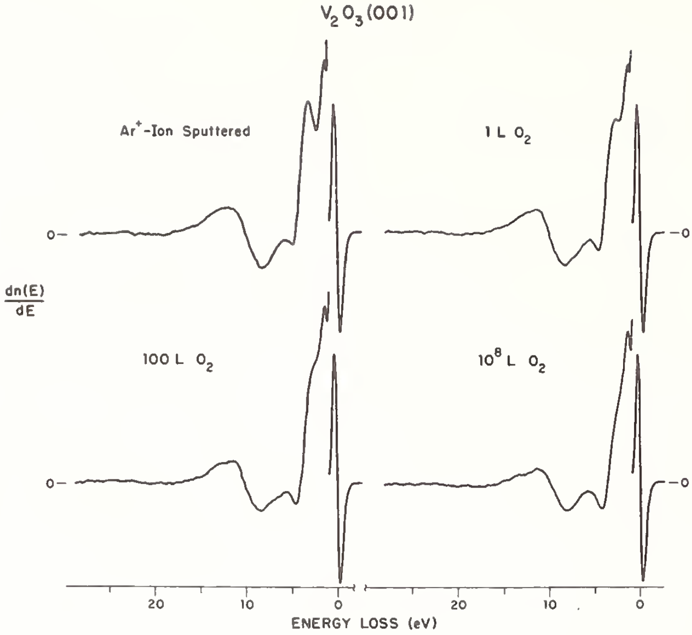

Fig. 8. Effect of O_2 exposure on the electron energy loss spectra for $V_2O_3(001)$.

In summary, we have begun to extract information on the surface electronic structure of a class of materials that has great academic and practical importance. Surface states are present that depend on crystal face symmetry, cation valence and ligand environment. The presence of magnetic ions, partially filled d-levels and phase transitions in these materials, together, of course, with their catalytic activity, makes the study of their surfaces extremely interesting, both experimentally and theoretically.

References

[1] Fujishima, A. and Honda, K., Nature 238, 37 (1972); Mavroides, J. G., Tchernev, D. I., Kafalas, J. A., and Kolesar, D. F., Mat. Res. Bull. 10, 1023 (1975).

[2] Tracy, J. C., Electron Emission Spectroscopy (W. Dekeyser et al., Eds.) D. Reidel, Dordrecht (1973), p. 305.

[3] Moore, C. E., Atomic Energy Levels, Vol. 1, N.B.S. Circular No. 467, U. S. Government Printing Office, Washington (1949).

[4] McClure, D. S., Solid State Phys. 9, 399 (1959).

[5] Wolfram, T., paper presented at this Workshop.

National Bureau of Standards Special Publication 455, *Electrocatalysis on Non-Metallic Surfaces*, Proceedings of Workshop held at NBS, Gaithersburg, Md., December 9-12, 1975. (Issued November 1976)

Dislocations in ZnO as Channels for Electron Transfer from Surface Species[1]

S. Roy Morrison and Thomas Freund[2]
Stanford Research Institute
Menlo Park, California 94022

The results reported show that dislocations strongly affect the properties of the ZnO electrode and that with the help of electrochemical measurements a fairly complete picture of the electrical and chemical behavior of dislocations can be developed. It is shown that dislocations in ZnO act as hole or electron traps in the space charge region, as recombination centers, as points of electric breakdown under anodic polarization, and as current paths leading to exchange current even in an indifferent electrolyte. The dislocations can be passivated by annealing or by precipitation of impurities. A qualitative model is presented that can account for the observed affects of dislocations on the solid state and electrode properties.

Key words: Dislocation; electrochemical; exchange current; semiconductor; traps; zinc oxide.

1. Introduction

In studies of ZnO as an electrode in aqueous solution, we [1,2,3][3] and others [4,5] have observed and reported that the dark anodic current is not associated with intentionally added reducing agents of intermediate redox potential. For example, when measuring electron exchange between ZnO and the redox couple ferro/ferricyanide, one finds that the cathodic current is proportional to the ferricyanide concentration, but the anodic current is independing of the ferrocyanide concentration. We have suggested that the anodic current is associated with flaws in the ZnO surface, and the current is limited by the rate at which anodic current can pass through the flaws. If such a model is valid, the influence of this behavior will be of significant interest in electrocatalysis at the semiconductor/electrolyte interface. As will be discussed in more detail below, at flaws the presence of active energy levels that are separate from the conduction and valence bands permits unwanted redox processes to occur, and thus the selectivity of the electrochemical process will be lowered. Such behavior will be deleterious also in basic studies of electrode reactions. For example, tunneling has become a popular and powerful technique [6,7] for studying energy levels in solution. However, to induce tunneling through a semiconductor surface barrier, very heavy doping of the solid is necessary. Such doping will often lead to flaws, in particular dislocations, in the material, and much of the so-called "tunneling current" may in actuality be current through the flaws.

---

[1] Supported in part by ARO-D

[2] Now at Xerox Corporation, Webster, New York, 14580

[3] Figures in brackets indicate the literature references at the end of this paper.

One important type of flaw that is almost always present is dislocation. This type of flaw is easily produced and removed. To test the influence of flaws on the electrode properties of ZnO (in particular the exchange current), we prepared a surface with an unusually high density of surface dislocation loops to determine the characteristics that dislocations imparted to the electrode properties.

A study of dislocations on the ZnO electrode was reported by Gerischer and his co-workers [8]. They concerned themselves primarily with the bulk properties (hole trapping in the space charge region) of the semiconductor, rather than the influence on electrode reactions. In our studies we examined both aspects of the dislocation behavior. In addition, we have been interested in possible techniques to remove the deleterious influence of dislocations, including high-temperature annealing and the precipitation of impurities at the dislocations to determine the effect on the electrode properties.

2. Experimental

Most of our work was done on the (0001) face of ZnO crystals obtained from 3M Corporation in St. Paul, Minnesota. Dislocations were introduced by lapping the crystals using 15-micron grit. The properties of the surface so treated were examined, then the samples were etched step by step until the effect of the dislocations was removed. The etch used was 85% H_3PO_4, which etches the $(000\bar{1})$ face at a rate of about 1 micron per minute, but does not etch the $(000\bar{1})$ face. On the $(000\bar{1})$ face it is found that only scratches and dislocations are etched.

Figure 1 shows a sketch to introduce the model assumed. For reference, Figure 1b shows an edge dislocation, which is the end of an extra half plane. The "dislocation pipe" so formed, shown encircled, is a linear flaw extending through the crystal beginning and ending on a surface. With our samples lapped on one side, the dislocation pipes must begin and end on the same surface, and Figure 1a shows the type of dislocation loops expected. By removing layers of the crystal surface in a stepwise fashion by etching, measurements can be made with successively lower dislocation density in the space charge region.

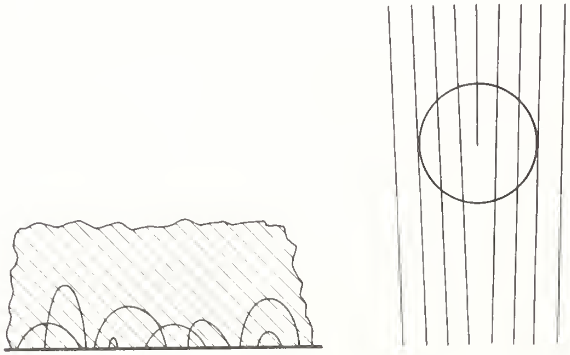

(a) (b) Fig. 1. Dislocations at a lapped surface.

The density of the space charge N_D near the surface was determined from the voltage dependence of the capacity [9] using eq (1):

$$V_S - kT/q = (1/2)\, qN_D A^2 \kappa\epsilon_o C^{-2} \qquad (1)$$

where N_D is the density of immobile positive charges in the space charge region, A is the area of the electrode, C is the differential capacity of the space charge depletion layer,

κ is the dielectric constant, ε_o is the permittivity of free space. The parameter V_s is the surface barrier potential given (in the depletion layer regime) by:

$$V_s = V_a + \text{const} \tag{2}$$

where V_a is the electrode potential of the ZnO (relative, say, to calomel). Most of the measurements reported below were made in one typical sequence. The exceptions are measurements of annealing and doping, where the effect of the dislocations was removed by a method other than etching.

Figure 2 shows a plot of the current/voltage characteristics for the same (0001) surface after (a) polishing, (b) etching 8 minutes, and (c) etching a total of 33 minutes. In all cases the readings labeled "dark" were taken after the sample had been left 16 hours (overnight) in the dark. The readings were all taken in the same order: beginning slightly anodic, decreasing to 0.4 volt cathodic, then increasing the voltage in the anodic direction. At each voltage the sample was held for 30 seconds before the reading. A definite procedure was adopted since the current is time dependent. The zero current potential of the electrode was close to the same value, (0.1 V relative to a saturated calomel electrode) in all three cases.

The curves show a substantially higher current, both in the anodic and cathodic directions, resulting from the presence of the dislocations.

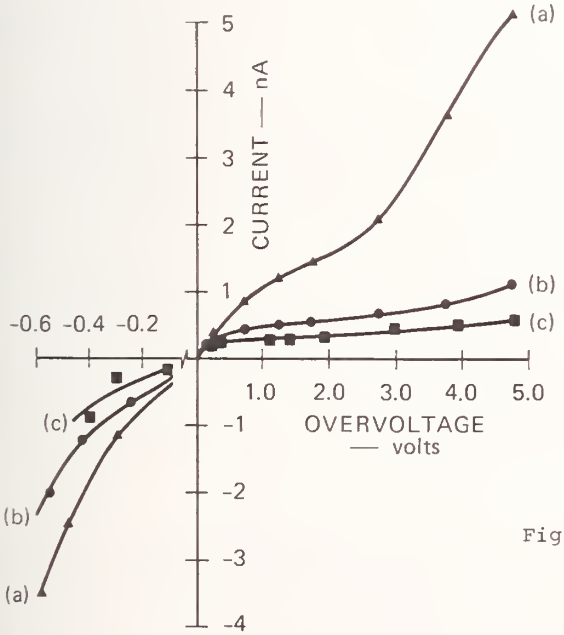

Fig. 2. Current/voltage electrode characteristics of ZnO(0001) surface.

Figure 3 shows various curves of C^{-2} versus voltage, needed to determine N_D by eqs. (1) and (2). The measurements were made on the same ZnO sample used in the experiments of Figure 2. However, the solid curves represent measurements on the opposite face (from those of Figure 2), the (000$\bar{1}$) face. First, the (000$\bar{1}$) face was polished and the capacity/voltage dependence measured. Curve (a) shows the "dark" measurements, curve (b) the results when the surface is illuminated by a tungsten lamp (the intensity will be discussed below). A much

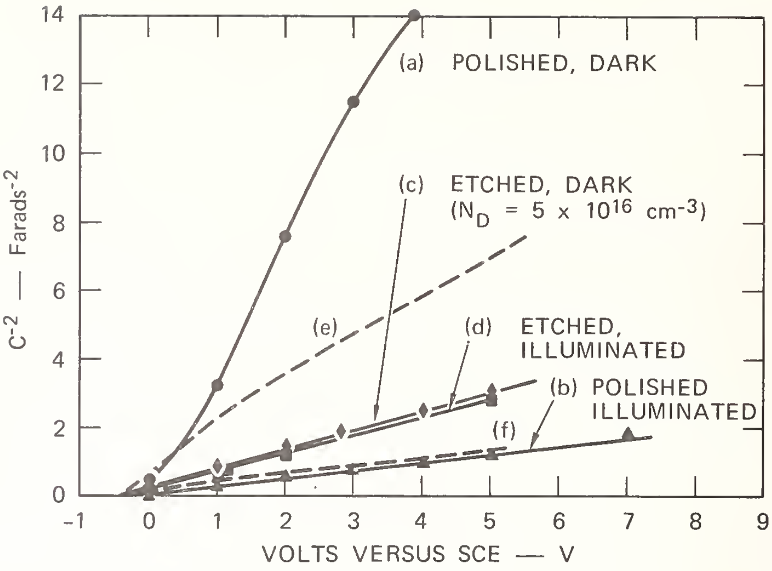

Fig. 3. Determination of net charge density in the space charge region.

higher capacity is observed during illumination. After these readings the $(000\bar{1})$ face was etched for 8 minutes in 85% H_3PO_4. As mentioned above, H_3PO_4 is a very slow etch on the $(000\bar{1})$ surface of ZnO, attacking primarily scratches and dislocations. After such a treatment, it is observed (curves c and d) that the capacity is at an intermediate value and is no longer sensitive to illumination.

We suggest that because the etch does not attack the $(000\bar{1})$ face but only the dislocations, only a modest H_3PO_4 etch is necessary to excavate dislocation pipes a few thousand angstroms and thereby remove dislocations from the space charge region. In the analysis we will relate the N_D variation with illumination to the dislocation density and curves (c) and (d) can be considered as the "blank", giving N_D for a dislocation-free sample.

The contrasting etching behavior of the (0001) face, the faces used for the stepwise etching experiments of Figure 2, is illustrated by curves (e) and (f) of Figure 3. These measurements were made after the sample was lapped and etched for eight minutes, and so can be compared directly to curves (c) and (d). In contrast to the $000\bar{1})$ face, after etching 8 minutes the capacitance is still photosensitive, indicating the presence of dislocations. This result is expected since H_3PO_4 does not rapidly and selectively etch dislocations on the (0001) face, but very slowly etches the entire surface layer.

As will be discussed in the Analysis section, the results in Figure 3 suggest that either electrons or holes can be trapped at dislocations. Clearly, if both electrons and holes can be trapped, the dislocation should act as a recombination center and a generation center for carriers. To examine the characteristics of dislocations as centers for electron-hole recombination, the photocurrent as a function of electrode potential was monitored.

Figure 4 shows the photocurrent, the total current under illumination, plotted as a function of inverse capacity. The light intensity was 7.5% of that used in the experiments of Figure 3. The surface area of the sample was 25 mm^2, the light source was a tungsten lamp. The photocurrent for the well-etched sample provides a useful measure of the absolute light intensity in these experiments. Later we will discuss the reason for the use of inverse capacity on the abscissa, and the interpretation of these results. However, it is

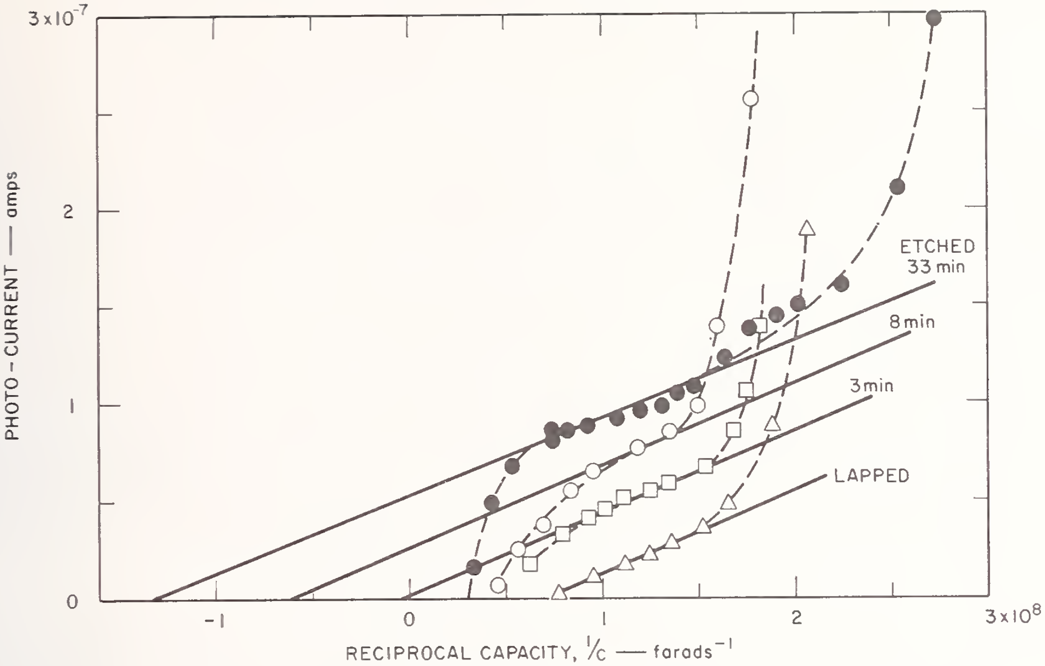

Fig. 4. Photocurrent vs reciprocal of the capacity for a specimen.

immediately apparent that the photocurrent at a given space charge thickness (a given capacity) is decreased by the presence of dislocations.

Summarizing, Figures 2-4 make it clear that the presence of dislocations causes excess exchange current at the electrode at zero net current, causes changes in N_D, and causes a decrease in the photosensitivity.

Experiments were performed attempting to passivate the dislocation activity. Results will be presented below showing the passivation when dislocations are annealed at high temperature. Such annealing is to be expected, and the result of interest in the present study is the temperature range on ZnO (T >900°C) at which it is observed.

The effect of a treatment in hydrogen in removing the deleterious effects of dislocations is shown in Figure 5. The procedure is based on saturating the sample with hydrogen (10) at a moderate temperature (300°C for the results of Figure 5) and passivating the dislocations by subsequent annealing at a lower temperature where the hydrogen concentration is supersaturated.

Figure 5 shows a series of measurments analogous to those of Figure 4, showing the hydrogen passivation effect. The light intensity for the measurements of Figure 5 is substantially higher than that for Figure 4. Curve (1) shows the photocurrent for a sample that was well etched, saturated with hydrogen by treatment before at 300°C in 1 atm H_2, then quenched to room temperature. Curve (2) shows the subsequent lowering of the photosensitivity by lapping to introduce dislocations, while maintaining the sample at room temperature to prevent hydrogen diffusion [10]. Curves (3), (4), and (5) are results after successive treatments at 250°C in helium. Curves (3), (4), and (5), compared to (2) show that helium annealing of the hydrogen-containing sample restores the photosensitivity to the polished sample, presumably by permitting hydrogen to diffuse to and to precipitate at the dislocations. We believe that the lower photosensitivity of curve (5) as compared with curve (4) results from too much annealing time--the hydrogen has had an opportunity to move to the surface and evaporate into the gas phase.

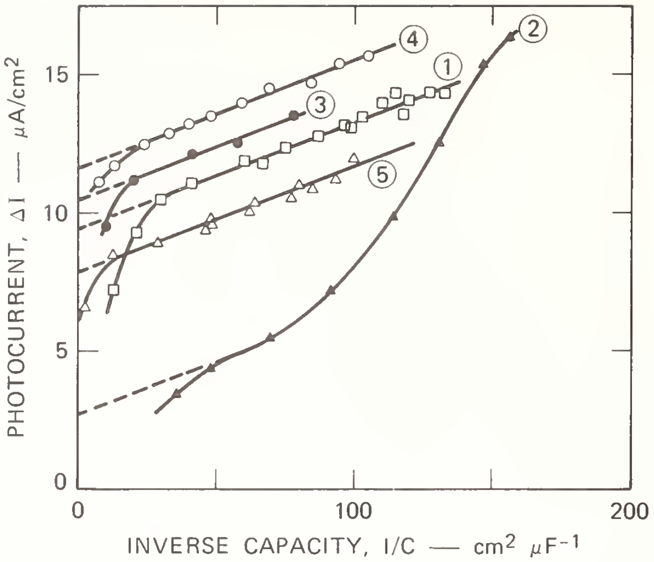

Fig. 5. Photocurrent vs reciprocal of the capacity for a specimen treated in hydrogen before the introduction of dislocations.

2.1. Analysis of the Results

The curves of Figure 2 show the influence of dislocations in causing a higher exchange current at the surface of a sample with no intentionally added redox couple. Suggested reasons for this activity will be discussed in the next section.

The results of Figure 3 suggest by the following argument that hole and electron trapping occurs when dislocations are present. The carrier dominant in the space charge region under illumination will be holes, the carrier dominant in the dark will be electrons. If either or both are trapped in the space charge region, the slopes in Figure 3 will differ depending on whether the sample is in the dark or illuminated. The curves for the (000$\bar{1}$) face after etching, curves (c) and (d), have identical slopes, indicating neither hole nor electron trapping. The slope of curves (c) and (d) thus gives the true donor density in the sample used, 5 x 10^{16} cm^{-3}. However with dislocations present, under illumination the slope of the C^{-2}/V curve is much lower than that of curves (c) and (d), indicating a much higher concentration of positive charge in the space charge region, i.e., hole trapping. On the other hand measurements in the dark with dislocations present show a much higher slope than curves (c) and (d), indicating electron trapping (the effective N_D is much less than the true donor density). Thus, dislocations can trap either electrons or holes.

The photocurrent data of Figure 4 are displayed in the form shown to permit calculation of the minority carrier diffusion length L_p, using the following model: If we assume that the tungsten lamp produces hole-electron pairs uniformly in the surface region of the crystal, and assume that holes produced in the space charge region will be swept to the surface by the electric field, then the total photocurrent J_p will be determined by the number of holes produced in the space charge region plus the number produced within a hole diffusion length L_p of the edge of the space charge region. Thus:

$$J_p = \alpha I(x_o + L_p) \tag{3}$$

where x_o is the thickness of the space charge region, the parameter I is the light intensity, and α is a proportionality constant. The parameter x_o is given by the parallel plate capacity formula:

$$C = \kappa\epsilon_o A/x_o \tag{4}$$

with κ the dielectric constant, and ϵ_o the permittivity of free space. Then (3) becomes:

$$J_p = \alpha I(A\kappa\epsilon_o C^{-1} + L_p) \tag{5}$$

A plot of J_p versus C^{-1}, as shown in Figure 4, should be a straight line with the intercept (at $J_p = 0$) yielding $-L_p$. Now by definition:

$$L_p = (D\tau)^{\frac{1}{2}} \tag{6}$$

where D is the diffusion constant for holes, a constant in this study, and τ is the lifetime of photoproduced holes. Thus, a variation of the intercept of the J_p/C^{-1} plot with dislocation density gives the variation in the minority carrier lifetime with dislocation density.

Three regions are apparent from Figure 4. Under highly cathodic conditions (large capacity), the current is more negative than the straight line region that we attribute to eq (5). At highly anodic voltages, the current is much higher than can be accounted for by hole current as per eq (5). The case of high anodic voltage corresponds to electrical breakdown. Thus, the display of the data according to J_p vo C^{-1} permits very clear the separation of breakdown current/photocurrent/cathodic region.

Table I shows the various parameters obtainable from Figure 4 where the breakdown field is obtained by calculating the electric field E at the surface from the capacity and the apparent donor density of the semiconductor using the Gauss relation

$$E = eN_D x_o/\kappa\epsilon_o \tag{7}$$

together with eq (5). The breakdown field E_B in Table I is defined as the value of E where the observed current is double that extrapolated from the straight line region.

In the presence of dislocations, the value of L_p decreases to the point where the apparent L_p is negative--recombination is occurring in the space charge region. The breakdown field also decreases with increasing dislocation density.

Measurements of L_p and E_B for a sample, which was first lapped to produce dislocations, then annealed in air at temperature T to determine if they are removed, are shown in Figure 6 as a function of the temperature T. It is observed that the dislocation loops appear to be removed by annealing at T > 900°C.

Table 1. Diffusion lengths and lifetimes of treated zinc oxide.

Treatment surface	L_p (cm)	τ[a] (s)	E_B (V/cm)
Lapped (0001)	-2×10^{-5}[b]	-----	1×10^{5}
Etched 3 min (0001)	1×10^{-6}[b]	1×10^{-12}[b]	1.8×10^{5}
Etched 8 min (0001)	2×10^{-5}	4×10^{-10}	2.4×10^{5}
Etched 33 min (0001)	4×10^{-5}	1.6×10^{-9}	7.4×10^{5}
Etched 3 min $(000\bar{1})$ ("dislocation free")	3×10^{-4}	1×10^{-7}	No breakdown observed up to 100V.

---

[a] Assuming D = 1 cm^2/s.

[b] The simple theory for L_p and τ is not applicable, although qualitative information is obtained from the calculated values of L_p.

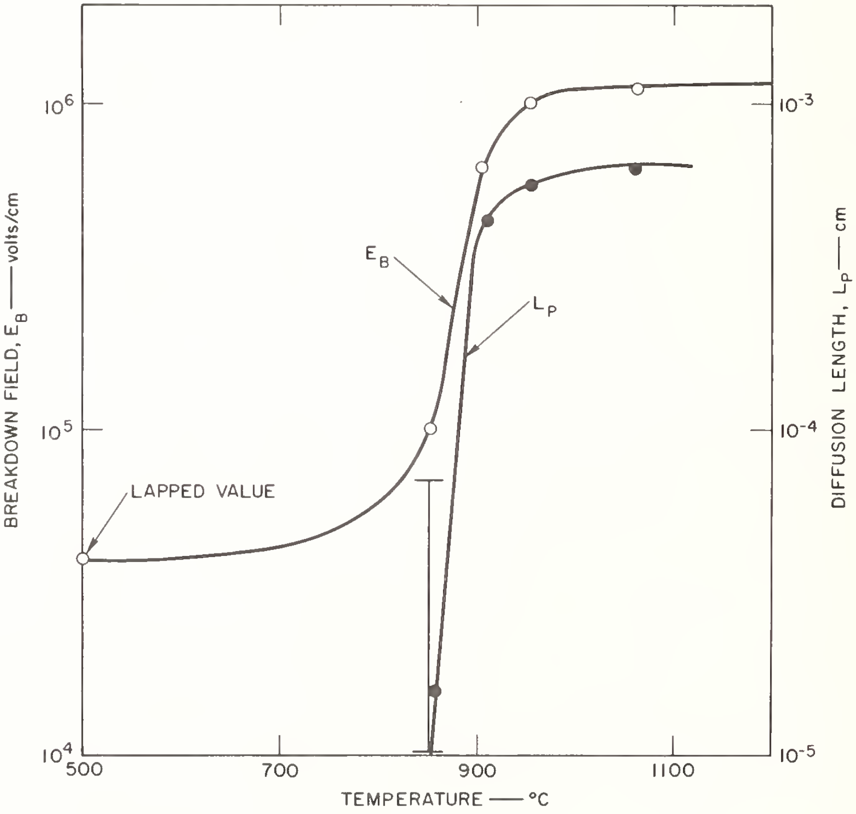

Fig. 6. Annealing of dislocations at high temperature, as observed by the effect of annealing treatments in room temperature measurements of the diffusion length and the breakdown field.

3. Discussion

From the above measurements we can (a) conclude that dislocations can have a significant effect on the electrode properties of a semiconductor electrode; (b) conclude that the dislocation effect can be removed either by a high-temperature anneal or by precipitation of a chemically active species on the dislocation. This section will be devoted to a discussion of a model for the dislocations that can account for the observed behavior and suggest why the dislocations should be so active at a semiconductor/electrolyte interface.

From modern theories of ionic semiconductors [11] as applied to states associated with incompletely coordinated ions (usually assumed to be at the surface) and qualitatively from the Madelung theory [12], it can be concluded that an incompletely coordinated anion may give rise to donor energy levels and that an incompletely coordinated cation to acceptor energy levels in the bandgap. These levels have orbitals derived from the atomic orbitals of the respective ions. At a dislocation, a line of incompletely coordinated anions and cations exists which may be alternating or may be dominated by either anions or cations, depending on the crystallographic direction of the dislocation as it wends its way through the crystal. Thus, we suggest that observed hole traps are associated with the anionic donors and the observed electron traps are associated with cationic acceptors.

These electron and hole traps are in a line, and normally some overlap will be expected between the orbitals of the anions, perhaps bridged by the cations or some overlap between the orbitals of the cations, perhaps bridged by the anions. For example, in many semiconductors, if the donor or acceptor impurity concentration rises to about 10^{18} to $10^{19}/cm^3$, so the impurities are on the average 10 to 20 Å apart, the orbital overlap is enough for conductance through the "impurity band". In the present case we suggest that the injection or extraction of electrons at the semiconductor/electrolyte interface is followed by "impurity band conduction" along the dislocation pipe through the thin (about 1000 Å) space charge region of the semiconductor. The pipes need not have a high conductivity, but the conductivity must be finite to explain the excess current in both the anodic and cathodic directions of Figure 2.

The next problem is the identification of the electrode reaction. In the cathodic direction we suggest that an electron migrating through the cationic levels to the surface still has enough energy for reduction of traces of dissolved oxygen, the same reaction that must be associated with the cathodic reaction due to conduction band electrons. The anodic reaction could conceivably be associated with the injection of electrons onto cationic energy levels at the dislocation from some unknown impurity in the solution. It seems more likely, however, that the anodic reaction is associated with the oxidation and dissolution of incompletely coordinated lattice oxide ions from the dislocation pipe by a reaction such as:

$$2O^{2-}_{L} + 2H^{+} \rightarrow H_2O_2 + 2e^{-} \tag{7}$$

Such a reaction corresponds electronically to the injection of an electron e^- onto the cationic acceptor level from the oxygen ion at the end of the dislocation pipe, and corresponds chemically to preferential etching of the crystal at a dislocation.

The model provides an explanation for the action of the dislocations as recombination centers and as centers of electrical breakdown. The action of the dislocations as recombination centers would correspond to capture of holes at the anionic donor levels, capture of electrons at the cationic acceptor levels, and the movement of the trapped electrons or holes along the dislocation pipe until they recombine. The action of the dislocations as centers of electric breakdown could be associated on the one hand with avalanche breakdown, where free electrons and holes by impact ionization excite electrons from the anionic donor levels to the valence band. On the other hand, it could correspond to Zener tunneling of either electrons from the donor levels to the conduction band or holes from the acceptor levels to the valence band. Either model would explain the breakdown data equally well.

The influence of hydrogen on the properties of the dislocations can be readily accounted for by the formation of HO_D^- groups (where O_D^{2-} is an incompletely coordinated oxygen ion at the dislocation) or of HZn_D^{2+} groups (where Zn_D^{2+} is an incompletely coordinated zinc ion). That is, a proton (in the case of HO_D^-) or a hydrogen atom (in the case of HZn_D^{2+}) occupies a coordination position of the otherwise coordinatively unsaturated ions, forming a chemically more stable complex. Such stabilization by complex formation would tend to increase the ionization potential of the donor (O_D^{2-}) or decrease the electron affinity of the acceptor Zn_D^{2+}. In energy level terminology the complex formation would make the traps shallower in both cases. Experimentally we find another donor (In) also tends to passivate the dislocations where an acceptor (Li) does not. The possible dependence on the donor characteristics is suggestive that the formation of the donor/acceptor complex HZn_D^{2+} may be the more important interaction.

4. Conclusions

We conclude directly from the evidence that electrode reactions normally not possible on ZnO become possible when dislocations are present. In particular, we interpret the observations as suggestive that extra levels are in the bandgap region of the ZnO. Ions in solution that cannot exchange electrons with the conduction band may be able to exchange electrons with these levels associated with dislocations.

The most interesting new observations in this work regarding the "bulk" properties of the electrode are that (a) the dislocations can act as channels for conduction of charge through the insulating space charge region between the surface and the bulk semiconductor, (b) dislocations are highly active as centers for electrical breakdown, and (c) the deleterious effects of the dislocations can be eliminated by the precipitation of certain impurities at the dislocation. In addition, the observations of others that dislocations can act as traps for carriers and as recombination centers have been confirmed for ZnO.

5. References

[1] Freund, T. and Morrison, S. R., J. Chem. Phys. 47, 1543 (1967).
[2] Freund, T. and Morrison, S. R., Surface Sci. 9, 119 (1968).
[3] Freund, T., J. Phys. Chem. 73, 468 (1969).
[4] Berghe, R.A.L.V., Cardon, F., and Gomes, W.P., Surface Sci. 39 368 (1973).
[5] Berghe, R.A.L.V. and Gomes, W. P., Ber. Bunsenges. Phys. Chem. 76, 481 (1972).
[6] Memming, R. and Möllers, F., Ber. Bunsenges. Phys. Chem. 76, 475 (1972).
[7] Gerischer, H., B. Pettinger and Schoppel, H.R., Ber. Bunsenges. Phys. Chem. 78, 451 (1974).
[8] Gerischer, H., Hein, F., Lubke, M., Meyer, E., Pettinger, B. and Schoppel, H. R., Ber. Bunsenges, Phys. Chem. 77, 284 (1973).
[9] Dewald, J.R., J. Phys. Chem. Solids 14 155 (1960).
[10] Lander, J. J. and Thomas, D. G., J. Chem. Phys. 25, 1136 (1956).
[11] Louis, E. and Yndurain, F., Phys. Stat. Solidi (b), 175 (1973).
[12] Levine, J. D. and Mark, P., Phys. Rev. 144, 751 (1966).

National Bureau of Standards Special Publication 455, *Electrocatalysis on Non-Metallic Surfaces*, Proceedings of Workshop held at NBS, Gaithersburg, Md., December 9-12, 1975. (Issued November 1976)

Characterization of Semiconductor Electrodes in Nonaqueous Solvents

Steven N. Frank, Daniel Laser, Kenneth L. Hardee and Allen J. Bard

Department of Chemistry
The University of Texas at Austin
Austin, Texas 78712

The large number of simple and reversible redox couples available in nonaqueous solvents allows convenient investigation of the band structures of semiconductors using electrochemical techniques. Comparisons of the cyclic voltammetric behavior of these couples at platinum and a semiconductor permits estimation of the relative energy levels of the conduction and valence bands and provides a means of mapping the gap region for intermediate levels and surface states. This technique is demonstrated with TiO_2 and n-type Si semiconductors. In spite of the large difference in band gaps between these semiconductors, their electrochemical behavior is similar and is ascribed to a similarity in the energies of their respective conduction bands and the energies of an intermediate energy level in TiO_2 and the valence band in Si.

Key words: Acetonitrile; cyclic voltammetry; electrochemistry; nonaqueous; semiconductor; silicon; titanium dioxide.

1. Introduction

Although nonaqueous solvents offer a number of distinct advantages when compared to water for electrochemical investigations with semiconductor electrodes, few studies have employed these solvents. Investigations of rather limited scope have been carried out with Ge [1,2],[1] SnO_2 [3], and more recently with GaP [4,5] and GaAs [5] in nonaqueous media. Among the forementioned advantages of nonaqueous solvents are the availability of a large number of kinetically simple and well understood charge transfer couples covering a broad potential region, an extended potential range due to increased solvent stability and fewer troublesome surface phenomena. Well-purified nonaqueous solvents are also expected to offer some relief from the undesirable electrode decomposition often found at positive potentials with certain semiconductors, since water is often a participating reactant in the decomposition reactions.

The current theory of the semiconductor-solution interface has been presented in several recent reviews [6,7] and papers [8]. Semiconductor behavior differs from that of a metal in several important respects. Unlike a metal, modulating the potential of a semiconductor results in little modulation of the potential at the surface of the semiconductor (unless the surface is degenerate) with most of the potential drop between the semiconductor and solution interiors occurring within the semiconductor space charge region, in which the concentration profiles of the charge carriers and band energies vary in an exponential fashion from the field-free interior to the semiconductor surface; the surface conduction and valence band energies remain essentially invariant with applied potential. Changes of the rates of electrochemical processes with potential result not from a variation of the energies of the bands as in the case of a metal but from changes in the

---

[1] Figures in brackets indicate the literature references at the end of this paper.

concentrations of the majority and minority charge carriers at the surface. The rather sizable photocurrents observed when a semiconductor is illuminated with light of energies greater than the band gap result from an increase in the number of minority carriers at the electrode surface.

The oxidized and reduced forms of the solution species can be represented by two guassian energy distributions that intersect at an energy corresponding to the standard potential of the redox couple [9]. Typically the widths of these distributions are 0.5 to 1.0 eV. Since the energies of these distributions are fixed relative to the bands of the semiconductor and electron transfer must be isoenergetic, the observed behavior may be no electron transfer, only oxidations or reductions (rectification), or both oxidations and reductions (metal-like behavior) depending upon the extent of overlap of the energy distributions of the solution species with bands of the semiconductor, the type of doping (acceptor or donor), the participation of minority or majority carriers, the band gap energy, the presence of surface states or energy levels in the forbidden band gap, and whether the electrode is illuminated.

Below we present the partial results of our investigations [10,11] of two semiconductors, n-type TiO_2, a wide band gap semiconductor (E_g = 3.2 eV) and n-type silicon, a narrow band gap semiconductor (E_g = 1.1 eV). Using the above principles and the behavior of the semiconductors in the presence of a number of solution redox couples, several aspects of the electronic structure of the semiconductors in contact with the nonaqueous solvent acetonitrile are explored. The location of the conduction and valence bands and intermediate energy levels are deduced for TiO_2. The behavior of a wide band gap versus a narrow gap material is contrasted.

2. Experimental

Solvent and compound preparation, electrode pretreatments, materials handling, and instrumental details are presented elsewhere [10-12]. Single crystal Si and both single crystal and chemically vapor deposited films of TiO_2 were employed. Tetrabutylammonium perchlorate was used as an electrolyte to increase solvent conductivity. The electrochemical cells were of a three compartment design that prevented mixing of the anode and cathode solutions. The potential of the semiconductor and platinum working electrodes was controlled versus a reference electrode. The cell voltage was applied between the working and a platinum counterelectrode.

The primary electrochemical technique used was cyclic voltammetry [13]. In brief this technique involves application of a triangular voltage wave form to the cell. For substances that are rapidly oxidized and reduced, so that the ratio of the oxidized to the reduced form obeys the Nernst relationship, the separation of the resulting current peaks for oxidation and reduction is about 58 mV for a one-electron process. The standard potential lies midway between the two peaks on the potential axis.

3. Results and Discussion

Figure 1 shows the potentials of the current peaks for the oxidation and reduction of a number of the substances used in these investigations both at platinum and the semiconductor electrodes. Also included are the estimated band energies for TiO_2 and Si, determined either from the behavior of the photopotential or the resistive component of the electrode impedance or from the behavior in the presence of the various solution redox couples [10,11]. The potentials given for the conduction bands in Figure 1 correspond closely to the flatband potential for the semiconductors (absence of a space charge region).

Since both semiconductors are n-type the majority charge carriers are electrons in the conduction bands. Possible currents due to minority carrier generation in the space charge region were calculated to be negligible. In order for there to be electron exchange between the semiconductor and solution, the energy distributions of the solution species must overlap an energy level in the semiconductor capable of accepting or donating electrons. For solution species with fairly negative standard potentials the energy distributions of both the oxidized and reduced forms will overlap the conduction band. In addition at potentials just slightly negative of the flatband potential the semiconductor surface becomes degenerate due to the large number of electrons at the surface and the semiconductor behaves like a metal. This metal-like behavior was observed at both TiO_2 and Si for substances with standard potentials negative of the flatband potentials. For substances with standard potentials a few hundred millivolts positive of the flat band, only the energy distribution for the oxidized form has good overlap with the conduction band and only reductions should be observed. As seen in the figure p-benzoquinone fulfills this criterion at TiO_2 and Si. p-Benzoquinone can be reduced but not reoxidized at TiO_2. The reduction occurs with considerable overpotential when compared to platinum; rapid reduction rates cannot occur positive of the flatband potential because of the depletion layer at the TiO_2 surface. A similar overpotential is observed for p-benzoquinone reduction at Si, although reoxidation is sometimes observed at Si with certain surface pretreatments which activate the electrode surface.

Compounds with standard potentials near the flatband potential may behave either as at a metal or with rectification depending on the particular shapes of their energy distributions. This transitional behavior was exploited to determine the location of the conduction band in TiO_2. Ru $(TPTZ)_2^{+3}$, $E^o \approx -0.8$ V (not shown), is reduced and reoxidized at TiO_2 in a manner similar to its behavior at platinum. Anthraquinone, $E \approx -0.9$, on the other hand, is reduced but its reoxidation is much slower than at platinum. On the basis of this behavior the conduction band for TiO_2 was assigned the level shown in Figure 1.

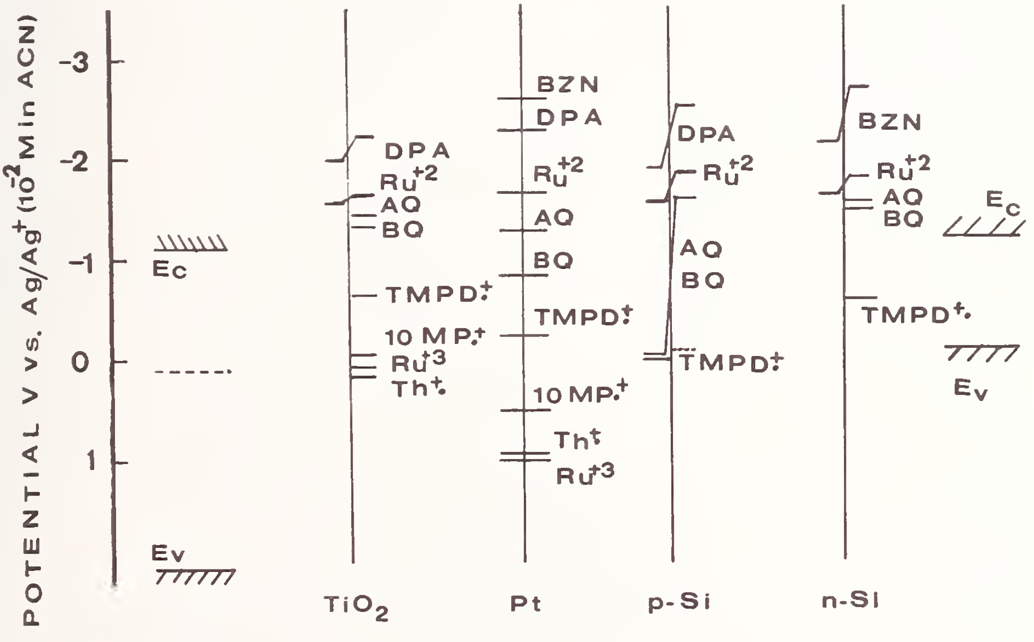

Fig. 1. Proposed band structures of TiO_2 and n- and p-type Si and the electrochemical behavior of various redox couples at these semiconductors and at Pt. Horizontal lines to the right of the vertical lines indicate the cyclic voltammetric peak potentials for reduction while those to the left indicate the potentials for oxidation.

For couples with very positive standard potentials significant overlap of their energy distributions with the conduction band is precluded. The reductions observed for these compounds at TiO_2 between -0.3 and -0.4 V must either occur by electron tunneling through the space charge or by an intermediate energy level at this position. At the carrier concentrations ($\approx 10^{16}$) with which we are concerned tunneling seems most unlikely [14] so that the existence of an intermediate level appears probable. This level along with the conduction band may also contribute to the reduction of $TMPD^+$. That this level can donate but not accept electrons is demonstrated by the lack of any reoxidation of TMPD and p-benzoqinone.

Illuminating the electrode with light of energies greater than the band gap creates electron-hole pairs near the electrode surface. Production of holes in the valence band provides a mechanism for removing electrons from the intermediate level. In line with this reasoning, the anion radical of benzoquinone is oxidized when the TiO_2 is illuminated (but not in the dark).

Although the band gaps of TiO_2 and Si differ by a factor of 3, the electrode behavior of the two is remarkably similar. (Extremely positive redox couples cannot be studied at Si due to oxidation of the Si surface.) This similarity results from the conduction bands of TiO_2 and Si being at nearly the same location and the intermediate energy level observed at TiO_2 occurring at almost the same place as the valence band of Si. In addition to the previously mentioned similarities both display almost identical behavior with anthraquinone. If one assumes that the valence band of Si and the intermediate energy level of TiO_2 can serve the same function with $TMPD^+$, it is not surprising that its reduction occurs within ≈60 mV on the two electrodes.

The holes created in the valence band by illuminating the Si can accept electrons from solution species. With illumination all of the compounds with standard potentials positive of the flat band are reoxidized at Si. An interesting aspect of the photooxidations at semiconductors which is demonstrated at both Si and TiO_2 is that the oxidations can occur at potentials negative of their oxidations at platinum (i.e., with "negative overpotential"). TMPD is oxidized at potentials nearly 1 volt more negative at Si under illumination, than at platinum. The main requirement for photoassisted oxidation is that the electrode potential be positive of the flatband potential so that holes are forced to the surface and electrons to the interior.

4. Acknowledgments

We wish to thank the National Science Foundation and the Robert Welch Foundation for support of this work.

5. References

[1] M. D. Krotova and Yu. V. Pleskov, Solid State Phys., 3, 2119 (1963).
[2] H. B. Mark, Jr. and B. S. Pons, Anal. Chem., 40, 110 (1966).
[3] T. Osa and T. Kuwana, J. Electroanal. Chem., 22, 389 (1969).
[4] R. Landsbergh, P. Janietz and R. Dehmlow, Z. Chem., 15, 38 (1975).
[5] R. Landsbergh, P. Janietz and R. Dehmlow, *ibid*., 15, 106 (1975).
[6] H. Gerischer, in "Physical Chemistry: An Advanced Treatise," Vol. 9A, H. Eyring, D. Henderson, W. Jost, eds., Academic Press, New York, 1970.
[7] H. Gerischer, in "Advances in Electrochemistry and Electrochemical Engineering," Vol. 1, P. Delahay and C. Tobias, eds., Interscience Inc., New York, 1961.
[8] W. P. Gomes and F. Cardon, Z. Phys. Chem., 86, 330 (1973) and references therein.
[9] R. A. Marcus, J. Chem. Phys., 43, 679 (1965).
[10] S. N. Frank and A. J. Bard, J. Amer. Chem. Soc., 97 (1975) (in press).
[11] D. Laser and A. J. Bard, J. Phys. Chem. (submitted).
[12] K. L. Hardee and A. J. Bard, J. Electrochem. Soc., 122, 739 (1975).
[13] R. S. Nicholson and I. Shain, Anal. Chem., 36, 706 (1964).
[14] B. Pettinger, H. R. Schöppel and H. Gerischer, Ber. Bunsenges. Phys. Chem., 78, 450 (1974).

Comment on Paper by S. N. Frank, *et al.*, "Characterization of Semiconductor Electrodes in Non-aqueous Solvents"

V. E. Henrich

Massachusetts Institute of Technology
Lincoln Laboratory
Wood Street
Lexington, MA 02155

It seems to me that your work on silicon might form the basis for a comparison between the silicon surface states in an electrolyte and the large body of work that has been done on the surface states on silicon under ultrahigh-vacuum conditions. This would be a very important step in bridging the gap between the ultrahigh-vacuum environment and the real world. Do you have sufficient data on silicon surface states, similar to that you showed for TiO_2, to permit such a comparison?

ELECTROCHEMICAL PROCESSES ON NON-METALLIC SURFACES - 1

National Bureau of Standards Special Publication 455, *Electrocatalysis on Non-Metallic Surfaces*,
Proceedings of Workshop held at NBS, Gaithersburg, Md., December 9-12, 1975. (Issued November 1976)

Chemical Theory of Chemisorption and Catalysis on the Surfaces of Non-Metals

Robert L. Burwell, Jr.
Ipatieff Laboratory
Department of Chemistry
Northwestern University
Evanston, Illinois 60201

This paper surveys chemisorption and catalysis on nonmetals primarily from the point of view of localized, coordinatively unsaturated surface (cus) sites and with use of analogies to the chemistry of coordination and organometallic complexes. Topics covered include chemisorption on oxides of main group elements and of transition elements, heterogeneous catalytic hydrogenation and oxidation on oxides of transition elements, and chemisorption on group IV elements and group III-V compounds.

Key words: Chemisorption; heterogeneous catalysis; catalytic oxidation; catalytic hydrogenation; surface coordinative unsaturation; cus.

The usual heterogeneous catalytic reaction appears to proceed by chemisorption of one or more reactants followed by surface reactions involving chemisorbed species and finally by desorption of products and regeneration of the catalytically active sites. In its present stage, the study of the mechanism of heterogeneous catalytic reactions is primarily concerned with the determination of the sequence of chemisorbed intermediates which constitutes the catalytic reaction. Inevitably, then, the study of chemisorption and the nature of the binding in the adsorption complex are essential to the study of mechanism.

The great majority of the more recent studies of chemisorption on non-metals has involved oxides or mixed oxides and almost exclusively adsorption from the gas phase. Studies of carbons, sulfides, silicon, and germanium constitute but a small fraction of total studies. This paper will consider primarily chemisorption and catalysis on oxides and usually on polycrystalline or amorphous ones. Oxides which have been investigated may be divided into two groups.

(a) Oxides of main group elements: SiO_2, Al_2O_3, SiO_2-Al_2O_3, and zeolites. These are important in technology both as adsorbents and as catalysts and supports for catalytically active ingredients.

(b) Oxides of transition elements, for example, Cr_2O_3, NiO, Co_3O_4, V_2O_5, $Bi_2O_3 \cdot MoO_3$, and also of post-transition elements like ZnO and also oxides of rare earth elements. Studies of chemisorption on these materials have primarily been motivated by interest in their catalytic properties.

In the 1950's there was a strong interest in interpreting chemisorption on oxides--even Al_2O_3 and Cr_2O_3 at lower temperatures--in terms of the band theory of semiconductors. In recent years, most interpretations have tended towards a localized bonding based on analogies with coordination and organometallic complexes. In this, the surface site is treated as a coordinatively unsaturated surface (cus) ion and the adsorbate as a ligand which completes or partially completes the coordination sphere of the (cus) ion. Ligand field theory provides a more elaborate extension of this approach. A survey of the crystal field and ligand field aspects is provided by D. A. Dowden, Catal. Revs., 5, 1 (1971). Some of the factors which led to this change of attitude are:

(a) The results of the earlier effort did not appear to be very useful.

(b) The earlier procedure ignored surface geometry, i.e., what crystal planes were exposed, the edge/face ratio of surface atoms, surface defects, etc., and also such chemical matters as the degree of hydroxylation of the surface.

(c) The earlier theory appeared to have no contact with the rest of chemistry.

(d) Few catalysts of any interest were typical semiconductors.

(e) The area of homogeneous catalysis by organometallic complexes developed and provided many examples of catalytic reactions rather similar to those in heterogeneous catalysis. Here a localized bond was necessarily involved. The existence of the homogeneous analogs proved nothing about heterogeneous catalysis, of course, but it did establish that band theories were not essential to explain all catalytic reactions.

Presumably there is an exact quantum mechanical solution to the nature of binding in any particular adsorption complex, but this solution is not accessible to present techniques and approximations must be used. The coordination complex approach might give a useful interpretation of the surface chemistry and catalytic behavior of an oxide or even of germanium, whereas it might be useless in interpreting the effect of chemisorption upon such bulk properties of the adsorbent as conductivity. That is, the effect upon the bulk might be a relatively small perturbation upon the actual binding in the adsorption complex and different approximations might, at this stage, be appropriate in discussing binding and conductivity.

Measurement of the extent of or the rate of the chemisorption of various adsorptives upon various adsorbents as a function of pretreatment, pressure, and temperature dates back more than fifty years. However, such investigations alone, although essential first steps, give little information about chemical binding. Analogies with molecular reactions were useful but most of the molecular analogs, particularly the organometallic complexes, have been discovered only in recent years. Infrared spectroscopy of adsorbed species has probably been the most important of the newer tools but electron paramagnetic resonance has also been important, particularly on oxides. Optical spectroscopy has also been useful. Mössbauer spectroscopy has been employed but it is limited by the small number of useful isotopes. X-ray photoelectron spectroscopy is beginning to have an impact. Although there are problems with this technique, it should prove useful in the so far difficult task of identifying the oxidation state of the metal ion in transition metal oxides and of changes which occur consequent to chemisorption. The techniques of surface chemical physics have so far been applied mainly to tungsten and a few other metals.

We present below a review of the kinds of chemisorbed species which have been proposed. The review is necessarily selective and the references have been chosen primarily to serve as leading references to the literature. It should be recognized that many of the species proposed as catalytic intermediates are speculative and are derived only from studies of catalytic reactions. In some cases additional support for such species has been provided by the techniques of the preceding paragraph and by isotopic tracer experiments, stereochemical experiments, reactant structure variation, etc. applied to the catalytic reaction [1].[1] The studies leading to the proposed chemisorbed species have almost all involved solid-gas systems, aqueous systems have rarely been examined, and, indeed, most of these chemisorptions are strongly inhibited by water vapor. That is, water molecules are strongly chemisorbed on most of the sites for chemisorption to be discussed.

It should be recalled that the most strongly adsorbed species is probably not a good catalytic intermediate. The very weakly adsorbed species may not be activated, the very strongly adsorbed species must be so low in the energy scale as to be relatively unreactive. Rather, the species of an intermediate energy of adsorption is most likely to be the most reactive.

---

[1] Figures in brackets indicate the literature references at the end of this paper.

Silica. Silica gel has been extensively investigated as an adsorbent. After preparation and drying at about 150 °C, the surface of silica gel is free of water vapor and covered with about 5 silanol (surface SiOH groups) per nm^2 [2]. Silica gel is a selective adsorbent. For example, it adsorbs olefins, arenes, and ethers much more strongly than alkanes because the silanol groups are strong hydrogen bond donors. However, unless one wishes to classify adsorption by hydrogen bonding as chemisorption, pure silica gel in its usual form does not exhibit chemisorption. Commercial silica gel contains about 0.05% Al_2O_3 which gives it a little of the characteristics of $SiO_2 \cdot Al_2O_3$ described below [3].

Alumina. The cubic aluminas (γ- , δ- , etc.) which come in high area forms are also covered with OH groups when equilibrated with water at room temperatures [4]. Upon heating, dehydroxylation occurs to produce Al^{3+} (cus) and O^{2-} (cus).

$$\begin{matrix} H & H \\ O & O \\ Al^{3+} & Al^{3+} \end{matrix} \longrightarrow \begin{matrix} & O^{2-} & \\ Al^{3+} & & Al^{3+} \end{matrix} + H_2O(g) \qquad (1)$$

O^{2-} (cus) may serve as a basic site to chemisorb acidic adsorptives [5]. Partially dehydroxylated aluminas chemisorb pyridine in two forms as shown by studies using infrared and Raman spectroscopy.

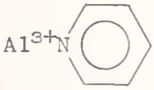

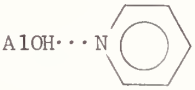

Silica-aluminas. Silica and alumina in which the ratio Si/Al is greater than about 3 form amorphous solid solutions. One can look upon this material as a condensation polymer of $Si(OH)_4$ and $Al(OH)_3OH_2$. Thus, each Al^{3+} will be accompanied by one H^+. One might schematically represent the undehydroxylated surface by

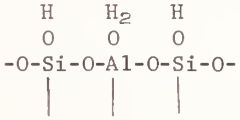

$$\begin{matrix} & H & & H_2 & & H & \\ & O & & O & & O & \\ -O- & Si & -O- & Al & -O- & Si & -O- \\ & | & & | & & | & \end{matrix}$$

As judged by indicator studies, some of the surface $AlOH_2$ groups are as strongly acidic as concentrated sulfuric acid [5]. Olefins, for example, propylene, appear to be converted to carbonium ions upon adsorption. Silica-alumina catalyzes reactions of hydrocarbons which closely resemble carbonium ion reactions. The material was used for many years as the catalyst in catalytic cracking of heavier petroleum stocks.

Zeolites. Zeolites are crystalline aluminosilicates with networks of small channels whose diameters are in the general range of 1 nm. As in silica-aluminas, an extra plus charge must accompany each Al^{3+} and, as the zeolites are synthesized, this extra plus charge is Na^+ but other positive ions can be introduced by ion exchange against Na^+. For example, Co^{2+} can be introduced and this ion can be amminated by treatment with ammonia. The cobalt ammine complex reacts with oxygen to form Co^{3+} $O\text{-}O^-$ as Howe and Lunsford have shown by EPR examination [6]. The Co^{2+} ions are too far apart for there to be any question that the binding is other than localized. Non-amminated ions of Co^{2+} exchanged into zeolites chemisorb carbon monoxide, nitric oxide, and methyl isocyanide [7].

Soft and hard acids and bases (SHAB). Pearson's concept of soft and hard acids and bases [8] is qualitatively useful in considering chemisorption and catalysis. In general, soft indicates large and polarizable; hard, small and less polarizable. The prototype of the hard acid is the proton, of the hard base, the hydroxide ion. The terms soft and hard must be distinguished from the terms weak and strong. Other things being equal, a soft acid prefers to combine with a soft base, a hard acid with a hard base. However, a strong, soft base may combine well with a hard acid, e.g., CH_3^- with H^+

Among bases, the order of increasing hardness is

$F^- > Cl^- > Br^- > I^-$

$O \gg S > Se > Te$ as in H_2O vs. H_2S

$N \gg P > As$ as in NH_3 vs. PH_3

Tetracyanoethylene, ethylene, carbon monoxide, H^-, and $C_2H_5^-$ are soft bases although consideration as acids or bases in the first three is complicated by back-donation of electrons.

Small, highly charged ions are hard acids: H^+, Li^+, Mg^{2+}, Al^{3+}, Fe^{3+}, and Cr^{3+}, also CO_2 and SO_3. Cu^+, Ag^+, Pt^{2+} are soft. The higher the charge on the ion of a given element, the harder it is. Thus, Co^{3+} is hard, Co^{2+} is intermediate, and Co(0) is soft. F^- binds more strongly to Al^{3+} than does I^- but the reverse is true to Ag^+. H_2O binds more strongly than does H_2S to Al^{3+} but the reverse is true to Ag^+. C_2H_4 and CH_3^- should bind weakly to Cr^{3+} (cus). H_2O should bind strongly and, indeed, water is a strong poison for heterogeneous catalytic reactions on chromia. Poisoning is a pervasive problem in heterogeneous catalysis and the SHAB concept is useful in predicting what compounds will be poisons for a particular catalyst.

Chromia (Cr_2O_3 of various degrees of hydration, crystalline or amorphous). Like alumina, chromia exposed to water at 25 °C has a surface which is fully hydroxylated, i.e., the surface is covered with OH^-. When such chromia is heated above about 200 °C, water is lost by condensation of surface OH^- to form pair sites, Cr^{3+} (cus) and O^{2-} (cus) [9]. A sample of amorphous chromia heated in an inert atmosphere (for example, flowing helium or a vacuum) to 400 °C, contains about one pair site per nm^2.

As could be predicted from the SHAB concept, the chemisorption of carbon monoxide on activated chromia is weak. At -78 °C, adsorption is complete and irreversible and the extent of such chemisorption can be used to measure the content in Cr^{3+} (cus). Warming to 0 °C liberates most of the carbon monoxide. One would hardly expect all Cr^{3+} (cus) to occur in identical geometries or to have the same degree of coordinative unsaturation. Initial dehydroxylation would generate Cr^{3+} (cus) in five-fold coordination (the coordination number in bulk is six) and O^{2-} coordinated to three Cr^{3+} rather than four as in bulk. More extreme degrees of dehydroxylation could generate Cr^{3+} in four-fold coordination. There is catalytic evidence for non-uniformity of Cr^{3+} (cus) [9] and Borello and Zecchina and also Peri have provided evidence from infrared spectroscopy that Cr^{3+} of C.N. = 4 exists [10].

A major difference between chromia and alumina is the possibility of changes in the oxidation number of chromium. Heated in oxygen at 450 °C, chromia is covered with a monolayer of Cr(VI) [11]. Heating in hydrogen or carbon monoxide at 500° appears to generate Cr(II) on the surface. Chromia is an oxidation catalyst and its action as such presumably involves alternation in the oxidation number of chromium. Oxygen adsorbs strongly on activated chromia. On chromias of lower degrees of hydroxylation, the initially formed adsorption complex is probably Cr^{4+} O_2^- [11] but on highly dehydroxylated chromia, the complex is probably Cr^{5+} O^{2-} [10]. These structures are rather speculative.

Chromia is also a catalyst under reducing conditions and, for example, it gives substantial rates in the hydrogenation of ethylene at -100 °C. There is still some question as to the relative degree of involvement of Cr^{2+} vs. Cr^{3+} in chromias which have not been exposed to reducing atmospheres at temperatures above 300 °C or so. However, it may be noted that Cr^{3+} (cus) should be more readily reduced than bulk Cr^{3+} because octahedrally coordinated Cr^{3+} is strongly stabilized by the crystal field stabilization energy but Cr^{2+} is destabilized in the crystal field of octahedral coordination. In bulk chromia, each Cr^{3+} is octahedrally surrounded by six O^{2-}. In what follows we will use Cr^{3+} (cus) as the example of the surface site.

H_2O adsorbs on the pair sites Cr^{3+} (cus) O^{2-} (cus) in what is the reverse of the dehydroxylation shown in eq (1). Formally, the water is dissociatively adsorbed as H^+ and OH^-. This process is heterolytic dissociative adsorption. At temperatures of 25 °C and above, hydrogen appears to adsorb heterolytically to give

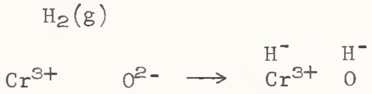

$$\overset{H_2(g)}{Cr^{3+}\quad O^{2-}} \longrightarrow \overset{H^-}{Cr^{3+}}\quad \overset{H^-}{O} \qquad (2)$$

and at 200 °C methane also adsorbs by dissociative heterolytic adsorption.

$$\overset{CH_4(g)}{Cr^{3+}\quad O^{2-}} \longrightarrow \overset{H_3C^-}{Cr^{3+}}\quad \overset{H^-}{O} \qquad (3)$$

The forms H^- and CH_3^- are the crystal field formalism of coordination chemistry. There is considerable charge redistribution and adsorbed species are much less ionic and basic than NaH and $NaCH_3$. It will be noted that heterolytic dissociative adsorption does not involve oxidation-reduction reactions in the adsorbent. There are a number of organometallic analogs to the adsorbed alkyl, one of which is p-tolylCr(III)Cl_2L_3 [12] where L is tetrahydrofuran coordinated through its oxygen atom and p-tolyl is formally

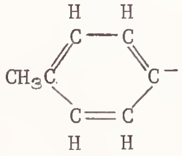

Alkanes exchange with deuterium in the presence of activated chromia at about 200 °C to give primarily the monodeuteroalkane. This reaction appears to proceed via heterolytic dissociative adsorption of alkane and deuterium as in eqs (2) and (3), followed by surface migration of H^+ and D^+, and then associative desorption. Hydrogenation, at least at temperatures above 25 °C, appears to proceed by a related mechanism: reaction of, for example, C_2H_4 with CrH to give $CrCH_2CH_3$ followed by reaction of the latter species with OH^- to regenerate the pair site and to form C_2H_6. There are hydrogenations homogeneously catalyzed by organometallic complexes which appear to proceed by a very similar mechanism [9]. In addition, it has been proposed that alkylethylenes can adsorb alternatively by heterolytic dissociation. With 1-butene the product would be $Cr(CH_2 \cdots CH \cdots CH\text{-}CH_3)\ OH^-$. Reversion to butylene could involve addition of H^+ to carbon-3 to form the isomeric 2-butene. The proposed intermediates derive largely from experiments using deuterium as an isotopic tracer. They are reasonable but somewhat speculative.

Reasonable, but even more speculative, is the proposal of reductive adsorption as in the following example.

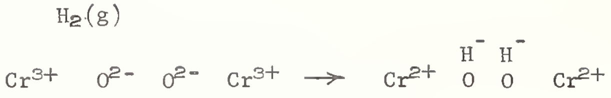

$$\overset{H_2(g)}{Cr^{3+}\ \ O^{2-}\ \ O^{2-}\ \ Cr^{3+}} \longrightarrow Cr^{2+}\ \ \overset{H^-}{O}\ \ \overset{H^-}{O}\ \ Cr^{2+} \qquad (4)$$

Such a form of chemisorbed hydrogen could lose water and generate coordinatively unsaturated and dehydroxylated surfaces containing Cr^{2+}. Continuing reaction and loss of water would result in reduction of Cr_2O_3 to CrO. It should be noted that the species formed in eq (4) is isomeric with that formed in eq (2). Probably the reductive adsorption form is favored at more elevated temperatures. Reductive adsorption of carbon monoxide can be represented,

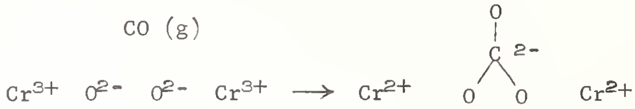

Co$_3$O$_4$. This oxide is an active catalyst for a number of reactions under reducing conditions and it rather resembles chromia in its overall behavior. It has been particularly studied by Ozaki [13]. The active sites are pair sites of cus cobalt and oxygen ions and hydrogen appears to adsorb heterolytically.

Zinc oxide. The species outlined above which were first proposed for chromia have been established more strongly as occurring on zinc oxide by R. J. Kokes who employed infrared spectroscopy as well as deuterium tracers [15]. Zinc oxide is particularly suitable for such a study. Its optical characteristics facilitate infrared studies and it is a much poorer catalyst. Thus, the surface intermediates are less reactive and more amenable to study. Kokes clearly established the occurrence of heterolytic dissociative adsorption of hydrogen and of propylene, the formation of a surface π-complex of ethylene, and reaction of adsorbed ethylene with Zn^{2+} H^- to give Zn^{2+} $C_2H_5^-$. The nature of surface intermediates for these reactions are better known on zinc oxide than on any other oxide.

Adsorption of Oxygen on Oxides of Transition Elements

Chemisorption of oxygen. The following forms of chemisorbed oxygen have been proposed, O^{2-} (oxide ion), O_2^{2-} (peroxide ion), O^-, O_2^- (superoxide ion), O_3^- (ozonide ion), and O_4^-. Substantial progress has been made in studying adsorbed oxygen because all but the first two are paramagnetic and subject to study by EPR. Moreover, the existence of ^{17}O of nuclear spin 5/2 has greatly facilitated this work. The hyperfine splitting observed with ^{17}O has permitted clear assignments and provided structural data. This subject has been reviewed by Lunsford [15]. It should be recalled that the reaction

$$O^{2-}(g) \longrightarrow O^-(g) + e^-(g)$$

is very strongly exoenergetic in the gas phase and that O^{2-} is stable against this reaction in solid ionic oxides because it is stabilized by the Madelung energy of the solid. Presumably, then, the reverse of the reaction above is less favored at the surface than in bulk and therefore, O^- would be relatively more stable at the surface than in bulk. Further, in the gas phase, N_2O^- decomposes to N_2 and O^- when the ion contains very small amounts of energy above its ground state. One might expect, then, that treatment with N_2O would be a method of choice in making O^- ads.

A number of studies of the adsorption of oxygen on reduced, supported molybdenum oxide have been reported [15,16]. O_2^- is formed and the two oxygen atoms are not equivalent. Further, there is some contribution from covalent bonding. At least with silica as the support, the O_2^- is stable to 100 °C. The EPR-invisible O^{2-} ion is probably also formed [16]. The O_2^- ion appears to be located at a positive ion on the surface and the situation is probably similar to that of a number of superoxide ions known in molecular complexes such as the Fe(II)-porphyrin complexes of myoglobin and hemoglobin. Molecular analogs to these are known in solution and they have been formed on the surface of imidazole-modified silica gel [17]. The reaction with oxygen can be represented

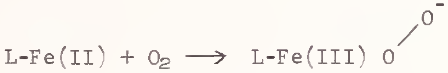

$$L\text{-}Fe(II) + O_2 \longrightarrow L\text{-}Fe(III)\ O{-}O^-$$

where four nitrogen atoms in the planar porphyrin molecule are coordinated to the iron atom in a plane perpendicular to the plane of the paper. L is an imidazole group. Co(II) complexes behave similarly. The reduced molybdenum catalysts exhibit the EPR signal of Mo(V) which declines in intensity as oxygen adsorbs. The process can probably best be represented as

$$Mo^{5+}\ (cus) + O_2(g) \longrightarrow Mo^{6+}\ O_2^-$$

with partial contribution from covalent bonding. However, ref. 16 considers that attachment occurs at surface Mo^{6+} although no explanation is given as to how an electron is transferred to the molecule of oxygen.

Treatment with N_2O leads to an EPR signal of O^-. This species reacts more rapidly with reducing agents than does O_2^- (ads).

An adsorbent prepared as V_2O_5/SiO_2 behaves rather similarly although some O^- appears during treatment with O_2. At 25 °C, O^-ads reacts rapidly with H_2, CH_4, C_2H_4, and CO. O_2^- is much less reactive. As judged by hyperfine splitting, O_2^- is in a form in which there is interaction with ^{51}V.

Little definite is known about adsorption of oxygen as what is formally O_2^{2-}, but, of course, it is invisible to EPR. It is well known in coordination complexes as, for example, in Vaska's compound [18].

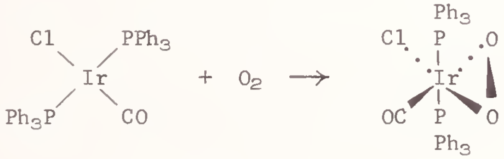

where Ph represents phenyl and the oxidation state of Ir increases from I to III consequent to the 'adsorption' of oxygen. A similar reaction may well occur in some cases on oxides or the like but most of the currently known examples in coordination chemistry involve metal atoms with $\underline{d}^8$ and $\underline{d}^{10}$ configurations. Such configurations are rare in oxides of catalytic interest.

Cimino and Stone separately and jointly have reported a series of important studies of solid solutions of oxides of transition elements in such insulating oxides as MgO and Al_2O_3 [19,20,21]. This work has provided information on two items: the adsorptive and catalytic effect of ions of different transition elements in the same environment, the effect of the dilution of a given ion upon these properties. It has been established that ions of transition metals have adsorptive and catalytic properties even in high dilution in insulating oxides where semiconductivity theory is clearly inappropriate. However, there is an effect of concentration. In particular, Stone [20] concludes that electronic interaction exists among neighboring Cr^{3+} ions in solutions of higher concentrations of Cr^{3+} in $(Cr^{3+}, Al^{3+})_2O_3$. At least under oxidizing conditions the purely localized treatment of adsorption and reactions on chromia given under <u>Chromia</u> is probably an oversimplification.

Adsorption of Oxygen on Oxides of Non-Transition Elements

Adsorption on these materials tends to proceed to a much smaller coverage than on the materials of the preceding group. Furthermore, since oxidation states more positive than Mg^{2+}, etc. are very high in energy, the formalism used to represent the adsorption of oxygen in the preceding section is inapplicable. MgO has been extensively studied. The electrons used in forming the EPR-visible species appear to come from traps and radiation either before or during adsorption is often needed to effect adsorption. N_2O under these conditions gives an O^- ads in which the extra electron is largely localized in one of the 2p orbitals of O^-. The extent of covalency in the binding is low. O_2^- is formed by exposure to oxygen, the two oxygen atoms are equivalent and the axis of O_2^- must be parallel to the plane of the surface (unlike the situation on the transition metal oxides of the preceding section). This is also true for TiO_2, ZnO, and SnO_2.

The ozonide ion O_3^- is formed by the following reaction on MgO

$$O^-\text{ads} + O_2(g) \longrightarrow O_3^-\text{ads}.$$

The species is not very stable and it slowly decomposes to O_2^- or O^-. At present, O_3^- appears to be a relatively uncommon form of adsorbed oxygen.

Charge Transfer Adsorption of Organic Molecules

The surface of MgO can adsorb certain organic molecules by charge transfer adsorption which is apparently of a different type than that involved in adsorbing oxygen. Thus, MgO after thermal activation adsorbs nearly a monolayer of nitrobenzene (NB) to form the nitrobenzene radical anion [22]. On partially dehydroxylated MgO, the process appears to be

$$\begin{array}{l} O^{2-}(\text{cus}) \\ OH^- \end{array} + NB \longrightarrow \begin{array}{l} O^-(\text{cus}) \\ OH^- \cdots NB^- \end{array}$$

whereas on highly dehydroxylated samples no proton hyperfine splitting is observed and the following process was suggested.

$$O^{2-}(\text{cus}) + NB \longrightarrow O^- \; NB^-$$

A number of examples of forming radical anions and also radical cations such as $(\text{phenyl})_3N^+$ has been observed on such insulating oxides as Al_2O_3 and Al_2O_3,SiO_2.

Heterogeneous Catalytic Oxidation

Many examples of heterogeneous catalytic oxidation exist. Some occur on metals, for example, the oxidation of NH_3 to NO (which is then converted to nitric acid), the oxidation of SO_2 to SO_3 on platinum, and the oxidation of hydrocarbons and carbon monoxide on platinum. Many examples in which oxides are the catalysts also exist, for example, the oxidation of SO_2 to SO_3 at about 450 °C on $V_2O_5,K_2O/SiO_2$ (an unusual case of heterogeneous catalysis because under operating conditions the catalytic ingredient is a melt of vanadium oxide dissolved in molten potassium pyrosulfate [23]), the oxidation of naphthalene to phthalic anhydride on a similar catalyst but at about 350 °C at which temperature the catalytic ingredient is probably solid, and the oxidation of methanol to formaldehyde on Fe_2O_3,MoO_3 at 375 °C. For a description of the catalysts and the operating conditions of industrial oxidation processes, see ref. 24.

It is not difficult to find catalysts which catalyze the oxidation of hydrocarbons to water and carbon dioxide and this can be accomplished even under the demanding conditions of treating automobile exhaust. The problem is selectively to oxidize the hydrocarbon part way. Ordinarily, the starting hydrocarbon is more resistant to attack than most imaginable intermediates. Sometimes, however, an intermediate possesses a rather high resistance to oxidation and good yields of the intermediate can be obtained, as, for example, in the oxidation of naphthalene to phthalic anhydride. Usually, the problem is more difficult and somehow one must find a catalytic system which for some reason does not further oxidize the desired product. This matter is very poorly understood but probably there is no general method for stopping the reaction at a desired point and the problem is almost as broad as chemistry itself. Enzymes give selective oxidation even of alkanes to perfection.

One must presumably activate either or both the hydrocarbon and the oxygen or other oxidizing agent. The chemical processes are usually complicated, the catalyst is often complicated, and operating temperatures are usually high. Only a few systems have received much fundamental scientific attention and we know something about the mechanism of the reaction in only a few cases. Further, there are not many homogeneous catalytic oxidations which are appropriate as analogs. The high operating temperature in most heterogeneous catalytic oxidations militates against this. However, a low temperature example follows.

The reaction between tert-butyl hydroperoxide and cyclohexene at about 80 °C produces cyclohexene oxide and tert-butyl alcohol,

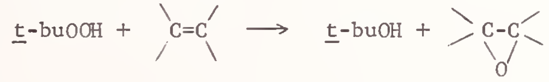

MoO_3 is a heterogeneous catalyst for the reaction and $MoO_2(acac)_2$ (acac is a bidentate, negatively charged ligand, the conjugate base of acetylacetone) and some other, but far from all, molybdenum complexes are homogeneous catalysts [25]. The system presents the advantage that the oxidation number of the molybdenum can be monitored by optical spectroscopy. Coordinatively unsaturated Mo species appear to be involved in both the heterogeneous and the homogeneous instances.

Where elemental oxygen is the oxidizing agent, either oxygen is incorporated into the product (e.g., $CO + 1/2O_2 \longrightarrow CO_2$), or, more commonly when a hydrocarbon is a reactant, oxygen appears both in an organic product and in water ($CH_3CH{=}CH_2 + O_2 \longrightarrow CH_2{=}CHCHO + H_2O$), or, in oxidative dehydrogenation ($CH_3CH{=}CHCH_3 + 1/2O_2 \rightarrow CH_2{=}CH\text{-}CH{=}CH_2 + H_2O$), oxygen appears only in water. We can imagine two extreme types of mechanisms:

(a) The oxygen in the product comes from adsorbed oxygen.

(b) The oxygen in the product comes from lattice O^{2-} which is replaced by adsorption of oxygen in a subsequent step.

For a simple example, consider the oxidation of carbon monoxide. In case (a), the sequence might be

$$M^{n+}(\text{cus}) + 1/2O_2 \longrightarrow M^{(n+1)+}\ O^-$$

$$M^{(n+1)+}\ O^- + CO \longrightarrow M^{n+}(\text{cus}) + CO_2$$

In case (b), the sequence could be

$$M^{n+}\ O^{2-} + CO \longrightarrow M^{(n-2)+} + CO_2$$

$$M^{(n-2)+} + 1/2O_2 \longrightarrow M^{n+}\ O^{2-}$$

Overall, $O_2(g)$ is the oxidizing agent, but in the step that forms CO_2: in case (a), both $M^{(n+1)+}$ and O^- are the oxidizing agents; in case (b) only M^{n+} is the oxidizing agent since the oxidation number of oxygen is the same in O^{2-} and in CO_2.

For an oxide which is reluctant to be reduced, such as Cr_2O_3, one might expect to observe case (a) under conditions such that oxidation to higher oxides is relatively slow. On the contrary one might expect to observe case (b) for an oxide like MoO_3 if reoxidation is rapid. That is, case (a) is to be expected where under operating conditions the catalyst is in the fully reduced form and case (b) is to be expected where it is in the fully oxidized form.

In actual examples of heterogeneous catalytic oxidation, the matter is complicated but it appears likely that case (a) often, probably usually, leads to non-selective, complete oxidation, whereas, selective oxidations are more likely to be favored by case (b).

Oxidations on Bismuth Molybdate. Bismuth molybdate, typically in the form Bi_2MoO_6, gives three remarkably selective oxidations at temperatures of about 450 °C [26,27].

$$CH_2{=}CH{-}CH_3 + O_2 \longrightarrow CH_2{=}CH{-}CHO + H_2O$$

$$CH_2{=}CH{-}CH_3 + NH_3 + 3/2O_2 \longrightarrow CH_2{=}CH{-}C{\equiv}N + 3H_2O$$

$$CH_3{-}CH{=}CH{-}CH_3 + 1/2O_2 \longrightarrow CH_2{=}CH{-}CH{=}CH_2 + H_2O$$

From isotopic labelling experiments using deuterium and ^{13}C it has been established that in the first reaction propylene is dissociatively adsorbed as some kind of allylic species. This step is rate limiting.

A remarkable feature of these reactions is that one may omit oxygen and find the reaction to proceed with the usual selectivity until the catalyst composition falls to $Bi_2MoO_{5.5}$. During this process the electrical conductivity increases and the EPR signal of Mo^{5+} appears. Treatment with oxygen restores the original properties and composition. Keulks has shown the acrolein formed initially from $^{18}O_2$ is nearly devoid of ^{18}O. Further, the oxidized catalyst does not exchange rapidly with $^{18}O_2$. It appears very probable, then, that the oxygen which is incorporated comes from the lattice.

The crystal structure of Bi_2MoO_6 consists of sheets of O^{2-}, $(Bi_2O_2)^{2+}$, and $(MoO_2)^{2+}$ alternating in the following manner

$$(Bi_2O_2)^{2+} \quad O^{2-} \quad (MoO_2)^{2+} \quad O^{2-} \quad (BiO_2)^{2+} \quad O^{2-} \quad \text{etc.}$$

The oxygen between the layers containing the metal ions is clearly very mobile and the possibility exists that the oxygen which replaces the O^{2-} consumed may be added at some distance from the point of loss.

The initial reaction may be

$$C_3H_6 + Mo^{6+} + O^{2-} \longrightarrow (MoC_3H_5)^{5+} + OH^-$$

During the subsequent stages, it appears likely that the adsorbed organic intermediates are not exposed to adsorbed oxygen and this may be the key to the selectivity.

Another component of selective oxidation catalysts, V_2O_5, has a crystal structure related to that of Bi_2MoO_6 [28]. Here planes containing vanadium and oxygen are separated by planes containing only O^{2-}.

One final comment must be made with respect to heterogeneous catalytic oxidations Free radicals may propagate from the surface of the catalyst into the gas phase and initiate reaction sequences in the gas phase. This is common in the oxidation of hydrocarbons in the liquid phase on oxides of transition elements [29] and it is likely that it is a side reaction in oxidations on Bi_2MoO_6.

Adsorption on Group IV Elements and on Group III-V Compounds. There has been a number of investigations of adsorption on elements of group IV and on group III-V compounds, many on single crystal surfaces by the methods of surface chemical physics. Research on these materials has not been motivated by interest in their adsorptive and catalytic utility (so far they have none) but, of course, by interest in their semiconductive properties. The conceptual approach to this work has often been different from that to the work considered earlier and intercomparisons are not always easy.

If one were to crush a crystal of diamond in an ultrahigh vacuum, one would break myriads of carbon-carbon bonds. One might expect that as a first approximation, one could consider the surface to react as if it were covered with free radicals even though the density of free radicals would be so high that there should be some kind of interaction among them which might even lead to surface reconstruction. One would expect hydrogen to chemisorb with some rather substantial activation energy to convert the diamond surface to an alkane one. Oxygen should chemisorb with a very small activation energy and initially to form alkylperoxy radicals, $\geqslant C\cdot + O_2 \longrightarrow \geqslant C\text{-}O\text{-}O\cdot$.

Adsorption experiments have been reported on silicon and germanium cleaved in an ultrahigh vacuum [30]. There is fast adsorption of HCl, HBr, H_2O, NH_3, and PH_3 at 25 °C. The adsorption is probably dissociative since one molecule of HCl adsorbs for every two surface atoms, one of H_2O for every four surface atoms. LEED studies have been reported for the adsorption of oxygen on single crystal surfaces of silicon and germanium cleaved in ultrahigh vacuum [31] and other experiments have been performed on the (111) faces of silicon crystals cleaved in an ultrahigh vacuum [32]. In the latter case, the sticking coefficient is about 0.001 and saturation corresponds to one atom of oxygen per surface atom. Results of this type have generally been interpreted in terms of "dangling bonds" on the clean adsorbent. The term must be a close cousin to "free radical."

The idea of surface coordinative unsaturation is less applicable here although the basic idea of unsaturation persists. Further, the materials are good semiconductors and one might expect to observe more substantial interactions between localized surface states and bulk than in most of the examples considered previously in this paper.

Oxygen adsorbs on the cleaved (110) surfaces of both n- and p-type GaAs to a saturation coverage of one atom of oxygen per pair of atoms of gallium and arsenic. The sticking coefficient is larger on n-type (3×10^{-5}) than on p-type (1.4×10^{-6}) [33]. It was suggested that the Oads is on As. However, an EPR signal of O_2^- has been observed on crushed GaAs [34]. The signal is due to a much weaker form of adsorbed oxygen, one which can be removed by desorption at -100 °C. The O_2^- is not ordered parallel to the surface and the signal intensity is ten-fold larger on n-type than p-type. On n-type AlSb 5% of the unpaired electron is in an ^{27}Al p-orbital.

Interpretation of chemisorption on single crystal planes of these materials may be complicated by surface reconstruction of the adsorbent, particularly with germanium and silicon. Further, there are apt to be problems associated with the role of surface defects and steps in experiments using the techniques of surface chemical physics. Special problems may be associated with adsorptives which generate adsorbates with a substantial and identical charge. Thus, on polar III-V compounds the ionic adsorption of oxygen to high coverage should be more difficult than that of hydrogen chloride which could adsorb heterolytically.

Summary

A summary of chemisorption and catalysis has been presented largely in terms of localized bonding and (cus) sites in analogy to inorganic and organometallic coordination chemistry. Of the approximate treatments yet considered, the author believes this approximation to be usually the most useful for the purposes of heterogeneous catalysis and of chemisorption itself. Presumably, in the future it will be replaced by a still better treatment. However, it should be noted that not all workers in the area employ the theoretical framework employed here. Band theory [35,36] continues to be employed by some workers [36,37] and, on some semiconductors, with little contribution from the chemical nature of surface [38].

References

[1] M. Boudart and R. L. Burwell, Jr., "Techniques of Chemistry," Vol. VI, Part 1, edited by E. S. Lewis, John Wiley and Sons, New York, 1974, p. 693.
[2] C. Okkerse, "Physical and Chemical Aspects of Adsorbents and Catalysts," edited by B. G. Linsen, Academic Press, London, 1970, p. 213.
[3] P. B. West, G. L. Haller, and R. L. Burwell, Jr., J. Catal., 29, 486 (1973).
[4] B. C. Lippens and J. J. Steggerda, "Physical and Chemical Aspects of Adsorbents and Catalysts," edited by B. G. Linsen, Academic Press, London, 1970, p. 171.
[5] K. Tanabe, "Solid Acids and Bases," Academic Press, New York, 1970.
[6] R. F. Howe and J. H. Lunsford, J. Amer. Chem. Soc., 97, 5156 (1975).
[7] P. Pichat, "Catalysis, Heterogeneous and Homogeneous," edited by B. Delmon and G. Jannes, Elsevier, Amsterdam, 1975, p. 183.
[8] R. G. Pearson, editor, "Hard and Soft Acids and Bases," Dowden, Hutchinson, and Ross, Inc., Stroudsburg, Pa., 1973.
[9] R. L. Burwell, Jr., G. L. Haller, K. C. Taylor, and John F Read, Advan. Catal. Relat. Subj., 20, 1 (1969).
[10] A. Zecchina, S. Coluccia, L. Cerruti, and E. Borello, J. Phys. Chem., 75, 2783 (1971). A. Zecchina, L. Cerruti, and E. Borello, J. Catal., 25, 55 (1972). J. B. Peri, J. Phys. Chem., 78, 588 (1974).
[11] M. P. McDaniel and R. L. Burwell, Jr., J. Catal., 36, 394 (1975).
[12] J. J. Daly, R. P. A. Sneeden, and H. H. Zeiss, J. Amer. Chem. Soc., 88, 4287 (1966).
[13] H. Nihara, T. Fukushima, K. Tanaka, and A. Ozaki, J. Catal., 23, 281 (1971).
[14] R. J. Kokes, Accts. Chem. Research, 6, 226 (1973).
[15] J. H. Lunsford, Catal. Revs., 8, 135 (1973).
[16] M. Che, A. J. Tench, and C. Naccache, J.C.S. Faraday Trans. I., 70, 263 (1974).
[17] O. Leal, D. L. Anderson, R. G. Bowman, F. Basolo, and R. L. Burwell, Jr., J. Amer. Chem. Soc., 97, 5125 (1975).
[18] F. A. Cotton and G. Wilkinson, "Advanced Inorganic Chemistry," Interscience Publishers, New York, 1972, p. 772.
[19] A. Cimino, V. Indovina, F. Pepe, and F. S. Stone, Gazz. Chim. Ital., 103, 935 (1973).
[20] T. A. Egerton, F. S. Stone, and J. C. Vickerman, J. Catal., 33, 299 (1974).
[21] A. Cimino, Chim. Ind. (Milan), 56, 27 (1974), a review of ions in oxide matrices.
[22] D. Cordischi, V. Indovina, and A. Cimino, J.C.S. Faradav Trans. I, 70, 2189 (1974).
[23] P. Mars and J. G. H. Maessen, Proc. Int. Congr. Catal. 3rd, 266 (1965).
[24] C. L. Thomas, "Catalytic Processes and Proven Catalysts," Academic Press, New York, 1970, chapters 18-20.
[25] F. Triforo, P. Forzatti, and I. Pasquon, "Catalysis, Heterogeneous and Homogeneous," edited by B. Delmon and G. Jannes, Elsevier, Amsterdam, 1975, p. 509.
[26] G. C. A. Schuit, J. Less-Common Metals, 36, 329 (1974).
[27] D. J. Hucknall, "Selective Oxidation of Hydrocarbons," Academic Press, London, 1974.
[28] W. M. H. Sachtler, Catal. Revs., 4, 27 (1970).
[29] L. Ya. Margolis, Catal. Revs., 8, 241 (1973).
[30] A. J. van Bommel and F. Meyer, Surface Sci., 8, 381 (1967).
[31] J. J. Lander and J. Morrison, J. Appl. Phys., 33, 2089 (1962); 34, 1411 (1963).
[32] H. Ibach, K. Dorn, R. Dorn, and H. Lüth, Surface Sci., 38, 433 (1973).
[33] R. Dorn, H. Lüth, and G. J. Russel, Phys. Rev. B., 10, 5049 (1974).
[34] D. J. Miller and D. Haneman, Phys. Rev. B, 3, 2918 (1971).
[35] A. Clark, "The Theory of Adsorption and Catalysis," Academic Press, New York, N.Y., 1970, chapter XV.
[36] F. F. Vol'kenshtein, "The Electronic Theory of Catalysis on Semiconductors," Pergamon Press, Oxford, 1963.
[37] A. C. Zettlemoyer and R. D. Iyengar, "The Solid-Gas Interface," edited by E. A. Flood, Marcel Dekker, Inc., New York, N. Y., 1967, Vol. 2, chapter 26.
[38] T. A. Goodwin and P. Mark, Progress in Surface Sci., 1, 1 (1971).

National Bureau of Standards Special Publication 455, *Electrocatalysis on Non-Metallic Surfaces*, Proceedings of Workshop held at NBS, Gaithersburg, Md., December 9-12, 1975. (Issued November 1976)

ELECTROCATALYSIS AT TRANSITION METAL OXIDE AND CARBIDE SURFACES

P. Stonehart

Advanced Fuel Cell Research Laboratory
Power Systems Division
United Technologies Corporation
Middletown, Connecticut 06457

Due to the cost of noble metal electrocatalysts, significant research has been carried out to find non-noble metal electrocatalytic materials. Transition metal oxides, usually doped tungsten oxides (bronzes), have been postulated previously due to their favorable electronic conductivity and stability in electrolytes. The surface chemistry of such electrocatalysts has been largely neglected but interesting parallels exist for the electron injection and extraction with heteropolyanions in solution. The heteropolyanions exhibit electrochemical properties of "bronze" crystals and can be considered to be microcrystallites. Optical studies show correlations between absorbance in the visible region and the electron density per transition metal atom. By and large, the transition metal oxide electrocatalysts have not yet fulfilled their expectations.

A related research direction has examined the activity of transition metal carbides for hydrogen oxidation in acid. Here it was found that tungsten carbide was the most active material but that it required a pretreatment. Surface studies established that the active form of the tungsten carbide electrocatalyst was slightly carbon deficient.

Key Words: Electrocatalysis; heteropolyanions; phosphotungstate complex ions; "spillover" effect; transition metal carbides; transition metal oxides; tungsten bronze; tungsten carbide.

It is only recently that electrocatalysis, as a distinct sub-area in the field of electrochemistry, has taken on increased emphasis. This has been due to more sophisticated developments in energy conversion devices, such as fuel cells and new battery systems. The field of gas-phase catalysis has advanced further than that of electrocatalysis, principally due to an understanding of the surface features on gas-phase catalysts and the importance of highly dispersed (small particle size) catalytic materials. Nevertheless, the concepts developed for highly dispersed gas-phase catalysts can be applied equally well to electrocatalytic materials [1,2][1] The singular difficulty in understanding the operation of electrocatalysts is the lack of surface diagnosis techniques that are capable of examining the electrocatalyst surface in the presence of the electrolyte. To overcome this deficiency, one has to draw analogies and inferences from other sources, as this paper will show.

Noble metal electrocatalysts mostly have been studied but due to the cost of these materials, significant research has been carried out to find non-noble electrocatalytic materials. Due to their stabilities in acid electrolytes, transition metal oxides (usually of tungsten and molybdenum) have been postulated as suitable materials. Empirically, it has been shown that the incorporation of transition metal oxides, together with platinum, into porous electrode structures produces a higher reaction rate both for hydrogen oxidation

---

[1] Figures in brackets indicate the literature references at the end of this paper.

and hydrogen oxidation in the presence of carbon monoxide compared to the reaction rate for platinum alone [3]. It has not been determined whether this increased activity was due to an electrocatalytic effect or simply due to the formation of an improved electrode structure. In addition, alkali doped tungsten oxides in conjunction with platinum have been shown to be beneficial for carbon monoxide electro-oxidation [4].

It is well known that the incorporation of alkali metals into tungsten oxides produces "bronzes" with very low electronic resistance (fig. 1). It is apparent that the conductivity of the "bronze" does not depend on the particular alkali metal, but does depend on the doping level. At low electrode potentials, hydrogen atoms enter the WO_3 structure to form the analogous "hydrogen bronze" [5,6], so that it is not necessary that an alkali metal bronze be formed initially. Unfortunately, although there is some considerable knowledge on the solid-state properties of these "bronzes," very little information exists concerning the surface structure, especially in the presence of an electrolyte.

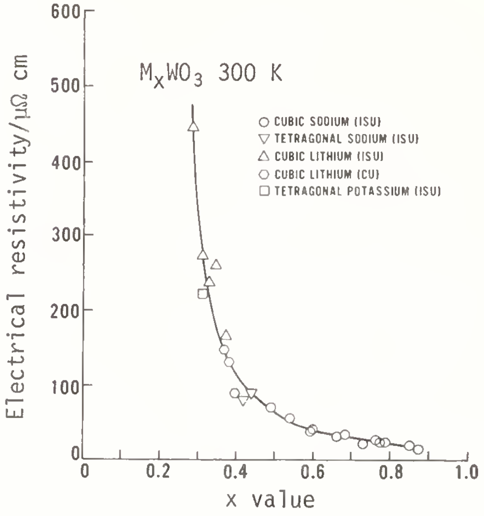

Fig. 1. Dependence of electrical resistivity on composition for some alkali-metal tungsten bronzes. Data from work at Iowa State University (ISU) and Cornell University (CU).

In order to identify the electrochemical processes occurring at the transition metal oxide surface, one may examine the properties of heteropolyanions. These can be considered as micro-crystallites of WO_3 and as such, the WO_3 groups are all surface entities. The two principle structures of heteropolyanions are: a) dodecametallo with the "Keggin" structure, and b) octadecametallo with the "Dawson" structure. These two structures are shown in figure 2. The former has an approximately spherical cage of 12(WO_3) groups surrounding a single hetero ion group, whereas the latter has 18(WO_3) groups in an elongated

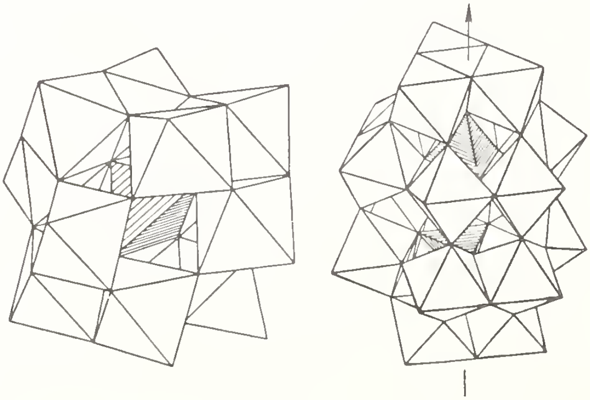

Fig. 2. (a) Dodecatungstophosphate ion, $[PW_{12}O_{40}]^{3-}$, ('Keggin structure') showing coordination polyhedra; (b) octadecatungstodiphosphate ion, $[P_2W_{18}O_{62}]^{6-}$, ('Dawson structure') showing coordination polyhedra.

cage surrounding two hetero ion groups. Since these ions have very few atoms, and as microcrystallites (clusters) the atoms are all surface entities, one is entitled to ask whether the electrochemical properties are at all representative of larger "bronze" particles.

An examination of the potentiodynamic electro-reduction of the $[PW_{12}O_{40}]^{3-}$ ion in acid on mercury [7] shows that addition of the first electron to the cage occurs in the vicinity of +0.2V versus hydrogen, shown as peak Ic in figure 3. Reoxidation of the reduced ion is shown by peak Ia. Addition of the second electron to the heteropolyanion occurs at more negative potentials, shown as peak IIc and the consequent reoxidation (removal of the second electron) as peak IIa. Two features may be noted. Firstly, the potential differences between peaks Ia and Ic are much less than between the peaks IIa and IIc. This means that the kinetic rate constant for addition and removal of the first electron to the WO_3 cage is greater than the corresponding rate constant associated with the second electron. Although only one electron is shared among $12(WO_3)$ groups to give $11W^{6+}$ and one W^{5+} (since the electron is not delocalized but probably hopping), it effectively hinders the addition of the second electron. Secondly, at the reversible hydrogen potential, only one electron is added to the cage. This would mean that for a hydrogen anode, either at or slightly positive to the reversible hydrogen potential, only a few tungsten atoms (1 in 12) would be expected to be as W^{5+}. The remainder are hexavalent. There is a real question, therefore, whether the surface of a "bronze" particle would exhibit the commonly assumed metallic conductivity or whether it would be semiconducting. The latter is more likely. In addition, although a variety of low surface area "bronzes" have been prepared for electrocatalytic studies, it has not been possible to prepare these compounds with useful high surface areas. McHardy [8] studied this problem and found that on introduction of alkali doped tungsten bronzes into an acid electrolyte, rapid leaching of the alkali metal occurred, producing a skin of WO_3 to the depth of 0.5 μm. It is not surprising, therefore, that when one micrometer particles of alkali doped tungsten bronzes are prepared, the only properties they exhibit in solution are those of stoichiometric WO_3 particles.

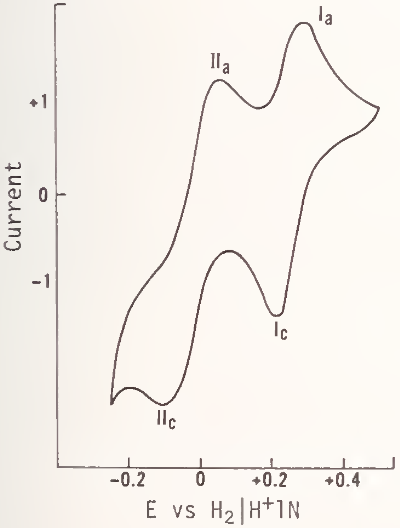

Fig. 3. Cyclic potentiodynamic i-V curves for $[PW_{12}O_{40}]^{3-}$ in 1 M H_3PO_4. v = 0.0925 V s^{-1}. I_c is the current peak associated with addition of the first electron and I_a is the current peak associated with oxidation of the $[PW_{12}O_{40}]^{4-}$ product. II_c and II_a are the corresponsing cathodic and anodic peaks associated with the second electron transfer. Stationary mercury electrode.

Even though these heteropolyanions contain so few atoms, one may conclude that the electrochemical properties are indeed representative of "bulk" materials. On comparing the potentiodynamic scans in figure 3 to potentiodynamic scans on sodium tungsten bronze crystals shown by Randin [9] in figure 4, the correspondence is obvious. Five different potentiodynamic scan rates are shown, but it is clear that the potentials of the peaks correspond to the first electron reduction and reoxidation (Ia and Ic) obtained with the heteropolyanions.

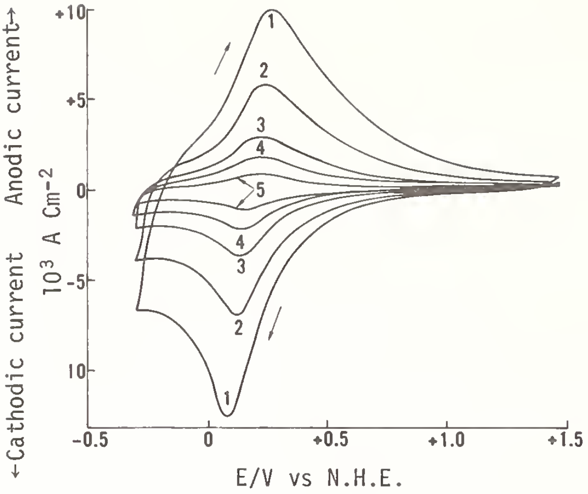

Fig. 4. Triangular voltage sweep curves for a sodium tungsten bronze electrode in helium-saturated 1 N H_2SO_4. Sweep rates: 1, 0.720; 2, 0.360; 3, 0.180; 4, 0.090; 5, 0.036 V s^{-1}

There is additional evidence from absorption spectra of the reduced heteropolyanions that these compounds can be considered as micro-crystallites of "bronzes." This subject is covered more fully in a discussion of the electrochemistry of transition metal oxide bronzes and related compounds published elsewhere [10]. It is somewhat surprising that so few atoms in a "cluster" exhibit properties manifest by bulk materials, except that is exactly what the theoreticians working on cluster calculations have been saying. Although the electrochemist is denied many of those surface techniques that are being employed to unravel mechanisms in gas-phase catalysis, by judicious choices of ionic species, such as the various heteropolyanions, it is possible to identify electron exchange processes occurring at the surfaces of solid electrocatalysts. Given the high sensitivity shown by electrochemistry for measuring reaction rates at fractional monolayer levels, then electrocatalysis becomes a sensitive surface probe [2].

Examining the electrocatalytic oxidation of hydrogen on platinum, and on tungsten oxide promoted by platinum, Hobbs and Tseung [3] showed an apparent maximum in the reaction rate as a function of platinum loading, shown in figure 5. This maximum is indicative of an electrocatalytic enhancement of the hydrogen oxidation rate at low platinum levels. The effect is made pronounced by the method of plotting the data, since the effect is negligible at higher platinum loadings where the high rate of hydrogen oxidation on platinum masks any enhancement due to the presence of tungsten oxide. A later paper by the same authors [11] showed an identical enhancement using nominally sub-stoichiometric tungsten oxide. The enhancement in the reaction rate occurred at the same nominal platinum loading. It is likely that the electrocatalytic materials were the same in both instances.

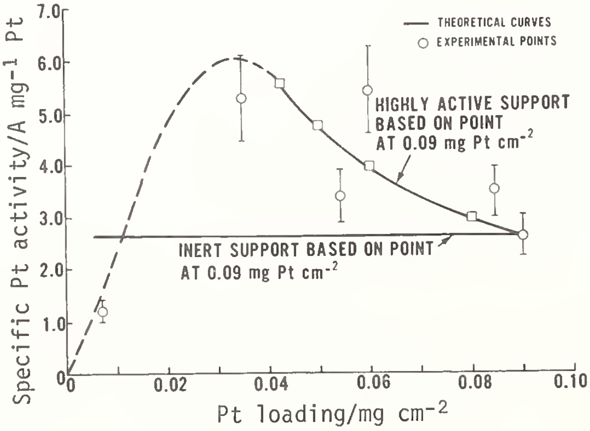

Fig. 5. Specific activity of supported Pt for hydrogen oxidation (current per mg Pt at +0.05 V) as a function of Pt loading on WO_3. The two theoretical curves were drawn assuming an inert support (——) and an active support (—□—), respectively. Poor activity at low loadings (---) was attributed to ohmic losses.

Since it has recently been shown experimentally [12] that the rate-determining step for hydrogen molecule oxidation on platinum in acid is dissociative chemisorption of the hydrogen molecule

$$H_2 \rightarrow 2H \text{ (Tafel Reaction)}$$

then two options are available for explaining the electrocatalytic enhancement by tungsten oxide. Either the adsorption isotherm for hydrogen atoms on the platinum surface is shifted to lower coverages (since hydrogen atoms are "poisons" for the hydrogen molecule dissociative chemisorption step), or the reduced tungsten oxide particles in the vicinity of a platinum crystallite become weakly active for hydrogen molecule oxidation on the oxide surface. The latter situation is considered more likely, although the reaction mechanism may not be the same as on the platinum surface. There is one further interesting point to note: the electrocatalytic enhancement of the hydrogen oxidation rate by tungsten oxide with low platinum loadings is exhibited in sulfuric acid electrolytes but not in phosphoric acid electrolytes. It may be conjectured that a surface phosphotungstate complex would be formed, preventing hydrogen molecule oxidation on the oxide. This is additional, although tenuous, evidence that the surface of tungsten oxide in sulfuric acid is a weak hydrogen molecule oxidation electrocatalyst.

Extensions of the studies on transition metal oxides have been those studies on transition metal carbides, which are also stable in acid. Several international groups have made contributions to the work, principally Böhm et al. [13], Mund et al. [14], Svata et al. [15], Palanker et al. [16], and Baresel et al. [17]. A screening program for the ability of transition metal carbides to oxidize hydrogen in sulfuric acid was performed by Mund et al. [14] and is given in table 1.

Table 1. Comparison of electrocatalytic activity among transition metal carbides.

Transition Metal carbide	H_2 oxidation 22 °C exchange current, i_o, A/cm^2
TiC	8×10^{-8}
ZrC	3×10^{-8}
VC	2×10^{-7}
Cr_3C_2	8×10^{-6}
Mo_2C	4×10^{-5}
WC	1×10^{-5}
Pt	3×10^{-2}

The exchange currents on tungsten carbide and molybdenum carbide are clearly superior but are still three orders of magnitude lower than platinum [12], which is included in table 1. A general consensus of this work on tungsten carbide electrocatalysts is that for the best hydrogen oxidation activity, the surface of the tungsten carbide must be slightly oxidized. This may be carried out either by gently heat treating in oxygen or by electrochemical oxidation in the presence of hydrazine. Whichever method is used, it serves to remove excess surface carbon and is also believed to render the tungsten carbide surface carbon deficient. Ross et al. [18] examined a variety of tungsten carbides and compared the electrocatalytic activity to the surface structure probed by Auger electron spectroscopy. In addition, gas-phase volumetric adsorption of hydrogen was measured. The results are reproduced in table 2.

Table 2. Correlation of gas-phase and electrochemical H_2 adsorption with the electrocatalytic activity of WC for H_2 oxidation in acid.

Preparation	Volumetric adsorption/ µmole BET m^{-2}	Capacitance (0-0.4 V)/ µF cm^{-2}	Current density/µA cm^{-2} at 0.2 V, 22 °C 1 M H_2SO_4	Reference
AEG-Telefunken	7	475	2	Ross et al. [18]
W_2C	2.5	330	1.9	
Ventron	0	62	0.2	
Starck	0	< 50	0.4	
MRC	0	< 50	0.2	
WO_3 + CO (600 °C)	0.5	<< 50	0.09	
W + CO (1100 °C)	N/A	1100 (geo.)	7 (geo.)	Sokolsky et al. [16]
W + C (2500 °C)	N/A	900 (geo.) 300 (real)	8 (geo.) 2.7 (real)	Mund et al. [14]

It is clear that there is a correlation between hydrogen uptake and the specific electrocatalytic rate for hydrogen oxidation, so there are special surface features required to make tungsten carbide an active electrocatalyst. The surfaces of tungsten carbides, depending on the mode of preparation and pretreatment, may range from having a large excess of metal atoms--in which case, irreversible surface oxide may be formed to act as a poison; to having a large excess of carbon, which is similarly inert for hydrogen oxidation. At some intermediate point, the surface is slightly carbon deficient, active, and does not form an irreversible oxide. The exact surface structure is not known at this time.

By comparison with platinum, the best tungsten carbide electrocatalyst reported is still significantly inferior, as is shown in figure 6. This figure was constructed using

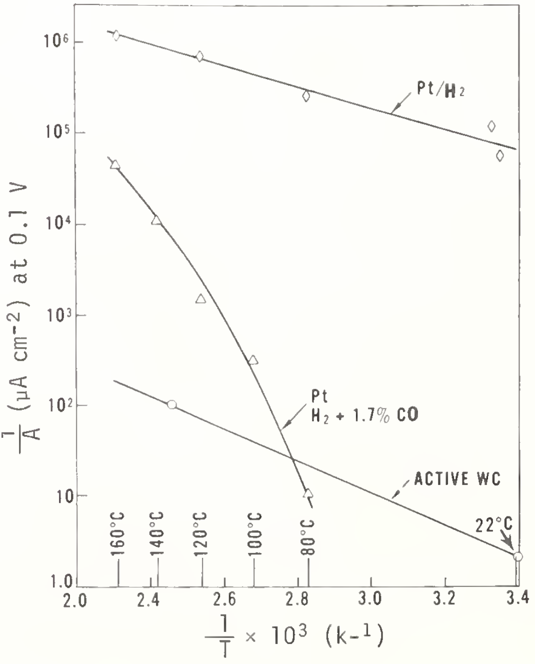

Fig. 6. Specific oxidation rate for hydrogen molecules in acid at 0.1 V vs. rhe. Data extracted from references [12] and [16].

published values of the kinetic rate constants for hydrogen oxidation of platinum in acid [12] and for the oxidation of hydrogen on tungsten carbide [16].

One important operational advantage of tungsten carbide over platinum is that it is poisoned by neither carbon monoxide nor hydrogen sulfide. In this regard, the tungsten carbide electrocatalysts when operating with contaminated hydrogen are superior to platinum at low temperatures. Even with contaminated hydrogen, platinum is still superior at the higher temperatures, since the adsorption isotherm coverages for carbon monoxide and sulfur on platinum decrease and the higher reactivity of the platinum comes intc force.

In conclusion, it is fair to state that although a start has been made towards our understanding of the factors controlling the operation of non-noble metal and nonmetallic electrocatalysts, we are still far behind the comprehension that exists for gas-phase catalysts. On the other hand, the field of electrocatalysis may well be developing faster since we were further behind. There is no doubt that transition metal compounds, due to their stability, will continue to play an important role in this field. As the diagnostic tools for probing the electrocatalyst surfaces are developed, together with the materials developments for new electrocatalysts, then we can expect rapid progress towards lower cost and more highly reactive electrocatalysts that are poison tolerant and decay resistant.

References

[1] Stonehart, P., Bett, J. A. S., and Kinoshita, K., in *Proceedings of Symposium on Electrocatalysis,* San Francisco, M. W. Breiter, ed. p. 275 (The Electrochemical Society, Princeton, New Jersey, 1974).

[2] Ross, P. N. and Stonehart, P., *J. Res. Inst. for Catalysis,* Hokkaido University, 22, 22 (1974); Stonehart, P. and Ross, P. N., *Catalysis Reviews,* 12, 1 (1975).

[3] Ziering, L. K., U. S. Patent No. 3,357,863; Hobbs, B. S. and Tseung, C. C., *J. Electrochem. Soc.* 120, 766 (1973).

[4] Niedrach, L. W. and Zeliger, H. I., *J. Electrochem. Soc.* 116, 152 (1969).

[5] Bagotsky, V. S. and Jofa, S. A., *C. R. (Doklady) Acad. Sci. U.S.S.R.* 53, 439 (1946).

[6] Glemser, O. and Naumann, C., *Z. Anorg. Chem.* 265, 288 (1951).

[7] Stonehart, P., Koren, J. G., and Brinen, J. S., *Anal. Chim. Acta,* 40, 65 (1968).

[8] McHardy, J. and Bockris, J. O'M., *J. Electrochem. Soc.* 120, 53 (1973).

[9] Randin, J. P., Vijh, A. K., and Chughtai, A. B., *J. Electrochem. Soc.* 120, 1174 (1973).

[10] McHardy, J. and Stonehart, P., in *International Reviews of Science,* Phys. Chem. Series 2, A. D. Buckingham and J. O'M. Bockris, eds., Volume 6, p. 171 (Butterworths, London-Boston, 1976).

[11] Hobbs, B. S. and Tseung, A. C. C., *J. Electrochem. Soc.* 122, 1174 (1975).

[12] Vogel, W., Lundquist, J., Ross, P., and Stonehart, P., *Electrochim. Acta,* 20, 79 (1975).

[13] Böhm, H. *Electrochim. Acta,* 15, 1273 (1970).

[14] Mund, K., Richter, G., and von Sturm, F., *Coll. Czech. Chem. Communs.* 36, 439 (1971).

[15] Svata, M. and Zabransky, Z., *Coll. Czech. Chem. Communs.,* 39, 1015 (1974).

[16] Palanker, V. Sh., Baybatyrov, E. N., and Sokolsky, D. V., *Electrochim. Acta,* 20, 51, 71 (1975).

[17] Baresel, D., Gellert, W., Heidemeyer, J., and Sharner, P., *Angew. Chem.* 83, 213 (1971); U.S. Patent No. 3,902,917.

[18] Ross, P. N., MacDonald, J., and Stonehart, P., *J. Electroanal. Chem.* 63, 450 (1975); Ross, P. N. and Stonehart, P., *J. Catal.* 39, 298 (1975).

National Bureau of Standards Special Publication 455, *Electrocatalysis on Non-Metallic Surfaces*,
Proceedings of Workshop held at NBS, Gaithersburg, Md., December 9-12, 1975. (Issued November 1976)

Adsorption and Oxidation of Bromide Ion on Tin Oxide Electrodes

H. Yoneyama and H. A. Laitinen
Department of Chemistry
University of Florida
Gainesville, Florida 32611

Adsorption of bromide ion on a tin oxide electrode proceeded at such a slow rate that adsorption equilibrium took longer than two days to be reached. The electrode became active for oxidation of bromide ion depending on the extent of soaking in an acidic bromide solution. It was found that hydration of the electrode is an important factor to determine its activity for electro-oxidation of bromide ion. An electrode having a high activity lost its activity owing to surface oxidation upon polarization into the discharge potential region of bromide ion.

Key words: Adsorption; anodic oxidation; electrocatalysis; semiconductor electrode; tin oxide electrode; transparent electrode.

1. Introduction

The tin oxide electrode has been used as a transparent electrode to enable spectrochemical measurements to be made in combination with electrochemical measurements [1][1]. In addition to its optical transparency, this electrode is superior to noble metal electrodes in that it can be used to a high anodic potential with a very low background current [2,3].

Redox reactions of several species have been investigated and it has already been clarified that a mechanism of electron tunneling through the space charge layer formed within the electrode near its surface prevails in electrochemical reactions of species having a more noble redox potential than the flat-band potential of the electrode, except for at least the oxygen evolution reaction [4,5,6].

The position of the Fermi level of redox species of one-electron transfer systems relative to electron levels in a tin oxide electrode should be the same when the redox species have the same redox potential. Inasmuch as the width of gaussian energy distribution of a species is larger than 0.5 V [7], no enormous difference in electrochemical behavior is to be expected for species having redox potentials different by values of the order of 0.01V. Comparison of the current-potential curves of iron (II) phenanthroline and hydrobromic acid, formal redox potentials of which are different by 0.05V, however, revealed an exception to the above expectation. As shown previously [4], the iron-phenanthroline redox couple shows highly reversible behavior both at a highly doped tin oxide electrode and at a platinum electrode, while the bromine/bromide couple shows highly irreversible behavior at a tin oxide electrode. It was already speculated in the previous paper that the abnormal behavior of bromide may be brought about by some interaction between the surface and bromide ion. This study was conducted to elucidate the interaction effect.

---

[1] Figures in brackets indicate the literature references at the end of this paper.

2. Experimental

Tin oxide electrodes were prepared in our laboratory by a method similar to that already reported [8]. An aqueous spraying solution was prepared from stannic chloride and hydrochloric acid containing the desired amount of antimony trichloride. The solution was repeatedly aspirated onto a quartz or glass plate heated at around 500°C.

After mechanical polishing with 0.05μ alumina, the electrode was washed in a stream of water by rubbing gently with paper towels. It was then dipped in isopropanol for one hour, washed with de-ionized water for 30 minutes, soaked in nitric acid for 30 minutes, and finally washed with de-ionized water for 30 minutes. The chemical pretreatment was followed by drying the electrode at 130°C for over 15 hours. Just before using the electrode, it was polarized twice by applying a triangular potential sweep at a sweep rate of 5 mV/sec between 0.2V/(vs.SCE) and a potential sufficient to give an anodic current of $10 \mu A/cm^2$. The first potential scan was aimed to remove impurities from the electrode surface and the second one to verify the cleanness of the electrode. The design of the cell used was similar to that reported earlier [3]. Electrical contact was made with a silver ring.

In order to monitor the amount of adsorbed bromide ion on the tin oxide electrode, conventional γ-counting was conducted using a sodium iodide scintillation crystal (Dumont 3292) as a detector. The electrode was washed with several portions of de-ionized water for 30 seconds followed by two 30 second washing intervals with flowing water in the mounted cell. The electrode was then de-mounted and washed for 30 seconds in each of three beakers of de-ionized water. The washing time (3 minutes total) was selected so as to achieve reproducibility with minimal loss due to desorption. A semilogarithmic plot of washing time against apparent amount of bromide suggested a first order desorption rate-limited process. The rate constant determined for the process was $0.086\ min^{-1}$. The amount of adsorption was determined from the counting results at 3 minutes, correcting to zero time by extrapolation using the experimental desorption rate constant.

Current-potential curves were obtained by a triangular potential sweep method at a sweep rate of 5mV/sec or 10mV/sec. The nominal carrier concentration of the electrode was determined by using Schottky-Mott plots of differential capacitances of the electrodes measured at 1 KHz.

3. Results

3.1 Radiochemical studies

Figure 1 shows the number of adsorbed bromide ions as a function of soaking time when an electrode ($N=1.5 \times 10^{20}$ carriers/cm^3) was soaked in hydrobromic acid solutions. Notice that the time scale is changed at a middle point of the abscissa. The figure shows firstly, that adsorption progressed very slowly and secondly, that the number of adsorbed bromide ions was dependent on the concentration of bromide ion in the solution.

Figure 2 shows the number of adsorbed bromide ions as a function of polarization potential just after the electrode was subjected to the pretreatment. The electrode was held at each polarization potential for 15 minutes. Preliminary results showed that 15 minutes of polarization was enough to give a fixed amount of adsorption. The figure shows that potential of maximum adsorption was different for two electrodes having different carrier concentrations.

Figure 3 shows current-potential curves of tin oxide electrodes in one molar hydrobromic acid. The potential necessary for discharge of bromide ion was different among the electrodes of different carrier concentrations on account of different tunneling probabilities. It is found by comparing this figure with figure 2 that the potential of the maximum adsorption corresponds to the potential at the leading edge of the anodic curve, and that a negligible amount of adsorbed bromide can be expected under conditions of steady state discharge of bromide ion.

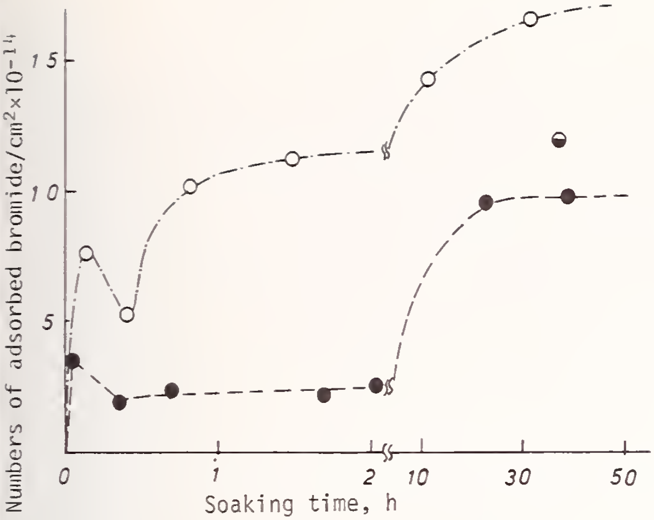

Fig. 1. Numbers of adsorbed bromide ion as a function of soaking time. $N = 1.5 \times 10^{20}$ carriers/cm^3. ○ = 1M HBr; ⊖ = 0.05M HBr; ● = 0.2M HBr.

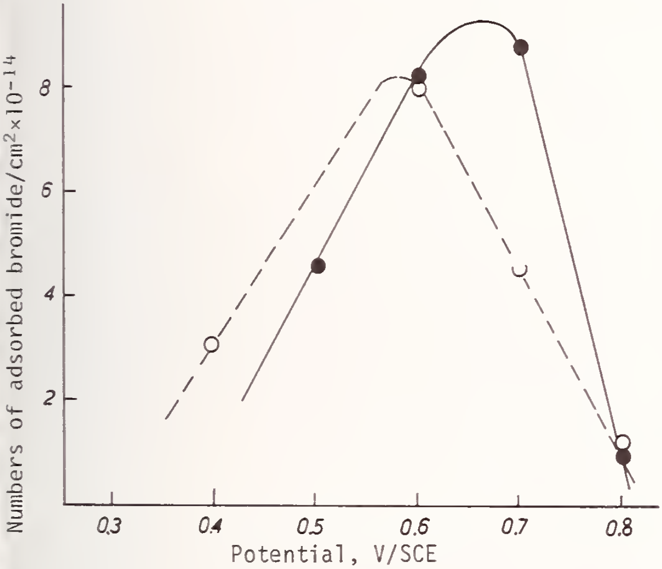

Fig. 2. Numbers of adsorbed bromide ion as a function of polarization potential. Polarization: 15 min in 1M HBr; ○, $N = 5.4 \times 10^{20}$ carriers/cm^3; ●, $N = 1.5 \times 10^{20}$ carriers/cm^3.

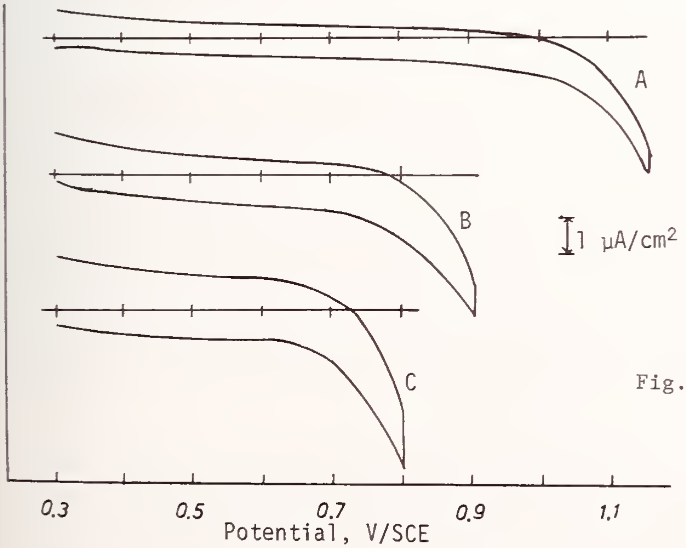

Fig. 3. Current-potential curves of tin oxide electrodes having different carrier concentrations. Polarization: 5mV/sec in 1M HBr;
A:$N = 8.2 \times 10^{18}$ carriers/cm^3;
B:$N = 1.5 \times 10^{20}$ carriers/cm^3;
C:$N = 5.4 \times 10^{20}$ carriers/cm^3.

3.2 Electrochemical studies

When a tin oxide electrode was soaked in 1M $HClO_4$ containing 10^{-2}M HBr, the current-potential curves were gradually changed with soaking time. A typical result is shown in figure 4. The potential at the leading edge of the anodic curve shifted in the negative direction and simultaneously a reduction peak of bromine became clear.

Figure 5 shows a comparison of current-potential curves between electrodes soaked under different conditions. The electrode giving the solid line was soaked for 5 hours in 1M $HClO_4$ containing 10^{-2}M HBr, while the electrode giving the dash-dotted curve was soaked in the same solution for a shorter time of 1.5 hours. However, only the latter electrode was soaked in 1M $HClO_4$ for 140 hours before soaking in the acidic bromide solution.

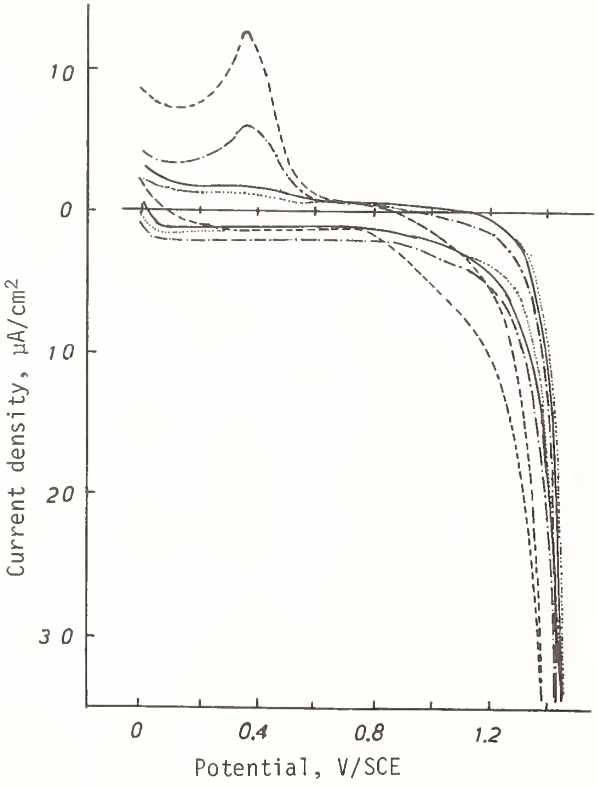

Fig. 4. Effect of soaking time on current-potential curves of a tin oxide electrode in 10^{-2}M JBr/1N $HClO_4$. N = 5.4 x 10^{20} carriers/cm^3; sweep rate 5mV/sec —— 0.25h; .... 19 h; .-.-.- 40h; ---- 125 h.

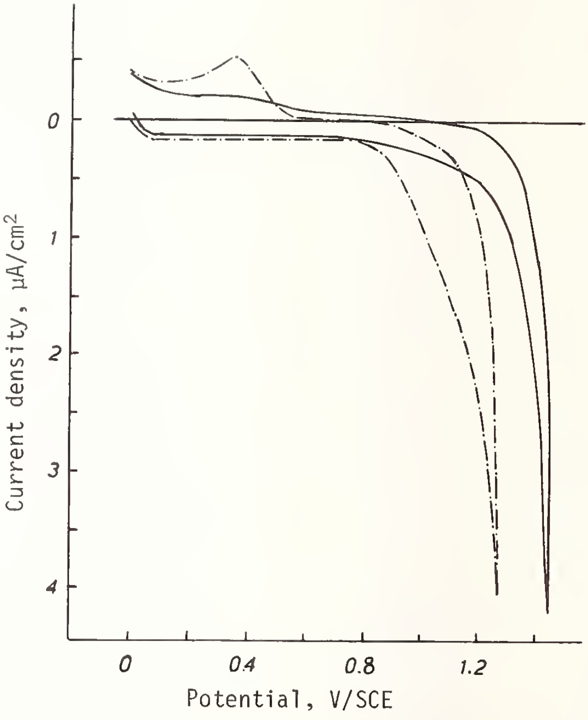

Fig. 5. Effect of soaking in 1N $HClO_4$ on current-potential curves of a tin oxide electrode in 10^{-2}M HBr/1N $HClO_4$. N = 5.4 x 10^{20} carriers/cm^3. sweep rate 10 mV/sec .-.-.- soaked in 1N $HClO_4$ for 140 h and then in 10^{-2}M HBr/1N $HClO_4$ for 1.5 h; ____ soaked in 10^{-2}M HBr/1N ClO_4 for 5 h.

From the results in this figure, therefore, it is recognizable that soaking in an acid solution, not necessarily in a bromide solution, is important for the electrode to increase activity for oxidation of bromide ion.

Figure 6 shows current-potential curves of a tin oxide electrode in 1M HBr when the electrode was soaked in the electrolyte for 24 hours. The potential sweep was continuously repeated. The first and third potential sweep started at 0V, while the second at 0.7V. The first potential sweep gave a sharp anodic peak, the area of which roughly corresponded to

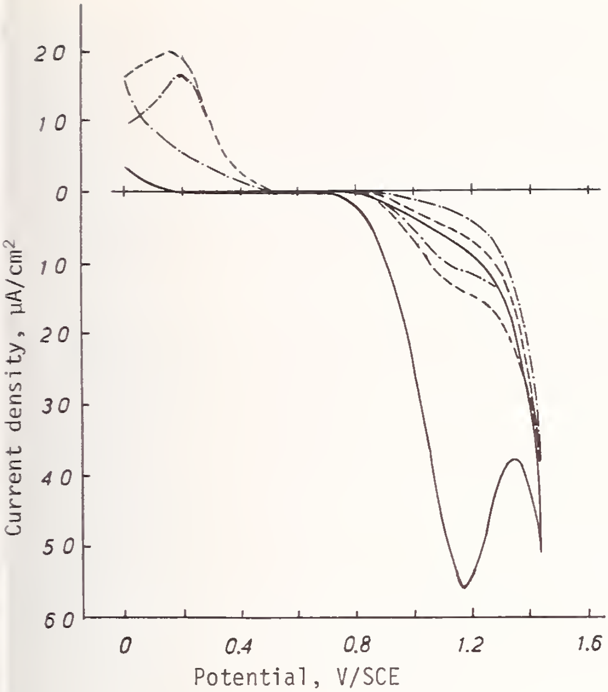

Fig. 6. Current-potential curves of a tin oxide electrode in 1M HBr. N = 2.1 x 10^{20} carriers/cm^3. Sweep rate 5mV/sec. The electrode was soaked in 1M HBr for 24 h. ____ 1st, ---- 2nd, .-.-.- 3rd.

seven times the number of Sn-0 sites on the surface if the roughness factor of the electrode surface was assumed to be two. Therefore, we cannot conclude that the peak corresponds only to oxidation of adsorbed bromide ions. With repetitive polarization cycles, however, the peak was successively depressed, and finally completely disappeared. Once the electrode had been brought into the stage, the anodic peak was never recovered by soaking again in the solution for the same period as before. However, a tendency to recover the activity for oxidation of bromide ion was noticeable by soaking the electrode for a period of the order of a week or longer.

4. Discussion

Judging from a recent study by the transmission infra-red technique on surfaces of tin oxide disks [9], prepared by pressing fine powders of hydrolysis products of tin chloride, the surface of a tin oxide electrode of the present study might have many different constituents such as coordinatively unsaturated tin site, hydroxyl groups, chlorine and coordinatively saturated tin sites, when the electrode was prepared at around 500°C. Relative numbers of the various sites would be dependent upon the exact conditions of preparation, and modified by the pretreatment of the electrode although not in a known manner. The exact physical as well as chemical conditions of the pretreated electrode were, therefore, unfortunately unclear, though the electrode surface was judged to be electrochemically clean.

Oxide electrodes usually show dependency of their flat-band potentials on the pH values of electrolytes. This is connected to dissociation of acidic surface hydroxyl groups [5,10]. The observation that the electrode pretreated in the manner mentioned in the experimental section showed a similar dependency, as had already been reported [3,4], suggests that some portion of the electrode surface was already occupied by hydroxyl groups, just when the pretreated electrode was soaked in a solution. Nevertheless, the present study can be successfully interpreted by taking into consideration of promotion of hydration with soaking time.

When a tin oxide electrode is soaked in an acid solution, the cyclic voltammogram of the electrode gradually changes with soaking time. The main changes are in the back ground current and anodic potential limit of the electrode. These changes are characteristic of hydrated electrodes [11] and were found to be removed by repetitive triangular potential sweeps made in a manner used in the pretreatment of the electrode. Therefore, the hydration structure seems not to be stable at a high anodic potential. Murray et.al. reported that treatment by hot concentrated HCl or 0.1M NaOH was necessary to impose immediate hydrolysis on the electrode [12]. These findings in addition to the present results support the idea that a tin oxide surface becomes hydrated at a slow rate.

It is clear from the result in figure 5 that the first important step to improve the activity for oxidation of bromide ion is the hydration step with formation of -Sn-OH sites. The results shown in figure 1 reflects the fact that the rate of hydration of the electrode surface was low. Possible soaking time of the order of days is required in 1M $HClO_4$ to complete this step.

The second step is adsorption of bromide ion on hydrated sites of the electrodes. In this process, adsorption must take place in such a manner to fulfill an equilibrium relation between the hydration sites and bromide ions in the solution, which is suggested in eq.(1),

$$-Sn-OH + H^+ + Br^- \rightleftarrows -Sn-Br + H_2O \qquad (1)$$

It will not take much time to complete this step which is analogous to complexation of aqueous tin (IV) ions by bromide.

The third step is oxidation of adsorbed bromide ions. Taking into account the fact that the oxidation wave at the first potential seen in figure 6 was higher by far than that expected for a monolayer coverage, a catalytic process possibly takes part in the oxidation process.

$$-Sn-Br \rightarrow -Sn^{(+)} + 1/2\ Br_2 + e^- \qquad (2)$$

$$Sn^{(+)} + Br^- \rightarrow Sn-Br \qquad (3)$$

From the point of view of semiconductor electrodes, appearance of the oxidation wave at a highly hydrated electrode suggested the formation of surface states, promoted by soaking. Surface states associated with the oxidation of bromide ion are -Sn-Br sites originating from hydrated sites.

Loss of the activity for oxidation of bromide ion by repetitive polarization run was seemingly brought about by oxidation of previously hydrated sites of the surface.

$$-Sn^{(+)} + H_2O \rightarrow -SnO + 2H^+ + e^- \qquad (4)$$

This view is supported by the result in figure 2 that a negligible amount of bromide ions is retained on the electrode surface when it is polarized under conditions of steady state discharge of bromide ions.

5. Conclusion

The present study revealed a case in which hydration of the electrode plays an important role in affecting the kinetics of charge transfer between electrode and solution species. Inasmuch as oxides are inevitably subjected to surface hydration though the rate and degree of hydration will vary for different oxides and conditions studied, careful consideration of the surface condition will be necessary when electrokinetic studies of adsorbable species are conducted at oxide electrodes.

6. Acknowledgement

We would like to thank the National Science Foundation for support of this program and also Professor M. L. Muga for kind advice in the radiochemical studies.

7. References

[1] Kuwana, T., Ber. Bunsenges. Phys. Chem., 77, 858 (1973).
[2] Strojek, J. W. and Kuwana, T., J. Electroanal. Chem., 16, 471 (1968).
[3] Laitinen, H. A., Vincent, C. A. and Bednarski, T. M., J. Electrochem. Soc., 115, 1024 (1968).
[4] Elliott, D., Zellmer, D. L. and Laitinen, H. A., J. Electrochem. Soc., 117, 1343 (1970)
[5] Möllers, F. and Memming, R., Ber. Bunsinges. Phys. Chem., 76, 469 (1972).
[6] Memming, R. and Möllers, F., ibid., 76, 475 (1972).
[7] Vanden Berghe, R. A. L. and Gomes, W. P., ibid., 76, 481 (1972).
[8] Kim,H. and Laitinen, H. A., J. Amer. Ceramic Soc., 58, 23 (1975).
[9] Thornton, E. W. and Harrison, P. G., J. Chem. Soc. Farady Trans.I, 71,461 (1975).
[10] Lohmann, F., Ber. Bunsenges. Phys. Chem., 70, 428 (1966).
[11] Kim, H. and Laitinen, H. A., J. Electrochem. Soc., 122, 54 (1975).
[12] Moses, P. R., Wier, L. and Murray, R. W., Anal. Chem., 47, 1882 (1975).

National Bureau of Standards Special Publication 455, *Electrocatalysis on Non-Metallic Surfaces*, Proceedings of Workshop held at NBS, Gaithersburg, Md., December 9-12, 1975. (Issued November 1976)

Cathodic Pyrophosphate-Lead Dioxide Electrode Reaction Properties

C. O. Huber, T. A. Berger, and R. E. Reim
Department of Chemistry and Laboratory for Surface Studies
University of Wisconsin-Milwaukee
Milwaukee, Wisconsin 53201

In the vicinity of +0.4 volts vs. S.C.E. in pH 8 solution pyrophosphate yields a cathodic current selective over orthophosphate at the lead dioxide electrode. Several aspects of this response were examined using α-electroplated lead dioxide on a platinum base and using mixed α-β wax-bound lead dioxide electrodes prepared from the powdered material. Scanning electron microscope results indicated the topographical nature of the wax-bound electrodes. Current-voltage plots indicated an absence of a limiting current and relatively high residual currents as the potential becomes more cathodic. Scanning cyclic voltammetry suggested adsorption of reactive species. Capacitance and coulometric studies indicated clear evidence of adsorption and showed that the current was necessary to the desorption step. Current vs. concentration studies allowed fits to electrosorption models within certain concentration ranges. From these data estimates of some thermodynamic quantities were made. An electrode reaction process involving quasi equilibrium adsorption of the electron transfer product followed by desorption of a plumbous-pyrophosphate complex is discussed.

Key words: Amperometry; cyclic voltammetry; electrosorption; Langmuir; lead dioxide; pyrophosphate; Temkin; wax-bound electrode.

1. Introduction

The conduction band of certain n-type metal oxide semiconductors involves the outer s orbital of the metal. Electron mobilities and electron densities are several magnitudes larger than for the usual transition metal oxides. Examples of this group are ZnO, SnO_2 and PbO_2.

Lead dioxide exists in α and β crystalline forms [1].[1] The structures have been described by Thomas and are closely related with octahedral packing. X-Ray analysis has been used to distinguish the α and β polymorphs [2,3] and to estimate individual concentrations in a mixture.

Resistivities of α and β lead dioxide at 25 °C are reported to be 1×10^{-5} ohm·m and 4×10^{-5} ohm·m, respectively. The temperature coefficient of

---

[1] Figures in brackets indicate the literature references at the end of this paper.

resistivity is positive and relatively large, +0.07%/°C. Hall effect studies have been reported to indicate concentrations of 10^{21} electrons per cm^3 [4].

Lead dioxide has been reported with stoichiometries from $PbO_{1.66}$ to $PbO_{1.98}$ with the latter value apparently more representative. Evidence to support the non-stoichiometry as due to interstitial excess lead atoms has been reported [4].

When lead dioxide is used as an electrode a cathodic current is obtained in the presence of pyrophosphate in the vicinity of +0.4 v vs. S.C.E. Orthophosphate does not show a corresponding current. Some aspects of the electrode reaction are presented and discussed here.

2. Electrode Preparation

In the work reported here, electroplated α lead dioxide was deposited onto platinum from an alkaline lead acetate bath at 0.04 A/m^2 [5]. All plating solutions were stirred. At the pH values used in the experiments reported here, the β crystal form would not be expected to persist [4], and therefore was not used. Wax- or plastic-bound lead dioxide electrodes were prepared by simply mixing 85% by weight of reagent grade powdered PbO_2 (as purchased) with the liquid form of the binding material. In the case of paraffin wax,the partially-hardened slurry was pressed to form cylinders 6.4 mm or 3.2 mm in diameter and 2-3 cm in length.

In the pressing step a connecting metal terminal was incorporated into one end of the electrode body. The other end was used as the electrode face. Sides were covered with wax. Completed electrodes had resistances of 1000 ohms or less. Molded electrodes using polyester resin were also prepared. No significant distinctions in the behavior based on the binder material could be observed. Surface renewal of these electrodes was easily accomplished via slicing or abrasion.

Scanning electron microscopy was used to examine the topography of the surface face of the wax-bound electrodes. The scans obtained and the associated data show that PbO_2 particles protrude from the surface (fig. 1), that the surface of PbO_2 particles are porous and intricate (fig. 2), and

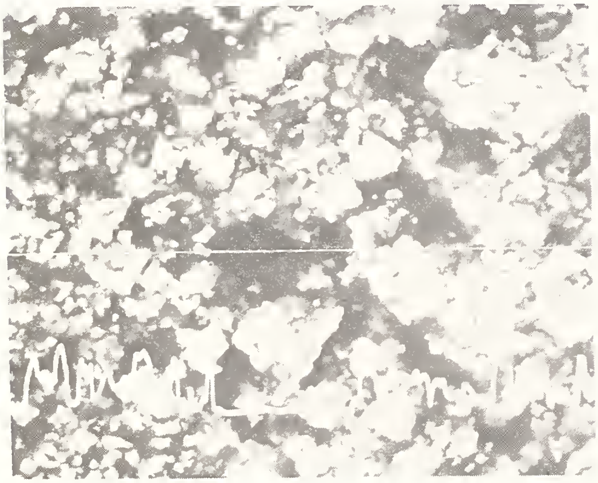

Fig. 1. Compositional scan of pressed wax-bound lead dioxide electrode surface. Superimposed line scan of total x-ray intensity. X 1000.

Fig. 2. Compositional scan of a typical lead dioxide particle. X 10,000.

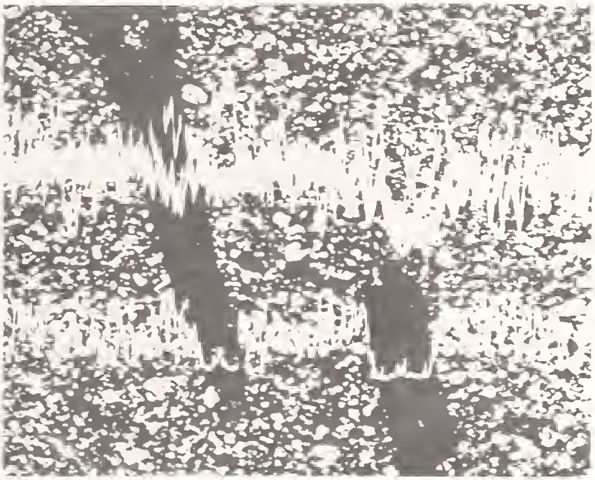

Fig. 3. Compositional scan of a polished wax-bound lead dioxide electrode surface with Pb x-ray line scan.

that attempts at polishing the surface generate a wax film which tends to obscure the lead dioxide from exposure to the solution (fig. 3). These SEM data and optical microscope studies showed that particle sizes remain unchanged during fabrication of the electrodes.

3. Results and Discussion

3.1 Current-Voltage Plots

Manually obtained current vs. voltage plots show that near 0.4 v vs. S.C.E. at pH 8 the residual current is very low. At more cathodic voltages other electrolyte constituents, and also orthophosphate when present, contribute to the observed current. A limiting current is not observed. The

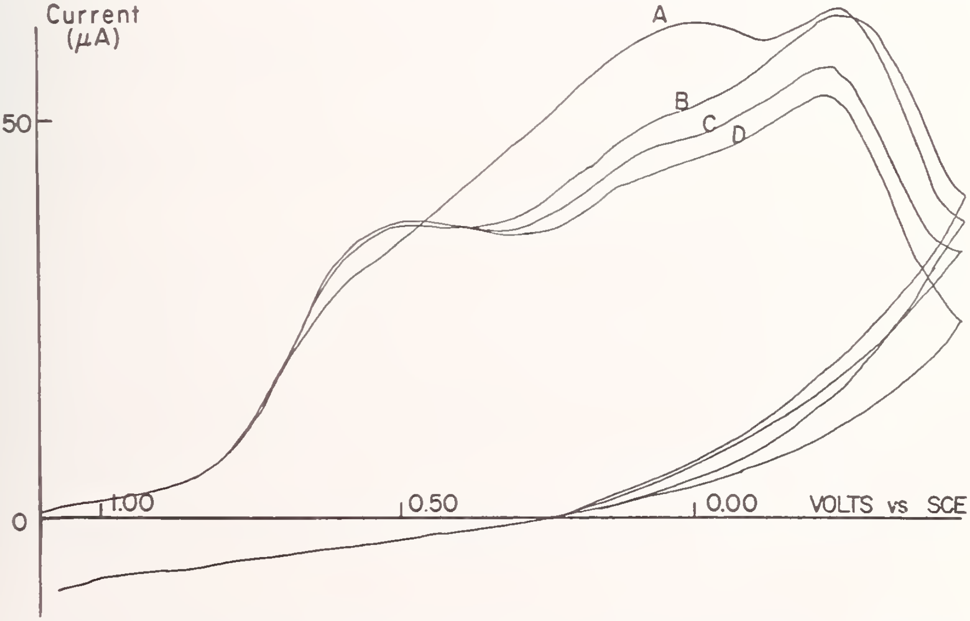

Fig. 4. Scanning voltammetry curves. 3.84 volts/min. After 50 cycles and: A, allowed to stand at open circuit for one minute; b, C, and D, cycled successively.

pyrophosphate current diminishes as pH increases above 8 whereas in the vicinity of pH 7 the selectivity to pyrophosphate over orthophosphate diminishes, thus pH 8.0 was selected for these studies.

Scanning voltammetry experiments with α electrodes, illustrated in figure 4, show that the electrode reaction is irreversible. A pre-peak attributable to adsorption of product appears on the second and successive scans. Both the parent peak and the post-peak (attributed to adsorbed reactant) decrease somewhat on successive scans. As scan rate is increased the height of the post-peak relative to the parent peak is observed to increase markedly, while that of the pre-peak decreases. These effects correspond to change in amounts of adsorbed electron transfer step reactant and product respectively.

3.2. Capacitance

The circuit described by McMullen and Hackerman [6] was modified slightly to provide for automatic applied D.C. potential control. Solutions were made from triple distilled, organic free water and reagent grade chemicals. Capacity measurements of α lead dioxide in ammonium nitrate buffer of pH 8.0 are presented in figure 5. Curves B and C show distinct enhancement of double layer capacity due to pyrophosphate. Comparisons of capacity measurements in buffer at a mercury electrode at -0.25 to -0.75 v *vs*. S.C.E. lead to a roughness factor for lead dioxide of 3.4, a value in good agreement with previous workers [7,8].

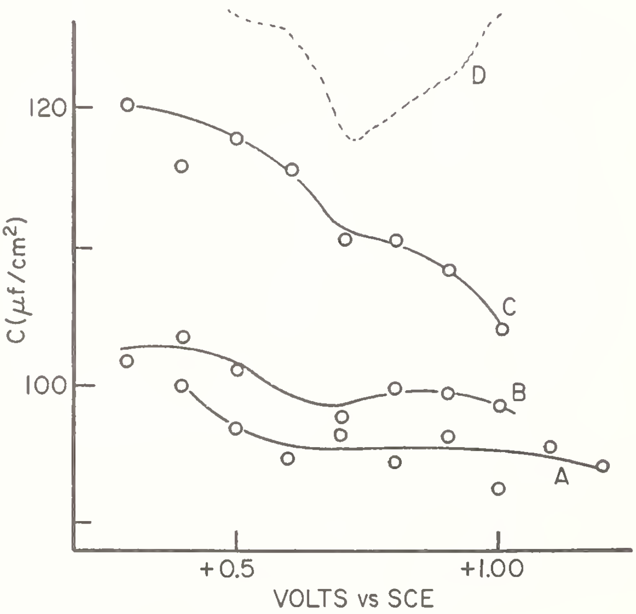

Fig. 5. Differential double layer capacity measurements on α-PbO_2 electrodes: A, in 0.1N NH_4NO_3 buffer of pH 8; B, same as A plus $1.1 \times 10^{-}$M $P_2O_7^{-4}$; C, same as A plus 3.1×10^{-2}M $P_2O_7^{-4}$; D, reported for 0.18M KNO_3 [7].

3.3. Coulometry

In these experiments the electrode was allowed to attain a stable residual current in pyrophosphate-free buffer. The electrode was then immersed in a buffered pyrophosphate solution and coulombs measured for a prescribed time, typically 4.0 minutes, with either open or closed (0.35 v *vs.* S.C.E.) circuit. The electrode was then removed from solution, rinsed with water, and placed in a new buffer containing no pyrophosphate at closed circuit. A decaying current-time (*i.e.*, stripping) curve was obtained indicating depletion of the surface pyrophosphate. Some results are summarized in figure 6 in which a saturation effect appears to be indicated.

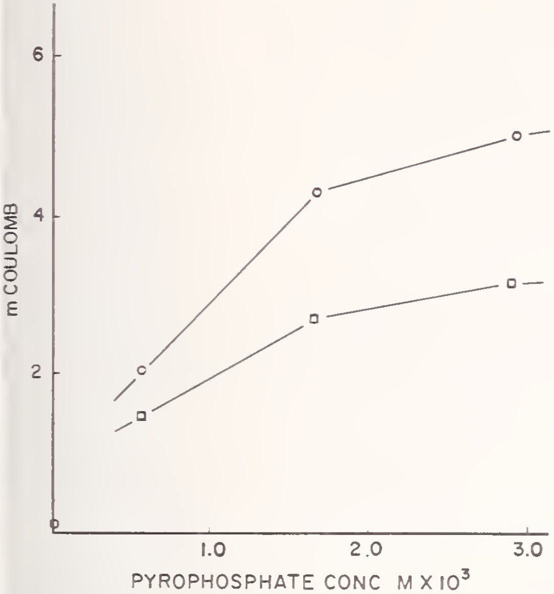

Fig. 6. Coulombs for adsorption and desorption of pyrophosphate. (⊙), Adsorption step; (⊡), Desorption step.

When the new buffer step was begun at open circuit for up to 4 minutes, the number of desorbed coulombs were within 5% of the number obtained with the circuit closed immediately. For the α electroplated electrode the time at open circuit could be as much as 30 minutes with no significant decrease in desorption coulombs. These results suggest that non-electroactive desorption is small, but that possibly the wax-bound electrodes are attacked more readily by solvent and buffer species than are the electroplated electrodes. The α-electroplated electrodes showed adsorption saturation effects in shorter times and with lower numbers of coulombs than the wax-bound version.

3.4. Amperometry

Potentiostatic current *vs.* concentration measurements allowed the best quantitative data because a given electrode surface could be used without disruption or disturbing while successive concentration increments were introduced and because competing effects of other anions could be minimized by maintaining a potential at which residual currents were very small.

With the wax-bound electrode a linear 1/i *vs.* 1/C relationship was found for lower pyrophosphate concentrations observed (0.4 to 3 × 10^{-4} *M*). The electroplated α-form did not yield such linearity. At somewhat higher concentrations both electrodes yielded linear i *vs.* log concentration data over at least a five-fold concentration range. The nominal (no roughness correction) current densities were in the range of 0.10 and 0.006 A/m^2 for the α-plated and the wax-bound electrodes, respectively.

A quasi equilibrium mechanism can be proposed:

$$\text{lattice } PbO_2 + HP_2O_7^{-3} \underset{k_{-1}}{\overset{k_1}{\rightleftharpoons}} \text{lattice } PbO_2 \cdot PbP_2O_7^{=} + 2e^- + H^+ \qquad (1)$$

$$\text{lattice } PbO_2 \cdot PbP_2O_7^{=} \xrightarrow{k_2} \text{lattice } PbO_2 + PbP_2O_7^{=} \qquad (2)$$

where $k_2 << k_1$ or k_{-1} and $i \simeq "i_2" = k_2\theta$. It can be shown [9] that applying a Langmuir model to this chemisorption process results in

$$\frac{1}{i} = \frac{1}{k_2} + \frac{1}{KCk_2} e^{-\frac{2F}{RT}\eta}$$

where $K = k_1/k_{-1}$ and C is pyrophosphate solution concentration. For small values of η the linear reciprocal current vs. reciprocal concentration observed was used to estimate the apparent adsorption equilibrium constant (Table I).

Table I

Thermodynamics Estimations
(ΔG°, ΔH° in kcal/mol)

Electrode	Model	Temp	K	ΔG°	ΔH°	ΔS°
Wax-bound	Langmuir	30°C	4 ± 1 × 10³	-5		
	Temkin	2.9°	0.85 × 10³	-3.7		
	Temkin	23°	2.6 × 10³	-4.6		
	Temkin	35°	5.8 × 10³	-5.3		
					9.9	42 e.u.
α-plated	Temkin	20°	0.62 × 10³	-3.6		
		30°	1.3 × 10³	-4.3		
		40°	2.0 × 10³	-4.7		
					10.5	49 e.u.
	Clausius-Clapeyron				10.4	

The Temkin isotherm adsorption model based on free energy of adsorbate deposition linearly dependent on surface coverage, θ, yields:

$$\theta = \frac{RT}{r} \ln(K^\circ C) + \frac{2F}{r}\eta$$

where K° is the apparent standard adsorption equilibrium constant and r is an empirical parameter [9]. The relationship applies to intermediate coverages. The linear i vs. ln concentration properties found for the system examined here correspond to the assumption that $i = k_2\theta$, i.e., that the desorption step energetics are relatively independent of coverage. This situation correlates to the product containing electrode material. The corresponding values obtained are summarized in Table I. Each of the evaluations was performed at three temperatures and with these data ΔS and ΔH values were estimated.

The heat of adsorption at the α-plated electrode was also computed using

$$\ln\frac{C_2}{C_1} = \frac{\Delta H^\circ}{R}\,\frac{T_2-T_1}{T_1T_2}$$

at constant apparent coverage (see Table I).

The free energy of formation of $Pb(P_2O_7)^=$ in water solution at 25° is 8.6 kcal/mol based upon stability constant values reported by Costly and Farr [10]. The data here suggest that the surface bond may resemble that of the soluble complex with the pyrophosphate ligand satisfying two of the octahedral coordination sites.

Heiland, Gileadi, and Bockris [11] have examined the adsorption of benzene on platinum and report an entropy change of 50 entropy units. They suggest that displacement of solvent molecules from surface sites might account for the relatively large positive entropy shift for larger molecules. Similar reasoning may be applied to the case of the relatively large pyrophosphate ion.

The similarlity of results with both the α-electroplated and the wax-bound α-β mixture electrodes used here suggests that these surface reactions are not specific for a particular crystal structure. Qualitative results in this laboratory using β-electroplated lead dioxide electrodes support this view.

4. References

[1] Thomas, U. B., Trans. Electrochem. Soc., 94, 42 (1948).
[2] Brar, A. S. and Dupo, R. F., J. Electrochem. Soc., 116, 116 (1969).
[3] Kordes, D., Chem. Ing. Tech., 38, 638 (1966).
[4] Mindt, W., J. Electrochem. Soc., 116, 1076 (1969).
[5] Ruetschi, P., Angstadt, R., and Cahan, B., ibid., 106 547 (1959).
[6] McMullen, J. J. and Hackerman, N., ibid., 106, 341 (1959).
[7] Carr, J. P., Hampson, N. A., and Taylor, R., J. Electroanal. Chem., 27, 109 (1970).
[8] Hampson, N. A., Jones, P. C., and Phillips, R. F., Can. J. Chem., 45, 2039 (1967).
[9] Gileadi, E., Kirowa-Eisner, E., and Penciner, J., *Interfacial Electrochemistry,* Addison-Wesley Publ. Co., Inc. (1975).
[10] Costly, B. D. and Farr, J. P. G., Chemistry and Industry (London), 42, 1435 (1968).
[11] Heiland, W., Gileadi, E., and Bockris, J. O'M., J. Phys. Chem., 70, 1207 (1966).

National Bureau of Standards Special Publication 455, *Electrocatalysis on Non-Metallic Surfaces*,
Proceedings of Workshop held at NBS, Gaithersburg, Md., December 9-12, 1975. (Issued November 1976)

ELECTROLYSIS BY FOREIGN METAL MONOLAYERS

R.R.Adžić, A.R.Despić, D.N.Simić and D.M.Dražić

Institute of Electrochemistry, ICTM and
Faculty of Technology and Metallurgy,
Belgrade, Yugoslavia

Catalytic effects of foreign metal monolayers deposited at underpotentials have been found in the case of Fe^{2+}/Fe^{3+} redox reaction on gold, oxygen reduction on gold, and oxidation of some small organic molecules on platinum. It was found that the catalytic effects of foreign metal monolayers originate in the change of surface electronic properties and the change of energy of adsorption of oxygen or oxygen-containing species for Fe^{2+}/Fe^{3+} and oxygen reduction respectively. In the case of formic acid oxidation foreign metal monolayers decrease the hydrogen adsorption on platinum thus preventing the formation of the main poisoning species.

Key words: electrocatalysis; foreign metal monolayers; Fe^{2+}/Fe^{3+} reaction; formic acid oxidation; oxygen reduction; underpotential deposition.

1. INTRODUCTION

Most of the work in electrocatalysis has so far been concerned with the effect of the nature of electrode material. However, it is quite conceivable that the state of the electrode surface can have profound influence on the rate of the heterogeneous reactions and one of the problems in the study of electrocatalysis in the past was the lack of detailed knowledge of the electrode surface layer and its relation to the bulk properties. Over the past few years various ultra-sensitive experimental techniques of studying surfaces have been developed that are capable of detecting minor amounts of material on the surface and providing other information needed to characterize a surface. Thus, in situ application of reflectance spectroscopy [1, 2, 3][1] recently revealed a large change of surface electronic properties of an electrode when foreign metal monolayers are deposited at potentials more positive than the reversible one (underpotential deposition). This is a consequence of a strong interaction of the valence orbitals of adsorbed atoms with a band structure of the substrate [1]. There is no general agreement about the nature of such layers but a prevailing view is that these layers are partially charged adsorbed atoms [1, 4, 5]. Their effective charge is presumably quite low [1, 5]. It seemed that underpotential deposition (UPD) of foreign metal monolayers is a convenient way to modify electrocatalytic properties of surfaces and in general to study the surfaces effects in electrocatalysis.

The catalytic effects of foreign metal monolayers have been established for several reactions. It was recently shown that such layers can substantially increase the rates of Fe^{2+}/Fe^{3+} couple on gold [6] and

---

[1] Figures in brackets indicate the literature references at the end of this paper.

oxygen reduction on gold [7], and the rate of formic acid oxidation on platinum [8, 9]. The purpose of this paper is to review some of these results and to report on more recent work on this subject.

2. EXPERIMENTAL

The studies have been carried out in 1 M $HClO_4$ solution prepared from triply distilled water with the first distillation from alkaline permanganate and closed in a pyrex glass electrolytic cell. A polycrystalline platinum plate to serve as the test electrode was polished to obtain a mirror finish. After polishing the electrode was washed with KOH and HNO_3 solutions and stored in triply distilled water. The counter electrode was also a platinum electrode. The reference electrode was a saturated sulphate electrode connected via Luggin capillary.

Nitrogen was bubbled through the electrolyte before measurements. It was purified by passing over copper turnings and then through molecular sieves. All measurements were carried out at room temperature.

Potential sweep and steady-state polarisation measurements were made first in the absence and then in the presence of known amounts of a cation in solution, whose catalytic activity was to be tested. The cation concentration was varied in the range between 10^{-6} and 10^{-2} M.

The standard circuitry included a Tacussel potentiostat, PAR Universal programmer and a Hewlett-Packard XY recorder. Potential sweeps have been made at a rate of 50 mV/sec. Steady-state data have been obtained by holding the electrode at a constant potential and following the decrease in current with time. The currents were read on a Data Precision digital multimeter after 90 sec.

3. RESULTS AND DISCUSSIONS

3.1. Fe^{2+}/Fe^{3+} redox reaction on gold

The kinetics of Fe^{2+}/Fe^{3+} redox couple has been determined on gold electrode in sulfuric acid solution in the potential range where the underpotential deposition of silver occurs. Subsequently silver was added to the electrolyte as Ag_2SO_4, in the concentration of 1.10^{-4} to 1.10^{-3} M. An immediate rise of current followed the addition of Ag^+ which persisted after sufficient time was allowed for adsorption of silver to attain equilibrium. A quantitative investigation has been made using potentiostatic techniques and running the redox process at low overpotentials so that the exchange current density could be determined from the linear part of the current-overpotential function in the absence and presence of silver in solution. Fig. 1 shows the effects of silver monolayer on the rate of Fe^{2+}/Fe^{3+} couple on gold. A two-fold increase in the exchange current density is seen in both anodic and cathodic polarizations.

Several phenomena have been considered as possible causes of this catalytic effect. It was shown that the double layer effect should decrease rather than increase the reaction rate [6]. The silver monolayer can change the electronic density-of-states at the surface which may be a possible explanation of this effect. Although the analogy is somewhat distant it appears that the resonance tunneling, observed with metal-adsorbed layer-vacuum interface [10], should also be considered as a possible explanation.

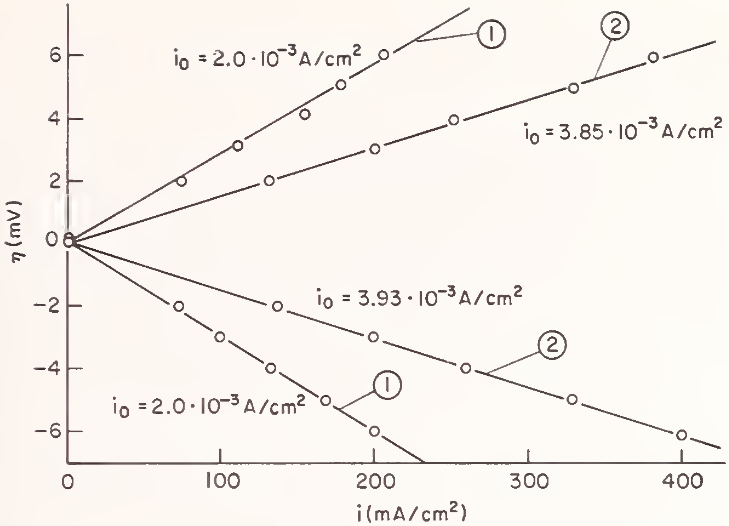

Fig. 1. Steady-state current-potential curves of gold in 2$\underline{M}$ H_2SO_4 containing 0.1$\underline{M}$ $FeSO_4$ and $Fe_2(SO_4)_3$. Curves 1, without Ag^+; curves 2, with $1.10^{-3}\underline{M}$ Ag^+ in solution

3.2. Oxygen reduction on gold

Gold is known as a poor catalyst for oxygen reduction. This was explained by its electronic structure which has no unpaired d-electrons which could engage in bonding with oxygen or oxygen-containing species [11], or by the fact that gold is a poor peroxide-decomposing catalyst [12]. It was shown that the monolayers of Bi, Pb, Tl formed by UPD have pronounced catalytic effect on oxygen reduction. The monolayer of Cd showed very small effect while Cu showed inhibitive effect [7]. Fig. 2 shows the effects of bismuth monolayer on oxygen reduction on gold in 1M $HClO_4$ electrolyte.

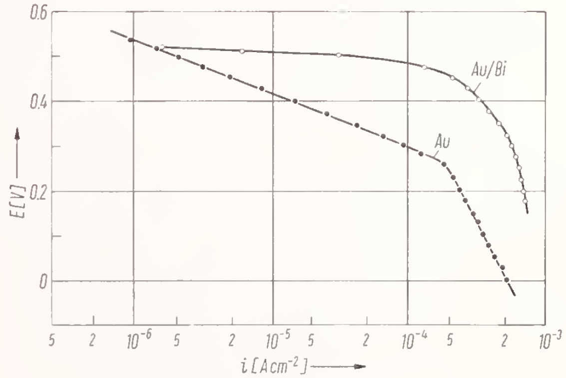

Fig. 2. Steady-state current-potential curve for oxygen reduction on bare gold, and gold covered with a monolayer of bismuth in 1$\underline{M}$ $HClO_4$.

It is seen that the linear Tafel relationship existing in the absence of Bi^{3+} turns into an almost horizontal line in the presence of the latter, up to the current density region in which the diffusion limiting current is expected.

In acid media significant UPD of Tl, Cd and Pb falls in the potential range where the oxygen reduction becomes controled by diffusion and hydrogen evolution commences. This prevents the estimation of the full merit of these metal adatoms as catalysts and the measurements at some more convenient pH are warranted.

The effect of depositing foreign metals on the decomposition of hydrogen peroxide as the intermediate in oxygen reduction has also been tested for the case of two metals with opposing effects on the latter, i.e. for Bi and Cu. Both metals exhibited similar and considerable electrocatalytic effects. Hence, the inhibitive effect of Cu concerns the initial stage of oxygen reduction, i.e. the formation of hydrogen peroxide.

It was suggested that the rate determining step for O_2 reduction on gold is the exchange of the first electron [13, 14]. The same behavior is found in this work [7]. If the rate-determining step is

$$O_2(ads) + e \rightarrow O_2^- (ads) \tag{1}$$

the reaction is led into the "peroxide path" and the most probable further step involves the reaction of O_2^- with hydronium ion followed by another electron transfer and formation of H_2O_2.

If in a peroxide free solution the first electron-transfer is rate-determining, preceded by one or the other type of adsorption of the oxygen molecules there are several possibilities of electrocatalysis [7]. However, the most probable possibility is the energy barrier for electron transfer changed favorably by the change in the energy of oxygen adsorption. In presence of a foreign adsorbed atom the potential at the boundary of the metal surface is perturbed sufficiently as to produce a new surface state. These surface states can play a role in determining adsorption properties of such electrodes, and lead to a more favorable adsorption of oxygen on covered gold then on the bare gold surface.

3.3. Oxidation of formic acid on noble metals

It was recently shown that the monolayers of Cd, Tl, Bi and Pb have striking catalytic effects on oxidation of formic acid on platinum [9]. The UPD of these cations follows the reduction of platinum oxide. Considerablly lower currents are obtained in the region of hydrogen adsorption indicating a supression of hydrogen adsorption by monolayers of these cations [9].

The potential sweep diagram in the presence of formic acid,without the addition of cations whose catalytic activity has been tested, is shown in Fig. 3 (dashed line). The addition of Pb^{2+}, which undergoes UPD in that potential range, is shown to have a profound effect, causing a large catalytic effect. The peak current in anodic direction is about two orders of magnitude larger than in pure formic acid solution. Similar, although smaller effects were observed by Schwarzer and Vielstich [15] produced by traces of lead in sulfuric acid solution. Other authors also have observed the benefitial effects on oxidation of formic acid on platinum of the substances normally regarded as poisons. Breiter [16] and Brummer et al. [17] have noticed the effects of copper monolayer and Angerstein-Kozlowska et al. [18] of electrodeposited mercury and acetonitril. The effects however were small and no systematic study was undertaken.

Quantitative investigation has been carried out of the steady-state polarization of the platinum electrode in pure formic acid and in the presence of different concentrations of Pb^{2+} ions. The obtained Tafel relationships are shown in Fig. 4.

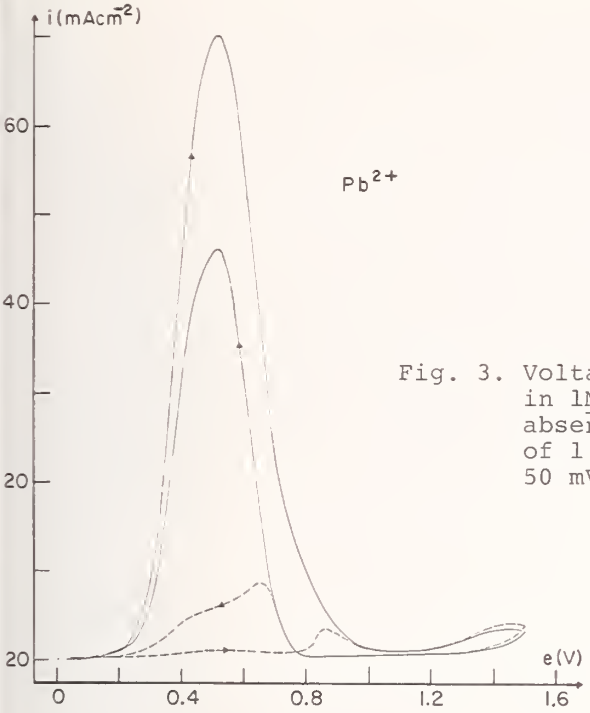

Fig. 3. Voltammetry curves of platinum electrode in 1M $HClO_4$ containing 0.265 M HCOOH in the absence (dashed line) and in the presence of 1.10^{-3}M Pb^{2+} (full line). Sweep speed 50 mVs^{-1}.

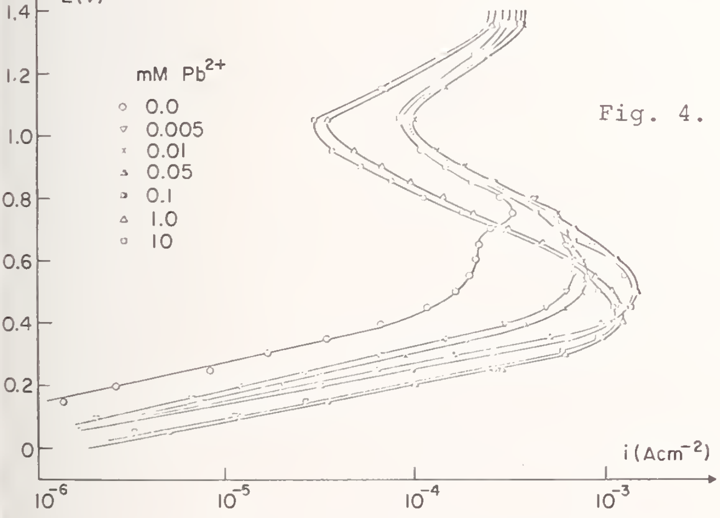

Fig. 4. Steady-state current-potential curves of platinum in 1M HClO containing 0.265M HCOOH in the absence and presence of Pb^{2+}. Lead concentration is indicated in the graph.

The curve in pure formic acid exhibits a linear Tafel region with a slope of ~ 120 mV and other well known features at more anodic potentials of oxide formation.

Addition of very small amount of Pb^{2+} (5.10^{-6}M) results already in catalysis of HCOOH oxidation. The effects are considerable in the linear Tafel region but even higher in the region of limiting current density. The Tafel slope seems to be preserved for that concentration but decreases somewhat as the concentration of Pb^{2+} is increased up to 1.10^{-4}M. Further increase of the Pb^{2+} concentrations increases the Tafel slope back to the value of 120 $mVdec^{-1}$.

At higher anodic potential the situation is somewhat different. The largest catalytic effect is obtained at the concentration of 5.10^{-5}M Pb^{2+}. With higher concentration there is a decrease of catalytic effect and even inhibition at more anodic potentials. At high oxide coverages the effects are small for all lead concentrations. However, only the effects at most cathodic potentials in these plots are of technological importance. It was shown [9] that the reaction order with respect to Pb^{2+} ions appears to be ~ 0.5. However, the changing Tafel slopes with increasing concentration make the meening of such a reaction order questionable.

The reaction mechanism of oxidation of HCOOH on bare platinum has been given very detailed consideration [cf.19]. The formation of several poisoning species makes these studies difficult. It seems that majority of authors agree that the main poisoning species is $\underset{xxx}{C}OH$ whose formation is strongly dependent on the amount of hydrogen adsorbed on the electrode. According Capon and Parsons [20] the carboxyl ad-radical $\underset{x}{C}OOH$, formed in an initial reaction of HCOOH with Pt,

$$HCOOH \longrightarrow \underset{x}{C}OOH + H^{+} + e \qquad (2)$$

reacts immediately with H ad to form $\underset{xxx}{C}OH$

$$\underset{x}{C}OOH + 2Had \longrightarrow \underset{xxx}{C}OH + H_2O \qquad (3)$$

In the main reaction pathway the carboxyl ad-radical undergoes further oxidation:

$$\underset{x}{C}OOH \longrightarrow CO_2 + H^{+} + e \qquad (4)$$

The monolayers of metals investigated decrease the hydrogen adsorption on platinum to a negligible value and thus they could decrease the rate of reaction. That this is the case was proved by the following experiments.

In the absence of foreign metal cations the electrode was held at the open circuit potential, which is in hydrogen adsorption region, for 5 min. The first sweep in the anodic direction (dashed line) shows considerably smaller current than that obtained under conditions of constant cycling as shown in Fig. 5. The same experiment performed in the presence of Pb^{2+} in solution showed different picture (Fig. 6). The first sweep in the anodic direction (full line) gives even higher current than the subsequent sweeps. This suggests that no or very litle poison was formed at open circuit potential in the presence of lead monolayer in contrast to the situation in the absence of lead. Desorption of lead during anodic sweep opens a fresh platinum surface which can sustain the observed huge currents. The difference in the currents associated with the first and subsequent sweep suggests that at higher anodic potentials there is a formation of poisoning species. The reaction giving the poisoning species probably does not involve adsorbed hydrogen in this case. This poison could be again $\underset{xxx}{C}OH$ formed by the disproportionation reaction, or intermediate $\underset{xx}{C}(OH)_2$ or dimer of formic acid anhydride. The catalytic effects at higher anodic potentials besides decreased hydrogen adsorption, if any at those potentials, may be due to the "third body" effect [18]. The adsorbed foreign metal atoms may block inhibitor adsorption or formation by blocking sites for adsorption. From this considerations it appears likely that the investigated catalytic adatoms have a dual effect on the oxidation of formic acid.

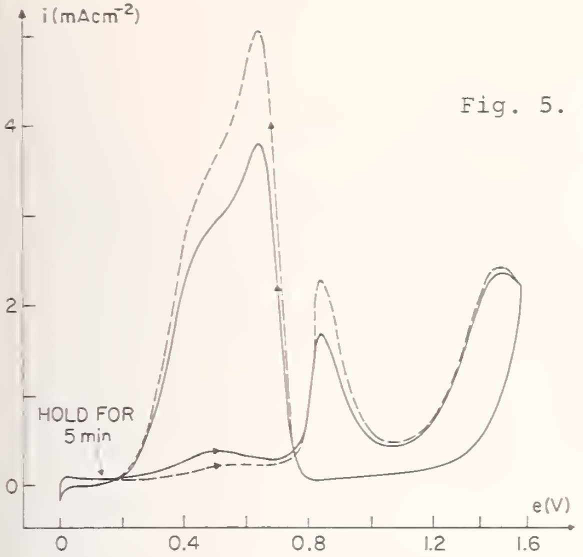

Fig. 5. Voltammetry curve of platinum electrode in 1M $HClO_4$ containing 0.265M HCOOH. First sweep after 5 min at open circuit (dashed line), second sweep (full line). Sweep speed 50 mVs^{-1}.

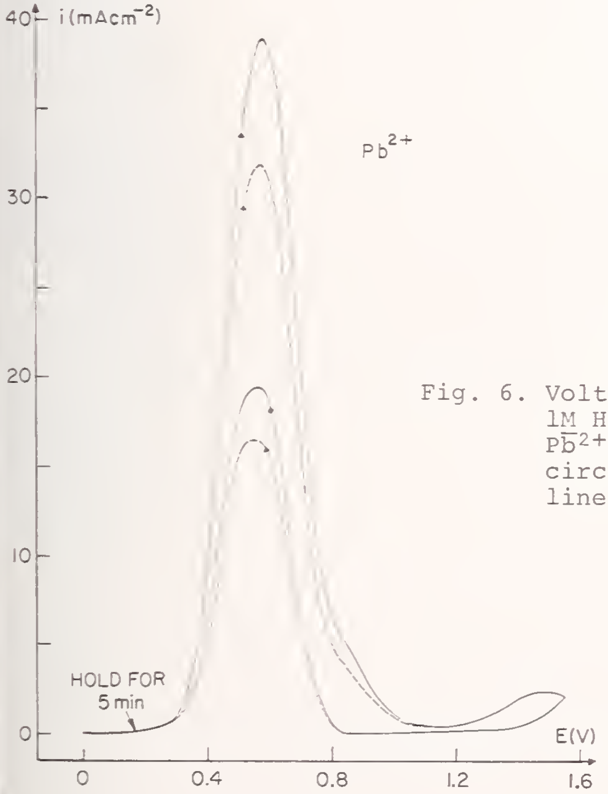

Fig. 6. Voltammetry curve of platinum electrode in 1M $HClO_4$ containing 0.265M HCOOH and 1 mM Pb^{2+}. First sweep after 5 min at open circuit (full line), second sweep (dashed line). Sweep speed 50 mVs^{-1}.

The experiments with Pd and Rh seem to confirm previous explanation. Palladium is known to form no poisoning species and in this case lead monolayer inhibits the reaction (Fig. 7). On the other hand, rhodium behaves similarly to platinum, and in the case of rhodium a large catalytic effects were again observed, as shown in Fig. 8. The effects of lead on oxidation of HCOOH on Ir were practically negligible.

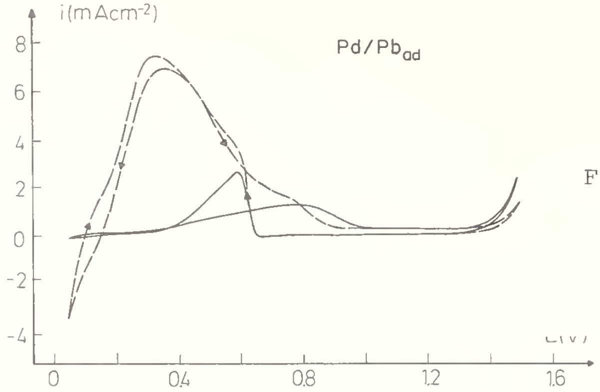

Fig. 7. Voltammetry curve of palladium electrode in 1M $HClO_4$ containing 0.265M HCOOH in the absence (dashed line), and in the presence of 1 mM Pb^{2+} (full line). Sweep speed 50 mVs^{-1}.

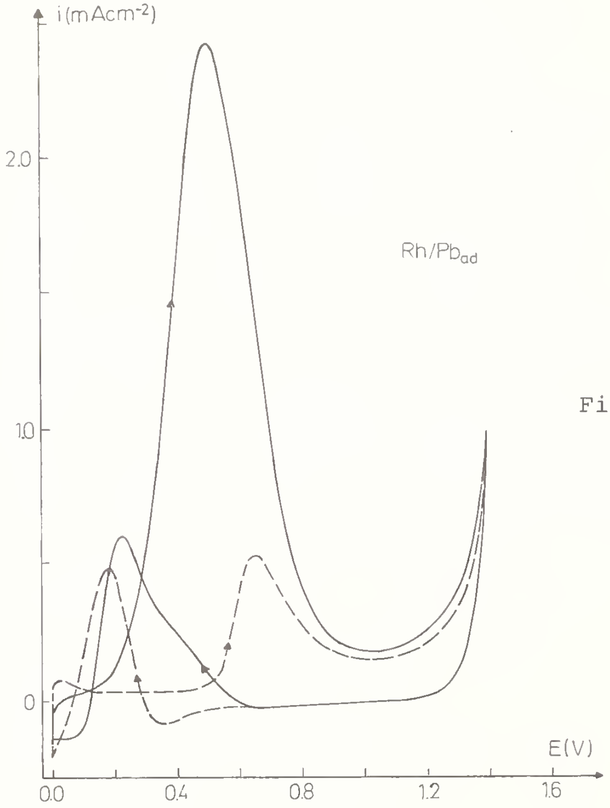

Fig. 8. Voltammetry curve of rhodium electrode in 1M $HClO_4$ containing 0.265M HCOOH in the absence (dashed line), and in the presence of 1 mM Pb^{2+} (full line). Sweep speed 50 mVs^{-1}.

It seems that the minimum polarity model which is used by some authors to explain catalytic effects of alloys can be applied to these systems. The model assumes a complete lack of interaction between neighbouring atoms, the adsorption and catalytic properties being a function of the localized properties of the individual surface atoms. In such a case one could regard the observed catalytic effects on Pt and Rh as an indication of their behaviour if no poisoning species were formed.

If this approximate measure of catalytic activity of Pt and Rh is taken, and that of Pd, Ir and Au obtained without foreign metal monolayers, and correlated with the metal heats of sublimation, one obtains the volcano type curve shown in Fig. 9.

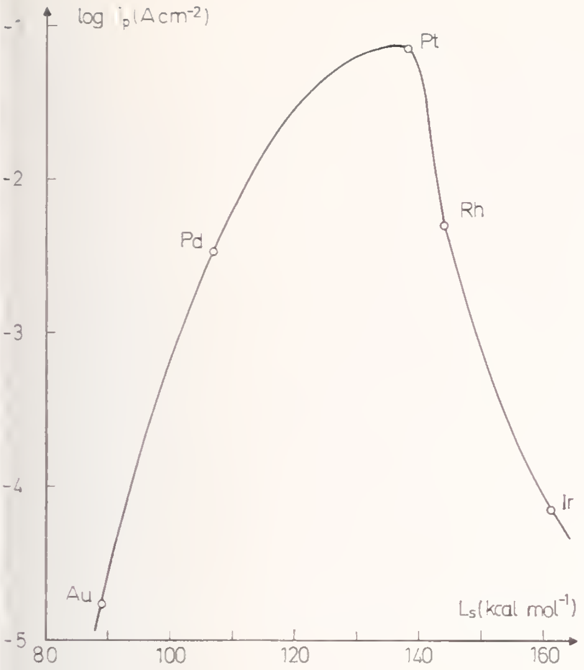

Fig. 9. Plot of the log of the current at the peak in anodic direction for some noble metals vs. their latent heat of sublimation.

Capon and Parsons [19] recently obtained similar curve by plotting the current at the cathodic peak vs. latent heat of sublimation. In this case the correlation of the log i_p was used as the theory requires, and it seems that more quantitative significance can be attached to this result.

4. CONCLUSIONS

Catalytic effects of foreign metal monolayers have been found for several electrode reactions. Fe^{2+}/Fe^{3+} couple belongs to the so called weak interaction case, while the oxygen reduction and formic acid oxidation are representatives of strong interaction case. This demonstrates the importance of surface properties of electrodes in electrocatalysis in general, and calls for a surface-oriented study of electrocatalysts.

The UPD of foreign metal monolayers was shown to be a quite convenient way of modifying surface properties of electrodes. By controlling the electrode potential one controls both the coverage by foreign metal adatoms and the state of their effective charge. However, this quantity is not readily obtainable and one should obtain at least the electrosorption valency of such species. Such data could help the interpretation of catalytic effects and eventually make possible the predictions of catalytic behavior of foreign metal monolayers.

It is likely that the coverages by foreign adatoms are different in the presence and in the absence of reacting species. Therefore, a determination of the coverages during the catalytic reactions is warranted.

REFERENCES

1. R.Adžić, E.Yeager and B.D.Cahan, J.Electrochem.Soc., 121 (1974) 474.
2. T.Takamura, Y.Sato and K.Takamura, J.Electroanal.Chem., 41 (1973) 31.
3. D.M.Kolb, D.Leutloff and M.Przasnysky, Surface Sci., 47 (1975) 622.
4. J.W.Schultze and K.J.Vetter, J.Electroanal.Chem., 44 (1973) 63.
5. D.M.Kolb, M.Przasnysky and H.Gerischer, J.Electroanal.Chem., 54 (1974) 25.
6. R.R.Adžić and A.R.Despić, J.Chem.Phys., 61 (1974) 3482.
7. R.R.Adžić and A.R.Despić, Ber.Bunsenges.Phys.Chem., submitted for publication.
8. R.R.Adžić, D.N.Simić, D.M.Dražić and A.R.Despić, J.Electroanal.Chem., 61 (1975) 117.
9. R.R.Adžić, D.N.Simić, A.R.Despić and D.M.Dražić, ibid., 65 (1975) 587.
10. J.W.Gadzuk, Phys.Rev. B1 (1970) 2110.
11. A.Damjanović and V.Brusic, Electrochim. Acta, 12 (1967) 1971.
12. J.P.Hoare, ibid., 11 (1966) 311.
13. G.Bianchi,, F.Mazza and T.Mussini, ibid., 11 (1966) 1509.
14. A.I.Krasilshchikov, Zh.Fiz.Khim., 26 (1952) 216.
15. E.Schwarzer and W.Vielstich,C.R., 3-ième Journ.Internat. d'Etude de Piles à Combustible, Presses Academique Européennes, Bruxelles 1969.
16. M.Breiter, Electrochem.Acta, 8 (1963) 447.
17. S.Brummer and A.C.Makrides, J.Phys.Chem., 68 (1964) 1448.
18. H.Angerstein-Kozlowska, B.MacDougall and B.E.Conway, J.Electrochem. Soc., 121 (1974) 756.
19. A.Capon and R.Parsons, J.Electroanal.Chem., 44 (1973) 239.
20. A.Capon and R.Parsons, ibid. 45 (1973) 205.

Comment on Paper by R. R. Adžić, *et al.*, "Electrolysis by Foreign Metal Monolayers"

B. D. McNicol

Shell Research, Ltd
Thornton Research Centre
P. O. Box 1
Chester, CH1 35H, England

I have a comment and a question on the paper by Adzic, *et al.* Shell has been working on Pt/Sn catalysts for methanol electro-oxidation for some time and the characteristics of these catalysts are rather similar to those catalysts described by Dr. Adzic. Some of our Pt/Sn catalysts were prepared by a special immersion technique developed by M. M. P. Janssen (Koninklijke/Shell Laboratorium, Amsterdam), whereby the Pt catalyst is electrochemically pretreated prior to immersion in a Sn salt solution. Cyclic voltammetry studies of such catalysts revealed that the hydrogen chemisorption regions of the profiles were reduced in intensity while the oxide formation and reduction regions were shifted significantly. The catalytic activity for methanol electro-oxidation on the Pt/Sn catalyst is about 100 times greater than that of pure Pt. The effect of the Sn promoter on the Pt has been interpreted as a ligand effect [1], thus modifying the Pt adsorption properties.

The method of preparation of the Pt/Sn catalysts seemed readily applicable to finely dispersed Pt such as Pt on carbon. However, with certain Sn salts it was found that the Sn was preferentially taken up by the carbon support. Therefore, I would like to ask whether Dr. Adzic has looked at the influence of metal cations in solution on the activity of supported Pt.

---

[1] Janssen, M. M. P. and Moolhuysen, J., manuscript submitted to *J. Catalysis* for publication.

ELECTROCHEMICAL PROCESSES ON NON-METALLIC SURFACES - 2

National Bureau of Standards Special Publication 455, *Electrocatalysis on Non-Metallic Surfaces*, Proceedings of Workshop held at NBS, Gaithersburg, Md., December 9-12, 1975. (Issued November 1976)

Mechanisms of Electrochemical Reactions on Non-Metallic Surfaces

Ernest Yeager
Department of Chemistry
Case Western Reserve University
Cleveland, Ohio 44106

Oxygen electrocatalysis has assumed new importance because of the involvement of the O_2 electrode in various fuel cells and electrolyzer systems. For O_2 electroreduction to proceed at reasonable current densities requires the adsorption of the O_2 molecule or ion on the electrode surface. Various models for the interaction of such O_2 species with surfaces and the corresponding pathways for the electroreduction are considered. Generally peroxide mechanisms are predominant in aqueous solutions on non-metallic as well as metal surfaces but this leads to less favorable operating potentials for O_2 cathodes. A number of reasonably effective O_2 electroreduction catalysts have been identified for alkaline solutions but so far only high area platinum appears to combine reasonable activity and stability in acid electrolytes. Various electrocatalysts for which results have been reported in the literature are summarized. The electrochemical behavior of various carbons and graphites, lithiated NiO and various defect metal oxides including RuO_2/Ti is considered in some detail relative to O_2 generation as well as reduction kinetics.

Key words: Carbon; electrocatalysis; nickel oxide; semiconductor electrodes; oxide electrodes; oxygen electrochemistry.

1. Introduction

With the energy problems facing many nations, renewed interest has developed in electrochemical energy conversion and storage, and among the various electrochemical devices, particularly fuel cells and water electrolyzers. An important part of most such devices is the oxygen electrode. Unfortunately it is one of the more troublesome parts. The irreversibility of the oxygen electrode leads to excessive voltage losses and restrictions on power densities of the cells. Furthermore, in an effort to achieve an acceptable level of performance, it has been necessary to resort to expensive precious metal oxygen electrocatalysts in very high area forms, which are difficult to maintain over long operating times.

In light of the importance of O_2 electrodes and problems associated with oxygen electrocatalysis, this lecture will be directed principally to oxygen electrode reactions on nonmetallic surfaces.

2. General features of oxygen electrode reactions

The pronounced irreversibility of the oxygen electrode reactions at moderate temperatures has severely complicated mechanistic studies. The exchange current densities for the oxygen electrode are very low--typically 10^{-10} to 10^{-11} A/cm^2 on an effective catalytic surface such as platinum. Consequently the current densities near the reversible potential are generally too low to permit measurements under conditions where the kinetics are sensitive to the reverse as well as forward reactions. Further, the experimentally accessible portions of the cathodic and anodic branches of the polarization curves are sufficiently separated in potential that the surface conditions differ very substantially. Therefore, the cathodic and anodic processes under these conditions are probably not the reverse of each other. To complicate the situation further, the oxygen electrode reactions may proceed through a large number of pathways. This explains why the mechanisms for O_2 generation and reduction are still not fully understood even on platinum, the most extensively used and most studied O_2 electro-reduction catalyst.

Before discussing O_2 electrocatalysis on specific non-metallic surfaces, some of the general features of the possible electrode mechanisms will be considered. O_2 reduction in aqueous solutions requires a strong interaction of O_2 with the electrode surface for the reaction to proceed at a reasonable rate. Three types of models for such interaction have been proposed [1,35][1]. These are shown in figure 1, together with the corresponding reaction pathways for O_2 reduction. The Griffiths model [2] involves a lateral interaction of the π orbitals of the O_2 interacting with empty d_{z^2} orbitals of a transition element, ion or metal atom with back bonding from at least partially filled d_{xz} or d_{yz} orbitals of the transition element to the π^* orbitals of the O_2. This type of interaction should lead to a weakening of the O-O bond with a corresponding lengthening of this bond. The Vaska complexes [e.g., $Ir(O_2)Cl(CO)(PPh_3)_2$] appear to form such complexes with O_2 [3,4]. These compounds are selective oxidation catalysts for cyclic olefins [5]. The formation of a strong metal-to-oxygen interaction results in a weakening of the O-O bond and an increment in the length of this bond [6]. Sufficiently strong interaction of this type may lead to the dissociative adsorption of O_2 with probably simultaneous proton addition and valency change of the transition element in the manner represented by Pathway I in figure 1, followed by reduction of the $M(OH)_2$ to regenerate the catalyst site. Sandstede et al.[7,8] have attempted to explain oxygen reduction with square pyramidal Co(II), Fe(II) and Fe(III) complexes as well as on the thiospinels on the basis of such π bonding. Tseung, Hibbs and Tantram [9] have proposed that O_2 reduction on Li-doped NiO changes from a non-dissociative to dissociative mechanism

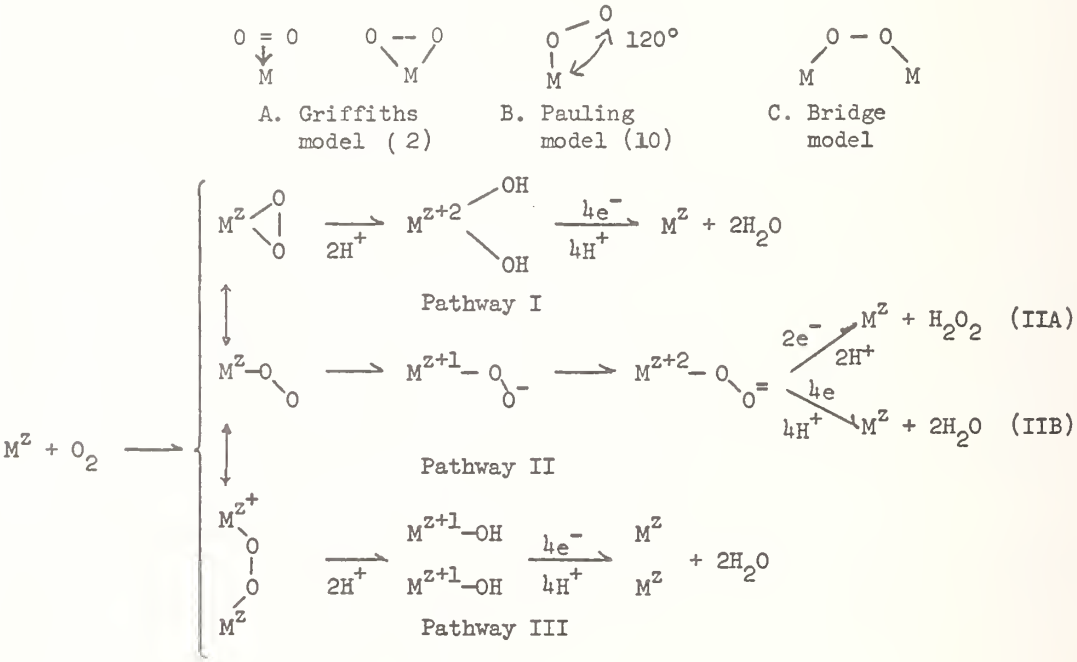

Figure 1. Models for adsorbed O_2 and corresponding reaction pathways for O_2 electroreduction.

---

[1] For reviews see ref. [1,35]. Figures in brackets indicate the literature references at the end of this paper.

above the Neel point (200°C for their ~10-atom % Li doped NiO) in order to explain the increment in catalytic activity in KOH hydrate melts above the Neel temperature.

It is indeed likely that O_2 reduction does proceed by a dissociative adsorption mechanism on some electrocatalysts. Up to date, however, no unambiguous experimental evidence appears to have been presented for O_2 reduction by such a mechanism on either metallic or non-metallic catalyst surfaces in aqueous solutions at moderate temperatures.

With most transition metal catalysts, the most probably structure for O_2 adsorption is the Pauling model [10] in which sp^2 orbitals of O_2 interact with d_{2} orbitals of the transition metal. The square pyramidal complexes of Fe(II) and Co(II)^{z}; which have good activity for O_2 reduction in acid solutions, appear to involve such an end-on interaction on the basis of esr and other evidence [11]. This adsorption of O_2 is expected to be accompanied by at least a partial and probably complete charge transfer to yield a superoxide and then peroxide state, as represented by Pathway II in figure 1. The adsorption of the O_2 on the square pyramidal complexes of Fe(II) and Co(II) may lead directly to the superoxide state. With somewhat similar oxyhemoglobin complexes of iron, various workers have proposed that O_2 binding to the iron involves O_2^- or $O_2^=$ states with Fe in the III valent state [12-14]. The change in valency state of the transition metal coupled with the change in O_2 oxidation state during formation of the O_2 adduct corresponds in principal to the redox electrocatalyst concept proposed by Beck <u>et al</u>. [15,16].

The further reduction of the O_2 beyond the peroxide state requires rupture of the O-O bond. Such can occur in Pathway IIB through the formation of $O^{\cdot -}$ or HO° free radicals in solution or the simultaneous reduction-bond cleavage (electrochemical desorption) to yield H_2O or OH^-. Neither of these processes are likely to be sufficiently fast at practical operating potentials for O_2 cathodes but the electrochemical desorption is a better candidate. The free energies of formation of the $O^{\cdot -}$ and HO· free radicals in solution are just too high to achieve sufficiently high concentrations for the subsequent homogeneous reactions to proceed at rates corresponding to reasonable current densities at acceptable electrode potentials. Substantial evidence exists for Pathway IIA yielding solution phase peroxide for various metallic and non-metallic electrode surfaces. With non-metallic electrodes such as carbon, graphite and lithiated NiO in aqueous alkaline solutions, significant amounts of peroxide are found in solution and the potential under open-circuit conditions follows the Nernst equation predictions for the O_2-HO_2^- couple [see e.g. ref. 17, 18]. Eventually the peroxide is further reduced at practical O_2 cathodes. The formation of solution phase peroxide as an intermediate, however, is unfortunate since it leads to less favorable operating potentials. With carbon electrodes in alkaline solutions, it is necessary to incorporate a peroxide reduction or decomposition catalyst in the electrode to prevent the buildup to high concentrations of the peroxide within the electrode structure. One possibility is to utilize the spillover effect with the peroxide produced at one site migrating on the surface to an adjacent or nearby site where the peroxide elimination step occurs. This indeed may occur to some extent with high area carbon electrodes containing peroxide elimination catalysts such as Pt or Ag.

Under some circumstances it is possible that the superoxide species $O_2^{\cdot -}$ may desorb to yield the solution phase species. This ion is formed as a reasonably stable entity during O_2 reduction in aprotic solvents [see e.g., ref. 19-22] and probably in carbonate melts [23]. The superoxide ion also has been proposed to be formed in aqueous solutions on Hg [24,25], amalgamated gold [26] and carbon paste [27] cathodes in the presence of surface active agents. Under these circumstances, Divisek and Kastening [24,25] propose that the surfactant molecules displace water molecules from the surface, impeding access of water to the adsorbed $O_2^{\cdot -}$, and thereby inhibiting further reduction. Dubrovina and Nekrasov [26] have proposed that the $O_2^{\cdot -}$ radical may be stabilized through the formation of a complex with the surfactant molecule. In the absence of adsorbed organic species, however, it does not appear that an $O_2^{\cdot -}$ desorption mechanism contributes significantly to the observed current. Rotating disk experiments have rather clearly demonstrated this for graphite [28] and also gold cathodes [29], as will be discussed for the former case later in this lecture.

Pathway III in figure 1 provides an alternate means for bringing about rupture of the O-O bond through the formation of an -O-O- bridge. Such a mechanism may come into play with the proper surface spacing of transition metal atoms or ions in a metal, oxide or thiospinel or in a bimetal complex such as a macrocyclic. The formation of the bridge species requires proper spacing of the two metal species plus partially filled d_{xz} or d_{yz} orbitals to participate in bonding with the sp^2 orbitals of the oxygen. Macrocyclic transition metal complexes of the type $M\text{-}O_2\text{-}M$ been synthesized [e.g., see ref. 30, 31, 36, 37] and appear to occur naturally in hemeythrin.

For any of the mechanisms in figure 1, considerable questions exist as to the reversibility of the O_2 adsorption step at the rather high rates involved with practical O_2 cathodes. For O_2 to bond to M^z will generally require the replacement of a water molecule or anion of the electrolyte--a situation which would normally be expected to be unfavorable to O_2 unless the O_2 adduct has a pronounced dipolar character ($M^{z+1}O\text{-}O^-$) [32, 33]. The reversibility of the formation of such adducts in water and other solvent systems is strongly dependent on the ligands and generally favored in the "picket fence" porphyrins in which the large rather bulky organic groups create an environment more conducive to O_2 uptake [34]. Porphyrins of this type are probably responsible for the relatively good performance of carbon cathodes as O_2 electrodes in blood, but it is doubtful whether they can be rendered sufficiently stable for prolonged use in the strongly acid and alkaline solutions of most fuel cells above 100°C.

At steady state any peroxide formed on the electrode surface must be subsequently further reduced or decomposed. When the O_2 reduction proceeds entirely through a peroxide state on the electrode surface and/or in the solution, the process is usually referred to as "series" whereas when O_2 reduction proceeds simultaneously by a dissociation step without a peroxide state as well as through a peroxide state, the processes are described as "parallel". Peroxide has been detected in the solution phase during O_2 reduction on many metallic and non-metallic electrodes (e.g., Pt, Au, Ag, Pb, Ni, NiO, carbon, graphite) in various aqueous electrolytes at $T < 100°C$. Consequently little doubt exists that the peroxide mechanism is often functional. Some authors have proposed that reduction also proceeds simultaneously through a dissociative adsorption mechanism as a parallel mechanism. Unfortunately the evidence is for the most part ambiguous.[2]

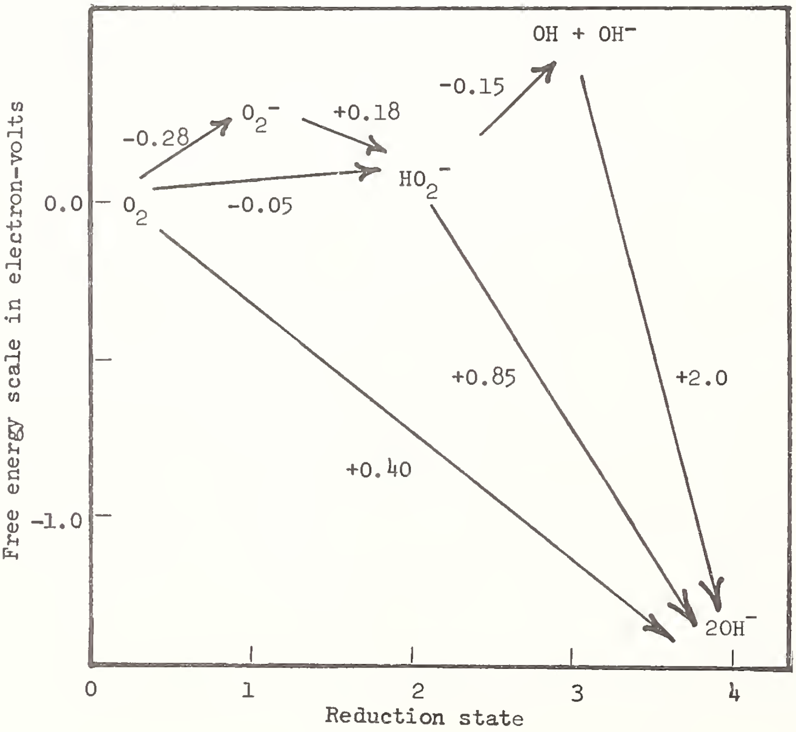

Fig. 2. Free energy relationships for the reduction of oxygen in basic solution at 25°C. Standard reduction potentials in volts are indicated on lines designating steps. Potential for O_2/O_2^- couple from ref. [25]. Multiply ordinates by 23 to obtain free energy in kcal/mol.

---

[2] Damjanovic, Genshaw and Bockris [39] have proposed that their rotating ring-disk data provide evidence for the parallel mechanism on Pt. Their treatment of the kinetics does not consider the peroxide desorption step. This would explain their results [40] without a parallel mechanism.

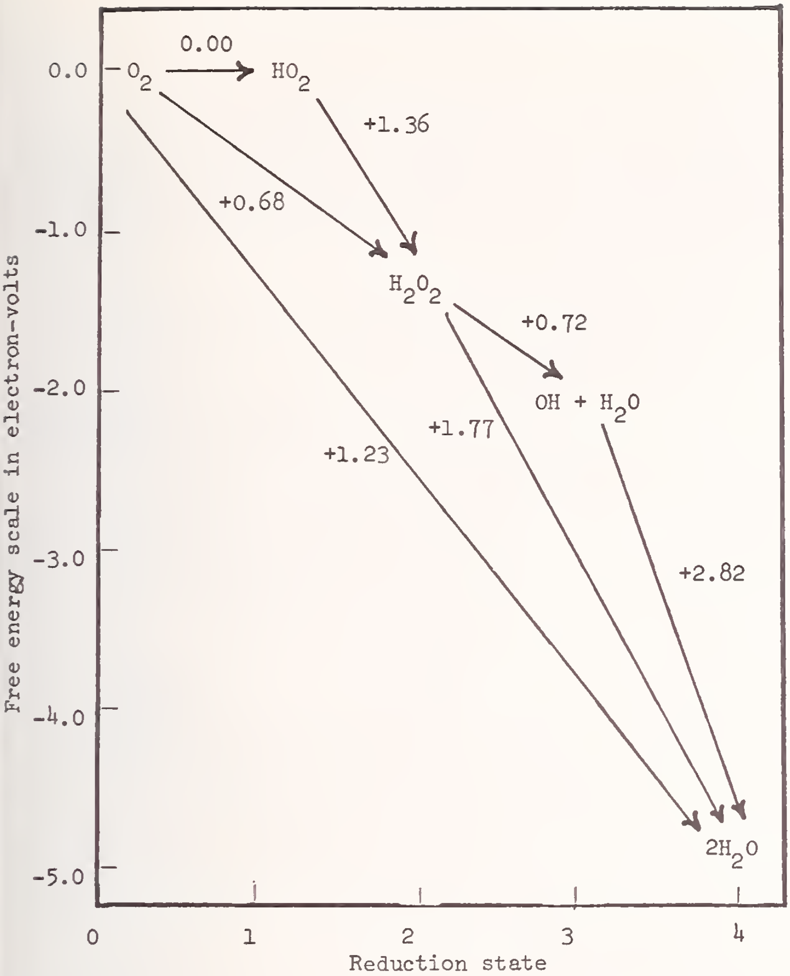

Fig. 3. Free energy relationships for the reduction of oxygen in acid solution at 25°C. Standard reduction potentials in volts are indicated on lines designating steps. Potential for O_2/HO_2 couple calculated from data for O_2/O_2^- (ref. 25) and pK = 4.88 for O_2^--HO_2 (ref. 38). (Multiply ordinates by 23 to obtain free energy in kcal/mol.)

The question of whether O_2 reduction can proceed by a parallel mechanism is more than just academic. The free energy changes and corresponding standard electrode potentials associated with the various O_2 couples are shown in figures 2 and 3 for alkaline and acid solutions. The standard electrode potential of the O_2 - peroxide couple is far less anodic than that for the four-electron O_2 reduction (by +0.45 and -0.53V in alkaline and acid solutions, respectively). Further the O_2-peroxide couple is usually much more reversible than the other steps shown in figures 2 and 3 with the result that the potential is often controlled predominantly by the O_2-peroxide step.

In principle it should be possible for the potential of the O_2-peroxide couple to approach the reversible potential for the four-electron reduction by depressing the peroxide concentration to the equilibrium value for the reaction

$$2HO_2^- = O_2 + 2OH^- \qquad (1)$$

In practice this has not proved possible even with extremely effective peroxide decomposing catalysts under open-circuit conditions because the equilibrium peroxide concentration is extremely low (i.e., 10^{-15}M HO_2^- in 1M caustic). With high area carbon electrodes on which the O_2-peroxide couple has a high exchange current density [e.g., 10^{-4} A/cm^2 (true area)] in alkaline solutions, it has been possible to improve very substantially the performance through the incorporation of very effective peroxide elimination catalysts [see e.g., ref. 41, 68].

3. Summary of Materials Examined as O_2 Electrocatalysts

Table I is a partial list of the various materials which have been examined as O_2 reduction electrocatalysts. Many of the compounds listed in this table have substantial electrocatalytic activity for O_2 reduction in alkaline solutions but do not have sufficient long-term stability. Only a few have significant activity in the concentrated acid solutions and only platinum in ultrahigh area form has combined sufficient activity and stability. A few of these systems will be considered in some detail.

Table 1. Compounds considered for O_2 electroreduction catalysts in the literature.

Type	Example		Literature reference
Metal chelates			
N_2S_2	diacetyl-di(thiophenylbenzhydrazone)[a]	[DT]	7,42,43
N_2O_4	bissalicylaldehyde-o-phenylenediamine[a]	[Pfeiffer]	7,42,43
N_4	tetraphenyl porphyrin[a]	[TP]	7,42,43
	phthalocyanines[a]	[PC]	7,42-44,47
S_4	bisdiphenyldithioethylene[a]		42,43
	polymeric versions of above		42,43
	hemin		48
	Order of activities: for N_4: $Fe > Co > Cu > Ni \sim Mn$ for N_2O_4: $Co > Mn > Fe > Cu > Ni$ for Co II: $N_2O_4 > N_4 > N_2S_2 > O_4 \sim S_4$ for Fe II: $N_4 >> N_2O_2 > N_2S_2 > O_4 \sim S_4$		
Thiospinels			
$Me^aMe_2{}^bS_4$	Me^a = Mn, Fe, Co, Ni, Cu, Zn Md^b = Ti, V, Cr, Fe, Co, Ni also seleno- and telluro-spinels activity: $Co_3S_4 > Ni_3S_4 > Fe_3S_4$		
Disulfides, diselenides, ditellurides			
	Co compounds active; for Cu, activity is highest with disulfide		
Oxides			
Spinels			
Spinels	$Me^aMe_2{}^bO_4$: Co_3O_4, Co_2NiO_4, $CoAl_2O_4$ active		52-55
Tungsten bronzes	M_xWO_3		57-60
Perovskites	Sr_xCoO_3 active		9,56
Other oxides:	NiO (lithiated)		9,18
	RuO_2		61
	Au_2O_3		62
Metals			
Pt and Pt family metals, alloys[b]			65-68, 83-85
Au and Au alloys			62,64
Ag			29,40,63
Carbons			
Ion implanted carbon			17,18,28,29,69,86

---

[a] Cations: Ti, V, Cr, Mn, Fe, Co, Ni, Cu, Zn

[b] The work on Pt is very extensive. For a review see references 75-78.

4. O_2 Electrocatalysis on Carbon and Graphite

On both carbons and graphites of low mineral content, the reduction of molecular O_2 proceeds to hydrogen peroxide in alkaline solution almost quantitatively at low peroxide concentrations. Typical current-voltage curves obtained with the rotating disk technique are shown in figure 4 for the edge and basal planes of stress-annealed pyrolytic graphite in 1M KOH. The hysteresis evident in these slow sweep curves (10 mV/sec) is caused by changes in the oxidation state of various groups present on the edge orientation. Isotopic experiments [70] involving O^{18} and the rotating disk experiments [28] indicate the following mechanism in NaOH and KOH solutions:

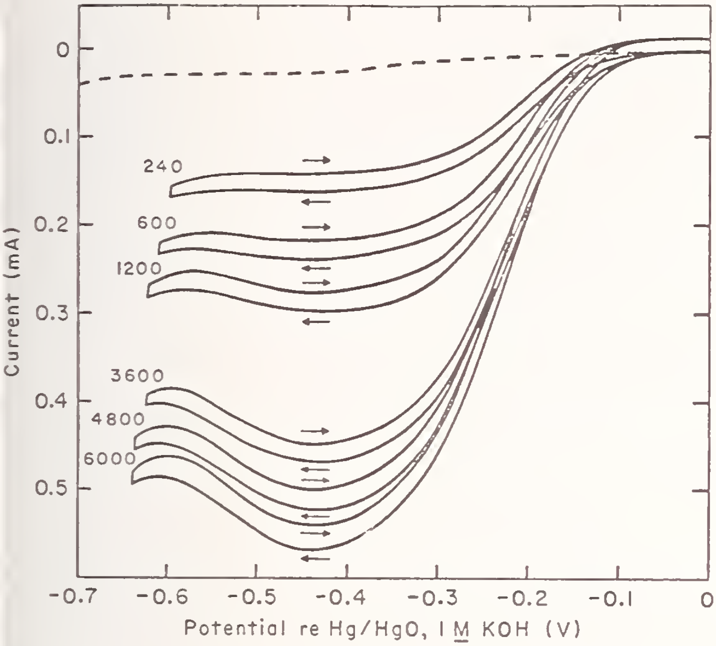

Fig. 4. Reduction of O_2 on high pressure annealed pyrolytic graphite. —— edge orientation, --- cleavage orientation. Electrolyte: 1 M KOH, pressure O_2: 0.97 atm, temperature: 22°C, electrode area: 0.22 cm^2. Rotation rates indicated on curves in rpm. Direction of sweep indicated by arrows. X-ray rocking angle of graphite $\Theta_{1/2}$ = 0.4°.

Step I. $$S + O_2 \rightarrow S - O_2 \qquad (2)$$

Step II. $$S - O_2 + e^- \rightarrow S - O_2^- \qquad (3)$$

Step III. $$\begin{array}{l} S - O_2^- \\ \vdots \\ S - O_2^- \end{array} + HOH \rightarrow \begin{array}{l} S + O_2H^- + OH^- \\ \vdots \\ S + O_2 \end{array} \qquad (4)$$

Step II is ordinarily rate controlling with a transfer coefficient of 0.50 but at high current densities, the potential-insensitive Step I becomes controlling. Corroborating evidence for such an O_2^- adsorption step is to be found in the reversible chemisorption of O_2 on carbon from the gas phase, presumably without bond cleavage, as revealed by esr studies [71]. Step III is quite surprising and is definitely a surface reaction rather than a second order solution-phase reaction between superoxide radicals ($O_2^{-}\cdot$ or $HO_2\cdot$). The fact that Step III is second order in the surface concentration of adsorbed O_2^- indicates that a direct interaction between two adsorbed O_2^- is required for this step. While the kinetic measurements have been carried out principally on various types of graphites, the results for various carbons [17] are sufficiently similar to suggest the same mechanism.

Of particular note is that with single crystal graphite and stress-annealed pyrolytic graphite, the O_2 reduction as well as peroxide oxidation reactions are very inhibited on the basal plane with the exchange current at least three orders of magnitude less on the basal plane than on the edge orientation. Imperfections in the basal plane set a lower limit to the checking of how far the exchange current is depressed on this plane.

This depression of the exchange current on the basal plane may be caused by

1. anisotropic surface-semiconductor properties of the graphite
2. the lack of suitable functional groups or adsorption sites on the basal plane.

The carrier concentration in graphite is rather low near the Fermi level and hence some significant fraction of the applied potential may fall across a space charge region for the basal plane. To check on this, a.c. impedance measurements have been carried out on this plane [72]. The differential capacitance curves and corresponding voltammetry curves are shown in figure 5 for both 1 N NaOH and 1 N H_2SO_4. These curves are in strong contrast to the corresponding curves for the edge orientation [73] which show much structure. The capacitance on the basal plane is much lower than on the edge orientation or on typical metals such as Hg or Au, suggesting that a significant potential drop occurs across a space charge region within the graphite. The potential dependence of the capacitance, however, is close to parabolic rather than the hyperbolic dependence expected for a semiconductor electrode. This may be caused by the high carrier concentration in the graphite; i.e.: $\sim 6 \times 10^{18}$ carriers/cm^3 [74]. Further, the capacitance curves give no indication of specific adsorption, even in the presence of relatively high concentrations of such anions as iodide [72].

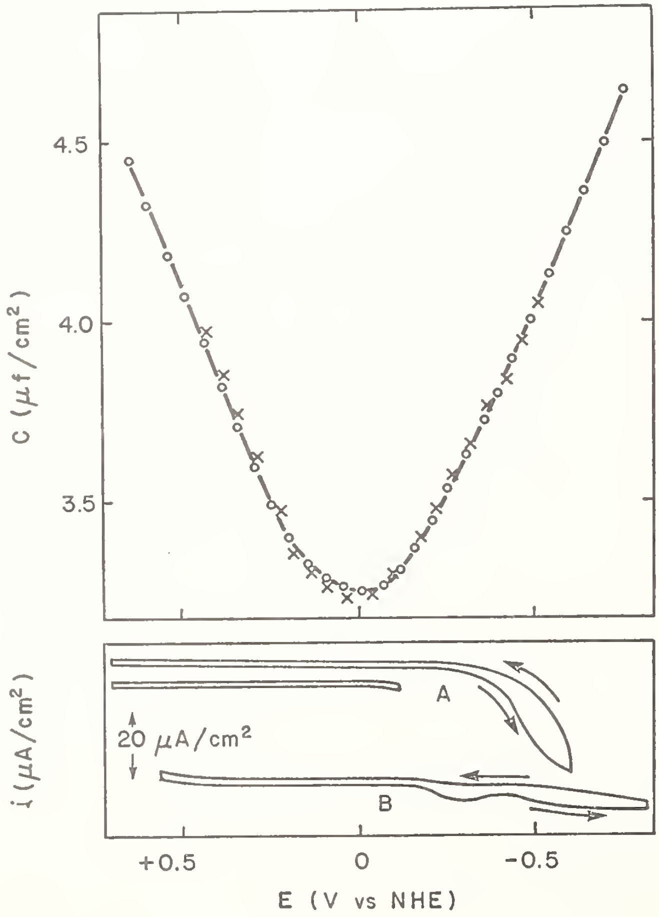

Fig. 5. Capacity-potential and current-potential curves for the basal plane of stress-annealed pyrolytic graphite ($\Delta\Theta_{\frac{1}{2}} \cong 0.4°$) in 1 N H_2SO_4 and 1 N NaOH solutions at 25°C and 1000 Hz (sine wave): x 1 N H_2SO_4; o 1 N NaOH. Scan rate for the current-potential curves 0.1 V/sec, direction of sweep indicated by arrows: A) 1 N H_2SO_4; B) 1 N NaOH.

To check further on the extent to which electrode reactions on the basal plane may be impeded by semiconductor effects, the behavior of the Fe(CN)$_6^{3-}$ - Fe(CN)$_6^{4-}$ redox couple has been examined on this surface [28]. The apparent exchange current density is appromiately 1/3 of that on the edge (1.1 mA/cm^2 on the basal plane as compared with 3.0 mA/cm^2 on the edge in 0.005 $\underline{M}$ $K_3Fe(CN)_6$ + 0.005 $\underline{M}$ $K_4Fe(CN)_6$ + 0.5 $\underline{M}$ K_2SO_4 at pH = 3 and 26°C). This difference may be caused by a difference in the ratio of true to apparent surface area or ionic double layer effects (different point of zero charge) as well as semiconductor effects but is certainly far less than the two orders of magnitude difference in the exchange current densities for the O_2 reduction on the basal and edge planes.

The most likely explanation for the suppression of O_2 reduction on the basal plane is the lack of suitable adsorption sites for O_2(ads), O_2^- (ads) and O_2H^-(ads) during the reduction. This raises the question as to what particular adsorption sites or functional groups are involved in the O_2 reduction on the edge surface. A large number of functional groups have been proposed to exist on carbon surfaces [79, 80] and some of these should persist on graphite as well as carbon at the potentials for O_2 reduction in alkaline solutions. Even so, it is far from clear which, if any, provide the adsorption sites involved in the O_2 reduction.

Garten and Weiss [81] some years ago proposed that quinone groups are involved in the following way:

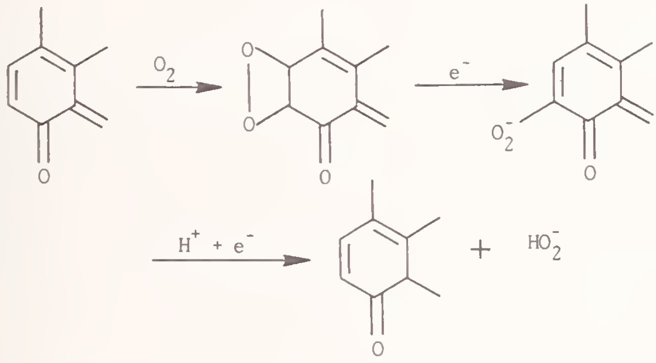

(5)

The O_2 first adds to the olefinic bond associated with the quinone group to form the hydroperoxide or molecular oxide. Electron transfer then occurs to form O_2^-(ads) and subsequently splits off as HO_2^- after a further electron transfer. Steps I and II of this mechanism are compatable with the kinetics but step III is not. The peroxide formation step is second order in O_2^-(ads) and hence appears to involve interaction between two O_2^-(ads) with simultaneous electron transfer either directly or through the carbon substrate. The nature of this interaction is not clear. A similar second order step involving O_2^-(ads) also appears to be involved in O_2 reduction on gold [29, 63].

5. O_2 Electrode Reactions on Nickel Oxide

Oxygen reduction at room temperatures proceeds through a peroxide mechanism on lithiated NiO in alkaline solutions [9, 18, 82]. In O_2-saturated alkaline solutions of HO_2^-, the open-circuit potential of anhydrous NiO produced by various methods corresponds to the thermodynamic value for the O_2 - HO_2^- couple with the proper dependence on HO_2^- activity [18].

The NiO most extensively studied in the author's laboratory [18, 82] is mosaic crystalline anhydrous NiO ([100] orientation) produced by hydrothermal growth on isomorphic MgO from the $NiBr_2$ - H_2O vapor phase at ∿600°C, using the method of Cech and Alessandrini [88]. The mosaic crystals are then doped with 0.1 - 1.0% Li by high temperature infusion (1450-1550°C). This material is a p-type semiconductor and hence processes such as O_2 reduction would be expected to be inhibited. Examination of redox couples such as ferri-ferrocyanide with the rotating disk technique do indicate such cathodic inhibition in acid solutions with the anode branch under combined kinetic and diffusion control [87]. Differential capacitance measurements in acid solutions indicate that most of the electrode potential change occurs across the space charge region within the NiO(Li) at electrode potentials cathodic to 0.8V vs. standard hydrogen electrode (SHE)[88]. In alkaline solutions, however, the ferri-ferrocyanide couple is no longer cathodically inhibited and both the cathodic and anodic branches are essentially diffusion controlled even at high rotation rates [87]. The flat band potential shifts in alkaline solutions from a positive to quite negative value relative to the reversible potential of this couple with the result that the potential changes occur principally across the Helmholtz layer. The reversible potential for the O_2-peroxide couple, however, is more negative and therefore O_2 reduction even in alkaline solutions is still quite inhibited [82]. The oxidation of HO_2^- to O_2 proceeds more readily but is still much less reversible than on carbon or graphite. Similar results have been observed on lithiated polycrystalline NiO produced by high temperature oxidation of nickel metal in air or O_2 [18].

O^{18} techniques have been used to demonstrate that the O_2 liberated during the oxidation of HO_2^- to O_2 at controlled potential on NiO in alkaline solutions originates only from the HO_2^- [82]. Thus the O-O bond does not appear to be broken during the oxidation process, and presumably also during the reverse reduction of O_2 to HO_2^-.

So far in this lecture, we have only considered the reduction of O_2. Nickel oxide is of some interest from the standpoint of the anodic generation of O_2, however, since nickel electrodes are used in water electrolysis in caustic and these electrodes develop anodic oxide layers under such conditions.

O_2 generation has been examined on mosaic NiO(Li) in acid solutions using O^{18} labelling techniques [90]. The dissolution of NiO in concentrated acid solutions is extraordinarily slow and is under pure kinetic control. After correction for lattice $O^=$ entering the solution through dissolution, a substantial fraction of the anodically generated O_2 has been found to originate from lattice oxygen ($\underline{\underline{1}}0\%$ at $\underline{1}.8$V vs. SHE). The proposed mechanism is the falling of p-carriers into surface O^- or OH^- traps. The subsequent formation of O_2 is then coupled to the NiO dissolution process and may proceed as follows:

$$\begin{array}{llcll}
\text{Step I:} & 2\,O^{2-} + 2p^{+} & \rightarrow & 2O^{-} & (6)\\
\text{Step II:} & 2\,O^{-} + 2H^{+} & \rightarrow & 2\,OH & (7)\\
\text{Step III:} & OH + OH & \rightarrow & H_2O + 1/2\ O_2 & (8)\\
\text{Step IV:} & 2Ni^{2+}_{lattice} & \rightarrow & 2Ni^{2+}_{aq} & (9)\\
\hline
 & 2NiO + 2H^{+} + 2p^{+} & \rightarrow & 2Ni^{2+}_{aq} + H_2O + 1/2\ O_2 & (10)
\end{array}$$

Steps I and II may be a single step or separate steps as shown. Step III undoubtedly involves several component steps. The overall process is independent of the steps. The standard free energy change for the overall process relative to the reaction $2H^+ + 2e \rightarrow H_2$ can be calculated from the standard free energies of formation as listed by Pourbaix [91]; NiO, ΔG°_f = -51.3 kcal/mole; Ni^{2+}, ΔG°_f = -11.53 kcal/mole; H_2O, ΔG°_f = -56.5 kcal/mole. The calculated relative standard free energy change for the overall reaction is +23.1 kcal/mole corresponding to a standard electrode potential of +0.5V.

Alternatively the O_2 formation from lattice oxide may involve two p carriers falling into a O^{2-} surface state; i.e.,

$$\begin{array}{llcll}
\text{Step I:} & O^{2-} + 2p^{+} & \rightarrow & O & (11)\\
\text{Step II:} & O & \rightarrow & 1/2\ O_2 & (12)\\
\text{Step III:} & Ni^{2+}_{lattice} & \rightarrow & Ni^{2+}_{aq} & (13)\\
\hline
 & NiO_{lattice} + 2p^{+} & \rightarrow & Ni^{2+}_{aq} + 1/2\ O_2 & (14)
\end{array}$$

where Steps I and II are multiple step processes. For the overall process, $\Delta G° = +39.8$ kcal/mole and $E° = 0.87V$.

The potentials for both of these overall reactions 10 and 14 are cathodic to that for the discharge of O_2 from water. Since the activity of Ni^{2+}_{aq} is far less than the unit value, the equilibrium potentials may be considerably less anodic than the standard values. This may be the explanation for the observation that at potentials even as small as +0.7V vs. SHE anodic currents were observed for NiO (0.26 atom % Li) in 1 N acid solutions. In the absence of such an anodic process a cathodic current is expected to attend the dissolution of the NiO due to the reduction of lattice Ni^{3+} (resulting from the Li doping) to Ni^{2+} [90].

The voltammetry curve for the [100] interface of the mosaic crystals indicates two peaks (fig. 6) in both acid and alkaline solutions, one at 0.95V vs. SHE (Peak I) and a second at 1.4V (Peak II). Both have a pH dependence of -60 mV/decade over the pH range 0-14. At slow sweep rates ($\leq$ 60 mV/sec), the anodic and cathodic sweep peak potentials coincide, indicating reversibility.

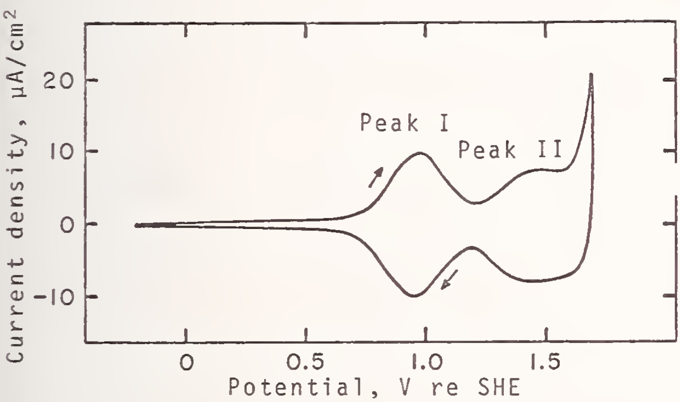

Fig. 6. Linear sweep voltammetry curve at 4.0 V/min for mosiac NiO (0.36 cation % Li) in helium-saturated 1.0 N H_2SO_4 at 25°C. Electrode area: 0.128 cm^2.

Yohe et al. [82] have compared the voltammetry results with the thermodynamic data compiled by Pourbaix [91] and concluded that peaks I and II probably correspond to the oxidation of Ni^{2+} to Ni^{+3} and Ni^{+3} to Ni^{+4}, respectively, coupled with the removal of protons from adjacent oxygen ions. These reactions appear to occur only at the electrode surface since the total charge under both peaks corresponds to less than a monolayer (65%) of the charge for the (100) plane, assuming one electron per Ni^{2+} ion for each peak, and an idealized (100) surface orientation with no surface roughness. The difficulty of converting all surface Ni^{2+} ions to a higher valency state is not surprising since complete conversion would probably involve very large surface excess charge. It is even possible that both peaks correspond to the Ni II - Ni III conversion with the marked difference in potential due either to different surface sites with differing charge compensation by surface $O^=$ and OH^- ions or to induced heterogeneity arising from a large increment in the free energy of oxidation for Ni II ions adjacent to an Ni III surface ion.

Another interesting feature is the extraordinarily slow rate of dissolution of the mosaic NiO(Li) in acid electrolytes and the pronounced potential dependence of the solution rate. At room temperatures the dissolution rate in acid solutions (e.g., 6 M H_2SO_4) is typically a few micrograms/cm^2-hr or less, making it possible to make use of this oxide as an electrode over very extended periods of time even in strong acids. To facilitate dissolution rate studies, the dissolution kinetics have been studied in the author's laboratory at temperatures just below the boiling points of the electrolytes. The dissolution rate is entirely under kinetic control [90]. In H_2SO_4 solutions the dissolution rate passes through a maximum as the potential is made increasingly anodic (fig. 7), in accord with the predictions of Engell [92] and Vermilyea [93] when the dissolution is controlled by the transfer of ions across the oxide-electrolyte interface. The maximum should correspond to a shift from control of the dissolution kinetics by the potential energy barrier for cation transfer to control by that for anion transfer across the interface. The theory

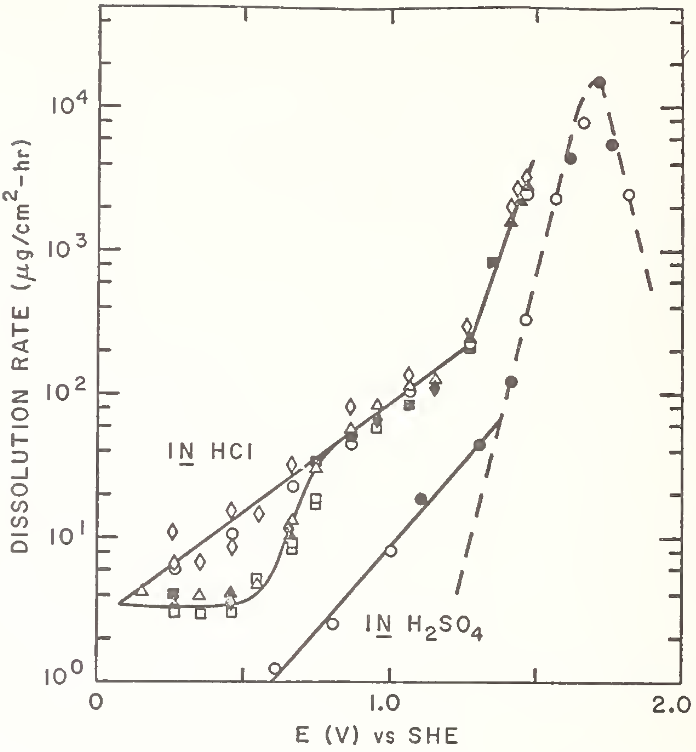

Fig. 7. Dissolution of lithiated nickel oxide in helium-saturated 1 N HCl and 1 N H_2SO_4 solution at 95°C [89]. Symbols corresponding to different group of electrodes:
○ ● Group 1, $(C_{Li})_{MS}$ = 0.88%; □■△ Group 3, $(C_{Li})_{MS}$ = 0.26%;
◇ Group 2, $(C_{Li})_{MS}$ = 0.33%; ▲◆ Group 4, $(C_{Li})_{MS}$ = 0.12%.
Dashed line: calculated from eq (1) with the following parameters: $\alpha_+ z_+ = 0.62$, $\alpha_- z_- = -0.62$, r_f = 15,000 µg/cm - h, ϕ_f = 1.68 V vs SHE. (Concentrations of Li in cation -%, based on the slopes of the Mott-Schottky plots.)

predicts Tafel linearity on either side of the maximum. It is not possible, however, to identify the specific ionic species being transferred over the potential energy barriers from the observed Tafel slopes, which yield α n (α = transfer coefficient, n = charge of species).

6. O_2 Electrocatalysis on other Oxides

The anodic generation of O_2 has been examined on a number of defect metal oxides, prepared by thermally decomposing a metal salt (usually the chloride) with titanium as the substrate. Potential-current curves obtained by O'Grady and Iwakura in the author's laboratory are shown in figure 8 for a few of these oxides [94]. The current-voltage curves at lower current densities ($<10^{-5}$ A/cm^2) are strongly influenced by the intrinsic changes in valency state of the oxide even though the data were acquired with decreasing current with three minutes at each data point. Since the current densities are apparent values, area differences may have influenced the relative positions of the curves. Of particular importance is the low Tafel slope (∿0.04V/decade) for several of the defect oxides (e.g., RuO_x, IrO_x).

The behavior of the corresponding pure metals as O_2 anodes is distinctly different from that of the defect metal oxides in figure 8 even though the metals are oxide coated at the potentials where O_2 generation occurs. Ruthenium metal is not stable as an O_2 anode in 4 M KOH. Active dissolution begins already at ∿1.3V vs. RHE.

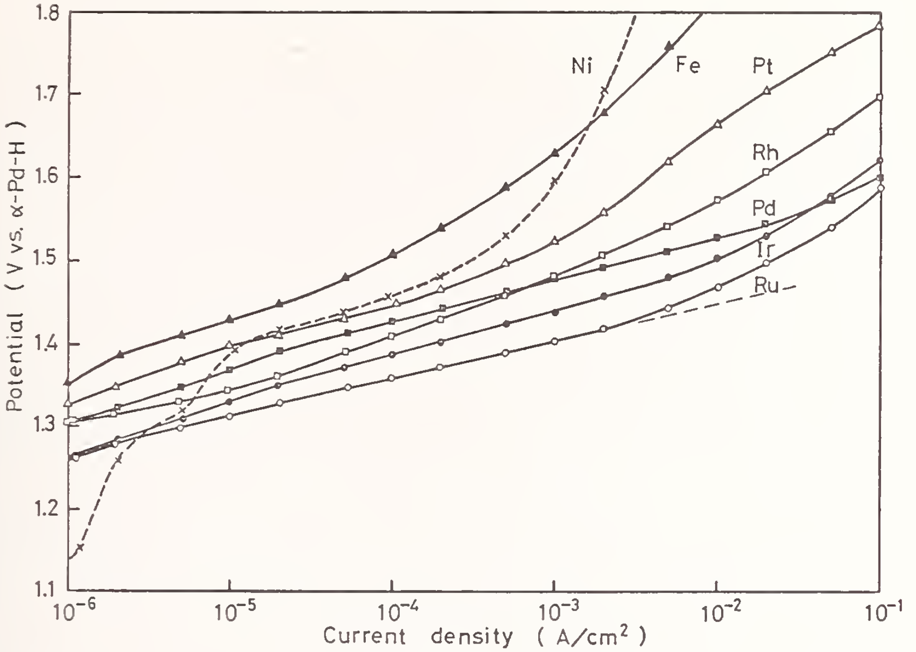

Fig. 8. O_2 generation on various metal oxides. Anodic polarization curves on metal oxides on Ti substrate in O_2-saturated 4 M KOH, obtained with 3 min/point after polarization with increasing current up to 0.1 A/cm^2 (dashed line represents IR drop corrected curve for RuO_x) [94].

The RuO_x catalyst appears to be similar to that used for the dimensionally stable anodes for Cl_2 generation [97]. This oxide has been investigated in some detail in the author's laboratory [61]. The O_2 generation reaction on RuO_x/Ti is first order in OH^- over the pH range 11 to 14. Unfortunately the stoichiometric number cannot be obtained because of interference from the intrinsic oxidation-reduction reactions of the RuO_2 at low current densities near the reversible potential for the 4-electron reaction.

O'Grady et al. [61] have found that[3] the Tafel slopes are independent of the catalyst loading over the ranges 10^{-8} to 10^{-5} moles Ru/cm^2 and the apparent exchange current densities are approximately proportional to the catalyst loading over this range. Such a proportion is to be expected since the true-to-apparent area ratio is also approximately proportional to the catalyst loading. The Ti only acts as a substrate and does not have any direct effect on the activity of the RuO_x per unit true area. For RuO_x coverage greater than 10^{-8} moles Ru/cm^2, ESCA did not indicate any Ti in the RuO_x.

Several of the reaction paths for O_2 generation tabulated by Damjanovic [76] for acid solutions can have Tafel slopes corresponding to $dV/d \ln i = 2RT/3F$ or 0.040 V/decade when modified to a form suitable for alkaline solutions. All have the common feature that the rate controlling step is a second electron rather than first electron transfer. With judicious choice of H_2O vs. OH^- as the reactant in the first and second electron transfer steps or proceeding proton transfer steps, it is possible to have the kinetics also first order in OH^-.

With electrode surfaces involving species with ionic character, O'Grady *et al.* [61] prefer to write the mechanism in such a way as to indicate the possibility of changes in the effective valency state of the catalyst sites. A simple mechanism compatible with the observed Tafel slope and reaction order is as follows:

---

[3] The next four paragraphs are quoted from reference 61 with only minor change.

$$\text{Step I:} \quad S^z + OH^- \underset{k_{-a}}{\overset{k_a}{\rightleftarrows}} (SOH)^z + e^- \text{ (fast)} \qquad (15)$$

$$\text{Step II:} \quad (SOH)^z \xrightarrow{k_b} (SOH)^{z+1} + e^- \text{ (slow)} \qquad (16)$$

followed by subsequent processes yielding finally O_2 and regenerating the site S^{+z}; for example,

$$\text{Step III:} \quad \begin{array}{c} (SOH)^{z+1} \\ + \\ (SOH)^{z+1} \end{array} \begin{array}{c} OH^- \\ \\ OH^- \end{array} \rightarrow \begin{array}{l} S - O\text{-}H\text{--}OH^- \\ \quad\; | \\ S - O\text{-}H\text{--}OH^- \end{array} \rightarrow \begin{array}{c} S^z \\ + \\ S^z \end{array} \begin{array}{c} O \\ | \\ O \end{array} \begin{array}{c} HOH \\ + \\ HOH \end{array} \qquad (17)$$

The sites are probably Ru^{4+} but also could be higher valency state Ru ions. These sites are probably hydrated although the waters of hydration are not shown in the mechanism.

In Step I the site S^z has been proposed by O'Grady et al. to be a Ru ion of the oxide lattice. Step I involves the oxidation of the Ru to a higher valency state with partial transfer of electron charge from the OH species to Ru forming a $(RuOH)^z$ complex. Such a process should require much less energy than the formation of an OH free radical or a rather weakly adsorbed OH radical. Step II involves the further oxidation to $(RuOH)^{z+1}$, possibly followed by the formation of $(RuO)^z$ before proceeding with Step III. The RuO_x electrode surface may have some of the same features as the $Ru(NH_3)_5ORu\text{-}(NH_3)_4ORu(NH_3)_5{}^{7+}$ ion, reported by Earley and Razavi [95, 96] to oxidize OH^- homogeneously to form O_2. These species have the structure $Ru\text{-}O\text{-}Ru\text{-}O\text{-}Ru^{7+}$. Earley and Razavi have pointed out that Ru has a tendency to form species of coordination number 7 and that there are low-lying antibonding π* orbitals which can accept electron charge from OH^-. Thus the $(RuOH)^z$ intermediate (other species in the inner coordination sphere not shown) seems reasonable."

From the applied standpoint, RuO_x does appear attractive for use as an O_2 anode electrocatalyst. While the exchange currents per unit true area are comparable to Pt in alkaline solutions, the much lower Tafel slope results in significantly lower overpotential at high current densities.

O_2 reduction on RuO_x in alkaline and acid solutions appears to involve a peroxide mechanism [61] although it is possible that "parallel" mechanisms are involved. Pronounced hysteresis and a lack of stability of the oxide have interfered with kinetic studies with the rotating disk technique.

7. Acknowledgment

The experimental data obtained in the author's laboratory and presented herein, have been obtained principally by the following colleagues and students:

Oxygen electrode studies on carbon:	I. Morcos
A.c. impedance measurements on graphite:	J. P. Randin
Redox couples on NiO(Li):	D. Tench, D. Yohe
Dissolution kinetics and O_2 generation on NiO(Li):	C. H. Lee, A. Riga
O_2 electrocatalysis on RuO_x and other defect oxides:	W. O'Grady, C. Iwakura and J. Huang

The author also acknowledges helpful discussions on O_2 electrocatalysis with his colleagues R. K. Sen, W. E. O'Grady and F. Urbach.

This work has been partially supported through grants from the U.S. Office of Naval Research and NASA-Ames.

References

[1] See e.g. McGinnety, J.A., in MTP International Reviews of Science, Inorganic Chemistry Series I, Vol. 5, D. Sharp, ed., Butterworths, London, 1972, p. 229.

[2] Griffiths, J.S., Proc. Roy. Soc. (A) 235, 23 (1956).

[3] Vaska, L., Science 140, 809 (1963).

[4] McGinnety, J., Doedens, R. and Ibers, J., J. Amer. Chem. Soc. 88, 3511 (1966).

[5] e.g., Collman, J., Kubola, M. and Hosking, J., ibid. 89, 4809 (1967).

[6] McGinnety, J., Payne, N. and Ibers, J., ibid. 91, 6301 (1969).

[7] Behret, H., Binder, H. and Sandstede, G., in Proc. of the Symposium on Electrocatalysis, M. Breiter, ed., The Electrochemical Society, Princeton, N.J. 1974, pp. 319-338.

[8] Behret, H., Binder, H. and Sandstede, G., Electrochim. Acta 20, 111 (1975).

[9] Tseung, A, Hobbs, B. and Tantram, A., ibid. 15, 473 (1970).

[10] Pauling, L., Nature 203, 182 (1964).

[11] See e.g., Hoffman, B., Diemente, D. and Basolo, F., J. Amer. Chem. Soc. 92, 61 (1970).

[12] Weiss, J.J., Nature 203, 183 (1964).

[13] Wittenberg, J., Wittenberg, B., Persach, J. and Blumberg, W., Proc. Nat. Acad. Sci. 67, 1846 (1970).

[14] Ochiai, E.I., J. Inorg. Chem. 36, 2129 (1974).

[15] Beck, F. Dammert, W., Heiss, J., Hiller, H. and Polster, R., Z. Naturforsh, 28A, 1009 (1973).

[16] Beck, F., Ber. Bunsenges. physik. Chem. 77, 353 (1973).

[17] Yeager, E., Krouse, P. and Rao, K., Electrochim. Acta 9, 1057 (1964).

[18] Yeager, E. and Kozawa, A., Kinetic Factors in Fuel Cell Systems: The Oxygen Electrode, Proc. 6th AGARD Meeting, Cannes, 1964, Pergamon Press, Oxford, 1965, pp. 769-793.

[19] See e.g., Maricle, D.L. and Hodgson, W.G., Anal. Chem. 37, 1562 (1965).

[20] Sawyer, D.T. and Roberts, J.C., J. Electroanal. Chem. 12, 90 (1966). Goolsby, A.D. and Sawyer, D.T., Anal. Chem. 40, 83 (1968).

[21] Peover, M.E. and White, B.S., Electrochim. Acta 11, 1061 (1966).

[22] Nekrasov, L.N., Pukhanova, L., Dubrovina, N. and Vykhodtseva, L., Elektrokhim. 6, 388 (1970).

[23] Appleby, J., Molten Carbonate Fuel Cells in Conference Proceedings, Fuel Cell Catalysis Workshop, Electric Power Research Institute, Palo Alto, California, EPRI SR-13, Special Report, August 1975, pp. 153-6.

[24] Kastening, B. and Kazemifard, G., Ber. Bunsenges. physik. Chem. 74, 551 (1970).

[25] Divisek, J. and Kastening, B., J. Electroanal. Chem. 65, 603 (1975).

[26] Dubrovina, N.I. and Nekrasov, L.N., Elektrokhim. 8, 1503 (1972).

[27] Brezina, M. and Hofanova-Matejkova, A., J. Electroanal. Chem. 44, 460 (1973).

[28] Morcos, I. and Yeager, E., Electrochim. Acta 15, 953 (1970).

[29] Yeager, E., Oxygen Electrode Kinetics on Various Electrode Surfaces, in Conference Proceedings, Fuel Cell Catalyses Workshop, loc. cit., pp. 49-59.

[30] Ochiai, E.I., Inorg. Nucl. Chem. Letters 10, 453 (1974).

[31] Traylor, T.G. and Chang, C.K., J. Amer. Chem. Soc. 95, 5810 (1973).

[32] Stynes, H.C. and Ibers, J.A., ibid. 94, 5125 (1972).

[33] Brimgar, W., Chang, C., Gerbel, J. and Traylor, T., ibid. 96, 5597 (1974).

[34] Collman, J., Gagne, R., Halbert, T., Marchon, J. and Reid, C., ibid. 95, 7868 (1973).

[35] Valentine, J.S., Chem. Revs. 73, 235 (1973).

[36] Bennett, M.J. and Donaldson, P.B., J. Amer. Chem. Soc. 93, 3307 (1971).

[37] Schaefer, W.P., Inorg. Chem. 7, 725 (1968).

[38] Behar, D., Czapski, G., Rabani, J., Dorfman, L. and Schwarz, E., J. Phys. Chem. 74, 3209 (1970).

[39] Damjanovic, A., Genshaw, M. and Bockris, J., J. Chem. Phys. 45, 4057 (1966).

[40] Damjanovic, A., Genshaw, M. and Bockris, J., J. Electrochem. Soc. 114, 1107 (1967).

[41] Yeager, E., The Sodium Amalgam-Oxygen Continuous Feed Cell, in Fuel Cells, Chapter 7, W. Mitchel, ed., Academic Press, New York City, 1963.

[42] Jahnke, H.F., Schönborn and Zimmerman, G., in Proc. of the Symposium in Electrocatalyses, M. Breiter, ed., The Electrochemical Soc., Princeton, N.J., 1974, pp. 303-319.

[43] Jahnke, H.F., Schönborn and Zimmerman, G., "Organic Dyestuffs as Catalysts for Fuel Cells" in Topics of Current Chemistry, Springer-Verlag, Heidelberg, Germany, 1975.

[44] Jasinski, R., J. Electrochem. Soc. 112, 526 (1965).

[45] Jahnke, H., Ber. Bunsenges. physik. Chem. 72, 1053 (1968).

[46] Heller, H., Polster, R., Beck, F. and Guthke, H., German Patent P 2046-345-1, Sept. 9, 1970.

[47] Savy, M., Bernard, C. and Magner, G., Electrochim. Acta 20, 383 (1975).

[48] Kozawa, A., Zilionis, V.E., Brodd, R. and Powers, R.A., J. Electrochem. Soc. 113, 1470, 1974 (1970).

[49] Kozawa, A., Zilionis, V.E. and Brodd, R.J., ibid. 118, 1705 (1971).

[50] Alt, H., Binder, H. and Sandstede, G., J. Cataly. 28, 8 (1973).

[51] Behret, H., Binder, H. and Sandstede, G., Electrochem. Acta 20, 111 (1975).

[52] Marko, A. and Kordesch, K., U.S. Patent 2,615,932 (1952).

[53] Clark, M., Darland, W. and Kordesch, K., "Carbon Fuel Fell Electrodes", Proc. Annual Power Sources Conference, 18th, Atlantic City, N.J., 1964, pp. 11-14.

[54] Savy, M., Electrochim. Acta 13, 1359 (1968).

[55] King, W. and Tseung, A., ibid. 19, 485 (1974).

[56] Tseung, A. and Bevan, H., J. Electroanal. Chem. 45, 429 (1973).

[57] McHardy, J. and Stonehart, P., in MTP International Reviews of Science, A. Buckingham and J. Bockris, eds., Series Z, Vol. 6, Butterworth, London, 1974.

[58] McHardy, J. and Bockris, J. Electrochem. Soc. 120, 53, 51 (1973).

[59] Randin, J.P., ibid. 120, 373 (1973); 121, 1209 (1974). Electrochim. Acta 19, 87 (1974).

[60] Fischman, J., Henry, J. and Tessore, S., ibid. 14, 1314 (1966).

[61] O'Grady, W.E., Iwakura, C., Huang, J. and Yeager, E., in Proc. of the Symposium on Electrocatalysis, loc. cit., pp. 286-302.

[62] Grevstad, P.E., Final Report, "Development of Advanced Fuel Cell Systems", Pratt and Whitney Aircraft Co., NASA Contract NAS3015339, Nov. 1972.

[63] Zurilla, R. and Yeager, E., "Oxygen Electrode Kinetics on Gold", Technical Report No. 23, Case Western Reserve University, ONR Contract N 0014-67-c-0389, May, 1969.

[64] "New Trends in Catalysis", Part II, Report Pennsylvania Research Associates, Inc., Philadelphia, Pa., NASA Contract NAS7-574, Annl. 1968; "The Role of Metal in Electrochemistry", ibid. Sept. 1970.

[65] Appleby, A.J., J. Electrochem. Soc. 117, 328 (1970).

[66] Vogel, W. and Lundquist, J., ibid. 117, 1512 (1970).

[67] Vogel. W., Lundquist, J. and Bradford, A., Electrochim. Acta 17, 1735 (1972).

[68] Kordesch, K. and Scarr, R., "Low Cost Oxygen Electrodes", Final Report, Union Carbide Corp., Consumers Products Division, Cleveland, Ohio, U.S. Army Contract DAADOZ-71-C-0297, July, 1973.

[69] Yeager, E., IVA Meddelande (Sweden) 134, 89 (1963).

[70] Davies, M., Clark, M., Yeager, E. and Hovorka, F., J. Electrochem. Soc. 106, 56 (1959).

[71] Singer, L. and Spry, W., Bull. Amer. Phys. Soc. 1, 214 (1956).

[72] Randin, J.P. and Yeager, E., J. Electroanal. Chem. 36 257 (1972); J. Electrochem. Soc. 118, 711 (1971).

[73] Randin, J.P. and Yeager, E., J. Electroanal. Chem. 58, 313 (1975).

[74] Klein, C.A., J. Appl. Phys. 33, 3338 (1962). Rev. Mod. Phys. 34, 72 (1962).

[75] Bockris, J. O'M. and Srinivasan, S., Fuel Cells: Their Electrochemistry, McGraw-Hill Book Co., New York City, 1969, pp. 412-468.

[76] Damjanovic, A., in Modern Aspects of Electrochemistry, J. Bockris and B. Conway, eds., Vol. 5, Plenum Press, New York City, 1969.

[77] Appleby, A.J. in Modern Aspects of Electrochemistry, loc. cit., Vol. 9, chapter 5, 1974.

[78] Hoare, J.P., Electrochemistry of Oxygen, Interscience, New York City, 1968.

[79] See e.g., Snoeyink, V.L. and Weber, W.J., in Progress in Surface and Membrane Science, J. Danielli, M. Rosenberg and D. Cadenhead, eds., Academic Press, New York, 1972, pp. 63-120.

[80] Panzer, R.E. and Elving, P.J., Electrochim. Acta 20, 635 (1975).

[81] Garten, V.A. and Weiss, D.E., Rev. Pure Appl. Chem. 7, 69 (1957). See also Garten, V.A. and Eppinger, K., Aust. J. Chem. 12, 394 (1959).

[82] Yoke, D., Riga, A., Greef, R. and Yeager, E., Electrochim. Acta 13, 1351 (1968).

[83] Stonehart, P., Kinoshita, K. and Bett, J.A.S., in Proc. of Symposium on Electrocatalysis, loc. cit. pp. 275-285.

[84] Bett, J.A.S., Lundquist, J.T., Washington, E. and Stonehart, P., Electrochim. Acta, 18, 343 (1973).

[85] Blurton, K.F., Greenberg, P., Oswin, H.G. and Rutt, D.R., J. Electrochem. Soc. 119, 559 (1972).

[86] Voinov, M., Buhler and Tannenberger, H., in Proc. of Symposium on Electrocatalysis, loc. cit., pp. 268-274.

[87] Tench, D.M. and Yeager, E., J. Electrochem. Soc. 121, 318 (1974).

[88] Tench, D.M. and Yeager, E., ibid. 120, 164 (1973).

[89] Cech, R. and Alessandrini, E., Amer. Soc. Met. Trans. Quart. 51, 150 (1959).

[90] Lee, C.H., Riga, A. and Yeager, E., The Dissolution Kinetics of Lithiated NiO in Aqueous Acid Solutions, in Mass Transport Phenomena in Ceramics, A.R. Cooper, and A.H. Heuer, eds., Plenum Publishing Co., New York City, 1975, pp. 489-499.

[91] Pourbaix, M., "Atlas of Electrochemical Equilibria in Aqueous Solutions", Pergamon Press, Oxford, 1966 (English translation by J.A. Franklin).

[92] Engell, H.J., Z. Physik. Chem. N.F. 7, 158 (1956).

[93] Vermilyea, D.A., J. Electrochem. Soc. 113, 1067 (1966).

[94] O'Grady, W., Iwakura, C., Huang, J. and Yeager, E., unpublished data.

[95] Earley, J. and Rajavi, H., Inorg. Nucl. Chem. Letters 9, 331 (1973).

[96] Earley, J. and Fealey, T., Inorg. Chem. 12, 323 (1973).

[97] e.g., South African Pat. 68/7371, 68/7482 (1968). German Pat. 2021422 (1969) 2014746, 1915951 (1970). British Pat. 1206863 (1970).

National Bureau of Standards Special Publication 455, *Electrocatalysis on Non-Metallic Surfaces*, Proceedings of Workshop held at NBS, Gaithersburg, Md., December 9-12, 1975. (Issued November 1976)

Photoelectrolysis of Water[1]

J. G. Mavroides, D. I. Tchernev, J. A. Kafalas, and D. F. Kolesar
Lincoln Laboratory, Massachusetts Institute of Technology
Lexington, Massachusetts 02173

The photoelectrolysis of water has been investigated by experiments on cells consisting of an illuminated n-type semiconductor anode, an aqueous electrolyte, and a platinized-Pt cathode. It has been found that such cells operate either in the photogalvanic mode (no H_2 evolved) or in the photoelectrolytic mode (H_2 evolved at the cathode by decomposition of water), depending on whether or not the electrolyte surrounding the cathode contains dissolved oxygen. In both cases, current flows through the external circuit and O_2 is evolved at the anode. For operation in the photogalvanic mode, maximum values of 80-85% for the external quantum efficiency (η) for current production have been measured at $h\nu \approx 4$ eV with both single-crystal and polycrystalline TiO_2 anodes. Similar results have been obtained with $SrTiO_3$ anodes. The internal quantum efficiencies, corrected for reflection and absorption losses, are close to 100%, indicating that the band bending in both cases under photogalvanic conditions is sufficient to separate the electron-hole pairs generated by photon absorption and also that the oxygen overvoltage for charge transfer at the semiconductor-electrolyte interface is negligible for illuminated anodes. For operation in the photoelectrolytic mode, η is only 1-2% for TiO_2 and $\sim$ 10% for $SrTiO_3$ if the anode and cathode are shorted together, but the efficiency can be greatly increased by applying a bias voltage. All the observations, including the increased efficiency for $SrTiO_3$, can be given a straightforward explanation in terms of the energy levels of the electrodes and the electrolyte.

Key words: Energy levels; photocatalytic electrodes; photoelectrolytic cells; photogalvanic cells; quantum efficiency; solar energy.

1. Introduction

About three years ago, Fujishima and Honda published a letter [1][2] in Nature on "Electrochemical Photoelectrolysis of Water at a Semiconductor Electrode". In this report, these authors suggested that an electrochemical cell consisting of an n-type single-crystal TiO_2 anode and platinum black cathode could be used with visible light to decompose water into H_2 and O_2. Aside from its purely scientific interest, this report has aroused considerable interest in possible utilization of the phenomenon for obtaining fuel, H_2, from solar energy. In order to further evaluate the potential of photoelectrolysis for this application we have investigated the physics and electrochemistry of this effect by experiments on cells with polycrystalline as well as single-crystal TiO_2 anodes[2]. This work then led to studies with $SrTiO_3$ anodes [3] and we report some of these results as well.

---

[1] This work was sponsored by the Department of the Air Force.

[2] Figures in brackets indicate the literature references at the end of this paper.

2. Energy Diagram of a Photoelectrolytic Cell

Figure 1 is a simplified energy diagram of a photoelectrolytic cell consisting of an n-type semiconducting anode, an acidic electrolyte, and a metallic counterelectrode. (An acidic electrolyte has been chosen for simplicity. An entirely equivalent discussion could be given for basic solutions.) The two electrodes are connected through an external circuit, so that the Fermi level is the same for both. Because of the difference in work function between the semiconductor and the electrolyte, the energy bands of the semiconductor are bent at the surface, so that the analog of a Schottky barrier exists at the semiconductor-electrolyte interface. The semiconductor surface is irradiated by photons of energy at least equal to its energy gap. The photon-generated hole-electron pairs do not recombine but are separated by the electric field of the barrier; the electrons move away from the surface into the bulk of the semiconductor and then through the external circuit to the Pt cathode, where they discharge H_2 by the reaction

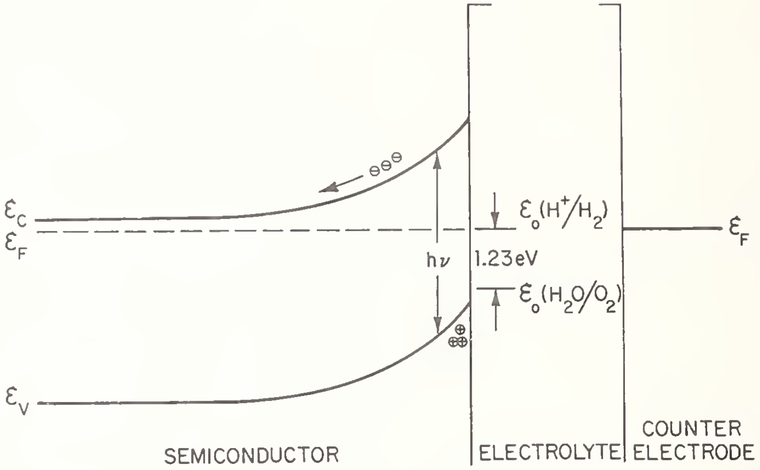

Fig. 1. Simplified Energy diagram of an ideal photoelectrolytic cell.

$$2e^- + 2H^+ \rightarrow H_2 \tag{1}$$

while the holes remain at the surface of the semiconductor anode, where they can interact with the electrolyte to produce O_2 by the reaction

$$2p^+ + H_2O \rightarrow 1/2\ O_2 + 2H^+ \tag{2}$$

The overall reaction is

$$H_2O \xrightarrow{2h\nu} H_2 + 1/2\ O_2 \tag{3}$$

From this brief description of the principle of operation, it is evident that a number of conditions are necessary for efficient photoelectrolysis: (1) The energy bands at the semiconductor-electrolyte interface must be bent in order to separate the holes and electrons excited by the light: Since the bending is due to the difference in work functions (or electrochemical potentials) between the semiconductor and the electrolyte, this puts an upper limit (for an n-type semiconductor) on the work function (or electron affinity) of the semiconductor; (2) the relevant electronic levels must line up, i.e., the hole states of the anode with $\mathcal{E}(H_2O/O_2)$ and the Fermi level $\mathcal{E}_F$ with $\mathcal{E}(H^+/H_2)$, in order to permit transfer of holes at the anode and electrons at the cathode; (3) the semiconductor must be chemically inert serving only to absorb light and produce the holes and electrons which make the above reactions possible and (4) the semiconductor must have an energy gap between 2 and 2.5 eV so as to make the most effective use of the sun.

At the present time it is not obvious that all these conditions can be met simultaneously. In particular, can we find a material with a small energy gap that does not dissolve under anodic polarization? All the common semiconductors, such as Ge, Si, CdS and GaP, dissolve under these conditions. In this talk we will discuss our results on TiO_2 and $SrTiO_3$ with the above criteria in mind. It should be pointed out at the onset that both of these materials are extremely stable and do not dissolve; they have energy gaps of ~ 3 eV, however, so that they are not suitable for efficient solar photoelectrodes.

3. Experiments with TiO_2 Anodes

The anode material used in most of our experiments was the rutile form of TiO_2. Some TiO_2 anodes were fabricated from single crystals, but most were polycrystalline disks prepared by hot-pressing powdered rutile at 750°C under a pressure of 10,000 psi. To make the disks conducting $[\rho \sim 1 - 10\ \Omega m\ (10^2 - 10^3\ \Omega\text{-cm})]$, they were heated in vacuum for three hours at ~ 800°C, which causes a loss of oxygen that makes them n-type and gives them a blue coloration. Other anodes were prepared by heating Ti foils at ~ 600°C in an oxygen atmosphere for periods of three hours or more to form polycrystalline TiO_2 films by thermal oxidation.

In initial experiments we used both the differential space-charge capacitance and AC photocurrent techniques to determine the flat-band potential of TiO_2 with respect to the saturated calomel reference electrode. This potential, $(\mathcal{E}_F)_{fb}$, is the particular value of the Fermi level for which the energy bands of TiO_2 are not bent. Therefore the amount of anode band bending for a given Fermi level, $\mathcal{E}_F$, is the difference between $\mathcal{E}_F$ and the flat band potential. With increasing pH, $(\mathcal{E}_F)_{fb}$ was found to vary linearly with a slope of 0.059 eV/pH (i.e. 2.303 e/kT), as expected if the principal effect of the change in pH is to vary the Fermi level in the solution. At pH = 0, $(\mathcal{E}_F)_{fb} \sim -0.2$ eV, which is close to $\mathcal{E}(H^+/H_2) = -0.24$ eV. (By convention, in an energy diagram like figure 1, levels lying above the saturated calomel electrode are negative, while those lying below it are positive.) This means that TiO_2 is quite different from the hypothetical semiconductor of figure 1, which exhibits significant band bending when $\mathcal{E}_F = \mathcal{E}(H^+/H_2)$. For TiO_2, since $(\mathcal{E}_F)_{fb} \approx \mathcal{E}(H^+/H_2)$, it seen that the band bending is very small. This situation, shown in figure 2, indicates a high electron-hole recombination rate. Thus the quantum efficiency for photoelectrolysis, η, which is defined as 100 times the ratio of the number of electrons flowing in the external circuit (N_e) to the number of photons incident on the cell, N_p, and calculated from the measured short circuit current density, J_{sc}, and light intensity, S, at each photon energy $h\nu$, i.e.

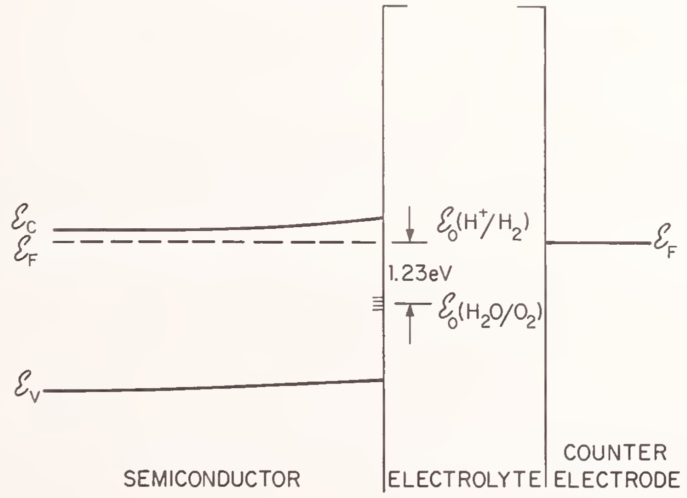

Fig. 2. Energy diagram of a TiO_2 electrochemical cell operating in the photoelectrolytic mode.

$$\eta = 100 \, \frac{N_e}{N_p} = 100 \, \frac{J_{sc}}{S} \, h\nu \qquad (4)$$

is only 1 to 2% at most in our best samples.

If the cell containing the illuminated TiO_2 anode and the platinized-Pt cathode is exposed to air so that the electrolyte surrounding the cathode contains dissolved oxygen, then charge transfer takes place at the platinum electrode and it assumes a potential close to the equilibrium potential of O_2. Thus the energy states of the counterelectrode are shifted downwards (relative to those of the electrolyte) by ~ 0.8 eV. This is indicated in figure 3. Now when photo-generated electrons are supplied to the cathode, the energetically favorable process is not the transfer of electrons from the cathode to the H^+/H_2 level according to eq (1) but rather their transfer to the H_2O/O_2 level, which causes the reduction of oxygen. In an acidic solution, the resulting chemical reaction is

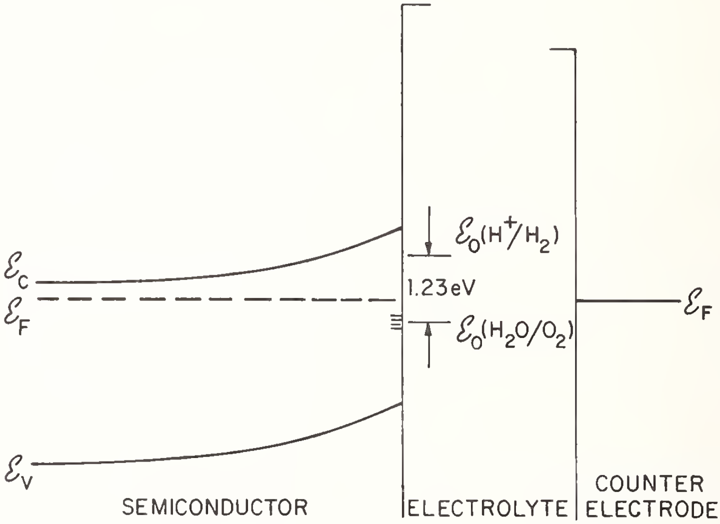

Fig. 3. Energy diagram of a TiO_2 electrochemical cell operating in the photogalvanic mode.

$$2e^- + 2H^+ + 1/2 \, O_2 \rightarrow H_2O \qquad (5)$$

Illumination of the anode thus causes the cell to function in the photogalvanic mode with significant band bending, but the passage of current through the external circuit although producing O_2 efficiently is not accompanied by the production of H_2. As will be discussed later, η here is almost 100%.

The remaining experiments on TiO_2 described here were designed to evaluate the performance of semiconducting anodes in the process of charge transfer across the semiconductor-electrolyte interface. To perform such an evaluation, it is necessary for the reactions at the anode, rather than those at the cathode, to be rate-limiting. This was accomplished by using a platinized-Pt cathode with a geometric area about 50 times that of the anode and operating with the electrochemical cell open to air, so that there was a plentiful supply of dissolved oxygen in the electrolyte surrounding the cathode. Under these conditions the cell operates in the photogalvanic mode, so that the current flow in the external circuit is determined by the photo-generation of electron-hole pairs at the anode, the separation of these pairs due to band bending, and the transfer of holes from the anode to the electrolyte. Anode performance was characterized by measuring the current flow. The gas evolved at the anode, which was collected by displacement of the electrolyte solution from an inverted buret, was identified as O_2 because it was completely absorbed by pyrogallol. The volume collected was found to be 80-85% of the value calculated by assuming that the current flow was entirely associated with the generation of O_2 according to eq. (2); we assume that the difference of 15-20% was due to collection losses.

The operating characteristics of a photogalvanic cell under constant illumination from a 150-W Xe source were measured for various values of pH. Typical results, obtained for pH=0, are plotted in figure 4. The upper curve gives the output voltage, V, as a function of the current drawn from the cell per cm^2 of illuminated TiO_2 surface. The lower curve gives the electrical power, P, extracted by the external load. The two curves can be fit to a fairly good approximation by a model that considers the cell as equivalent to a constant voltage source in series with an internal resistance. Here, the open circuit voltage is 0.52 V and the internal resistance is ~ 350 Ω. For operation in the short-circuit mode, the anode current density J_{sc} is 19 A/m^2 (1.9 mA/cm^2). When the pH of the electrolyte was increased, J_{sc} initially increased quite rapidly but then reached a limiting value of ~ 25A/m^2 (2.5 mA/cm^2) for pH values of about 5 or higher.

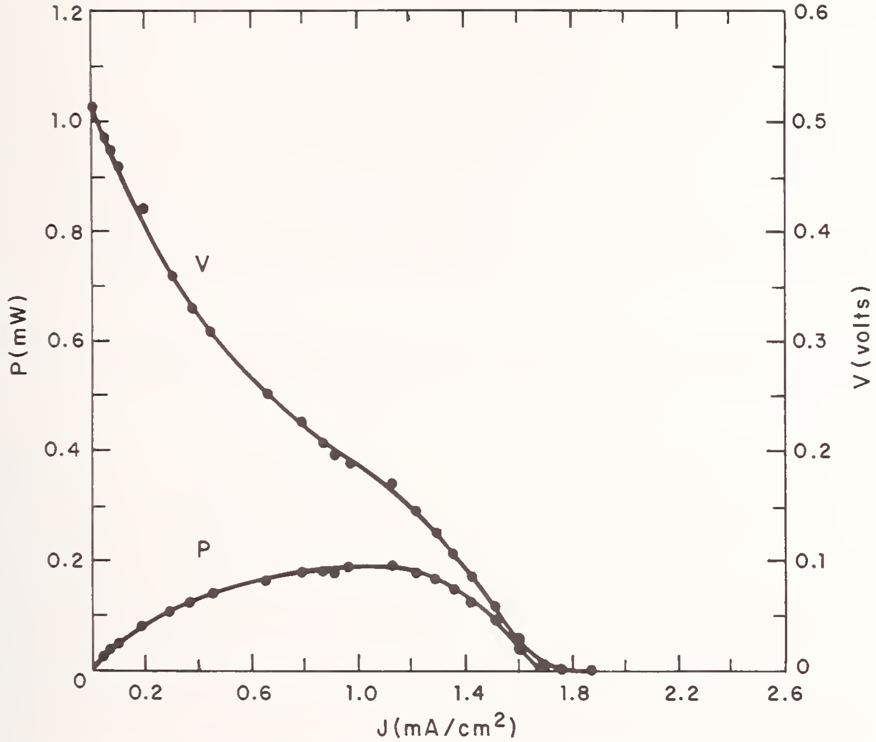

Fig. 4. Operating characteristics of a TiO_2 photogalvanic cell showing the variation of output voltage (V) and power (P) as a function of current density (J). pH=0.

The external quantum efficiency for current production was measured as a function of photon energy on an optimized photogalvanic cell for light intensities in the linear region. The anode was illuminated by monochromatic light from a source consisting of a 1000-W Xe lamp and a grating monochromator. The light intensity incident on the cell was measured as a function of hν by means of a thermopile power meter that had a flat response down to 0.25 μm.

Figure 5 shows the values of η vs hν for TiO_2 films on Ti foil that had been thermally oxidized under different conditions and measured in a non-buffered electrolyte of pH = 13. For film "a" (7 μm thick), η reaches a maximum value of 84% at λ = 0.34 μm (~ 3.5 eV), while film "b" (<2 μm thick) has a maximum of 83% at 0.30 μm (~ 4 eV). The positions of the quantum efficiency peaks correspond to 3 major absorption peaks in TiO_2 that occur at about 3.5, 4 and 4.7 eV (0.34, 0.30 and 0.26 μm) respectively. The relative intensities of the efficiency peaks depend on preparation procedure and oxide

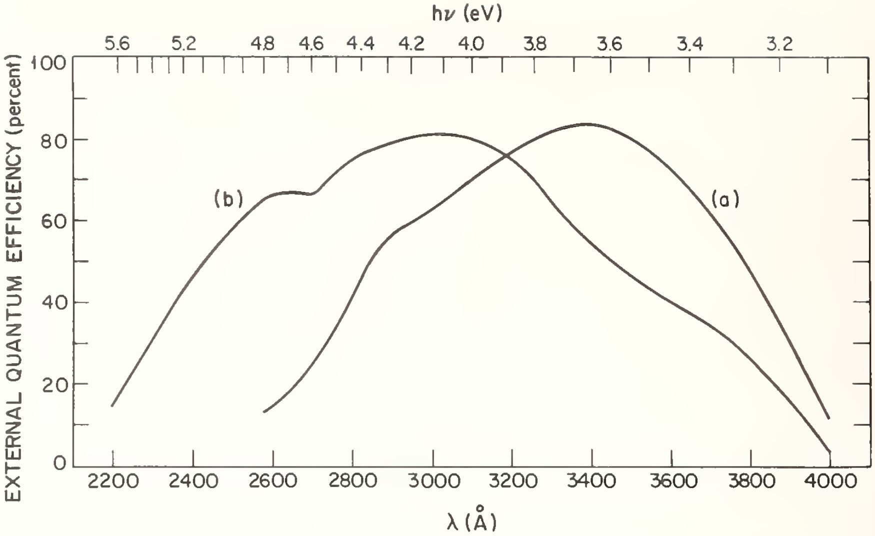

Fig. 5. Variation of external quantum efficiency with wavelength of a TiO_2 photogalvanic cell for two different thermally oxidized TiO_2 foil anodes. pH = 13.

layer thickness. Equally high efficiencies are also obtained with single crystals and hot-pressed disks.

When the maximum measured η values are corrected by taking account of estimated reflection losses at the interfaces and absorption losses in the electrolyte, we find that the internal quantum efficiency is close to 100% for both single-crystal and polycrystalline TiO_2 anodes. This high quantum efficiency shows that the band bending in TiO_2 under photogalvanic conditions (~ 0.8 eV) is sufficient to separate all the hole-electron pairs generated by photon absorption. It also shows that the anodes have hole states (probably surface states) which are close to the H_2O/O_2 level of the electrolyte. Other evidence for such states, lying in the energy gap, has already been presented at this workshop: Professor Bard's elegant work on the exploration of these states by means of solution redox couples, the Lincoln Laboratory study of surface states using ultrahigh-vacuum energy loss spectroscopy and Professor Wolfram's theoretical work on the origin of these states. The observation of such high efficiencies implies that, for illuminated anodes of TiO_2, the oxygen overvoltage for charge transfer at the semiconductor-electrolyte interface is negligible.

4. Experiments with $SrTiO_3$ Anodes

The $SrTiO_3$ anodes used in the experiments reported here were n-type disks 5 to 15 mm in diameter that had been cut from a single crystal (Titanium Pigment Division of National Lead Industries). Preliminary experiments with an anode prepared by hot-pressing powdered $SrTiO_3$ gave results similar to those obtained with single-crystal material. The material was reduced by annealing in H_2 at atmospheric pressure for about 3 hours at 900° C. After reduction $SrTiO_3$ changed from insulating to conducting, with a resistivity ~ 0.15 Ωm (15 Ω-cm), and from colorless and transparent to blue-black and opaque. An ohmic contact was made to each disk by ultrasonically soldering In to its back surface and attaching a Pt wire to the In. The entire disk, except for the front surface, was then coated with insulating epoxy or stop-off lacquer.

Again photoelectrolytic cells were prepared by immersing a $SrTiO_3$ anode and a platinized-Pt cathode into an aqueous electrolyte contained in a fused-quartz vessel. Each electrode was capped with a inverted buret filled with electrolyte, so that the gas evolved could be collected by liquid displacement for volumetric measurement and chemical analysis. Provision was made for flushing the electrolyte with either N_2 or Ar in order to remove dissolved O_2 so that the cell operated in the photoelectrolytic mode. Measurements were generally made after the solution had been purged for several hours.

Figure 6 is a plot of the variation of small signal ac photocurrent with electrode potential at pH = 13.3. One can use such a plot to estimate the flat band potential from the value of voltage at which the photocurrent goes to zero. Two curves are shown here -- one for TiO_2 and the other for $SrTiO_3$. Also shown is the equilibrium hydrogen potential $\mathcal{E}(H_2/H^+)$ for this pH. These results indicate that the band bending for photoelectrolysis is very small for TiO_2 and ~ 0.2 volts more for $SrTiO_3$. This is consistent with the difference in work function, or electron affinity, of ~ 0.2 volt that we have measured by the Kelvin contact potential method in air.

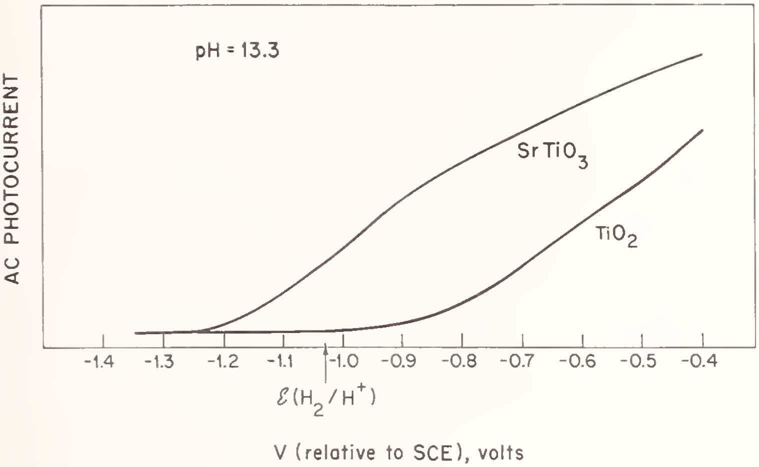

Fig. 6. Influence of electrode potential on small signal ac photocurrent in an aqueous electrolyte.

This ~ 0.2 volt larger band bending in $SrTiO_3$ results in a quantum efficiency for photoelectrolysis about one order of magnitude larger than that found for TiO_2; i.e., $\eta = 10\%$ at $h\nu = 3.8$ eV. The gases evolved at the electrodes were collected and analyzed. At high pH values (pH > 13) the volumes of gas collected at the cathode and anode were found to be over 90% of the values calculated from the integrated electron current by assuming that only the reactions given by eqs. (1) and (2) are taking place. These results are consistent with the conclusion that photoelectrolysis is the only reaction occurring.

Summary

In summary it is especially significant that we have been able to give a straightforward interpretation of our experimental results on photogalvanic and photoelectrolytic cells in terms of the energy levels of the electrodes and the electrolyte. This application of theoretical energy-level concepts, discussed earlier in this workshop by Professor Gerischer and derived from both solid state physics and electrochemistry, should greatly facilitate the search for new electrode materials by making it possible to specify what properties are necessary for efficient photoelectrolysis.

References

[1] Fujishima, A and Honda, K., Nature 238, 37 (1972).

[2] Mavroides, J. G., Tchernev, D. I., Kafalas, J. A., and Kolesar, D. F., Mat. Res. Bull. 10, 1023 (1975).

[3] Mavroides, J. G., Kafalas, J. A., and Kolesar, D. F., Appl. Phys. Lett. (to be published).

National Bureau of Standards Special Publication 455, *Electrocatalysis on Non-Metallic Surfaces*, Proceedings of Workshop held at NBS, Gaithersburg, Md., December 9-12, 1975. (Issued November 1976)

ELECTROCHEMICAL PROCESSES ON STRONTIUM TITANATE ELECTRODES

D. M. Tench and D. O. Raleigh
Rockwell International/Science Center
Thousand Oaks, California 91360

The electrochemical properties of n-type single-crystal $SrTiO_3$ electrodes (10^{18}-10^{19} carriers/cm^3) were investigated in acidic sulfate solutions, with special attention to the hydrogen evolution reaction. AC impedance measurements, together with the voltammetric behavior of the ferro-ferricyanide couple and the onset of anodic photocurrent, established that the flat band potential, U_{fb}, lies about 250 mV cathodic to the reversible hydrogen electrode potential.

Slow-sweep cyclic voltammetry with a rotating electrode assembly established several hydrogen discharge mechanisms in moderately acidic solutions. Anodic to U_{fb}, chemical desorption ($H_{ads} + H_{ads} \rightarrow H_2$) appears to be rate limiting. At more cathodic potentials, electrochemical desorption ($H_3O^+ + e^- + H_{ads} \rightarrow H_2 + H_2O$) dominates. At still more cathodic potentials, where proton discharge becomes diffusion-limited, hydrogen discharge from H_2O appears to dominate. Anomalous current behavior at low pH values (~ 0.5) suggests possible proton diffusion into the electrode. ESCA measurements showed that the first few atomic layers of the $SrTiO_3$ surface, when brought in contact with aqueous solutions, become depleted in Sr.

Key words: Semiconductor electrode; hydrogen evolution; perovskite surface composition; oxide electrode; flat band potential; rotating electrode voltammetry.

1. Introduction

Transition metal oxides of the ABO_3 perovskite structure have attracted considerable attention as possible catalysts and electrocatalysts. Rare-earth cobaltites, manganites and ruthenates have shown catalytic activity for olefin hydrogenation [1][1], CO oxidation [2] and NO reduction [3,4]. Strontium-doped lanthanum cobaltite, $La_{1-x}Sr_xCoO_3$, has been reported to show reversible oxygen electrode behavior [5,6]. $SrTiO_3$ electrodes have been used for the photoelectrolytic decomposition of water, with considerably improved quantum efficiency over TiO_2 electrodes [7].

Previous theoretical work at the Science Center has indicated that the d-band perovskites are unique among transition metal oxides in having a high concentration (10^{14} cm^{-2}) of electronic surface states of almost pure d-orbital character, with the appropriate symmetry for catalytic activity [8,9]. Strontium titanate has been studied extensively as a representative d-band perovskite [8-13]. The pure compound is a broad-band insulator with a 3.2eV band gap, but may be heavily n-doped ($\sim 10^{20}$ cm^{-3}) by hydrogen reduction [14], resulting in specific conductivities up to ~ 1 Ω^{-1} cm^{-1}. The carriers populate a $pd\pi^*$ conduction band, with which are associated a high concentration of surface d-band states with the t_{2g} orbital symmetry, located in a double-peaked energy distribution in the band gap [8]. Since surface states of this symmetry have been proposed to be instrumental in the dissociative adsorption of common diatomic gas molecules [8], it was of interest to determine the properties of n-$SrTiO_3$ electrodes with respect to the hydrogen evolution reaction in aqueous media.

---

[1] Figures in brackets indicate the literature references at the end of this paper.

2. Experimental

Single crystals of $SrTiO_3$ from NL Industries, Inc. were cut into samples 1 mm thick and 4 mm square, having a 100 orientation (111 faces gave similar results, but more hysteresis). These samples were then lapped on 600 grit SiC paper and etched in 85% H_3PO_4 for 15 min. at room temperature. Various concentrations of n-carriers were introduced by quenching in a 4% H_2 (in N_2) reducing atmosphere from elevated temperatures (900-1150°C). Ohmic electrical contacts were prepared by electroless deposition of nickel on one side of the crystals, heat treating at 400°C for ~1/2 hr. [15], then attaching a Pt lead wire using Ag-epoxy resin.

Each crystal was mounted flush with the end of a Kel-F cylinder by compression molding at elevated temperatures. Electrical contact was made through a threaded brass cylinder molded concentrically into the other end. This configuration minimizes the possibility of contamination, permits the use of strong echants, and is well-suited for rotating electrode studies [16]. Before use, the electrodes were polished on 3 μm alumina powder in water and etched for ~1/2 hr. in 85% H_3PO_4 at 100°C to remove mechanically disrupted surface layers.

The main compartment of the Pyrex electrochemical cell contained 50-100 ml of electrolyte, and had an optical glass bottom. All cell connections were made via a gas-tight Teflon top. A controlled atmosphere (argon, unless otherwise specified) could be maintained even with rotating electrodes, since the shaft clearance was less than 1 mm. Separate compartments contained a Pt counter electrode and a commercial saturated calomel reference electrode, which was positioned several mm from the crystal via a Luggin capillary. For a.c. impedance measurements, a 30 cm^2 mercury pool in the main compartment was used for the counter electrode [17]. The external Pt counter electrode, however, gave comparable results. All electrolytes were prepared with reagent grade chemicals and de-ionized water.

For the current-potential measurements, a Princeton Applied Research (PAR) Model 173 potentiostat/galvanostat with a PAR Model 176 current follower was used in the three electrode mode to control the electrode potential. Data were recorded on a Hewlett-Packard Model 7004B x-y recorder. The electrode rotation rate was controlled and monitored with a Motomatic Model E-550-M controller and motor. A.C. impedance measurements were made using a direct biased General Radio Type 1650-A impedance bridge with an external polystyrene decade capacitor and an external function generator. Identical results within 5% were obtained by measuring the current response to an a.c. signal with a PAR Model HR-8 lock-in amplifier. In both cases, a signal of 15 mV peak to peak was used across the cell. Photocurrents were measured using monochromatic light chopped at 90 Hz and phase sensitive detection.

3. Results and Discussion

3.1. Potential Distribution

To identify the potential region where sufficient charge carriers are available at the semiconductor surface to sustain electrochemical reactions, the a.c. impedance characteristics of the semiconductor-electrolyte interface were first studied. The flat band potential, U_{fb}, and bulk carrier concentration, N, are obtained from the intercept and slope of a plot of C^{-2} vs. U, according to the well-known Mott-Schottky approximation [18] for exhaustive depletion of charge carriers

$$\frac{1}{C_{SC}^2} = \frac{8\pi}{\varepsilon_{SC} eN} \left(U - U_{fb} - \frac{1}{f}\right) \tag{1}$$

where C_{SC} = semiconductor space charge capacitance, ε_{SC} = dielectric constant in space charge region, e = electronic charge, and f = e/kT.

Plots according to this equation are shown in figure 1 at pH 3.0 for $SrTiO_3$ electrodes containing various concentrations of charge carriers. Frequency dispersion of capacitance was found to be less than 5% from 100 to 1000 Hz. The carrier concentrations shown were calculated using the bulk value [19] of 305 at 25°C for ε_{SC}. Considerable curvature is evident at more anodic potentials, especially for large N. This presumably results from dielectric saturation, as has been observed for $KTaO_3$ electrodes [20]. For each carrier concentration, there is an appreciable linear region which extrapolates to a value of $U_{fb} \cong -0.42$ V vs. standard hydrogen electrode (SHE). This good agreement for U_{fb} over the

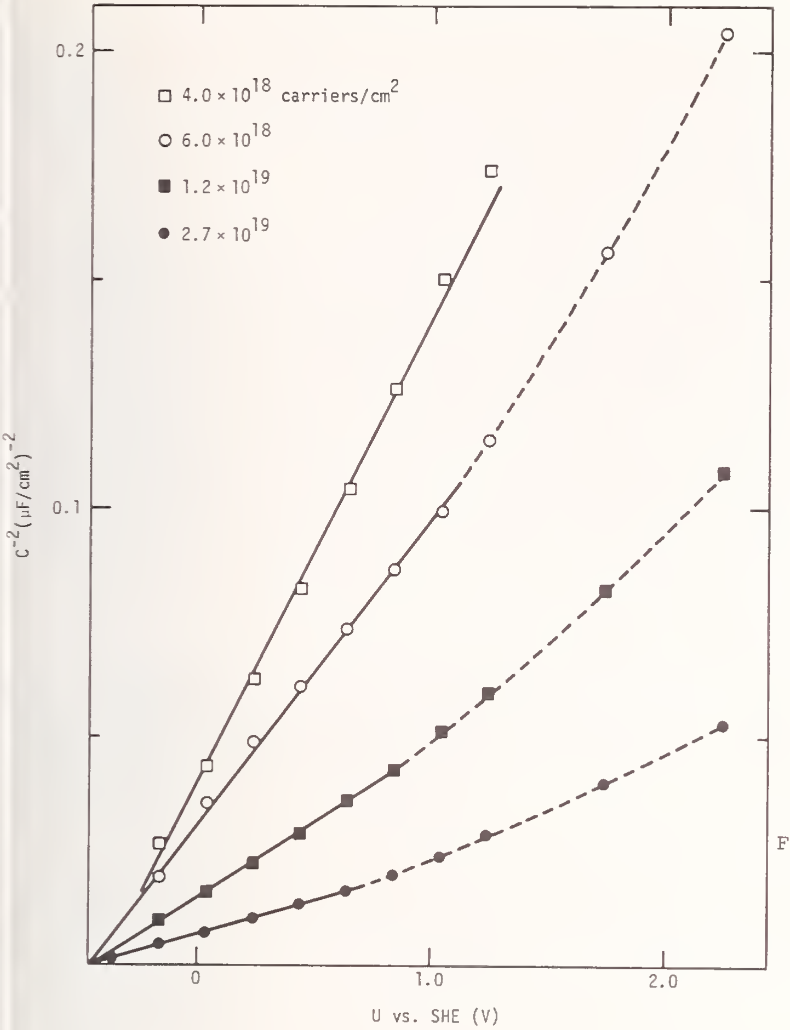

Fig. 1. Plots of C^{-2} vs. U for $SrTiO_3$ electrodes of various carrier concentrations at 1000 Hz in argon-saturated 0.5 M K_2SO_4 (pH 3.0).

range of 10^{18}-10^{19} carriers/cm^3 suggests that the capacitance of the Helmholtz layer is sufficiently large (~ 20 μcoul/cm^2) that its effect on the total electrode capacitance is small [21]. The pH dependence of U_{fb} is -70 mV/pH in acidic solutions, and is somewhat more in basic media, as illustrated in figure 2. Thus, U_{fb} always lies about 250 mV cathodic to the potential of the reversible hydrogen electrode in acid solutions. In this case, an appreciable contribution to the overvoltage for hydrogen evolution can be expected from the depletion of charge carriers in the semiconductor space charge region. A small but significant difference in the Mott-Schottky slope in 1N H_2SO_4 should be noted, which seems to be related to a change in the electrode surface, as will be discussed below.

The potential distribution at the interface was checked by studying the slow sweep (10 mV/sec) voltammetric behavior of the ferro-ferricyanide couple on rotating $SrTiO_3$ electrodes in pH 3.0 and 7.0 potassium sulfate solutions. As expected, the anodic branch is inhibited and cathodic current does not begin to flow until 300-400 mV anodic to the U_{fb} values indicated by the impedance studies. With increasingly negative voltage, the cathodic currents rise with negligible hysteresis to diffusion limits, i_L, plots of which exhibit the expected [22] linear dependence on the square root of the rotation rate, intersecting the origin. The slopes of these "Levich plots" yield a value of 6.2×10^{-6} cm^2/sec for the diffusion coefficient of the Fe $(CN)_6^{-3}$ species, which agrees well with the literature value of 7.2×10^{-6} cm^2/sec [23]. Figure 3 shows Tafel plots of log $[i/(i_L-i)]$ vs. U which are linear, except for minor deviations in the more acidic electrolyte, and exhibit slopes of 60-70 mV/decade.

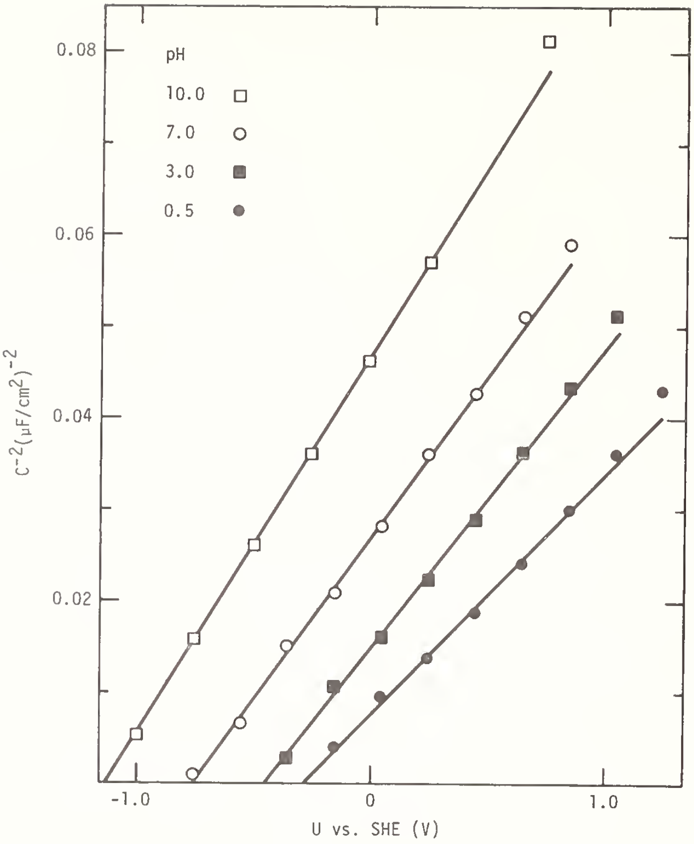

Fig. 2. Plots of C^{-2} vs. U for $SrTiO_3$ (1.2×10^{19} carriers/cm^3) at 1000 Hz in argon-saturated 0.5 M sulfate solutions of various pH values.

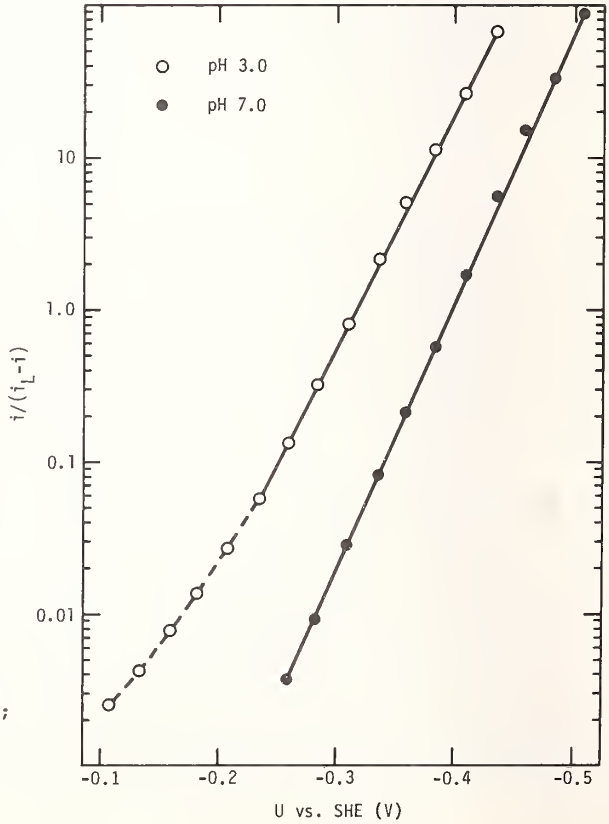

Fig. 3. Plots of $\log[i/(i_L-i)]$ vs. U for reduction of ferricyanide ion at 2500 rpm and 10 mV/sec on $SrTiO_3$ (1.2×10^{19} carriers/cm^3) in 0.5 M K_2SO_4 (pH 3.0 and 7.0) containing 2.5×10^{-3} M $K_3Fe(CN)_6$ and $K_4Fe(CN)_6$; i_L = 1.80 mA/cm^2 (pH 3.0) and 1.82 (pH 7.0).

When back reaction and double layer effects may be neglected and the symmetry factor is 0.5, the current-overpotential relationship for a first-order process involving a one-electron transfer, like ferricyanide reduction, may be written as [16]

$$\eta = \frac{1}{f(1-\gamma/2)} \left(\ln \frac{i}{i_L - i} - \ln \frac{i_o}{i_L}\right) \tag{2}$$

where η = overpotential, γ = fraction of the total electrode potential drop occurring across the Helmholtz region, i = current at overpotential η, i_L = diffusion limiting current, and i_o = exchange current. This equation assumes that the charge carrier concentration at the interface follows the Boltzmann distribution. If γ is a constant, it is evident that a plot of $\log[i/(i_L-i)]$ vs. U will yield a straight line of slope $59/(1-\gamma/2)$ mV/decade. Thus, when all of the electrode potential change occurs across the Helmholtz layer, $\gamma = 1$ and the Tafel slope is 118 mV/decade. For the other extreme, when all of the potential change is across the semiconductor space charge region, $\gamma = 0$ and the Tafel slope is 59 mV/decade. Thus, it appears that practically all of the potential change occurs across the space charge region for $SrTiO_3$ (10^{18}-10^{19} carriers/cm^3) at potentials anodic to the U_{fb} values determined in the impedance studies. A final confirmation of U_{fb} for $SrTiO_3$ was obtained by noting the onset of anodic photocurrent. This was observed to occur in pH 3.0 potassium sulfate solution at -0.40 V vs. SHE, in good agreement with the impedance value of -0.42 V.

3.2. Proton Reduction Anodic to U_{fb}

Figure 4 shows a typical linear sweep voltammetric curve covering the hydrogen evolution region at 10 mV/sec for a freshly prepared rotating $SrTiO_3$ electrode in argon saturated 0.5 M K_2SO_4 (pH 2.9). The current scale on the left side is magnified 100-fold to better illustrate the relatively small currents in this voltage region. No dependence of the current on charge carrier concentration was observed from 4×10^{18} to 3×10^{19} carriers/cm^3. Two cathodic waves are evident.

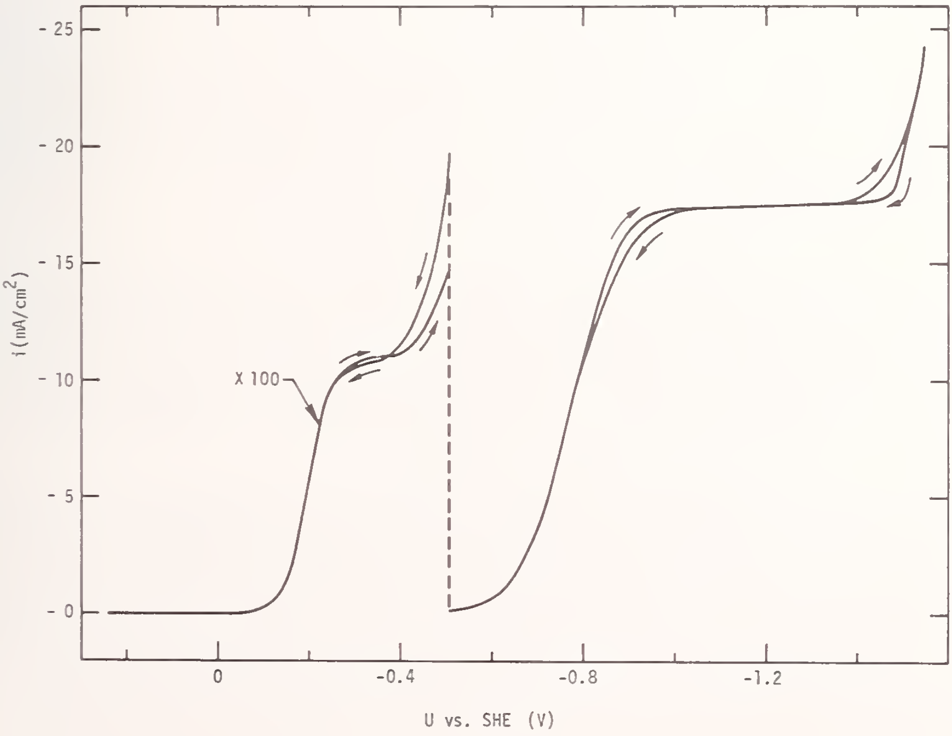

Fig. 4. Linear sweep cyclic voltammogram at 10 mV/sec for $SrTiO_3$ (4.0×10^{18} carriers/cm^3) at 3600 rpm in argon-saturated 0.5 M K_2SO_4 (pH 2.9).

The first wave occurs anodic to U_{fb} and reaches a plateau in the μA range. This current plateau is observed to be rotation-rate dependent and is decreased by a factor of 10 by bubbling H_2 through the solution. Although this wave is difficult to reproduce exactly from experiment to experiment, it does not seem to depend on pH (from pH 0.5 to 5.0). The sulfate and K^+ species are not directly involved, since comparable results were obtained in 1.0 M $NaClO_4$ (pH 3.0).

Levich plots of limiting current density vs. the square root of rotation rate, ω, are linear for this first wave, but intercept the abscissa at $\omega^{\frac{1}{2}} \cong 30$ $rpm^{\frac{1}{2}}$ without passing through zero. The latter effect is probably caused by interference from the much larger second wave and does not preclude a first order diffusion process. Tafel plots of log $[i/(i_L-i)]$ vs. U for the first wave are linear with slopes of 40-55 mV/decade, as figure 5 illustrates.

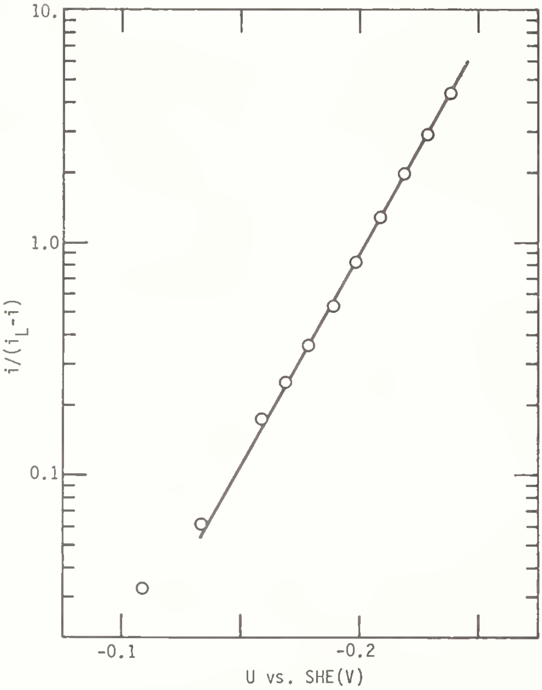

Fig. 5. Plot of log$[i/(i_L-i)]$ vs. U for proton reduction at 10 mV/sec on $SrTiO_3$ (4.0×10^{18} carriers/cm^3) at 3600 rpm in argon-saturated 0.5 M K_2SO_4 (pH 2.9); $i_L = 0.12$ mA/cm^2.

These data are consistent with hydrogen evolution rate-limited by a chemical desorption step ($H_{ads} + H_{ads} \rightarrow H_2$), with the plateau resulting from full coverage of the electrode [24]. The higher Tafel slopes than theoretical (30 mV/decade) probably result from the large fraction of the total potential drop occurring across the space charge region in this potential range, but could also be the result of interference from the larger second wave.

3.3. Surface Coverage

The coverage of the electrode surface with adsorbed hydrogen (H_{ads}) was investigated by chronopotentiometry and by moderately fast linear sweep cyclic voltammetry in pH 3.0 sulfate solutions. For the chronopotentiometric experiments, the electrode was pre-polarized cathodically with a constant current, then switched to a constant anodic current of reduced magnitude, and the electrode potential followed as a function of time. As shown in figure 6, an inflection point was observed, which presumably corresponds to the depletion of H_{ads} by re-oxidation at the electrode surface. For pre-polarization currents of -67 to -330 μA/cm^2 and subsequent anodic currents of 3.3 to 10 μA/cm^2, the charge passed up to the inflection point is always 260-340 μcoul/cm^2. Approximate monolayer coverage by adsorbed hydrogen would seem to be indicated.

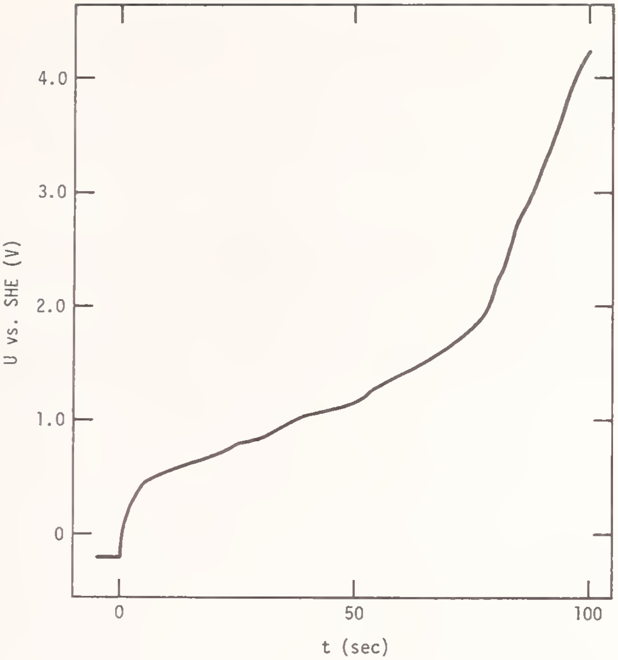

Fig. 6. Chronopotentiometric curve of U vs. t for $SrTiO_3$ (1.2×10^{19} carriers/cm^3) in argon-saturated 0.5 M K_2SO_4 (pH 3.0) at +3.3 $\mu A/cm^2$ after pre-polarizing at -67 $\mu A/cm^2$.

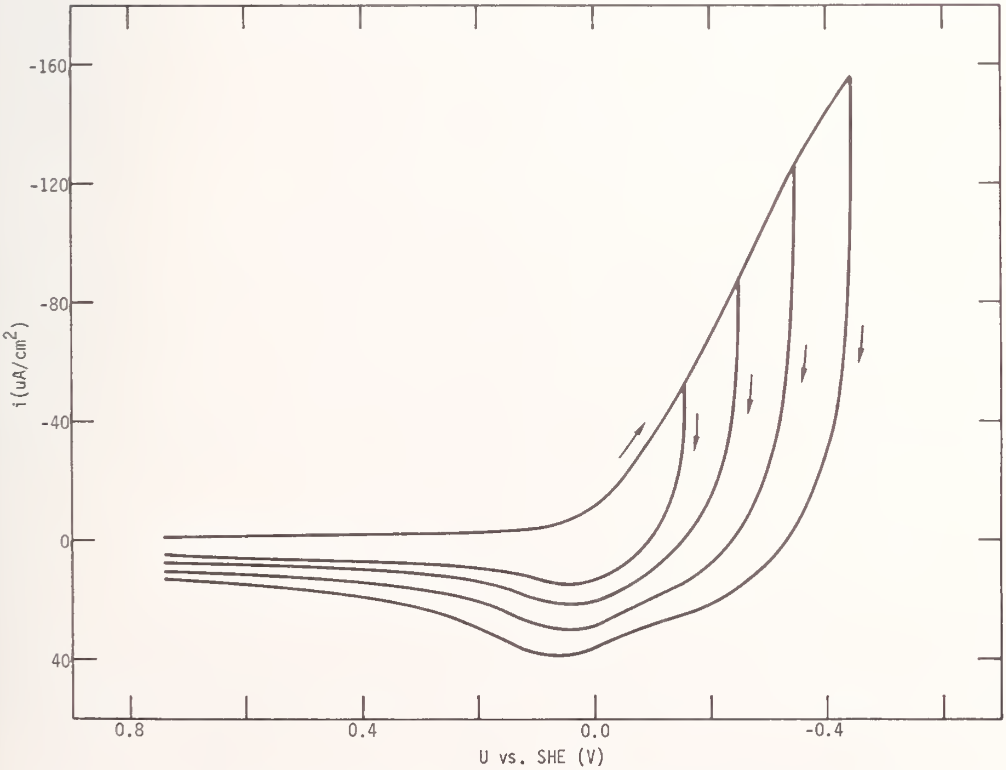

Fig. 7. Linear sweep cyclic voltammogram at 100 mV/sec for $SrTiO_3$ (2.7×10^{19} carriers/cm^3) in argon-saturated 0.5 M K_2SO_4 (pH 2.9).

Figure 7 shows representative linear sweep cyclic voltammetric curves at 100 mV/sec. For each curve, a broad anodic peak is observed slightly positive to SHE. The integrated areas under these peaks (to +1.7 V where the sweep was reversed) presumably correspond to the charge required to re-oxidize H_{ads} on the electrode surface. When the sweep is reversed at -0.44 V, this charge is 325 μcoul/cm^2 and seems to increase only slightly at more cathodic sweeps. For sweep reversals at -0.34, -0.25 and -0.15 V, the respective charges passed are 235, 150 and 115 μcoul/cm^2.

Thus, about 300 μcoul/cm^2 of charge is required to re-oxidize H_{ads} in the vicinity of the first plateau, and at least this amount at more negative potentials. If we assume one H_{ads} per O or Ti site on a 100 surface, about 200 μcoul/cm^2 of charge would correspond to full coverage. Therefore, it is possible that adsorption occurs on both O and Ti sites or that more than one H_{ads} can occupy the same site. Alternatively, a surface roughness factor of 1.5 could be responsible for the additional charge. In any case, it seems reasonable to assume that full coverage obtains at potentials cathodic to the beginning of the first plateau.

3.4. Proton Reduction Cathodic to U_{fb}

At voltages cathodic to the first wave in figure 4 and to U_{fb}, the current rises to a second plateau, which appears to be limited by diffusion of protons to the surface. In this potential range, linear Levich plots which pass through the origin are obtained, as exemplified in figure 8. The diffusion coefficient for protons, D_{H^+}, was calculated from their slopes. Because of the relatively high values measured at low pH (e.g., 4.5×10^{-4} cm^2/sec at pH 3.0), D_{H^+} was determined in 0.1 $\underline{M}$ K_2SO_4 (pH 3.2) and found to be 1.7×10^{-4} cm^2/sec, in agreement with the value reported by Breiter and Hoffmann [25].

A typical Tafel plot for the second wave of figure 4 is shown in figure 9 for the anodic sweep. Since this wave occurs cathodic to U_{fb}, all of the potential drop is assumed to be across the Helmholtz layer, so that the normal kinetic treatments used for metal electrodes are applicable. At all rotation rates to 4900 rpm, the Tafel slopes are 120-130

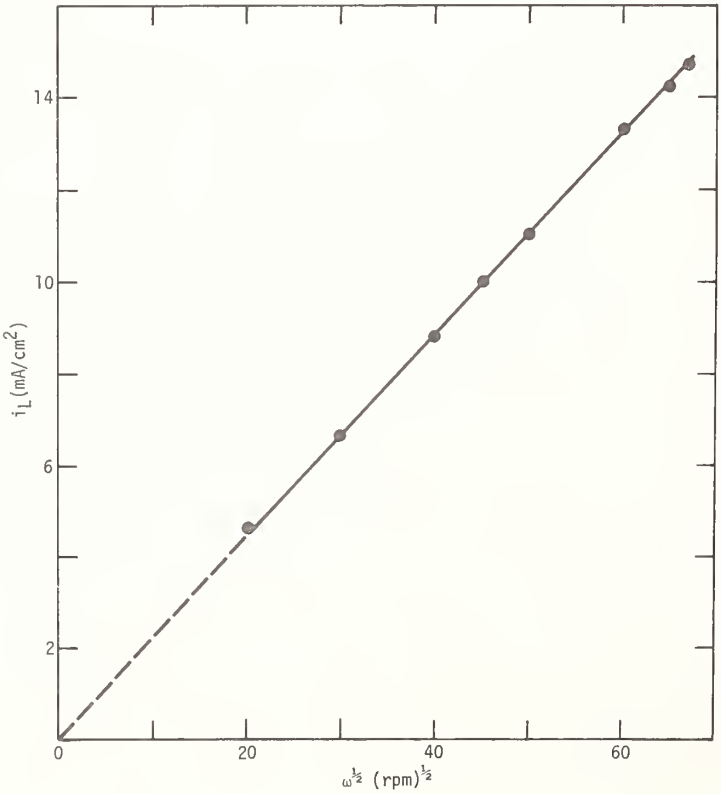

Fig. 8. Plot of i_L vs. $\omega^{1/2}$ for the second proton reduction wave on $SrTiO_3$ (4.0×10^{18} carriers/cm^3) in argon-saturated 0.5 $\underline{M}$ K_2SO_4 (pH 3.05).

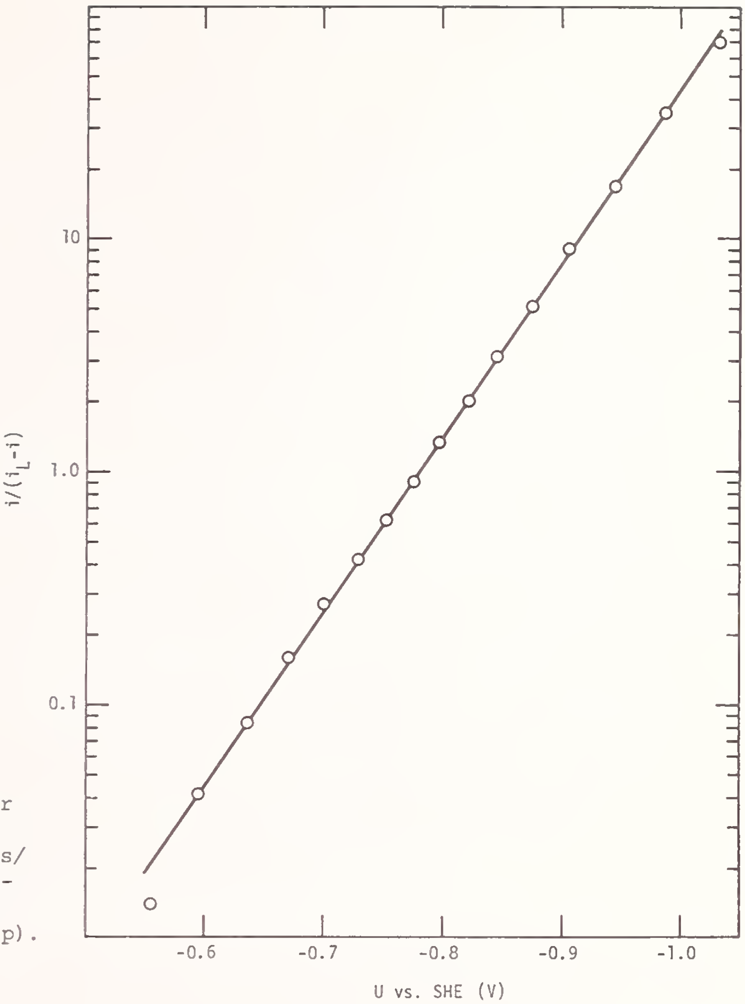

Fig. 9. Plot of log[i/i_L-i)] vs. U for proton reduction at 10 mV/sec on $SrTiO_3$ (4.0×10^{18} carriers/cm^3) at 3600 rpm in argon-saturated 0.5 M K_2SO_4 (pH 2.9); i_L = 17.5 mA.cm^2 (anodic sweep).

mV/decade, with the smaller slopes occurring for the cathodic sweeps. At the full electrode coverage assumed here, the only rate limiting step consistent with a 120 mV/decade Tafel slope is electrochemical desorption [24]. This mechanism involves the discharge of a hydrated proton in solution at the Helmholtz plane, in concert with coalescence with an adsorbed hydrogen atom to form H_2 gas: $H_3O^+ + e^- + H_{ads} \rightarrow H_2(g) + H_2O$. Since this process requires an appreciable potential drop across the Helmholtz region, it would not occur readily anodic to U_{fb}. At still more negative potentials (cathodic to the second plateau of fig. 4), one expects hydrogen discharge via proton abstraction from H_2O molecules: $H_2O + e^- + H_{ads} \rightarrow H_2(g) + OH^-$.

3.5. Dependence on pH

Figure 10 shows steady-state voltammetric sweeps at pH values from 0.5 to 5.2 in the voltage range of the second wave of figure 4. The results obtained in the pH range 2 to 5 are consistent with the previously discussed behavior at pH $\approx$ 3.0. At pH 2.3 a current-voltage curve corresponding to the "pre-plateau" region of the second wave at pH 3.05 is obtained, with higher currents, as expected at this increased proton concentration. Plots of log i vs. U at this pH were seen to be linear over two decades, with slopes of 120-130 mV/decade. At pH 5.2, the proton diffusion limited wave of pH 3.05 is seen to be absent, presumably because of the lower proton concentration, and the onset of appreciate current corresponds to proton abstraction from H_2O.

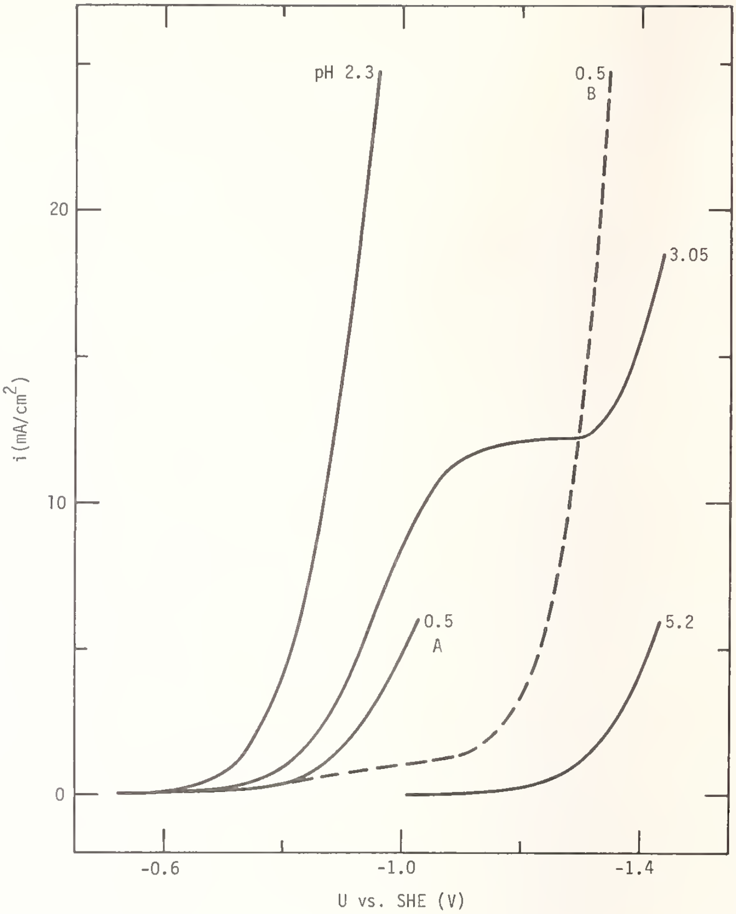

Fig. 10. Steady-state cathodic voltammetric sweeps at 10 mV/sec for $SrTiO_3$ (1.2×10^{19} carriers/cm^3) at 2500 rpm in argon-saturated 0.5 M sulfate solutions of various pH values. Curves A and B are for freshly prepared and aged electrodes, respectively.

At low pH values, anomalous current-voltage behavior is observed. The current is considerably lower than expected, and there is a pronounced "aging" effect. Curve A of figure 10 is for a freshly prepared electrode immersed in the electrolyte at pH 0.5. After several minutes, a steady-state is reached, given by Curve B. Tafel plots in this case are reasonably linear, but have slopes in the 180-190 mV/decade range. In addition, at higher pH (>2.0), many electrodes showed an order of magnitude current suppression during the first few voltammetric cycles after immersion in solution, but then recovered with time and approached the behavior of fresh electrodes. These effects would appear to be caused by some change in the nature of the electrode surface. Because of the apparent suppression of discharge from H_3O^+ at these pH values, one might hazard a guess that proton diffusion into the electrode is involved, which could electrostatically suppress the discharge mechanism involving the charged electrolyte species H_3O^+. This, however, is mere speculation.

3.6. Surface Studies

To determine whether the bulk composition $SrTiO_3$ is indeed the composition obtaining at the crystal surface, the surface Ti/Sr ratio for several crystals was measured by the ESCA technique before and after various treatments. The results are shown in Table 1. A pulverized single crystal was used as a standard, to calibrate the Ti/Sr ESCA peak height ratio. After quenching in 4% H_2/N_2, the surface is seen to be severely depleted in Sr, probably reflecting evaporative loss at elevated temperatures, resulting in a rutile (TiO_2) surface. Mechanical polishing with 3 μm alumina powder and water reduces the Ti/Sr ratio considerably. Etching in 85% H_3PO_4 at 100°C for 30 min. reduces this ratio still more, whereas cycling a $SrTiO_3$ ($\sim 10^{18}$ carriers/cm^3) electrode between +0.2 and -1.5 V re SHE in 0.5 M K_2SO_4 (pH 2.9) produced no further reduction. This suggests that a somewhat Ti-rich surface might be stable in aqueous or at least acidic media.

Table 1. Surface Ti/Sr atomic ratios determined by ESCA for single crystalline $SrTiO_3$ ($\sim 10^{18}$ carriers/cm^3) after hydrogen reduction and various surface pretreatments.

Sample Preparation	Ti/Sr Atomic Ratio
Pulverized single crystal	1.00
Quenched in hydrogen only	2.01
Mechanically polished only	1.56
Etched only	1.32
Etched after mechanically polishing	1.38
Electrochemically cycled after polishing and etching	1.36
Freshly cleaved	1.06
Exposed to water after cleaving	1.44

To test the effect of water on the surface, a crystal was freshly cleaved in air and quickly transferred into the vacuum chamber. The Ti/Sr ratio was similar to those observed for pulverized samples. After exposing this cleaved surface to de-ionized water for 2 min., however, the Ti/Sr ratio (1.44) was found to be practically the same as for etched crystals (1.3-1.4).

These results show that the $SrTiO_3$ surface becomes severely depleted in Sr when it is brought into contact with water or aqueous electrolytes. If we consider an escape depth for ESCA electrons from $SrTiO_3$ of 1.8-2.0 nm, the Ti/Sr ratio observed (1.3-1.4) would correspond to total removal of Sr in the interface region, leaving two atomic layers of only titanium and oxide ions at the surface, or some equivalent distribution. As a first guess, this composition could reflect the good solubility of SrO in aqueous media. The resultant surface composition might either reflect a TiO_2 structure, or else the perovskite structure might be retained, with protons replacing Sr ions.

The results raise serious questions about the validity of extrapolating bulk properties to electrode surfaces, not only for $SrTiO_3$, but for perovskites in general. At least in the case of $SrTiO_3$, the nature and availability of surface states is uncertain. Also, as we have suggested earlier, the structural nature of the electrode surface may be potential dependent, accounting for some of the anomalies reported in this work.

4. Summary and Conclusions

For $SrTiO_3$ electrodes, U_{fb} is always about 250 mV negative of the reversible hydrogen electrode potential in the same electrolyte. At potentials anodic to U_{fb}, hydrogen evolution proceeds only slowly, with chemical desorption ($H_{ads} + H_{ads} \rightarrow H_2$) as the rate limiting step. This would result from the fact that most of the electrode potential change occurs across the semiconductor space charge region, so is not available to drive the electrochemical reaction. At full electrode coverage by H_{ads}, a current plateau is observed in the µA range. This plateau is important for theoretical reasons, but has not previously been unambiguously observed [26]. This is because, for metal electrodes, practically all of the electrode potential is usually available to drive electrochemical reactions over the whole available voltage range.

At potentials cathodic to U_{fb} on $SrTiO_3$, electrochemical desorption ($H^+ + H_{ads} + e^- \rightarrow H_2$) becomes the rate limiting step for the hydrogen evolution reaction. This change in mechanism occurs because, cathodic to U_{fb}, a sufficient fraction of the electrode potential appears across the Helmholtz layer to drive the electrochemical desorption reaction.

Thus, it is clear that a perovskite with a U_{fb} value at least 250 mV more positive is required to lower the overpotential for the hydrogen evolution reaction. In this case, electrochemical desorption should become the rate limiting step at the reversible hydrogen potential. A material on which hydrogen is more weakly adsorbed would also be desirable, since this should increase the rates of both the chemical and electrochemical desorption steps. Finally, since the surface structure of $SrTiO_3$ has been shown to be altered by aqueous solutions, care should be exercised when dealing with other perovskites.

5. Acknowledgments

The authors express their appreciation to Mr. Cameron Ogden for performing many of these experiments and to Dr. Leonard Szalkowski for carrying out the ESCA measurements.

6. References

[1] Pedersen, L. A. and Libby, W. F., Science 176, 1355 (1972).

[2] Voorhoeve, R.J.H., Remeika, J. P., Freeland, P. E. and Matthias, B. T., *ibid.* 177, 353 (1972).

[3] Voorhoeve, R.J.H., Remeika, J. P. and Johnson, Jr., D. W., *ibid.* 180, 62 (1973).

[4] Voorhoeve, R.J.H., Remeika, J. P. and Trimble, L. E., Mat. Res. Bull. 9, 1393 (1974).

[5] Meadowcroft, D. B., Nature 226, 847 (1970).

[6] Tseung, A. C. C. and Bevan, H. L., J. Electroanal. Chem. 45, 429 (1973).

[7] Mavroides, J. G., *et al.*, "Photoelectrolysis of Water", p. 221, These Proceedings.

[8] Morin, F. J. and Wolfram, T., Phys. Rev. Lett. 30, 1214 (1973).

[9] Wolfram, T. and Morin, F. J., Appl. Phys. 8, 125 (1975).

[10] Wolfram, T., Kraut, E. A., and Morin, F. J., Phys. Rev. B7, 1677 (1973).

[11] Kraut, E. A., Wolfram, T. and Hall, W. F., Phys. Rev. B6. 1499 (1972).

[12] Wolfram, T., Phys. Rev. Lett 29, 1383 (1972).

[13] Morin, F. J. and Oliver, J. R., Phys. Rev. B8, 5847 (1973).

[14] Yamada, H. and Miller, G. R., J. Solid State Chem. 6, 169 (1973).

[15] Turner, D. R. and Sauer, H. A., J. Electrochem. Soc. 107, 250 (1960).

[16] Tench, D. M. and Yeager, E., J. Electrochem. Soc. 121, 318 (1974).

[17] Tench, D. M. and Yeager, E. J. Electrochem. Soc. 120, 164 (1973).

[18] Schottky, W., Z. Physik 113, 367 (1939); Mott, N. F., Proc. Roy. Soc. (London) A171, 27 (1939).

[19] Linz, A., Phys. Rev. 91, 753 (1953).

[20] Boddy, P. J., Kahng, D. and Chen, Y. S., Electrochim. Acta 13, 1311 (1968).

[21] De Gryse, R., Gomes, W. P., Cardon, F. and Vennik, J., J. Electrochem. Soc. 122, 711 (1975).

[22] Riddiford, A. C., Adv. Electrochem. and Electrochem. Eng. 4, 76 (1966).

[23] Jahn, D. and Vielstich, W., J. Electrochem. Soc. 109, 849 (1962).

[24] Vetter, K. J., Electrochemical Kinetics, Academic Press, New York, p. 516-614, (1967).

[25] Breiter, M. and Hoffmann, K., Z. Elektrochem. 64, 462 (1960).

[26] Vetter, K. J., *loc. cit.*, p. 521.

National Bureau of Standards Special Publication 455, *Electrocatalysis on Non-Metallic Surfaces*, Proceedings of Workshop held at NBS, Gaithersburg, Md., December 9-12, 1975. (Issued November 1976)

ELECTROCHEMICAL ACTIVITY OF POLYMERIC AND MONOMERIC IRON PHTHALOCYANINES AS A FUNCTION OF THEIR SPECTRAL PROPERTIES

A. J. Appleby and M. Savy

Laboratoire d'Electrolyse du C.N.R.S.
92-Bellevue, France.

Samples of monomer and polymer iron phthalocyanines, prepared both in situ on carbon supports or in the form of thin films, using a gas-phase synthesis method, and by dissolution of liquid-phase preparations in sulfuric acid followed by reprecipitation on carbon, were examined by optical and Mössbauer spectroscopy. Their electrochemical activities for oxygen reduction were examined under steady-state conditions using the ultra-thin porous electrode technique, as a function of O_2 partial pressure, pH (11.8 - 16.4) and H_2O_2 additions. In addition, rotating ring-disk electrode experiments were conducted. Analysis of reaction orders and comparison of activities with those of the support have allowed the most probable mechanism to be determined, in which the rate-determining step is a chemical dissociation of the O - O bond. Correlations between electrochemical activities and spectral properties indicate the role of polymerization and of the spin configuration of the central iron atom in promoting catalysis. These effects result from reoxidation of Fe^{II}iS to Fe^{III}HS or iS, which is favorized by interaction between the polymer π electrons and the d electrons of the iron.

Key words: Electrocatalysis; electronic structure; hydrogen peroxide; iron phthalocyanines; Mössbauer; optical spectra; oxygen; reaction mechanisms; ring-disk electrodes.

1. Introduction

Study of the influence of electronic parameters of the active surface in heterogeneous catalysis is of great theoretical and practical interest. In electrochemistry, the major process of technical importance, and one of the slowest, is the reduction of molecular oxygen to water in a four-electron process. This reaction has received extensive study on metal surfaces, and, following previous work on hydrogen evolution [1][1], many correlations between properties related to substrate electronic parameters (e.g., d-orbital vacancies, heats of adsorption and sublimation) and reaction rates have been proposed. This is particularly true for oxygen reduction on the noble metals in acid solution [2].

It is well known that most catalytic processes are characterized by relations of volcano type [3,4,5], in which reaction rates as a function of bond-strength reach a maximum value. In the most simple cases, involving reversible adsorption of reaction intermediates and no simultaneous irreversible adsorption of other species, the maximum corresponds to a site occupation of 0.5 by adsorbed reaction intermediates, either as reactants or products in the rate-determining step [4]. For such cases, it is easy to show that reduction of rate as bond-strength increases (on the falling side of the volcano) results from a diminution of available sites and from the fact that desorption becomes rate-determining [4]. On the rising side of the volcano, adsorption is rate-determining. Thus, in the most general case, a certain minimum bond strength for chemisorption of the reaction intermediates is required for maximum rates.

---

[1] Figures in brackets indicate the literature references at the end of this paper.

Formation of this 'most favorable' bond between a reactant or product and the substrate will require as a first condition sites presenting partially filled MO levels of the same energy as those of the intermediate species [6]. The existence of this favorable bonding will also depend on the wave function and steric availability of the d-electron cloud at the site, which may be modified by the electronic properties of the surrounding environment. Such ideas are difficult to test in the case of metallic electrodes, owing to the problem of the precise definition of surface states. However, stable chelate compounds of well-defined structure and composition, whose electronic properties can be determined, are very suitable for fundamental studies of catalysis. The effect of MO energy levels on catalytic processes can be determined by examining the effect of the nature and degree of oxidation of the central ion; similarly, the effect of d-electron density may be demonstrated by changing the π electron properties of the surrounding organic structure. This paper describes the identification of the electronic characteristics of mono- and polymer iron phthalocyanines, and their effect on the electrocatalytic reduction of oxygen in alkaline solution. A summary of previous work on oxygen reduction on these substrates has been given elsewhere [7].

In previous work [8,9], it was found that the increase in the number of unpaired electrons, detected by optical and ESCA spectroscopy, was accompanied by an increase in the electrochemical activity for the reduction of oxygen on thin-layer phthalocyanine monomers in both acid and alkaline solution. However, the techniques used in this work were not able to differentiate between the activities of different lattice sites in terms of their oxidation states and spin configurations. In the present work, we have made these correlations using a combination of optical reflectance spectroscopy, Mössbauer spectroscopy, and electrochemical experiments on supported monomeric and polymeric iron phthalocyanines prepared by gas-phase and liquid-phase methods [8-10].

The mechanism of the oxygen reduction process on the polymer iron phthalocyanine was determined using two types of electrochemical experiments on carbon supported material, viz.
a) - Steady-state measurements as a function of pH in the alkaline range and as a function of oxygen partial pressure. The apparatus, ultra-thin porous electrode preparation and measurement techniques have been previously described [8-10].
b) - Rotating ring-disk electrode measurements, to detect the presence of free intermediates (O_2H^- ion) produced in the reaction.
A certain number of experiments were performed on Eastman Kodak monomeric iron phthalocyanine supported on carbon black, prepared by precipitation from concentrated sulfuric acid solution [10]. Blank experiments on the support were also conducted.

2. Experimental

2.1 Optical Spectra

Three types of iron phthalocyanines were examined:
1) - Thin vacuum-deposited films of blue (electrochemically inactive) and green (active) forms of the monomer carried on gold foils. Preparation is given in Refs. 8,9.
2) - Iron polyphthalocyanines, consisting mainly of the dimer [9] in 10% by weight loading on acetylene black (Lannemezan Y), active carbon (Norit BRX) and high-surface area ground graphite supports. The phthalocyanines were prepared in situ using a gas-phase technique [10].
3) - Pure mono (Eastman Kodak) and gas-phase and liquid-phase polymer [10] preparations in the form of powders.

Transmission spectra (for the thin film materials) and reflection spectra (for the powders) were obtained both in the dry state and in contact with 1N KOH solution, both in the presence of air.

2.2 Mössbauer Spectra

Mössbauer spectra for monomeric and polymeric powders were obtained using a $^{57}Co/Cu$ source at 293°K, and two different absorber temperatures (293° and 77.4°K). In separate experiments, thin film monomers similar to those used in the optical spectra experiments, but in this case vacuum-deposited onto Mylar instead of onto gold foils, were examined. For these materials, spectra were obtained only at liquid nitrogen temperature, since at room temperature absorption proved to be insufficient. Experimental details have been given elsewhere [7].

2.3 Electrochemical Measurements

Steady-state results: Steady-state measurements were performed on ultra-thin porous electrodes of the type first described by Vogel and Lundquist [11]. These electrodes, which had catalyst weights in the 0.1 mg/cm^2 range, allow pure kinetic measurements to be made on finely-powdered electrode materials without diffusion limitations [10]. Experimental techniques have been given elsewhere [10]. Experimental results obtained on phthalocyanines supported on acetylene black and high-surface-area graphite materials were compared with those for the pure supports. All preparations (gas-phase or liquid-phase reprecipitated from concentrated sulfuric acid) were in 10% by weight loading. Polarization - log current density results at 1 atm. O_2 partial pressure were obtained in 1N K_2CO_3 (pH 11.8), 1N K^+ carbonate buffer (pH 13.0), 1N KOH (pH 13.9), and in a series of KOH solutions varying from 2N to 12N concentration (pH 14.2 to 16.4). pH values in the latter solutions were calculated from activity coefficient values given in Ref. 12. Results were also obtained over a range of oxygen partial pressures varying from 5 x 10^{-3} atm. to 1 atm. in 2N KOH. Finally, the effect of the addition of hydrogen peroxide on the rest potentials of the electrodes and on steady-state polarization results was determined in the presence of oxygen at 1 atm. partial pressure. Concentrations of 10^{-3} M, 10^{-2} M and 10^{-1} M were examined. Results were compared with those obtained on a pure carbon material (Norit BRX, 10 mg/cm^2). All experiments were conducted at 25°C.

Ring-disk electrode experiments: A ring-disk electrode (Tacussel) with a cavity shaped in the gold disk was used [13]. The ring was gold with a gold-black electrodeposit. The iron polyphthalocyanine on carbon black support was introduced into the cavity in the form of a paste containing purified mineral oil [13], after which the surface was accurately smoothed. Collection efficiency was determined to be 0.17. These experiments were conducted at ambient temperature (20°C).

3. Results and Discussion

3.1 Spectra

The optical spectra obtained are shown in Figs 1a,b,c. The most striking observation involves the change in the structure of the spectra on wetting the materials with KOH in the presence of oxygen. In the latter case, only two spectral peaks are observed, which are identical for all the phthalocyanines studied.

Curve 2 in Fig. 1b represents the reflection spectrum obtained on the monomer gas-phase preparation powder. The position of the two main peaks on this curve shows them to be the same as the two similar peaks on curve 1. They show the presence of the Fe^{II} triplet state (see below). After drying in air at room temperature, the spectra were identical to those obtained before wetting. Since a transformation involving the bulk phthalocyanine would be unlikely to be reversible, and can in any case be excluded for the reflectance spectrum data, we conclude that wetting results in a modification of the oxidation state and spin configuration of the outer monolayers of the phthalocyanine. Reflection spectra for monomeric powders (Eastman Kodak and gas-phase preparations) are shown in Fig. 1c. Spectra for both monomers are identical. Globally, a shift of the principal absorption peaks towards longer wavelengths is observed, in the order:

Liquid-phase preparation > Gas-phase > Monomer

From ESCA data [8,9], the position of the main absorption peak for the liquid-phase polymer preparation corresponds to Fe^{III} HS. The corresponding peak in the case of the monomer is that for Fe^{II} iS. Since the shift to longer wavelengths increases with increasing spin [8,9], we conclude that either Fe^{II} HS or Fe^{III} iS must be present in the gas-phase preparation, in agreement with the observed order of absorption peak wavelength, i.e.

$$Fe^{III}\ HS(5/2) > Fe^{II}\ HS(2),\ Fe^{III}\ iS(3/2) > Fe^{II}\ iS(1)$$

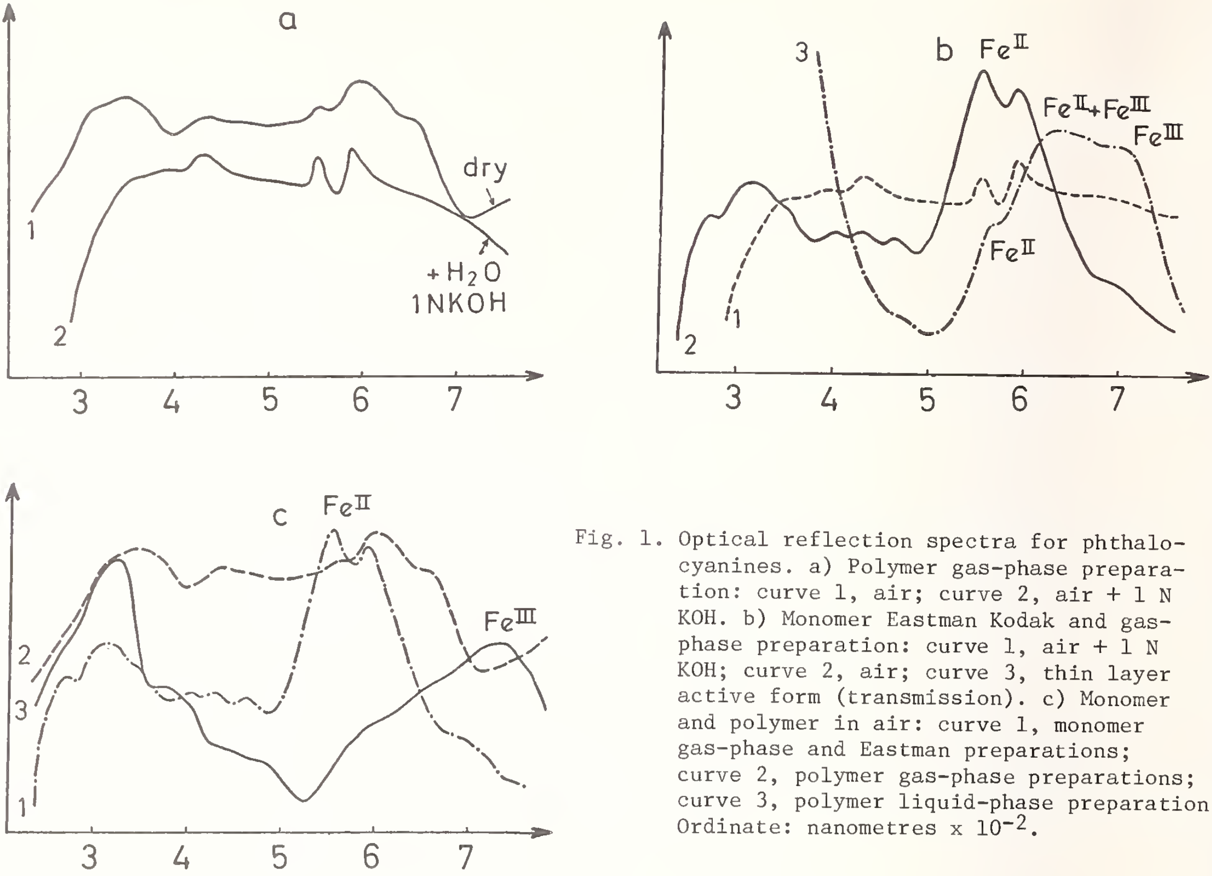

Fig. 1. Optical reflection spectra for phthalocyanines. a) Polymer gas-phase preparation: curve 1, air; curve 2, air + 1 N KOH. b) Monomer Eastman Kodak and gas-phase preparation: curve 1, air + 1 N KOH; curve 2, air; curve 3, thin layer active form (transmission). c) Monomer and polymer in air: curve 1, monomer gas-phase and Eastman preparations; curve 2, polymer gas-phase preparations; curve 3, polymer liquid-phase preparation. Ordinate: nanometres x 10^{-2}.

Mössbauer data (Quadrupole splitting, QS, and Isomer shift, IS[2]) are summarized in Table 1. QS values are oxidation-number independent and are normally on the order of 0.5 (in mm/s units) [14]: higher values indicate low ligand symmetry, e.g. C_{2V}. The IS values may be compared with literature data for identification of the species present. These are indicated in the Table, and are discussed in detail in Ref. 7. The major conclusions are that the polymeric materials consist largely of Fe^{III} HS (liquid-phase preparation) and Fe^{III} iS (gas-phase preparation). The inactive monomer, on the other hand, consists of Fe^{II} (triplet state). These are in agreement with the tentative conclusions of the optical data. However, comparison with the optical spectra obtained after wetting shows that the presumed inactive species in the monomer (Fe^{II} triplet) is also present at the surface (but not in the interior) of the polymers.

3.2 Electrochemical Data

The effect of pH (v. NHE) is shown in Fig. 2. The polarization results obtained showed no hysteresis and a reproducibility to within 3mV at the same current density (outside of the diffusion region) for different samples of the same preparation. Over most of the pH range studied, the initial Tafel slope was close to 30mV/decade. This was followed by a section of smoothly increasing slope leading into the diffusion region. In highly-concentrated KOH solutions, the Tafel-like regions were much shorter than in 1 or 2N KOH (for the latter on the order of 2 decades), since oxygen solubility falls off rapidly with increasing concentration. In N K_2CO_3, the slope observed was somewhat higher, perhaps suggesting a change in reaction mechanism at lower pH (see below).

---

[2] Upper-case I is used to distinguish isomer shift (IS from intermediate spin (iS).

Table 1. Mössbauer data, ^{57}Co(Cu) source.

	δ_1[a]		$\frac{1}{2}\Delta_1$	δ_2		$\frac{1}{2}\Delta_2$	δ_3		$\frac{1}{2}\Delta_3$	δ_4		$\frac{1}{2}\Delta_4$	δ_5		$\frac{1}{2}\Delta_5$
Monomer (90 K)	0.18	A[b] 56	1.16	0.16	B 15	0.54	0.12	C 23	0.23	0.01	0 5	1.62	-0.27	E 1	1.83
Monomer (298 K)	0.14		1.24	0.10		0.57	0.07		0.25	-0.02		1.76	0.39		1.09
Foil blue (90 K)	0.16	A_1 45	1.13	-0.11	8_1 24	0.70 ?	-0.03	C_1 29	0.23 ?						
Foil green (90 K)	0.24	A_1 43	1.22	-0.04	B_1 28	0.55	0.32	C_1 29	0.36						
	Triplet Fe^{2+}			Fe^{3+} HS or Fe^{2+} LS			Fe^{3+} green HS			Fe^{3+} LS					
	δ_1		$\frac{1}{2}\Delta_1$	δ_2		$\frac{1}{2}\Delta_2$	δ_3		$\frac{1}{2}\Delta_3$						
Polymer (298 K)	0.004	A_2 80	0.90	-0.10	8_2 15	1.35	0.44	C_2 5	0.66						
Polymer (90 K)	0.03	A_2 84	0.83	-0.06	8_2 12	1.24	0.26	C_2 4	0.49						
	Fe^{3+} iS			monomer Triplet Fe^{2+}			Fe^{3+} HS								

---

[a] Units δ_i and Δ_i are in millimeters.

[b] Indicates percentage of each form present.

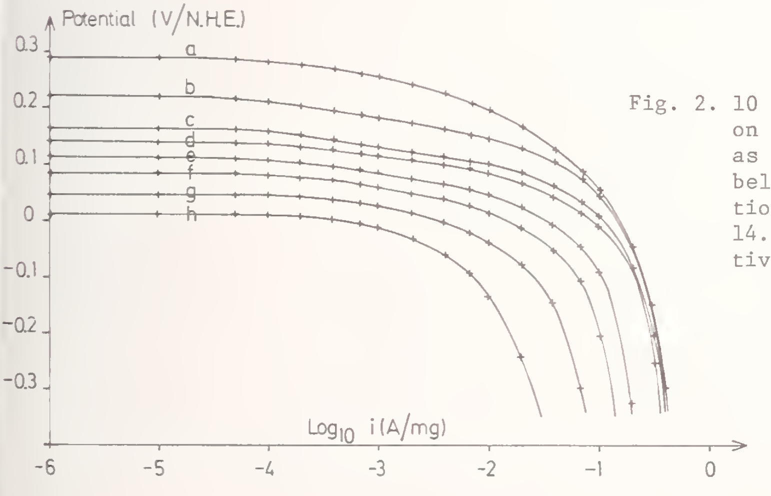

Fig. 2. 10 wt % gas-phase polyphthalocyanine on acetylene black: V--log i curves as a function of pH (v. NHE--curves below are v. hydrogen in same solution). a-h: pH 11.8, 13.0, 13.9, 14.2, 14.8, 15.2, 15.8, 16.4 respectively.

The effect of oxygen partial pressure in 2N KOH is shown in Fig. 3a. Fig. 3b gives a log-log reaction-order plot for current densities in the Tafel range (925mV v. hydrogen in the same solution). The experimental reaction order was 1.08. This value was used to correct the current density data at constant potential in Fig. 2 for the effect of oxygen solubility, so that the reaction order for OH^- could be determined. This required a consideration of the change in water activity with KOH concentration [15], both on the kinetics of the process (since one molecule of water is required for each OH^- liberated), and on the H_2 potential scale used. A complete analysis has been given (7). It was concluded that the most probable chemical reaction orders were +2 in H_2O and -1 in OH^-.

V - log i plots at 1 atm. O_2 partial pressure in 6N KOH for all the phthalocyanine prearations (monomer, gas- and liquid-phase polymer), together with the untreated carbon supp-

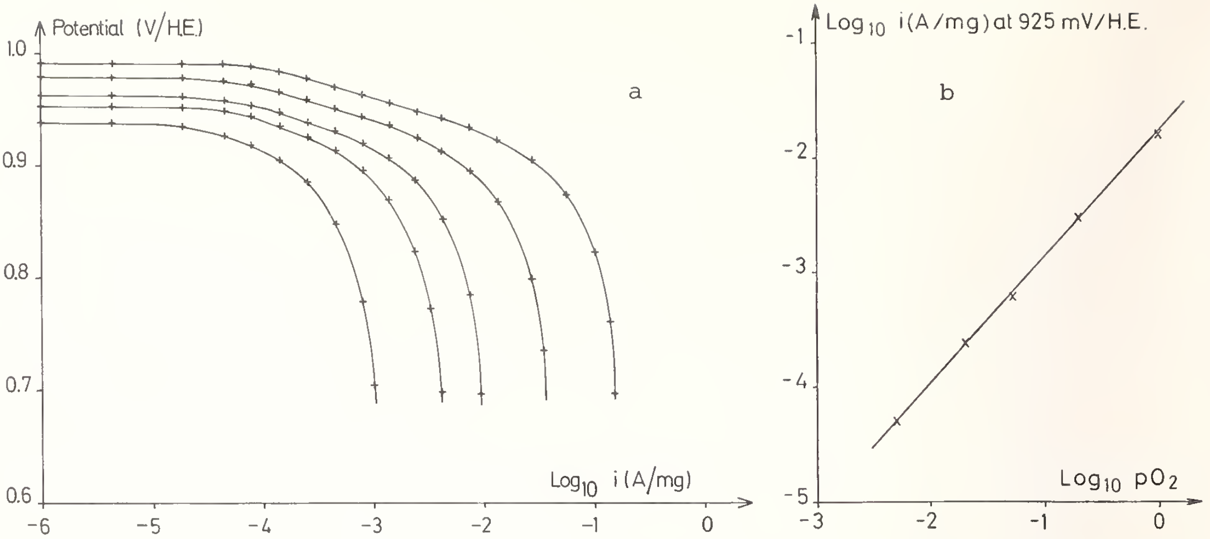

Fig. 3. 10 wt % gas-phase polyphthalocyanine on acetylene black: left, V--log i curves as a function of O_2 partial pressure (left to right, 0.005, 0.02, 0.053, 0.02 and 1 atm); right, reaction order plot (925 mV). Slope = 1.08.

ort, are shown in Fig. 4a. It is evident that the polymeric phthalocyanines confer activity much greater than that of the support in the non-diffusion-limited region (see Fig. 4b). In contrast, the effect of the monomer is largely to mask the intrinsic support activity. The liquid-phase polymer preparation shows an activity somewhat less than that of the gas-phase species.

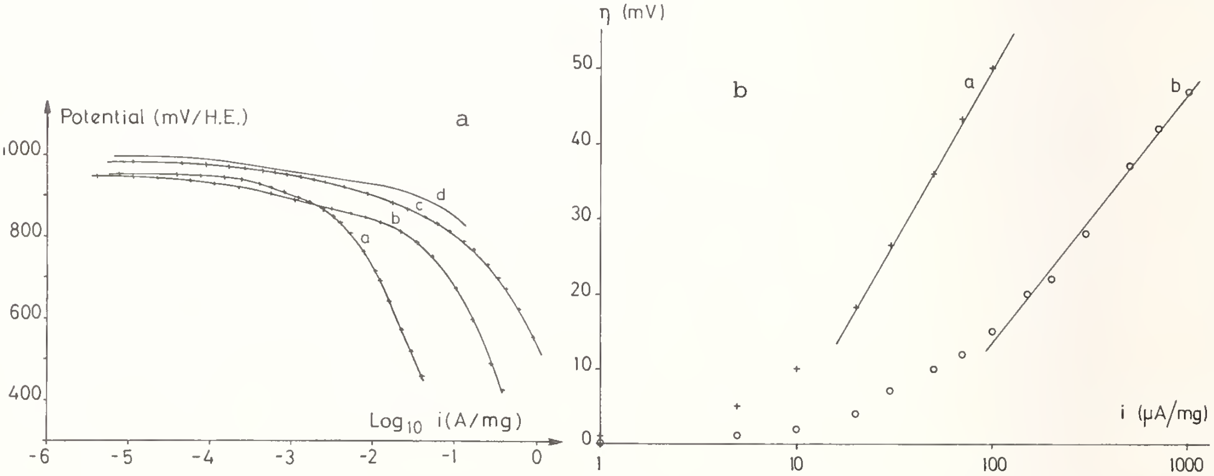

Fig. 4. Oxygen reduction in 6N KOH: left, 10 % loadings on acetylene black: a, monomer; b, support alone; c, liquid-phase polymer; d, gas-phase polymer; right, a, support alone; b, gas-phase polymer (10 wt % on 400 m^2/g graphite dust).

The effect of hydrogen peroxide additions in the presence of oxygen (1 atm.) is shown in Fig. 5a for phthalocyanine electrodes, and in Fig. 5b for electrodes of Norit BRX carbon black. In both cases, hydrogen peroxide is reduced on the material, and the current increases linearly with H_2O_2 concentration. However, the fact that hydrogen peroxide additions do not depress the rest potential of the phthalocyanine material is remarkable, and implies that the O_2/H_2O_2 couple is not reversible in this case (i.e., that H_2O_2 is not oxidized on the phthalocyanine surface).

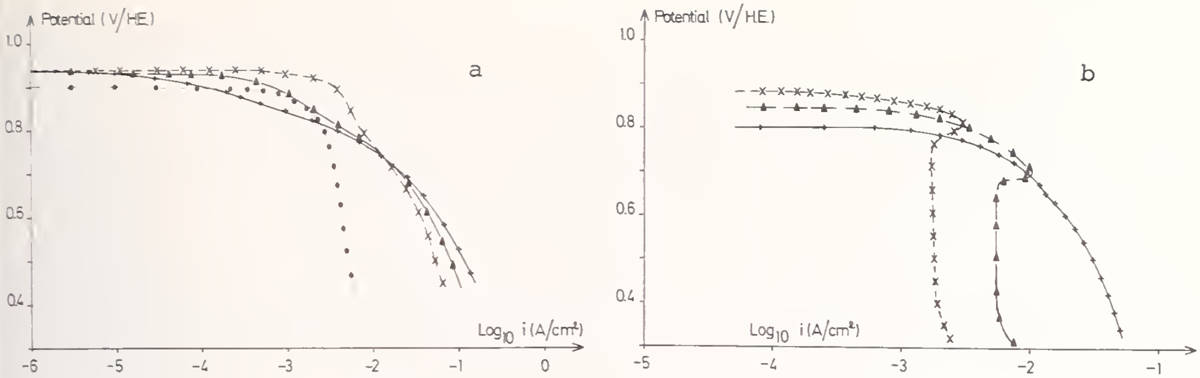

Fig. 5. V--log i curves in presence of H_2O_2 at 1 atm O_2. H_2O_2 concentrations are (left to right, in diffusion region): gas-phase phthalocyanine (left), 0.1, 0.01 M and zero (dashed curve is nickel support); BRX carbon (right), 0.01, 0.1 and 1.0 M.

Ring-disk electrode data in carbonate buffer and KOH solutions are given in Fig. 6a,b. Only negligible quantities ($<1\%$) of HO_2^- are formed above 600mV v. hydrogen. The larger quantities (increasing with pH up to 13.6% at 200mV in 5N KOH) at low potentials are perhaps due to direct reduction of oxygen on uncovered parts of the carbon black support. This is in accord with the horizontal disk current/ring current vs $\omega^{-\frac{1}{2}}$ plot shown in Fig. 7, which indicates a reaction product that is stable in contact with the catalyst [16]. This cannot be the case for phthalocyanines, which decompose HO_2^- rapidly. The half-wave potential in N KOH is independent of rotation rate (Fig. 6b), so the reaction is activation controlled.

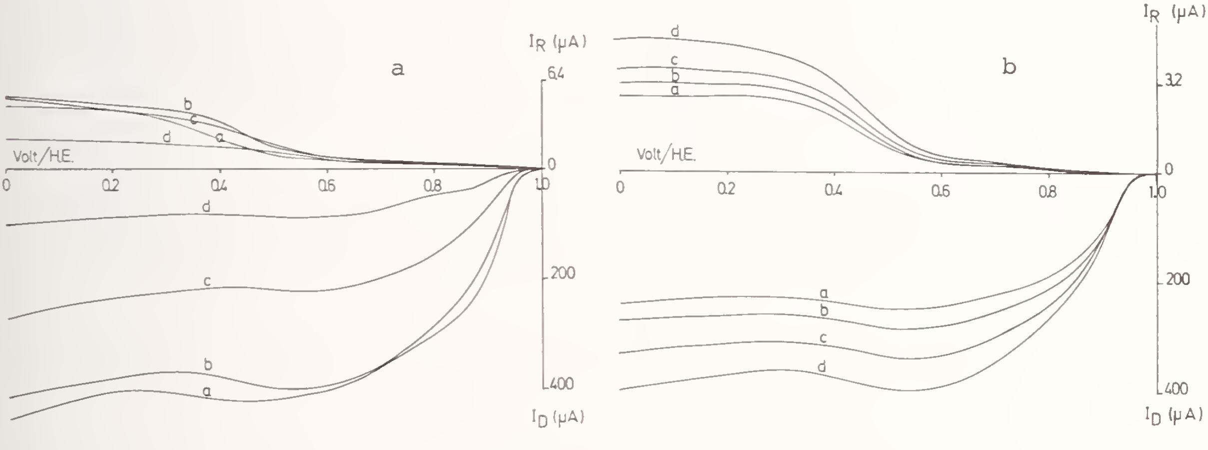

Fig. 6. Ring-disk electrode data (collection efficiency = 0.17); I_R = ring current; I_D = disk current: left, results as function of concentration at 2400 rpm; a - c, 5, 2.5 and 1 N KOH; d, N carbonate buffer, pH 13.3; right, N KOH; a - d, 900, 1200, 1800 and 2400 rpm respectively. Gas-phase polyphthalocyanine on acetylene black, 1 atm O_2.

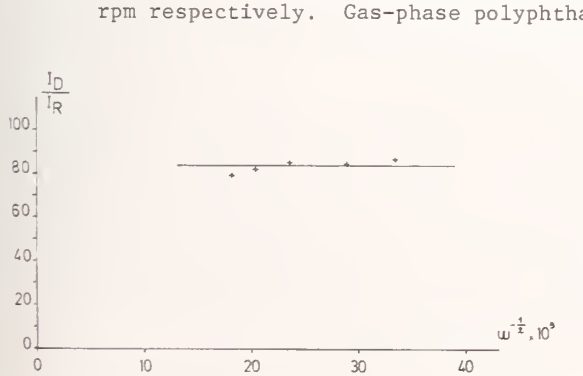

Fig. 7. I_D/I_R as a function of root rpm ($\omega^{\frac{1}{2}}$). Conditions as in figure 6 (left).

3.3 Reaction Mechanism On Polyphthalocyanines

The data in Figs. 2 and 3, obtained on gas-phase iron polyphthalocyanine preparations, show that the reaction is first order in O_2, and probably of order -1 in OH^-. An order of +2 in H_2O is probable. The Tafel slope is low: about 30mV/decade, or RT/2F. The value of α, defined as in Ref. 21, is therefore close to 2.0. The reaction is not controlled by the diffusion of a dilute product from the electrode surface, as demonstrated by the rotating-disk electrode half-wave potential data. α will normally be given by the expression [21]:

$$\alpha = n/\nu + \beta n' \beta n' \tag{1}$$

where n is the number of electrons reversibly transferred before the rate-determining step, whose stoichiometric number is ν, and for which the symmetry factor is β. n' values other than 0 (chemical process) and 1 (electrochemical process) may be excluded on activation energy grounds [22].

It is important to point out that Equation 1 will only apply to metallic or degenerate semiconductor electrodes for 1 - 1 coupled process [17], for reactions involving complete transfer of charge across the double-layer in the rate-determining-step (r.d.s.). Three other possible limiting cases have been discussed in the literature:
a) The presence of a purely resistive or barrier-layer film on the electrode surface [18].
b) Charge-transfer across the wide-gap bulk semiconductor-solution interface [19].
c) Reactions involving adsorption of reaction intermediates at some point within the Helmholtz double layer, so that charge is transferred across less than the bulk material - solution potential difference in the r.d.s., in previous steps, or both [20]. This effect may be in addition to those described in a) and b) above.

In case a), a second charge-transfer barrier occurs across the potential drop region in the film itself. This leads to an effective β value whose reciprocal is equal to the sum of the reciprocals for double layer and film transfer, so that very low apparent symmetry factors and high Tafel slopes result [18]. For case b), β will be effectively equal to unity for a cathodic process involving electron transfer from the conduction band (normally the predominant process at an intrinsic or n-type semiconductor), and zero for hole exchange to the valence band [19]. In both cases, the initial term will remain the same in Equation 1 (for 1 - 1 coupled processes), since it follows from the change in electrochemical potential in passing from the process reactants in their initial state (chemical species in the bulk solution, electrons at the Fermi level) to the state following the r.d.s. In general, case a) will always lead to higher Tafel slopes than those predicted from Equ. 1, whereas case b) will normally lead to slopes that are lower. As Gnanamuthu and Petrocelli have shown, the slopes for case c) will always be higher than predicted from Equ. 1 [20].

In the present work, α was determined to be close to 2 in the current density range between 10^{-4} and 10^{-2} A/mg, in particular in 1N and 2N KOH. If for the moment we assume that Equ. 1 applies (1 - 1 coupled processes under Langmuir conditions), then with $\alpha = 2$. possible values of n/ν are:

$n/\nu = 2$; $n' = 0$, for all β values (chemical r.d.s.; all cases except c)

$n/\nu = 1$; $n' = 1$, for β equal to 1 (semiconducting electrodes, case b).

Other possibilities certainly exist. However, processes involving cases a) and c) are improbable, owing to the very low observed Tafel slope: indeed, if case a) applies, electron transfer of primary type will be expected to be rate-determining (slope >2RT/F). Other possible types of mechanism (e.g., processes other than those of 1 - 1 coupled type, such as mechanisms III - V in Ref. 20) can be eliminated on reaction order grounds. Reactions occurring under high-coverage Langmuir conditions can be similarly rejected, since they will normally be zero-order in O_2 [2]. Temkin-type processes are formally possible, and result in higher effective values of β(e.g. $\beta = 1$ on metallic electrodes, c.f. Refs. 2,22). However, they imply fractional orders in OH^- [2,22]. We may therefore conclude that the most probable mechanism at low current density in the strongly alkaline range involves two electron transfers before a chemical r.d.s., or one electron transfer before an electron transfer r.d.s., provided, in the latter case, that the substrate can be regarded as a typical bulk semiconductor.

We suggest the following possible process:

$$O_2 \longrightarrow O_{2\ ads} \qquad \text{(rapid)} \qquad \text{I}$$

$$O_{2\ ads} + H_2O + e^- \longrightarrow HO_{2\ ads} + OH^- \qquad \text{(rapid)} \qquad \text{II}$$

$$O_2H_{\ ads} + H_2O + e^- \longrightarrow H_2O_{2\ ads} + OH^- \qquad \text{III}$$

$$H_2O_{2\ ads} \longrightarrow 2\ OH_{\ ads} \qquad \text{IV}$$

in which step IV (or possibly step III, for bulk semiconducting electrodes) is the r.d.s. Electron microscope studies have shown [9] that in 10% loadings on acetylene black, phthalocyanines consist of relatively uniform 20-30Å thick layers, whose surface area is somewhat less than that of the support [10]. A semi-infinite linear surface model is therefore proposed, in which electron transfer from the carbon to the surface takes place via a hopping process ($Fe^{II} \rightleftharpoons Fe^{III} + e^-$), which, at least at lower current densities, is not rate-limiting. Case b) (step III rate-determining), which can only apply on bulk semiconductors whose thicknesses are greater than the Debye length, can therefore be excluded. A rate-determining chemical step is therefore most probable. Since $H_2O_{2\ ads}$ in step III is not likely in strongly alkaline solution, the most probable process is I and II followed by:

$$HO_{2\ ads} + e^- \longrightarrow HO_{2\ ads}^- \qquad \text{(rapid)} \qquad \text{V}$$

$$HO_{2\ ads}^- + H_2O \longrightarrow 2\ OH_{\ ads} + OH^- \qquad \text{(r.d.s.)} \qquad \text{VI}$$

An alternative sequence may involve disproportionation as the r.d.s. (c.f. Ref. 23), i.e., V followed by:

$$HO_{2\ ads}^- + OH_{\ ads} \longrightarrow OH^- + HO_{2\ ads} \qquad \text{VII}$$

$$2\ HO_{2\ ads} \longrightarrow 2\ OH_{\ ads} + O_2 \qquad \text{VIII}$$

in which either VII or VIII is rate-determining, and in which O_2 is recycled. At low pH (11.8), the mechanism may change, perhaps to a second electron transfer step. Similarly, at higher current densities than 10^{-2} A/mg, the slow bending of the V - log i curve (compare plot for active carbon, Fig. 4a) implies a change in r.d.s., which probably becomes electron transfer through the phthalocyanine film.

Finally, it has been suggested iron phthalocyanines serve only to decompose peroxide produced by reduction of oxygen on the carbon support [24]. This is unlikely, in view of direct electron microscope evidence [9], and of the smaller limiting currents in the presence of phthalocyanine, indicating a masking effect [10]. As Goldstein and Tseung [25] have indicated, a simple reaction scheme involving decomposition will give a maximum of only a factor of 2 increase over the intrinsic carbon activity at the same overpotential. This is confirmed by a more complex model [26], which also shows that Tafel slopes will be expected to be similar on coated and uncoated supports. In practice, the enhancement factor will be less than 2, due to the masking effect of the catalyst and the fact that the efficiency of H_2O_2 production on carbon is not 100% [13]. Fig. 4b indicates a factor of ca 10 increase in activity, together with a change in Tafel slope. The hypothesis given in Ref. 24 can therefore be rejected.

4. Correlation with Spectroscopic Data

As indicated above, the oxidation state of the iron and its spin configuration determine the rate of electrosorption of molecular oxygen and of subsequent electron-transfer steps. Hoxever, reflection spectra results in KOH and oxygen show that the interface consists of a low-activity species (Fe^{II} triplet). If we compare the present data with that previously given [10], it is clear that the polymeric forms are still much more active than the monomer, which consists largely of the above iron species. Mössbauer and reflection spectral data on the dry polymer show Fe^{III} iS to be the predominant species in the gas-phase preparation (Fe^{III} HS in the liquid-phase material). These species can be presumed to be present inside the wetted polymer. There is no contradiction between the catalytic theory and the experimental data if it is assumed that initial absorption of oxygen molecules occurs within the bulk of the catalyst layer, producing oxygenated radicals which react at the interface after migration. An initial reaction path, consisting first of a chemisorption step activated by the iron spin configuration ($Fe^{III} - O_2$, iS or HS) in the bulk material, followed by reaction with water at the interface (corresponding to steps I and II), can be proposed:

$$O_2 + PPc\ Fe^{III} - O_2^- \longrightarrow O_2^* - PPc\ Fe^{III} - O_2^- \qquad \text{(in bulk)}$$
$$PPc\ Fe^{III} - O_2^- + H_2O \longrightarrow PPc\ Fe^{II} - O_2H + OH^- \qquad \text{(interface)}$$

These are followed at the interface by III and subsequent steps given above. The increased activity of Fe^{III} iS over Fe^{III} HS (gas- and liquid-phase preparations) may perhaps be explained by the greater ease of electron transfer in the absence of a change of spin. The effect of polymerization is to stabilize the Fe^{III} species, via π-d electron interaction. This lowers the activation energy for electron transfer, as shown by the fact that oxygen electrosorption appears to be rate-determining on the monomer [8].

5.Conclusions

Iron phthalocyanines have been studied by Mössbauer and optical reflectance spectroscopy and by steady-state and rotating-disk electrochemical techniques. While reduction of molecular oxygen on the monomer materials in alkaline solution is relatively slow, an increase in activity by over an order of magnitude is seen on polymer samples, particularly those prepared in situ on carbon supports by a gas-phase method. The Mössbauer and optical data indicate that this increase in activity is associated with the presence of Fe^{III} iS or HS sites within the polymer. An increase in the electron transfer rate appears to occur in parallel with an increase in oxygen adsorption rate on the polymer. Oxygen is reduced in a direct or pseudo- 4-electron process, and the most probable r.d.s. is the breaking of the O - O bond, either directly or via a disproportionation process, taking place after two rapid electron transfers. Since optical reflection spectra in the presence of oxygenated KOH are similar for both monomer and polymer, and correspond to Fe^{II} iS, we suggest that adsorption occurs initially in the bulk material, the oxygenated radicals thereafter diffusing to the interface. This agrees with previous work showing an increase in activity with increasing thickness for monomer films [8,9], for which absorption is rate-determining. The enhanced activity of polymers may be accounted for by the increased d-electron density resulting from π electron overlap in the conjugated rings. This increases both heats of adsorption of oxygenated radicals and electron transfer rates.

6. References

[1] Bockris, J. O'M. and Wroblowa, H, J. Electroanal. Chem. 7, 428 (1964).
[2] Appleby, A. J., in 'Modern Aspects of Electrochemistry, Vol. 9' (J. O'M. Bockris, Ed.) Plenum, New York 369 (1974).
[3] Balandin, A. A., 'The Problems of Chemical Kinetics, Catalysis and Reactivity', Acad. of Sciences, Moscow (1955).
[4] Gerischer, H., Bull. Chim. Soc. Belge 67, 506 (1958).
[5] Parsons, R., Trans. Faraday Soc. (London) 54, 1053 (1958).
[6] Savy, M., Andro, P., Bernard, C. and Magner, G., Electrochim. Acta 18, 191 (1973); Alt, H., Binder, H. and Sanstede, G., J. Catalysis 28, 8 (1973).
[7] Appleby, A. J., Fleisch, J. and Savy, M., J. Catalysis, to be published.
[8] Savy, M., Bernard, C. and Magner, G., Electrochim. Acta 20, 383 (1975).
[9] Savy, M., Andro, P. and Bernard, C., Ibid. 19, 403 (1974).
[10] Appleby, A. J and Savy, M., Ibid., to be published.
[11] Vogel, W. M. and Lundquist, J. L., J. Electrochem. Soc. 117, 1512 (1970).
[12] 'Sprovochnik Khimika, Vol. 3', Khimiya, Moscow 595 (1964).
[13] Appel, M., Thesis, Conservatoire National des Arts et Métiers, Paris (1974).
[14] Greenwood, N. N. and Gibb, T. C., 'Mössbauer Spectroscopy', Chapman and Hall, London (1971).
[15] Bro, P. and Kang, H. Y., J. Electrochem. Soc. 118, 1430 (1971).
[16] Damjanovic, A., Genshaw, M. A. and Bockris, J. O'M., J. Chem. Phys. 45, 4057 (1966).

[17] Riddiford, A. C., J. Chem. Soc. 1175 (1960); Electrochim. Acta 4, 170 (1961).
[18] Meyer, R. E., J. Electrochem. Soc. 107, 847 (1960).
[19] Green, M., in 'Modern Aspects of Electrochemistry, Vol. 2' (J. O'M. Bockris, Ed.) Butterworth, London 343 (1959).
[20] Gnanamuthu, D. S. and Petrocelli, J. V., J. Electrochem. Soc. 114, 1036 (1967).
[21] Parsons, R., c.f. Hoar, T. P., in 'Proc. 8th. Meeting C.I.T.C.E., Madrid, 1956', Butterworth, London 439 (1958).
[22] Damjanovic, A. and Brusic, B., Electrochim. Acta 12, 615 (1967).
[23] Hoare, J. P., J. Electrochem. Soc. 112, 849 (1965).
[24] Conference Proceedings: Fuel Cell Catalysis Workshop, Palo Alto, Ca., January 1975; E.P.R.I. SR-13, 89-90, August 1975.
[25] Goldstein, J. R. and Tseung, A. C. C., J. Phys. Chem. 76, 3646 (1972).
[26] Appleby, A. J. and Savy, M., to be published.

National Bureau of Standards Special Publication 455, *Electrocatalysis on Non-Metallic Surfaces*, Proceedings of Workshop held at NBS, Gaithersburg, Md., December 9-12, 1975. (Issued November 1976)

Electrocatalytic Activity of Phthalocyanines for Oxygen Reduction

R. J. Brodd, V. Z. Leger, R. F. Scarr, and A. Kozawa

Union Carbide Corporation
P. O. Box 6116
Cleveland, Ohio 44101

A survey of the activity of phthalocyanines as catalysts for oxygen reduction has identified several metal phthalocyanines with good activity. The central metal ion evidently controls the overall activity of the phthalocyanines for oxygen reduction. Ferric phthalocyanine had the best overall activity and approaches platinum in ability to catalyze the oxygen reduction reaction. The structure also influences the phthalocyanic activity. For copper as the central ion the order of activity is: polycopper phthalocyanine > copper phthalocyanine > copper porphyrazine. The substrate also influences the activity of the phthalocyanine as does solution composition. A mechanism for oxygen reduction is proposed which includes a hydrogen peroxide adsorption-desorption step. Rotating ring-disk results satisfactorily fit this model.

Key words: Ferric phthalocyanine; kinetics; oxygen reduction; phthalocyanine catalysts.

1. Introduction

The oxygen reduction reaction on solid electrodes is one of the fundamental reactions in electrochemistry. The reaction proceeds at a useful rate only on "active" surfaces as the reaction is highly irreversible (low exchange current). The search for catalysts for this reaction - other than noble metals - frequently follows a path suggested by biological compounds. Several biological agents, e.g., catalase, haemin, hemoglobin speed hydrogen peroxide decomposition and the transfer of oxygen in biological processes. The solubility of most of the biologically active materials mitigates against their use in practical oxygen electrode systems. Structurally similar compounds, porphyrins and phthalocyanines, have been shown to have catalytic activity for the electrochemical oxygen reduction reaction in acid, base, and saline electrolytes [1-4][1].

2. Effect of Phthalocyanines

Using a rotating disk electrode technique, the activity for oxygen reduction of phthalocyanine compounds with various central metal ions was determined on a pyrolytic carbon electrode in isotonic saline solution. The phthalocyanines purchased from Eastman Chemicals Co. were applied to the electrode surface from pyridine solution. The valence state of the central ion was not verified experimentally. Typical results are shown in

---

[1] Figures in brackets indicate the literature references at the end of this paper.

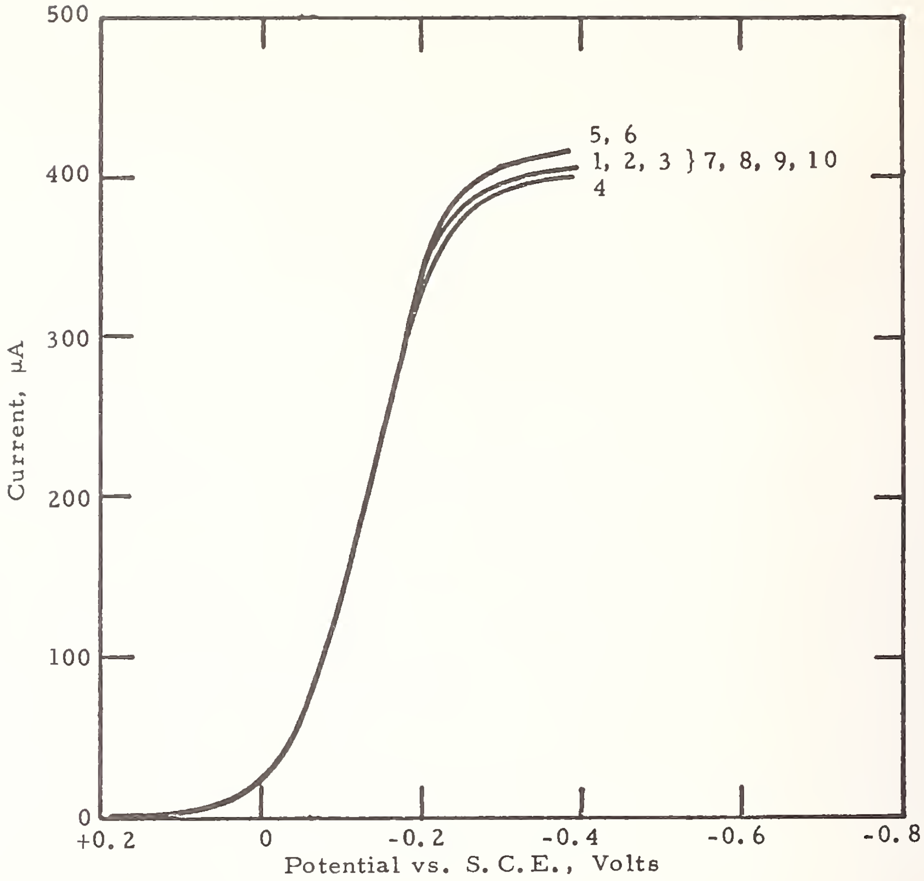

Figure 1. Ten successive current-potential curves taken at a ferric phthalocyanine-graphite electrode in 0.05 M sodium acetate (oxygen-saturated) solution at 23°C; electrode area: 0.268 cm^2. Solution was renewed after third and seventh runs.

figure 1. The activity is judged by the potential at which the activity for oxygen reduction was noted as well as the shape of the reduction curve. The overall effectiveness of the phthalocyanine for catalyzing the oxygen reduction reaction depends markedly on the central metal ion. The most effective central metal ion was Fe^{+3}. The relative order of effectiveness for central metal ions was found to be: $Fe^{+3} > Fe^{+2} > Co^{+2} > Al^{+3} > Cr^{+3} > Cu^{+2} > Ni^{+2} > Sn^{+2}$ with little or no activity for: UO_2^{+2}, Ga^{+3}, Sb^{+3}, Na^{+1}, Zn^{+2}, Ag^{+1}, Ru^{+3}. Generally transition metals were most effective as catalysts. However, Al^{+3} and Sn^{+2} exhibited some activity. The order of activity agrees fairly well with previous reports in view of the varying conditions. Savy [5-7] reported the activity of $Fe^{+3} > Fe^{+2}$ but found $Ni^{+2} > Cu^{+2}$ in contrast to that reported here. T. Beck [8] reported essentially the same order as Savy in acid solutions using gold electrodes. Alt, et al [9], however, report that the activity of $Fe^{+2} > Fe^{+3}$ based on theoretical arguments.

The activity of the phthalocyanine compounds resides in the ability of the central metal ion to coordinate (react with) oxygen. One visualizes that the phthalocyanine compound orients itself flat on the surface, the conjugated benzene rings of the phthalocyanine parallel to the hexagonal carbon structure of the base plane of pyrolytic graphite. Molecular oxygen coordinates with the central ion to form the O_2^- ion. Subsequent electron transfer may occur through the phthalocyanine molecule accompanied by proton addition. Hydrogen peroxide forms then splits to produce hydroxide as the final product.

The influence of structure of the organic portion of the molecule is demonstrated with copper as the central ion.

decreasing activity ↓
Polycopper phthalocyanine
Copper phthalocyanine
Copper octaphenylporphyrazine

The polymeric form has the highest activity. Similar results have been reported for ferric compounds in acid and basic solutions. Evidently the increased conjugated π bond character of the polymerized compound enhances the ability of the central metal ion to enter into the oxygen reduction reaction. Substitution on the ring structures also influences the electron density on the central metal ion and thereby the catalytic activity.

3. Effect of Electrode Material

The substrate has a definite effect on the ability of ferric phthalocyanine (FePc) to function as a catalyst. Graphite seems to be specific in its ability to utilize phthalocyanines as a catalyst. On graphite, the activity of FePc approaches that of a platinum electrode. When deposited on platinum or nickel the activity of the phthalocyanine catalyzed electrodes for oxygen reduction decreased. On some electrode materials, the FePc has essentially no enhancement of the oxygen reduction reaction.

The specificity of graphite may be related to the structure of the base plane. The carbon atoms in graphite form a ring structure closely resembling the benezene ring. The π bond character of the phthalocyanine could interact with the carbon surface in such a way as to enhance the catalytic activity of the phthalocyanine for molecular oxygen reduction.

4. Stability

To be useful in practical applications, the phthalocyanine catalyst must retain its activity over a wide range of potential and pH. In neutral and basic solutions the FePc is stable over the potential range from oxygen to hydrogen evolution. Repeated potential excursions have essentially no effect on activity as shown in Figure 1 for saline solution. Figure 2 for sulfuric acid solutions shows that an irreversible reaction occurs with FePc when the potential approaches the -0.3 V versus saturated calomel. Potential excursions beyond this point destroys the catalytic activity of the FePc. At room temperature, the FePc activity remains stable near the oxygen potential in acid, basic and neutral solutions. In phosphoric acid at 125°C FePc quickly transforms into phthalic acid with no catalytic activity.

5. Method of Catalyst Application

Four methods of catalyst application have been evaluated. Vapor deposition and evaporation of a pyridine solution on the electrode surface generally produce electrodes of equal catalyst activity. Due to the high resistivity of the phthalocyanine, care must be exercised to prevent buildup of thick films which lower activity. Deposition of the catalyst by slow dilution of a concentrated sulfuric acid solution produced the most uniform deposits and electrodes with the highest activity. It was thought that a different modification of the FePc crystal was produced by this technique but this could not be established experimentally. It was possible to deposit thin films of 10-100 $\mu g/cm^2$ of catalyst on graphite electrodes with activity closely approaching that of platinum for oxygen reduction.

A variation of the acid deposition technique also produced electrodes of good activity. The FePc was first precipitated at 0°C from concentrated sulfuric acid as described above. This procedure produced extremely small catalyst particles which could be filtered out.

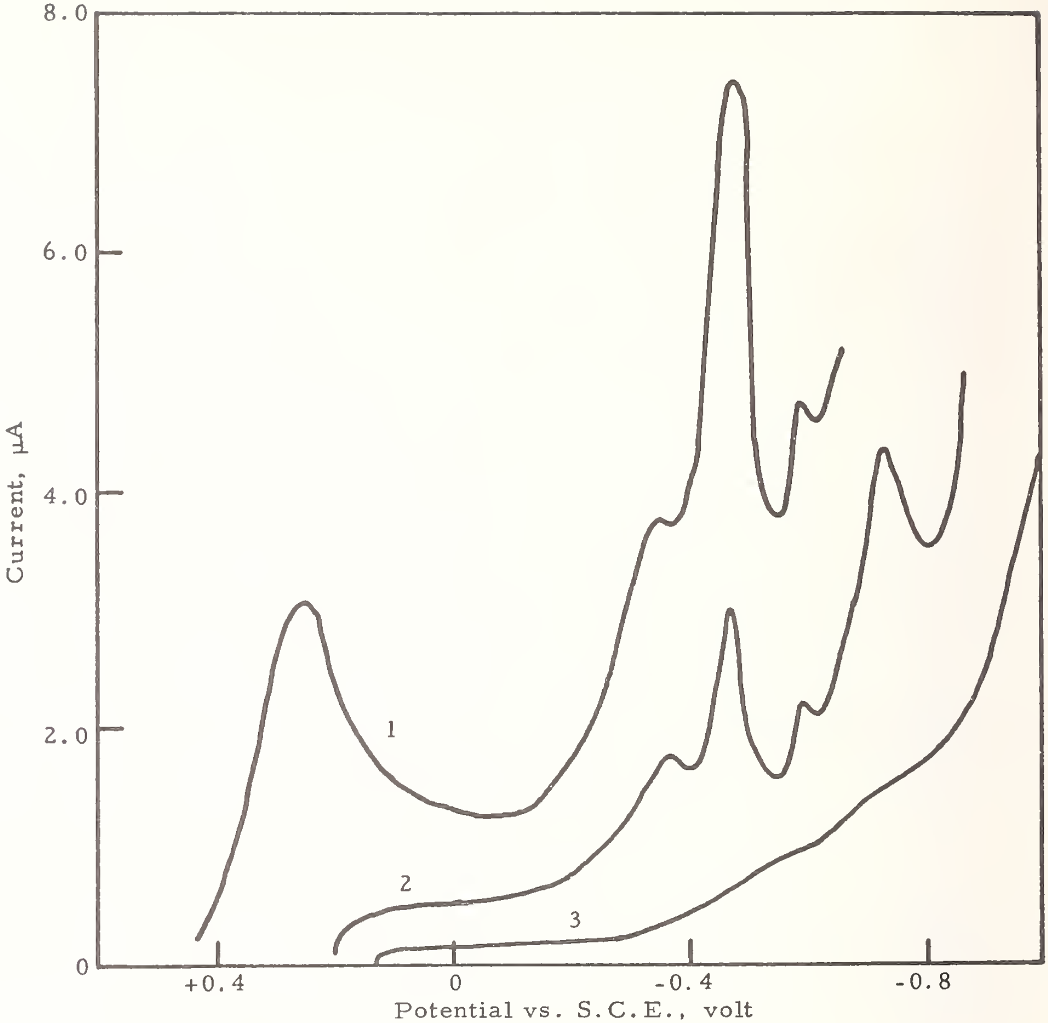

Fig. 2. Current-potential curves in 0.05 M H_2SO_4 + 0.15 M NaCl, nitrogen-saturated; electrode area: 0.268 cm^2. (1) Ferric phthalocyanine-graphite electrode (1st sweep); (2) Ferric phthalocyanine-graphite electrode (2nd sweep); (3) Graphite electrode.

These particles were suspended in acetone and sprayed onto electrode structures with an air brush.

6. Porous Oxygen Electrode Performance

"Teflon"-bonded porous fuel cell type oxygen electrodes were constructed using several different active carbons [10]. Table 1 lists several properties of the carbons used in electrode fabrication. The most important parameter was the ability of the carbon to decompose hydrogen peroxide. Heat treatment of the carbon in H_2O and CO_2 environments increased their ability to decompose hydrogen peroxide. Attempts to differentiate between carbons using ESR were partially successful. The signal enhancement in air versus in vacuum qualitatively may be related to the strength of the carbon-oxygen surface bond [11]. However, a clear relationship between ESR results and carbon activity was not established. Other factors which appeared to be of greater importance in choosing an active carbon included surface area to resistivity ratio and carbon crystallite size from x-ray line broadening.

Table 1

Effect of Carbon Support on Catalyst Activity in Saline Solution.

	Electrode Potential vs Calomel Reference				
Nuchar Type	OCV	1 mA/cm^2	H_2O_2 Decomposition Rate Constant	S. A. /pX10^{-4}	BET Surface Area m^2/g
C-190-N	0.212	-0.246	8	1.05	800
CN	0.202	-0.275	11	1.00	960
WV-L	0.168	-0.215	45	1.38	890
WV-H	0.160	-0.224	27	1.57	1100

The carbon was catalyzed with FePc before and after electrode fabrication with little effect on the overall electrode performance. Over 3700 hours of continuous operation were attained for several electrodes in saline solution. Failure was associated with delamination of the carbon matrix from the nickel conductor mesh, rather than deterioration of the catalytic activity.

7. Comparison of Pt and Carbon Surfaces

Using a rotating ring-disk technique, the activity of platinum and carbon surfaces for oxygen electroreduction was compared in alkaline solution. Various reaction models were used to fit the results from the experiments. This type of analysis permits a direct evaluation of the effect of various catalysts on each specific kinetic step of oxygen reduction. In order to satisfactorily fit the experimental results, the following model was used:

$$\begin{tikzcd} O_2 \arrow[r, shift left, "K_1"] & HO_2^-\,(ads) \arrow[l, shift left, "K_3"] \arrow[r, "K_2"] \arrow[d, shift right, "K_4"'] & OH^- \\ & HO_2^- \arrow[u, shift right, "K_{-4}"'] \arrow[r] & \text{ring.} \end{tikzcd} \tag{1}$$

An interesting feature of the model is the inclusion of an adsorption-desorption for hydrogen peroxide, steps K_{-4} and K_4. The platinum results could be fitted satisfactorily without the adsorption step in the model. However, for graphite the inclusion of a slow desorption step was essential in order to account for the observed behavior. Apparently the polar HO_2^- ion is more strongly adsorbed on the carbon surface than on a platinum surface. This may lead to increased surface coverage on the carbon and may account in part for the slower peroxide reduction rate. The results in Table 2 suggest that platinum surfaces are 10 to 30 times as active for oxygen reduction as are carbon surfaces. This difference arises primarily from the ability of platinum to support a higher rate of hydrogen peroxide reduction and the slow initial oxygen reduction step on the carbon surface. The FePc catalyzed carbon surface approaches the activity of platinum. The overall reaction rate is about the same for both electrodes as indicated by the disk current, but the rates on the various steps in the reduction process differ. There is more peroxide reduction on the FePc catalyzed surface which closely parallels a platinized platinum surface activity. The rate constants for the FePc catalyzed surface were fit for a specific set of experimental data and will vary slightly with catalyst loading.

Table 2

Rate Constants for Oxygen Reduction Reaction on Platinum and Catalyzed and Uncatalyzed Pyrolytic Graphite Electrodes in 1 N KOH.

	Platinum	Pyrolytic Graphite	FePc on Pyrolytic Graphite
K_1 (cm/s)	0.15	0.013	0.10
K_2 (cm/s)	1.0	0.03	5.4
K_3 (cm^4/mil s)	10^7	10^6	10^7
K_4 (cm/s)	4	0.08	0.013
K_{-4} (cm/s)	3.6×10^{-2}	3.0×10^{-4}	3.9×10^{-2}

8. Acknowledgement

The authors gratefully acknowledgement the partial financial support from the National Institute of Health, Artificial Heart Program, Contract No. PH-43-68-1391.

9. References

[1] A. Kozawa, V. E. Zilionis, R. J. Brodd, and R. A. Powers, "Artificial Heart Program Conference Proceedings" National Heart Institute, June 9-11, 1969 Washington, D. C., Chap. 71, p. 849.

[2] A. Kozawa, V. E. Zilionis, and R. J. Brodd, J. Electrochem. Soc. 117, 1469 (1970).

[3] A. Kozawa, V. E. Zilionis, and R. J. Brodd, J. Electrochem. Soc. 117, 1474 (1970).

[4] A. Kozawa, V. E. Zilinois, and R. J. Brodd, J. Electrochem. Soc. 118, 1705 (1971).

[5] M. Savy, C. Bernard, and G. Magner, Electrochim. Acta 20, 383 (1975).

[6] M. Savy, P. Andro, C. Bernard, and G. Magner, Electrochim. Acta 18, 191 (1973).

[7] M. Savy, P. Andro, and C. Bernard, Electrochim. Acta, 19, 403 (1974).

[8] F. Beck, Ber. Bunsenges Physik Chem. 77, 353 (1973).

[9] H. Alt, H. Bender, W. Linder, and G. Sandstede, J. Electro Anal. Chem. 31, App. 19 (1971).

[10] R. J. Brodd and A. Kozawa in Methods in Electrochemistry, A. Salkind and E. B. Yeager, Eds., J. Wiley & Sons, in press.

[11] L. S. Singer in Proceeds of the 5th Carbon Conf., Pergammon Press, New York 1963, Vol 2, p. 37.

National Bureau of Standards Special Publication 455, *Electrocatalysis on Non-Metallic Surfaces*, Proceedings of Workshop held at NBS, Gaithersburg, Md., December 9-12, 1975. (Issued November 1976)

Continued Growth of Anodic Oxide Films at Platinum and the Mechanism and Catalysis of Oxygen Evolution

A. Damjanovic[1]

It is shown on the example of oxygen evolution at platinum that thin anodic oxide films may profoundly affect kinetics and mechanism of an electrochemical reaction. At any potential above 1.0V an "insulating" oxide film grows over the electrode surface. The potential difference across the anode is then divided into the potential difference across the oxide film and that across the electrolyte double layer. The film is a barrier to electron transfer and together with the reaction across the double layer controls the kinetics and mechanism of the reaction. The exchange current density of the reaction decreases exponentially with thickness of the film. Only when the distribution of potential across the oxide film and double layer is taken into account, it is possible to explain the observed fractional reaction order with respect to activity of hydrogen ions and to propose a mechanism of the reaction that explains this reaction order. In the proposed mechanism a chemical step that follows first electrochemical step controls the rate in the double layer.

Key words: Anodic films; dual barrier, electrocatalysis; oxygen evolution; platinum anodes; reaction mechanism.

I. Introduction

Thin surface oxide or hydroxide films form at sufficiently high potentials even at anodes of noble metals such as gold or platinum. These films may affect kinetics of an electrode reaction; usually they decrease the reaction rate. For instance, the rate of anodic oxidation of hydrogen [1][2] and hydrocarbons [2] decreases by orders of magnitude once an electrode has reached the potential at which an oxide film initiates and grows over the electrode surface. Cathodic reactions too, e.g. of oxygen reduction [3], are affected by surface oxide films. Though it has been evident for some time that a thin anodic film decreases the rates of various electrode reactions, little attention has been paid in the past to analyze in some details its effect on the kinetics and mechanism,-- and hence electrocatalysis,-- for these reactions. The knowledge of the nature and properties of the anodic oxide films,-- and in particular of the kinetic character of film growth,-- that is essential for such an analysis was frequently lacking. It will be illustrated here by the example of anodic evolution of oxygen at platinum that only when the presence and kinetic character of film growth is taken into account one can avoid erroneous conclusion about the reaction mechanism and factors affecting the catalysis.

---

[1] Address: 809 Harbor Square, Rochester, New York 14617.

[2] Figures in brackets indicate the literature references at the end of this paper.

II. Oxide Film Formation

At a platinum anode an oxide film grows at any constant current density (e.g. 10^{-2} - 10^4 Am^{-2}) whenever the electrode potential exceeds 1.0V (vs HE). As shown by a number of workers, -- and notably by Vetter and Schultze [4], -- the potential, V, at a constant current density increases linearly with time or integrated charge, q, as shown in figure 1. Significantly, the dV/dq slopes are proportional [5] to log current density (fig 2). As shown with a rotating disk-ring electrode, in the linear V-time region and before a critical potential is reached (cf. N in fig 1) current is used up entirely for the formation of an

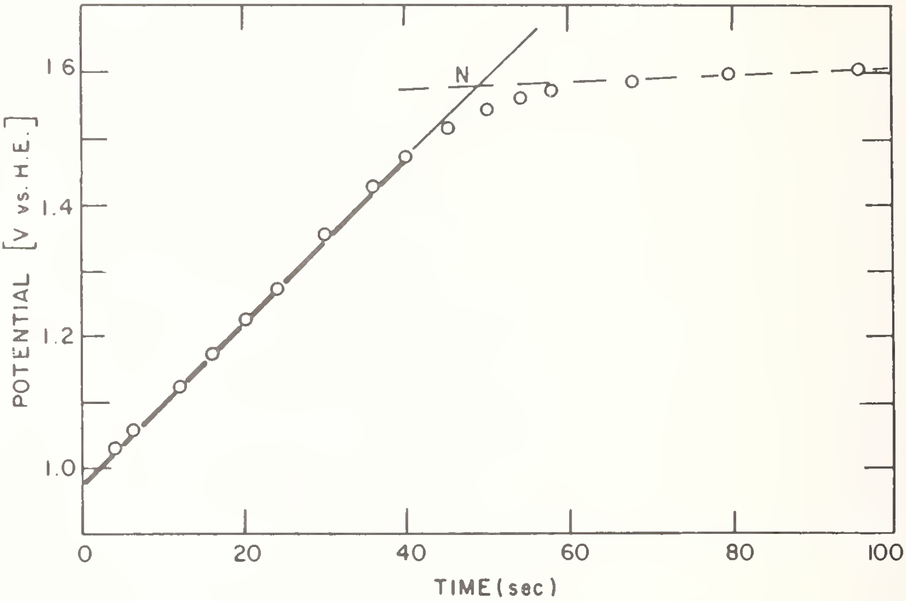

Fig. 1. Change of potential with time at Pt anodes at a constant current density of polarization ($i = 2\times10^{-1}Am^{-2}$). The linear region is followed by a quasi-steady state. Oxygen starts to evolve after point N [5].

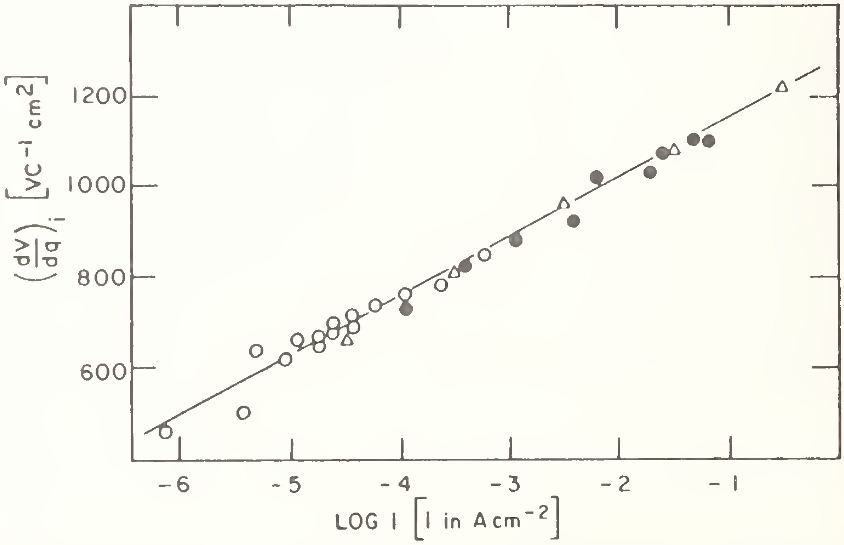

Fig. 2. The dependence of $(\partial V/\partial q)_i$ on current density of polarization [5].

anodic oxide film (with no O_2 evolution though the electrode potential exceeds the reversible O_2 potential by as much as 0.3 to 0.4V). After the critical potential, -- which increases as the applied constant current density increases, -- oxygen starts suddenly to evolve and soon becomes predominant reaction. The rate of oxide growth is then substantially reduced. These changes in the anodic processes are reflected in the V-t and V-q diagrams: the potential 'flattens off' and assumes a 'steady state' value. As will be discussed below, in this region too, neither potential nor film thickness remains constant; they continue to increase with time of polarization but now very slowly.

The rate of growth of anodic films in the linear potential region is well accounted for by the formalism of the Mott-Cabrera model of growth for high field assisted ionic diffusion. For this model the rate equation can be written as:

$$i_{og} = zeN\nu \exp\left[-\frac{\Delta G^*}{RT}\right] \exp\left[\frac{zF\lambda(V-V_0)}{dRT}\right]$$

$$= i_{og,o} \exp\left[\frac{\alpha\Delta V_{of}}{d}\right] \quad . \qquad (1)$$

Here, V_0 is the potential at which a film starts to grow[3], ΔV_{of} is the potential difference across the film, d is (average) film thickness (V_{of}/d is hence field within the oxide film), z is the charge and λ 'half jump' distance of migrating ions. N represents a concentration term and ΔG^* is zero field activation energy. Other symbols have their usual significance. From figure 2 and with a reasonable value for the conversion factor to relate q to d, the transfer coefficient, α, has been found [5] to be 16nm V^{-1}. This leads to $\lambda \approx 0.2$nm and $z = 2$. Anodic film is, therefore, a divalent oxide phase in accordance with a previous ellipsometric study [6].

Experiments at various temperatures gave $\Delta G^{\ddagger} \approx 25$ kcal mol^{-1}, and $N\nu \approx 3.10^{31}$ s^{-1} m^{-2}. This product is a characteristic of the rate determining step. With the mean frequency $\nu = 3.10^{12}$ s^{-1}, -- calculated from the Debye temperature, -- N is very closely equal to the density of atoms in the surface of the metal. This remarkable agreement strongly suggests that a process at the metal/oxide interface, -- rather than within the oxide phase, -- controls the rate of oxide film formation[4].

The most important outcome of these studies of oxide film growth is the realization that a strong field ($\approx 5.10^8$ Vm^{-1}) must exist within a growing oxide film [4,5,8]. Hence, the electrode potential difference, ΔV, must be distributed between the potential difference across the oxide film itself, ΔV_{of}, and that across the oxide film -- electrolyte double layer, ΔV_{dl}. Such a potential distribution is expected to affect both kinetics and mechanism of an electrode reaction that occurs at oxide covered electrodes [9].

Ellipsometry has shown that after the critical potential (N in fig 1) at any constant current density of polarization, i_p, film thickness increases logarithmically with time (cf. fig 3) in such a way that [10]:

$$\left(\frac{\partial d}{\partial \log t}\right)_{ip} = \text{const} \neq f(i_p) \qquad (2)$$

and

$$\left(\frac{\partial d}{\partial \log i_p}\right)_t = \text{const} \neq f(t) \qquad (3)$$

The rate of this slow, extended growth is described by equation:

$$i_{og} = i_{og,o} \exp\left[-\frac{d}{d_0} + \frac{aF\Delta V}{RT}\right] \qquad (4)$$

---

[3] V_0 is close to 0.9 V vs. HE.

[4] Contrary to some literature readings, the same rate equation as above describes initial stages of oxide film growth irrespective of the mode of polarization [7].

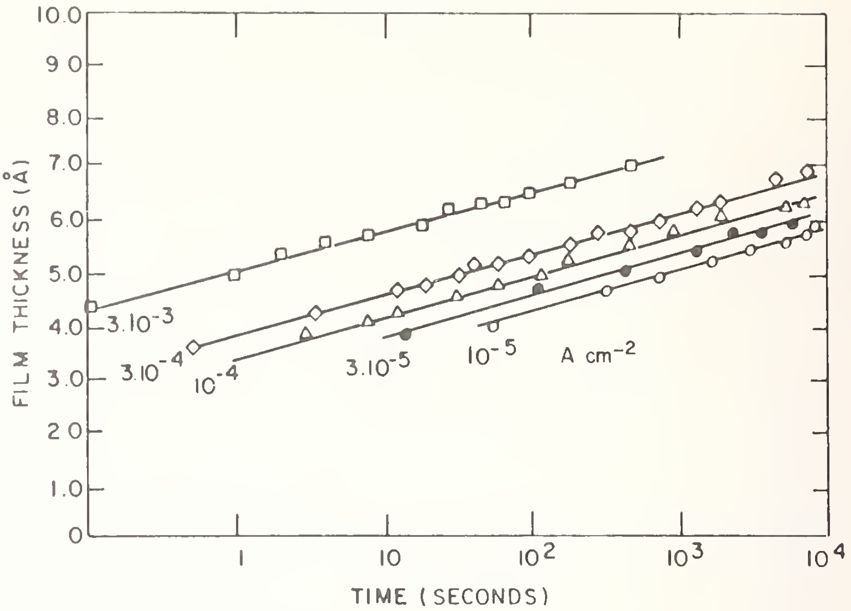

Fig. 3. Thickness of anodic oxide films at platinum as function of time at constant current densities of polarization [10].

that is diametrically different from the equation of initial growth (cf. eq (1)). Similar relationship is obtained for the extended growth at a constant potential mode of polarization [10]. Apparently, relationship given by eq (4) does not reflect any particular change in ΔV_{of} which is now controlled by the major ongoing reaction, the oxygen evolution reaction, and which even at a constant mode of polarization is not constant any longer. Rather, this relationship reflects a genuine change in the mechanism of growth. The change occurs only after O_2 starts to evolve and has become a major reaction. This is an unexpected result, the meaning of which is as yet unclear. The growth according to eq (4) has previously been observed at other metal electrodes, e.g. at iron electrodes [11]. However, in the latter case oxide growth is the only reaction (no O_2 evolution) that occurs at the electrode and the change of potential with time reflects the mechanism of oxide growth only.

III. Oxide Films and Oxygen Evolution

It has recently been shown [12] that both the ellipsometric thickness of anodic films and electrode potential change linearly with logarithm of current density, i_p, with which a prereduced electrode is anodically polarized for a given time. For all times of polarization the dV/d log i_p slopes are close to 170 mV and dd/d log i_p to 0.1 nm (figs 4 and 5). After an electrode has been polarized for a given time with a constant current density and the current density, i, is decreased in steps, no change in thickness, d, is observed (from A to B in fig 5). In contrast to this, ΔV decreases as i is decreased (fig 4). The dV/d log i slopes are now close to the frequently reported value of 115 mV or to 2.3 (2RT/F). Thus, the linear V-log i relationship with the slopes $\partial V/\partial \log i = 120$ mV,-- observed for over several decades of current density [13, 14],-- is obtained only at electrodes that were anodically pretreated at a higher potential or current density to form a stable oxide film, and when it was ensured that the thickness of the film remained unchanged during measurements. The slope is then independent of film thickness [9], i.e.:

$$\left(\frac{\partial V}{\partial \ln i}\right)_d = \frac{2RT}{F} \neq f(d) \tag{5}$$

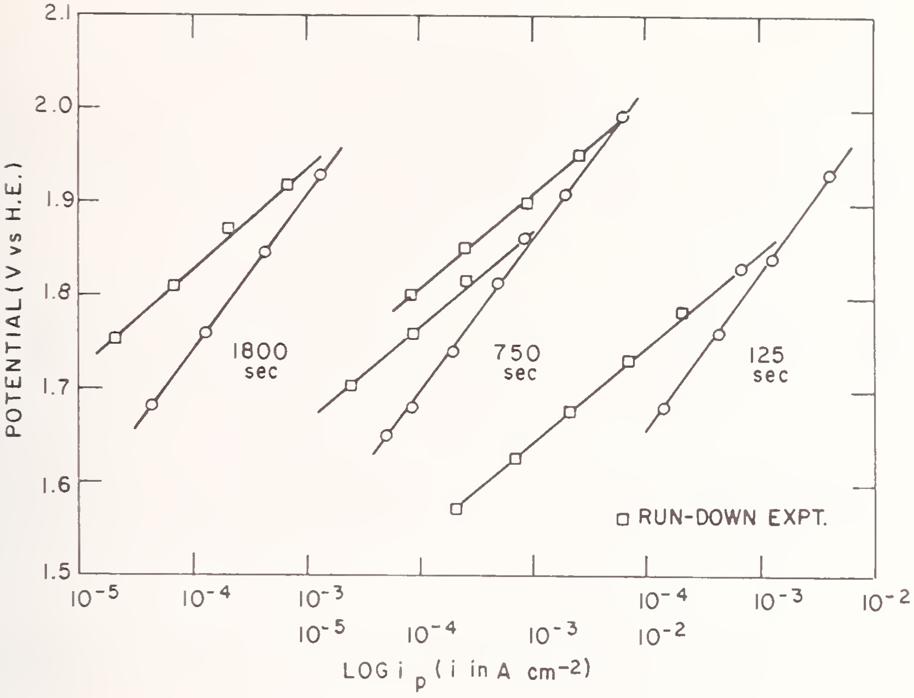

Fig. 4. Electrode potentials after 125, 750 and 1800 seconds at a given current density of polarization (circles). Squares represent subsequent potential--current density relationships at decreasing current densities [12].

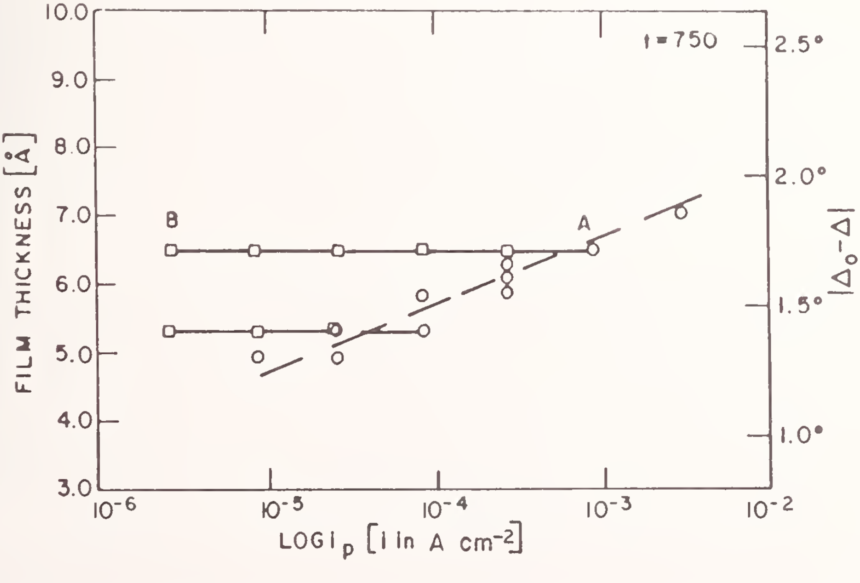

Fig. 5. Thickness of anodic oxide films after 750 seconds at a given current density of polarization (circles). Squares represent subsequent thickness--current denstiy relationships at decreasing current densities [12].

It has been shown [12] that log i is linearly related both to V and to d, and that the function[5]:

$$i_{O_2} = C \exp \left(- \frac{\delta d}{2}\right) \exp \left(\frac{F\Delta V}{2RT}\right) \tag{6}$$

gives the dependence of the rate of oxygen evolution on electrode potential and film thickness. For constant thickness, current density is given by:

$$i = i_o \exp \left(\frac{F\Delta V}{2RT}\right) \tag{7}$$

with exchange current density equal to:

$$i_o = C \exp \left(- \frac{\delta d}{2}\right) \tag{8}$$

Thus, the exchange current density,-- a measure of the catalytic activity,-- decreases exponentially with the thickness of the oxide film. Unless the effect of film thickness is taken into account, any correlation of the catalytic activity with a particular physical parameter at various anodes (e.g. with bond strength of adsorption of reactants or reaction intermediates or with work function of anode material) is, therefore, of dubious validity.

As a consequence of the increase of film thickness with logarithm of time, potential too at a constant current density increases with the logarithm of time (cf. fig 6). The V-log i lines at various constant current densities are, therefore, parallel between themselves and equally spaced for an equal increment of log i.

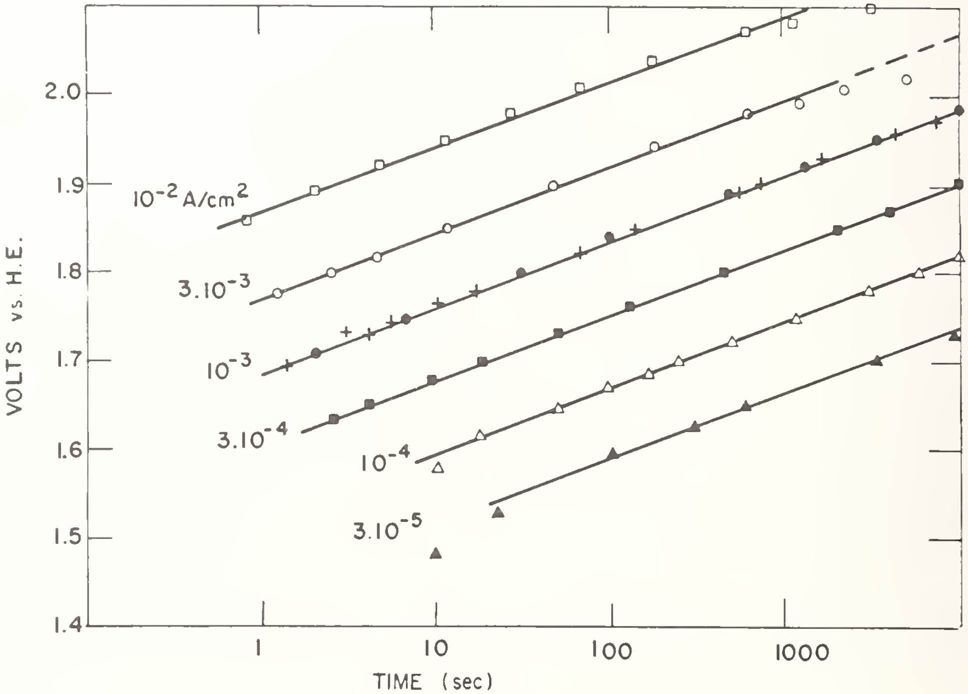

Fig. 6. Potentials at platinum as function of times at different constant current densities of polarization [10].

---

[5] The same relationship was obtained by Schultze and Vetter [15] from different experiments and with different arguments.

IV. Mechanism of Reaction

In some earlier studies of O_2 evolution, either the presence of oxide films at electrodes was ignored or insufficient care was taken to keep film thickness constant in solutions of different pH. This then led to erroneous conclusion that the reaction was pH independent and that the first electrochemical step was rate determining [13]. Recent experiments have shown, however, that for the same thickness of the oxide film the rate is represented by equation

$$i = k\,[H^+]^{-1/2} \exp\left[\frac{FV}{2RT}\right] \tag{9}$$

i.e., the reaction order with respect to H^+ is negative and fractional (not zero!). The fractional reaction order precludes the first electrochemical step as rate determining. Moreover, fractional reaction order could not be accounted for by any simple analysis either under Langmuir or Temkin conditions of adsorption. It is explained [9] in terms of a dual barrier model [16, 17] according to which there is a potential difference both across the oxide film and across the oxide/electrolyte interface, i.e. it is explained only after the presence of anodic oxide films is considered in the analysis. According to this model, current densities across the oxide film and across the double layer are given respectively by [12]:

$$i_{of} = X_o \exp(-\delta d) \exp\left[\frac{F\Delta V_{of}}{RT}\right] \tag{10}$$

and [9]:

$$i_{dl} = A\,[H^+]^{-1} \quad \exp\left[\frac{F\Delta V_{dl}}{RT}\right]\ . \tag{11}$$

Here, X_o and A are constants independent of pH. Evidently, only reaction across the double layer is pH dependent but with no fractional reaction order. Analysis has shown further that the observed current density is given by [9]:

$$i = i_{dl} = i_{of} = (AX_o)^{1/2}\ [H^+]^{-1/2} \exp\left(-\frac{\delta d}{2}\right) \cdot \exp\left[\frac{F\Delta V}{2RT}\right] \tag{12}$$

which for a constant thickness reduces to eq (9) and thus accounts for the unusual pH dependence of the reaction. It is suggested that the rate determining step for the reaction across the double layer is a chemical step which follows the first, fast electrochemical step. The rate across the oxide film is most likely controlled by the quantum mechanical tunneling process, but as yet there is no satisfactory account for this equation.

V. In Conclusion

In conclusion, it is illustrated here on the example of oxygen evolution at platinum anodes that a thin, 'insulating' anodic oxide film may profoundly affect the rate of an electrochemical reaction. The observed change in the catalytic activity of the oxygen electrode is related to the change in thickness of the oxide film. Oxide film affects also the mechanism of the reaction. Hence, whenever an electrode surface is covered by an oxide film, its presence has to be taken into account in analyses of mechanisms and catalysis of electrode reactions. Of course, an anodic oxide film at an electrode does not have to be 'insulating' in which case the rate of a reaction should not be greatly affected by the thickness of the oxide film. Oxygen evolution at nickel anodes is perhaps an example for this. However, even at platinum,-- when an oxide film is formed at very high current densities (e.g. $i \geq 10^3\ Am^{-2}$) for a longer time,-- there is experimental evidence [18] that a 'conductive' oxide phase eventually forms. Thus, at a high current density electrode potential first increases with time, as expected when an 'insulating' oxide film forms, but then it decreases substantially with further polarization (reactivation of the electrode) though film thickness continues to increase [18]. Apparently, divalent oxide is transformed to a higher valence 'conductive' oxide phase. The latter experimental evidence suggests one avenue for a revived search and 'tailoring' of new catalysts for oxygen electrode reaction.

VI. References

[1] Schuldiner, S., J. Electrochem. Soc. 115, 362 (1968).
[2] Wroblowa, H., Piersma, B. J. and Bockris, J. O'M., J. Electroanal. Chem. 6, 401 (1963).
[3] Damjanovic, A. and Bockris, J. O'M., Electrochim. Acta 11, 376 (1966).
[4] Vetter, K. J. and Schultze, J. W., J. Electroanal. Chem. 34, 141 (1972).
[5] Damjanovic, A., Ward, A. T., Ulrick, B. and O'Jea, M., J. Electrochem. Soc. 122, 471 (1975).
[6] Visscher, W., Optics 26, 402 (1967).
[7] Harris, L. B. and Damjanovic, A., J. Electrochem. Soc. 122, 593 (1975).
[8] Ord, J. L. and Ho, F. C., J. Electrochem. Soc. 118, 46 (1971).
[9] Damjanovic, A. and Jovanovic, B., J. Electrochem. Soc. 123, 374 (1976).
[10] Ward, A. T. and Damjanovic, A., Submitted to J. Electrochem. Soc.
[11] Sato, N. and Cohen, M., J. Electrochem. Soc. 111, 512 (1964).
[12] Damjanovic, A., Ward, A. T. and O'Jea, M., J. Electrochem. Soc. 121, 1186 (1974).
[13] Bockris, J. O'M. and Hug, A. K. M. S., Proc. Roy. Soc. (London) A237, 277 (1956).
[14] Damjanovic, A., Dey, A. and Bockris, J. O'M., Electrochim. Acta 11, 791 (1966).
[15] Schultze, J. W. and Vetter, K. J., Electrochim. Acta 18, 889 (1973).
[16] Meyer, R. E., J. Electrochem. Soc. 107, 847 (1960).
[17] MacDonald, J. J. and Conway, B. E., Proc. Roy. Soc. 269, 419 (1962).
[18] Vissher, W. and Blijlevens, M., Electrochim. Acta 19, 387 (1974).

ELECTROCHEMICAL PROCESSES ON NON-METALLIC SURFACES - 3

National Bureau of Standards Special Publication 455, *Electrocatalysis on Non-Metallic Surfaces*, Proceedings of Workshop held at NBS, Gaithersburg, Md., December 9-12, 1975. (Issued November 1976)

Electrochemical Surface Reactions on Non-metals

R. Memming

Philips GmbH, Forschungslaboratorium Hamburg
2000 Hamburg 54, Germany

Various surface reaction of semiconductors during electrochemical polarization are investigated which are of interest in connection with catalytic and photo-electrocatalytic processes. Examples for the anodic and cathodic decomposition are given and discussed with regard to the stability of electrode materials. In addition the formation of semiconducting layers on metal electrodes is described and their analysis and characterization investigated as far as electron transfer is concerned. Reactions at bronze electrodes leading to semiconducting surface films are included.

Key words: Anodic decomposition; cathodic decomposition; electrochemistry; inorganic bronze electrodes; inorganic bronze electrodes; metal electrodes; semiconductor electrodes; stability, surface layers; surface reactions.

1. Introduction

Since there is such a great demand for less expensive electrodes for fuel cells and suitable materials for photoelectrolytic devices the electrochemical properties of quite a large number of non metallic electrodes have been studied in the recent past. Unfortunately, not only oxidation and reduction of hydrogen and oxygen, respectively, were observed but also other processes such as electrochemical decomposition or film formation have been detected. These surface reactions could be divided into several processes such as

semiconductor → decomposition
semiconductor → formation of insulating film
semiconductor → formation of metallic film
metals (or metal-like conductor) → formation of semiconducting film
metals (or metal-like conductor) → insulating film

In the present paper examples of these processes are given and the stability of the electrode material correlated to the band gap of the semiconductor. The main emphasis is put on the analysis and characterization of the semiconducting properties of semiconductor electrodes, of semiconducting films on a metal substrate and of bronze electrodes.

2. Electrochemical Decomposition and Stability of Semiconductor Electrodes

Most semiconducting materials can be decomposed in aqueous solutions by anodic oxidation or cathodic reduction. It is useful to distinguish between element and compound semiconductors since in the first type the bonding is pure covalent whereas in compounds a certain degree of ionic bond exists. In all cases the electronic states at the surface have a key function in the reaction mechanism as demonstrated schematically for the dissolution of an element semiconductor in fig. 1. In this figure A represents a surface atom of an element semiconductor to which two hydroxyl groups are bonded. Principally the anodic dissolution occurs in two steps by which the chemical bond between two neighbours has to be broken under the influence of an applied electrical field. The latter process, however, is only possible if the surface density of holes is sufficiently large. In the first reaction step a surface radical is formed. Since the chemical bond between the surface atom A and the crystal is now much weaker the energy level of the surface radical should not be located anymore within the valence band but it should occur above the valence band as indicated in the lower part of fig. 1a. The next reaction step (complete separation of the surface atom) is characterized by an electron transfer from the surface level E_t into the valence or into the conduction band. In the first case also holes are required at the surface. A conduction band process, however, is only possible for a rather small energy distance of E_t relative to the conduction band, i.e. such a process can occur only with small band gap semiconductors. It has been observed with germanium electrodes [1][1] (E_g = 0.8 eV) but with no other semiconductor.

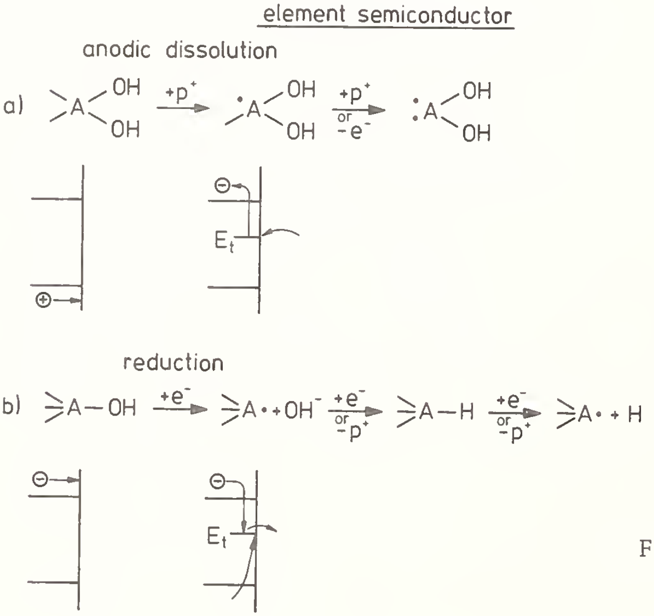

Fig. 1. Elementary process of anodic dissolution and reduction of element semiconductors.

As mentioned above the anodic dissolution mechanism represented in fig. 1a contains only the most important reaction steps. In this example two charges are required for the dissolution process as it was found e.g. for Si-electrodes in hydrofluoric solutions [2]. In most other cases four charges are required. Then the unpaired electron remains at the crystal surface and has to be neutralized either by electron transport to the back side contact or by a further hole from the valence band [1,2]. The crystal surface

---

[1] Figures in brackets indicate the literature references at the end of this paper.

is restored by chemical reaction with the reacting molecules such as OH^--molecules. It should be emphasized that the dissolution current i^+ is proportional to the density of holes at the surface, p_s, i.e.

$$i^+ \sim p_s \quad . \tag{1}$$

Assuming Boltzmann distribution then p_s is related to bulk hole density p_o by

$$p_s = p_o \exp\left(+ \frac{eU_{sc}}{kT}\right) \quad , \tag{2}$$

in which U_{sc} represents the potential across the space charge layer. Since in most cases the externally applied potential only occurs across the space charge layer the anodic current is given by

$$i^+ \sim \exp\left(eU_{sc}/kT\right) = \exp\left(e\Delta U_E/kT\right) \quad (U_E = \text{electrode potential}). \tag{3}$$

In this case a Tafel slope of 60 mV/decade is expected as it was proved for various semiconductors [2,3].

The same principle scheme is valid for cathodic processes (fig. 1b). In this case an electron transfer from the conduction band across the interface leads to a separation of an OH^--group from the surface. A radical is formed again and the subsequent step may occur either by charge transfer via the conduction or the valence band [4,5].

These basic reaction steps also occur in the decomposition process of compound semiconductor electrodes. The main difference from element semiconductors is due to possible differences in the bonding character. The bonding could be of covalent or of ionic nature. Two examples are GaP- and ZnO-electrodes. For instance in the case of GaP in which the bonding is mainly covalent, the anodic dissolution in acid solutions is given by [6]

$$GaP + 3H_2O + 6p^+ \longrightarrow Ga^{3+} + H_3PO_3 + 3H^+ \tag{4}$$

whereas in alkaline solutions:

$$GaP + 4OH^- + 3p^+ \longrightarrow GaO_2^- + P + 2H_2O \ .$$

The surface structure is shown in fig. 2. Although the chemical bonding is more covalent differences occur in acid and alkaline solutions. If both atoms are dissolved electrochemically then six charges are necessary for the dissolution of one GaP-molecule as observed in acid solutions. Since in alkaline solutions only three charges are consumed it may be concluded that one electron of each bond remains at the phosphorus atom, i.e. neutral phosphorus is formed which is dissolved slowly in a subsequent step. Breaking one bond, for instance by trapping a hole at the surface, the corresponding phosphorus surface atom is left with an unpaired electron (fig. 2a). The energy of this unpaired electron does not coincide with the valence band, its position is somewhat above the valence band, as indicated by the energy diagram in fig. 2. Principally the unpaired electron can be transferred into the valence band. On the other hand the transition probability from this energy state into the valence band must be very low in alkaline solutions because only three charges are consumed. The different behavior in acid and alkaline solutions are rather difficult to interpret. A more speculative explanation could be the assumption that the phosphor radicals are stabilized in acid solutions by H_3O^+-ions bridged to the surface atoms as shown in fig. 2b leading to a downwards shift of the radical energy level.

The situation is somewhat different for compounds of more ionic bonding such as ZnO and other II-VI-compounds. It is assumed that hydroxyl groups are bonded to the more positively charged $Zn^{\delta+}$-atom. According to Gerischer [7] the anodic dissolution can be described as follows:

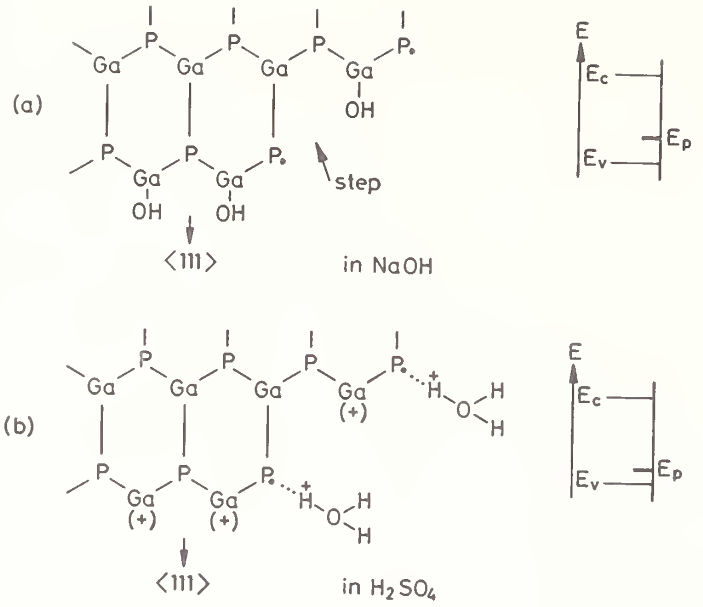

Fig. 2. Surface structure of GaP lattice during anodic dissolution and energy diagram. (a) in NaOH; (b) in H_2SO_4.

$$\begin{aligned} O_s^{2-} + p^+ &\xrightarrow{\text{slow}} O_s^- \\ O_s^- + O_s^{2-} + p^+ &\xrightarrow{\text{slow}} (O\text{-}O)^{2-} \\ (O\text{-}O)^{2-} + 2p^+ &\xrightarrow{\text{fast}} O_2 \\ 2Zn_s^{2+} + aq &\xrightarrow{\text{fast}} 2Zn^{2+} + 2\,aq \\ 2ZnO + 4p^+ &\longrightarrow 2Zn^{2+} + O_2 \end{aligned} \qquad (6)$$

In this case the hole p^+ produced by light excitation is trapped at a more negatively charged oxygen atom at the surface (O_s^{2-}) and oxygen is evolved in two subsequent steps leading also to a dissolution of Zn. According to Justice and Hurd [8] the anodic current is quantitatively due to dissolution.

During cathodic polarization the reverse process was observed. In this case electrons are trapped at a more positively charged Zn-atom at the surface resulting in the reduction of Zn^{2+} to Zn and of oxygen to H_2O according to the mechanism given by

$$\begin{aligned} Zn_s^{2+} + e^- &\longrightarrow Zn_s^+ \\ Zn_s^+ + e^- &\longrightarrow Zn \\ O_s^{2-} + 2H^+ &\longrightarrow H_2O \\ ZnO + 2e^- + 2H^+ &\longrightarrow Zn + H_2O \end{aligned} \qquad (7)$$

These reactions are typical for various other II-VI-compounds. For instance anodic polarization of CdS results into the dissolution of cadmium. In this case, however, sulfur remains as an insulating layer at the surface [9]. On the other hand cathodic polarization leads to the formation of a metallic film on the surface.

In table 1 the decomposition products of various semiconductor electrodes during anodic and cathodic polarization are summarized.

Table 1. Decomposition products of various semiconductor electrodes during anodic and cathodic polarization.

Electrode material	E_g, eV	Anodic decomposition products		Cathodic decomposition products	
Ge(n,p)	0.8	Ge^{4+}	[1]	H_2	[1]
Si(n,p)	1.1	Si^{2+}, Si^{4+} (in HF)	[2]	H_2	[2]
GaAs(n,p)	1.4	Ga^{3+}, A^{3+}	[10]	AsH_3, H_2	[10]
CdSe(n,p)	1.75	Cd^{2+}, Se^{o}	[9]	Cd, (H_2Se)	[9]
GaP(n,p)	2.35	Ga^{3+}, P^{o} or P^{3+}	[6]	H_2; (PH_3 < 0.1%)	[6]
CdS(n)	2.4	Cd^{2+}, S^{o}	[9]	Cd, H_2S	[9]
WO_3(n)	2.5	O_2		H_xWO_3, H_2	[11]
SiC(n,p)	3.0	Si^{4+}, C (in HF)	[12]	H_2	[12]
ZnO(n)	3.2	Zn^{2+}, O_2	[8]	Zn, H_2O	[8]
TiO_2(n)	3.2	(Ti^{4+}), O_2	[13]	Ti, H_2	[14]
K_3TaO_4(n)	3.5	O_2	[15]	?	
SnO_2(n)	3.8	O_2	[16]	H_2, Sn (in HCl)	[16]

According to this table the most stable or inert electrode materials exhibit a large band gap. This result seems to be quite reasonable since various authors have found a linear relationship between band gap E_g and average bond energies of binary compounds [17]. Materials of large bond energies are expected to be relatively stable. This result is important especially for the selection of electrode materials in photo-electrocatalytic devices in which mainly TiO_2 has been used. In connection with these problems it should be mentioned that several materials show a quasi stable behavior in the dark, e.g. n-type electrodes in the anodic range where the current is limited to a very low value due to the absence of holes. Any excitation of holes by light absorbed by the electrode, however, may lead to anodic dissolution or film formation. Whether dissolution or formation of an insulating film occurs depends mainly on the electrolyte used. For instance SiC seems to be a very stable electrode in aqueous solutions. However, this stability is only due to the formation of an oxide film which also limits the electron transfer [12]. Only in hydrofluoric acid anodic dissolution was observed.

3. Characterization of Electrode Surfaces

Some information about the electrochemical behavior can be already obtained from current-potential measurements. Taking n-SnO_2 as an example the anodic current is limited to a very low value up to large anodic potentials (fig. 3). This current rise is due to oxygen evolution caused by electron tunneling through the space charge region[16,18,20]. This tunneling process only occurs with heavily doped electrode materials. For lower dopings this current rise does not occur or only at much higher potentials. In the lower potential range the current is limited to a very low value because holes are required for this process. Light excitation leads to current increase (fig. 3). The corresponding photocurrent sets in at the flat band potential and is proportional to the light intensity. Its absolute value is also dependent on the recombination of electron-hole pairs. In some cases such as SnO_2 and TiO_2 the recombination depends on the doping and on the crystal structure. For instance much larger photocurrents were found with single crystals of these compounds than with polycrystalline layers [16,19].

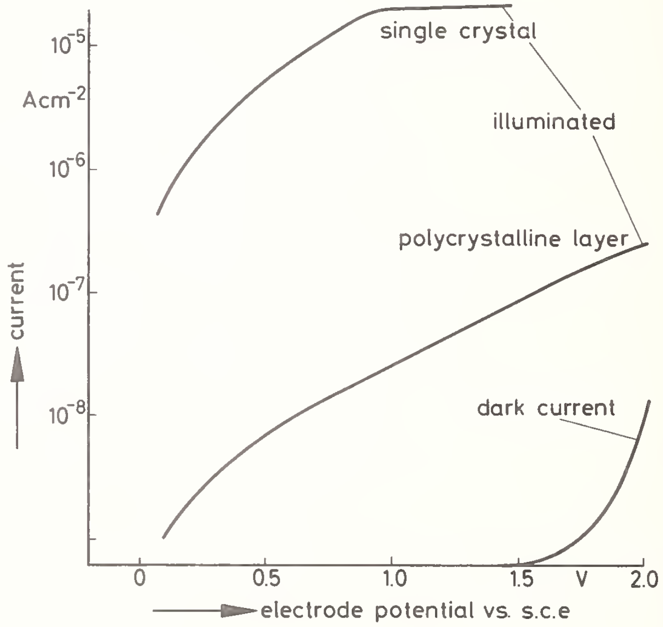

Fig. 3. Current vs. potential for SnO_2-electrodes in 1 N H_2SO_4 (vs. SCE).

The flat band potential U_{fb} and the donor density N_D are usually obtained from measurements of the space charge capacity C_{sc} vs. electrode potential U_E. In the Schottky-Mott form the capacity is given by

$$\frac{1}{C^2} = \frac{2}{\varepsilon\varepsilon_o e N_D} (U_E - U_{fb} - \frac{kT}{e}) \qquad (8)$$

The donor density N_D can be derived from the slope of the curve provided that any externally applied potential occurs only across the space charge layer.

4. Electrochemical Process at Oxide Covered Metal Electrodes

4.1 Characterization of oxide layers

In many electrochemical experiments semiconducting oxide films are formed on metal electrodes. In some cases such as platinum these oxide films are very thin and the current is mainly determined by electron tunneling through the oxide layer [21] (< 20 Å). These thin layers cannot really be characterized by semiconducting properties because the lattice periodicity is too short. Thicker oxide layers (> 100 Å), however, exhibit semiconducting properties. These properties are mainly derived from measurements of the photocurrent or of the space charge capacity in the oxide. Usually the latter method is used and the results are plotted as $1/C^2$ vs. electrode potential U_E (Schottky-Mott). In many cases a linear dependence has been obtained and from the slope of such a curve the donor density has been derived. It is rather surprising, however, that this linear relation could be verified for many oxide films formed on metal electrode although the composition should vary from the metal-oxide to the oxide-electrolyte interface considerably as schematically shown in fig. 4b. Accordingly the donor density should decrease from the metal towards the oxide surface resulting in a corresponding band bending shown in fig. 4c. In fact different slopes and consequently different donor densities were obtained for different oxide thicknesses on niobium electrodes [22,23] as demonstrated by Schottky-Mott-plots of the capacity in fig. 5. According to Heusler and coworkers [23] the donor density N_D decreases inversely proportionally to the square of the thickness d, i.e. $N_D = kd^{-2}$ in which k is a constant. This relation was not only found for Nb_2O_3 but also for TiO_2 on titanium [24]. The question arises, however, whether under these circumstance the slope of the Schottky-Mott-plot still

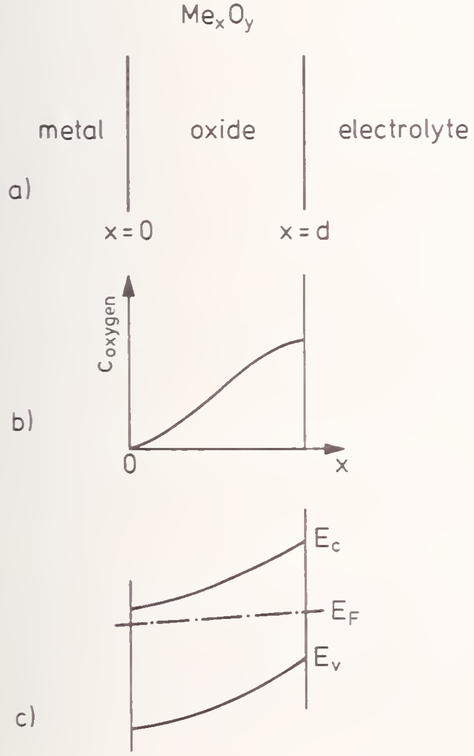

Fig. 4. Schematic presentation of a) metal/oxide/electrolyte interface; b) oxide distribution; c) potential distribution.

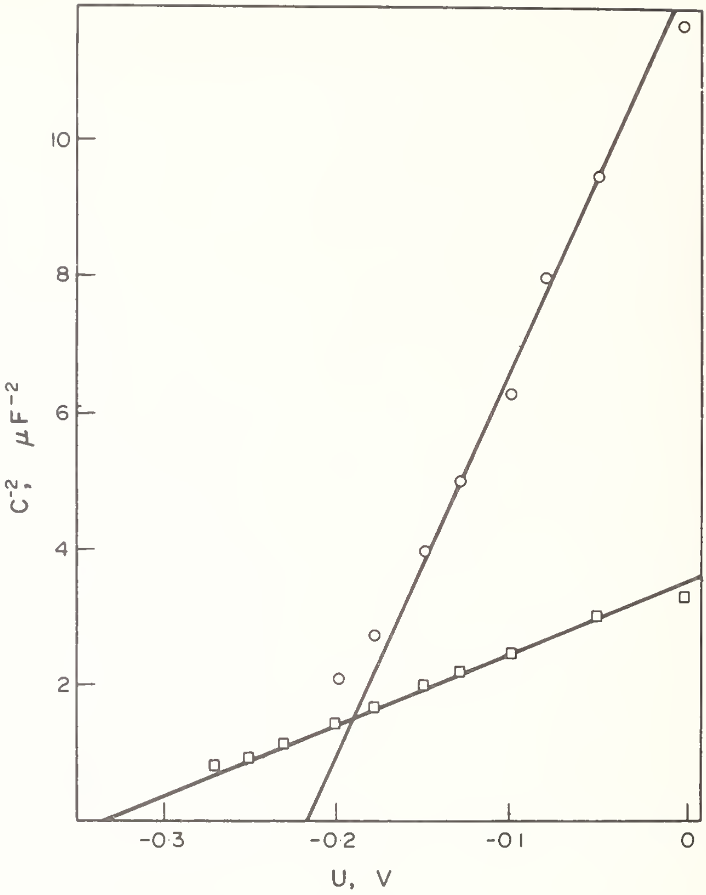

Fig. 5. Schottky-Mott plot of space charge capacity for niobium with oxide films (Nb_2O_3) in 0.1 M oxalic acid, 15 nm (□) and 28 nm (○) oxide thickness (taken from K. E. Huesler [22]).

determines the donor density in bulk of the oxide. This problem can be solved by an approximate solution of the Poisson equation which is given for n-type semiconductor by

$$\frac{d^2y}{dx^2} = \alpha(N-n_o e^{-y}) \sim \alpha N \tag{9}$$

in which $\alpha = \frac{e^2}{\varepsilon\varepsilon_o kT}$, N donor density, n_o electron density in the bulk. y is the potential in the space charge region in kT-units. The above equation is valid for upwards band bending, i.e. for an exhaustion region (fig. 6b). Assuming a donor density of

$$N = \frac{k}{(a-x)^2} \quad \text{(see fig. 6a)} \tag{10a}$$

the donor density at the surface is given by

$$N_o = \frac{k}{a^2} \sim \frac{k}{d^2} \tag{10b}$$

Integrating the Poisson equation one obtains a potential distribution of

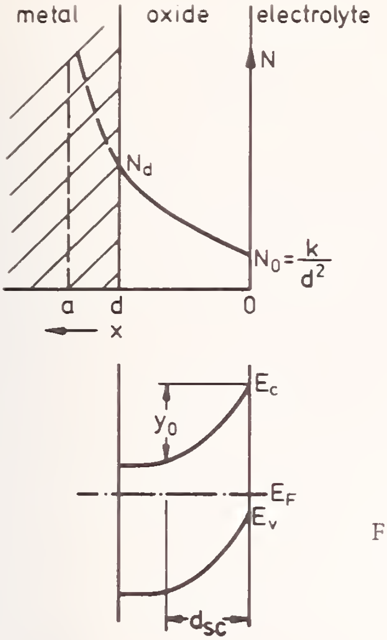

Fig. 6. Schematic presentation of a) donor distribution, b) energy diagram at metal/oxide/electrolyte interface.

$$y = -k \ln(1 - \frac{x}{a}) + Kx + y_o \qquad (11)$$

or after expanding the first term into a series:

$$y = k(\frac{x}{a} + \frac{x^2}{a} + \ldots) + Kx + y_o \text{ for } \frac{x}{a} < 1 \quad . \qquad (11a)$$

Terminating the series after the square term one obtains for the Schottky-Mott-equation $(C = \varepsilon\varepsilon_o \frac{d(dy/dx)}{dy_o})$

$$\frac{1}{C^2} = \frac{2\ kT}{\varepsilon\varepsilon_o e^2 N_o}\ y_o \qquad (12)$$

i.e. the slope is determined by the donor density N_o at the oxide-electrolyte interface. A similar result is obtained assuming an exponential dependence between donor density and thickness and subsequent series development. In a certain potential range in which the thickness of the space charge layer is still much smaller than that of the oxide layer this approximation is valid and the surface donor density N_o may be derived from a Schottky-Mott-plot. It must be emphasized that these capacity-potential dependences are not sensitive to the donor distribution within the oxide.

4.2 Surface Reactions

The electrochemical processes at oxide film covered metal electrodes can be determined by the semiconducting properties of the oxide film in the same way as found for single crystals. For instance the current potential curve of polycrystalline TiO_2 on Ti is identical to that of single crystals, i.e. the anodic current is limited to a very low level due to the lack of holes required for oxygen evolution [13,19] (fig. 7) whereas the anodic current is increased by illumination. The photocurrent depends considerably on the pretreatment of the oxide layer [25]. Other electron transfer processes such as

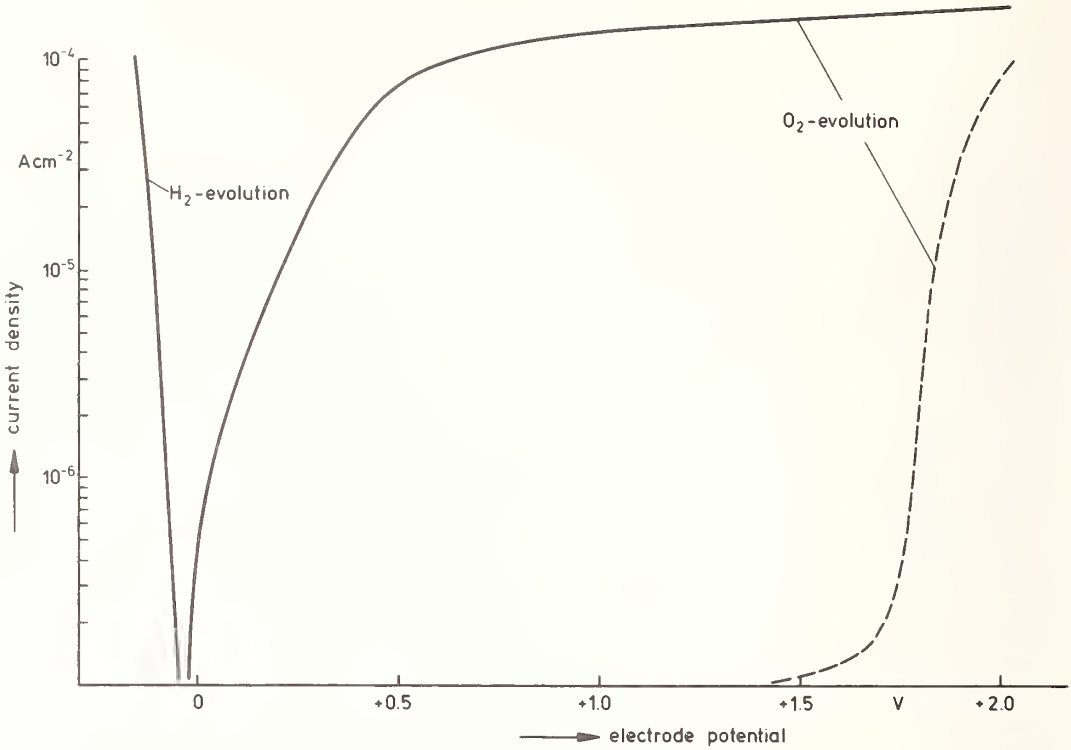

Fig. 7. Dark and photocurrent vs. electrode potential for TiO_2 layer (d = 0.4 µm) on Ti substrate in 0.1 N H_2SO_4.

redox reactions proceed at TiO_2-layers in the usual way although the exchange current via the conduction or the valence band is rather small due to the large band gap [19,21]. On the other hand the spectral distribution of the photocurrent may depend on the substrate used as a film support as it was also found for TiO_2-layers. In fig. 8 the spectral distribution of the anodic photocurrent is shown, as measured with TiO_2 deposited by pyrolytic decomposition on SnO_2. According to this figure the spectral distribution depends very much on the thickness of the TiO_2-layer if the electrode was illuminated through the electrolyte whereas it was independent of the thickness illuminating the system through the backside. Light was not absorbed by SnO_2 because the band gap (3.8 eV) is larger than for TiO_2 (3.1 eV). In the first case the maximum occurred at rather short wavelengths using o.1 µ thick TiO_2-layer. This maximum occurs at the same wavelength as found for backside illumination (compare fig. 8a and b). This result indicates that the highest yield for the photocurrent was obtained if electron-hole pairs were created near the interface SnO_2-TiO_2, i.e. the charge carriers were separated by the electric field at this interface causing hole injection into TiO_2 which are then consumed at the TiO_2/electrolyte interface. On the other hand illumination of a thicker TiO_2-layer (> 1 µ) by light passing through the electrolyte leads to a charge seperation at the TiO_2/electrolyte interface due to the electric field of the space charge layer below this surface. In this case the spectral distribution of the photocurrent is identical to that found for single crystals [26]. This substrate effect is expected to depend also on the relative position of the Fermi level in TiO_2 and consequently on the doping and preparation technique of the oxide.

The question arises, however, whether always semiconducting properties of an oxide layer determines the charge transfer process across the interface. Mostly capacity measurement were performed in order to prove whether an externally applied potential occurs across the space charge. As outlined in the previous section this type of measurement yields reasonable Schottky-

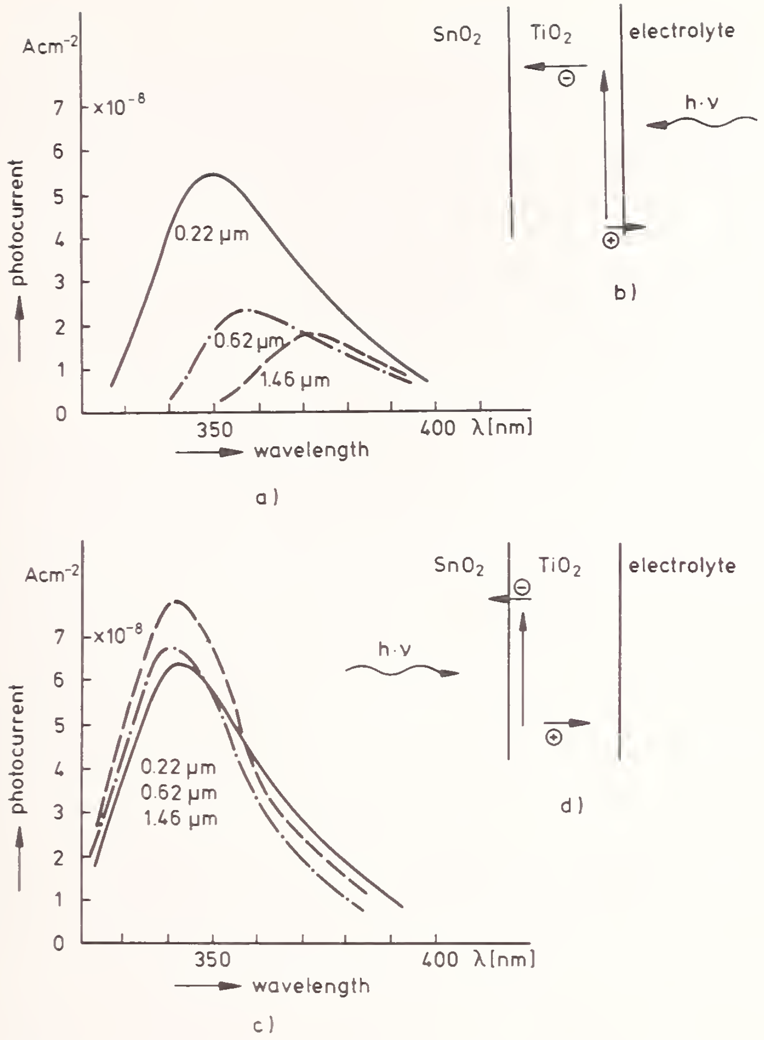

Fig. 8. Spectral distribution of photocurrent for TiO_2 on SnO_2-substrate a) illumination through electrolyte; c) illumination through substrate; b) and d) excitation process.

Mott-dependences in a limited potential range for oxide films grown on a metal electrode. This has been proved also for TiO_2 on Ti-electrodes [19,24] and the flat band potential could easily be determined. In some other cases, however, rather porous oxide films are formed on the metal electrodes such as for instance Ag_2O on silver. Ag_2O is readily formed on a Ag-electrode in alkaline solution above around 0.3 V (vs. SCE) (fig. 9). The further oxidation to AgO occurs above 0.65 V. Ag_2O and AgO are also expected to show semiconducting properties. However, they are difficult to characterize since no reasonable Schottky-Mott-plots were obtained from capacity measurements. On the other hand, after having formed Ag_2O on silver by anodic polarization according to the reaction

$$2\ Ag + 2\ OH^- \longrightarrow 2\ Ag_2O + H_2O + 2e^- \qquad (13)$$

anodic photocurrents were observed due to light absorbed by Ag_2O. Göhr [27] interpreted this photoeffect by assuming a photodissociation. According to our own measurements [28], however, the photocurrent could be related quantitatively to the further oxidation to AgO, as also confirmed by Conway [29].

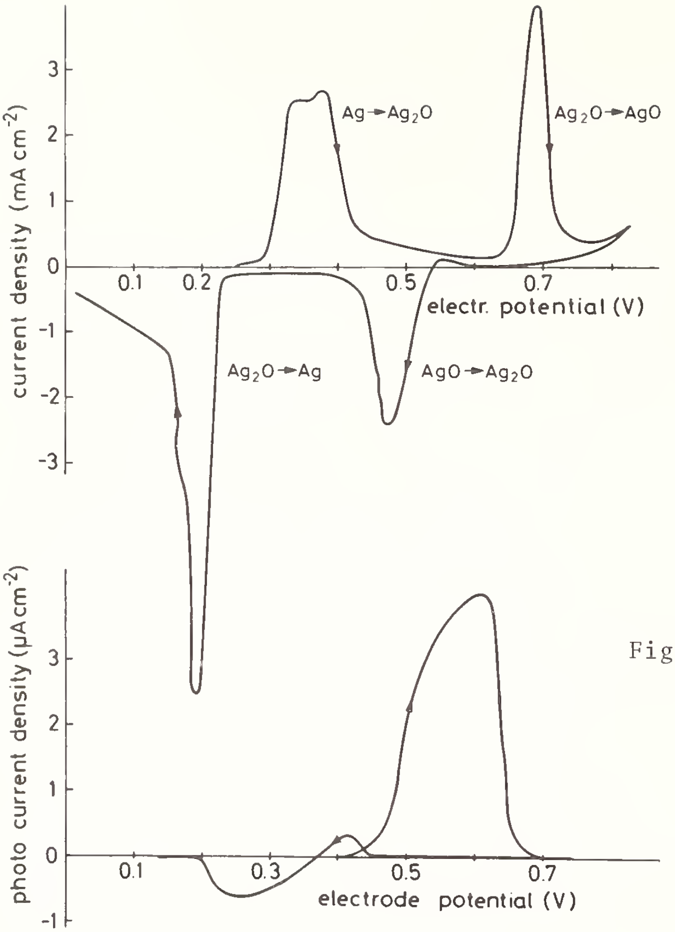

Fig. 9. Current-potential curve for silver electrode in 1 N KOH, sweeping speed 50 mV/sec. a) dark current; b) differential photocurrent.

It is interesting to note that the photocurrent sets in at a potential (0.4 V) 0.25 V lower than that where the oxidation occurred in the dark (fig. 9b). This is a typical semiconductor effect and could be interpreted by assuming the flat band potential to be around 0.4 V so that the energy bands are bent upwards above this potential. The corresponding electric field forces the holes created by light excitation towards the surface where they are consumed for further oxidation. Accordingly the second oxidation may described by

$$Ag_2O + 2\,p^+ + 2\,OH^- \longrightarrow 2\,AgO + H_2O \quad . \qquad (14)$$

This description is oversimplified since also ionic conduction is required for this process.

It should be mentioned that the photocurrents caused by light absorption in Ag_2O are partly also due to a bulk photoeffect since the conductivity of this oxide is very low. This assumption is supported by the result that AgO formed during illumination is not reduced at the usual potential (around 0.5 V) but in the potential range where Ag_2O is reduced to Ag. In this range also a cathodic photocurrent was observed (fig. 9b). The reduction of AgO is inhibited since AgO formed during light excitation is still separated from the metal electrode by low conducting Ag_2O. Further details are given in a previous paper [28].

5. Electrochemical Processes at Tungsten Bronzes

Sodium tungsten bronzes have been studied extensively because this material seemed to be quite promising for oxygen reduction reaction [30,31]. This bronze of the composition Na_xWO_3 with $x > 0.25$ shows metallic conduction. Different models for the conduction band of bronzes have been postulated and have been reviewed recently [32,33]. The electrical properties change for low x-values and it seems that below $x = 0.25$, sodium tungsten bronzes are semiconductors. At least pure WO_3 ($x = 0$) is a semiconductor with a band gap of 2.5 eV.

Although the sodium tungsten bronzes are very resistant towards acids it has been shown [30,31] that on anodic polarization sodium diffuses out of the bronze surface according to

$$\frac{1}{x}\, Na_xWO_3 \longrightarrow Na^+ + \frac{1}{x}\, WO_3 + e^- \qquad (15)$$

leaving a semiconducting surface on the metallic bronze electrode. This was proved by ion probe analysis [30]. Indications for a semiconducting surface layer were already obtained by Hardy and Bockris [30] who observed an anodic photocurrent after having polarized the bronze electrode anodically. The photocurrent occurred above light energies of about 2.2 eV. Since this energy corresponds roughly to the band gap of WO_3 it has to be assumed that a WO_3-layer exists on the bronze electrode. The photoprocess initiated by light absorbed by WO_3 must be a valence band process according to

$$WO_3 + 2\,OH^- + 2\,p^+ \longrightarrow WO_3 + H_2O + 1/2\ O_2 \qquad (16)$$

This is in agreement with current-potential measurements at WO_3-electrodes performed by Hobbs and Tseung [11] who found a small anodic current in the dark which is typical for n-type semiconductors.

Randin [34] has analyzed and characterized the bronze electrodes by capacity measurements. He obtained very nice Schottky-Mott-plots after anodic treatment of the electrodes and derived from the slope of the curves donor densities of the order of 10^{19} - 10^{20} cm^3. Moreover, he correlated the donor density to the concentration of sodium ($N_d = N_{Na^+}$). It was concluded that the sodium concentration must be much smaller than that obtained by ion probe measurements.

According to our analysis of Schottky-Mott curves for an inhomogeneous distribution of donor states (section 4.1) only the density of donor states at the very surface can be derived from the slope of the capacity curves which may be indeed very low. As mentioned before the Schottky-Mott-plot is insensitive to the distribution of donor states. Since in some cases a linear relation between $1/C^2$ and U_E was found in a potential range of about 7 V ($y_o = 300$) the thickness of the semiconducting surface layer can be estimated by using eqs (10) to (12) and one obtains $d \sim 300$ Å for $N_o = 10^{20}$ cm^{-3} which is in agreement with the ion probe measurements.

6. Concluding Remarks

It has been demonstrated that many compound semiconductors undergo electrochemical decomposition. Only few of them, such as oxides, are relatively stable. However, these materials have a large band gap. This fact leads to problems as far as photogalvanic systems are concerned. In order to obtain a large quantum efficiency for conversion of solar energy into chemical energy semiconductor electrodes with a band gap much smaller than that of TiO_2 are needed. The second condition, that the flat band potential is more negative than the hydrogen potential, required for photogalvanic system, is fulfilled for most n-type semiconductors [12].

7. References

[1] Beck, F. and Gerischer, H., Ztschr. f. Elektrochemie 63, 500 (1959).
[2] Memming, R. and Schwandt, G., Surf. Sci 4, 109 (1966).
[3] Mehl, W. and Lohmann, F., Ber. Bunsenges. Phys. chem. 71, 1055 (1967).
[4] Gerischer, H. and Mindt, W., Surf. Sci. 4, 440 (1966).
[5] Memming, R. and Neumann, G., Surf. Sci. 10, 1 (1968).
[6] Memming, R. and Schwandt, G., Electrochim. Acta 13, 1299 (1968).
[7] Gerischer, H., J. Electrochem. Soc. 113, 1174 (1966).
[8] Justice, D. D. and Hard, R. M., J. Electrochem. Soc. 118, 1417 (1971).
[9] Williams, R., J. Chem. Phys. 32, 1505 (1960).
[10] Gerischer, H. and Mattes, J., Ber. Bunsenges. Phys. Chem. 69, 578 (1965).
[11] Hobbs, B. S. and Tseung, A. C. C., J. Electrochem. Soc. 120, 766 (1973).
[12] Gleria, M. and Memming, R., J. Electroanal. Chem. and Interfac. Electrochem. 65, 163 (1975).
[13] Boddy, P. J., J. Electrochem. Soc. 115, 199 (1968).
[14] Gissler, W., Lensi, P. L. and Pizzini, S., J. Appl. Electrochem., in press.
[15] Boddy, P. I., Kahng, D. and Chen, Y. S., Electrochim. Acta 13, 1311 (1968).
[16] Möllers, F. and Memming, R., Ber. Bunsenges., Phys. Chem. 76, 469 (1972).
[17] Vijh, A. K., J. Electrochem. Soc. 117, 173C (1970).
[18] Memming, R. and Möllers, F., Ber. Bunsenges., Phys. Chem. 76, 475 (1972).
[19] Möllers, F., Tolle, H. J. and Memming, R., J. Electrochem. Soc. 121, 1160 (1974).
[20] Memming, R., Proc. of Symposium Electrocatalysis, Electrochem. Soc. Princeton 1974, p. 178, ed. by M. Brieter.
[21] Schultze, J. W. and Vetter, K. J., Electrochim. Acta 18, 889 (1973).
[22] Heusler, K. E. and Schulze, M., Electrochim. Acta 20, 237 (1975).
[23] Stützle, D. and Heusler, K. E., Ztschr. Phys. Chem. N.F. 65, 201 (1969).
[24] Allard, K. D., Ahrens, M. and Heusler, K. E., Werkstoffe u. Korr. 26, 694 (1975).
[25] Gissler, W., submitted to J. Appl. Electrochem.
[26] Hardee, K. L. and Bard, A. J., J. Electrochem. Soc. 122, 739 (1975).
[27] Göhr, H. and Breitenstein, A., Electrochim. Acta 13, 1377 (1968).
[28] Memming, R., Möllers, F. and Neumann, G., J. Electrochem. Soc. 117, 451 (1970).
[29] Tilak, B. V., Perkins, R. S., Kczlowska, H. A. and Conway, B. E., Electrochim. Acta 17, 1447 (1972).
[30] Bockris, J. O'M. and McHardy, I., J. Electrochem. Soc. 120, 61 (1973).
[31] McHardy, H. and Bockris, J. O'M., J. Electrochem. Soc. 120, 53 (1973).
[32] Hagenmuller, P., Proj. Solid State Chem. 5, 71 (1971).
[33] Dickens, P. G. and Whittingham, M. S., Quart. Rev. 22, 30 (1968).
[34] Randin, J. P., Electrochim. Acta 19, 83 (1974).

National Bureau of Standards Special Publication 455, *Electrocatalysis on Non-Metallic Surfaces*,
Proceedings of Workshop held at NBS, Gaithersburg, Md., December 9-12, 1975. (Issued November 1976)

Oxygen Evolution on Semiconducting Oxides

A.C.C. Tseung and S. Jasem
Department of Chemistry
The City University
St. John Street
London, E.C.1

The oxygen evolution reaction is of particular interest to secondary metal air batteries and water electrolysis plants. However, most of the earlier work has been on precious metals and there are no guidelines for the choice of semiconducting oxides as oxygen evolving electrodes. In this study, the role of the metal/metal oxide or the lower metal oxide/higher metal oxide couple in determining the minimum voltage required for the evolution of oxygen is emphasized, together with other essential requirements such as electrical resistivity electrode microstructure, corrosion resistance and catalytic properties. A survey of various metal oxides based on the above criterion suggested that $NiCo_2O_4$ is of particular interest and teflon bonded electrodes based on this material gave over 13,000 A/m^2 at 1.63 V vs DHE, 70°C, 5N KOH.

Key words: Nickel cobalt oxides; oxygen evolution, Pourbaix diagram; semiconducting oxides; spinels; teflon bonded electrodes

1. Introduction

The oxygen evolution reaction on semiconducting oxides has not been studied in detail. Hoare [1][1] suggested that the mechanism of O_2 evolution in alkaline media could involve:

$$(H_2O)_{ads} \xrightarrow{slow} (OH)_{ads} + H^+ + e$$

$$(OH)_{ads} + (OH)_{ads} \rightleftharpoons (O)_{ads} + H_2O$$

$$(O)_{ads} + (O)_{ads} \rightleftharpoons (O_2)_{ads}$$

$$(O_2)_{ads} \rightleftharpoons O_2$$

However, this does not indicate whether such reactions occur on metal oxide surfaces. In the case of oxygen on Pt[1], it has been shown that unless the Pt electrode is anodically polarized beyond the equilibrium potential of the PtO/PtO_2 couple, oxygen evolution cannot proceed. Similar arguments apply to all other metals, since oxygen evolution can only proceed when the potential of the electrode is higher than the metal/metal oxide couple or the lower metal oxide/higher metal oxide couple if there is more than one form of oxide.

---

[1] Figures in brackets indicate the literature references at the end of this paper.

2. General Considerations

2.1 Metal/Metal Oxide and Lower Metal Oxide/Higher Metal Oxide Couples

Since Hoare [1] has shown that in all the metals studied, the oxygen produced initially reacts with the bare metal surface to form surface oxides and hence the potential at which oxygen can start to evolve from the oxide surfaces is related to the metal/metal oxide couple or if there is more than one form of oxide, the lower metal oxide/higher metal oxide couple. Thus, the ideal couple will be lower or similar to the theoretical potential of the oxygen electrode.

The data for the various oxide couples can easily be obtained from the Pourbaix Diagrams [2].

2.2 Electrical Resistivity

It is impractical to use solid semiconducting oxide electrodes since the ohmic losses will be too high. However, it has recently been shown [3-5] that teflon bonded porous electrodes, supported on nickel screens, are far more efficient than solid electrodes for oxygen evolution. Since the catalyst/teflon mixture is in close contact with conducting nickel wires, the likely ohmic losses in such electrodes can easily be estimated if we assume that almost all the ohmic losses occur in the catalyst/teflon mixture [6]. If we assume that current is being collected on four sides of the square holes in the nickel mesh, we have

$$IR = \frac{\rho i L^2}{16t}$$

Where I is the total current, Amps; R is the total resistance of the electrode, ohm ; i, current density, A/cm^2; L, length of each side of the square hole in the nickel mesh, cm; ρ, resistivity of the catalyst/teflon layer, ohm-cm, t, thickness of catalyst/teflon layer. Taking the typical case of teflon bonded porous electrode supported on 100 mesh nickel screen, L is 0.04 cm and t is 0.025 cm. Hence if the catalyst/teflon layer has a resistivity of 100 ohm cm, and operating at 0.5A/cm^2, the IR loss will be about 0.2 V. However if the resistivity ρ is 10^3 ohm cm, the IR loss will be over 2 V. Hence the resistivity of the catalyst/teflon layer should be below 100 ohm-cm. In actual practice, taking into account the increased resistivity due to the presence of teflon particles and contact resistance between the catalyst powder, the maximum allowable bulk resistivity of the semiconducting oxide for use in such electrodes will be about 10-15 ohm-cm.

2.3 Corrosion Resistance

It is important to know the stability of the candidate oxide materials under the operating conditions (i.e. pH 14, 1.3-2V). In the absence of detailed experimental data, the best guide is the Pourbaix diagram [2], whereby stability is defined as when the equilibrium concentration of the metal ion in solution is less than 10^{-6} ions/l.

2.4 Catalytic Properties of Semiconducting Oxides

It is difficult to be certain which of the available data on semiconducting oxides would be of relevance in predicting which oxides are of interest in oxygen evolution reactions. In any case, it should be able to desorb the oxygen molecule from the surface relatively easily. Since the O_2 reduction reaction on most of the common oxides has been studied, their activity could be used as a guide-high activity implies that oxygen is not too strongly chemisorbed on the surface.

2.5 Electrocatalyst Microstructure

In order to maximize the area available for oxygen evolution reaction, it is necessary to use teflon bonded porous electrodes[5]. Therefore, the electrocatalyst aggregates must be strong enough to withstand the gas pressure built up inside the pores; hence, the semiconducting oxides should be prepared by chemical methods to ensure there are solid bonds between the particles inside each electrocatalyst aggregate [4]. Of the numerous methods available for the preparation of high surface area semiconducting oxides, freeze drying[7] and co-precipitation methods[8] are particularly useful.

2.6 List of Candidate Materials

Table 1 lists the conductivity, corrosion resistance, oxygen reduction performance as well as the equilibrium metal/metal oxide or lower metal oxide/higher metal oxide couples of a selected number of candidate materials. The physical properties listed are for the higher metal oxides. Obviously, if the oxides whose equilibrium potential is lower than or close to that of the oxygen electrode possess adequate conductivity, corrosion resistance and ability to reduce oxygen (implying low heat of oxygen adsorption), they will start to evolve O_2 sooner than other oxides and be expected to give higher anodic current at a given overpotential. An examination of Table 1 shows that it is difficult to get suitable oxides which can satisfy all the above requirements, but the oxide couples on Ni and Co seem to satisfy most of the requirements except for their high electrical resistivity. However, the spinel Co_2 NiO_4,[9]possess relatively low resistivity ($\sim$ 10 ohm cm) and is therefore chosen for detailed study.

Table 1. Properties of semiconducting oxides.

Oxide	Electrical conductivity	Corrosion resistance at pH = 14	Oxygen reduction	Potential vs NHE volt
La/La_2O_3	Poor	Good	Poor	-2.069
Ti_2O_3/TiO_2	Poor	Good	Poor	-0.556
V_2O_4/V_2O_5	Poor	Poor	Poor	-0.666
Cr_2O_3/CrO_2	Poor	Poor	Poor	+1.284
MoO_2/MoO_3	Poor	Poor	Poor	-1.09
W_2O_5/WO_3	Poor	Poor	Poor	-0.029
Mn_2O_3/MnO_2	Fair	Doubtful	Fair	+1.014
Co_2O_3/CoO_2	Poor	Good	Poor	+1.447
lower Co_2NiO_4/Co_2NiO_4	Good	Good	Good	+1.4
Ni_2O_3/NiO_2	Poor	Good	Poor	+1.434
RuO_2/RuO_4	Good	Poor	Good	+1.387
Rh_2O_3/RhO_2	Good	Doubtful	Good	+1.73
PdO_2/PdO_3	Good	Good	Good	+2.03
OsO_2/OsO_4	Good	Poor	Good	+1.00
Ir_2O_3/IrO_2	Good	Poor	Good	+0.93
PtO/PtO_2	Good	Good	Good	+1.7
Cu_2O/CuO	Poor	Doubtful	Poor	+0.667
AgO/Ag_2O_3	Good	Poor	Good	+1.57
Au_2O_3/AuO_2	Good	Doubtful	Poor	+2.63

RuO_2-TiO_2 would seem to be the next best candidate material. This was substantiated by recent studies of Srivinsan et al. [10].

3. Materials and Methods

The $NiCo_2O_4$ samples were prepared by freeze drying [9] of mixed nitrate solutions, followed by vacuum decomposition at 250°C and subsequent heat treatment at 400°C for 10 hours in air. The BET area was $41 m^2/g$ and x-ray diffraction confirmed that only spinel $NiCo_2O_4$ was present. The resistivity of the powder was less than 10 ohm cm. The powder was mixed with teflon dispersion (ICI Fluon) and painted onto either 100 mesh nickel or platinum screens, dried at 110°C for 1 hour and finally cured for an hour at 300°C to form teflon bonded electrodes. The catalyst/teflon ratio was 10/3 in all cases. The electrode was immersed in a thermostated glass cell containing 5N KOH. A piece of 5 x 5 cm gold foil was used as the counter electrode. The potential of the working electrode was measured against a dynamic hydrogen electrode (DHE) and the potential was controlled by a 3A Chemical Electronics Potentiostat. An interruptor technique [11] was used to measure the ohmic drop between the Luggin capillary and the working electrode.

4. Results and Discussion

4.1 Oxygen Evolution on Metal Substrates

The anodic performances of a 1 cm^2 nickel screen and a porous nickel plaque electrode at 1.638 V vs DHE are shown in figure 1. The performances of both electrodes decreased from 20×10^2 A/m^2 to less than 7×10^2 A/m^2 over a period of 40 hours, suggesting that the growth of high resistance nickel oxide films has greatly reduced the activity of the electrodes.

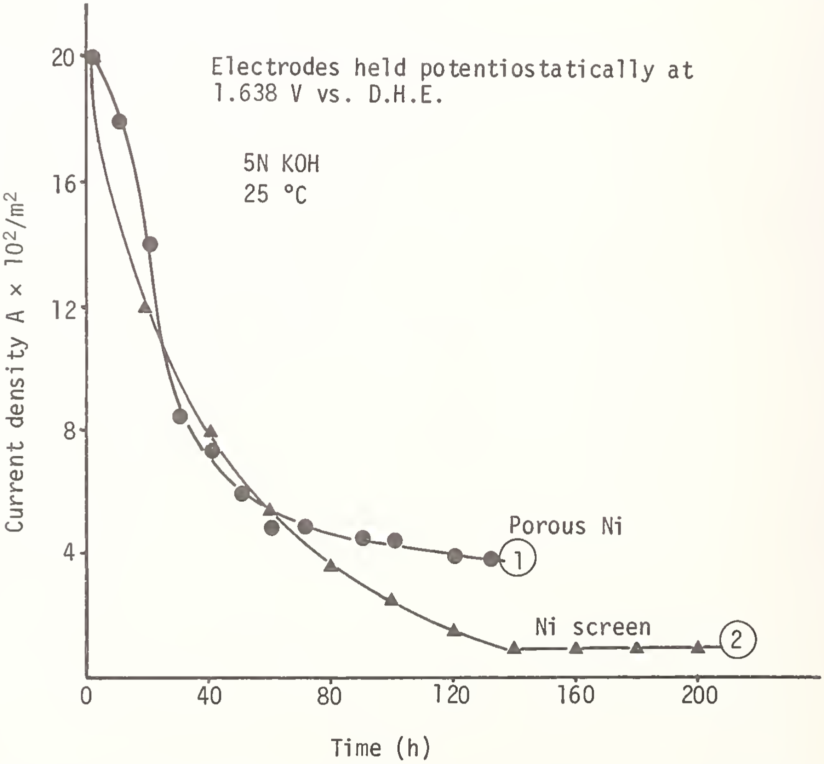

Fig. 1. Oxygen evolution on 100 mesh Ni screen and porous nickel as a function of time.

In addition, it is worth noting that despite the very much higher nickel area in the porous plaque, the activity is similar to that of the nickel screen electrode, suggesting that when oxygen is produced inside pores, it will have to build up a high enough pressure to expel the electrolyte from the pores before oxygen could escape; hence only the mouth of the pores could function[5]. Thus, it is necessary to use teflon bonded porous electrodes to maximize the area available for oxygen evolution. Furthermore, the results confirmed our earlier hypothesis - oxygen evolution on nickel began at about 1.45 V, just above the potential of lower nickel oxide/higher nickel oxide couple.

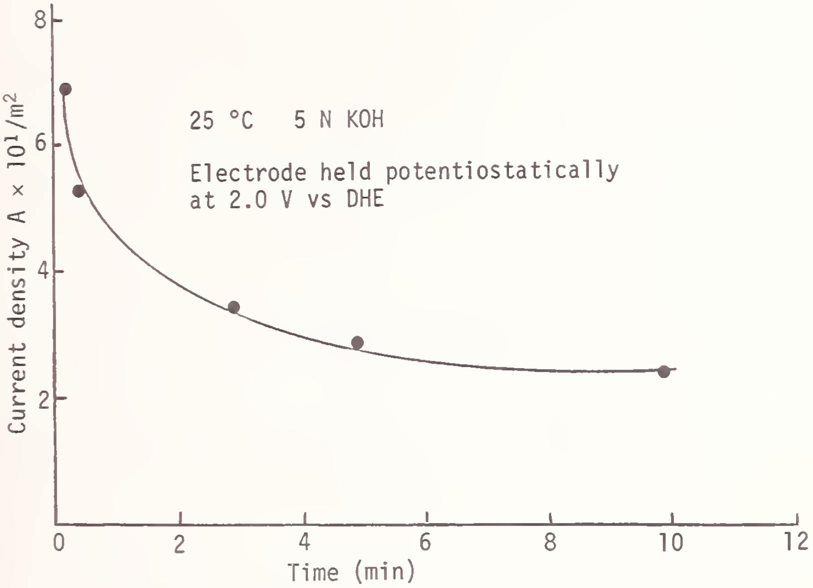

Fig. 2. Oxygen evolution on Pt screen as a function of time.

The results for oxygen evolution on Pt screen (fig. 2) showed a similar trend - though the performance decreased to a lower, steady level after only 20 minutes. The results indicated that initially some of the anodic current is used to build up the PtO_2 layer. Once the process has reached an equilibrium state, oxygen evolution proceeds on the PtO_2 surface. However, it is worth noting that the over-voltage is very much higher than on nickel, and this is in agreement with the higher potential of the PtO/PtO_2 couple.

4.2 Oxygen Evolution on Teflon Bonded $NiCo_2O_4$ Electrodes

The results obtained on nickel screens suggest that they can give a significant amount of current initially and cannot be neglected in our study. On the other hand, Pt screen is far more passive and the oxygen evolution reaction reaches a steady value within 20 minutes. Figure 3 shows the performance of teflon bonded $NiCo_2O_4$ electrode supported on 100 mesh Ni screens. It is interesting to note that the iR corrected results showed that over 13 × 10^3 A/m^2 could be obtained at 1.63 V vs DHE and to 70°C (fig. 3). The corresponding result for $NiCo_2O_4$ supported on Pt screen is 10.5 × 10^3 A/m^2 at 1.71 V (fig. 4), since $NiCo_2O_4$ alone contributed to most of the activity in this case. In this study, no attempt has been made to study the Tafel relationships since it is meaningless to apply the Tafel equation to gas-evolving porous electrodes--we cannot ascertain the contribution to the overall electrode polarization from mass transfer effects (emptying of electrolytes inside the pores, blockage of electrode area by gas bubbles, etc). We plan to study the problem in more detail by using potentiostatic pulse techniques [12] to eliminate mass transfer effects at a later date.

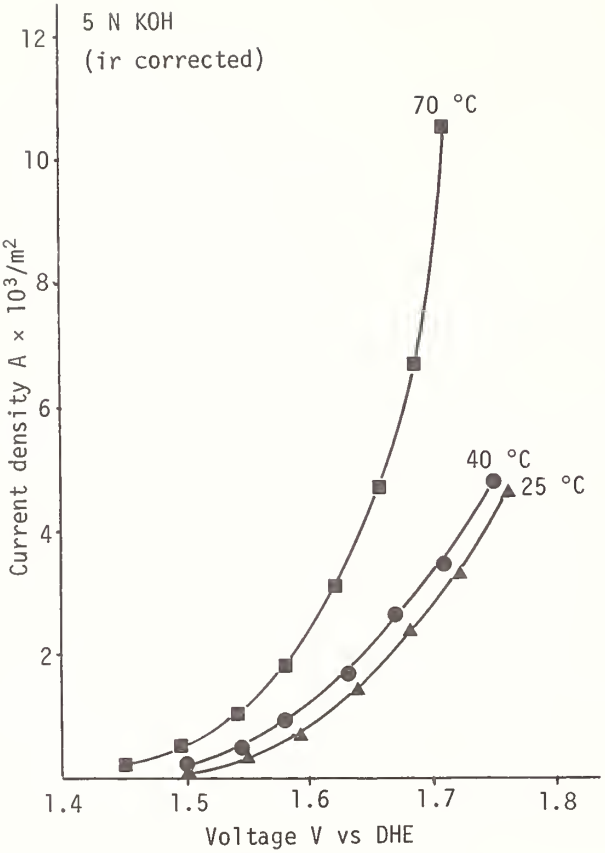

Fig. 3. Oxygen evolution on $NiCo_2O_4$ (Ni screen as current collector).

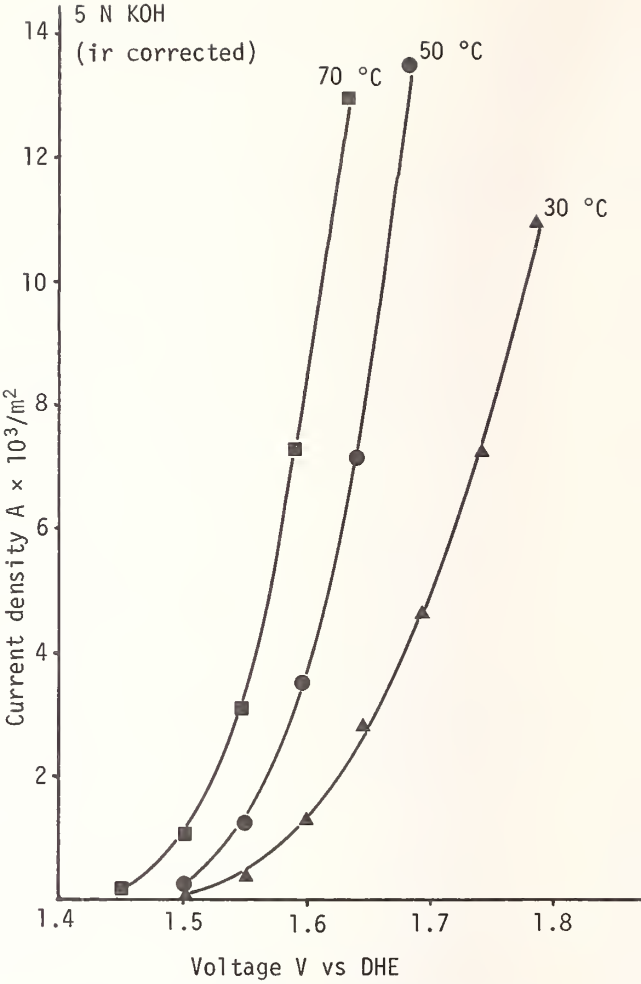

Fig. 4. Oxygen evolution of $NiCo_2O_4$ (Pt screen as current collector).

4.3 Stability of $NiCo_2O_4$ Electrodes

Figure 5 confirmed that the performance of teflon bonded $NiCo_2O_4$ electrode supported on Pt screen did not change with time. In practice, Ni screens would have to be used as the current collector and the temperature of operation would definitely be higher than 25°C. Figure 6 showed that after an initial decay in performance at 80°C, the performance of teflon bonded $NiCo_2O_4$ on Ni screen remained stable and that the initial decay was mainly associated with the growth of insulating nickel oxide film on the Ni screen. Over a total test period of 300 hours there were no visible signs of physical deterioration in the electrode and atomic absorption analysis of the KOH solution after the endurance test did not reveal the presence of Ni or Co ions (sensitivity of apparatus 2 ppm).

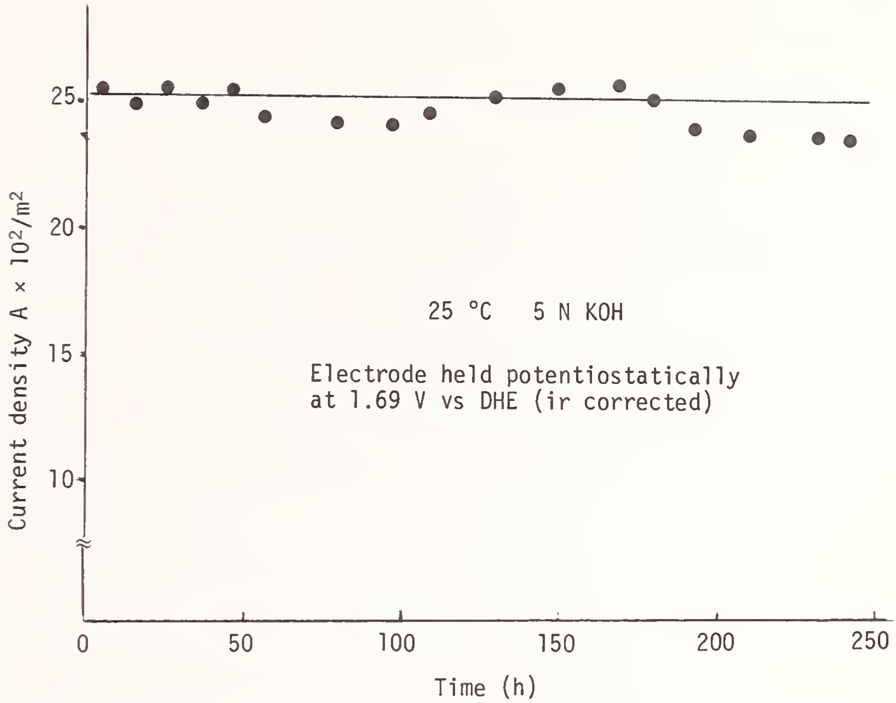

Fig. 5. Long term test for oxygen evolution on $NiCo_2O_4$ (Pt screen as as current collector) 5 N KOH, 25^oC.

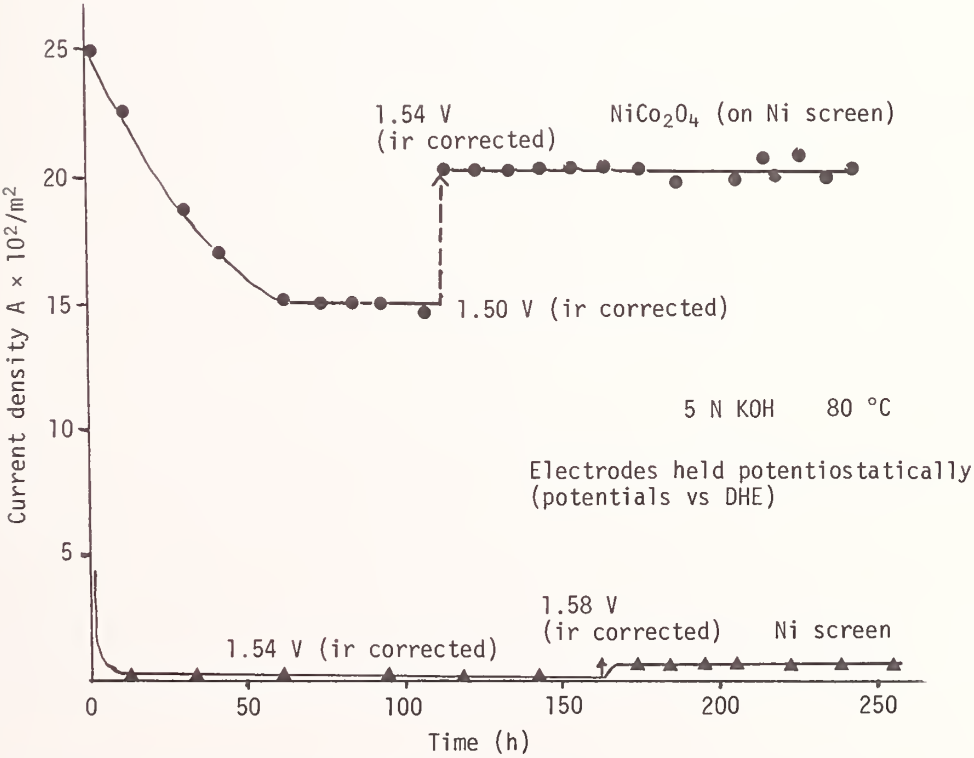

Fig. 6. Long term test for oxygen evolution on $NiCo_2O_4$ (Ni screen as current collector) 5 N KOH, 80^oC.

5. References

[1] T.P. Hoare. The Electrochemistry of Oxygen. Interscience (1968).

[2] M. Pourbaix, Atlas d'Equilibres Electrochemiques à 25°C., Gauthiers-Villars, Paris (1963).

[3] P.R. Vassie, A.C.C. Tseung, Electrochimica Acta, 20, 759 (1975).

[4] P.R. Vassie, A.C.C. Tseung, Electrochimica Acta, 20, 763 (1975).

[5] A.C.C. Tseung, P.R. Vassie, Electrochimica Acta (in the press).

[6] A.C.C. Tseung, unpublished results.

[7] A.C.C. Tseung, H.L. Bevan, J. of Mat.Sci.,5,604 (1970)

[8] A.C.C. Tseung, J.R. Goldstein, J. of Mat. Sci., 7,1383 (1972)

[9] W.J. King, A.C.C. Tseung, Electrochimica Acta, 19,485 (1974)

[10] S. Srivinsan et al. Paper presented at the NBS Meeting on Electrocatalysis on non-metallic surfaces, Washington, Dec., 1975.

[11] K.R. Williams, An Introduction to Fuel Cells, Elsevier, Amsterdam (1966)

[12] B.S. Hobbs, P.R. Vassie, A.C.C. Tseung, in Electrochemical Engineering Symposium, Inst. of Chem. Eng., Edit. J.D. Thornton, 1.123 (1971).

National Bureau of Standards Special Publication 455, *Electrocatalysis on Non-Metallic Surfaces*, Proceedings of Workshop held at NBS, Gaithersburg, Md., December 9-12, 1975. (Issued November 1976)

Mixed Oxides as Oxygen Electrodes

G. Singh, M. H. Miles and S. Srinivasan
Department of Applied Science
Brookhaven National Laboratory
Upton, New York 11973

The irreversibility of the oxygen electrode reaction on metals and alloys is the main cause of efficiency losses in fuel cells, water electrolysis cells and some battery systems. Oxygen evolution always occurs on oxide covered surfaces while the reduction reaction generally takes place on bare metallic surfaces but can do so on oxides. Since the most likely candidates for reversible oxygen electrodes are oxides, mixed oxides or compound oxides, three types of oxides - NiO_x, $NiCo_2O_4$ and $RuO_2|TiO_2$ were examined as oxygen electrodes in KOH solution. When these oxide electrodes were prepared by thermal decomposition of their salts on a substrate, ratios of true to apparent surface areas of the electrodes were quite high (over 200) and the transfer coefficients, obtained from the Tafel lines for oxygen evolution in the temperature range 25 - 100°C, were 1.5, as compared with about half that value on nickel electrodes. Above 100°C $NiCo_2O_4$ and $RuO_2|TiO_2$ electrodes corroded in the strong (50%) KOH environment. Mixed oxides are more stable than simple oxides in the region of potential where oxygen reduction occurs. From the values of the Tafel slopes and exchange current densities for oxygen evolution and reduction on $NiCo_2O_4$ (a spinel) and $RuO_2|TiO_2$, it is clear that reversibility of this electrode reaction was not obtained. Other mixed oxides (including spinels and perovskites) will have to be investigated with the aim of developing reversible oxygen electrodes.

Key words: Electrocatalysis; nickel-cobalt oxide; nickel oxide; oxide electrodes; oxygen electrode reaction; ruthenium dioxide/titanium dioxide; spinel.

1. Introduction

The oxygen electrode reactions are of special importance in water electrolysis, fuel cells and some battery systems (e. g., zinc-air, aluminum-air, and iron-air) because activation overpotential at this electrode is the chief cause of efficiency losses in these devices. Oxygen evolution always takes place on oxide covered metallic surfaces whereas oxygen reduction occurs on bare metallic surfaces but in some cases on oxides or mixed oxides. Thus, the most likely candidates for reversible oxygen electrodes are oxides, mixed oxides or compound oxides. Mixed oxides, including spinels, appear to be better catalysts for several reactions than simple oxides. One particular feature of mixed oxides is their increased stability over the simple oxides. In spinels, the mixed valences of the cations help in the reversible adsorption of oxygen by providing donor-acceptor sites for chemisorption.

With a view to understanding and developing reversible oxygen electrodes, the electrocatalytic activities of a simple oxide (NiO_x) and of the mixed oxides $NiCo_2O_4$ and $RuO_2|TiO_2$ for oxygen evolution and of the mixed oxides for oxygen reduction were determined in the present work. There is some evidence that the spinel $NiCo_2O_4$ is a good electrocatalyst for oxygen reduction [1][1]. The mixed oxide $RuO_2|TiO_2$ has been extensively used in the chlorine industry [2]. It also has shown promise as a good electrocatalyst for the oxygen electrode reaction [3].

2. Experimental

The nickel-cobalt oxide electrodes were prepared by two methods. In the first [4], the two nitrates, $Ni(NO_3)_2 \cdot 6H_2O$ and $Co(NO_3)_2 \cdot 6H_2O$ were weighed in the exact proportion of Ni:Co = 1:2 and dissolved in water. The solution was evaporated to dryness until there were no more NO_2 fumes. The black powder was heated in an electric furnace in air for 48 hours at a temperature of 325 - 350°C. The spinel, $NiCo_2O_4$, was mixed with Teflon 30 emulsion and shaken well. Teflon 30 and $NiCo_2O_4$ were in the proportion of approximately 20:80 by weight. A nickel screen was dipped in the above solution and a coating of $NiCo_2O_4$ was deposited on it. The nickel screen was heated in an electric furnace for about an hour at 310°C. The electrode thus prepared was used for determining its electrocatalytic activities for the oxygen electrode reactions.

In the second method, nickel oxide (NiO_x) and nickel-cobalt oxide ($NiCo_2O_4$) were prepared by thermal decomposition on a substrate. Details of the preparation of the nickel-cobalt oxide electrode are as follows: Nickel nitrate and cobalt nitrate, mixed in stoichiometric amounts were dissolved in 1-butanol. A clean piece of a metal (Ni or Ti) or stainless steel was spot welded to a wire of the same metal or alloy and washed. It was heated for five minutes in an oven at 250°C and then dipped in the solution of the nitrates. It was placed in the oven again at 250°C for 2 - 3 minutes and this process was repeated about 10 times. At the end of this operation, the temperature of the oven was raised to 350°C and the electrode heated in it overnight. The electrode was cooled and washed. It had about 1 - 5 mg of $NiCo_2O_4$ per cm^2 of the metal plate. The nickel oxide electrode was prepared in a similar manner. The ruthenium dioxide-titanium dioxide electrodes for the oxygen evolution and reduction studies were obtained from T. Bomaraju of Hooker Chemical Company, Niagara Falls.

The electrochemical measurements, to determine electrocatalytic activities, consisted of steady-state potentiostatic measurements using a PAR (Model #173) potentiostat. The electrolyte used was 30% KOH. The oxygen evolution studies were conducted at 25, 50, 80 and 100°C while the oxygen reduction studies were carried out at temperatures of 25, 50 and 80°C. For comparison of electrocatalytic activities, the oxygen reduction studies were also done on platinum at the same temperatures. The true surface areas of the electrodes were determined using cyclic voltammetric techniques. For this purpose, the electrodes were maintained at the highest potential used for oxygen evolution studies. The cyclic voltammograms were then recorded in a small range (about 100 mv), starting at a much lesser potential (say 1 volt vs. RHE), as a function of sweep rate. As a check, the surface areas in one set of experiments were also obtained by BET measurements.

With $NiCo_2O_4$ and $RuO_2|TiO_2$, preliminary electrocatalytic studies for oxygen evolution were also carried out at temperatures up to 150°C.

3. Results

The Tafel lines for oxygen evolution at the four temperatures on nickel-cobalt oxide, prepared by the thermal decomposition method, are shown in figure 1. From figure 2, it is clear that the electrocatalytic activities of the three oxide systems for this reaction at 80°C show little difference. Figures 3 and 4 show the methodology of obtaining the true surface areas of the electrodes. By limiting the cyclic voltammogram to a narrow range of potential, the double layer charging currents are constant, with the anodic current being equal in magnitude to the cathodic current at each sweep rate (fig. 3). A plot of the charging current versus the sweep rate is linear, as expected, and it passes through the origin (fig. 4). Similar results were obtained on the nickel-cobalt oxide electrodes.

The performance of the Teflon bonded nickel-cobalt oxide electrode was much less satisfactory than that of the electrodes prepared by the thermal decomposition method.

---

[1] Figures in brackets indicate the literature references at the end of this paper.

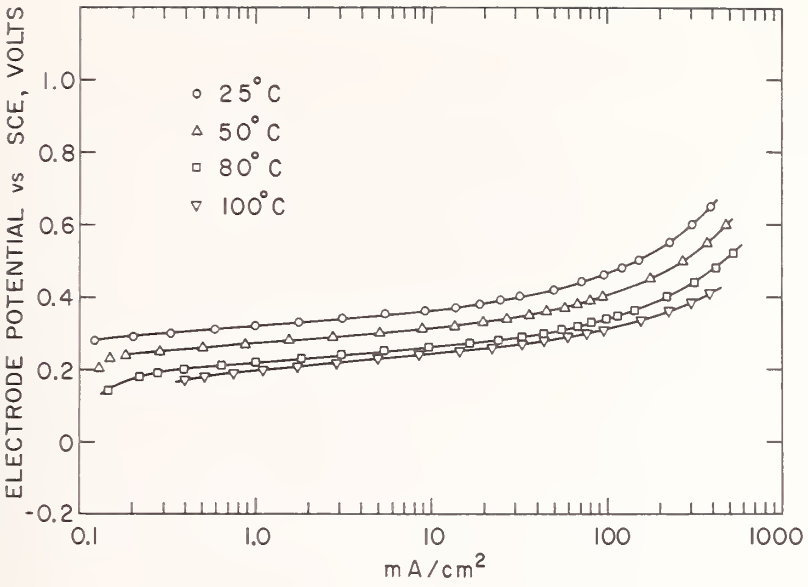

Fig. 1. Potential-current density relations for oxygen evolution on NiCo$_2$O$_4$, deposited thermally on nickel plate, in 30% KOH at 25, 50, 80 and 100°C.

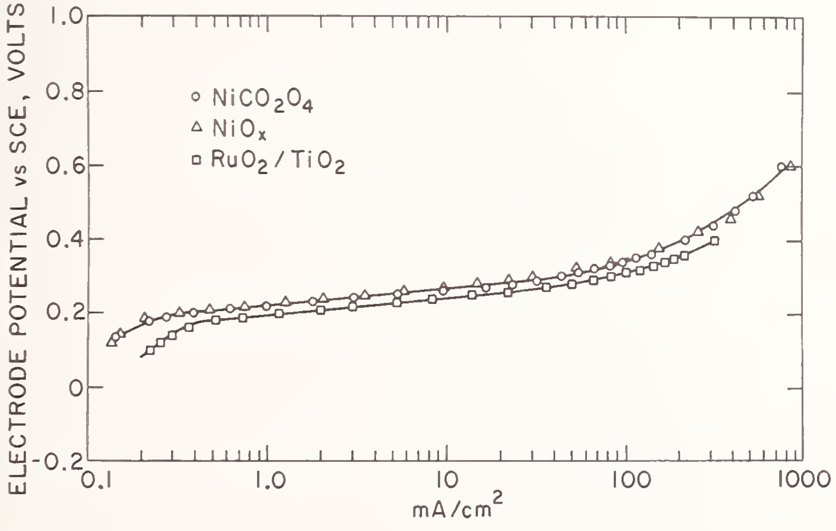

Fig. 2. Potential-current density relations for oxygen evolution on NiO$_x$, NiCo$_2$O$_4$ and RuO$_2$|TiO$_2$ electrodes, prepared by the thermal decomposition method, in 30% KOH at 80°C.

The stability of the electrodes was considerably better in the latter case.

Though the NiCo$_2$O$_4$ and RuO$_2$|TiO$_2$ electrodes showed a good performance for oxygen evolution, and were stable at temperatures below 100°C, they were quite unstable at higher temperatures. This is probably due to the formation of cobaltates and ruthenates in the strongly alkaline environment.

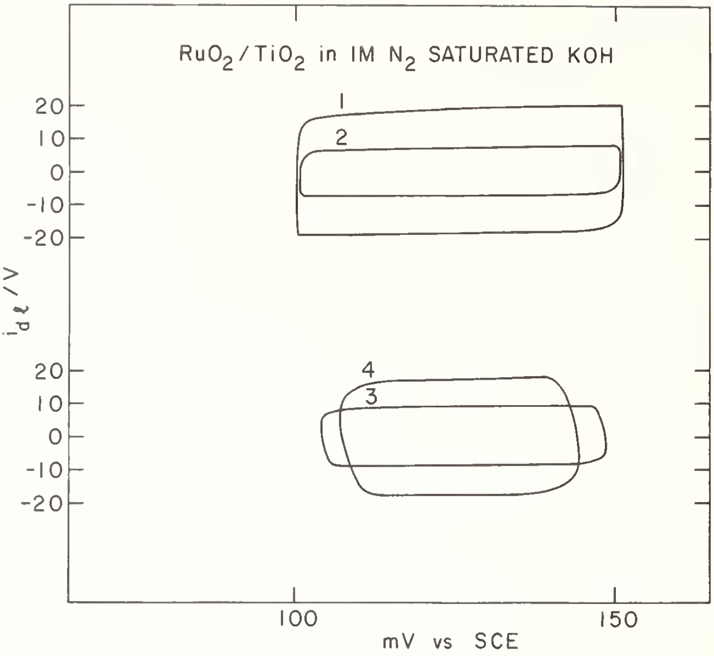

Fig. 3. Cyclic voltammograms on $RuO_2|TiO_2$ electrodes in 1M nitrogen saturated KOH at four sweep rates. Designations 1, 2, 3 and 4 represent sweep rates of 10, 20, 50 and 100 $mVsec^{-1}$.

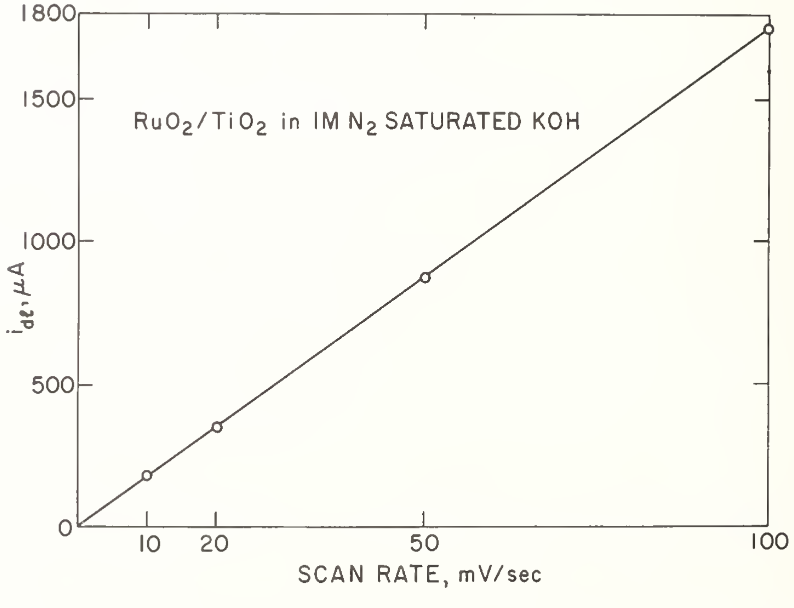

Fig. 4. Double layer charging current (from fig. 3) versus sweep rate.

Results of oxygen reduction at 80°C on Pt, $NiCo_2O_4$ and $RuO_2|TiO_2$ from 30% KOH solution are graphically represented in figure 5. The current is partly due to the reduction of the lattice oxide, which is quite evident in figure 6 which shows the current-potential relations on a nickel-cobalt oxide electrode in 30% at 80°C with oxygen or argon being bubbled through the electrolyte. The spinel $NiCo_2O_4$ appears to be less stable than the mixed oxide $RuO_2|TiO_2$ in the region of potential where oxygen reduction occurs at appreciable rates.

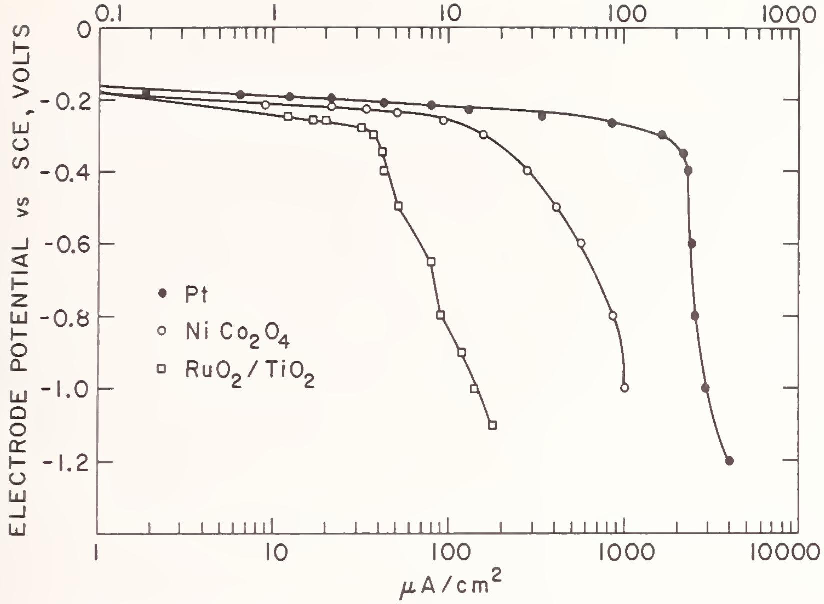

Fig. 5. Potential-current density relations for oxygen reduction on Pt, $NiCo_2O_4$ and $RuO_2|TiO_2$ in 30% KOH at 80°C.

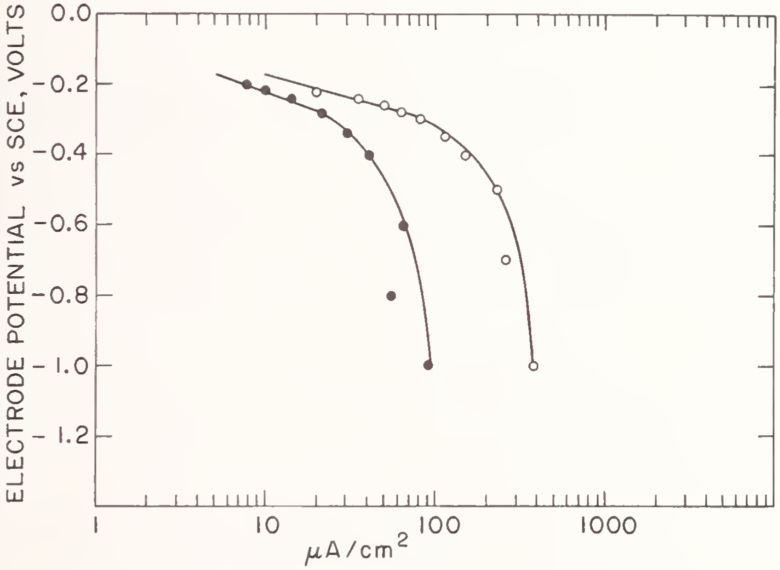

Fig. 6. Potential-current density relations on $NiCo_2O_4$ in 30% KOH with oxygen (o) or argon (●) bubbling through the electrolyte.

4. Discussion

4.1 The Oxygen Evolution Reaction on the Oxide Electrodes

The kinetic parameters for the oxygen evolution and reduction reactions on the oxide electrodes in 30 wt % KOH are presented in Table 1.

Table 1. Kinetic parameters for the oxygen evolution and reduction reactions in 30 wt % KOH.

Electrode	Temp (°C)	Tafel slope (V)	α[a]	$i_o (A/cm^2)$[b] $\times 10^9$	$\Delta E^{\neq}$[c] Kcal/mol
		Evolution			
$NiCo_2O_4$	25	0.040	1.48	1.78	9.2
	50	0.040	1.60	5.31	
	80	0.042	1.67	29.9	
	100	0.046	1.61	54.7	
RuO_2/TiO_2	80	0.045	1.56	194.5	9.2
NiO_x	80	0.047	1.49	71.0	8.2
		Reduction			
Pt	80	0.033	2.1	8.7×10^{-4}	
$NiCo_2O_4$	80	0.060	1.2	6.8×10^{-1}	
RuO_2/TiO_2	80	0.070	1.0	1.0	

---

[a] Transfer coefficient.

[b] Exchange current densities are given in terms of geometric areas. The roughness factors of various electrodes are, Pt = 2, $NiCo_2O_4$ = 400, and RuO_2/TiO_2 = 700.

[c] Arrhenius activation energy.

One of the most striking features is that the electrode kinetic parameters for all the three oxides are quite similar (cf. fig. 2 and Table 1), even though their structural and electronic properties are quite different. The transfer coefficient (α) for the oxygen evolution reaction on nickel electrodes (in the form of wires, foils or screens) is about 0.7 at temperatures below 100°C [5], while in the present study on nickel oxide prepared by the thermal decomposition method it is 1.5. This value of α on NiO_x, $NiCo_2O_4$ and $RuO_2|TiO_2$ indicates that the rate determining step for oxygen evolution on these electrodes is the second electron transfer step, as for example in the reaction sequence [3]:

$$S^Z + OH^- \rightleftarrows (SOH)^Z + e_o^- \qquad \text{fast} \qquad (1)$$

$$(SOH)^Z \rightarrow (SOH)^{Z+1} + e_o^- \qquad \text{slow} \qquad (2)$$

$$\begin{array}{llllll} (SOH)^{Z+1} & + OH^- \rightarrow & S\text{-}O\text{-}H\ldots OH^- & \rightarrow & S^Z + & O\ HOH \\ & & & & & |\ + \\ (SOH)^{Z+1} & OH^- & S\text{-}O\text{-}H\ldots OH^- & & S^Z & O\ HOH \end{array} \qquad (3)$$

where S^Z represents the substrate.

The exchange current densities on these oxides, based on the true surface areas, are lower than on nickel electrodes, because of the lower Tafel slopes on the former systems. However, at desirable current densities (say 200 mA cm^{-2} -geometric) the overpotentials for oxygen evolution on the oxide electrodes prepared by the thermal decomposition method are at least 150 mV less than on nickel (wire, screen or foil electrodes). This result has practical implications in developing more efficient (from energy considerations) water electrolysis cells.

Ruthenium dioxide on titanium dioxide is only a slightly better electrocatalyst than nickel cobalt oxide or nickel oxide. Both these mixed oxide systems are not stable at temperatures above 100°C in 50% KOH. It has been previously suggested [6] that the lower overvoltage for oxygen evolution on ruthenium in acid solution is due to the presence of ruthenium ions in solution produced by the anodic dissolution of the metal. In alkaline solution, it is very probable that the ruthenium ion is not involved in the overall reaction path due to the fact that the other oxide systems as well show similar electrode kinetic parameters. It is very probable that in this medium, it is necessary to create the conditions for a lower activity of adsorbed hydroxyl radicals, which causes the oxygen evolution to be controlled by the second electron transfer step (cf. reaction path represented by eqs. 1 - 3). In practically all water electrolysis cells, nickel is used as the oxygen electrode and is in the form of nickel clad iron electrodes, sintered nickel plaques or screens. Since the present work shows that nickel oxide prepared by the thermal decomposition method has electrocatalytic activities similar to nickel-cobalt oxide as well as ruthenium dioxide but considerably superior to nickel in the above forms, the present approach to preparation of oxygen electrodes, using nickel, is suggested.

4.2 The Oxygen Reduction Reaction on the Oxide Electrodes

The Tafel slopes for oxygen reduction on $NiCo_2O_4$ and in $RuO_2|TiO_2$ are about twice that on platinum. Based on the true surface area, the exchange current densities for oxygen reduction on the oxide electrodes are only slightly higher than on platinum. In a previous study [7], it was shown that oxygen reduction to hydroxyl ions on the spinel $NiCo_2O_4$ does not proceed through a peroxide intermediate. The present work (fig. 6) confirms another investigation [8] that this spinel is not stable in alkaline environments under conditions of oxygen reduction.

From the values of the transfer coefficients and exchange current densities in Table 1, it is also apparent that oxygen evolution and reduction occur on these mixed oxides by different mechanisms. The exchange current densities are considerably lower for oxygen reduction than for oxygen evolution. It is planned to investigate other oxide systems with the hope of developing reversible oxygen electrodes for regenerative fuel cells and battery systems.

5. Conclusions

In alkaline solution, nickel oxide (NiO_x), the spinel $NiCo_2O_4$ and the mixed oxide $RuO_2|TiO_2$ are good electrocatalysts for oxygen evolution but not for oxygen reduction. The superior performance of these oxides, as compared with that of conventional metal electrodes (e. g.,nickel), for oxygen evolution is due to the method of preparation of high surface area electrodes. Oxide electrodes prepared by the thermal decomposition method have a higher electrocatalytic activity and stability than the Teflon bonded electrodes. The mechanism of the oxygen evolution reaction on oxide electrodes, prepared by the former method, involves a rate determining electrochemical desorption of the adsorbed hydroxyl radical while on nickel electrodes in the form of wire, foil or screen, the r.d.s. is probably a chemical desorption of the adsorbed hydroxyl radical. Mixed oxides are more stable than simple oxides in the region of potential where oxygen reduction occurs. Other mixed oxides (including spinels and perovskites) will have to be investigated with the aim of developing reversible oxygen electrodes.

6. Acknowledgements

This work was performed under the auspices of the U. S. Energy Research and Development Administration. The authors wish to thank Miss Patricia J. Dwyer for carrying out the experimental studies on oxygen reduction and Mr. F. J. Salzano for his interest and encouragement of the work.

7. References

[1] King, W. J. and Tseung, A. C. C., Electrochim. Acta 19:485, 1974.
[2] DeNora, O., Chem. Ing.-Techn., 42:222, 1970.
[3] O'Grady, W., Iwakura, C., Huang, J. and Yeager, E., Proceedings of the Symposium on Electrocatalysis, M. Breiter Ed., 286, The Electrochemical Society, Princeton,

New Jersey, 1974.

[4] Knop, O., Reid, K. I. A., Sutarno and Nakagawa, Y., Can. J. Chem., 46:3463, 1968.

[5] Miles, M. H., Kissel, G., Lu, P. W. T., and Srinivasan, S., J. Electrochem. Soc., 123:332, 1976.

[6] Burketz, L. D., and O'Meara, T. O., J. Electroanal. and Interf. Electrochem., 36:App. 25, 1972.

[7] Shumilova, N. A., and Kruscheva, E. I., paper presented at 10th Intersociety Energy Conversion Engineering Conf., Wilmington, Delaware, Aug. 18-22, 1975.

[8] King, W. J., and Tseung, A. C. C., Electrochem. Acta, 19:493, 1974.

National Bureau of Standards Special Publication 455, *Electrocatalysis on Non-Metallic Surfaces*, Proceedings of Workshop held at NBS, Gaithersburg, Md., December 9-12, 1975. (Issued November 1976)

Surface and Electrocatalytic Properties of Tungsten Bronzes[1]

M. F. Weber and H. R. Shanks

Energy and Mineral Resources Research Institute
Iowa State University, Ames, Iowa 50010

Tafel plots have been obtained for the oxygen reaction in acid solution on several alkali tungsten bronzes having different crystal structures. Platinum doped sodium tungsten bronze crystals were studied and the results compared with those of platinum free crystals of the same composition. In both cases sodium tungsten bronzes were found to be poor electrocatalysts for the cathodic reduction of oxygen. Similar results are reported for other alkali tungsten bronzes and for tungsten trioxide. Anodic treatment of the crystals affected the electrocatalytic activity of only the sodium tungsten bronze and the effect was a negative one. Cyclic voltammetry was employed to study the effects of the anodic treatment which created a sodium depletion layer on the sodium tungsten bronze surface. The existence and depth of the sodium depletion layer was determined by an Auger Electron Spectroscopy depth profile.

Key words: Tungsten bronzes; oxygen reduction; electrocatalyst; Auger Electron Spectroscopy; sodium depletion; Tafel plots.

1. Introduction

Tungsten bronzes are nonstochiometric compounds of the form M_xWO_3, where M is a metal ion and x is a number between 0 and 1. The limiting composition "MWO_3" has the perovskite structure (ABO_3). As the x-value or metal ion content of the bronze decreases, the structure passes through several different phases. For example, in the sodium tungsten bronze system (Na_xWO_3) a cubic structure is found for x in the range $0.49 < x < 0.93$, a tetragonal phase for $0.25 < x < 0.49$, a second tetragonal phase for $0.07 < x < 0.25$, an orthorhombic phase for $0.01 < x < 0.07$ and the monoclinic phase of WO_3 for very low x values [1][2]. In general, the crystal symmetry decreases as the x-value decreases. Most of the tungsten bronzes are resistant to acids. In particular, sodium tungsten bronze is not visibly attacked even by aqua regia over very long periods of time. However, all tungsten bronzes are attacked by alkaline solutions.

In recent years, reports [2-5] of high electrocatalytic activity for oxygen reduction by $Na_{0.7}WO_3$ crystals containing traces of platinum stimulated a large research effort to investigate this effect and substantiate these reports [6-9]. The later research results differed from the earlier reports, in that no exceptional electrocatalytic properties of $Na_{0.7}WO_3$ for oxygen reduction were found, even with crystals doped with up to 1000 ppm platinum.

---

[1] This work was supported in part by a grant from the National Science Foundation.

[2] Figures in brackets indicate the literature references at the end of this paper.

2. Experimental

The alkali tungsten bronzes were prepared by the electrolysis of a fused salt of the appropriate alkali tungstate and tungsten trioxide as described by Shanks [1]. The crystals of WO_3 were prepared by vapor transport, following the techniques of Sawada and Danielson [13]. Since Bockris and McHardy [5] have suggested that Al_2O_3 and platinum together as impurities affect the electrocatalytic properties of the sodium tungsten bronzes, a special effort was made to eliminate any uncontrolled source of these impurities. High purity sodium carbonate and tungsten trioxide were used as starting materials for the growth of undoped and platinum doped (up to 800 ppm) high purity sodium tungsten bronzes. Typical mass spectrographic analysis results for crystals grown from this material and for the starting materials are shown in Table 1. From these results it appears that Mo, Fe, and Ti tend to concentrate in the crystals during electrolysis since the concentration found in the crystals were greater than in the melt. In addition, the impurity concentrations decreased as successive crystals were grown from a given melt, indicating depletion of the impurity in the melt. Platinum doping of the Na_xWO_3 crystals was achieved by using a platinum anode in the melt, and vanadium doping by adding V_2O_5 to the melt.

Table 1. Mass Spectrographic Analysis of Starting Material and Na_xWO_3 Crystal (concentrations in ppm).

Impurity	WO_3	Na_2CO_3	$Na_{0.7}WO_3$	Impurity Source
C			30	S[a]
Al	2	0.2	0.2	S
Si			<2	Electrodes
P	500	<0.2	0.2	S
Cl	10	60	9	S
K	10	2	70	Crucible
Ca	1	<3	100	Crucible
Ti	0.7	3	50	S
Fe	3	5	20	S
Mo	30	<5	100	S
Au	0.3	0.5	<0.1	Electrode
Pb	3	<1	<0.3	S
V	<0.06	<2	1	S
Co	0.1	13	<0.1	S
Ni	0.3	2	0.9	S
Pt	<10	<3	<0.6	S

[a] Starting material.

The crystals used in the experiments were all mounted in teflon and received a metallographic polish with different sizes of alumina down to 3 µm. The sample and sample holder were then cleaned with isopropanol and then with boiling conductivity water. Electrical connection was made to the back of the samples by means of a stainless steel 2/56 threaded screw which made physical contact with the crystal as shown in figure 1. All data are given with respect to the apparent surface area of the electrode.

All electrochemical studies were done in a standard three compartment cell of pyrex construction, using triple distilled water and ultra pure acid. The electrolyte used was 0.1 N H_2SO_4 in all cases. The reference electrode was a palladium bead saturated with hydrogen and immersed in an electrolyte having the same composition as that in the main compartment of the cell. This reference electrode was constructed using the design of McHardy [14] and is shown in figure 2. The reference electrode was separated from the main compartment by means of a Luggin capillary and closed stopcock. The counter electrodes for all experiments was either a sodium tungsten bronze crystal with an exposed area

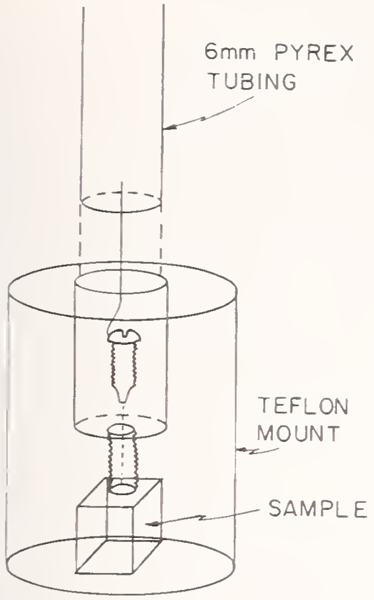

Fig. 1. Sample mounting and electrical connection.

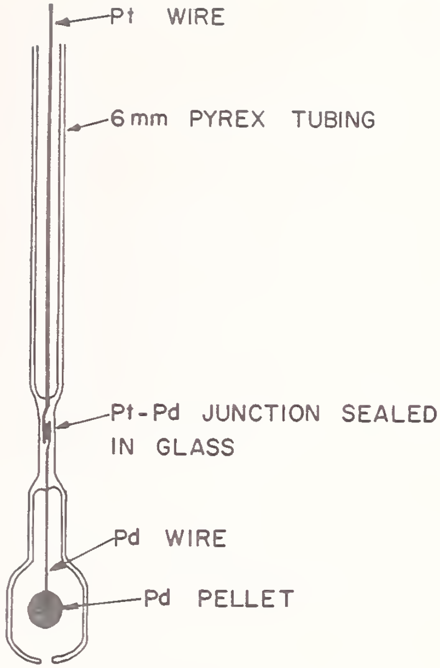

Fig. 2. Palladium-hydrogen reference electrode.

of about 1 cm^2 or a spectroscopic grade graphite rod. Before taking data the solution was pre-electrolysed potentiostatically with a gold electrode held at 1.3 V NHE. In this manner, no impurities were introduced into the solution by possible dissolution of the pre-electrolysis electrode.

Extensive efforts were made to purify the gases bubbled into the cell. The starting material for the oxygen gas was Air Products "zero oxygen" which was further purified by passing it over hot platinized asbestos. The trace amounts of CO_2 generated by this process were removed by then passing the gas over moist KOH and then through two traps containing Linde type 13x molecular sieve. The gas used to provide an inert atmosphere in the cell whenever needed was Matheson "zero helium" which was further purified by passing it over heated oxide free calcium and magnesium chips. The helium was then passed through two liquid N_2 cold traps, one containing activated charcoal and the other, Linde type 13x molecular sieve.

The Tafel plots were obtained by the constant current method, starting at 10 A/m^2 and decreasing the current in steps to 10^{-2} A/m^2. Individual data points were taken at intervals of two hours or greater to allow the potential to reach equilibrium. The currents were generated and the potentials measured using a PAR model 173 potentiostat/galvanostat in the galvanostatic mode. The cyclic voltammetry curves were obtained by using the same apparatus in the potentiostatic mode with a triangular wave input from a Wavetek model 111 signal generator. All measurements were made at room temperature.

3. Results

Tafel plots have been obtained for oxygen reduction in acid solution on various alkali tungsten bronzes with different crystal structures. The bronzes studied included hexagonal $K_{0.33}WO_3$, tetragonal I $Na_{0.4}WO_3$, high purity cubic $Na_{0.7}WO_3$ undoped and doped with up to 800 ppm platinum, cubic $Na_{0.7}WO_3$ doped with 0.12% vanadium, cubic $Na_{0.90}WO_3$, cubic and tetragonal II Li_xWO_3, and single crystal monoclinic WO_3. The rest potentials varied greatly from sample to sample, with potentials (vs. NHE) ranging from 0.62 V for tetragonal II Li_xWO_3 and 0.45 V for WO_3 to -0.17 V for hexagonal $K_{0.33}WO_3$.

Cathodic measurements were performed on freshly polished crystals both before and after prolonged anodic polarization, since anodic potentials were thought to alter the x-value of a bronze surface. Typical cathodic Tafel lines obtained on the crystal before any anodic treatment are shown in figure 3. Data for all the samples are not shown because many samples exhibited similar Tafel lines. The Tafel lines for $Na_{0.9}WO_3$ and $Na_{0.7}WO_3$ are the same, and remain unchanged when doped with platinum (800 ppm) or vanadium (0.12%). All noncubic samples and cubic Li_xWO_3 exhibited higher overpotentials than $Na_{0.7}WO_3$, and are the same as the values for WO_3, except the hexagonal $K_{0.33}WO_3$ crystal which exhibited still higher overpotentials than WO_3. Very high overpotentials were observed in the current range 10^{-2} A/m^2 to 10 A/m^2 on all samples including Pt-doped (800 ppm) $Na_{0.7}WO_3$ and very high purity $Na_{0.7}WO_3$. Below 10^{-2} A/m^2 the potentials drifted to the rest potentials listed above suggesting the Tafel relationship no longer holds. Tafel lines for all samples extended below zero volts NHE, the lowest curve being the one obtained for $K_{0.33}WO_3$, which had a rest potential of -0.17 V. For this sample, the Tafel line for oxygen reduction was only 100 mV above the Tafel line for hydrogen reduction.

Anodic current-voltage measurements were performed on all samples, but no Tafel lines as such, could be obtained. The overpotentials increased rapidly with increasing anodic current and, for many samples, exceeded five volts at a current density of 10 A/m^2. However, at low current densities the potentials dropped well below 1.0 V NHE. On the $K_{0.33}WO_3$ sample the potential dropped to 0.5 V NHE at the rather high current density of 10 A/m^2. These low potentials may be due to a corrosion mechanism.

In the following discussion the anodic current-voltage measurements will be referred to simply as an "anodic treatment," and the samples treated in this manner as "anodized" samples. The maximum anodic current used on all samples was 10 A/m^2. The anodic treatment had no effect on the cathodic Tafel lines of any crystals except cubic Na_xWO_3 crystals, and even there the effect was not large. The Tafel lines for the cubic Na_xWO_3 crystals, before and after the anodic treatment, are shown in figure 4. The overpotentials of anodized cubic Na_xWO_3 samples are close to those of WO_3 and the noncubic bronzes.

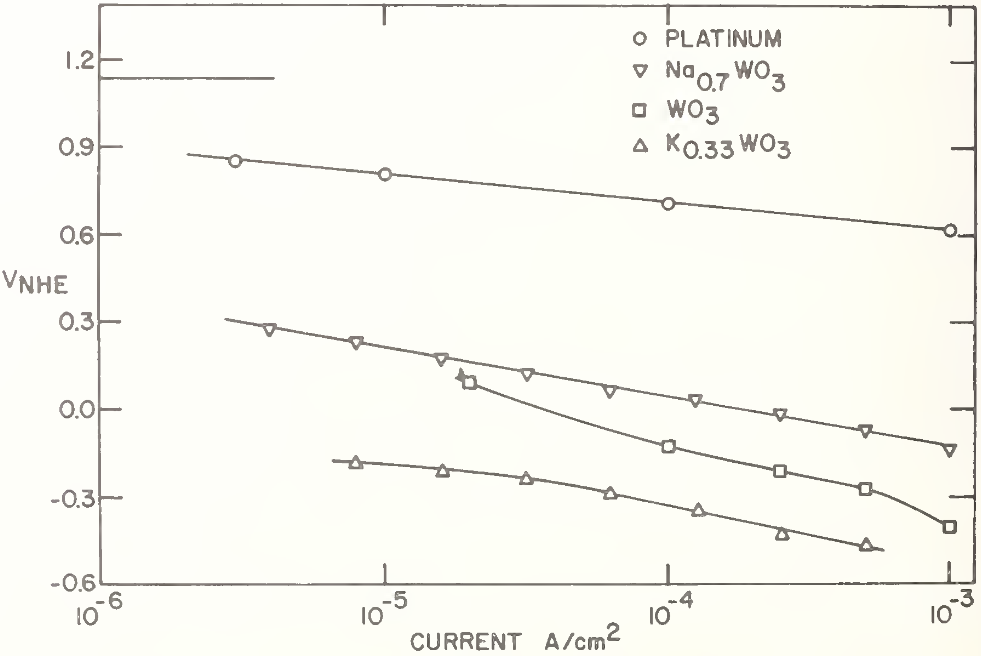

Fig. 3. Representative Tafel plots of unanodized tungsten bronzes compared to a plot for pure platinum (□ represents WO_3 and all noncubic bronzes except $K_{0.33}WO_3$).

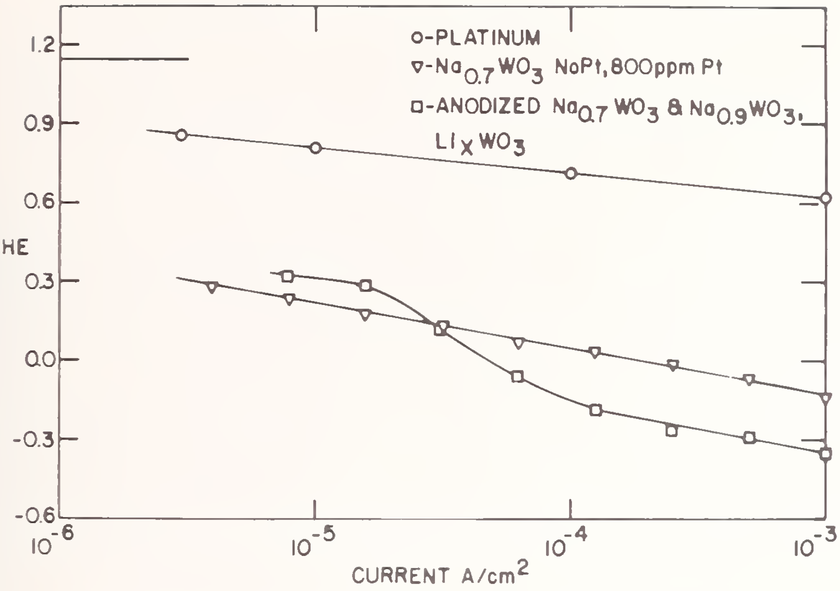

Fig. 4. Tafel plots of anodized and unanodized cubic Na_xWO_3 compared to a plot for pure platinum. The curves represent both undoped crystals, and crystals doped with Pt and V.

Cyclic voltammetry was performed on samples of each crystal structure. Very different results were obtained for the cubic Na_xWO_3 crystals when compared to the noncubic crystals. A typical curve for an anodized sample of $Na_{0.9}WO_3$ is shown in figure 5. A well defined oxidation-reduction peak occurs near 0.2 V NHE as has been reported in the literature [12]. However, the curve for the same crystal before the anodic treatment is considerably different. The peak current at a given sweep rate is an order of magnitude smaller before the anodic treatment is performed, as shown in figure 6. This oxidation-reduction peak has been attributed to the movement of hydrogen ions in and out of the crystal lattice [12]. The

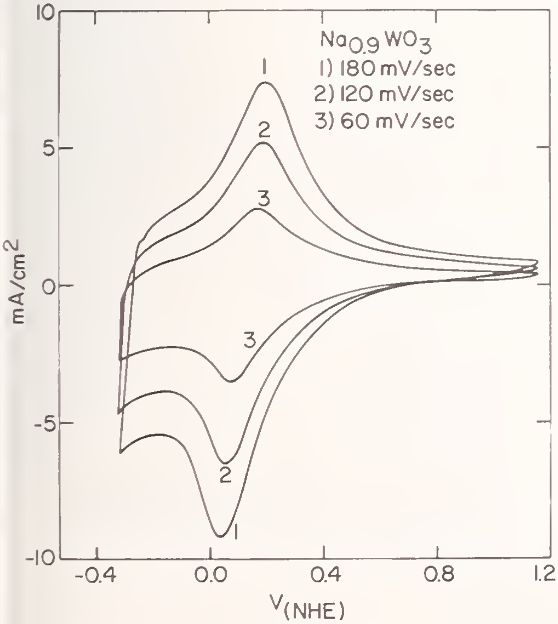

Fig. 5. Cyclic voltammetry curves for anodized cubic $Na_{0.9}WO_3$.

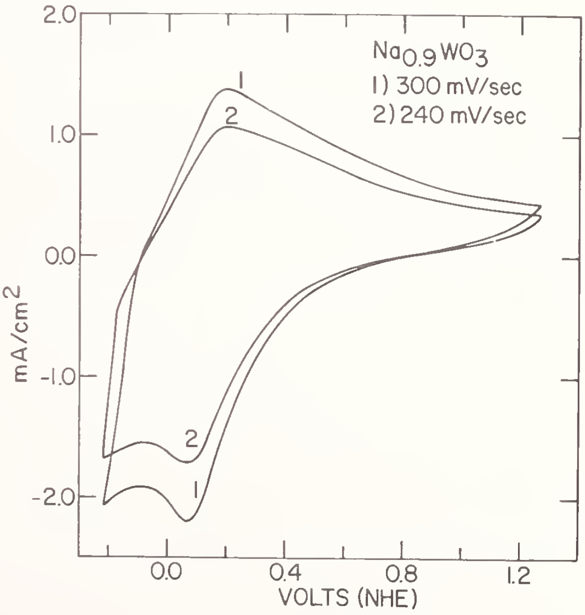

Fig. 6. Cyclic voltammetry curves for unanodized cubic $Na_{0.9}WO_3$.

data presented here are consistent with this idea because the anodic treatment removes many of the sodium ions from the lattice, allowing more hydrogen ions to enter the lattice.

For the noncubic crystals the oxidation peak broadens and the current density is much larger at higher potentials than for cubic Na_xWO_3 crystals. The prolonged anodic current is most likely a corrosion current, and is quite large on the $K_{0.33}WO_3$ crystal. On the noncubic samples the reduction peak became only a slight shoulder superimposed on the hydrogen evolution peak. The cyclic voltammetry curves for a WO_3 crystal, shown in figure 7, are representative of the curves of most of the noncubic bronze crystals and cubic Li_xWO_3. The only difference on some crystals was an even broader oxidation peak. The peak currents were not affected by the anodic treatment except on $K_{0.33}WO_3$ which had slightly higher peak currents after the anodic treatment. All the cyclic voltammetry curves, both before and after the anodic treatment, are stable curves. For example, the curves for the unanodized $Na_{0.9}WO_3$ sample are from approximately the 100th cyclic sweep.

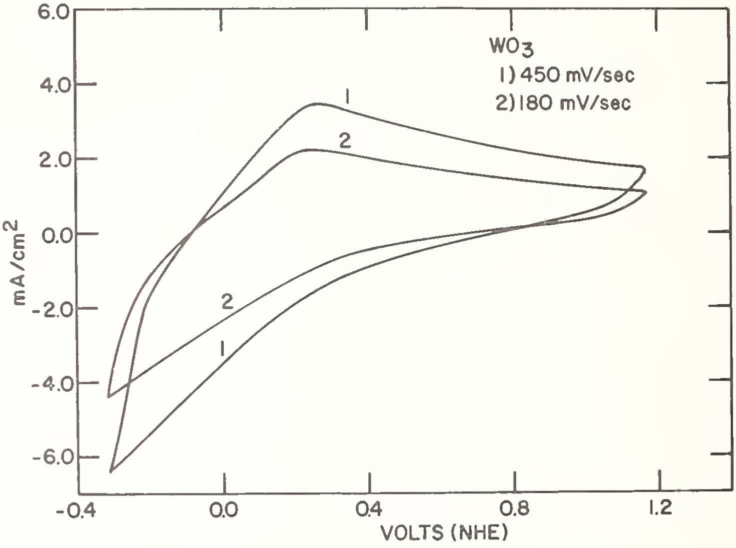

Fig. 7. Cyclic voltammetry curves for WO_3 (also representative of curves for noncubic bronzes).

The extent and depth of sodium depletion from a cubic sodium tungsten bronze crystal, with an x-value of 0.70, has been determined by Auger Electron Spectroscopy. Depth profiles of the sodium-tungsten ratio were obtained on both a freshly polished crystal and on a polished and anodized crystal. The latter sample was anodized with a current of 10 A/m^2 at 4 V for 2 hours. The results of the Auger depth analysis are shown in figure 8. The freshly polished crystal contained a constant sodium x-value of 0.70 at all depths. The

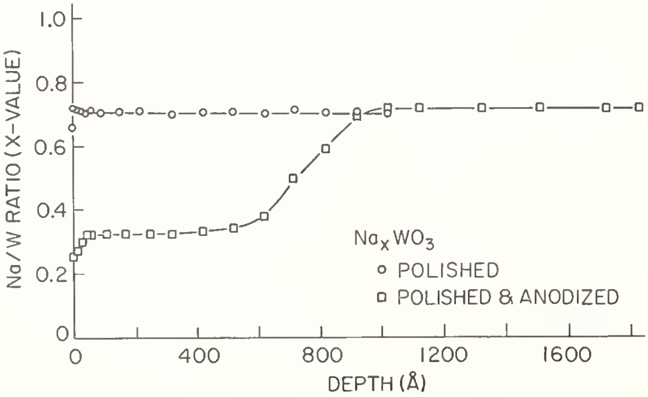

Fig. 8. Auger electron spectroscopy depth profile of the sodium-tungsten ratio for cubic $Na_{0.7}WO_3$.

surface layers of the anodized crystals were not pure WO_3 as expected, but contained some sodium. The x-value at the surface of the anodized crystal was about 0.25 and increased to 0.33 at a depth of 50 Å. The x-value was constant at 0.33 to a depth of 500 Å and then increased gradually to the bulk value of 0.70 at a depth of 1000 Å.

4. Conclusions

From the evidence presented here in the Tafel plots it can be concluded that doping of cubic sodium tungsten bronzes with platinum does not affect their electrocatalytic activity for oxygen reduction in acid solutions. Although none of the other tungsten bronzes studied here were doped with platinum, the results are expected to be the same due to the similarity of their Tafel plots with those of WO_3 and undoped cubic Na_xWO_3.

Although a more extensive Auger analysis of anodized cubic Na_xWO_3 crystals is needed, it can be concluded that the crystals of cubic Na_xWO_3 do not have a layer of WO_3 on their surfaces, even when moderately anodized. The x-value of the sodium depletion layer, as determined by the Auger analysis, is near a critical x-value for lattice stability and the metal-semiconductor transition. A further decrease in the x-value (<0.25) would require a major change in the lattice to the tetragonal II structure. The energy requirements of this transition may prohibit the formation of a lower x-value bronze or WO_3 on the crystal surface.

5. References

[1] Howard R. Shanks, Journal of Crystal Growth 13/14, 433 (1972)

[2] D. B. Sepa, A. Damjanovic, and J. O'M. Bockris, Electrochim. Acta, 12, 746 (1967)

[3] A. Damjanovic, D. Sepa, and J. O'M. Bockris, J. Res. Inst. Catalysis, Hokkaido Univ., 16, 1 (1968).

[4] J. McHardy and J. O'M. Bockris, in "From Electrocatalysis to Fuel Cells," G. Sandstede, Editor, p. 109, University of Washington Press, Seattle, Washington (1972).

[5] J. O'M. Bockris and J. McHardy, J. Electrochem. Soc., 120, 61 (1973)

[6] B. Broyde, J. Catalysis, 10, 13 (1968)

[7] R. D. Armstrong, A. F. Douglas, and D. E. Williams, Energy Conversion, 11, 7 (1971)

[8] J. Heffler and H. Böhm, Metaloberflaeche-Angew. Electrochem., 27, 77 (1973)

[9] Jean-Paul Randin, J. Electrochem. Soc., 121, 1029 (1974)

[10] M. V. Vojnovic, D. B. Sepa, and D. S. Ovcin, Croat. Chem. Acta, 44, 89 (1972)

[11] J. McHardy and J. O'M. Bockris, J. Electrochem. Soc., 120, 55 (1973)

[12] J. P. Randin, A. K. Vijh, and A. B. Chughtai, Ibid, 120, 1174 (1973)

[13] S. Sawada and G. C. Danielson, Phys. Rev. 113, 1005 (1959)

[14] J. McHardy, Ph.D. Thesis, University of Pennsylvania, Philadelphia, Pennsylvania (1972)

National Bureau of Standards Special Publication 455, *Electrocatalysis on Non-Metallic Surfaces*, Proceedings of Workshop held at NBS, Gaithersburg, Md., December 9-12, 1975. (Issued November 1976)

The Electrochemistry of Molybdenum Oxides

Jean Horkans, M. W. Shafer, and R. Peekema

IBM, Thomas J. Watson Research Center
Yorktown Heights, New York 10598

The general electrochemistry of four oxides of mylybdenum, MoO_2, Mo_4O_{11}, Mo_8O_{23}, and Mo_9O_{26}, and the reduction of oxygen on these oxides, in 1 N H_2SO_4 have been investigated on natural faces of single crystals. These compounds are found to undergo electrochemical oxidation and reduction in the potential range between 0.13 and 0.73 V vs NHE. Oxygen does not influence the oxidation of MoO_2 and Mo_4O_{11}, but promotes the anodic dissolution of Mo_8O_{23} and Mo_9O_{26}. Oxygen reduction is supported on all these oxides at low currents and high overpotentials. Large effects of crystal orientation are observed. The chemical composition of the crystal has a much smaller effect. This is apparently due, at least in part, to a change of surface composition with changing electrode potentials. Thus, at a given potential, the compositions of the surface layers of all samples may be similar.

Key words: Electrochemistry; molybdenum oxides; orientation effects; oxygen reduction.

1. Introduction

Stable metal oxide electrodes offer a possible alternative to the use of metals as catalysts for oxygen reduction. The use of an oxide may allow the minimization of corrosion and offer the possibility of investigating both the oxygen reduction and oxygen evolution on surfaces of the same chemical composition. One such material to be investigated was sodium tungsten bronze [1][1], but it was disappointing as an oxygen catalyst [2]. A logical group of materials for a systematic investigation as oxygen electrodes is the transition metal oxides, which offer a range of chemical and electronic properties. Of these, the oxides of molybdenum and tungsten are particularly attractive because of their good electronic conductivity and their stability.

Although in a real catalyst it is necessary to have high surface areas to maximize the current, a basic understanding of catalysis and the nature of interactions at catalyst surfaces may be advanced by an investigation of electrode processes at single crystal faces. Single crystals of MoO_2, Mo_4O_{11}, Mo_8O_{23}, and Mo_9O_{26} have been grown and investigated as electrodes. In this paper we discuss the ability of these surfaces to sustain the O_2 reduction reaction as a function of both chemical composition and crystal orientation.

2. Experimental

Single crystals of the four oxides studied were grown by vapor transport using Mo metal and MoO_3 powder as starting materials and I_2 as the transporting agent. Crystals of the desired compositions were obtained by varying the Mo/MoO_3 ratio and the growth temperature, which was between 790°C and 950°C [3]. Crystal habit could also be changed slightly by adjusting the growth conditions. The size and quality of the crystals varied with composition.

---

[1] Numerals in brackets indicate the literature references at the end of this paper.

Mo_4O_{11} being the largest, with faces up to several cm^2 and Mo_9O_{26} being the smallest (3-4 mm^2) and poorest quality. Crystal morphology also changes markedly with composition. The crystals were identified and oriented using X-ray diffraction methods.

Contact was made to the crystals by attaching a Au wire with Ag-filled epoxy. The Au wire, the contact, and all of the crystal except the face of interest were then masked off using Miccrostop (Michigan Chrome and Chemical Co.), a polyvinyl ketone used as a plater's mask. The inertness of this material under the conditions of the investigation was established by partially masking off wires of Pt and Au and running their cyclic voltammetry in 1 N H_2SO_4. No anomalous features attributable to contamination were observed. In the case of several of the molybdenum oxide crystals it was possible to examine several natural faces of the same crystal by cleaning the crystal and remasking.

Measurements involved potentiostatic linear sweep and steady state measurements with a three-electrode system. All measurements were done in 1 N H_2SO_4 through which either He or N_2 was being bubbled. A three compartment cell was used, the compartments being separated by glass frits. The counter electrode was a Pt foil and the reference electrode was Hg/Hg_2SO_4. All potentials are quoted vs. the normal hydrogen electrode.

The steady state data were taken with the electrode potential being changed in the negative direction. Each point represents 10-15 minutes. Data are not always reproducible when the direction of the potential change is reversed, as will be discussed below.

3. Results and discussion

The molybdenum-oxygen system contains a number of compounds, of which MoO_2 and MoO_3 are best known. Between these compositions, five other distinct phases have been identified and their crystal structures have been determined by Magneli [4,5] and Kihlborg [6]. The structural studies have shown that all the compounds can be classified as belonging to one of several basic structural types. The four compounds we studied are of either the rutile or ReO_3 type. The MoO_2 is a rutile type, which is common to many of the transition metal dioxides and has the molybdenum in only one coordination, i.e. MoO_6 octahedra, which share both corners and edges. The high conductivity of this compound is due to the short Mo-Mo distance along the direction in which the MoO_6 octahedra are joined by edges (c axis).

The basic structural unit of the other oxides, Mo_4O_{11}, Mo_8O_{23}, and Mo_9O_{26}, is of the ReO_3 type. In this structure the MoO_6 octahedra are linked exclusively at the corners. The oxygen deficiency of these compounds, i.e. the deviation from pure MoO_3, can be accounted for by connecting MoO_6 units in other ways. In Mo_8O_{23} and Mo_9O_{26} the appropriate fraction share edges, and in Mo_4O_{11} there are MoO_4 tetrahedra joining the basic ReO_3-type slabs. A detailed description of these structures and their relationship to each other is given by Kihlborg [6].

The transport properties of the four oxides have been measured by the four-probe method as a function of temperature. A summary of their room temperature resistivities and the pertinent structural data is given in table 1.

As expected, the resistivities increase as the composition approaches the stoichiometric MoO_3, which is a rather good insulator. The conduction mechanism of the ReO_3-type oxides is complex and presently not understood.

The cyclic voltammetry (CV) of two faces of MoO_2 in 1 N H_2SO_4 is shown in figure 1. The solid line indicates the behavior in the absence of O_2 and the dashed line that in O_2-saturated solution. Even in the absence of O_2, currents flow over the entire potential range shown. Although the general appearance of the CV for the two faces shown here is similar, the currents are more than an order of magnitude larger for the $(10\bar{1})$ face than for the (100) face. The $(2\bar{1}\bar{1})$ face exhibits currents intermediate to the two faces of figure 1. A reduction of the surface occurs cathodic to ∿ 0.4V and oxidation occurs beyond ∿ 0.65V in the anodic sweep. In the absence of O_2, the total charge consumed in oxidation is essentially equal to that consumed in reduction on the (100) and $(2\bar{1}\bar{1})$ faces. However, on the $(10\bar{1})$ face the cathodic charge is substantially larger than the anodic charge. The shape of the voltammograms is quite dependent on the potential range scanned.

Table 1. Structural data and resistivities of molybdenum oxides.

Compound	Symmetry	Lattice constants (Å)	Resistivity (300 K) (ohm cm)
MoO_2	monoclinic[a]	a = 5.61 b = 4.85 c = 5.62	1.2×10^{-4}
Mo_4O_{11}	orthorhombic[b]	a = 24.49 b = 5.45 c = 6.75	2×10^{-4}
Mo_8O_{23}	monoclinic[b]	a = 16.88 b = 4.05 c = 13.39	6×10^{-1}
Mo_9O_{26}	monoclinic[b]	a = 8.14 b = 11.89 c = 21.23	4×10^{1}

[a] Brandt and Skapski [7]

[b] Kihlborg [6].

When O_2 is present, the anodic current is basically the same as in He-saturated solution, but larger reduction currents are observed due to oxygen reductions. The proportional increase in current on addition of O_2 is of the same order on the $(10\bar{1})$, (100), and $(21\bar{1})$ faces but the absolute magnitude of the increase is quite different.

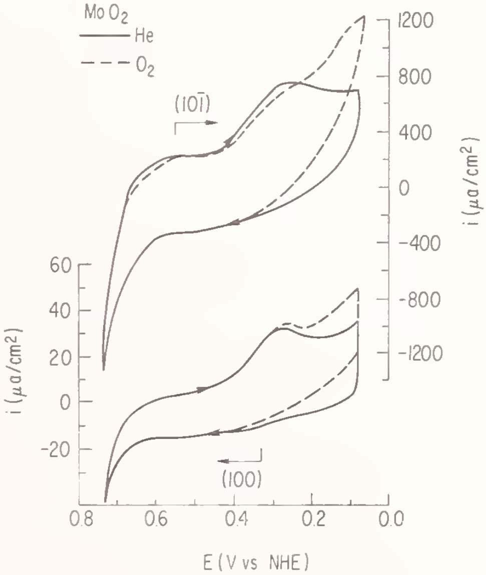

Fig. 1. Cyclic voltammetry of the $(10\bar{1})$ and (100) faces of MoO_2 in He-saturated (——) and O_2-saturated (---) 1 N H_2SO_4. Sweep speed 10 mV/s.

Steady state measurements for O_2 reduction on MoO_2 are summarized on figure 2. The background currents in the absence of O_2 have been subtracted from the total currents in O_2-saturated solution to obtain the data of figure 2. There is no substantial linear region and a limiting current is reached at quite low current values. Cathodic to ∿ 0.10V the background currents become larger compared to the O_2-reduction currents. Anodic to ∿ 0.45V an anodic background current flows.

Reproducibility of the steady state measurements is poor due to irreversible changes in the oxidation state of the electrode surface with changes of potential. The curves in figure 2 will retrace when the direction of the potential change is reversed until a potential is reached where large anodic currents associated with oxidation of the MoO_2 surface begin to flow.

Figure 2 thus indicates that the O_2 reduction reaction can be observed on these surfaces, uncomplicated by reactions of the electrode surface itself, only between about 0.30 and 0.45V. The overpotential for O_2 reduction is high. Both the magnitude of the current and the overpotential are of the order of those reported by Randin [2] for the Pt-free Na_xWO_3.

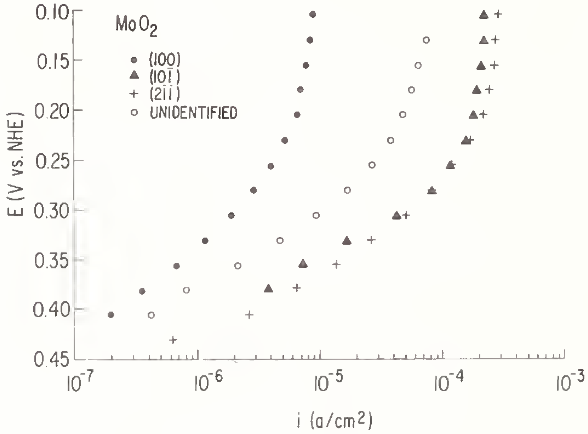

Fig. 2. Steady state masurements for O_2 reduction in 1 N H_2SO_4 on several faces of a MoO_2 single crystal.

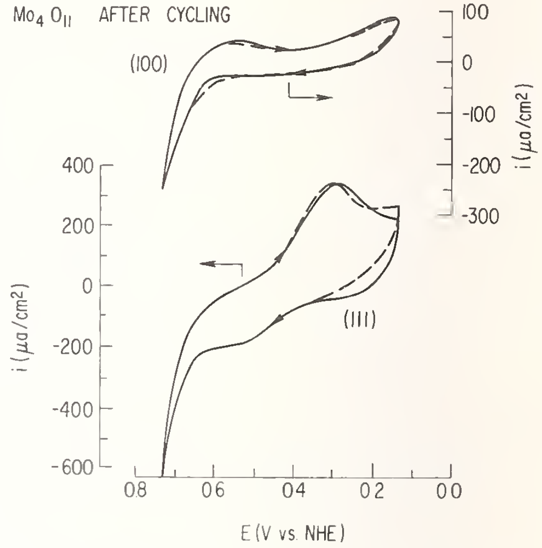

Fig. 3. Cyclic voltammetry of the (100) and (111) faces of Mo_4O_{11} in He-saturated (——) and O_2-saturated (---) 1 N H_2SO_4. Sweep speed 10 mV/s.

A complicating factor in the interpretation of the steady state measurements is the fact that, due to the oxidation and reduction of the surface which are apparent from the CV, the nature of the surface at any given potential is ill-defined. It cannot be assumed to consist only of Mo (IV). A rather large effect due to orientation is observed: O_2 reduction currents are more than an order of magnitude higher on the (10$\bar{1}$) face than on the (100) face. All of the faces studied support only small O_2-reduction currents.

The CV of two faces of Mo_4O_{11} is shown in figure 3. As in the case of MoO_2, significant currents flow over the entire potential range studied, both in the presence and absence of O_2. These currents are larger for the (111) face than for the (100) face. Oxygen causes larger cathodic currents to flow on the (111) face but has little effect on the (100) face.

The steady state data on these two faces are shown in figure 4. The results are similar to those obtained on MoO_2. Small O_2 reduction currents are observed between about 0.25 and 0.40V. These are larger on the (11$\bar{1}$) face than on the (100) face. Cathodic to ∿ 0.15V the background current becomes large compared to the O_2 reduction current.

The higher oxides, Mo_8O_{23} and Mo_9O_{26}, show somewhat different behavior in the cyclic voltammetry (fig. 5) than MoO_2 and Mo_4O_{11}. (Only one face of each of these crystals was examined.) Oxygen increases not only the cathodic current, but also the anodic current. In the absence of O_2, the anodic and cathodic charge consumed during one complete cycle are equal. When O_2 is present, the anodic charge is significantly larger than the cathodic charge. Apparently O_2 promotes the dissolution of Mo_8O_{23} and Mo_9O_{26} and the increased currents observed are apparently due to dissolutions. The steady state data for Mo_8O_{23} and

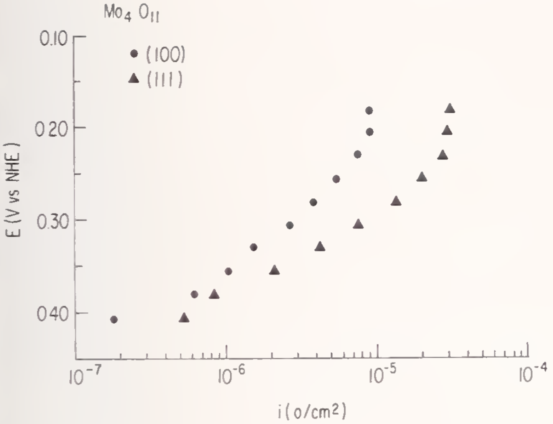

Fig. 4. Steady state measurements for O_2 reduction on 1 N H_2SO_4 on the (100) and (111) faces of a Mo_4O_{11} single crystal.

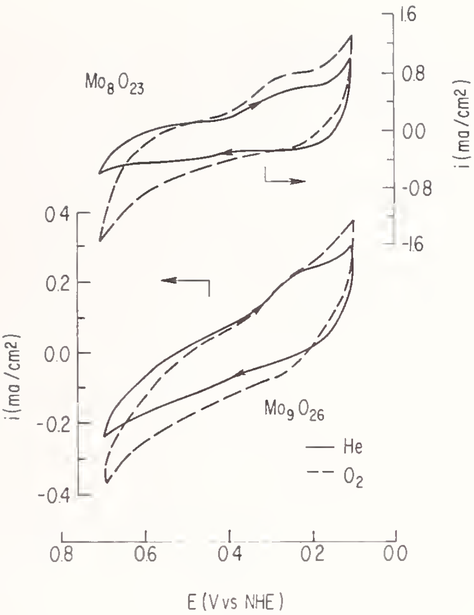

Fig. 5. Cyclic voltammetry of unidentified single crystal faces of Mo_8O_{23} and Mo_9O_{26} in He-saturated (——) and O_2-saturated (---) 1 N H_2SO_4. Sweep speed 10 mV/s.

Mo_9O_{26} show the same general trends as for MoO_2 and Mo_4O_{11}, but they apparently are less reliable because of reduction of the oxide surface.

As mentioned earlier, the shape of the CV depends strongly on the potential range over which the electrode is cycled. Figure 6 shows the CV of a number of samples which have been cycled only between 0.43 and 0.73V. These potentials are not sufficiently cathodic to cause significant reduction of the surface. Comparison with figures 1, 3, and 5 shows that the current-voltage characteristic in this potential region is substantially different than when the cathodic potential limit of the scan is 0.13V. Anodic currents occuring in figure 6 are apparently due to the anodic dissolution of the oxides. This is found to be highly dependent on both the chemical composition of the oxide and the crystal face being studied.

The higher oxides Mo_8O_{23} and Mo_9O_{26} show no tendency to dissolve anodically in this potential range. Substantial dissolution currents flow on Mo_4O_{11} above ∿ 0.65V. These are highly dependent on orientation. The (100) face of Mo_4O_{11} exhibits an unusual oscillatory current which Peekema and Shafer [8] have attributed to dissolution of the 12Å layers perpendicular to the [100] direction which make up the Mo_4O_{11} structure. Since the [111] direction has no simple relationship to the periodicity in the structure, no structure in the CV is seen for the anodic dissolution of the (111) face.

There is no periodicity of this type in the MoO_2 structure. All faces show CV in this region similar to that for (100) as seen in figure 6, although the magnitude of the current varies.

The question of the nature of the surface reactions which occur in the absence of O_2 in solution has been addressed only in a preliminary way to date. The large number of possible oxidation states which can be assumed by molybdenum complicate this process. Pourbaix [9] indicates that at the more cathodic end of the potential region scanned, it may be possible to form Mo (III), which would probably exist in solution. The formation of Mo(III) is unlikely in our solution because sulfate is not a good complexant for this species: its absence has been confirmed by chemical analysis for molybdenum in solution after severe cathodic treat-

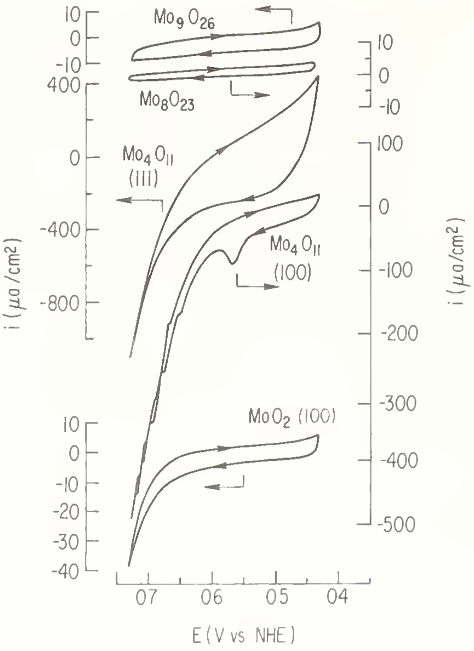

Fig. 6. Dissolution of molybdenum oxides. Cyclic voltammetry of MoO_2, Mo_4O_{11}, Mo_8O_{23}, and Mo_9O_{26} samples in He-saturated 1 N H_2SO_4 which have never been cycled into potential regions where cathodic currents flow.

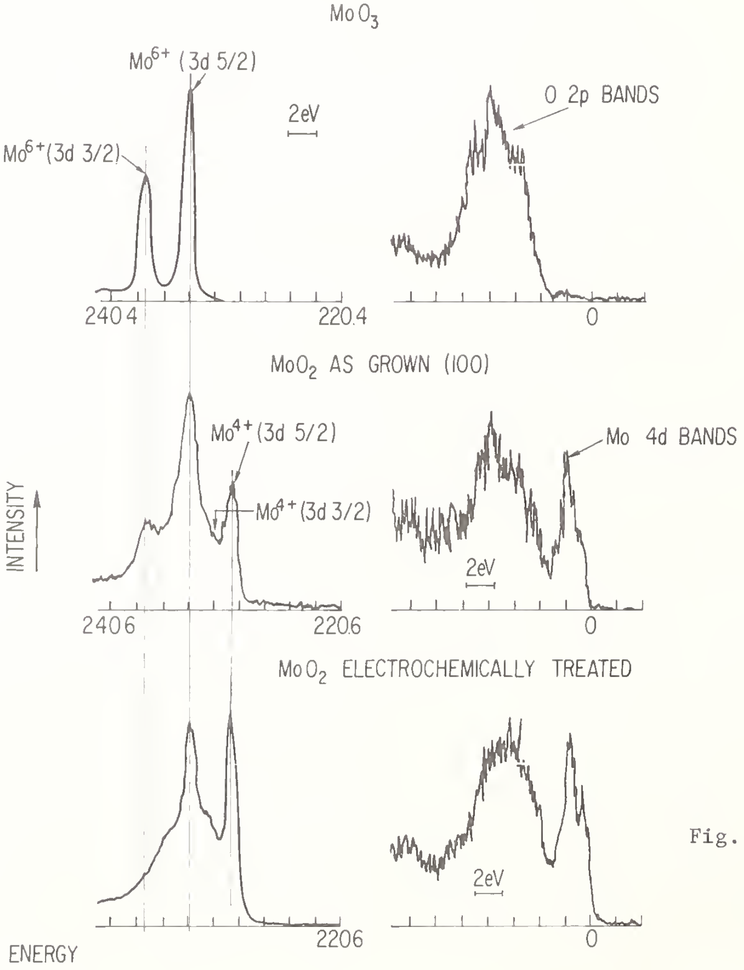

Fig. 7. ESCA data for as-grown MoO_3 and for MoO_2 as-grown and after electrochemical cycling.

ment of a sample of Mo_4O_{11}. Another possible oxidation state of molybdenum is +5, which is stable in the absence of O_2. An EPR study of Mo_4O_{11} in H_2SO_4 showed Mo (V) formation only when the sample was being actively dissolved anodically. Thus, in a potential range in which anodic dissolution does not occur, it appears that only the +4 and +6 oxidation states of molybdenum need to be considered in dealing with the electrochemistry of its oxides.

Qualitative information about the effects of electrochemical cycling on the electrode surface was obtained using ESCA, as illustrated in figure 7. At the top of the figure are shown the Mo (VI) 3d peaks and the oxygen 2p bands of a sample of as-grown MoO_3. Beneath this are the same spectral regions of two MoO_2 (100) samples, as-grown and after extensive cycling between 0.13 and 0.73V. (The last potential seen by the electrode before removal from solution was 0.43V.) The as-grown MoO_2 sample is seen to have a considerable amount of Mo (VI) on the surface. After cycling, the amount of Mo (VI) is reduced and the Mo (IV) has increased, as indicated by the growth of the Mo (IV) 3d peaks relative to the Mo (VI) 3d peaks and the increase of the molybdenum 4d band. This surface was in contact with air for several hours before measurement, so the actual amount of Mo (VI) at the time of removal from solution may have been even less. Similar results were obtained for Mo_4O_{11} although the relative increase of Mo (IV) is less dramatic. More quantitative information of this kind is certainly desirable. It would require instituting better handling techniques in transferring the sample from the solution to the vacuum chamber and more careful potential control.

4. Conclusions

The electrochemistry of the molybdenum oxides shows many broad similarities among MoO_2, Mo_4O_{11}, Mo_8O_{23}, and Mo_9O_{26}. In the potential range between 0.13 and 0.73 V in 1 N H_2SO_4, these compounds undergo a highly irreversible reduction and oxidation of the surface. These reactions lead to high background currents in the steady state measurements and interfere with the measurement of O_2 reduction except in the narrow range between about 0.2 and 0.4 V.

Oxygen reduction occurs on these surfaces at a high overpotential. Only small O_2 reduction currents are sustained. Oxygen promotes the dissolution of Mo_8O_{23} and Mo_9O_{26}. All results are highly dependent on crystal orientation.

The fact that all these oxides exhibit similarities in their electrochemistry may not mean that chemical composition and electronic conductivity do not play in important role. Instead, it may mean that the surface oxidation and reduction reactions that occur in this potential range cause all the surfaces to have similar composition at a given electrode potential, independent of the composition of the bulk. The lack of specific information about the surface composition makes the modeling of the interactions at the surface dangerous.

5. Acknowledgement

The authors gratefully acknowledge the assistance and support of R. Figat for crystal growth, T. Penney for resistivity data, R. Pollak and H. Hughes for ESCA data and interpretation, R. Title and W. Fitzpatrick for EPR studies, B. Gilbert for wet chemical analysis and J. Angilello for crystal orientation.

6. References

[1] For example, D. B. Sepa, A. Damjanovic, and J. O'M. Bockris, Electrochem. Acta, 12, 746 (1967); J. McHardy and J. O'M. Bockris, J. Electrochem. Soc., 120, 53 (1973); J. O'M. Bockris and J. McHardy, ibid., 120, 61 (1973).
[2] J.-P. Randin, J. Electrochem. Soc., 121, 1029 (1974).
[3] M. W. Shafer, R. A. Figat, and T. Penney, to be published.
[4] A. Magneli, Acta Chem. Scand., 2, 501 (1948).
[5] A. Magneli, ibid., 2, 861 (1948).

[6] L. Kihlborg, *Arkiv för Kemi*, *21*, 471 (1963).

[7] B. G. Brandt and Skapski, *Acta Chem. Scand.*, *21*, 661 (1967).

[8] R. M. Peekema and M. W. Shafer, Abstract no. 59, Electrochemical Society Meeting, Dallas, October, 1975.

[9] M. Pourbaix, *Atlas of Electrochemical Equilibria* (Pergamon, Oxford, 1966) p. 275.

National Bureau of Standards Special Publication 455, *Electrocatalysis on Non-Metallic Surfaces*,
Proceedings of Workshop held at NBS, Gaithersburg, Md., December 9-12, 1975. (Issued November 1976)

Titanates As Oxygen Electrodes

U. Bertocci, M. I. Cohen, J. L. Mullen and T. Negas

Institute for Materials Research
National Bureau of Standards
Washington, D.C. 20234

Single crystal or polycrystalline compacts of five, TiO_2-based, oxide materials were investigated as oxygen electrodes. Potentiostatic and potentiodynamic measurements were accomplished at room temperature using neutral borate or 5M H_3PO_4 and inert (Ar) or oxygen environments. Observations of electrochemical behavior during illumination also were made.

Materials display slow, but continuous, changes in features of potentiodynamic scans, as well as changes in current with time at constant potential. Failure to attain steady-state conditions is attributed to specimen mechanical/chemical inhomogeneities and changes prior to and during measurement, variable surface conditions, together with electrode pre-treatment. For example, cathodic currents for O_2 reduction tend to increase after cathodic polarization, while H_2-evolution is hindered by dissolved O_2. Illumination increases the current density for O_2 reduction at very negative potentials while current decreases are apparent during H_2-evolution in Ar.

Results indicate that these oxides are not promising as electrocatalysts for O_2-reduction, although for a definitive assessment, well-defined and closely controlled surface conditions are necessary.

Key words: Electrocatalyst; hydrogen evolution; lanthanum titanate; oxygen electrode; photo-assisted electrolysis; rutile.

1. Introduction

Transition metal oxides have shown interesting catalytic properties. Some of these materials, particularly those with perovskite structure, have been found to be effective catalysts in gas phase reactions [1][1], but they have been little studied as electrodes [2]. It was felt, therefore, that it would be interesting to examine these materials as electrocatalysts, particularly as oxygen electrodes in electrolytes, such as concentrated phosphoric acid, which are proposed for the operation of low temperature fuel cells [3].

Due to its high resistance to acid attack and to the fact that its conductivity is controllable by doping or reduction [4], TiO_2 was chosen for these investigations.

Reports of electrochemical behavior are few, primarily being limited to photoassisted decomposition of water by TiO_2 [5-10], although some information as to the general electrochemical behavior of rutile is available [11].

In the lanthanum titanate series, it appears that the conductivity can be varied from metallic to semiconducting to insulator, by varying the lanthanum oxide/titanium oxide ratio [12].

---

[1] Figures in brackets indicate the literature references at the end of this paper.

In this paper we will report on the behavior, as oxygen electrodes, particularly on the cathodic side, of five materials: reduced TiO_2, Nb and Ta doped TiO_2, $La_{0.75}TiO_3$ and $La_{0.92}TiO_3$.

2. Experimental

2.1. Preparation

Reduced rutile was prepared by heating a TiO_2 single crystal [13] at 1200 °C in a H_2 atmosphere. After reduction, the material had 6 x 10^{21} charge-carriers/cm^3 at room temperature. The Nb doped TiO_2 (0.1%Nb) was also a single crystal [13]. Ta doped TiO_2 (95:5) was prepared by heating at high temperature (1600 °C) a mixture of TiO_2 and Ta_2O_5. The material was further homogenized by grinding the resultant mass and pressing the power into pellets, followed by further sintering at the same temperature. The two lanthanum titanates were made by melting in gettered argon a mixture of the starting materials (TiO_2, Ti and $La(OH)_3$), followed by extensive annealing of the compound in gettered argon. Materials prepared in this manner were polycrystalline.

The samples were mounted in epoxy resin after indium soldering to a copper block. The part exposed to the solution, having surface areas ranging from 0.3 to 0.5 cm^2, was ground flat and then polished. 1 μm diamond powder was the final polishing stage. Electrical contact was made in a conventional way by a screw into the copper block [14]. The electrode surface was, in general, smooth although there were some small holes and cracks.

2.2 Electrochemical Measurements

Investigations were carried out at room temperature (23 °C) in a buffer solution made of a 1:1 by volume mixture of saturated H_2BO_3 and $Na_2B_4O_7$ (pH ∿7.5), as well as in 5M H_3PO_4. A saturated calomel electrode was used as reference. The reversible hydrogen electrode potential was -685 mV vs. SCE in the neutral solution and -240 mV vs. SCE in phosphoric acid. Measured values and those calculated from pH measurements agreed within 10 mV.

The measurements were taken either by slow potentiodynamic sweeps or by stepwise potentiostatic runs. Corrections for the ohmic drop in the neutral borate solution (where the resistance was measured as $30\Omega \cdot cm^2$)[2] were calculated and applied to the plots. In acidic solution the ohmic resistance, measured by applying a square wave current signal to the electrode and observing the voltage response, was less than $5\Omega \cdot cm^2$ and its effect was negligible, since the current density was seldom more than 1 mA/cm^2. Measurements were taken in a closed cell, either under an inert atmosphere (Ar) or with oxygen. Both gas bubbling and stirring with a magnetic stirrer were used for O_2 elimination if an inert atmosphere was desired and to enhance oxygen transport to the electrode when in a O_2 atmosphere.

2.3. Effect of Light

Observations have been made also on the effect of illumination on the electrochemical behavior of the materials. The light source was a 200 W quartz-iodine lamp, whose beam was focussed on the electrode surface by means of mirrors. Since the beam, however, entered the cell through a Pyrex glass window, most of the energy in the short wavelength region did not reach the electrode.

3. Experimental Results

3.1. Doped TiO_2

The results of the stepwise potentiostatic runs, on the cathodic side, for the three doped TiO_2 electrodes are given in figures 1, 2 and 3. The data, all referred to the reversible hydrogen electrode (RHE), cover both neutral and acidic electrolyte in the presence and in the absence of oxygen. The primary non-steady-state feature observed was that polarization of the electrode to a certain potential tended to increase, at least temporarily, the cathodic current density which could be obtained at more positive potentials. The effect

---

[2] The unit $\Omega \cdot cm^2$ is the ratio of voltage to current density.

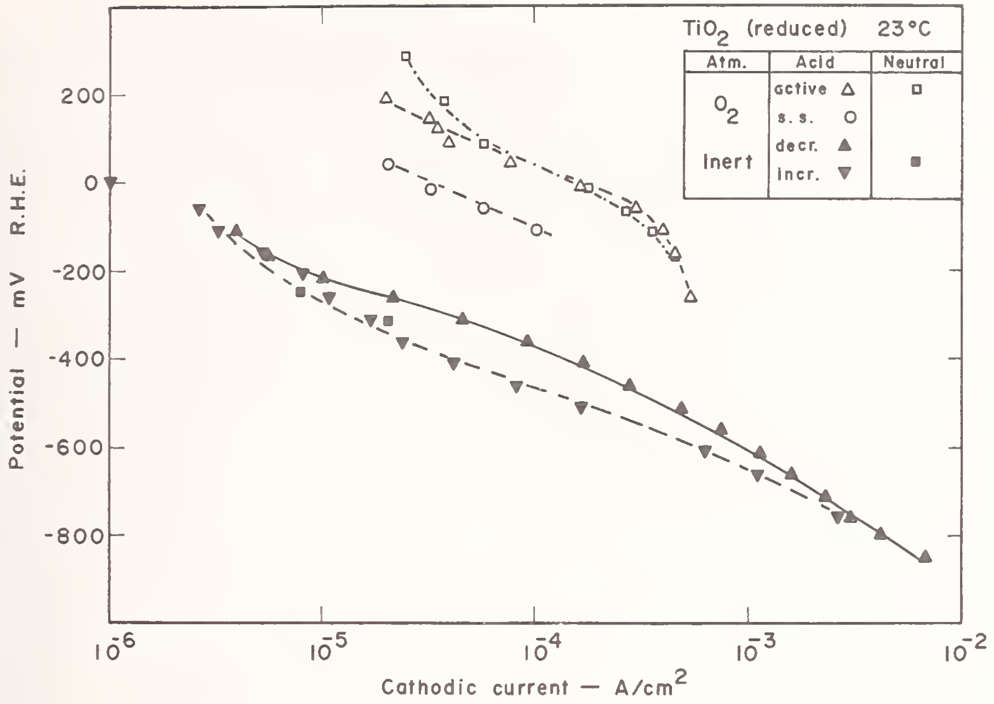

Fig. 1. Cathodic current density-potential curves for reduced rutile in acidic and neutral solution.

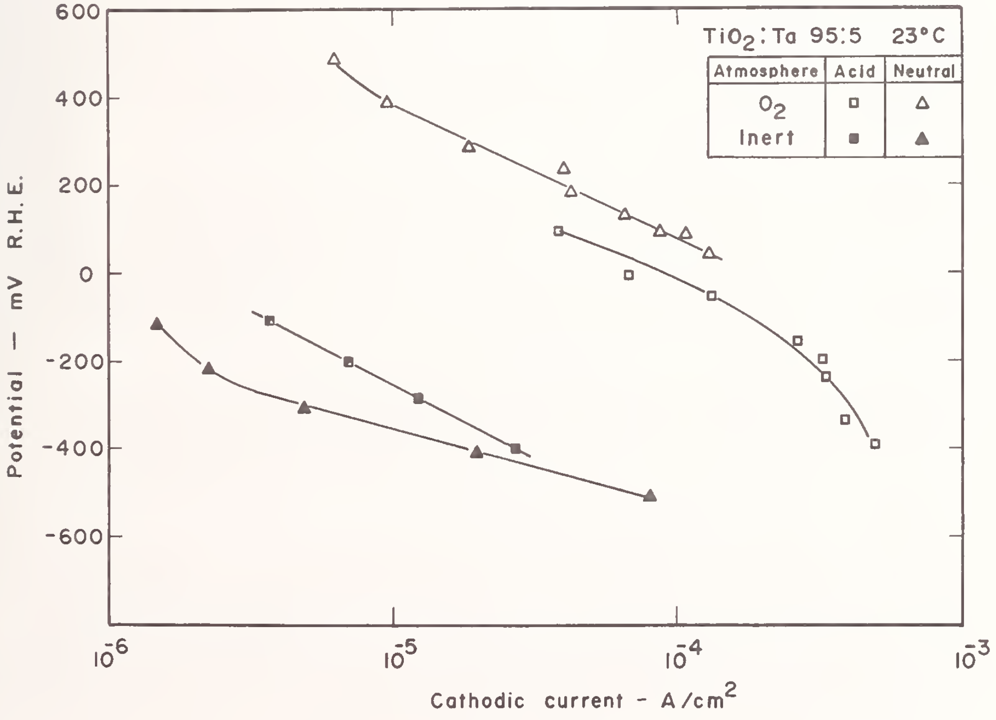

Fig. 2. Cathodic current density-potential curves for Ta-doped TiO_2 in acidic and neutral solution.

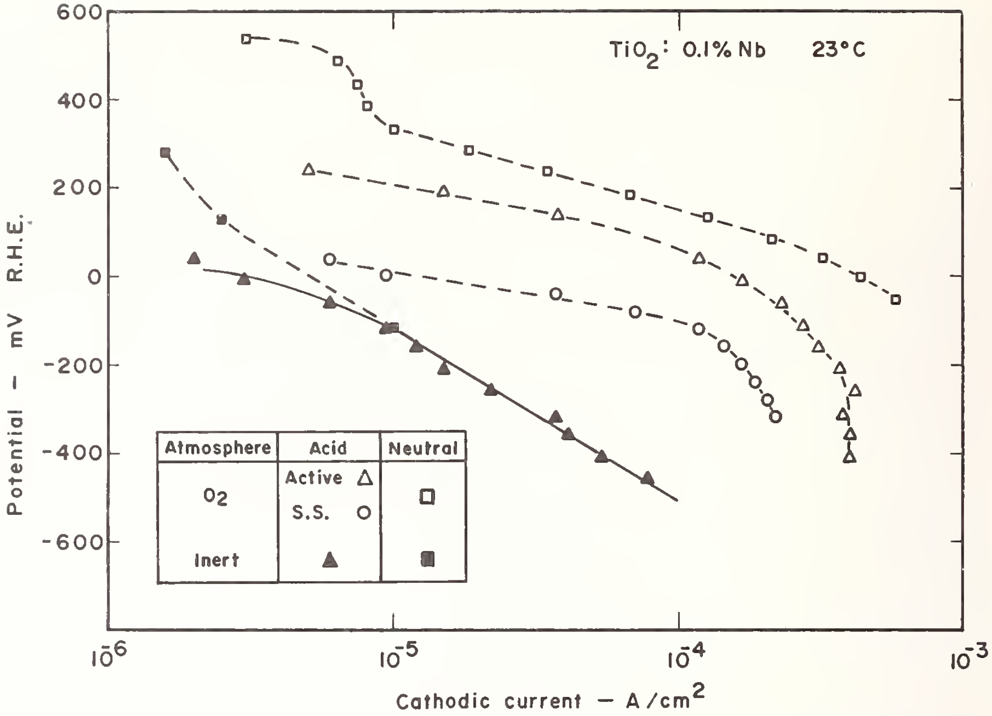

Fig. 3. Cathodic current density-potential curves for Nb-doped TiO_2 in acidic and neutral solution.

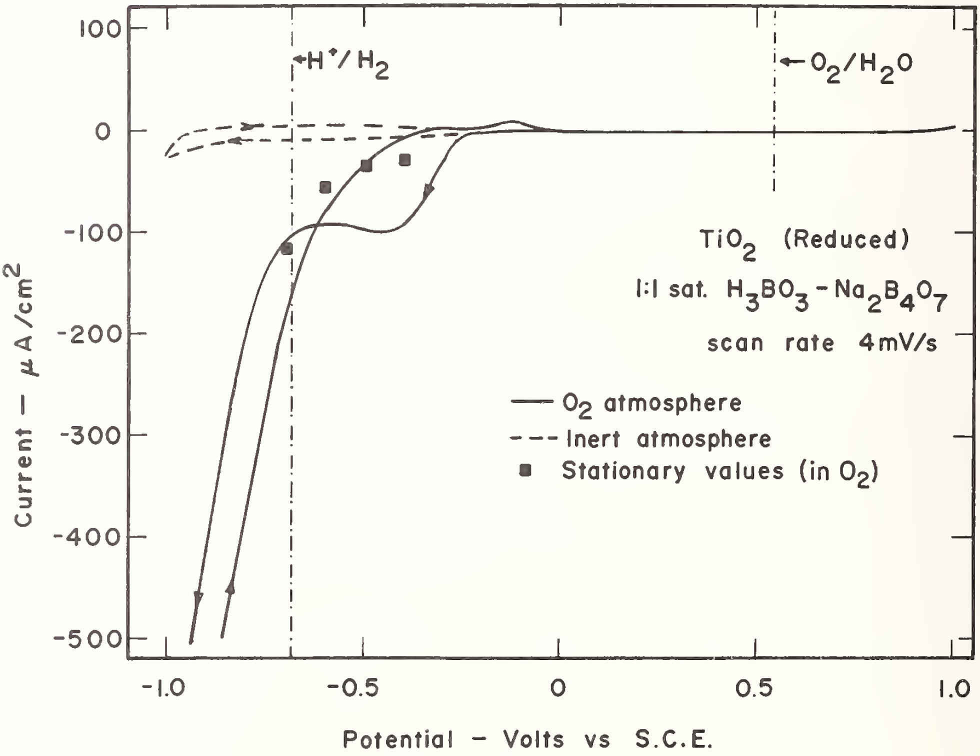

Fig. 4. Potentiodynamic scan for reduced rutile in 1:1 saturated H_3BO_3-$Na_2B_4O_7$ solution. Scan rate 4 mV/s.

was particularly pronounced if the pre-treatment consisted of polarizing to a negative value such as to obtain vigorous (50-100 mA/cm^2) hydrogen evolution. Accordingly, as shown in the figures, the current density was in general larger during the "return" runs, when the potential was increased (in a positive direction) stepwise, than when the potential was decreased stepwise. A number of points are marked "active" and "steady state". The "active" values were obtained after strong cathodic polarization, and tended to decay towards the "steady state" value in times of the order of several minutes. It should be noticed that activation was particularly effective in increasing the rate of oxygen reduction.

The potentiodynamic scans in an O_2 atmosphere have shown the presence of a cathodic peak located about 200 mV more positive than the potential for steady state O_2 reduction. This peak, which is shown in figure 4, decreases by repeated cycling and reappears only after long times (of the order of one hour) at open circuit. However, larger cathodic currents in the same potential region (approximately +300 mV vs. RHE) are so persistent that they appear also in the potentiostatic stepwise runs, as shown in figure 5.

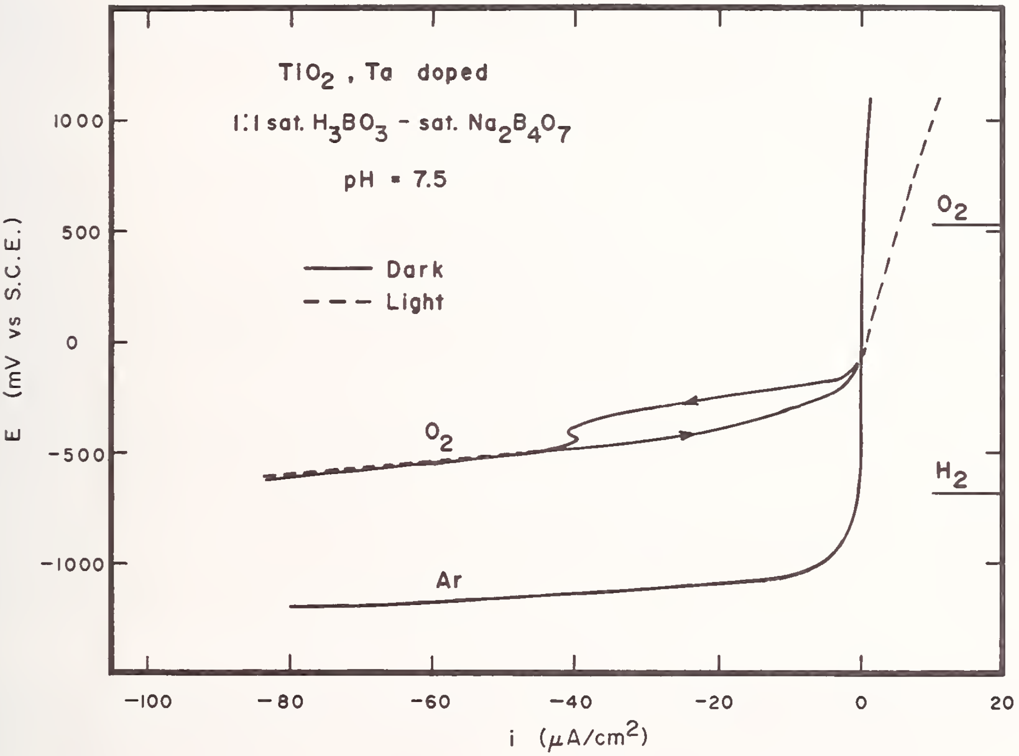

Fig. 5. Current density-potential curves for Ta-doped TiO_2 in 1:1 saturated H_3BO_3-$Na_2B_4O_7$ solution. H_2 and O_2 refer to equilibrium potentials for the two reactions.

The effect of illumination on the electrochemical response of doped TiO_2 electrodes was similar for all three. Figure 5 shows the effect for Ta doped TiO_2 and figure 6 shows the light effect in more detail for the Nb doped TiO_2.

Microscopic observations of the electrode surface before and after the measurements gave no indication that these materials were being attacked.

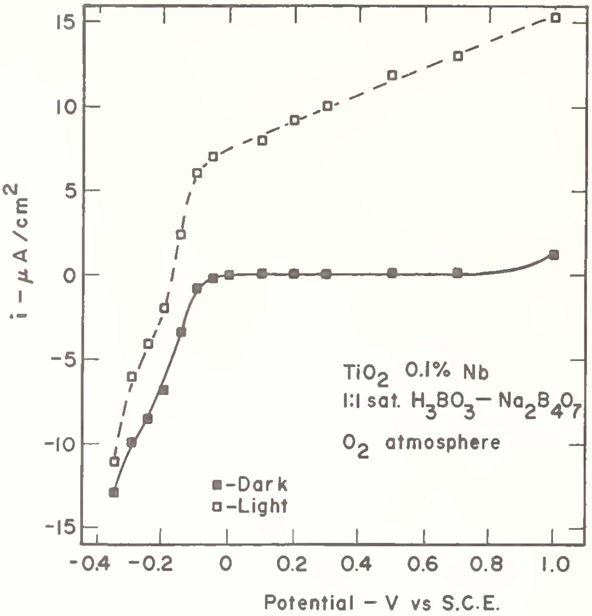

Fig. 6. Effect of illumination on current-potential curves for Nb-doped TiO_2 in 1:1 saturated H_3BO_3-$Na_2B_4O_7$ solution.

3.2. Lanthanum Titanates

The current-potential curves for cathodic reduction on the more metallic of the two titanates investigated, $La_{0.92}TiO_3$, are given in figure 7 and those for $La_{0.75}TiO_3$ in figure 8. The effects of "activation" of the electrode surface are similar to those observed on doped TiO_2. As shown in figure 8, hydrogen evolution in acidic solution was found to

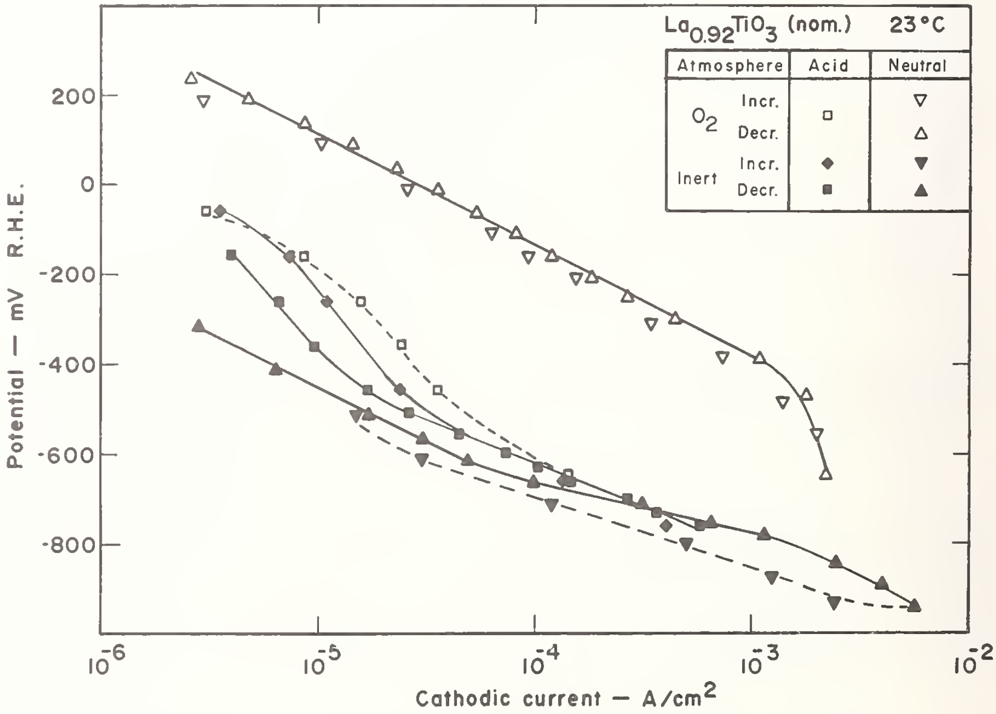

Fig. 7. Cathodic current density-potential curves for $La_{0.92}TiO_3$, in acidic and neutral solution.

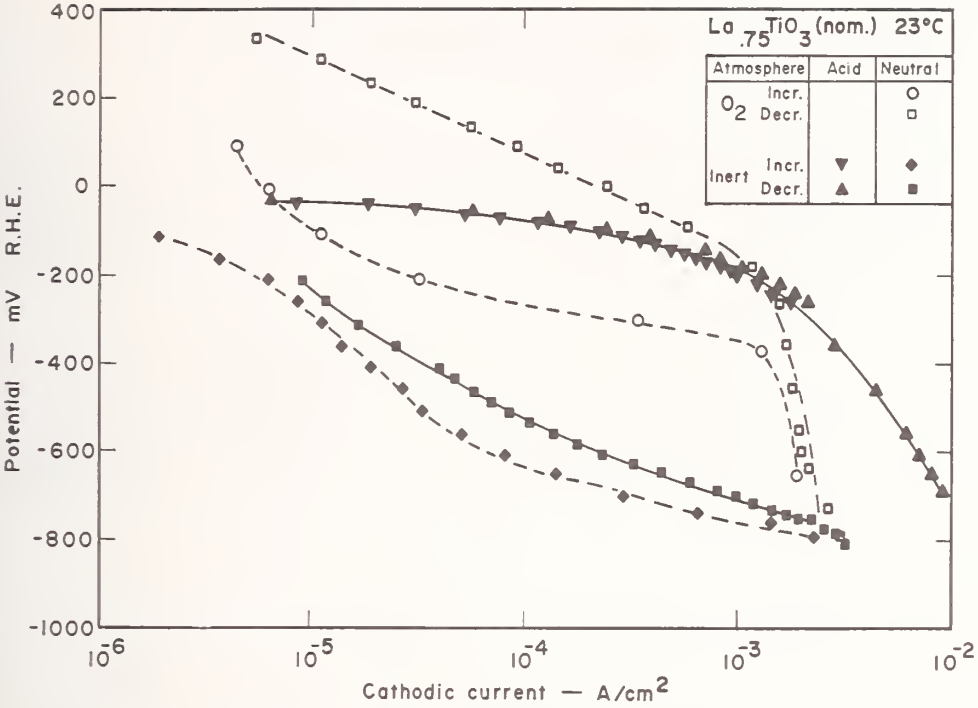

Fig. 8. Cathodic current density-potential curves for $La_{0.75}TiO_3$, in acidic and neutral solution.

occur on $La_{0.75}TiO_3$ much more easily than for any other condition, including the same electrode in neutral borate. Therefore, the occurrence of oxygen reduction on this electrode in phosphoric acid could not be established, since O_2 bubbling in the cell did not make any appreciable difference in the current density at constant potential.

The reason for this conspicuous lowering of the H_2 overvoltage in H_3PO_4 might be etching of the surface, which was observed on both titanates in acid. Figures 9 and 10 show the surface of the two electrodes after the measurements. The overvoltage decreases, therefore, might be due to production of a more active surface as well as an increase in real surface area due to etching.

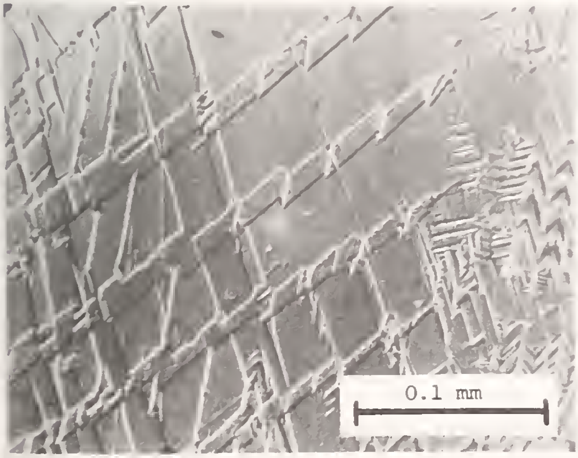

Fig. 9. Photomicrograph of a $La_{0.92}TiO_3$ electrode surface after measurements in H_3PO_4. Nomarski interference contrast.

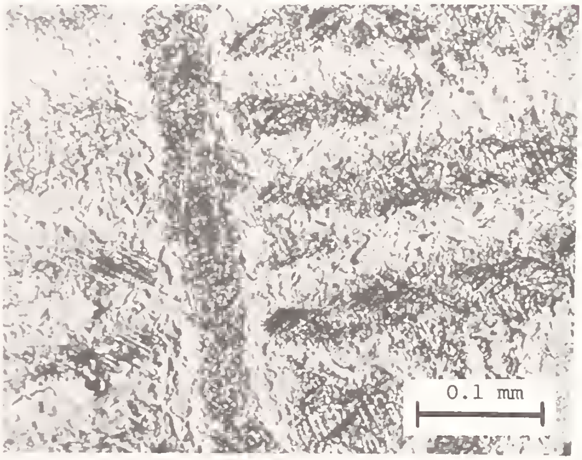

Fig. 10. Photomicrograph of a $La_{0.75}TiO_3$ electrode surface after measurements in H_3PO_4. Nomarski interference contrast.

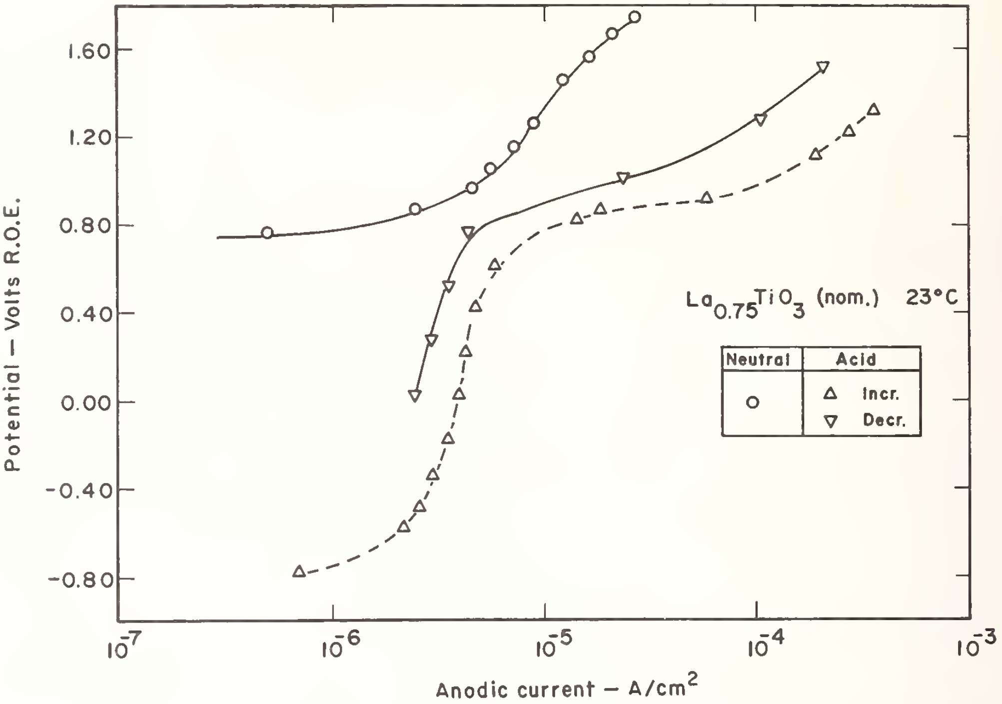

Fig. 11. Anodic current density-potential curves for $La_{0.75}TiO_3$ in acidic and neutral solution.

The attack seems to involve anodic dissolution: in figure 11 are some anodic current-potential curves, showing that in H_3PO_4 a non-negligible anodic current, of the order of several microamperes per square centimeter is recorded at potentials well below that necessary for oxygen evolution in the dark.

4. Discussion

The results presented here show that none of the materials tested in this work seem to be promising as electrodes for the electrochemical reduction of oxygen. The best performance was observed on Nb doped TiO_2, but it was only a current density of the order of 10^{-4} A/cm^2 for potentials less than 200 mV positive with respect to the RHE. It is true that in a practical fuel cell the higher operating temperature should decrease the kinetic hindrance, but during the course of this work it was observed that in acid electrolyte the electrocatalytic properties with respect to oxygen reduction were, if anything, worse than in neutral solution.

The problem of obtaining reproducible current-potential curves even in the absence of detectable surface attack, might be linked to inhomogeneities such as compositional changes (inferred, for instance, from variations in points to point light absorption properties) or voids and cracks, and point to the desirability to work with good single crystals of known orientation. The beneficial effect of cathodically polarizing the electrode for the subsequent oxygen reduction seems to indicate that on these materials, as is the case with Pt and Ir, oxygen adsorption is a hindrance for the oxygen reduction reaction [15,16]. The slow changes in current with time at constant potential, as well as the slow changes in the features of the potentiodynamic scans, show that any adsorption and desorption processes, if present, have long relaxation times.

The difficulty in reaching steady-state conditions, prevents an attempt to investigate the kinetics in greater detail. The slope of the semilogarithmic plots seem to change in a continuous fashion, or, at least, are broken into several segments. In general, the slopes are fairly high (200 to 300 mV/decade of current density) in all conditions, and this holds for O_2 reduction as well as H_2 evolution. This behavior, not dissimilar to that observed for O_2 reduction on noble metals, might be due to a potential dependent adsorption isotherm [17]. The exchange current densities obtained by extrapolation have to be considered only of orientative value: for H_2 evolution i_o should be less than 10^{-7} A/cm^2 and for O_2 reduction less than 10^{-10} A/cm^2 in the most favorable cases.

The effect of light in producing an anodic current on doped TiO_2, caused, presumably, by photoassisted oxygen evolution has been reported by several authors [5-10]. As a consequence of this fact, there is a potential range (see fig. 6) where illumination shifts the current from anodic to cathodic. However, it is interesting that light increases, however slightly, the cathodic current density for oxygen reduction at very negative potentials, as indicated in figure 5. In inert atmospheres, during H_2 evolution, light illumination, on the contrary causes a transient corresponding to a current decrease.

5. Acknowledgements

We should like to thank the Environmental Protection Agency for its partial support of this program; also A. D. Franklin, W. S. Horton and H. P. R. Frederikse, who provided much useful discussion. In particular, we would like to thank N. L. Loeffler of the University of Tennessee Space Institute who provided us with La_xTiO_3 samples and with much useful information.

6. References

[1] R. J. H. Voorhoeve, J. P. Remeika, P. E. Freeland and B. T. Matthias, Science 177 353 (1972).
[2] P. J. Boddy, D. Kahng, Y. S. Chen, Electrochem. Acta 13, 1311 (1968).
[3] A. E. Gillis, Advanced Development. In: Seventh Status Report on Fuel Cells, J. R. Huff (ed.) U. S. Army Mobility Equipment Research and Development Center, Ft. Belvoir, Va. Report 2039 NTIS No. AD-755 (1972).
[4] H. P. R. Frederikse, JAP Supplement, 32, 2211 (1961).
[5] A. Fujishima, K. Honda, S. Kikuchi, Kogyo Kagaku Zasshi, 72, 108 (1969).
[6] A. Fujishima, K. Honda, Nature, 238, 37 (1972).
[7] J. G. Mavroides, J. A. Kafalas, Lincoln Lab., MIT, Solid State Research, 2 (1974).
[8] M. S. Wrighton, D. S. Ginley, P. T. Wolezanski, A. B. Ellis, D. L. Morse, A. Linz, Proc. Nat. Acad. Sci. USA, 72, 739 (1975).
[9] K. L. Hardee, A. J. Bard, J. Electrochem. Soc. 122, 739 (1975).
[10] A. Fujishima, K. Kohayakawa, J. Electrochem. Soc. 122, 1487 (1975).
[11] J. W. Diggle, Oxides and Oxide Films, M. Dekker, Inc., N. Y. Vol. I (1972) and Vol. II (1973).
[12] N. L. Loeffler, University of Tennessee Space Institute, Private Communication.
[13] Crystals Grown by Flame Fusion Technique. Dopants Added to Starting Materials.
[14] M. Stern, A. C. Makrides, J. Electrochem. Soc. 107, 782 (1960).
[15] J. P. Hoare in "Encyclopedia of the Electrochemistry of the Elements", A. J. Bard, Editor, Chapter 4, p. 307. M. Dekker, N. Y. (1974).
[16] J. P. Hoare, J. Electrochemical Chem. 18, 251 (1968).
[17] A. J. Appleby, J. Electrochemical Chem. 27, 335, 364 (1970).

ELECTROCHEMISTRY AT SOLID ELECTROLYTE INTERFACES

National Bureau of Standards Special Publication 455, *Electrocatalysis on Non-Metallic Surfaces*, Proceedings of Workshop held at NBS, Gaithersburg, Md., December 9-12, 1975. (Issued November 1976)

Ionic Transport and Electronic Exchange at Solid Electrolyte Interfaces

M. W. Breiter and G. C. Farrington
General Electric Research and Development Center
P. O. Box 8
Schenectady, New York 12301

Interest in highly conductive solid electrolytes, compounds that display conductivities comparable to aqueous electrolytes at room temperature, is great because of their many potential applications. This paper reviews conduction mechanisms and charge transfer at solid electrolytes having fast ionic transport. For the discussion, solid electrolytes have been grouped into stoichiometric compounds, doped compounds and non-stoichiometric compounds; interfaces are classified as two-phase and multi-phase boundaries.

Key words: Charge transfer processes, conduction mechanisms, interfacial phenomena, solid electrolyte

1. Introduction

Solid compounds with greater ionic conductivities than electronic conductivities have long been known. [1][1] Usually, ionic mobility in such compounds is appreciable only at elevated temperatures. In recent years, new materials which in certain temperature ranges display ionic conductivities comparable to aqueous electrolytes at room temperature have been found. Interest in these solid electrolytes is great because of their potential application in fuel cells and batteries for the production and storage of electrical energy, in electrolyzers for the production of certain gases, and in sensors for monitoring gases or dissolved species in liquids.

Conduction mechanisms in highly conducting solid electrolytes have been extensively reviewed [2-5], but less information is available [4] on electrochemical processes occurring at interfaces where one boundary is established by the solid electrolyte. A previous review of this area was written by Raleigh [4]. The emphasis of the present paper is on conduction mechanisms and charge transfer processes at interfaces with solid electrolytes of fast ionic transport.

2. Characterization and Conduction Mechanisms of Solid Electrolytes

Solid electrolytes with fast ionic transport fall in three broad categories:

---

[1] Figures in brackets indicate the literature references at the end of this paper.

1. Stoichiometric compounds, for instance, AgI
2. Doped structures, like calcia stabilized zirconia.
3. Non-stoichiometric compounds, such as beta alumina.

Ionic conductivities of examples for each class are plotted versus reciprocal temperature in figure 1. For comparison, the conductivity of a "regular" ionic conductor, LiF, is also shown.

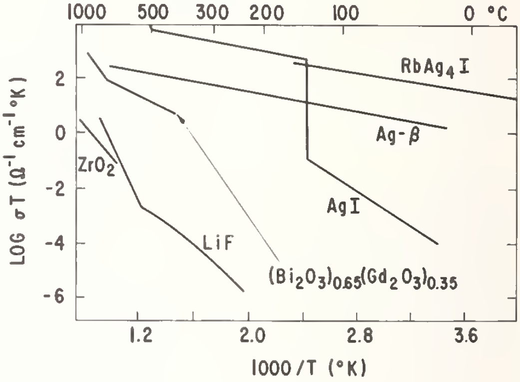

Fig. 1. Plots of the product of conductivity and absolute temperature, T, versus temperature for different solid electrolytes.

The shape and region of high conductivity of each curve in figure 1 reflect its underlying mechanism of conduction. The curve for LiF, for example, consists of two parts. Ionic conductivity is appreciable only within several hundred degrees of the melting point and results from thermal generation of current-carrying defects in the crystal lattice. At temperatures below the point where the concentration of thermally generated defects is comparable to the impurity concentration, conduction is dominated by fixed impurities.

The curves for ionic conductors of class 1 consist of two parts separated by a sharp transition region in which a phase change occurs. Relatively large conductivity is observed above the transition region and normal, thermally induced conductivity in the lower temperature phase. In the high conductivity phase, a large number of interstitial sites is provided for the small cations in the rigid anion structure. The cations may be considered to be in a molten state, migrating through the fixed anion sublattice in a disordered fashion. In contrast, the phase below the transition temperature is cation-ordered.

Compounds of class 2 are mixtures of oxides and display large oxygen ion mobilities at high temperatures. Doping of a suitable oxide with another oxide in which the cation has a lower valency leads to formation of a cubic phase with a large anion vacancy concentration. The extent of doping is considerable. Calcia stabilized zirconia is a classic example for group 2. The conductivity of a class 2 conductor is largest at one particular doping level, for instance, at about 12 mole % CaO for calcia stabilized zirconia. Usually this doping level is not identical with the maximum miscibility of the two oxides. A detailed understanding of conductivity in compounds of class 2 is complicated by problems of metastability and partial ordering.[6]

Sodium beta alumina, formulated as $(1+x)Na_2O \cdot 9Al_2O_3$, is the best known example of a class 3 compound. The normal beta-phase contains 15-30 percent excess sodium ions which are compensated either by aluminum vacancies or oxygen interstitials. All the sodium ions are located in planes perpendicular to the c-axis which are separated by four oxygen-aluminum planes. Rapid ion migration occurring in these planes is two dimensional, in contrast to three dimensional conductivity in compounds of class 1. As shown in figure 2, there are three sites, d, b, and MO available for Na^+ ions in the conducting

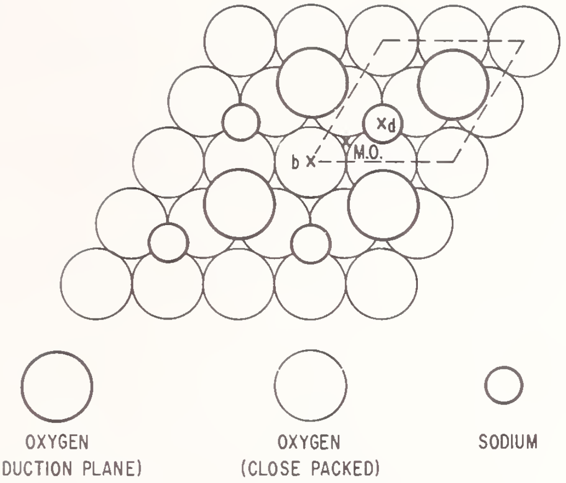

Fig. 2. Ionic arrangement in conduction plane of sodium beta alumina.

plane. The distribution of the Na^+ ions among the sites changes with their concentration and temperature, becoming more uniform with increasing temperature.

Sodium beta" alumina differs somewhat in composition from sodium beta alumina and contains a Na^+ ion excess of about 50 percent. These ions reside in nearly equivalent sites. The beta" phase has higher conductivity, 0.3 Ω^{-1} cm^{-1} vs. 1.2 $\Omega^{-1}cm^{-1}$ at 300°C [7], in comparison to beta alumina.

The preceding discussions of conduction mechanism are strictly valid only for ideally pure single crystals. Additional effects, especially grain boundary resistance, must be considered for polycrystalline samples of classes 2 and 3. Grain boundary resistivity is not significant for class 1 compounds in which appreciable conduction is only found at temperatures one to several hundred degrees below their melting points where single crystal and polycrystalline specimens display identical behavior. In fact, grain boundary resistivity may actually be smaller [4] than bulk resistivity for some class 1 compounds.

Grain boundary impedance has been measured for stabilized zirconia [8,9] and sodium beta alumina. [10,11] The frequency dependence of the impedance was analyzed to separate bulk resistivity, grain boundary resistivity and electrode polarization. Figure 3 shows results obtained with $(Sc_2O_3)_{0.1}(ZrO_2)_{0.9}$ between 550° and 571°C. The ratio between grain boundary resistivity, R_b, and

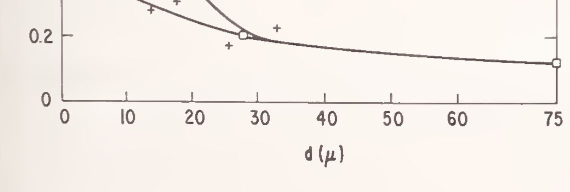

Fig. 3. Ratio of grain boundary resittivity to crystal resistivity as function of the average grain size for two different samples of stablized zirconia.

that of the crystal interior, R_c, is plotted as a function of average grain size for two specimens sintered at different temperatures. The relative contribution of grain boundary resistance increases as the grain size decreases and the number of grain boundaries becomes larger. The ratio R_b/R_c is still < 1 at the smallest grain size for $(Sc_2O_3)_{0.1}(ZrO_2)_{0.9}$. As demonstrated [10] for Na^+ beta alumina specimens containing small amounts of additives, R_b/R_c also depends upon temperature because the two conduction processes have different activation energies. More recent results for beta alumina will be discussed later. Other factors affecting solid electrolyte impedance have been discussed in reference 12.

3. Characterization of Interfaces

Interfaces between a solid electrolyte and other compounds may be separated into two classes:

1. Two-phase boundaries

2. Multi-phase boundaries

Class 1 represents the simplest case of direct contact between a solid electrolyte and another compound. Two-phase boundaries may be further subdivided:

- Interfaces with blocking electrodes

- Interfaces with non-blocking electrodes

    a. Electrode reversible to conducting ion

    b. Electrode not reversible to conducting ion

- Interfaces between solid electrolytes and other electrolytes.

Multi-phase interfaces, at which at least two additional phases contact a solid electrolyte within the same area, are more difficult to classify. The simplest case is a three-phase boundary between a solid electrolyte, an electronic conductor, and a third phase which is either a liquid or gas.

Although individual interface behavior is discussed, experimental interfacial studies require at least two interfaces. To isolate the behavior of one particular interface, the cell must be constructed to eliminate effects of the secondary interface on an experimental or theoretical basis. As with aqueous systems, the simplest approach is to minimize the contributions of the secondary interface compared to those of the interface under study.

Practical preparation of interfaces of type 1 and 2 involves numerous considerations. The reader is referred to the excellent discussion of this subject by Raleigh in chapter IIIA of reference 4.

If inert electronic conductors are employed as contacts, the potential range of study may be chosen so that faradaic reactions do not occur. The electronic conductor then behaves as an ideally polarizable electrode. Many examples can be found in the literature in which Pt or Au/ionic crystal interfaces are used in studying ionic mobility and intrinsic polarization effects within crystals. In many, the electrode contacts are only assumed to act as blocking electrodes even though this point is crucial to successful interpretation of results.

But, blocking behavior cannot be assumed without proof. Charge transfer reactions may no more be absent at an interface such as Pt/beta alumina merely because of the unlikely role of Pt as parent of ions injectible into beta alumina than at a Pt/non-aqueous electrolyte or Pt/aqueous electrolyte interface at which Pt is an equally unlikely source of ions. A Pt/electrolyte interface can, of course, approximate an ideally polarized electrode; but, regardless of the electrode composition or physical state, that behavior must be established experimentally, taking into consideration such factors as the decomposition potential of the electrode and the electrolyte, and the presence of tertiary substances capable of redox behavior at the electrode. Only then can the electrical response of the electrolyte be interpreted on the basis of models assuming blocking behavior.

In theory, a Pt/beta alumina interface or its equivalent should approximate an ideally polarizable electrode over a wide potential range in the absence of species capable of bringing about charge transfer such as adsorbed H_2O or H_2. Beyond this, the range of ideal polarizability is limited by decomposition of the beta alumina, which involves Na^+ reduction at one potential extreme and O^{--} oxidation at the other. This represents a range of ideal behavior much wider than typical liquid electrolyte systems. To date, no detailed experimental exploration of blocking electrode/beta alumina interfaces has appeared.

General models for the AC behavior of solid electrolyte interfaces have been developed for different conditions by Macdonald. [13,14] Simple models for interfaces with blocking electrodes without specific ion adsorption, for interfaces with blocking electrodes with specific ion adsorption, and for interfaces with non-blocking electrodes were proposed by Armstrong [15]. The models refer to solid electrolytes of class 1 or class 3 with high cation conductivity. The solids are assumed to consist of cations which are all equivalent and all mobile and of immobile anions. Because of their large mobile ion concentrations, diffuse double layer contributions at such solid electrolyte interfaces are considered negligible. This is a generalization of a concept proposed previously by Hull and Pilla [16] for the graphite/silver iodide system. Only the concentration of cations in the first layer differs from that of the bulk, resulting in a compact double layer. The situation is similar to that in concentrated aqueous solutions where the diffuse double layer is negligible in comparison to the Helmholtz layer.

Analogue circuits [15] describing some of the main features of solid electrolyte/electrode interfaces are shown in figure 4a and 4b. Both circuits consist of two separate circuits in series, reflecting the interfacial impedance and the impedance of the solid electrolyte between the interface and measurement probe. If the frequency is below ca. 100 kHz, the capacitance, C_{El}, of the solid electrolyte is negligible. The circuit for an interface with blocking electrodes (fig. 4a), then, simplifies to a series circuit of double layer capacity C_d and electrolyte resistance R_{El} if specific adsorption of ions, represented by C_{ad} and R_{ad}, and the Warburg impedance, W, are absent. According to Armstrong [15], the Warburg impedance only exists at blocking interfaces if two mobile cations are present, one in excess of the other. In the circuit for non-blocking electrodes (fig. 4b),

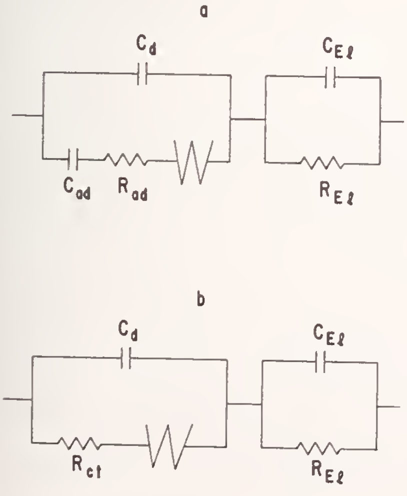

Fig. 4. Analogue circuits for the interface electrode/solid electrolyte:

a. for blocking electrode
b. for non-blocking electrode

R_{ct} represents the charge transfer resistance. It contains no Warburg component if only the reaction $M \rightleftarrows M^+ + e^-$ with one cation occurs. The possibility of an adsorbed intermediate leads [15] to introduction of R_{ad} and C_{ad} into figure 4b. The applicability of these interfacial models and their respective analogue circuits will be discussed on the basis of experimental results for different interfaces in subsequent chapters.

4. Electrochemical Processes at Interfaces with Stoichiometric Compounds (Class 1)

Interface studies with stoichiometric compounds may be grouped into two broad categories

- electronic conductor/solid electrolyte
- aqueous electrolyte/solid electrolyte

Investigations of the second category are less common because of the problem of solid electrolyte dissolution in water.

4.1. Studies of Electronic Conductor/Solid Electrolyte Interfaces

The transient behavior of graphite/AgI and Pt/AgI interfaces was investigated by Hull and Pilla [16] in cells of the type Ag/AgI/M at room temperature. Cells were assembled by pressing the powdered constituents together with 40,000 psi into pellets. A small silver wire was embedded in each solid electrolyte as a reference electrode. Ohmic potential drop inside the solid electrolyte was electronically compensated.

Interfacial behavior during a voltage sweep of 5 mV/sec., starting at 0.46 V vs. Ag/AgI, is represented in figure 5. No appreciable Faradaic current is observed to flow across the graphite/AgI interface until a potential of about -0.03 V is reached during the cathodic sweep. Silver deposition commences abruptly at this point. After sweep reversal, silver deposition occurs at lower potentials than during the preceding cathodic sweep. This implies that silver is more easily plated on silver islands than on free graphite sites. Removal of the silver deposit occurs in the broad anodic peak between 0 and 0.2V. Contrasting behavior occurs at a Pt/AgI interface. Silver is continuously plated out during the cathodic sweep, starting with the formation of a monolayer at underpotentials as in aqueous solutions.

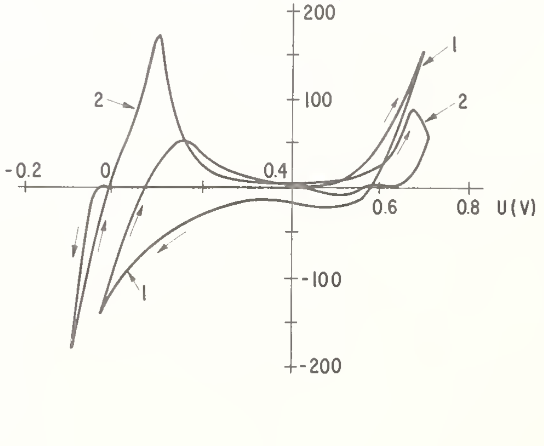

Fig. 5. Current-potential curves, measured at 5 mV/s in the cell of the type Ag/AgI/M at room temperature: curve 1, S=2 (platinum), curve 2, S = 1 (graphite).

Iodine is produced at about 0.5V for graphite and 0.46V for platinum during the anodic sweep. Graphite and platinum display similar electrocatalytic behavior as in aqueous solutions.

Both voltage sweep and galvanostatic studies have demonstrated that graphite/AgI approximates an ideally polarized electrode between 0.5V and 0.35V. Such a potential range does not exist for platinum. This behavior is very similar to that of graphite/silver bromide and platinum/silver bromide interfaces at higher temperature (244° - 292°C). A more detailed study of halogen discharge on graphite electrodes from three different halide solid electrolytes was recently reported by Raleigh. [17]

Detailed studies of the kinetics of Faradaic interfacial processes have been carried out for Ag/Ag_3SI [18,20] and Ag/Ag_4RbI_5 [21,25]. Anodic current-voltage curves [18] of Ag in the cell $Ag/Ag_3SI/(C)I_2$ at 25°C and 45°C are shown in figure 6. Although these curves and similar cathodic current-potential curves in reference 19 have shapes usually found when diffusion is rate-determining, analysis under this assumption leads [18] to incorrect values of the diffusion layer thickness. The interpretation that homogeneous reaction between interstitial silver ions, ion vacancies, and ions in regular lattice positions is rate-determining yields a theoretical expression [18] which adequately describes the experimental results over about a decade of current density. But the sharp increase of potential with current density in figure 6 must be explained [18] by an additional process, namely precipitation of a substance of lower conductivity, such as AgI, at higher currents. Since linear plots of current density versus potential are not given in reference 18, it is difficult to decide if, as suggested [18], the sharp current increase represents transition to a limiting current.

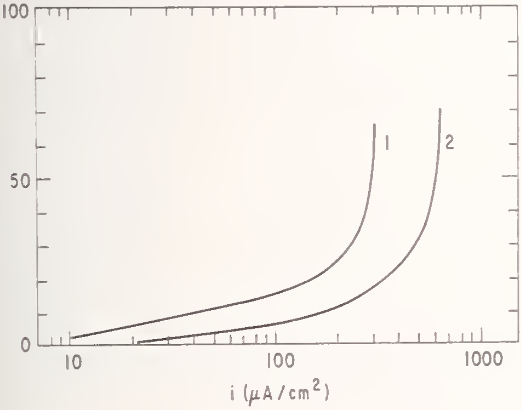

Fig. 6. Anodic current-potential curves, measured at two temperatures in the cell $Ag/Ag_3SI/C,I_2$.

Interfacial polarization is eliminated [18] by amalgamation of the silver electrode. It was proposed [22] that this implies a heterogeneous rather than homogeneous reaction is rate-determining. Further results [19,20] are free of this objection, but lead to similar conclusions as reference 18. Other interpretations for the behavior of amalgamated silver electrodes must be found.

A linear plot of overvoltage versus current density revealed the existence of a limiting current during cathodic deposition of silver onto silver in the cell $Ag/Ag_3SI/Ag$. The interpretation [17] that the rate-determining step is transition of silver ions from regular lattice positions to interstitial positions leads to an adequate theoretical description of the observed phenomena.

Impedance measurements [20] of the interface Ag/Ag_3SI between 100 Hz and 100,000 Hz in a three-electrode cell without polarization and at -0.046 V led to a Warburg-type frequency dependence of the Faradaic impedance components, R_s and $1/\omega C_s$, in a series circuit after correction for ohmic potential drop inside the solid electrolyte and for double layer capacity. The latter value was determined experimentally according to the procedure in reference 26. R_s vs. $\omega^{-1/2}$ goes through zero and $1/\omega C_s$ vs. $\omega^{-1/2}$ intersects the ordinate as a positive value corresponding to about 100 $\mu F/cm^2$. This is attributed to an adsorption capacity. It was proposed [20] that the rate-determining transition [19] of an ion from a regular lattice position to an interstitial position is so slow that it does not affect the impedance in the given frequency range.

Two conclusions may be drawn from the results with Ag_3SI:

a. The assumptions made [15] in modeling interfaces between solid electrolytes and non-blocking electrodes are inadequate in this case.

b. The charge transfer step is rapid.

The first conclusion is based on results from DC and AC studies, the second conclusion on AC measurements.

The anodic behavior of the interface, Ag/Ag_4RbI_5, was studied [21,22] in the cell, $Ag/Ag_4RbI_5/Ag$, with a silver reference electrode. Figure 7 shows current-potential curves at 0°C and 25°C. The IR drop is eliminated. At small current densities, a Tafel line with a slope of 20 mV is found. A second Tafel line with a slope of about 110 mV appears to occur [21,22] at larger currents at 25°C. However, the strong temperature dependence of this second region, the gradual increase [21] of overvoltage with time, and the curvature of the Tafel plot [22] raise serious doubts to the conclusions [22] that either ion-transfer or surface diffusion of adatoms is rate-determining there. Impedance measurements [23,25] of the Ag/Ag_4RbI_5 interface also lead to ambiguous conclusions.

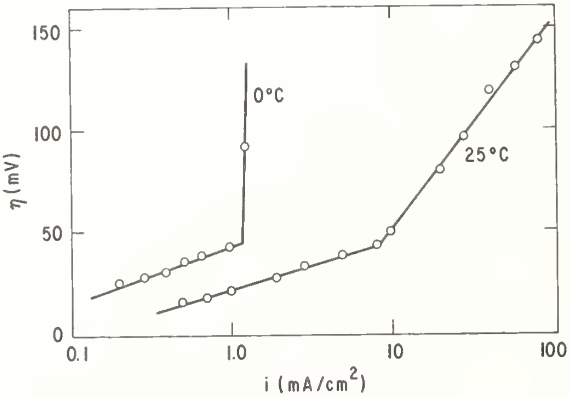

Fig. 7. Anodic current-potential curves, measured at two temperatures in the cell $Ag/Ag_4RbI_5/Ag$.

Since the analogue circuits contain more than two elements, different circuits [23,25] allow the same degree of approximation to the experimental results. In general, the large number of parameters determined from experimental data in the description of an electrode/solid electrolyte interface by analogue circuits poses serious difficulties for reliable interpretation.

4.2 Studies of Solid Electrolyte/Aqueous Electrolyte Interfaces

Solid electrolyte/liquid electrolyte interfaces in the system $Ag_3SI/AgNO_3+KNO_3$ have been studied at room temperature by DC [27,28] and AC measurements [29]. The contributions of current lead contacts to Ag_3SI were minimized by a special cell construction [27]. The potential drop across the interface, measured against a calomel electrode, varied [27] with silver ion activity in a Nernstian relationship. Cathodic polarization curves of silver deposition displayed limiting current behavior identical [28] for rotating discs of Ag_3SI and of Ag. Mass transport of ions in the liquid solution is rate-determining. If the electronic conductivity of Ag_3SI is sufficiently small, silver ions migrate into interstitial lattice positions. If not, silver deposition occurs on the solid electrolyte surface in a parallel reaction.

In contrast to the cathodic process, transfer [28] of silver ions from the solid electrolyte into the liquid electrolyte requires a larger overvoltage than the comparable anodic process on silver metal (see fig. 8). The current-potential curves do not depend upon rotation speed and silver ion concentration in the liquid electrolyte. Above 4 mA/cm^2, the anodic current-potential curves become Tafel lines, $\eta = a + b \log i$, with b equal to 0.38 V for Ag_3SI and 0.28 V for Ag. It was suggested [27] that transfer of ions from interstitial positions into the liquid electrolyte is not rate-determining but that supply of silver ions to the interface in Ag_3SI is slow.

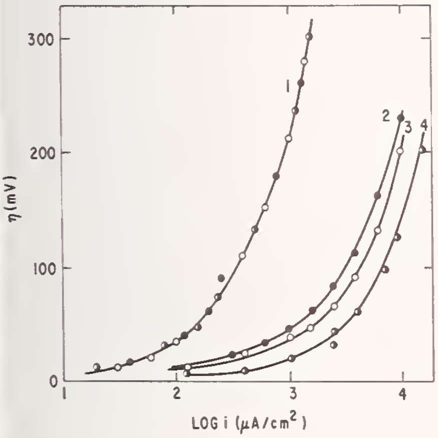

Fig. 8. Dependence of rate of silver ion transfer from Ag_3SI (curve 1) and Ag (curves 2 to 4) into liquid electrolyte upon electrode potential at rotating disc electrode: ● 0.01 M $AgNO_3$ + 0.09 M KNO_3, 0 rotations/min; ◑ 0.05 M $AgNO_3$ + 0.09 M KNO_3, 60 rotations/min; o 0.05 M $AgNO_3$ + 0.09 M KNO_3, 100 rotations/min.

Further experiments examined the capacity of the interface, $Ag_4SI/AgNO_3$+ KNO_3, and found it much smaller than that of the interface, $Ag/AgNO_3$ + KNO_3, at 100 kHz. It was concluded []9] that the double layer capacity is determined by the double layer inside the solid electrolyte. Cathodic polarization decreased the double layer capacity of an $Ag_4SI/AgNO_3$ + KNO_3 interface and anodic polarization increased it. These results were attributed to a change of the space charge inside the solid electrolyte. The effective thickness of the space charge layer becomes smaller by the introduction of more interstitial silver ions under cathodic polarization. The reverse is true for anodic polarization.

Studies [27,29] of solid electrolyte/liquid electrolyte interfaces are not in agreement with the predictions of the models. [15]

5. Electrochemical Processes at Interfaces with Doped Compounds

Although many investigations of two-phase boundaries have been carried out with electrolytes of classes 1 and 3, few have appeared for doped compounds of class 2. The primary reason is that interest in multi-phase boundaries has been greater with doped compounds because of their potential use as oxide ion conductors in such devices as high temperature fuel cells.

The simplest use of multi-phase interfaces with doped conductors is in potentiometric study of oxide ion activity. For example, the cell, Pt/Fe, FeO/$(ZrO_2)_{0.85}(CaO)_{0.15}$/Ni,NiO/Pt, has been used to determine the free energy of formation of NiO. [30] Similar cells have been used as current sources in coulometric titrations [31,32] and in oxygen transfer studies. [33,34] The mixture of metal and oxide serves both as an electronically conducting contact and as an oxide ion reservoir. The interface is of the multi-phase type. In a coulometric titration, oxide ion depletion at the negative interface is compensated by metal ion reduction.

The three-phase interface which has received major attention in fuel cell research is the combination of an oxide ion conductor, electrocatalyst, and molecular oxygen. As with analogous three phase boundaries in aqueous electrolytes, the electrocatalyst strongly influences interfacial behavior.

Current-voltage curves obtained [36] for a Pt/$(ZrO_2)_{0.9}(CaO)_{0.1}$/Pt cell at 1000°C are replotted in figure 9. The electrodes were adherent, porous, fine-grained platinum deposits on both sides of closed, stabilized zirconia tubes. The inner electrode was exposed only to pure oxygen gas and served as both counter and reference electrode. The composition of the gas mixture at the outer platinum electrode was varied. Current-voltage curves remained linear up to 250 mA/cm^2 at 1000° and the DC resistance taken from the slope of the i-U curve was equal to the AC resistance, determined separately when both electrodes were exposed to pure oxygen. Polarization effects were absent under these conditions implying that the inner electrode could be used as a reference electrode. The influence of the oxygen partial pressure on oxygen evolution is negligible up to 0.58% O_2. In contrast, oxygen reduction is accompanied by considerable polarization in argon-oxygen mixtures dilute in oxygen. The shapes of the cathodic i-U curves in figure 9 indicate that a limiting current which depends upon the oxygen content is reached. A more detailed study reveals [37,38] that the appearance of the limiting current becomes less pronounced and desappears when the required potential approaches and surpasses 2V, e.g., at relatively high ohmic resistance of the electrolyte. At currents above the limiting current, an additional process of direct exchange between the electrode and the electrolyte occurs, [37,38] leading to electronic conductivity. The electrolyte itself is reduced.

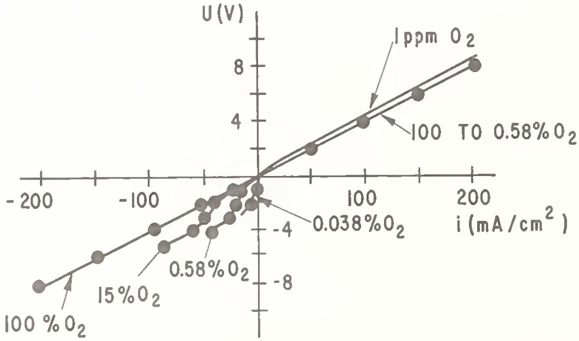

Fig. 9. Current-voltage characteristics for Pt/$(ZrO_2)_{0.9}(CaO)_{0.1}$/Pt at 1000 °C for different gas mixtures.

Since polarization effects are absent, mechanistic conclusions for the separate steps in the process of oxygen evolution cannot be drawn at present. Mass transport [36,39,40] in the gas phase at 1000°C, diffusion of oxygen atoms in the adsorbed phase [37] at 810°C, and diffusion through the platinum electrode [38,41] at 520° to 560°C have all been suggested as rate-determining steps for oxygen reduction at currents below the limiting current. These deductions are based on interpretation of DC measurements. It was pointed [42] out recently that a transition in the rate-determining step from oxygen diffusion through the platinum to mass transport in the pores, should occur as temperature, oxygen pressure, and porosity change. This may explain the discrepancy between various hypothesized rate-determining steps. It is clear that at high potentials either oxygen transfer [38,41] into the electrolyte or electronic conduction [38] within the electrolyte is controlling.

One kinetic step in the net reaction was postulated [8] as rate-determining on the basis of impedance masurements on Pt/$(ZrO_2)_{0.9}(Y_2O_3)_{0.1}$/Pt over a wide range of oxygen pressure between 400° and 800°C. The analogue circuit for interpreting the impedance data is that in figure 4b with the Warburg impedance taken as zero and a third ohmic resistance added in series. The components on the right side of the analogue circuit are proportional [8] to the length of the solid electrolyte and thus reflect [8,43] contributions from grain boundary and crystal impedance. The values of $1/C_d$ and R_{ct} are proportional [8] to the geometric surface area of the platinum electrode. They result from interfacial processes. The resistance, R_{ct}, increased by about a factor five at 400°C when the porous platinum electrode was replaced by a nonporous one. The latter result was attributed [8] to a diminished number of three-phase boundaries. Direct evidence for such an effect was previously given [44] by DC measurements. In general, R_{ct} became [8,43] very small at temperatures above 800°C. The latter result is in agreement with the conclusion [36,39,40] from DC measurements that mass transport in the gas phase, which is not reflected in the impedance, becomes rate-determining at 1000°C. It was suggested [8] on the basis of the dependence of R_{ct} upon oxygen pressure that the electronic transfer step between adsorbed oxygen atoms and oxygen ions or the dissociation step of molecular oxygen is rate-determining at the three-phase boundary. The latter interpretation which should hold for temperatures below 800°C is inconsistent with the conclusion from DC studies that diffusion of oxygen in the adsorbed phase [37] or through the platinum electrode [38,41] is the slowest step. However, recent AC studies [45,46] of the system indicate that the simple analogue circuit is not adequate and suggest [45] that the formation of a platinum oxide affects the impedance.

The behavior of the interface, metal/stabilized ZrO_2, was also investigated [47-49] in the presence of an inert gas in which the content of molecular oxygen had been reduced as far as experimentally feasible. Under this condition, solid platinum [48] or liquid silver [47,49] or liquid tin [48] approximate ideally polarizable electrodes. Since the resistance and capacity in a series circuit did not change [50] significantly with frequency above about 100 kHz, the capacity at 400 kHz was taken as the double layer capacity. Plots of this capacity versus potential, referred to a platinum electrode in air, had [48] parabolic shapes with sharp minima for liquid metals at 975°C. The double layer capacity curve with platinum was less symmetrical, [47] but also displayed a minimum. The minimum was attributed to the point of zero charge, assuming a space charge layer inside the stabilized zirconia. As expected, the capacity-potential curves became [49] wider with increasing yttria content, that is, increasing defect concentration. The described results [47-50] are not in agreement with a model for the interface in which only a compact double layer is considered.

6. Electrochemical Processes at Interfaces with Non-Stoichiometric Compounds

These studies fall in two groups:

- M/M^+-beta alumina
- M^+-beta alumina/liquid electrolyte

M/M^+-beta alumina represents a broad group of beta alumina interfaces in which M is the reduced form of the primary mobile ion within the beta alumina structure. M^+ can be Na^+, Li^+, K^+, Rb^+, Tl^+, or Ag^+ in beta alumina; only Na^+ has been reported to be mobile within beta" alumina.

Not all substituted beta aluminas are stable in contact with their parent alkali metals. For example, molten Li metal reduces [51] Na^+-beta alumina at 450°C. Na/beta alumina and Na/beta" alumina are believed to be stable at least to 400°C based on results of Na/S battery research. Ag and Tl should also be stable in contact with beta or beta" alumina.

The M^+-beta alumina/M^+-liquid electrolyte interface presents an unusual opportunity to study ionic transport between dissimilar electrolytes over a wide range of chemical conditions because of the chemical stability of beta alumina. M^+ can be any of the ions mobile within beta alumina such as Na^+, Li^+, K^+, Tl^+, or Ag^+. Only Na^+-beta alumina/Na^+ containing electrolyte has been discussed in detail in the literature.

6.1 Studies of M/M^+-Beta Alumina Interfaces

M/M^+-beta alumina approximates an ideally non-polarizable electrode. Deviation from ideality can arise from space charge effects within the solid electrolyte, which should be insignificant because of its high charge carrier concentration, and from transition and crystallization overpotentials. Transition overpotential, or energy required to bring about ionic transition from the solid electrolyte structure to the metallic electrode, should be the primary component of overpotential at a liquid metal/beta alumina interface. Crystallization overpotential may occur in addition to transition overpotential at a solid metal/solid electrolyte interface. Published work has so far only described charge transfer at Na/beta alumina and Na/beta" alumina interfaces.

Studies [52] of interfacial transport in symmetric cells of the type Na/beta" alumina/Na from 150-350°C at frequencies between 10^{-2} and 10^4 Hz revealed no evidence of charge transfer polarization on finely polished discs. In contrast, a marked effect of surface roughness on the impedance exists as expected from theoretical predictions [26] for aqueous systems. Wetting of beta alumina with sodium is also strongly affected by surface preparation. This agrees with the observation [53] that Na begins to wet monofrax beta alumina only above 300°C.

Significant interfacial polarization was observed [54] in a freshly prepared Na/beta alumina/Na cell with two probe conductivity measurements at 150°C from 1 to 140 mA/cm^2 using single crystal boules of beta alumina. No polarization was detected at 150°C after the cell was heated to 300°C for one hour. This appears to be another manifestation of Na wetting of beta alumina. No interfacial polarization could be observed above 150°C after wetting, but it was apparent at temperatures below 150°C, especially below 97°C, the melting point of Na. The experiments with solid Na appear to be the first AC examination of polarization at a solid Na/beta alumina interface. As expected, polarization increases with decreasing temperature.

Other Na/beta alumina interfacial data are sparse. Will [55], in examining the performance of the Hg(Na)/beta alumina/Br_2 battery, reported there is insignificant polarization at the liquid Hg(Na)/beta alumina interface. In contrast, polarization effects become noticeable [56] at temperatures below about 150°C in symmetrical cells of the type Hg(Na)/beta alumina/Hg(Na). Armand [57] briefly discussed the difficulties of preparing an oxide-free solid Na/beta" alumina interface and found at an imperfect Na/beta" alumina interface, held under compression, a current of approximately 0.1 mA/cm^{-2} can be drawn for an average time of 30 min. before contact is lost due to Na depletion. This corresponds to the removal of less than five monolayers of Na.

Whittingham and Huggins [58] studied the interfacial response of solid Ag/Monofrax beta alumina contacts prepared by painting the solid electrolyte with Ag resinate solution and annealing for 12 hours at 800°C. No frequency dependent impedance attributable to interfacial polarization was observed from 10^2 to 10^5 Hz at 25°C.

Liquid Na/beta alumina is the inverse of most electrochemical interfaces at which the electrode is solid and the electrolyte liquid. Just as meticulous electrode preparation is essential in a study of solid electrode/liquid electrolyte charge transfer kinetics, similar care must be applied to electrolyte preparation in solid electrolyte investigations. The few studies available show that the exchange current at a carefully prepared Na/beta or beta" alumina interface is very large above 150°C. Between 150°C and 97°C, interfacial polarization becomes apparent, although insufficient data are available to identify its origin. Below 97°C, polarization increases steadily as temperature decreases. Few data are available in this temperature range where effects of electrode depletion, poor electrode/electrolyte contact, and inhomogeneous current density should be most pronounced.

6.2 Studies of M^+-Beta Alumina/M^+-Liquid Electrolyte Interfaces

Na^+-beta alumina/Na^+ liquid electrolyte is a two-phase system with a single mobile ion common to each phase.

Kinetic considerations predict [59] that the i/U relationship between interfacial polarization, η, and current density, i, is

$$i = i_o\left[\exp \frac{\alpha zF\eta}{RT} - \exp \frac{-(1 - \alpha)zF\eta}{RT}\right] \qquad (1)$$

in which α is the transfer coefficient, i_o, the equilibrium exchange current density, and z the charge of the mobile ion.

The i/U relationship for Na^+ entry into and exit from beta alumina across a propylene carbonate interphase should be described by equation (1) in which ion exit from the solid electrolyte is considered a positive current occurring at a positive overpotential. This assumes that transport is hindered primarily by transition overpotential.

Voinov and Tannenberger [60] examined interfacial transport across a beta alumina/propylene carbonate + NaI + I_2 interface using a polycrystalline beta alumina tube which dipped halfway into and was halfway filled with the propylene carbonate solution. Four electrodes were used, one current-carrying electrode in each electrolyte compartment and two reference electrodes. One reference electrode was positioned halfway between the outer current carrying electrode and the beta alumina surface and the other was wrapped around the outside top of the tube and wetted with electrolyte solution. This electrode placement insured that only interfacial polarization from the outside interface was measured. It did not, however, eliminate ohmic polarization from bulk propylene carbonate resistivity. Current through the outer electrodes was stepped while monitoring the potential difference between the reference electrodes.

The results showed Na^+ exit from beta alumina into propylene carbonate to be a slow process with a high activation energy. Extended Na^+ injection into beta alumina was accompanied by steadily increasing interfacial polarization for both ion entry and exit. This was attributed to irreversible accumulation of H^+ ions in the beta alumina and a concurrent decrease in local conductivity. Since neither the beta alumina nor the propylene carbonate were specially dried, water was surely adsorbed at the interface and could serve as a source of H^+.

It is reasonable that a hydrogen ionic species can be injected into beta alumina from a water contaminated interface. The hypothesis that this is irreversible, however, is inconsistent with the mechanism which produces it. Any ion diffusing into the conduction plane in an electric field should diffuse out in a field of opposite polarity. H_3O^+ is also more likely to diffuse into the conduction plane in the presence of excess H_2O than H^+

because it is a larger ion and should have a larger diffusion coefficient within beta alumina.

These minor objections do not diminish the broader conclusion of Voinc and Tannenberger that water significantly influences beta alumina interfacial transport. Because of water's uncertain effect, the results reported do no reflect intrinsic polarization at a beta alumina/propylene carbonate interface.

Farrington [59,61] also studied Na$^+$ transport across a polycrystalline beta alumina/propylene carbonate interface. In his procedure, a polished disc of polycrystalline beta alumina, dried at 10^{-5} torr and 400°C for 24 hours, was held by silicone rubber gaskets between two chambers of a Teflon polymer electrolysis cell. The cell compartments were filled with a carefully dried solution of 0.01 M NaClO$_4$ + 0.10 M tetrabutylammonium tetrafluoborate in propylene carbonate. The apparatus incorporated four electrodes, an outer current-carrying pair of Pt foil, and an inner reference pair of Tl (Hg) dissolved in Au wire. One reference electrode dipped directly into the propylene carbonate near one disc face, and the other was inserted in a hole drilled into the beta alumina halfway between each face. Interfacial overpotential at the surface between the reference electrodes was separated from bulk propylene carbonate and beta alumina resistivity by a galvanostatic transient technique, which took advantage of the longer time constant (10^{-3} sec.) of interfacial polarization compared to bulk resistivity (10^{-5} sec.). Constant current maintained unidirectional ion flow to differentiate ion entry into the solid electrolyte from ion exit.

No interfacial polarization overpotential is apparent from 30 μA/cm^2 to 10^4 μA/cm^2 at 23°C for Na$^+$ transport across a propylene carbonate/beta alumina interface that has been scrupulously dried.

Interfacial polarization is apparent for Na$^+$ exit from polycrystalline beta alumina previously exposed to 100 percent relative humidity as figure 10 shows. In this plot, bulk iR drop has been subtracted. Overpotential follows a Tafel relationship for which the transition coefficient (α) is 0.24 at 23°C and 0.22 at 62°C and the exchange current (i_o) is 3.0×10^{-6} at 23°C and 2.4×10^{-5} A/cm^2 at 62°C.

Ion entry into beta alumina from propylene carbonate proceeds without observable interfacial overpotential across a carefully dried interface at current densities less than 10^3 μA/cm^2. Entry across a hydrated interface

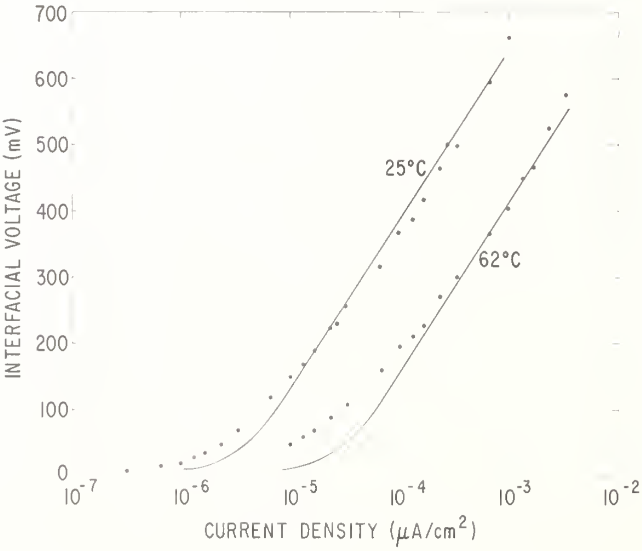

Fig. 10. Current voltage relationship for Na$^+$ exit from a hydrated beta alumina interface into 0.01 M Na$^+$ in propylene carbonate; (●) experimental; (—) calculated; at 25 °C, α = 0.24, i = 3.0×10^{-6} A/cm^2; at 62 °C, α = 0.22, i_o = 2.4×10^{-5} A/cm^2.

should follow the same Tafel relationship that describes ion exit under identical conditions. But, as ions are injected, large increases in interfacial voltage drop occur, the same phenomenon observed by Voinov and Tannenberger [60]. The increased resistivity can be reversed by extended electrolysis of ions out of the interface. H_3O^+ injection into the beta alumina is a reasonable explanation for the phenomenon.

Farrington's work suggests that Na^+ ion transport across a beta alumina/propylene carbonate interface occurs through an adsorbed intermediate state in which the ion is neither within the beta alumina conduction plane nor solvated in the liquid electrolyte. At 1310 μA/cm² interfacial overpotential remains unchanged when 9 coulombs of Na^+ passed out of the interface. However, at 3290 μA/cm² a steep voltage transition occurs after only two coulombs have passed. This increase is repeatable, initial behavior being restored at zero current. As the interface is increasingly hydrated, the height of the transition and the current density above which it occurs decrease.

These data are consistent with the transport mechanism shown in Eqn. 2 According to this

$$Na^+_\beta \rightleftarrows Na^+_{ads} \rightleftarrows Na^+_{pc} \qquad (2)$$

mechanism, interfacial transport is primarily influenced by species which compete with Na^+ for surface adsorption sites, of which water is one, or influence the rate of Na^+ adsorption and desorption. Although the results reported were for Na^+ transport, similar behavior can be expected with other ions mobile within beta alumina such as Ag^+, Li^+, and K^+.

The work summarized here clearly indicates that Na^+ beta alumina/propylene carbonate interfacial transport can be described in low current densities by a Tafel relationship. This implies that the space charge region within beta alumina at the interface is insignificant. However, the Tafel relationship has been experimentally seen only at interfaces first exposed to water vapor. Similar Tafel polarization surely occurs at a dry interface, but its magnitude is small in comparison to the voltage drop arising from current flow through the beta alumina and propylene carbonate and is, therefore, not detected.

6.3 Studies of Multi-Phase Interfaces

The interface between Na^+-beta alumina and sulfur or a mixture of sulfur and polysulfides, contained in a carbon fiber matrix, is the well known example of a multi-phase boundary in the sodium-sulfur battery. This cell operates at temperatures between 300°C and 350°C. Measurements of the cell voltage as a function of the cell current revealed [62] an ohmic relation between these two parameters, independent of the state of charge and of the rechargeability of the cell. These results and impedance measurements [63] lead to the conclusion that a hindrance of kinetic steps at the said interface does not exist at current densities of up to 100 mA/cm², referred to the geometric area of the beta alumina tube. Electrochemical processes involving the sulfur electrode are responsible for the behavior of the cell impedance towards the end of the discharge or charge cycle.

Acknowledgement

The support of the work on interfacial phenomena in sodium-sulfur cells by EPRI is acknowledged.

References

[1] See R. T. Foley, J. Electrochem Soc., 116, 13C (1969).

[2] D. O. Raleigh, Progress in Solid State Chemistry, H. Reiss, ed., Pergamon Press, New York, 1967, Vol. 3, Chap. 3.

[3] M. J. Rice and W. L. Roth, J. Solid State Chem., 4, 294 (1972).

[4] D. O. Raleigh, J Electroanalyt Chem, Vol. 6, A. J. Bard, ed., Marcel Dekker, New York, 1973.

[5] M. S. Whittingham, Electrochim. Acta, 20, 575 (1975).

[6] R. E. Carter and W. L. Roth, Electromotive Force Measurements in High-Temperature Systems, C. B. Alock, ed., Institution of Mining and Metallurgy, London, 1968.

[7] First Quarterly Report [1 July 73-30 Sept. 73] for NSF Contract NS-C805, submitted Oct. 73 by Ford Motor Co.

[8] J. E. Bauerle, J. Phys. and Chem. Solids, 30, 2657 (1969).

[9] M. V. Inozemtsev, M. V. Perfilev, and A. S. Lipilin, Elektrokhim., 10, 1471 (1974).

[10] R. W. Powers and S. P. Mitoff, J. Electrochem. Soc., 122, 226 (1975).

[11] G. C. Farrington, J. Electrochem. Soc., 121, 1314 (1974).

[12] R. D. Armstrong, T. Dickinson, and P. M. Willis, J. Electroanalyt. Chem., 53, 389 (1974).

[13] J. R. Macdonald, J. Chem. Phys., 58, 4982 (1973).

[14] J. R. Macdonald, J. Electroanalyt. Chem., 53, 1 (1974).

[15] R. D. Armstrong, J. Electroanalyt. Chem., 52, 413 (1974).

[16] M. N. Hull and A. A. Pilla, J. Electrochem. Soc., 118, 72 (1971).

[17] D. O. Raleigh, J. Appl. Electrochem., 5, 55 (1975).

[18] T. Takahashi and O. Yamamoto, Electrochim. Acta, 11, 911 (1966).

[19] S. V. Karpachev, Yu M. Ovchinikov, and L. D. Yushina, Elektrokhim., 8, 788 (1972).

[20] L. D. Yushina, S. V. Karpachev, and Yu S. Fedyaev, Elektrokhim., 8, 788 (1972).

[21] T. Takahashi and O. Yamamoto, J. Electrochem. Soc., 117, 1 (1970).

[22] R. D. Armstrong, T. Dickinson, H. R. Thirsk and R. Whitfield, J. Electroanalyt. Chem., 29, 301 (1971).

[23] R. D. Armstrong, T. Dickinson, and R. Whitfield, J. Electroanalyt. Chem., 39, 257 (1972).

[24] B. Scrosati and A. D. Butherus, J. Electrochem. Soc., 119, 128 (1972).

[25] N. G. Bukun and A. M. Mikhailova, Elektrokhim., 9, 1872 (1973).

[26] R. DeLevie, Electrochim. Acta., 10, 395 (1965).

[27] Yu V. Shirokov, V. S. Borovkov, P. D. Lukovtsev, *Elektrokhim.*, 5, 1211 (1969).

[28] Yu V. Shirokov, P. D. Lukovtsev, V. S. Borovkov, *Elektrokhim.*, 7, 575 (1971).

[29] Yu V. Shirokov, P. D. Lukovtsev, V. S. Borovkov, *Electrokhim.*, 7, 393, (1971).

[30] K. Kiukkola and C. Wagner, *J. Electrochem. Soc.*, 104, 379 (1957).

[31] C. B. Alcock and T. N. Belford, *Trans. Faraday Soc.*, 60, 822 (1964).

[32] T. N. Belford and C. B. Alcock, *Trans. Faraday Soc.*, 61, 433 (1965).

[33] W. L. Worrell and J. L. Iskoe, *Fast Ion Transport in Solids*, W. van Gool, ed., North-Holland, Amsterdam, 1973, p. 513.

[34] L. F. Donaghey and R. Pong, *J. Electrochem. Soc.*, 121, 506 (1974).

[35] H. H. Mobius and B. Rohland, *Z. Chem. Lpz.*, 4, 158 (1966).

[36] T. H. Etsell and S. N. Flengas, *J. Electrochem. Soc.*, 118, 1890 (1971).

[37] M. Kleitz, J. Besson and C. Deportes, *Rev. Energ. Primaire*, 2, 35 (1966).

[38] R. J. Brook, W. L. Pelzmann and F. A. Kroger, *J. Electrochem.,Soc.*, 118, 185 (1971).

[39] S. V. Karpachev and Yu M. Ovchinnikov, *Elektrokhim.*, 5, 200 (1969).

[40] C. S. Tedmon, Jr., H. S. Spacil, and S. P. Mitoff, *J. Electrochem. Soc*, 116, 1170 (1969).

[41] H. Yanagida, R. J. Brook, and F. A. Kroger, *J. Electrochem. Soc.*, 117, 593 (1970).

[42] F. A. Kroger, *J. Electrochem. Soc.*, 120, 75 (1973).

[43] See also M. V. Perfilyev, *Elektrokhim.*, 7, 792 (1971).

[44] S. V. Karpachev and A. T. Filiayev, *Elektrokhim.*, 2, 1330 (1966).

[45] E. Schouler, M. Kleitz and C. Deportes, *J. Chim. Phys.*, 70, 923 (1973).

[46] E. Schouler and M. Kleitz, *J. Electroanalyt. Chem.*, 64, 135 (1975).

[47] S. V. Karpachev and A. T. Filiayev, *Elektrokhim.*, 2, 617 (1966).

[48] A. T. Filiayev, I. D. Remez and S. V. Karpachev, 7, 257 (1972).

[49] I. D. Remez, S. V. Karpachev, L. M. Solov'eva, V. N. Chebotin, and A. T. Filyaev, *Elektrokhim.*, 11, 292 (1975).

[50] A. T. Filiayev, S. V. Karpachev and I. D. Remez, *Elektrokhim.*, 6, 283 (1970).

[51] G. C. Farrington and W. L. Roth, unpublished.

[52] R. D. Armstrong, T. Dickinson, and J. Turner, *J. Electroanalyt. Chem.*, 44, 157, (1973).

[53] A. Imai and M. Harata, Jap. J. Appl. Phys., 11, 180 (1972).

[54] W. L. Fiedler, H. E. Kautz, J. S. Fordyce, and J. Singer, J. Electrochem Soc., 122, 528 (1975).

[55] F. G. Will and S. P. Mitoff, J. Electrochem. Soc., 122, 457 (1975).

[56] R. D. Armstrong, T. Dickinson, and J. Turner, J. Electrochem. Soc., 118, 1135 (1971).

[57] M. B. Armand, Fast Ion Transport in Solids, W. vanGool, ed., American Elsevier, New York, (1973), p. 670.

[58] M. S. Whittingham and R. A. Huggins, J. Electrochem. Soc., 118, 1 (1971).

[59] G. C. Farrington, Report No. 75CRD193, GE CR&D, Schenectady, New York, (1975); J. Electrochem. Soc., in press.

[60] M. Voinov and H. Tannenberger, Electrochim. Acta., 19, 959 (1974).

[61] G. C. Farrington, Report No. 75CRD146, GE CR&D, Schenectady, New York (1975); J. Electroanalyt. Chem. submitted for publication.

[62] Sodium-Sulfur Battery Development for Bulk Energy Storage, EPRI 128-2, Interim Report, September 1975.

[63] M. W. Breiter, Proc. 4th Australian Electrochem. Conf., in print.

National Bureau of Standards Special Publication 455, *Electrocatalysis on Non-Metallic Surfaces*,
Proceedings of Workshop held at NBS, Gaithersburg, Md., December 9-12, 1975. (Issued November 1976)

Influence of Water on Beta Alumina Interfacial Ion Transport

Gregory C. Farrington
General Electric Research and Development Center
P. O. Box 8
Schenectady, New York 12301

Water, adsorbed on a beta alumina surface, significantly influences the nature of Na^+ ion transport across a non-aqueous electrolyte/beta alumina interface and the behavior of a Pt/beta alumina interface. Na^+ interfacial exchange current at 23°C between beta alumina and propylene carbonate decreases with increasing surface hydration. Adsorbed water undergoes a number of faradaic reactions at a Pt/beta alumina interface, which otherwise should approximate an ideally polarizable or "blocking" electrode. This paper discusses the effects of adsorbed water on ion and electron transport at these two interfaces.

Key words: Beta alumina; blocking electrode; interface; solid electrolyte; water.

Introduction

Beta alumina (ca. 1.2 $Na_2O \cdot 9Al_2O_3$) is a solid ionic conductor in which a variety of monovalent cations, including Na^+, Ag^+, H^+, and H_3O^+, are mobile. Its structure [1][1] and conductivity [2,3] have been previously discussed. Breiter and Farrington [4] have reviewed the electrochemistry of charge transport at a beta alumina interface. Farrington [5,6] has described experimental investigations of Na^+ transport at liquid electrolyte/beta alumina interfaces. Selected portions of these data will also be presented in this discussion of the influence of adsorbed H_2O on charge transfer at propylene carbonate/beta alumina and Pt/beta alumina interfaces.

H_2O and Na^+ both adsorb on an alpha alumina surface. Raman analysis of water adsorbed on alpha alumina concludes that Na^+ ions and water molecules compete for Lewis acid sites [7]. Na^+ adsorption is thought to cause alpha-alumina catalyst "poisoning" in Na^+-containing environments. Infrared spectroscopic analysis of pyridine adsorption on alpha alumina concludes that pyridine adsorbs at non-protonic Lewis acid sites in the absence of water. Proton activity is observed in the presence of water. Similar adsorption behavior may be expected for beta alumina.

The interaction of molecular water and beta alumina may not be confined to surface adsorption. Kline <u>et al.</u> [8], in broadband NMR measurements, found that the ^{23}Na spectrum in beta alumina, which is sharply narrowed by rapid localized ion motion at room temperature, broadens in the presence of water vapor. Heating restores a normal spectrum. Weight change measurements corroborate the reversibility of the exchange [9]. This has been interpreted

---

[1] Figures in brackets indicate the literature references at the end of this paper.

as evidence that molecular H_2O reversibly diffuses directly into the beta alumina conduction plane, decreasing local Na^+ motion and conductivity.

Water is also a source of ionic hydrogen species such as H_3O^+ and H^+, both of which can replace Na^+ in beta alumina. H_3O^+-beta alumina has been prepared by exchanging Na^+ beta alumina in concentrated H_2SO_4 [10]. H^+-beta alumina is synthesized by exposing Ag^+ beta alumina to a reducing atmosphere of H_2 [11]. Both H^+ and H_3O^+ ions, therefore, are capable of diffusing spontaneously or under the influence of a field into the beta alumina structure.

The energy required to bring about ion transfer between two dissimilar chemical environments such as between solid and liquid electrolytes appears as an interfacial polarization. Kinetic considerations [6] predict the i/V relationship relating interfacial polarization, η, and current density, i, to be

$$i = i_o \left[\exp \frac{\alpha z F \eta}{RT} - \exp \frac{-(1 - \alpha) z F \eta}{RT} \right] \tag{1}$$

in which α is the transfer coefficient, i_o, the equilibrium exchange current density, and z the charge of the mobile ion. The i/V relationship for Na^+ entry into and exit from beta alumina across a propylene carbonate interface should be described by eq. (1) for which ion exit from the solid electrolyte is considered a positive current occurring at a positive overpotential.

Results of a preliminary examination [12] of beta alumina/propylene carbonate interfacial transport at 25°C performed in this laboratory revealed that the interfacial impedance for Na^+ entry and exit increases after exposure of the beta alumina to water vapor. Similar effects were noted by Voinov and Tannenberger [13] who speculated that protons may be irreversibly driven into the beta alumina under the influence of an electric field, increasing its resistivity.

The following discussion describes the use of a galvanostatic technique to distinguish interfacial polarization from effects of bulk resistivity during Na^+ ion transfer across a propylene carbonate/beta alumina interface. The influence of adsorbed H_2O on interfacial transport is described.

Cyclic voltammetry was used to examine the electrochemical behavior of adsorbed H_2O at a Pt/beta alumina interface. A Pt/Na-beta alumina interface should approximate an ideally polarizable electrode over a potential range limited only by Na^+ reduction and O^{--} oxidation. This is a broader range of ideal polarizability than is encountered with typical Pt/liquid electrolyte interfaces. Adsorbed H_2O should limit the range of ideal polarizability of a Pt/Na^+-beta alumina interface since H_2O can be oxidized to H_3O^+, an ion mobile within the beta alumina structure.

Experimental

Beta alumina ceramic discs were prepared from Alcoa 'XB-2' beta alumina powder. The powder was ground with ZrO_2 grinding media, dried under vacuum, screened, and hydrostatically pressed into rods approximately 1.6 cm. in diameter and 15 cm long. The rods were cut into 1.6 cm segments and fired at 1700°C. The resulting ceramic was single phase, polycrystalline beta alumina of 98 percent theoretical density, containing approximately one percent MgO and one percent ZrO_2.

Rods were sliced into samples 1.3 cm in diamter and 4 mm thick. A 0.6 mm hole was drilled 3 mm into each sample from its circumference. Sample faces were polished through 600A grit SiC paper, washed in methanol, and fired for 24 hours at 700°C. Between individual experiments, samples were wet polished with methanol through 600A grid SiC paper, rinsed with methanol, and baked at 400°C at 10^{-3} torr for seven days or at 10^{-5} torr for six hours. They were transfered in vacuo to a Vacuum Atmospheres Ar drybox, polished briefly on dry 600A grit SiC paper, and mounted in the experimental cell shown in figure 1 between silicone rubber gaskets. In the following discussions beta alumina prepared by this procedure is referred to as "dry" or "anhydrous." "Hydrated" beta alumina is that which has been treated as above but exposed to 100 percent relative humidity at 23°C for 20 minutes before mounting.

Burdick and Jackson "Spectroscopic" propylene carbonate was dried by multiple percolation through a 16 cm x 2 cm column of alumina which had been activated at 500°C in vacuo for 24 hours. Baker anhdrous reagent NaI and Southwestern Analytical anhydrous tetrabutylammonium tetrafluoborate ($TBABF_4$) were baked 48 hours at 110°C in vacuo before dilution. Two electrolyte solutions were prepared: 1) 0.010 M NaI + 0.100 M $TBABF_4$ and 2) saturated NaI and $TBABF_4$. Solution 1 was the test solution and is referred to in this paper by its Na^+ concentration. The second was used in the unmonitored compartment of the experimental cell.

The assembled cell (fig. 1) incorporated four electrodes, an outer current-carrying pair of Pt foil (1 and 4) and an inner reference pair (2 and 3). Au wire dipped into Tl amalgam was used for reference electrodes. A small amount of electrolyte was injected into the sample reference electrode hole to provide satisfactory ionic contact to the beta alumina.

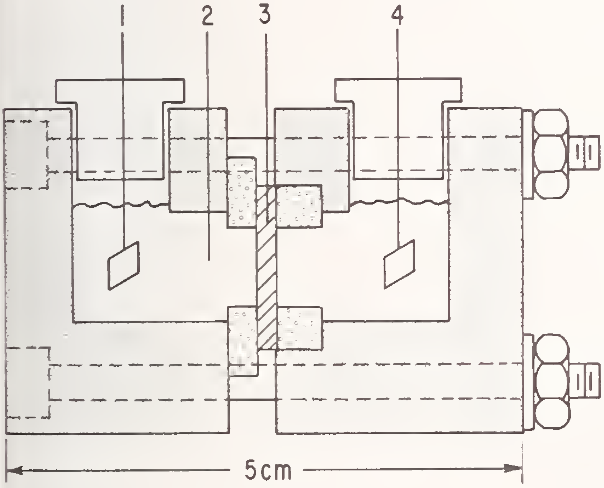

Fig. 1. Experimental cell; solid dots, Teflon; open circles, silicone rubber; slashes, beta alumina.

To study the behavior of a Pt/beta alumina interface, Pt electrodes, 1000 Å thick, were sputtered onto both faces of a 1.2 cm diameter, 4 mm thick, polished disc of polycrystalline beta alumina. A reference electrode hole, 0.6 mm in diameter, was drilled 3 mm into the disc from its edge. Cyclic voltammetric results were carried out in H_2O vapor using a Au wire dipped in Tl (Hg) as reference electrode. A small amount of propylene carbonate electrolyte was injected into the reference electrode hole to insure good electrode/beta alumina contact. Cyclic voltammetry results, thus, are referred to the $Tl°/Tl^+$ couple in anhydrous propylene carbonate. The $Tl°/Tl^+$ couple has a standard potential of -0.34 V vs. N.H.E. in acidic aqueous media.

The technique of galvanostatic analysis has been described previously [3,6]. In brief, it consists of applying single, fast-rise-time constant current square waves of varying widths to electrodes 1 and 4 in figure 1 while monitoring the differential voltage response across electrodes 2 and 3. A typical result showing voltage vs. elapsed time during a constant flux of Na^+ ions exiting hydrated beta alumina into propylene

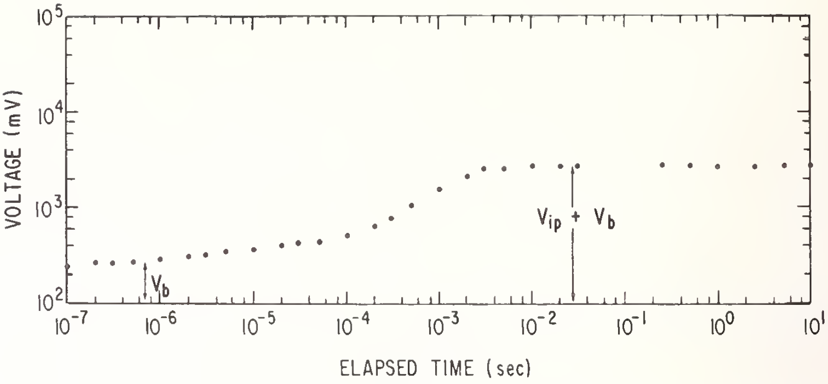

Fig. 2. Voltage ($V_b + V_{ip}$) vs. elapsed time; Na^+ exit from hydrated interface at 1.38×10^{-4} A/cm^2; V_b is bulk voltage drop, V_{ip} is interfacial polarization, 23°C.

carbonate is shown in Fig. 2. The time constants for bulk propylene carbonate and beta alumina resistivity (V_b) are much shorter than the rise time of the square wave ($t_r \sim 10^{-6}$ sec), so V_b is constant from 10^{-5} sec to dc. Interfacial polarization (V_{ip}), in contrast, has a time constant of approximately 10^{-3} sec. It is this difference between bulk and interfacial time constants which permits isolation of interfacial polarization by this technique.

Results - Interfacial Ion Transport

Figures 3 and 4 present plots of total voltage ($V_{ip} + V_b$) vs. applied current for Na^+ entry and exit across a dry beta alumina/propylene carbonate interface. V_{ip} is undetectable within measurement accuracy. Both plots are ohmic over the current ranges shown and have identical slopes corresponding to the resistance expected for bulk beta alumina and propylene carbonate.

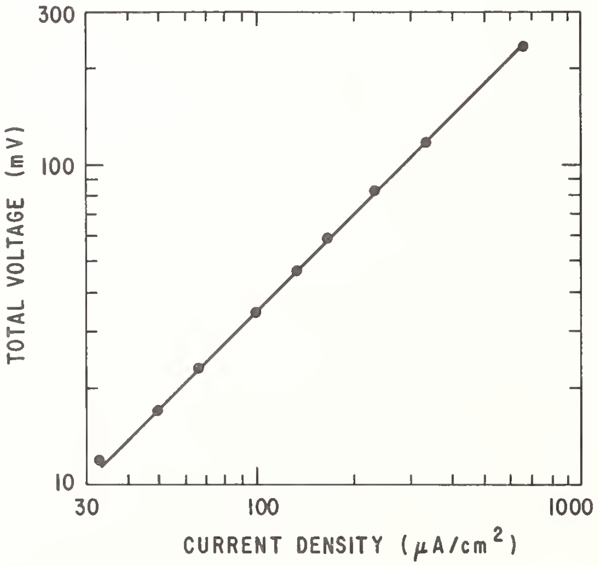

Fig. 3. Voltage ($V_b + V_{ip}$) vs. current density; Na^+ entry into dry beta alumina; slope = 1.00; 23°C.

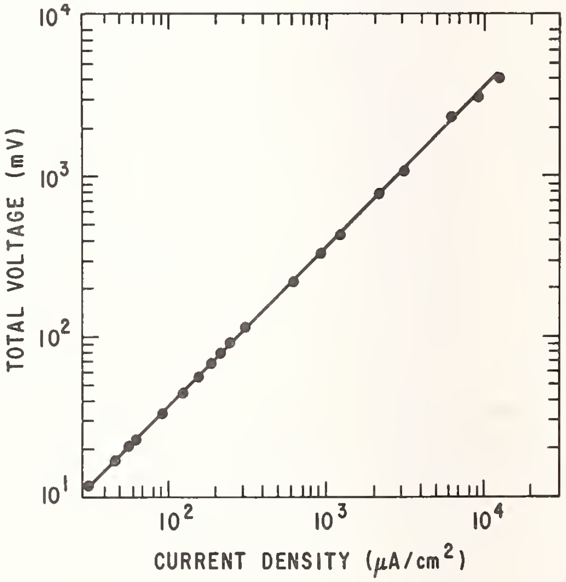

Fig. 4. Voltage ($V_b + V_{ip}$) vs. current density; Na^+ exit from dry beta alumina; slope = 1.00; 23°C.

In contrast, significant charge transfer polarization is detectable during ion transport across a hydrated interface. Typical resistivity/time response is shown in Figure 2. The potential attributable to interfacial polarization is readily separable from bulk resistivity. Figure 5 shows characteristic plots of V_{ip} vs. current density for Na$^+$ exit from a hydrated interface at two temperatures.

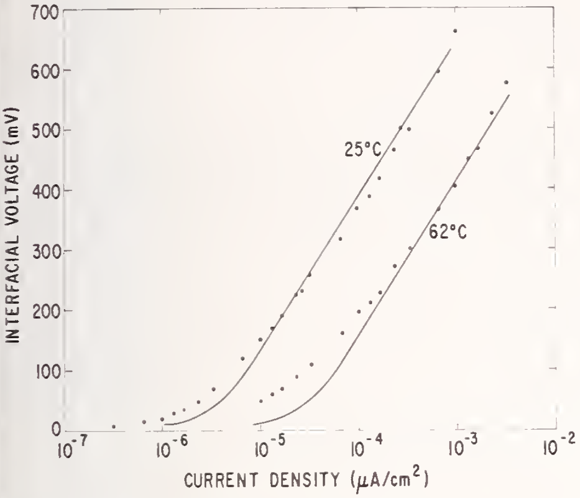

Fig. 5. Interfacial overpotential (V_{ip}) vs. current density; Na$^+$ exit from hydrated beta alumina; (•) points are observed while solid lines are calculated.

Interfacial polarization for Na$^+$ exit from a hydrated interface clearly follows the Tafel relationship described in eq. (1) for which the transition coefficient (α) was found to be 0.24 at 23°C and 0.22 at 62°C by plotting ln i vs. η. The interfacial exchange current (i_o) is 3.0×10^{-6} A/cm^2 at 23°C and 2.4×10^{-5} A/cm^2 at 62°C. Tafel behavior implies that any space charge region within the beta alumina is insignificant, a result that was expected for such an electrolyte having a large density of charge carriers.

Non-ohmic transition polarization must also arise during ion transport across an anhydrous interface. However, the Na$^+$ exchange current appears to be much larger at a dry interface and polarization is too small to be detected. A lower limit on i_o for dry interfacial Na$^+$ transport, estimated from figure 3, is 2×10^{-4} A/cm^2, at 23°C.

These results illustrate the dramatic effect of water on beta alumina interfacial transport. Adsorbed water decreases the equilibrium exchange current for Na$^+$ at a propylene carbonate/beta alumina interface. Previous results of Farrington [5] indicate that this decrease is a function of the extent of surface hydration, the exchange current increasing with decreasing hydration.

Tafel-type polarization observed for ion exit from a hydrated interface should also occur during ion entry through such an interface. However, the interfacial voltage drop is not constant but steadily increases during ion flux into beta alumina through a hydrated interface. This effect is significant over the entire range of current density examined in this work, 10^{-7} to 10^{-2} A/cm^2. Initial interfacial behavior is restored by extended electrolysis of ions out of the solid electrolyte.

These results are consistent with the hypothesis that reversible H_3O^+ substitution into beta alumina is the crucial factor behind the interfacial voltage drop increase during ion entry. Water, adsorbed on the beta alumina interface, is a source of H_3O^+ ions which can substitute for Na$^+$ in the beta alumina structure. Voinov and Tannenberger [13] suggested and Farrington [5] experimentally corroborated that H_3O^+ or a similar ionic hydrogen species competes with Na$^+$ for injection into beta alumina at a hydrated interface.

H_3O^+ substitution is accompanied by an increase in electrolyte resistivity which is manifested as a gradual increase in interfacial voltage drop during ion entry.

Further studies suggest that interfacial Na^+ transport occurs through an intermediate state in which Na^+ is adsorbed on the beta alumina surface. Under anhydrous conditions (fig. 6), the total voltage during ion exit undergoes a sharp increase after approximately 1 coulomb has passed at a current density of 3290 $\mu A/cm^2$ (curve A). At a lower current, 1310 $\mu A/cm^2$ (curve B), no transition is observed even with passage of 10 coulombs.

Hydration of the interface decreases the current density at which a voltage transition is observed and decreases its sharpness as figure 7 demonstrates. Curve A was observed with a beta alumina disc first exposed to 100 percent relative humidity for 20 minutes then baked in vacuo for six hours at 400°C and curve B with a disc that had been hydrated without bakeout.

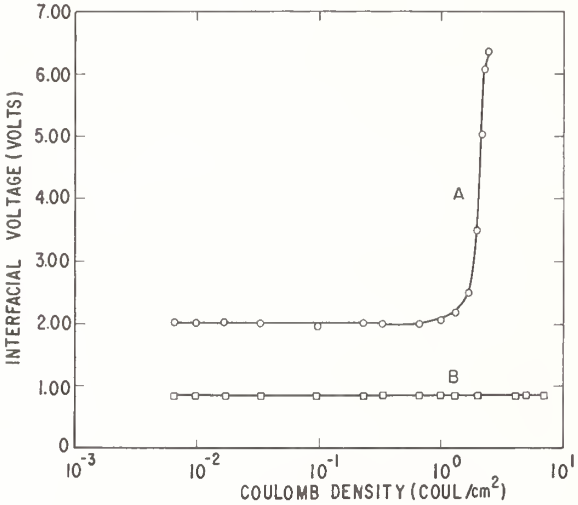

Fig. 6. Voltage ($V_b + V_{ip}$) vs. coulomb density; Na^+ exit from dry interface; curve A, 3.290×10^{-3} A/cm^2; 23°C; curve B, 1.310×10^{-3} A/cm^2.

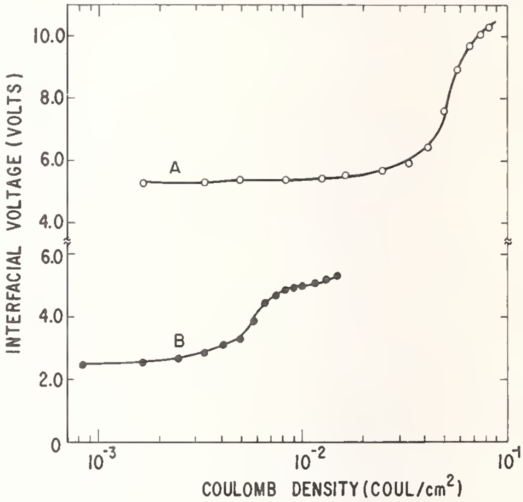

Fig. 7. Voltage ($V_b + V_{ip}$) vs. coulomb density; Na^+ exit from beta alumina; A, partially dried beta alumina; B, hydrated beta alumina; both at 3.290×10^{-3} A/cm^2 and 23°C.

All three plots are consistent with the hypothetical mechanism for Na^+ transport across a beta alumina/propylene carbonate interface shown in eq. (2) in which Na^+ exists in a surface adsorbed state intermediate between bulk beta alumina and propylene carbonate solvation.

$$Na^{+}_{\beta Al_2O_3} \rightleftarrows Na^{+}_{ads} \rightleftarrows Na^{+}_{pc} \qquad (2)$$

According to this mechanism, ion solvation occurs as a step in maintaining adsorption equilibrium and is independent of ion transport into or out of the beta alumina structure so long as the transport rate is less than the adsorption/desorption rate. Solvent structure and dielectric constant should exert their most significant effects on interfacial transport in influencing adsorption/desorption rate and equilibrium.

Pt/Beta Alumina Interface

The effects of H_2O surface adsorption and H_3O^+ injection into the conducting planes of beta alumina can be independently observed by cyclic voltammetry at a Pt/beta alumina interface. Results are shown in figure 8.

Little cell current is observed upon initial polarization at 0 V vs. $Tl°/Tl^+$. Positive potential sweep encounters several oxidation peaks (A-C) which can be attributed to H_2O oxidation to H_3O^+. Sweep reversal produces one significant peak at D which can be associated with reduction of a product, presumably O_2, formed at A-C.

At potentials less than -0.40V, a second major reduction peak appears (E). The current increases dramatically beyond -0.75V. Sweep reversal reveals peak F, not observed on initial cell polarization. The rapid decay of current in F suggests it corresponds to depletion of a particular species previously produced in peaks D or E.

The characteristics of peaks E and F are consistent with the hypothesis that E corresponds in part to reduction of adsorbed H_2O with simultaneous Na^+ migration out of the solid electrolyte to the surface. The overall reaction is

$$4H_2O + 4Na^+_{beta} + 4e^- \rightarrow 2H_2 + 4NaOH \qquad (3)$$

Peak F, then, represents reoxidation of H_2 and reinjection of Na^+ into beta alumina. Both H_2 and Na^+ exist at the interface only as the result of electrochemical production at E.

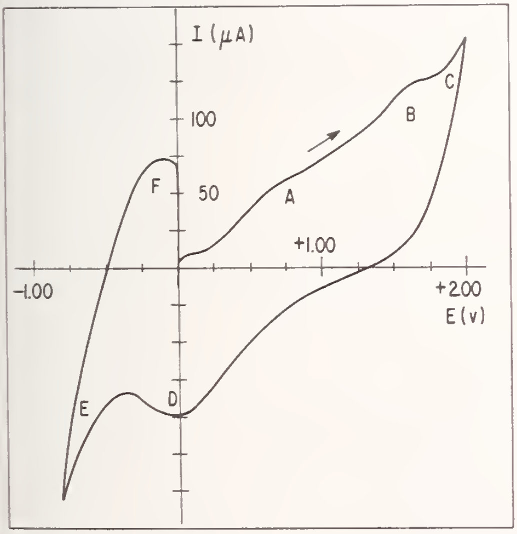

Fig. 8. Cyclic voltammogram of reaction of gaseous H_2O at Pt/beta alumina interface; sweep rate = 0.200 V/sec; 23°C; electrode area = 0.78 cm^2; potentials referred to Tl(Hg) - Tl couple in propylene carbonate.

As the complete sweep cycle shown in figure 8 is repeated, all peaks decrease in magnitude, particularly A-C. Evidently, H_3O^+ ions gradually substitute into the beta alumina adjacent to the interface and significantly decrease its conductivity. This observation is consistent with the results previously described which indicate that extended Na^+ entry into beta alumina across a hydrated interface leads to a progressive increase in interfacial voltage, presumably from buildup of H_3O^+ ions in the beta alumina.

Summary and Conclusions

No interfacial polarization can be detected at an extremely dry propylene carbonate/beta alumina interface from 3×10^{-5} to 1×10^{-2} A/cm^2 at 23°C.

If the beta alumina is first exposed to water vapor, significant interfacial polarization is apparent. Polarization follows a Tafel relationship for which the transition coefficient (α) is 0.24 at 23°C and 0.22 at 62°C. The interfacial exchange current (i_o) is 3.0×10^{-6} A/cm^2 at 23°C and 2.4×10^{-5} A/cm^2 at 62°C.

Na^+ ion transport across a beta alumina/propylene carbonate interface occurs through an intermediate adsorbed state in which the ion is neither within the beta alumina structure nor solvated in the non-aqueous electrolyte. Interfacial Na^+ ion transport is primarily influenced by those species which either compete with Na^+ for surface adsorption sites, of which water is one, or influence the rate of Na^+ ion adsorption and desorption. This latter step should be affected by interfacial ionic composition and by the solvent and its dissolved secondary components.

H_2O adsorbs at a Pt/beta alumina interface and can be oxidized to ionic species, presumably H_3O^+, mobile within the beta alumina structure. The possible presence of trace H_2O must be considered in any experimentation assuming blocking behavior at a Pt/beta alumina interface or its equivalent. Meticulous interface preparation including isolation from normal atmosphere must be exercised if an inert metal/beta alumina interface is to approximate an ideally polarizable, or blocking electrode. The presence of trace water is surely responsible for the satisfactory behavior of Pt and Au contacts in low frequency impedance measurements on Na^+-beta alumina [14,15,16] and may also account for unexpectedly large capacitance observed in several investigations [14,17] of Pt/beta alumina/Pt or Au/beta alumina/Au cells.

Acknowledgements

Dr. R. W. Powers kindly supplied samples of beta alumina used in this work.

References

[1] W. L. Roth, J. Solid State Chem., 4, 60 (1972).

[2] M. S. Whittingham and R. A. Huggins, J. Chem. Phys., 54, 414 (1971).

[3] G. C. Farrington, Report No. 75CRD193, GE CR&D, Schenectady, New York (1975); J. Electrochem. Soc., in press.

[4] M. W. Breiter and G. C. Farrington, this volume.

[5] G. C. Farrington, Report No. 75CRD146, GE CR&D, Schenectady, New York (1975); J. Electrochem. Soc., submitted for publication.

[6] G. C. Farrington, J. Electroanal. Chem., submitted for publication.

[7] G. Careri, V. Mazzacurati, M. Sampoli, and G. Signorelli, J. Catal., 26, 494 (1972).

[8] D. Kline, H. S. Story, and W. L. Roth, J. Chem. Phys., 56, 5180 (1972).

[9] W. L. Roth, General Electric Research and Development Center, Report No. 74CRD054, (1971).

[10] H. Saalfeld, H. Matthies, and S. K. Datta, Berichte Deutsche Keram. Ges. 45, 212 (1968).

[11] G. P. Kummer, J. Solid State Chem., 7, 141 (1972).

[12] G. C. Farrington, abstract, Symposium on Interfacial Phenomena, Amer. Inst. Chem. Eng., 67th Meeting, December 1974, Washington, DC.

[13] M. Voinov and H. Tannenberger, Electrochim. Acta., 19, 959 (1974).

[14] A. Imai and M. Harata, Jap. J. Appl. Phys., 11, 180 (1972).

[15] J. H. Kennedy and A. F. Sammells, J. Electrochem. Soc., 119, 1609 (1972).

[16] R. W. Powers and S. P. Mitoff, J. Electrochem. Soc., 122, 226 (1975).

[17] S. P. Mitoff and R. J. Charles, J. Appl. Phys., 43, 927 (1972).

National Bureau of Standards Special Publication 455, *Electrocatalysis on Non-Metallic Surfaces,*
Proceedings of Workshop held at NBS, Gaithersburg, Md., December 9-12, 1975. (Issued November 1976)

Overvoltage Phenomena in Solid-Oxide Electrolyte Cells at Elevated Temperatures

W. L. Worrell
Department of Metallurgy and Materials Science
University of Pennsylvania
Philadelphia, Pennsylvania 19174

To develop a more quantitative understanding of the factors which establish overvoltages in solid-oxide electrolyte cells, constant currents have been passed through two types of symmetrical cells. At temperatures between 800 and 1000°C, constant and reproducible cell overvoltages are obtained when the imposed current is less than 50 μA. The cell overvoltage (η) is directly proportional to the current (I), and the interfacial resistance, defined as equal to η/I, is constant for each cell at constant temperature. Assuming that oxygen concentration gradients in the metal portion of the electrodes establish the cell overvoltages, a quantitative expression has been derived to calculate the interfacial resistance for each cell. Reasonable agreement between calculated and experimental values of the interfacial resistance is obtained for cells having two-phase metal-metal oxide electrodes. This agreement indicates that oxygen is transferred between metal particles and the electrolyte rather than through oxide particles in the electrodes. For cells with oxygen-saturated copper electrodes, the solubility-diffusivity product of oxygen in solid copper has been calculated from the overvoltage data.

Key words: Copper electrodes; interfacial resistance; metal-metal oxide electrodes; oxygen transport; steady-state overvoltages.

1. Introduction

An understanding of the factors which establish cell overvoltages is important because large overvoltages are detrimental to the useful application of many electrochemical cells. The chemical potential difference between two electrodes establishes the open-circuit or thermodynamic cell voltage. Under closed-circuit conditions, the cell voltage is usually less than the thermodynamic value, and the difference between the thermodynamic and the measured voltage is the overvoltage. Phenomena which are responsible for the overvoltage can be conveniently divided into interfacial and transport effects. Interfacial effects include slow electron transfer and chemical reactions at the electrode-electrolyte interface. Slow transport in the electrolyte or in the electrodes causes concentration gradients in the respective phases.

Electrochemical cells using zirconia-based electrolytes have been used in a number of coulometric titration and oxygen diffusivity studies [1].[1] Raleigh has reviewed studies of electrode processes in solid-state cells [2]. Except for our work with two-phase electrodes [3,4], previous investigations have been conducted using single-phase solid electrodes. In

---

[1] Figures in brackets indicate the literature references at the end of this paper.

this paper, our experimental measurements of steady-state overvoltages in cells using a $ZrO_2(CaO)$ electrolyte at elevated temperatures are summarized, and the method used to quantitatively calculate such overvoltages is described.

2. Experimental Aspects

In our overvoltage investigations using a zirconia-based electrolyte and solid electrodes, two symmetrical electrochemical cells were employed [3-5]. Two-phase metal-metal oxide electrodes were used in the first cell,

$$M, MO|ZrO_2(CaO)|M, MO, \tag{A}$$

where M, MO was Cu, Cu_2O; Fe, FeO or Ni,NiO. These metal-metal oxide electrodes are most commonly used in thermodynamic and kinetic cell studies [1]. In cell (A) the zirconia electrolyte was sandwiched between two identical electrode pellets. The electrolyte was a commercial-grade ZrO_2 (7.5 wt. pct CaO) disc, 0.25 to 0.6 cm thick and ~1.2 cm diam., obtained from the Zirconium Corp. The preparation and characterization of M, MO electrode pellets have been described [3,4].

In the second cell,

$$Cu, Cu_2O|Cu|ZrO_2(CaO)|Cu|Cu, Cu_2O \tag{B}$$

the electrodes were oxygen-saturated copper foils of precisely known thickness. Copper foils 3.2×10^{-3} cm in thickness were used in one series of experiments, while foils having a thickness of 1.27×10^{-2} cm were used in another series. To saturate the copper electrodes with oxygen, cell (B) was heated to a temperature of 1060°C and was held for approximately two days before beginning experimental measurements. To maintain oxygen saturation in the electrodes, the copper foils were sandwiched between the electrolyte and a Cu, Cu_2O pellet.

Two critical experimental precautions were necessary to obtain reproducible results. Although measurements were made under an atmosphere of purified argon, metal foils of copper or iron were placed within 0.5 cm of the cell to minimize any harmful reactions between impurities in the argon and the electrodes. Intimate electrode-electrolyte contact was also essential for accurate measurements. Preliminary measurements showed that excellent interfacial contact could be obtained by using an alumina push-rod to press the electrodes and the electrolyte together. The alumina rod could be moved by adjusting a brass screw at the top of the reaction tube. Using this design, the measured steady-state cell voltages were stable and independent of the argon gas flow rate. After an experiment, the interfacial adherence was so strong that the electrolyte would fracture internally rather than separate from the electrode.

Detailed descriptions of our experimental apparatus and technique are available [3-5], and only a brief summary is necessary here. The experimental technique was a galvanostatic one in which constant currents were imposed across cells (A) and (B), and the cell voltage was measured as a function of time at temperatures between 800 and 1000°C. The voltage drop across a standard decade resistance box provided a highly precise measurement of the current through the cell. Cell voltages were measured (±0.02 mV) using a Keithly 630 high impedence (10^{13} ohms) potentiometric electrometer. When the imposed current was above 50 µA, the cell voltage continuously increased with time and never reached a steady-state value. Figure 1 shows an example of this behavior for cell (A) with Cu, Cu_2O electrodes. At lower currents, steady-state cell voltages were obtained as shown in figure 2. Only steady-state values were used in our quantitative analysis.

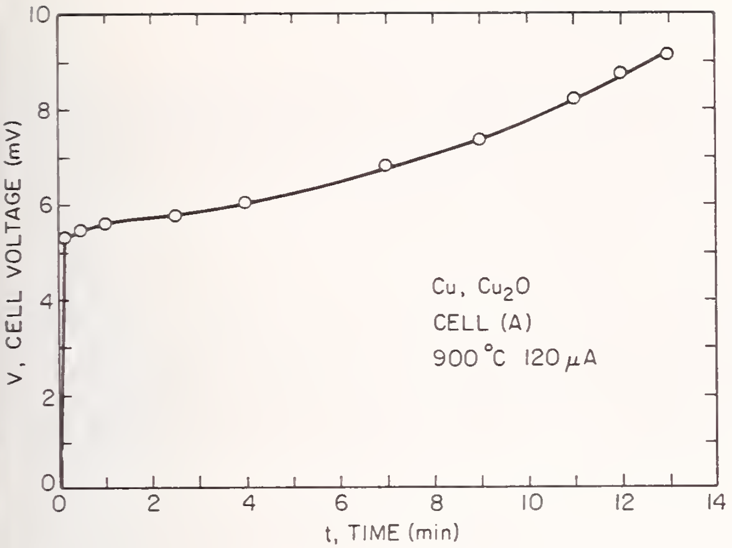

Fig. 1. Typical cell coltage versus time behavior for cell (A) at currents above 50 μA. The electrodes are Cu, Cu_2O mixtures.

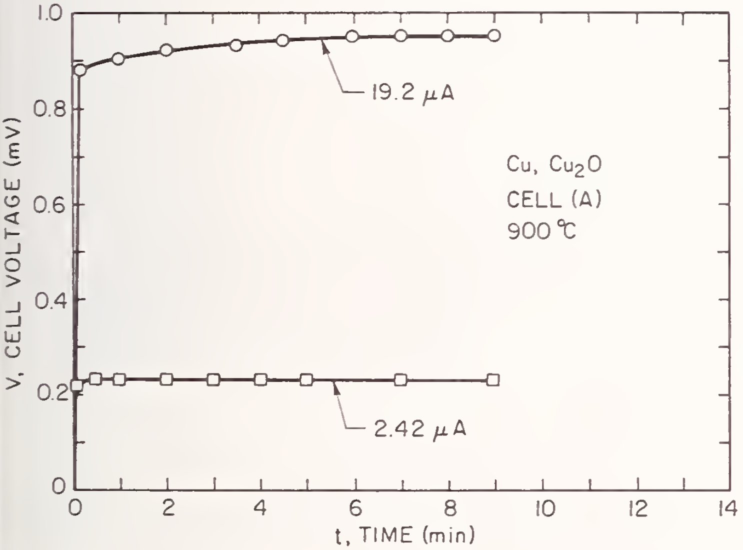

Fig. 2. Typical cell voltage versus time behavior for cell (A) at currents below 50 μA. The electrodes are Cu, Cu_2O mixtures.

For cells (A) and (B), the steady-state cell voltage (V) is the sum of the $I\Omega$ drop across the electrolyte and the overvoltage (η); thus,

$$V = I\Omega + \eta. \tag{1}$$

To determine the overvoltage, the dc resistance (Ω) of the cell must be known. With the Ni, NiO electrodes, the steady-state cell voltages were very large, and the ac cell resistance could be used for Ω in Eq. (1) with negligible error. For these cells, the $I\Omega$ term was less than 1% of the cell voltage. However, a direct measurement of the dc cell resistance was necessary for the other cells. Therefore after the steady-state voltage measurements, the dc resistance was measured directly by taking oscillographs of the change in cell voltage during the first tenths of a second after current was started or stopped.

3. Results

Values of η calculated using eq.(1) for cell (A) at 900°C are shown in figure 3. Results are shown on a log η versus log I plot so that results from the three different electrode cells can be compared. Figure 3 is not a Tafel plot. Over the experimental range of 0.5 to 50 µA, a linear relationship is observed between log η and log I. The slope of each of the three lines in figure 3 is unity; thus, a constant interfacial resistance (R_η) is observed, where

$$R_\eta \equiv \eta/I. \qquad (2)$$

At 900°C R_η is 12±2 ohms for the Cu, Cu_2O cell, 120±20 ohms for the Fe, FeO cell and 1200±200 for the Ni, NiO cell. Similar results have also been obtained for cell (A) at 800 and 1000°C. However, values for R_η at 800°C are higher, while values of R_η at 1000°C are lower than those at 900°C.

Steady-state overvoltages determined for cell (B) at constant temperature and constant electrode thickness also exhibit the behavior shown in figure 3. Experimentally determined values of the interfacial resistance for cell (B) are tabulated as a function of temperature and electrode thickness in Table 1.

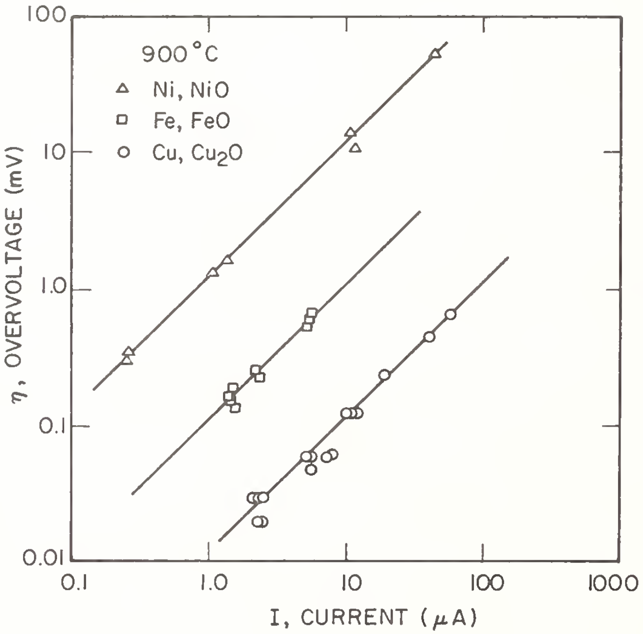

Fig. 3. Overvoltage versus current for cell (A) at 900 °C. Results are shown for three different two-phase electrode cells; the three electrodes are Cu, Cu_2O; Fe, FeO; and Ni, NiO.

Table 1. Values of R_η for cell (B).

3.2×10^{-3} cm Cu Electrode		1.27×10^{-2} cm Cu Electrode	
T, °C	R_η, ohms	T, °C	R_η, ohms
800	145.5	796	625.0
841	65.4	853	255.0
900	21.7	903	106.0
944	12.0	951	49.2
1000	4.5		

4. Discussion

Only oxygen ions move through the zirconia electrolyte, and the cell current density (i) is directly related to the oxygen flux (J) in the cell by

$$i = 2FJ, \tag{3}$$

where F is the Faraday constant. Because the metal particles or foil at each electrode are saturated with oxygen, oxide should be reduced at one electrode and formed at the other when oxygen ions are transported across the electrolyte. Assuming all the oxygen which enters the sink electrode forms oxide, one calculates a maximum formation rate for the oxide layer of 0.4 to 0.7 Å $\mu A^{-1} min^{-1}$. Thus, for a typical experimental current of 10 μA for 10 min, a 40-70 Å thick layer of oxide is formed.

4.1 Calculation of Interfacial Resistance.

The basic question is what establishes the constant interfacial resistance (R_η) when the cell current is less than 50 μA. The most likely cause of R_η is either a slow charge-transfer reaction at the electrode-electrolyte interface or slow transport of oxygen in the electrodes. It should be noted that oxygen-ion transport in the electrolyte determines the ohmic resistance (Ω) of the zirconia electrolyte and makes no contribution to the interfacial resistance. Overvoltage decay times of 5 to 150 min and the absence of a Tafel slope indicates that the observed overvoltages are not caused by a slow charge-transfer reaction. Thus, slow oxygen transport in the electrodes must be responsible for the observed overvoltages and for R_η

Oxygen transport in the two-phase electrodes of cell (A) could be through either the metal or oxide particles. However, for cell (B), oxygen transport through the oxygen-saturated copper foil electrodes is the only possibility. Assuming that oxygen concentration gradients in the metal (either particles or foil) electrodes establishes the cell overvoltage, the following equation has been derived [4,5] to calculate the interfacial resistance for cells (A) and (B):

$$R_\eta = \frac{RT\Delta x}{nF^2A\ C_O D_O}, \tag{4}$$

where R is 8.314 J $mol^{-1}K^{-1}$, F is 96,487 J $V^{-1}eq^{-1}$, n is 2 eq mol^{-1} for oxygen, T is in K, A(cm^2) is the electrolyte-metal electrode interfacial area, Δx(cm) is the oxygen diffusion distance in the metal electrode, and $C_O D_O$ (mol $cm^{-1}s^{-1}$) is the solubility-diffusivity product for oxygen in the metal.

Estimates of the metal particle-electrolyte interfacial area ($A \approx 0.5\ cm^2$) and of the average metal particle size (2×10^{-3} cm) have been made using photomicrographs of the electrode-electrolyte interfaces of cell (A). The average oxygen diffusion distance (Δx) in the metal particles is estimated to be 1/3 of the average particle size. With these assumptions and available data for $C_O D_O$, values of R_η calculated from eq.(4) are compared with the experimental values from cell (A) at 900°C in Table 2.

As shown in Table 2, calculated and measured values are in good agreement for the Cu, Cu_2O electrodes and in fair agreement for the Fe, FeO and Ni, NiO electrodes. Some uncertainty in the calculated values is due to the oxygen solubility-diffusivity product. Although $C_O D_O$ for copper and iron is fairly well established (within a factor of two), the data for nickel are very uncertain and could be in error by as much as a factor of 10 to 50 [11]. Another major uncertainty in the calculated values shown in Table 2 arises from the estimation of Δx, which is probably accurate only within a factor of four.

A major advantage of cell (B) is that the diffusion distance (Δx) is simply the thick-

Table 2. Comparison of calculated and experimental values of R_η at 900 °C for cell (A).

Electrodes	$(C_O D_O)^a$ in Metal	R_η (cal)	R_η (meas)
Cu, Cu_2O	1.5×10^{-10} [8]	5	12
	7.1×10^{-11} [5]	10	12
Fe, FeO	2.5×10^{-12} [6]	279	120
Ni, NiO	1.4×10^{-13} [7]	4988	1200

[a] Units are mol $cm^{-1}s^{-1}$.

ness of the copper foil electrodes, which can be precisely fixed and varied experimentally. At constant temperature, the interfacial resistance measured from cell (B) should be directly proportional to the electrode thickness. As shown in Table 1, this is observed within the experimental uncertainty. The measured values of R_η tabulated in Table 1 can be used with eq.(4) to calculate values of $C_O D_O$ for copper. For this calculation, the interfacial area for cell (B) is 0.785 cm^2. In figure 4, calculated values of $C_O D_O$ are compared with results from three other investigations [8-10] in which different experimental techniques were used. The good agreement shown in figure 4 indicates that eq.(4) is valid and that oxygen concentration gradients in the metal electrodes do establish the overvoltages in cell (B).

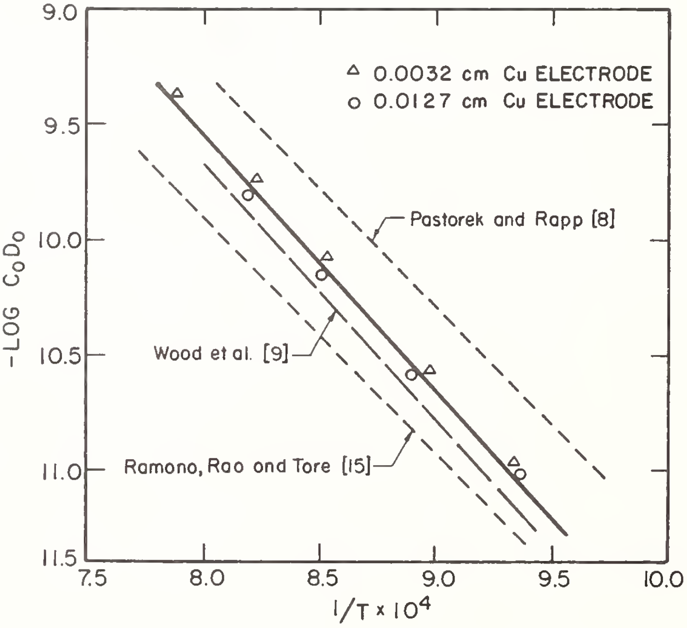

Fig. 4. The solubility-diffusivity product of oxygen in solid copper as a function of reciprocal temperature. The points and solid line represent values for $C_O D_O$ calculated using eq. (4) and overvoltage data from cell (B). The three dashed lines are experimental results from other investigations [8-10].

4.2 Further Comments Concerning Equation (4).

A number of ancillary experiments [4] showed that the overvoltage of cell (A) is independent of the direction of current and is produced equally at each electrode. During current flow, oxygen enters the sink electrode by diffusing through the oxygen-saturated metal and forming oxide at an oxide-metal interface. During a typical experiment, calculations using eq.(1) indicate a 40-70 Å layer of oxide should form, which is a negligible thickness compared to the estimated diffusion distance of 6.7×10^{-4} cm for cell (A). At currents below 50 µA the diffusion distance is essentially constant, and constant values of R_η are obtained. At higher currents, the oxide layer thickness could become significant, and the oxygen diffusion distance could vary with time. For oxygen to enter the metal electrodes, there must be a small supersaturation of oxygen in the metal at the electrode-electrolyte interface. For an overvoltage value of 10 mV, the ratio of the supersaturated oxygen content to the solubility value is only 1.2. Currents above 50 µA produce a large oxygen flux into the metal electrode, and the supersaturation oxygen content of the metal could become so large that oxide layers are nucleated at the electrode-electrolyte interface. Under these conditions steady-state overvoltages for cell (A) would never be observed.

The agreement shown in Table 2 requires that the major oxygen transport across electrode-electrolyte interfaces in cell (A) is between the electrolyte and metal particles in the electrodes. There is evidently negligible oxygen transport between the electrolyte and metal oxide particles in the electrodes. Ductile metal particles in the electrodes can deform under cell pressure to fit into microcracks and crevices on the electrolyte surface, which results in intimate contact between the metal particles and the electrolyte. Our initial results were a function of cell pressure until pressures were high enough to insure good electrode-electrolyte adherence.

In the derivation of eq.(4), short circuit diffusion paths for oxygen such as grain boundaries and surfaces of the metal particles have been ignored. Experimental temperatures are close to the melting points of the metals (particularly copper), which minimizes the influence of short-circuit diffusion.

Our experimental approach can be used to investigate overvoltage phenomena in other electrochemical cells. However, eq.(4), or one similar to it, applies only to those cases in which cell overvoltages are established by concentration gradients in the electrodes. One example is a study of the oxygen transfer kinetics between Ga, Ga_2O_3 electrodes and a $ZrO_2(CaO)$ electrolyte at temperatures between 800 and 900°C [12]. The experimental results followed eq.(4), and it was concluded that oxygen transport through liquid gallium in the two-phase electrodes established the cell overvoltages.

5. Conclusions

Assuming that oxygen concentration gradients in the metal portion of the two-phase electrodes establish the overvoltages in cell (A), calculated values of R_η are in reasonable agreement with experimental values. This agreement indicates that the major oxygen transport across the electrode-electrolyte interface is between the electrolyte and metal particles in the electrode. As shown in figure 3, overvoltages produced by Cu, Cu_2O electrodes are ten times less than those produced by Fe, FeO electrodes and 100 times less than those produced by Ni, NiO electrodes. Thus, Cu, Cu_2O electrodes are the preferred two-phase electrodes for use in coulometric titration and diffusivity studies.

Overvoltage data from cell (B) have been used with eq.(4) to determine values for the oxygen solubility-diffusivity product in solid copper. The good agreement between these values and other data shown in figure 4 indicates that steady-state overvoltages in cell (B) are established by oxygen concentration gradients in the copper foil electrodes.

Equation (4) can be used to calculate R_η and overvoltages for any solid-oxide electrolyte cell in which the overvoltages are established by slow oxygen transport in oxygen-saturated metal electrodes.

6. Acknowledgment

The financial support of this program by the National Science Foundation and the Laboratory for Research on the Structure of Matter at the University of Pennsylvania is gratefully acknowledged.

7. References

[1] Worrell, W. L., Amer. Ceram. Soc. Bull. **53**, 425 (1974).

[2] Raleigh, D. O., Electroanal. Chem. **6**, 87 (1973).

[3] Worrell, W. L. and Iskoe, J. L. in *Fast Ion Transport in Solids, Solid State Batteries and Devices*, (W. van Gool, Ed.) North-Holland Publ. Co., 513 (1973).

[4] Iskoe, J. L., Ph.D. Dissertation, University of Pennsylvania (1972).

[5] Ramanarayanan, T. A. and Worrell, W. L., Metal. Trans. **5**, 1773 (1974).

[6] Swisher, J. H. and Turkdogan, E. T., Trans. TMS-AIME **239**, 426 (1967).

[7] Barlow, R. and Grundy, P. J., J. Mat. Sci. **9**, 797 (1969).

[8] Pastorek, R. L. and Rapp, R. A., Trans. TMS-AIME **245**, 1711 (1969).

[9] Wood, S., Adamonis, D., Soffa, W. A., and Meier, G. H., ONR Report NRO 31-749 (1973).

[10] Ramana Rao, A. V. and Tare, V. B., Z. Metallkund. **63**, 70 (1972).

[11] Kerr, W. R., and Rapp, R. A., to be published.

[12] Donaghey, L. F. and Pong, R., J. Electrochem. Soc. **121**, 506 (1974).

PANEL DISCUSSION

Panel on Major Problems, Advances, and Opportunities Revealed by Workshop

Chairman: Prof. Dr. Heinz Gerischer, Fritz Haber Institute der Max Planck Gesellschaft, Berlin

Panelists:
Dr. William Gadzuk, National Bureau of Standards
Dr. Jerome Kruger, National Bureau of Standards
Prof. Robert de Levie, Georgetown University
Dr. Ralph J. Brodd, Union Carbide Corp.
Dr. Ugo Bertocci, National Bureau of Standards
Prof. Allen J. Bard, University of Texas at Austin
Prof. A. C. C. Tseung, The City University, London
Prof. Norman Hackerman, Rice University
Dr. Sigmund Schuldiner, Bureau of Mines
Prof. J. Ross MacDonald, University of North Carolina
Dr. Douglas O. Raleigh, Rockwell International

Reporter: Dr. Alan D. Frankin, National Bureau of Standards

Panel on Major Problems, Advances, and Opportunities Revealed by Workshop

A. D. Franklin

Reporter for the Panel
Institute for Materials Research
National Bureau of Standards
Washington, DC 20234

Summary of Discussion

Theory

The theoretical papers read at the Workshop dealt mainly with chemisorption rather than with electrocatalysis as such. Because of the great complexity of real catalytic systems, it cannot be expected that theory at present will be able to deal in detail with catalytic problems. Rather, theory can develop ideas and concepts which can guide researchers in developing strategies for investigating and understanding real catalytic systems.

Two trends in chemisorption theory are evident. On the one hand, calculations are being made of the electron states of clusters of atoms that represent small particles, including adsorbed species. Molecular orbital theory plays a dominant role here. Electron energy spectra can be calculated and compared to experimental observations, especially for energy differences. Of particular interest would be calculations on alloy clusters, to explore size effects on alloy catalytic properties, and on clusters containing lattice defects, although clearly the cluster size would have to be large enough to make a lattice defect meaningful.

This kind of theory is closely related to the chemists' view of specific chemical bonds between adsorbate molecules and atoms of the catalyst surface. Such theory is useful to understanding mechanisms and reaction paths, but is not reliable for predicting energy levels of electrons in surfaces and chemical bonds because of neglect of delocalizing effects of the electron states in the solid.

On the other hand, band theory has been extensively used to describe electrochemical reactions on semiconductors based on experimental analyses on the energetic position of band edges, at the interface between semiconductors and electrolytes. Specific adsorption sites are introduced as surface states, and the nature of these states is the probable meeting ground for the molecular orbital and band approaches. Indeed, Wolfram showed that the two descriptions converge when considering surface states in the energy gap of the semiconductor, both giving localized electron states capable of interacting strongly with anti-bonding states of adsorbed species. That this kind of theory is applicable to electrochemical situations is demonstrated by the observation in Wolfram's calculations of a group of surface states about 1.5 eV below the conduction band in n-type TiO_2, agreeing well with a peak in the same energy in the electron energy loss spectrum for reduced TiO_2 *in vacuo*, reported in the paper by Henrich, Zeiger, and Dresselhaus, and with a peak found by Lu, Pollak, and Raccah near 1.7 eV in the electro-reflectance spectrum of reduced TiO_2 in contact with 1 M aqueous KCl solution. In addition, Frank, Laser, Hardee, and Bard in their paper report a concentration of surface states about 1.2 eV below the conduction band in n-type TiO_2, from redox behavior of a number of redox couples in acetonitrile with TiO_2 as the working electrode.

Characterization

Adequate characterization of electrocatalyst specimens, like the characterization of materials in many other kinds of studies, involves determining a number of things. The specimen purity and stoichiometry must be determined, as the potential role of lattice oxygen in the activity of WC for the electrochemical oxidation of H_2 shows. The paper of Morrison and Freund demonstrates that lattice defects can be important, and Tseung and Jasem showed that activity for O_2 reduction may correlate with magnetic susceptibility.

Analytical chemistry techniques for measuring very low concentrations of reactants and products in the electrolyte near the electrocatalyst can be helpful in sorting out the reactions taking place and the concentration levels at which impurities might become important. An example is found in the oxygen electroreduction, where a variety of intermediate oxygen-containing species occur, and the problem arises of assessing the balance between the reduction paths leading to H_2O and H_2O_2.

Techniques for probing the nature of the surface and the species formed on it by chemisorption fall into two classes. On the one hand, there are very sensitive and powerful methods for studying surfaces under high vacuum or other ultra-clean conditions, such as LEED, ESCA, Auger spectroscopy, etc., while on the other hand, there are now a number of techniques capable of studying the surface *in situ*, in contact with an electrolyte and with an applied potential. These include optical techniques such as internal reflection absorption and Raman spectroscopy and electroreflectance, and also include electrochemical methods like linear sweep voltammetry and a.c. impedance. The paper by Conway reviews the tremendously useful information available from linear sweep voltammetry, and Bard and coworkers, in their paper quoted above, use linear sweep voltammetry with a series of redox couples in a non-aqueous solvent to probe the surface states of the electrode material.

The problem with applying the ultra-clean techniques to understanding electrochemical processes is how to assess the correspondence between the nature of the surface as seen by the measurement and the surface as it exists in the electrochemical situation, in contact with the electrolyte and under the influence of the applied potential. In general, changes undoubtedly take place on the surface as the sample is removed from the electrolyte and prepared for and transferred to the ultra-clean environment. However, examples do exist in which good correspondence has been seen between measurements made under electrochemical conditions and those on ostensibly the same surfaces under high vacuum or controlled gas environments. For instance, the phenomena of under-potential deposition discussed in the paper by Adžić, and coworkers arises because the substrate-adsorbate interaction is energetically stronger than is the self-interaction of the adsorbate. In effect, the heat of adsorption of the first monolayer is larger than the heat of vaporization of the bulk. It is therefore expected, provided that the surfaces are essentially the same, that the amount by which the under potential for monolayer deposition differs from the thermodynamic potential for bulk deposition should correlate with the difference between the temperature for flash desorption of bulk deposited layers and that for the last layers of adsorbate to vaporize, and indeed such a correspondence is observed for metals on metals.

Optical techniques, such as internal reflection infrared or Raman spectroscopy, offer the hope of probing in a fundamental way the nature of surface species *in situ* in the electrochemical environment. A cautionary note must be sounded, however. Even such a seemingly simple system as CO adsorbed from the gas phase on Ni surfaces has yet to be unscrambled in spite of work over three decades using highly sophisticated optical techniques.

Characterization of nonmetallic electrocatalytic surfaces and materials may require measurements not always used in electrochemical studies. An example arises from the work reported in this Workshop by Morrison and Freund, pointing out the role dislocations may play in determining the electrochemical behavior. Characterization with respect to dislocations and similar lattice defects may be very important in some cases. Similarly, the discussion brought out that the actual composition of WC electrocatalysts may be quite complex, involving perhaps excess W, substitutional oxygen, or dissolved gases, and that these compositional anomalies may be very significant in determining electrochemical behavior. The paper by Tseung and Jasem brought out a possible correlation between electrocatalytic activity and magnetic susceptibility in some of the transition metal oxides, opening up the possibility of using magnetic measurements as a tool of characterization.

From another standpoint, very sensitive analytical chemistry techniques for the quantitative assessment of very low concentrations of reactants and products can be valuable in sorting out actual reaction mechanisms at various potentials. Such chemical studies *in situ* during the course of electrochemical reactions on the surface can help elucidate the role of impurities. Because of the variety of oxygen species possible, they may be particularly valuable for studying oxygen reduction.

In situ studies under electrochemical conditions are particularly important for oxide semiconductors or metallic compounds. These materials are apt to be relatively strong Lewis acids or bases and, as mentioned above, to interact strongly with H_2O. Furthermore, as often demonstrated (*e.g.*, the paper by Weber and Shanks on sodium tungsten bronzes in this Proceedings), the nature of the surface is influenced by the electrochemical reactions being catalyzed. Extrapolation from the bulk properties to the surface is seldom possible, and the surface must be studied under dynamic conditions to understand how it influences the electrochemical reactions.

Influence of the Support on the Catalytic Activity of the Electrocatalyst, and Vice Versa

The paper by Stonehart reviewed some of the evidence for the so-called "spill-over effect," in which the support appears to take a more active catalytic role with the catalyst present than it is capable of in the absence of the catalyst. Several mechanisms for this effect appear possible. Examples are Pt on graphite and the earlier work of Hobbs and Tseung on Pt on WO_3.

One possibility is that the support acts as a cocatalyst. In this mode, the support possesses some catalytic activity that operates in a way synergistic to that of the catalyst itself. By shifting concentrations of reactants or products critical to the main reactions, the support may be able to affect the overall reaction rates in a way not possible in the absence of the supported catalyst. A possible example of this mode is the enhancement of the oxygen reduction activity of graphite by the addition of phthalocyanines on the surface. One suggestion is that the role of the phthalocyanine may be to decompose H_2O_2 produced by the reduction of oxygen on the graphite surface, but note evidence to the contrary in the paper of Appleby and Savy. This catalytic activity for oxygen reduction is observed when the phthalocyanine is added to a graphite surface, but not when it is deposited on surfaces of NiO or Au. The presence of the phthalocyanine also enhances the life of the graphite, which again may be due to the removal of H_2O_2.

A second mechanism possible for this apparent synergistic effect between catalyst and support is the modification of the catalyst properties by the support. For instance, it is well known that the different crystallographic faces of a given substance possess different catalytic activities. Deposition of the catalyst on a given support may result in a preponderance of particularly favorable crystal faces exposed to the electrolyte and therefore catalytic activity enhanced over that of the same catalyst on other supports or unsupported. Similarly, favorable structural defects may be stabilized by deposition of the catalyst on a given substrate.

A third mechanism that might in some cases explain an apparent influence of the substrate on the catalyst is the storage or enhanced dissemination of reaction products. By reducing the back reactions, the rate of the overall catalyzed reaction can be increased.

Finally, there may be some similarity between the interaction of, *e.g.*, Pt and graphite and that of Pb adsorbed on Pt. The paper by Adžić and colleagues shows that in the latter case, the adsorption of H on the Pt is inhibited, and reactions such as the oxidation of formic acid, with which adsorbed H interferes, are enhanced.

Photoelectrolysis

Since the work of Fujishima and Honda (Bull. Chem. Soc., Japan, 44, 1148(1971); Nature, 238, 37 (1972)) demonstrating direct decomposition of water in a photocell, there has been interest in the possibility of energy conversion using the electrochemical activity induced by the absorption of light at the electrocatalytic surface. Scientifically, there is interest because the phenomena appear to be amenable to treatment by rather well-established solid state concepts and it appears to be a reasonable testing ground for the applicability of such theory to electrochemical reactions. As a practical source of hydrogen or a practical means of converting solar to electrical or chemical energy, it is still uncertain. Too much energy is wasted with such a wide band gap semiconductor as

TiO_2 for practical application, but other, better materials may be found.

"Engineered" Surfaces

A concept that is being actively explored is to attach molecular compounds of known catalytic activity to substrates capable of acting not only as supports but also as electronic connectors with external circuitry. Not only must the substrate be a good conductor, but the fixing of specific functional groups must allow rapid electron transfer to the substrate. Graphite has been a favorite substrate to which to fix various polycyclic compounds with controlled functional groups, particularly in a search for oxygen reduction catalysts. One apparent problem is to maintain stability in the presence of the reactive species formed during the electrochemical reactions. A three-dimensional structure with self-renewing surface might work.

Catalysts for the direct oxidation of hydrocarbons and for the reduction of oxygen to water rather than hydrogen peroxide might be sought in this way. The suggestion was made that the splitting of the oxygen-oxygen bond needed for reduction to water might go well with coordination compounds involving low-valence states of second and third row transition elements, *e.g.*, Ir^+. In such studies, the mode of adsorption should be determined, whether it involves isolated molecules, clusters, or monolayers of adsorbate. By observing the change in activity of the adsorbate in going from the solution to the adsorbed state, one might obtain some information on the mutual interaction between the adsorbate and substrate.

Interfaces Involving Solid Electrolytes

In a very general way, electron exchange of reactants/products with the electrodes and ion exchange with the electrolyte appear to be very rapid, and early fears of large activation barriers, particularly with respect to the ion exchange with the electrolyte, appear to be unfounded. Indeed, examples of slow processes of this kind are hard to find. The electroreduction of CO_2 with Pt on a stabilized zirconia electrolyte is one possibility. The paper by Farrington in this Proceedings suggests that the transfer of Na^+ between β-Al_2O_3 and propylene carbonate when H_2O (or other protonated species) is present may be another.

Most theories of the development of electrode polarization involve the concept of the blocking electrode. Like the perfect insulator, the completely blocking electrode is an idealization, not really reproduced by any real electrode. A very useful form taken under simplified conditions by the theories of electrode polarization is the equivalent circuit, and it must be remembered that these are idealizations so that complete correspondence with experimental data must not be expected.

As work on solid electrolytes and their interfaces with various electrodes has proceeded, it has been found that the concepts and instrumental methods of aqueous electrochemistry have been very useful.

NBS-114A (REV. 7-73)

U.S. DEPT. OF COMM.
BIBLIOGRAPHIC DATA SHEET

1. PUBLICATION OR REPORT NO. NBS SP-455

2. Gov't Accession No.

3. Recipient's Accession No.

4. TITLE AND SUBTITLE

PROCEEDINGS OF WORKSHOP ON ELECTROCATALYSIS ON NON-METALLIC SURFACES

5. Publication Date November 1976

6. Performing Organization Code

7. AUTHOR(S) A. D. Franklin , Editor

8. Performing Organ. Report No.

9. PERFORMING ORGANIZATION NAME AND ADDRESS

NATIONAL BUREAU OF STANDARDS
DEPARTMENT OF COMMERCE
WASHINGTON, D.C. 20234

10. Project/Task/Work Unit No.

11. Contract/Grant No.

12. Sponsoring Organization Name and Complete Address *(Street, City, State, ZIP)*

Same as 9.

13. Type of Report & Period Covered Final

14. Sponsoring Agency Code

15. SUPPLEMENTARY NOTES

Library of Congress Catalog Card Number: 76-600062

16. ABSTRACT *(A 200-word or less factual summary of most significant information. If document includes a significant bibliography or literature survey, mention it here.)*

This book presents the proceedings of a Workshop on Electrocatalysis on Non-metallic Surfaces, held at the National Bureau of Standards, Gaithersburg, Maryland, on December 9-12, 1975. The Workshop was sponsored by the Institute of Materials Research, NBS, the Division of Materials Research of the National Science Foundation, and the Division of Conservation Research and Technology of the Energy Research and Development Administration. The purpose of the Workshop was to review the most recent experimental and theoretical investigationson electrocatalysis on non-metals and related topics, and to bring together electrochemists, surface scientists, and solid state physicists and chemists involved in research related to this topic. A total of 31 invited and contributed papers are here presented, together with a summary report of the final panel discussion. These proceedings are arranged to reflect, with some small exceptions, the program of the Workshop. The main groupings of papers are: I. Theory of Electrocatalysis and Related Topics; II. Characterization; III. Electrochemical Processes on Non-metallic Surfaces; and IV. Electrochemistry at Solid Electrolyte Interfaces. In addition, a final panel discussion (V) considered major problems, advances, and opportunities revealed by the Workshop.

17. KEY WORDS *(six to twelve entries; alphabetical order; capitalize only the first letter of the first key word unless a proper name; separated by semicolons)*

Catalysis; characterization; chemisorption; electrocatalysis; electrochemistry; electrode processes; non-metals; photoelectrolysis; solid electrolytes; surfaces

18. AVAILABILITY ☒ Unlimited

☐ For Official Distribution. Do Not Release to NTIS

☒ Order From Sup. of Doc., U.S. Government Printing Office Washington, D.C. 20402, SD Cat. No. C13. 10:455

☐ Order From National Technical Information Service (NTIS) Springfield, Virginia 22151

19. SECURITY CLASS (THIS REPORT) UNCLASSIFIED

20. SECURITY CLASS (THIS PAGE) UNCLASSIFIED

21. NO. OF PAGES 372

22. Price

☆ U.S. GOVERNMENT PRINTING OFFICE : 1976 O—223-773

NBS TECHNICAL PUBLICATIONS

PERIODICALS

JOURNAL OF RESEARCH reports National Bureau of Standards research and development in physics, mathematics, and chemistry. It is published in two sections, available separately:

- **Physics and Chemistry (Section A)**

Papers of interest primarily to scientists working in these fields. This section covers a broad range of physical and chemical research, with major emphasis on standards of physical measurement, fundamental constants, and properties of matter. Issued six times a year. Annual subscription: Domestic, $17.00; Foreign, $21.25.

- **Mathematical Sciences (Section B)**

Studies and compilations designed mainly for the mathematician and theoretical physicist. Topics in mathematical statistics, theory of experiment design, numerical analysis, theoretical physics and chemistry, logical design and programming of computers and computer systems. Short numerical tables. Issued quarterly. Annual subscription: Domestic, $9.00; Foreign, $11.25.

DIMENSIONS/NBS (formerly Technical News Bulletin)—This monthly magazine is published to inform scientists, engineers, businessmen, industry, teachers, students, and consumers of the latest advances in science and technology, with primary emphasis on the work at NBS. The magazine highlights and reviews such issues as energy research, fire protection, building technology, metric conversion, pollution abatement, health and safety, and consumer product performance. In addition, it reports the results of Bureau programs in measurement standards and techniques, properties of matter and materials, engineering standards and services, instrumentation, and automatic data processing.

Annual subscription: Domestic, $9.45; Foreign, $11.85.

NONPERIODICALS

Monographs—Major contributions to the technical literature on various subjects related to the Bureau's scientific and technical activities.

Handbooks—Recommended codes of engineering and industrial practice (including safety codes) developed in cooperation with interested industries, professional organizations, and regulatory bodies.

Special Publications—Include proceedings of conferences sponsored by NBS, NBS annual reports, and other special publications appropriate to this grouping such as wall charts, pocket cards, and bibliographies.

Applied Mathematics Series—Mathematical tables, manuals, and studies of special interest to physicists, engineers, chemists, biologists, mathematicians, computer programmers, and others engaged in scientific and technical work.

National Standard Reference Data Series—Provides quantitative data on the physical and chemical properties of materials, compiled from the world's literature and critically evaluated. Developed under a world-wide program coordinated by NBS. Program under authority of National Standard Data Act (Public Law 90-396).

NOTE: At present the principal publication outlet for these data is the Journal of Physical and Chemical Reference Data (JPCRD) published quarterly for NBS by the American Chemical Society (ACS) and the American Institute of Physics (AIP). Subscriptions, reprints, and supplements available from ACS, 1155 Sixteenth St. N.W., Wash. D. C. 20056.

Building Science Series—Disseminates technical information developed at the Bureau on building materials, components, systems, and whole structures. The series presents research results, test methods, and performance criteria related to the structural and environmental functions and the durability and safety characteristics of building elements and systems.

Technical Notes—Studies or reports which are complete in themselves but restrictive in their treatment of a subject. Analogous to monographs but not so comprehensive in scope or definitive in treatment of the subject area. Often serve as a vehicle for final reports of work performed at NBS under the sponsorship of other government agencies.

Voluntary Product Standards—Developed under procedures published by the Department of Commerce in Part 10, Title 15, of the Code of Federal Regulations. The purpose of the standards is to establish nationally recognized requirements for products, and to provide all concerned interests with a basis for common understanding of the characteristics of the products. NBS administers this program as a supplement to the activities of the private sector standardizing organizations.

Consumer Information Series—Practical information, based on NBS research and experience, covering areas of interest to the consumer. Easily understandable language and illustrations provide useful background knowledge for shopping in today's technological marketplace.

Order above NBS publications from: Superintendent of Documents, Government Printing Office, Washington, D.C. 20402.

Order following NBS publications—NBSIR's and FIPS from the National Technical Information Services, Springfield, Va. 22161.

Federal Information Processing Standards Publications (FIPS PUBS)—Publications in this series collectively constitute the Federal Information Processing Standards Register. Register serves as the official source of information in the Federal Government regarding standards issued by NBS pursuant to the Federal Property and Administrative Services Act of 1949 as amended, Public Law 89-306 (79 Stat. 1127), and as implemented by Executive Order 11717 (38 FR 12315, dated May 11, 1973) and Part 6 of Title 15 CFR (Code of Federal Regulations).

NBS Interagency Reports (NBSIR)—A special series of interim or final reports on work performed by NBS for outside sponsors (both government and non-government). In general, initial distribution is handled by the sponsor; public distribution is by the National Technical Information Services (Springfield, Va. 22161) in paper copy or microfiche form.

BIBLIOGRAPHIC SUBSCRIPTION SERVICES

The following current-awareness and literature-survey bibliographies are issued periodically by the Bureau:

Cryogenic Data Center Current Awareness Service. A literature survey issued biweekly. Annual subscription: Domestic, $20.00; Foreign, $25.00.

Liquified Natural Gas. A literature survey issued quarterly. Annual subscription: $20.00.

Superconducting Devices and Materials. A literature survey issued quarterly. Annual subscription: $20.00.

Send subscription orders and remittances for the preceding bibliographic services to National Bureau of Standards, Cryogenic Data Center (275.02) Boulder, Colorado 80302.

U.S. DEPARTMENT OF COMMERCE
National Bureau of Standards
Washington, D.C. 20234

OFFICIAL BUSINESS

Penalty for Private Use, $300

POSTAGE AND FEES PAID
U.S. DEPARTMENT OF COMMERCE
COM-215

U.S.MA

SPECIAL FOURTH-CLASS RATE
BOOK

AMERICAN REVOLUTION BICENTENNIAL
1776-1976

75 YEARS
NBS
1901-1976